The Role of Particle Cavitation in the Toughening of Polymers

by

Ulf Dieter Baumann

Maîtrise de Sciences de Gestion,
Université PARIS-NORD (1991)

Submitted to the Department of Mechanical Engineering
in partial fulfillment of the requirements for the degree of

MASTER OF SCIENCE IN MECHANICAL ENGINEERING

at the

MASSACHUSETTS INSTITUTE OF TECHNOLOGY

June 1998

Author .....
Department of Mechanical Engineering
May 25, 1998

Certified by .....
Mary C. Boyce
Associate Professor
Thesis Supervisor

Certified by .....
David M. Parks
Professor
Thesis Supervisor

Accepted by .....
Ain A. Sonin
Chairman, Department Committee on Graduate Students

The Role of Particle Cavitation in the Toughening of Polymers

by

Ulf Dieter Baumann

Submitted to the Department of Mechanical Engineering
on May 25, 1998, in partial fulfillment of the
requirements for the degree of
MASTER OF SCIENCE IN MECHANICAL ENGINEERING

Abstract

The deformation mechanisms in particle-modified polymer systems under notch conditions were studied using the finite element method. A unit cell approach was used to develop and implement a micromechanical model for polymer systems with compliant cavitating particles. The model contains matrix properties that are either anisotropic or isotropic. The anisotropic matrix was modeled after a semi-crystalline polymer with a high degree of preferential crystal orientation in the ligaments between neighboring particles, whereas the isotropic matrix was modeled after a matrix polymer whose mechanical response in the vicinity of a particle is unchanged from that of the bulk. The particle had the properties of a fluid-filled cavity that transitions into a hollow cavity upon particle cavitation. The unit cell model was deformed under varying degrees of triaxial stress, ranging from simple tension to a state of stress corresponding to that found at a notch tip. The studied parameters include the particle pressure, the macroscopic stress-strain response of the unit cell and the evolution of matrix plasticity as functions of macroscopic axial strain.

The results of the study indicate that two general regimes can be identified in the deformation of particle-modified polymer systems with respect to particle cavitation. Prior to cavitation, the simulations are characterized by high macroscopic stresses and relatively low levels of matrix plasticity at any given strain. Subsequently to cavitation (including pre-existing cavities), the simulations exhibit relatively low stresses at given strains and undergo substantially more plastic deformation in the matrix. The pressure at which the particle cavitates was found to have negligible influence on the matrix plasticity or the macroscopic stress-strain response of the unit cell, as long as the particle cavitation occurred.

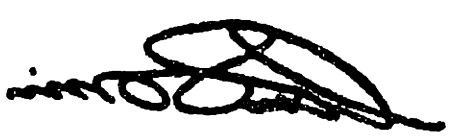

The anisotropic matrices were found to exhibit a high degree of localization of their matrix plasticity in clearly identifiable shear bands that were mostly situated along the diagonal of the unit cell and in tangential orientation. In the isotropic matrices, the observed localization of matrix plasticity was limited to the region near the particle equator due to the plastic thinning of the inter-particle ligaments.

Thesis Supervisor: Mary C. Boyce
Title: Associate Professor

Thesis Supervisor: David M. Parks
Title: Professor

Contents

1 Introduction **25**

2 Background **27**

2.1 Approaches to Toughening 28

2.2 The Competition between Brittleness and Ductility 29

2.3 Toughening Mechanisms 30

2.3.1 Argon et al.: Rubber-Toughened Nylon 33

2.3.2 Borggreve, Dijkstra, Gaymans et al. 38

2.3.3 Bucknall, Lazzeri, Zhang et al. 40

2.3.4 Kinloch, Huang, Guild et al. 41

2.4 Discussion 42

3 Cavitation Criteria for Rubber Particles **44**

3.1 Introduction 44

3.2 Literature Review on Particle Cavitation Criteria 46

3.3 Conclusion 63

4 Micromechanical Model **65**

4.1 Introduction 66

4.2 Geometry of Unit Cell and Particle 68

4.3 Geometric Boundary Conditions 70

4.4 Material Behavior 71

4.4.1 The Isotropic Matrix 72

4.4.2 The Anisotropic Matrix 72
4.4.3 The Rubber Particle 76
4.5 Loading Conditions 80
4.5.1 Thermal Contraction 80
4.5.2 Macroscopic Loading Conditions 86
4.6 Data Reduction 92
4.7 Software and Hardware Used 93
4.8 Procedure 93

5 Results **95**

5.1 Introduction 95
5.2 Uniaxial Tension of Bulk Nylon with a Pre-Existing Cavity 96
5.2.1 Introduction 96
5.2.2 Evolution of the Finite Element Mesh 97
5.2.3 Evolution of the Stress State 97
5.2.4 Macroscopic Strain History 101
5.2.5 Evolution of the Equivalent Plastic Strain 109
5.2.6 Macroscopic Stress-Strain Response 109
5.3 Example of a More Involved Simulation: "25ani-60-45-133" 114
5.3.1 Introduction 114
5.3.2 Evolution of the Finite Element Mesh 116
5.3.3 Evolution of the Stress State 116
5.3.4 Macroscopic Strain History 132
5.3.5 Plastic Deformation of Matrix 133
5.3.6 Macroscopic Stress-Stain Response 144
5.3.7 Volumetric Strain History of the Unit Cell 148
5.3.8 Evolution of the Pressure in the Particle 149
5.3.9 Volumetric Strain in the Particle and Cavity 150
5.4 Effect of Varying the Triaxial Stress State Σ 152
5.4.1 Introduction 152

5.4.2 Effect of Varying Σ on Particle Pressure and Particle Cavitation 152
5.4.3 Effect of Varying Σ on the Macroscopic Stress-Strain Response of Unit Cells with Non-Cavitating Particles 156
5.4.4 Effect of Varying Σ on the Macroscopic Stress-Strain Response of Unit Cells with Pre-Existing Cavities 161
5.4.5 Effect of Varying Σ on the Matrix Plasticity of Unit Cells with Non-Cavitating Particles 166
5.4.6 Effect of Varying Σ on the Matrix Plasticity of Unit Cells with Pre-Existing Cavities 191
5.4.7 Effect of Varying Σ on the Yield Point 218
5.5 Effect of Varying the Cavitation Strength of the Particle P_{cr} 227
5.5.1 Introduction 227
5.5.2 Effect of Varying P_{cr} on the Macroscopic Stress-Strain Response of the Unit Cell 228
5.5.3 Effect of Varying P_{cr} on the Matrix Plasticity 233
5.5.4 Effect of Varying P_{cr} on the Yield Point of the Unit Cell . . . 261
5.5.5 Summary 262
5.6 Effect of Matrix Properties: Anisotropic vs. Isotropic 264
5.6.1 Effect of Changing the Matrix Properties on the Yield Point of the Unit Cell 264
5.6.2 Effect of Changing the Matrix Properties on the Macroscopic Stress-Strain Response of Unit Cell with a Pre-Existing Cavity 266
5.6.3 Effect of Changing the Matrix Properties on the Macroscopic Stress-Strain Response of Unit Cell with a Non-Cavitating Particle 268
5.6.4 Effect of Changing the Matrix Properties on the Evolution of Matrix Plasticity in Unit Cells with a Pre-Existing Cavity . . 273
5.6.5 Effect of Changing the Matrix Properties on the Evolution of Matrix Plasticity in Unit Cells with a Non-Cavitating Particle 274

5.6.6 Effect of Changing the Matrix Properties on the Macroscopic Strain Response of Unit Cell and Particle 275

6 Discussion **282**

A Codes and Abreviations **293**

B Formulation of the Rubber Particle User Element **295**

B.1 The Particle Element 295

B.2 Constitutive Model 295

B.3 Subroutine Calls 296

B.4 Algorithm 297

B.4.1 Computing the Volume 297

B.4.2 Computing Volumetric Strain and Pressure 298

B.4.3 Computing Nodal Forces 298

B.4.4 Computing The Jacobian 300

B.5 Cavitation 300

B.5.1 Cavitation Criterion 301

B.5.2 Simple Cavitation 301

B.5.3 Force Relaxation 301

B.6 Thermal Strain 302

B.7 Example of a Typical Input Deck 304

B.8 Subroutine Code 305

C Formulation of the Triaxial Loading Condition **343**

C.1 MPC Implementation 343

C.2 UEL and DLOAD Implementation 348

C.2.1 Discussion of the Implementation 349

D Matlab Scripts **354**

List of Figures

2-1 Schematic representation of the lamella orientation of textured Nylon-6, after [51]. 35

2-2 Schematic representation of the organization of Nylon crystals on a surface. After [49]. 36

2-3 Engineering stress vs. engineering strain of free-standing thin films of polyamide 6 crystallized between polystyrene layers. After [49]. . . . 37

3-1 Strain energy, surface energy and total energy associated with internal rubber cavitation as function of particle diameter. After [32]. 50

3-2 Relationship between the minimum particle diameter required for cavitation and the relaitve volume strain (Δ). The dotted lines are the critical conditions corresponding to a particle size of $200nm$ and a relative volume strain of 1%. After [32] 51

3-3 Calculated potential energy of a cavitated rubber particle as a function of the reduced radius of the void (r/R) for particles of radius R ranging from 0.1 to $100\mu m$. Values calculated at a fixed volume strain of 0.0004. After [24]. 53

3-4 Examples of information obtained form stress-whitening experiments on PVC/MBS blends: average stress-whitening intensity, the percentage whitening and the tensile stress as a function of the tensile strain: (a) large particles, (b) small particles. The stress-strain response is the same for both particle sizes. From [31]. 55

3-5 Comparison of the percentage whitening as a function of tensile strain for four different PVC/MBS blends. Rubber cavitation strains are indicated by the solid lines. From [31]. 57

3-6 Relationship between the minimum particle diameter required for cavitation and the longitudinal strain ϵ or the volumetric strain Δ. The experimental data is obtained from analyses as shown in the plots of percentage whitening vs. strain. The continuous line is the theoretical result from equation 3.10. The material parameters used are described on page 52. From [31]. 58

4-1 Development of the cylindrical unit cell from a regular array of particles inside a representative volume element whose shape is a cylinder with hexagonal base. 67

4-2 Schematic of the quarter-segment of the unit cell that was used in the finite element simulations. Shown are the initial radius R^0 of the unit cell, and the initial radius r^0 of the particle. 68

4-3 The undeformed mesh. $\Phi = 25\%$. 69

4-4 Example of a deformed mesh. 69

4-5 Example of an undeformed (black) and a deformed (grey) meshes. $\Phi =$ 25%. Note how the mesh boundaries match at the vertical mid-plane of symmetry (bottom) and the axis of symmetry (left). 70

4-6 Boundary conditions of the 2-D quarter segment of the axiasymmetric unit cell. 71

4-7 Stress-strain plots for various ploymers, among which Nylon-6 (PA6) and the linear approximation used in the simulations. G'Sell[40]. . . . 73

4-8 Schematic showing where in the matrix mesh the element 820 is located. 75

4-9 Element 820 in its undeformed configuration. Global and local directions. 75

4-10 Element 820 in its deformed configuration. Global and local directions. 76

4-11 Schematic of the simple cavitation implementation. The pressure P is reduced to zero when the volumetric strain Ψ reaches a critical value Ψ_{cr}. 78
4-12 Schematic of the force-relaxation algorithm for particle cavitation. Once the volumetric strain Ψ has reached a critical value Ψ_{cr}, the pressure is reduced to zero over a non-zero interval of ε_{zz}. 79
4-13 Volume as a function of temperature in Nylon. After[60, 55] 82
4-14 Volume as a function of temperature in rubber. After[50] 82
4-15 Schematic of the unit cell subjected to simple tension. 87
4-16 Blunted crack tip and surrounding flow field, after[48]. 88
4-17 Flow field for a blunted notch, after[3]. 88
4-18 Triaxiality ratio in core region as function of groove angle, after [48]. . 90
4-19 Triaxiality ratio in root region as function of x'/a, after [48]. 90
4-20 Schematic of the unit cell under triaxial loading: subjected to axial tension by means of displacement u_z of the top boundary, and to a laterally applied distributed load σ_{rr}. 91
4-21 Schematic representation of the numerical study. 94

5-1a 25iso-00-45-033: Undeformed mesh at start of simulation. $\varepsilon_{zz} = 0$. . . 98
5-1b 25iso-00-45-033: Deformed and undeformed meshes at $\varepsilon_{zz} = 1.5\%$. . . 98
5-1c 25iso-00-45-033: Deformed and undeformed meshes at $\varepsilon_{zz} = 2.5\%$. . . 99
5-1d 25iso-00-45-033: Deformed and undeformed meshes at $\varepsilon_{zz} = 3.5\%$. . . 99
5-1e 25iso-00-45-033: Deformed and undeformed meshes at $\varepsilon_{zz} = 4.5\%$. . . 100
5-1f 25iso-00-45-033: Deformed and undeformed meshes at $\varepsilon_{zz} = 5.5\%$ . . 100
5-2a 25iso-00-45-033: Stress components at $\varepsilon_{zz} = 1.5$. 102
5-2b 25iso-00-45-033: Stress components at $\varepsilon_{zz} = 2.5\%$. 103
5-2c 25iso-00-45-033: Stress components at $\varepsilon_{zz} = 3.5\%$. 104
5-2d 25iso-00-45-033: Stress components at $\varepsilon_{zz} = 4.5\%$. 105
5-2e 25iso-00-45-033: Stress components at $\varepsilon_{zz} = 5.5\%$. 106
5-2f 25iso-00-45-033: Stress components at $\varepsilon_{zz} = 6.5\%$. 107

5-3 25iso-00-45-033: Strain space evolution: ε_{zz} as function of ε_{rr}. 108

5-4 25iso-00-45-033: (a) macroscopic axial true stress σ_{zz} and (b) cell volumetric strain Ψ_c as functions of macroscopic axial true strain ε_{zz}. . . 108

5-5a 25iso-00-45-033: Contour Plots of the equivalent plastic strain ε^p_{equiv} at $\varepsilon_{zz} = 1.5\%$. 110

5-5b 25iso-00-45-033: Contour Plots of the equivalent plastic strain ε^p_{equiv} at $\varepsilon_{zz} = 2.5\%$. 110

5-5c 25iso-00-45-033: Contour Plots of the equivalent plastic strain ε^p_{equiv} at $\varepsilon_{zz} = 3.5\%$. 111

5-5d 25iso-00-45-033: Contour Plots of the equivalent plastic strain ε^p_{equiv} at $\varepsilon_{zz} = 4.5\%$. 111

5-5e 25iso-00-45-033: Contour Plots of the equivalent plastic strain ε^p_{equiv} at $\varepsilon_{zz} = 5.5\%$. 112

5-5f 25iso-00-45-033: Contour Plots of the equivalent plastic strain ε^p_{equiv} at $\varepsilon_{zz} = 6.5\%$. 112

5-6a 25ani-60-45-133: Undeformed mesh at start of simulation. 117

5-6b 25ani-60-45-133: Deformed and undeformed meshes after completion of cooling. $\varepsilon_{zz} = 0$. 117

5-6c 25ani-60-45-133: Deformed and undeformed meshes at $\varepsilon_{zz} = 1.5\%$. . . 118

5-6d 25ani-60-45-133: Deformed and undeformed meshes at $\varepsilon_{zz} = 2.5\%$. . . 118

5-6e 25ani-60-45-133: Deformed and undeformed meshes at $\varepsilon_{zz} = 3.5\%$. . . 119

5-6f 25ani-60-45-133: Deformed and undeformed meshes at $\varepsilon_{zz} = 4.5\%$. . . 119

5-6g 25ani-60-45-133: Deformed and undeformed meshes at $\varepsilon_{zz} = 5.5\%$ . . 120

5-7a 25ani-60-45-133: Stress components after completion of cooling. $\varepsilon_{zz} = 0$. 122

5-7b 25ani-60-45-133: Stress components at $\varepsilon_{zz} = 1.5\%$. 123

5-7c 25ani-60-45-133: Stress components at $\varepsilon_{zz} = 2.5\%$. 124

5-7d 25ani-60-45-133: Stress components just before cavitation. $\varepsilon_{zz} = 2.81\%$. 125

5-7e 25ani-60-45-133: Stress components just after cavitation. $\varepsilon_{zz} = 2.82\%$. 126

5-7f 25ani-60-45-133: Stress components at $\varepsilon_{zz} = 3.5\%$. 127

5-7g 25ani-60-45-133: Stress components at $\varepsilon_{zz} = 4.5\%$. 128

5-7h 25ani-60-45-133: Stress components at $\varepsilon_{zz} = 5.5\%$. 129
5-8 25ani-60-45-133: Strain space evolution: ε_{zz} as function of ε_{rr}. 132
5-9a 25ani-60-45-133: Contour plots of ε^p_{equiv} at $varepsilon_{zz} = 1.5\%$. . . . 135
5-9b 25ani-60-45-133: Contour plots of ε^p_{equiv} at $varepsilon_{zz} = 2.5\%$. . . . 136
5-9c 25ani-60-45-133: PEEQ just before cavitation. $varepsilon_{zz} = 2.81\%$. 136
5-9d 25ani-60-45-133: PEEQ just after cavitation. $varepsilon_{zz} = 2.82\%$. . 137
5-9e 25ani-60-45-133: Contour plots of ε^p_{equiv} at $varepsilon_{zz} = 3.5\%$. . . . 138
5-9f 25ani-60-45-133: Contour plots of ε^p_{equiv} at $varepsilon_{zz} = 4.5\%$. . . . 138
5-9g 25ani-60-45-133: Contour plots of ε^p_{equiv} at $varepsilon_{zz} = 5.5\%$. . . . 139
5-10a25ani-60-45-133: Plastic strain components at $\varepsilon_{zz} = 1.5\%$. 140
5-10b25ani-60-45-133: Plastic strain components at $\varepsilon_{zz} = 2.5\%$. 141
5-10c25ani-60-45-133: Plastic strain components just before cavitation. $\varepsilon_{zz} =$ 2.81%. 142
5-10d25ani-60-45-133: Plastic strain components just after cavitation. $\varepsilon_{zz} =$ 2.82%. 143
5-10e25ani-60-45-133: Plastic strain components at $\varepsilon_{zz} = 3.5\%$. 145
5-10f 25ani-60-45-133: Plastic strain components at $\varepsilon_{zz} = 4.5\%$. 146
5-10g25ani-60-45-133: Plastic strain components at $\varepsilon_{zz} = 5.5\%$. 147
5-11 25ani-60-45-133: Macroscopic stress σ_{zz} and volumetric strain Ψ_m of the unit cell as functions of macroscopic axial true strain ε_{zz}. 148
5-12 25ani-60-45-133: Macroscopic deviatoric true stress $\hat{\sigma}_{zz}$ as function of macroscopic true axial strain ε_{zz}. 149
5-13 25ani-60-45-133: Particle pressure P and volumetric strain $\Psi_{p/c}$ of the particle as functions of macroscopic axial true strain ε_{zz}. 150
5-14 (a) particle pressure P and (b) particle volumetric strain Ψ as functions of macroscopic axial true strain ε_{zz}. Anisotropic matrix. 153
5-15 (a) particle pressure P and (b) particle volumetric strain Ψ as functions of macroscopic axial true strain ε_{zz}. Isotropic matrix with non-cavitating particle. 154

5-16 (a) macroscopic true axial stress σ_{zz} and (b) volumetric strain Ψ_m as functions of macroscopic axial true strain ε_{zz}. Anisotropic matrix with non-cavitating particle. 159

5-17 Macroscopic true deviatoric axial stress $\hat{\sigma}_{zz}$ as function of macroscopic axial true strain ε_{zz}. Anisotropic matrix with non-cavitating particle. 160

5-18 (a) macroscopic true axial stress σ_{zz} and (b) cell volumetric strain Ψ as functions of macroscopic axial true strain ε_{zz}. Isotropic matrix with non-cavitating particle. 161

5-19 Macroscopic true deviatoric stress $\hat{\sigma}_{zz}$ as function of macroscopic axial true strain ε_{zz}. Isotropic matrix with non-cavitating particle. 162

5-20 (a) macroscopic true axial stress σ_{zz} and (b) cell volumetric strain Ψ_m as functions of macroscopic axial true strain ε_{zz}. Anisotropic matrix with pre-existing cavity. 164

5-21 Macroscopic deviatoric true axial stress $\hat{\sigma}_{zz}$ as function of macroscopic axial true strain ε_{zz}. Anisotropic matrix with pre-existing cavity. . . . 165

5-22 (a) macroscopic true axial stress σ_{zz} and (b) cell volumetric strain Ψ as functions of macroscopic axial true strain ε_{zz}. Anisotropic matrix with pre-existing cavity. 166

5-23 Macroscopic true deviatoric stress $\hat{\sigma}_{zz}$ as function of macroscopic axial true strain ε_{zz}. Isotropic matrix with pre-existing cavity. 167

5-24a25ani-nv-45-033: Equivalent plastic strain ε^p_{equiv} at $\varepsilon_{zz} = 1.5\%$. Anisotropic matrix with non-cavitating particle. 169

5-24b25ani-nv-45-033: Equivalent plastic strain ε^p_{equiv} at $\varepsilon_{zz} = 2.5\%$. Anisotropic matrix with non-cavitating particle. 169

5-24c25ani-nv-45-033: Equivalent plastic strain ε^p_{equiv} at $\varepsilon_{zz} = 3.5\%$. Anisotropic matrix with non-cavitating particle. 170

5-24d25ani-nv-45-033: Equivalent plastic strain ε^p_{equiv} at $\varepsilon_{zz} = 4.5\%$. Anisotropic matrix with non-cavitating particle. 170

5-24e25ani-nv-45-033: Equivalent plastic strain ε^p_{equiv} at $\varepsilon_{zz} = 5.5\%$. Anisotropic matrix with non-cavitating particle. 171

5-24f25ani-nv-45-033: Equivalent plastic strain ε^p_{equiv} at $\varepsilon_{zz} = 6.5\%$. Anisotropic matrix with non-cavitating particle. 171
5-25a25ani-nv-45-066: Equivalent plastic strain ε^p_{equiv} at $\varepsilon_{zz} = 1.5\%$. Anisotropic matrix with non-cavitating particle. 172
5-25b25ani-nv-45-066: Equivalent plastic strain ε^p_{equiv} at $\varepsilon_{zz} = 2.5\%$. Anisotropic matrix with non-cavitating particle. 172
5-25c25ani-nv-45-066: Equivalent plastic strain ε^p_{equiv} at $\varepsilon_{zz} = 3.5\%$. Anisotropic matrix with non-cavitating particle. 173
5-25d25ani-nv-45-066: Equivalent plastic strain ε^p_{equiv} at $\varepsilon_{zz} = 4.5\%$. Anisotropic matrix with non-cavitating particle. 173
5-25e25ani-nv-45-066: Equivalent plastic strain ε^p_{equiv} at $\varepsilon_{zz} = 5.5\%$. Anisotropic matrix with non-cavitating particle. 174
5-25f25ani-nv-45-066: Equivalent plastic strain ε^p_{equiv} at $\varepsilon_{zz} = 6.5\%$. Anisotropic matrix with non-cavitating particle. 174
5-26a25ani-nv-45-133: Equivalent plastic strain ε^p_{equiv} at $\varepsilon_{zz} = 1.5\%$. Anisotropic matrix with non-cavitating particle. 175
5-26b25ani-nv-45-133: Equivalent plastic strain ε^p_{equiv} at $\varepsilon_{zz} = 2.5\%$. Anisotropic matrix with non-cavitating particle. 175
5-26c25ani-nv-45-133: Equivalent plastic strain ε^p_{equiv} at $\varepsilon_{zz} = 3.5\%$. Anisotropic matrix with non-cavitating particle. 176
5-26d25ani-nv-45-133: Equivalent plastic strain ε^p_{equiv} at $\varepsilon_{zz} = 4.5\%$. Anisotropic matrix with non-cavitating particle. 176
5-26e25ani-nv-45-133: Equivalent plastic strain ε^p_{equiv} at $\varepsilon_{zz} = 5.5\%$. Anisotropic matrix with non-cavitating particle. 177
5-26f25ani-nv-45-133: Equivalent plastic strain ε^p_{equiv} at $\varepsilon_{zz} = 6.5\%$. Anisotropic matrix with non-cavitating particle. 177
5-27a25ani-nv-45-233: Equivalent plastic strain ε^p_{equiv} at $\varepsilon_{zz} = 1.5\%$. Anisotropic matrix with non-cavitating particle. 178
5-27b25ani-nv-45-233: Equivalent plastic strain ε^p_{equiv} at $\varepsilon_{zz} = 2.5\%$. Anisotropic matrix with non-cavitating particle. 178

5-27c25ani-nv-45-233: Equivalent plastic strain ε^p_{equiv} at $\varepsilon_{zz} = 3.5\%$. Anisotropic matrix with non-cavitating particle. 179
5-27d25ani-nv-45-233: Equivalent plastic strain ε^p_{equiv} at $\varepsilon_{zz} = 4.5\%$. Anisotropic matrix with non-cavitating particle. 179
5-27e25ani-nv-45-233: Equivalent plastic strain ε^p_{equiv} at $\varepsilon_{zz} = 5.5\%$. Anisotropic matrix with non-cavitating particle. 180
5-27f25ani-nv-45-233: Equivalent plastic strain ε^p_{equiv} at $\varepsilon_{zz} = 6.5\%$. Anisotropic matrix with non-cavitating particle. 180
5-28a25iso-nv-45-033: Equivalent plastic strain ε^p_{equiv} at $\varepsilon_{zz} = 2.5\%$. Isotropic matrix with non-cavitating particle. 182
5-28b25iso-nv-45-033: Equivalent plastic strain ε^p_{equiv} at $\varepsilon_{zz} = 3.5\%$. Isotropic matrix with non-cavitating particle. 183
5-28c25iso-nv-45-033: Equivalent plastic strain ε^p_{equiv} at $\varepsilon_{zz} = 4.5\%$. Isotropic matrix with non-cavitating particle. 183
5-28d25iso-nv-45-033: Equivalent plastic strain ε^p_{equiv} at $\varepsilon_{zz} = 5.5\%$. Isotropic matrix with non-cavitating particle. 184
5-28e25iso-nv-45-033: Equivalent plastic strain ε^p_{equiv} at $\varepsilon_{zz} = 6.5\%$. Isotropic matrix with non-cavitating particle. 184
5-29a25iso-nv-45-066: Equivalent plastic strain ε^p_{equiv} at $\varepsilon_{zz} = 1.5\%$. Isotropic matrix with non-cavitating particle. 185
5-29b25iso-nv-45-066: Equivalent plastic strain ε^p_{equiv} at $\varepsilon_{zz} = 2.5\%$. Isotropic matrix with non-cavitating particle. 185
5-29c25iso-nv-45-066: Equivalent plastic strain ε^p_{equiv} at $\varepsilon_{zz} = 3.5\%$. Isotropic matrix with non-cavitating particle. 186
5-29d25iso-nv-45-066: Equivalent plastic strain ε^p_{equiv} at $\varepsilon_{zz} = 4.5\%$. Isotropic matrix with non-cavitating particle. 186
5-29e25iso-nv-45-066: Equivalent plastic strain ε^p_{equiv} at $\varepsilon_{zz} = 5.5\%$. Isotropic matrix with non-cavitating particle. 187
5-29f25iso-nv-45-066: Equivalent plastic strain ε^p_{equiv} at $\varepsilon_{zz} = 6.5\%$. Isotropic matrix with non-cavitating particle. 187

5-30a25iso-nv-45-133: Equivalent plastic strain ε^p_{equiv} at $\varepsilon_{zz} = 1.5\%$. Isotropic matrix with non-cavitating particle. 188
5-30b25iso-nv-45-133: Equivalent plastic strain ε^p_{equiv} at $\varepsilon_{zz} = 2.5\%$. Isotropic matrix with non-cavitating particle. 188
5-30c25iso-nv-45-133: Equivalent plastic strain ε^p_{equiv} at $\varepsilon_{zz} = 3.5\%$. Isotropic matrix with non-cavitating particle. 189
5-30d25iso-nv-45-133: Equivalent plastic strain ε^p_{equiv} at $\varepsilon_{zz} = 4.5\%$. Isotropic matrix with non-cavitating particle. 189
5-30e25iso-nv-45-133: Equivalent plastic strain ε^p_{equiv} at $\varepsilon_{zz} = 5.5\%$. Isotropic matrix with non-cavitating particle. 190
5-30f25iso-nv-45-133: Equivalent plastic strain ε^p_{equiv} at $\varepsilon_{zz} = 6.5\%$. Isotropic matrix with non-cavitating particle. 190
5-31a25iso-nv-45-233: Equivalent plastic strain ε^p_{equiv} at $\varepsilon_{zz} = 2.5\%$. Isotropic matrix with non-cavitating particle. 192
5-31b25iso-nv-45-233: Equivalent plastic strain ε^p_{equiv} at $\varepsilon_{zz} = 3.5\%$. Isotropic matrix with non-cavitating particle. 192
5-31c25iso-nv-45-233: Equivalent plastic strain ε^p_{equiv} at $\varepsilon_{zz} = 4.5\%$. Isotropic matrix with non-cavitating particle. 193
5-31d25iso-nv-45-233: Equivalent plastic strain ε^p_{equiv} at $\varepsilon_{zz} = 5.5\%$. Isotropic matrix with non-cavitating particle. 193
5-31e25iso-nv-45-233: Equivalent plastic strain ε^p_{equiv} at $\varepsilon_{zz} = 6.5\%$. Isotropic matrix with non-cavitating particle. 194
5-32a25ani-00-45-033: Contour plots of ε^p_{equiv} at $\varepsilon_{zz} = 1.5\%$. 196
5-32b25ani-00-45-033: Contour plots of ε^p_{equiv} at $\varepsilon_{zz} = 2.5\%$. 197
5-32c25ani-00-45-033: Contour plots of ε^p_{equiv} at $\varepsilon_{zz} = 3.5\%$. 197
5-32d25ani-00-45-033: Contour plots of ε^p_{equiv} at $\varepsilon_{zz} = 4.5\%$. 198
5-32e25ani-00-45-033: Contour plots of ε^p_{equiv} at $\varepsilon_{zz} = 5.5\%$. 198
5-32f25ani-00-45-033: Contour plots of ε^p_{equiv} at $\varepsilon_{zz} = 6.5\%$. 199
5-33a25ani-00-45-066: Contour plots of ε^p_{equiv} at $\varepsilon_{zz} = 1.5\%$. 200
5-33b25ani-00-45-066: Contour plots of ε^p_{equiv} at $\varepsilon_{zz} = 2.5\%$. 200

5-33c25ani-00-45-066: Contour plots of ε^p_{equiv} at $\varepsilon_{zz} = 3.5\%$. 201
5-33d25ani-00-45-066: Contour plots of ε^p_{equiv} at $\varepsilon_{zz} = 4.5\%$. 201
5-33e25ani-00-45-066: Contour plots of ε^p_{equiv} at $\varepsilon_{zz} = 5.5\%$. 202
5-33f25ani-00-45-066: Contour plots of ε^p_{equiv} at $\varepsilon_{zz} = 6.5\%$. 202
5-34a25ani-00-45-133: Contour plots of ε^p_{equiv} at $\varepsilon_{zz} = 1.5\%$. 203
5-34b25ani-00-45-133: Contour plots of ε^p_{equiv} at $\varepsilon_{zz} = 2.5\%$. 203
5-34c25ani-00-45-133: Contour plots of ε^p_{equiv} at $\varepsilon_{zz} = 3.5\%$. 204
5-34d25ani-00-45-133: Contour plots of ε^p_{equiv} at $\varepsilon_{zz} = 4.5\%$. 204
5-34e25ani-00-45-133: Contour plots of ε^p_{equiv} at $\varepsilon_{zz} = 5.5\%$. 205
5-34f25ani-00-45-133: Contour plots of ε^p_{equiv} at $\varepsilon_{zz} = 6.5\%$. 205
5-35a25ani-00-45-233: Contour plots of ε^p_{equiv} at $\varepsilon_{zz} = 1.5\%$. 206
5-35b25ani-00-45-233: Contour plots of ε^p_{equiv} at $\varepsilon_{zz} = 2.5\%$. 206
5-35c25ani-00-45-233: Contour plots of ε^p_{equiv} at $\varepsilon_{zz} = 3.5\%$. 207
5-35d25ani-00-45-233: Contour plots of ε^p_{equiv} at $\varepsilon_{zz} = 4.5\%$. 207
5-35e25ani-00-45-233: Contour plots of ε^p_{equiv} at $\varepsilon_{zz} = 5.5\%$. 208
5-35f25ani-00-45-233: Contour plots of ε^p_{equiv} at $\varepsilon_{zz} = 6.5\%$. 208
5-36a25ani-00-45-233: Contour plots of ε^p_{equiv} at $\varepsilon_{zz} = 1.5\%$. Cmax = 7.5%. 210
5-36b25ani-00-45-233: Contour plots of ε^p_{equiv} at $\varepsilon_{zz} = 2.5\%$. Cmax = 7.5%. 210
5-36c25ani-00-45-233: Contour plots of ε^p_{equiv} at $\varepsilon_{zz} = 3.5\%$. Cmax = 7.5%. 211
5-36d25ani-00-45-233: Contour plots of ε^p_{equiv} at $\varepsilon_{zz} = 4.5\%$. Cmax = 7.5%. 211
5-36e25ani-00-45-233: Contour plots of ε^p_{equiv} at $\varepsilon_{zz} = 5.5\%$. Cmax = 7.5%. 212
5-36f25ani-00-45-233: Contour plots of ε^p_{equiv} at $\varepsilon_{zz} = 6.5\%$. Cmax = 7.5%. 212
5-37a25iso-00-45-066: Contour plots of ε^p_{equiv} at $\varepsilon_{zz} = 1.5\%$. 213
5-37b25iso-00-45-066: Contour plots of ε^p_{equiv} at $\varepsilon_{zz} = 2.5\%$. 213
5-37c25iso-00-45-066: Contour plots of ε^p_{equiv} at $\varepsilon_{zz} = 3.5\%$. 214
5-37d25iso-00-45-066: Contour plots of ε^p_{equiv} at $\varepsilon_{zz} = 4.5\%$. 214
5-37e25iso-00-45-066: Contour plots of ε^p_{equiv} at $\varepsilon_{zz} = 5.5\%$. 215
5-37f25iso-00-45-066: Contour plots of ε^p_{equiv} at $\varepsilon_{zz} = 6.5\%$. 215
5-38a25iso-00-45-133: Contour plots of ε^p_{equiv} at $\varepsilon_{zz} = 1.5\%$. 216
5-38b25iso-00-45-133: Contour plots of ε^p_{equiv} at $\varepsilon_{zz} = 2.5\%$. 216

5-38c25iso-00-45-133: Contour plots of ε^p_{equiv} at $\varepsilon_{zz} = 3.5\%$. 217
5-38d25iso-00-45-133: Contour plots of ε^p_{equiv} at $\varepsilon_{zz} = 4.5\%$. 219
5-38e25iso-00-45-133: Contour plots of ε^p_{equiv} at $\varepsilon_{zz} = 5.5\%$. 219
5-38f25iso-00-45-133: Contour plots of ε^p_{equiv} at $\varepsilon_{zz} = 6.5\%$. 220
5-39a25iso-00-45-233: Contour plots of ε^p_{equiv} at $\varepsilon_{zz} = 1.5\%$. 220
5-39b25iso-00-45-233: Contour plots of ε^p_{equiv} at $\varepsilon_{zz} = 2.5\%$. 221
5-39c25iso-00-45-233: Contour plots of ε^p_{equiv} at $\varepsilon_{zz} = 3.5\%$. 221
5-39d25iso-00-45-233: Contour plots of ε^p_{equiv} at $\varepsilon_{zz} = 4.5\%$. 222
5-39e25iso-00-45-233: Contour plots of ε^p_{equiv} at $\varepsilon_{zz} = 5.5\%$. 222
5-39f25iso-00-45-233: Contour plots of ε^p_{equiv} at $\varepsilon_{zz} = 6.5\%$. 223
5-40 Macroscopic true axial strain at yield ε^y_{zz} as function of triaxiality Σ. Anisotropic matrix with pre-existing cavity ("Cavity") and non-cavitating particle ("Particle"). 224
5-41 Macroscopic true axial stress at yield σ^y_{zz} as function of triaxiality Σ. Anisotropic matrix with pre-existing cavity ("Cavity") and non-cavitating particle ("Particle"). 225
5-42 Macroscopic true axial stress at yield σ^y_{zz} as function of triaxiality Σ. Isotropic matrix with pre-existing cavity ("Cavity") and non-cavitating particle ("Particle"). 226
5-43 Macroscopic true axial strain at yield ε^y_{zz} as function of triaxiality Σ. Isotropic matrix with pre-existing cavity ("Cavity") and non-cavitating particle ("Particle"). 226
5-44 (a) macroscopic true axial stress σ_{zz} and (b) cell volumetric strain Ψ as functions of macroscopic axial true strain ε_{zz}. Anisotropic matrix. $\Sigma = 0.33$. 229
5-45 (a) macroscopic true axial stress σ_{zz} and (b) cell volumetric strain Ψ as functions of macroscopic axial true strain ε_{zz}. Anisotropic matrix. $\Sigma = 0.66$. 230

5-46 (a) macroscopic true axial stress σ_{zz} and (b) cell volumetric strain Ψ as functions of macroscopic axial true strain ε_{zz}. Anisotropic matrix. $\Sigma = 1.33$. 231
5-47 (a) macroscopic true axial stress σ_{zz} and (b) cell volumetric strain Ψ as functions of macroscopic axial true strain ε_{zz}. Anisotropic matrix. $\Sigma = 2.33$. 232
5-48 (a) macroscopic true axial stress σ_{zz} and cell volumetric strain Ψ as functions of macroscopic axial true strain ε_{zz}. Isosotropic matrix. $\Sigma =$ 0.33. 233
5-49 (a) macroscopic true axial stress σ_{zz} and cell volumetric strain Ψ as functions of macroscopic axial true strain ε_{zz}. Isosotropic matrix. $\Sigma =$ 0.66. 234
5-50 (a) macroscopic true axial stress σ_{zz} and cell volumetric strain Ψ as functions of macroscopic axial true strain ε_{zz}. Isosotropic matrix. $\Sigma =$ 1.33. 235
5-51 (a) macroscopic true axial stress σ_{zz} and cell volumetric strain Ψ as functions of macroscopic axial true strain ε_{zz}. Isosotropic matrix. $\Sigma =$ 2.33. 236
5-52a25ani-40-45-066: Contour plots of ε^p_{equiv} at $\varepsilon_{zz} = 1.5\%$. 237
5-52b25ani-40-45-066: Contour plots of ε^p_{equiv} at $\varepsilon_{zz} = 2.5\%$. 237
5-52c25ani-40-45-066: Contour plots of ε^p_{equiv} at $\varepsilon_{zz} = 3.5\%$. 238
5-52d25ani-40-45-066: Contour plots of ε^p_{equiv} at $\varepsilon_{zz} = 4.5\%$. 238
5-52e25ani-40-45-066: Contour plots of ε^p_{equiv} at $\varepsilon_{zz} = 5.5\%$. 239
5-52f25ani-40-45-066: Contour plots of ε^p_{equiv} at $\varepsilon_{zz} = 6.5\%$. 239
5-53a25ani-40-45-133: Contour plots of ε^p_{equiv} at $\varepsilon_{zz} = 1.5\%$. 241
5-53b25ani-40-45-133: Contour plots of ε^p_{equiv} at $\varepsilon_{zz} = 2.5\%$. 241
5-53c25ani-40-45-133: Contour plots of ε^p_{equiv} at $\varepsilon_{zz} = 3.5\%$. 242
5-53d25ani-40-45-133: Contour plots of ε^p_{equiv} at $\varepsilon_{zz} = 4.5\%$. 242
5-53e25ani-40-45-133: Contour plots of ε^p_{equiv} at $\varepsilon_{zz} = 5.5\%$. 243
5-53f25ani-40-45-133: Contour plots of ε^p_{equiv} at $\varepsilon_{zz} = 6.5\%$. 243

5-54a25ani-nv-45-233: Contour plots of ε^p_{equiv} at $\varepsilon_{zz} = 1.5\%$. $Cmax = 7.5\%$. 244
5-54b25ani-nv-45-233: Contour plots of ε^p_{equiv} at $\varepsilon_{zz} = 2.5\%$. $Cmax = 7.5\%$. 245
5-54c25ani-nv-45-233: Contour plots of ε^p_{equiv} at $\varepsilon_{zz} = 3.5\%$. $Cmax = 7.5\%$. 245
5-54d25ani-nv-45-233: Contour plots of ε^p_{equiv} at $\varepsilon_{zz} = 4.5\%$. $Cmax = 7.5\%$. 246
5-54e25ani-nv-45-233: Contour plots of ε^p_{equiv} at $\varepsilon_{zz} = 5.5\%$. $Cmax = 7.5\%$. 246
5-54f25ani-nv-45-233: Contour plots of ε^p_{equiv} at $\varepsilon_{zz} = 6.5\%$. $Cmax = 7.5\%$. 247
5-55a25iso-40-45-133: Contour plots of ε^p_{equiv} at $\varepsilon_{zz} = 1.5\%$. 249
5-55b25iso-40-45-133: Contour plots of ε^p_{equiv} at $\varepsilon_{zz} = 2.5\%$. 249
5-55c25iso-40-45-133: Contour plots of ε^p_{equiv} at $\varepsilon_{zz} = 3.5\%$. 250
5-55d25iso-40-45-133: Contour plots of ε^p_{equiv} at $\varepsilon_{zz} = 4.5\%$. 250
5-55e25iso-40-45-133: Contour plots of ε^p_{equiv} at $\varepsilon_{zz} = 5.5\%$. 251
5-55f25iso-40-45-133: Contour plots of ε^p_{equiv} at $\varepsilon_{zz} = 6.5\%$. 251
5-56a25iso-55-45-133: Contour plots of ε^p_{equiv} at $\varepsilon_{zz} = 1.5\%$. 252
5-56b25iso-55-45-133: Contour plots of ε^p_{equiv} at $\varepsilon_{zz} = 2.5\%$. 252
5-56c25iso-55-45-133: Contour plots of ε^p_{equiv} at $\varepsilon_{zz} = 3.5\%$. 253
5-56d25iso-55-45-133: Contour plots of ε^p_{equiv} at $\varepsilon_{zz} = 4.5\%$. 253
5-56e25iso-55-45-133: Contour plots of ε^p_{equiv} at $\varepsilon_{zz} = 5.5\%$. 254
5-56f25iso-55-45-133: Contour plots of ε^p_{equiv} at $\varepsilon_{zz} = 6.5\%$. 254
5-57a25iso-40-45-233: Contour plots of ε^p_{equiv} at $\varepsilon_{zz} = 1.5\%$. 255
5-57b25iso-40-45-233: Contour plots of ε^p_{equiv} at $\varepsilon_{zz} = 2.5\%$. 255
5-57c25iso-40-45-233: Contour plots of ε^p_{equiv} at $\varepsilon_{zz} = 3.5\%$. 256
5-57d25iso-40-45-233: Contour plots of ε^p_{equiv} at $\varepsilon_{zz} = 4.5\%$. 256
5-57e25iso-40-45-233: Contour plots of ε^p_{equiv} at $\varepsilon_{zz} = 5.5\%$. 257
5-57f25iso-40-45-233: Contour plots of ε^p_{equiv} at $\varepsilon_{zz} = 6.5\%$. 257
5-58a25iso-60-45-233: Contour plots of ε^p_{equiv} at $\varepsilon_{zz} = 1.5\%$. 258
5-58b25iso-60-45-233: Contour plots of ε^p_{equiv} at $\varepsilon_{zz} = 2.5\%$. 259
5-58c25iso-60-45-233: Contour plots of ε^p_{equiv} at $\varepsilon_{zz} = 3.5\%$. 259
5-58d25iso-60-45-233: Contour plots of ε^p_{equiv} at $\varepsilon_{zz} = 4.5\%$. 260
5-58e25iso-60-45-233: Contour plots of ε^p_{equiv} at $\varepsilon_{zz} = 5.5\%$. 260
5-58f25iso-60-45-233: Contour plots of ε^p_{equiv} at $\varepsilon_{zz} = 6.5\%$. 261

5-59 Anisotropic vs. isotropic matrix: macroscopic yield strain ε_{zz}^{y} as function of Σ. Pre-existing cavity. 265
5-60 Anisotropic vs. isotropic matrix: macroscopic yield stress σ_{zz}^{y} as function of Σ. Pre-existing cavity. 265
5-61 Anisotropic vs. isotropic matrix: macroscopic yield strain ε_{zz}^{y} as function of Σ. Coherent particle. 266
5-62 Anisotropic vs. isotropic matrix: macroscopic yield stress σ_{zz}^{y} as function of Σ. Coherent particle. 267
5-63 25xxx-00-45-033: (a) macroscopic axial true stress σ_{zz} and (b) cell volumetric strain Ψ as function macroscopic true axial strain ε_{zz}. $\Sigma =$ 0.33. Cavity. 268
5-64 25xxx-00-45-066: (a) macroscopic axial true stress σ_{zz} and (b) cell volumetric strain Ψ as function macroscopic true axial strain ε_{zz}. $\Sigma =$ 0.66. Cavity. 269
5-65 25xxx-00-45-133: (a) macroscopic axial true stress σ_{zz} and (b) cell volumetric strain Ψ as function macroscopic true axial strain ε_{zz}. $\Sigma =$ 1.33. Cavity. 269
5-66 25xxx-00-45-233: (a) macroscopic axial true stress σ_{zz} and (b) cell volumetric strain Ψ as function macroscopic true axial strain ε_{zz}. $\Sigma =$ 2.33. Cavity. 270
5-67 25xxx-nv-45-033: (a) macroscopic axial true stress σ_{zz} and (b) cell volumetric strain Ψ as function macroscopic true axial strain ε_{zz}. $\Sigma =$ 0.33. Coherent particle. 271
5-68 25xxx-nv-45-066: (a) macroscopic axial true stress σ_{zz} and (b) cell volumetric strain Ψ as function macroscopic true axial strain ε_{zz}. $\Sigma =$ 0.66. Coherent particle. 271
5-69 25xxx-nv-45-133: (a) macroscopic axial true stress σ_{zz} and (b) cell volumetric strain Ψ as function macroscopic true axial strain ε_{zz}. $\Sigma =$ 1.33. Coherent particle. 272

5-70 25xxx-nv-45-233: (a) macroscopic axial true stress σ_{zz} and (b) cell volumetric strain Ψ as function macroscopic true axial strain ε_{zz}. $\Sigma =$ 2.33. Coherent particle. 272
5-71 25xxx-00-45-033: Macroscopic strain space evolution: ε_{zz} vs. ε_{rr}. $\Sigma =$ 0.33. Cavity. 277
5-72 25xxx-00-45-066: Macroscopic strain space evolution: ε_{zz} vs. ε_{rr}. $\Sigma =$ 0.66. Cavity. 277
5-73 25xxx-00-45-133: Macroscopic strain space evolution: ε_{zz} vs. ε_{rr}. $\Sigma =$ 1.33. Cavity. 278
5-74 25xxx-00-45-233: Macroscopic strain space evolution: ε_{zz} vs. ε_{rr}. $\Sigma =$ 2.33. Cavity. 278
5-75 25xxx-00-45-033: Macroscopic strain space evolution: ε_{zz} vs. ε_{rr}. $\Sigma =$ 0.33. Coherent particle. 279
5-76 25xxx-00-45-066: Macroscopic strain space evolution: ε_{zz} vs. ε_{rr}. $\Sigma =$ 0.66. Cavity. 280
5-77 25xxx-00-45-133: Macroscopic strain space evolution: ε_{zz} vs. ε_{rr}. $\Sigma =$ 1.33. Cavity. 280
5-78 25xxx-00-45-233: Macroscopic strain space evolution: ε_{zz} vs. ε_{rr}. $\Sigma =$ 2.33. Cavity. 281

A-1 Explanation of Simulation Code 293

B-1 Examples of axisymmetric elements that can be modeled using the UEL subroutine 296
B-2 Continuous and discrete version of the surface integral. 297
B-3 Illustration of node and surface segment numbering 299
B-4 Constitutive model for the case of "Simple Cavitation" 301
B-5 Constitutive model for the case of "force relaxation algorithm" 302
B-6 Flow chart of the "force relaxation algorithm" 303

C-1 Schematic of the USER MPC implementation 344

C-2 Schematic of the triaxiality implementation using a UEL 349

List of Tables

4.1 Properties of Nylon in the temperatures regimes above and below T_g. Properties of rubber. From[60, 50] 84

4.2 Residual stresses due to cooling and matrix crystallization. 85

5.1 25iso-00-45-033: Charateristic Parameters. 96

5.2 25iso-00-45-033: Overview of graphs and contour plots. 97

5.3 25ani-60-45-133: Charateristic Parameters. 114

5.4 25ani-60-45-133: Overview of graphs and contour plots. 115

5.5 Macroscopic axial yield stress σ_{zz}^{y} and macroscopic axial yield strain ε_{zz}^{y} as function of triaxiality Σ. Anisotropic and isotropic matrices with cavity. 225

5.6 Macroscopic axial yield stress σ_{zz}^{y} and macroscopic axial yield strain ε_{zz}^{y} as function of triaxiality Σ. Asnisotropic and isotropic matrices with coherent particle. 226

A.1 Symbols and their meaning. 294

Chapter 1

Introduction

The field of polymer modification has long held research interest. Numerous methods for blending, grafting and other processes have been developed, and many are employed successfully in industry today. Some of these processes are little understood in spite of their widespread use. One such example is the toughening of polymers by incorporation of particles of a second phase into an otherwise homogeneous matrix polymer. The particles may be made from a compliant elastomeric material or from a stiff material, such as ceramics. For certain combinations of volume fraction and particle size, the blended materials are known to exhibit an increase in toughness when measured in notched Izod impact tests. Depending on the particle/matrix polymer system, the increase in toughness ranges from small amounts to dramatic jumps. Although this phenomenon has been known to exist for several decades, a comprehensive theory explaining the underlying causes for the toughening still does not exist.

In the work presented here, some of the aspects of rubber-toughening are studied. Using numerical methods, a micromechanical model of a rubber particle-toughened material is analyzed regarding the effects of the characteristic parameters of such materials on its mechanical response to different kinds of tensile deformation. Particular emphasis is given to studying the role of the particle and the particle cavitation event in the toughening process.

Chapter 2 will review some of the published literature on the particle-toughening

of polymers, and will discuss some of the experimental observations and hypothesized mechanisms in the toughening process.

In chapter 3 a review of proposed and confirmed cavitation criteria for rubber particles is given.

Chapter 4 introduces the micromechanical model and the numerical analyses that were used to investigate some of the issues in particle toughening.

The results are presented and analyzed in chapter 5, and general trends in the model's macroscopic stress- and strain-reponses, matrix plasticity evolution, particle cavitation etc. are identified.

Finally, in chapter 6 follows a discussion of the results with regard to the reported experiments and theories from the literature on toughening mechanisms.

Appendices B and C explain the implementation of the user-defined subroutines used in the finite element analysis, and appendix A explains some of the codes and variables used in this thesis. In appendix D some of the Matlab scripts used in the data reduction are listed.

Chapter 2

Background

Polymers are widely used as structural and engineering materials and replace more and more traditional metal parts. Their applications range from consumer goods and appliances to the automotive and defense industries. One limitation to the use of polymers is their tendency to exhibit brittle behavior in the presence of notches.

The interest in polymers in general and in some of the toughened varieties of these materials is so great and the number of potential applications so large that, according to a survey published by "Modern Plastics International" in 1989, the number of new resins based on Nylon alone that were to be introduced during that year exceeded 100. The total number of available Nylon-based resins at that time was more than 1000 [2].

Polymers usually exhibit intrinsic brittleness at temperatures that are sufficiently far below the polymer's glass-transition temperature T_g. In this 'virgin glassy state' [65] the polymer is in a non-equilibrium state in which its free volume is frozen-in at T_g. The density of the polymer and thus the local free volume depend upon the rate at which it is cooled from T_g. The tendency toward brittle behavior is also found to depend on the cooling rate. Therefore, it is postulated by some, the change in free volume causes the embrittlement of the polymer whereas the polymer's molecular parameters, such as entanglement density and characteristic parameters, are unchanged across T_g. This analysis is generally true only for amorphous polymers, but it can be applied to semi-crystalline polymers if the degree of crystallinity is not

too high. The deformation in the crystalline part of semicrystalline polymers involves lamellar slippage, stress-induced changes in orientation and crystal transformation. Semicrystalline polymers can therefore be thought of as amorphous matrices that include dispersed crystalline domains. Which one of the two domains of the polymer dominates the mechanical response of the material depends on the type of polymer.

While many polymers have the potential for brittle behavior, they also have the potential for ductile or yielding behavior. Several methods of manipulating these materials have been developed to either control the brittle behavior and/or to increase the propensity to deform in a ductile manner and thereby increase the toughness. Some of theses methods and the theory behind them are discussed in the next section.

2.1 Approaches to Toughening

Most engineering polymers are known to undergo a ductile-to-brittle transition when the temperature decreases, at high strain rates and/or in the presence of notches. To lower the yield strength, the polymer can be plasticized by adding a diluent such as water, resulting in a lowering of its glass-transition temperature. Because of the problems that the migration and/or inhomogenous distribution of the diluents may cause, it is much preferred to improve the polymer's brittleness through rubber modification, i.e. the incorporation of a soft second phase of dispersed particles. Both methods, however, decrease the blend's modulus. In some systems, the use of stiff particles can produce an increase in the modulus and in the toughness at the same time.

Improving the toughness of rigid polymers by incorporating a suitable elastomeric phase in the form of small particles is widely practiced. The obtained improvements depend on a variety of factors, such as particle volume fraction, particle size, the thermal and mechanical properties of matrix and particles, the degree of dispersion of the elastomers, use of grafting agents, etc. A variety of opinions exists in the literature about the importance and role of these factors and the underlying mechanisms of the toughening process. Examples of polymers that can be successfully toughened by

incorporating elastomeric particles are semi-crystalline polymers, such as Nylon, and glassy polymers, such as PMMA and PS. Recently the incroporation of stiff particles was reported to cause toughening in PE and Nylons.

2.2 The Competition between Brittleness and Ductility

From a mechanics perspective, the competition between brittleness and ductility can be reduced to the question of whether yield occurs and enough plastic deformation takes place to alleviate stress before it reaches the critical magnitude for brittle fracture to occur. The plastic deformation is to allow for the dissipation of as much elastic strain energy in the stressed material as possible in order to reduce the amount of energy that is available in the vicinity of the notch or crack tip to contribute to the advancement of the crack and to the creation of new free surface area. In the corresponding problem in metals, the competing mechanisms are characterized by the brittle strength σ_B and the yield strength σ_Y. σ_B is relatively independent of temperature and is typically the cleavage strength, whereas σ_Y has a strong dependence on strain rate and temperature [8]. The notion of yield strength is further qualified by the requirement that the ensuing plastic flow has to be large enough to alleviate the stress state before brittle failure occurs. When a polymer exhibits a brittle behavior, its brittle strength is lower than the stress required for yield. In the case of a ductile polymer it is the reverse. The toughening of a polymer must therefore act to either increase its brittle strength or lower its yield strength or a combination thereof.

In terms of stress requirements, the brittle strength mostly depends on tensile stresses, whereas the yield strength only depends on the deviatoric part of the stress state. In the case of an isotropic material, the propensity of the material to yield is well characterized by the von Mises equivalent stress measure. In anisotropic materials a more complex measure is required, such as the Hill yield criterion. If a mean normal stress is added to the current (predominantly tensile) stress state, such as in

the vicinity of a notch, the stress deviator is not affected and the von Mises stress remains constant. If, however, only one of the normal components of the stress state is removed, the deviatoric stress will increase. The latter case can take place in the vicinity of an interface from which all tractions are suddenly removed, as in the case of a cavitating particle or in the case of particle/matrix interface decohesion.

In certain materials, the presence of inhomogeneities, such as cavities or particles without grafting, may cause such levels of stress concentration that the local stresses reach the material's brittle strength before yield occurs, which can lead to an embrittlement of the blend. For certain semicrystalline polymers Argon, Cohen and Muratoglu [13] indicated that when such inhomogeneities of a size ranging from 25 to $50\mu m$ are present, the resulting brittle strength is on the order of 40 - $55MPa$[1]. When the inhomogeneities are "well-controlled" and on the order of only a few microns, however, the brittle strength rises above the yield strength and plastic flow occurs. Once the plastic deformation is initiated, it alleviates some of the effects of the impurities [13].

These general rules, however, have to be put into perspective by considering the vast differences between polymers in terms of their molecular characteristics, amorphous and crystalline domains, and their resulting brittle and ductile behavior.

2.3 Toughening Mechanisms

The observation that the incorporation of micron- and sub-micron-sized particles helps to make polymers more ductile has lead to the widespread use of various types of small particles as modifiers. The materials used for such particles include elastomers, such as rubber, thermoplastics, such as polyethylene, and rigid particles, such as calcium carbonate. In particular the incorporation of rubber particles in several polyamides was observed to cause a dramatic increase in fracture toughness under impact loading. The increase in Izod impact energy reaches factors on the order of

[1]This statement seems to refer to blends where the inter-particle distance is larger than the critical value as reported by Wu [62] in Nylon-6/rubber blends.

20 and even 30 [63]. The causes and underlying mechanisms for the toughening have generated widespread research interest and the question about their nature has lead to some disagreement in the scientific community.

In the published literature, there currently exists no theory that convincingly explains the toughening of all particle-modified polymers with one mechanism. There is evidence that a fundamental differentiation has to be made between the mechanisms responsible for the toughening of different types of particle-polymer systems. These mechanisms have to include both the mechanics of the heterogeneous system of the blend and the processes on the microstructural level of the matrix polymer.

The ways in which a polymer or polymer blend can dissipate energy when subject to impact loading is limited to crazing and/or some other form of brittle fracture, yielding or both. Wu [63] suggested the division of all polymers into two categories with regards to their fracture behavior, possible routes to toughening them and the role of the particle in rubber-toughening these polymers.

Type I includes brittle polymers in which crazing is the main fracture mechanism. Examples are polystyrene and poly(methyl methacrylate). Under impact loading they have low crack initiation and low crack propagation energies which result in low notched and unnotched impact strengths. They can be rubber-toughened by increasing the crazing of the matrix. Regarding the role of the particle size in particle-toughened blends, Wu summarizes the published literature as follows. In ABS the toughness increases with increasing particle size. In epoxy resin the toughness was found to increase, decrease or be independent of particle size. In polystyrene both increasing and decreasing toughness was reported with increasing particle size. In polypropylene the toughness was found to increase with decreasing particles size. Wu points out that there generally exists an optimum particle size at which the toughness is at a maximum. Some examples of reported optimal particle sizes for maximum toughness of the blends are 2-5μm in polystyrene, 0.1 - 1μm in poly(styrene-acrylonitrile) and 0.3μm in poly(methyl methacrylate). The mechanisms through which the particle size plays a role in the toughening is craze initiation and craze termination. At a given volume fraction, smaller particles are said to provide more craze

initiation sites, as well as craze termination sites. The smaller the particle, however, the less efficient it is for the termination of a craze. The particle size may also have an influence on the particle's potential to provide a craze initiation site, depending on how important a role particle cavitation plays relative to the stress concentration in the matrix due to the presence of the particle. Wu points out an observed correlation of the optimum particle size with the thickness of crazes in a given polymer. A critical requirement for the efficiency of particles to act as craze termination sites is their good adhesion to the matrix. Wu points out that the lack of consistency in the experimental results reported by various researchers could be due to the oversight of the importance of the adhesion between particle and matrix, which is rarely reported or measured. [2]

Type II polymers are ductile and their main fracture mechanism is yielding. Examples are Nylon, poly(ethylene terephthalate) and polycarbonate. The initiation of a crack requires high levels of energy, but the propagation of a crack little. The mechanism for rubber toughening in these polymers is to increase matrix yielding. The toughness in blends of type II polymers exhibits a sharp tough-to-brittle transition when the particle size reaches a critical value under constant particle volume fraction and constant adhesion. Wu points out that in these polymers the surface-to-surface distance provides a critical parameter that uniquely characterizes the toughening condition, independently of particle size or volume fraction. For the blend to have a tough response it is sufficient to adjust particle volume fraction and size so that the inter-particle distance is less than the critical value.

In order to illustrate Wu's point, rubber-toughened Nylon-6 will be chosen as an example for a type II particle-polymer system for which a relatively complete explanation of the toughening mechanism and its underlying microstructural phenomena has been proposed by the group of Argon, Bartczak, Cohen and Muratoglu who have published several papers on the subject [8, 11, 13]. Subsequently, the work of some

[2]Even Sue's [43] reported 'croids' should fit into Wu's type I polymers. A croid is a craze-like damage zone that was found to be a collection of line arrays of highly cavitated rubber particles around which the matrix appeared to have deformed plastically, whereas the matrix outside of these zones appeared to be undeformed.

of the other groups who have contributed to the study of toughening mechanisms in polymers will be review.

2.3.1 Argon et al.: Rubber-Toughened Nylon

Numerous researchers studied the particle toughening of polyamides by making blends with varying particle volume fractions and varying particle sizes. It was widely recognized that both of these parameters played an important role in the toughening mechanism, since a jump in toughness was observed at a critical particle size for a given particle volume fraction. Similarly a toughness jump was observed for a critical volume fraction at a given particle size. The significant correlation between the two, however, was overlooked. In his 1985 paper Wu [63] reported that particle size and particle volume fraction can be related through a single parameter, which is the inter-particle distance ID. He found that toughness jumps are observed in blends of Nylon-6,6 and rubber when the distance from the surface of one particle to the surface of its neighboring particles is less than a critical value. Equation 2.1 shows how the critical inter-particle distance ID_{cr} relates to the particle volume fraction Φ and the particle diameter d.

$$ID_{cr} = d\left[\left(\frac{\pi}{6\Phi}\right)^{\frac{1}{3}} - 1\right] \tag{2.1}$$

Because of the underlying assumptions of a regular cubic arrangement of the particles inside the matrix and of a negligible variation of particle sizes, the equation is an estimate. The value for the critical inter-particle distance identified by Wu for the case of Nylon-6,6 was $0.3\mu m$.

Wu first proposed an explanation based on the idea of stress field overlap [63]. He reasoned that the stresses around the particles due to the stress-intensifying effect of the particles were only slightly affected by the presence of their neighbors when the distance between the neighboring particles is larger than critical. The stresses were simply additive. When the distance was smaller than the critical inter-particle distance, however, the interactions of the stress fields become so large that the result-

ing stress state promotes matrix yielding in the ligaments and cause the transition to the blend's tough behavior. This explanation is contradicted by continuum mechanics considerations. The magnitude of the stress concentration scales with the particle size d and the particle center-to-center distance L. Since stresses are scale-independent, larger particles should result in the same yield-promoting stress state when the inter-particle distance is larger than the critical distance. In other words, the stress state is constant if the ratio $\frac{d}{L}$ is held constant while changing the particle size, which contradicts Wu's experimental observations [11].

Only with the observations of Lin [51] and Muratoglu [49] a consistent interpretation of Wu's critical inter-particle distance could be found. Lin and Argon [51, 10, 9] provided a crystallographic and mechanical characterization of Nylon-6. They demonstrated that the microscopic mechanical properties of quasi-single crystal Nylon-6 are highly anisotropic. A thermoplastic semicrystalline polymer with a crystallinity that is usually between 30 and 50%, Nylon-6 is characterized in the bulk as consisting of crystalline spherulites surrounded by an amorphous matrix. The crystalline domains appear in the form of lamellae with a monoclinic crystal structure. In textured Nylon-6 the crystalline lamellae exhibit three prominent slip systems on the (001) and (100) planes. The (001) [010] chain slip system corresponds to the hydrogen-bonded plane and has the lowest slip resistance, $16MPa$ [51]. The next-easier slip systems are the (100) [010] chain system and the (001) [100] transverse slip system both with a slip resistance of $23MPa$. All other slip systems have significantly higher resistances to slip and hence the plastic behavior of the crystallite components of Nylon-6 can therefore be characterized by these two slip systems. Figure 2-1 shows a schematic of the crystalline structure within a lamellae of a Nylon-6 crystal.

Muratoglu [49] performed experiments in which he produced films of Nylon-6 on a silicon substrate, ranging in thickness from $0.15\mu m$ to $2.20\mu m$. Using x-ray diffraction on the films he found that in Nylon-6 the (002) planes of the crystalline component are preferentially oriented parallel to the surface of the substrate on which they are grown, as shown schematically in figure 2-2.

With increasing thickness of the films, the degree of preferential crystallographic

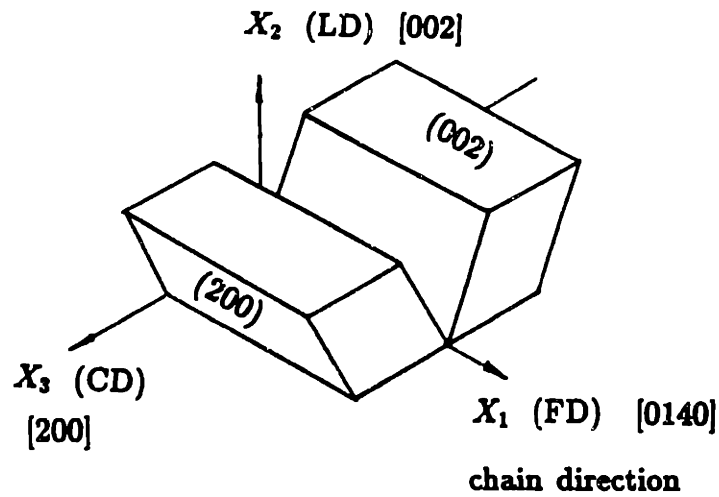

Figure 2-1: Schematic representation of the lamella orientation of textured Nylon-6, after [51].

orientation decreased. Using rubber to create sandwich configurations of rubber/Nylon-6/rubber, Muratoglu showed that the preferred orientation exists throughout the Nylon film when its thickness is less than a critical value of approximately ($0.5\mu m$ to) $0.7\mu m$. Since the Nylon chains are parallel to the (002) plane, they are thought of as lying parallel to the substrate surface during crystallization.

In another set of experiments Muratoglu [49] subjected thin films of Nylon-6 with varying thicknesses to tensile loads. He reported that the flow stress and the apparent modulus decreased with increasing film thickness, as shown in figure 2-3. The thinner the films, the higher is the degree of orientation according to the above observations. In the thinnest films most of the Nylon is expected to be fully oriented with its (002) plane parallel to the film surface. In this configuration the critical resolved shear stress on the (002) plane is nearly zero, and the corresponding easy slip system is not available for deformation. Hence the less easy slip systems determine the film's plastic response, and its yield stress is relatively high. As the film thickness increases, the degree of orientation of the Nylon crystals decreases. This allows for the critical resolved shear stress in more and more of the films' through-thickness to be non-zero, so that in those parts of the films the more easy slip systems become available for plastic deformation and the yield stress of the film decreases.

The above findings indicate that Wu's critical inter-particle distance is in fact the

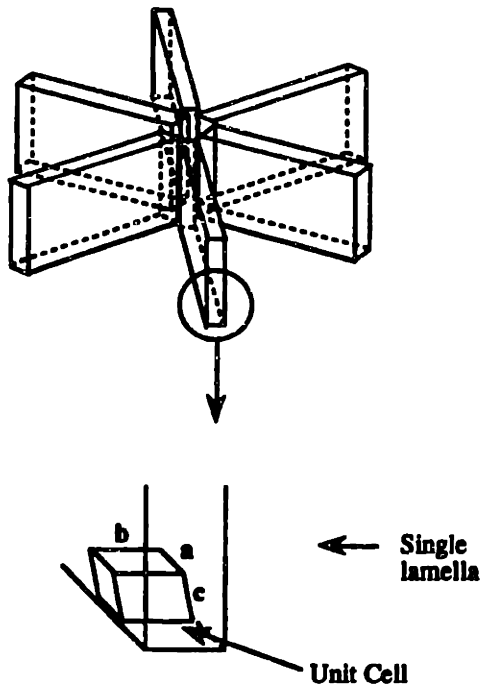

Figure 2-2: Schematic representation of the organization of Nylon crystals on a surface. After [49].

maximum distance over which the perfect alignment of crystalline Nylon can exist. When two (rubber) particles are at a distance from each other that is smaller than the critical distance ID_{cr}, then the Nylon ligament between the two particle surfaces is preferentially textured with the Nylon's chain axis tangential to the particle interface. When the distance is too large, the degree of preferential orientation decreases more and more until bulk spherulitic Nylon surrounds each particle.

As a consequence of the high degree of orientation in the thin ligaments, the slip resistance on the slip systems parallel to the particle surfaces (002) is low. This means that there exists much less resistance to plastic deformation in shear in the ligaments of those particles that are closer together than the critical inter-particles distance.

In a transmission electron microscopy (TEM) study, Muratoglu [49] established that the microstructure that was expected from his thin-film experiments does indeed exist in the bulk of rubber-modified Nylon-6. The generated micrographs showed that in those samples where the inter-particle distance is below the critical distance, the overlap of interface-induced orientation of the crystalline morphology results in a high

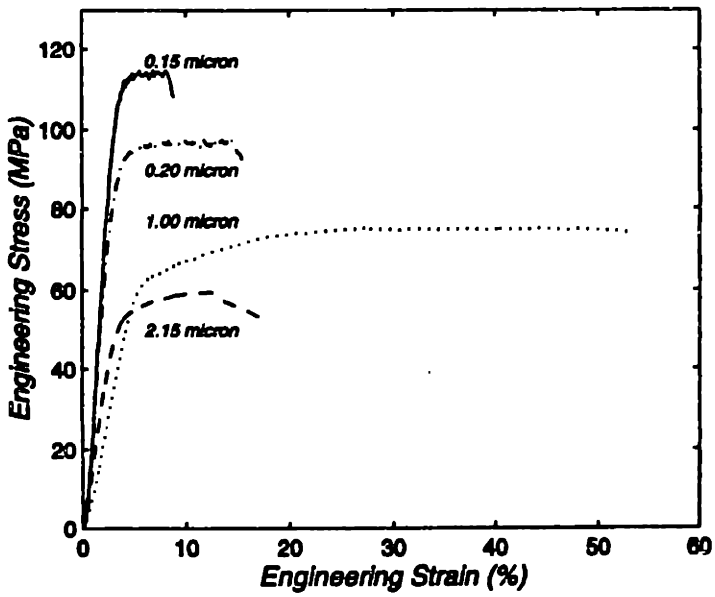

Figure 2-3: Engineering stress vs. engineering strain of free-standing thin films of polyamide 6 crystallized between polystyrene layers. After [49].

degree of material with preferred orientation of the hydrogen-bonded planes parallel to the matrix-particle interface in the interparticle zone [11].

The particluar morphology of the Nylon near the particle/matrix interface and the associated easy shear deformation cause the yield stress of the blend to be significantly lower than the stress at which brittle fracture occurs. This is, according to Argon and co-workers, the explanation for the dramatic increase in impact toughness that Nylon-6 exhibits whenever $ID \leq ID_{cr}$. The proposed explanation seems to be confirmed by the results obtained from studying particle/Nylon-6 blends where the particle was made from a stiff material. Bartzak, Argon, Cohen and Muratoglu [8] reported a jump in toughness in a system of Nylon with $CaCO_3$ particles when the inter-particle distance was reduced below a critical value, very much like in the rubber/Nylon-6 system.

Bartzak et al. [69] reported similar findings in blends of HDPE with rubber and with $CaCO_3$ particles. As in Nylon-6 and Nylon-6,6, the crystallinity was found to be essentially unchanged in the blends relative to bulk HDPE, but it was observed that the presence of particles produces special forms of preferential crystallization near the particles. The inter-particle distance was found to be the sole parameter to control

the notch toughness of these blends.

A number of other groups have contributed to the study of rubber/Nylon and other systems. Some of their work will be reviewed below.

2.3.2 Borggreve, Dijkstra, Gaymans et al.

The group of Borggreve, Dijkstra and Gaymans and co-workers performed a number of experimental, analytical and numerical studies of particle-modified polymer systems, such as rubber/Nylon and rubber/PS. In their work, the authors generally do not take into account morphological changes, such as the amorphous and crystalline domains in a semi-crystalline polymer, as reported by Lin [51]. Their explanations of the experimental results, as well as the authors' modelling, are based on the assumption that the matrix polymer has isotropic properties.

In one of their 1994 papers [28], the group studied stress fields around compliant particles using analytical and finite element methods. The properties of the systems they modeled were chosen to match those of Nylon-6 with rubber or LDPE particles. All results were based on isotropic linear elasticity, so that no microstructural effects were included in the model. The authors studied the hydrostatic stress σ^h and the von Mises equivalent stress σ^{mises} in models where the matrices surrounded (i) a solid particle and (ii) a cavity while subjected to either uniaxial or biaxial tension. The transition from the model with a particle to that with a cavity was thought to represent a particle cavitation event. It was reported that during the "cavitation process" under simple tension, σ^h and σ^{mises} did not change significantly in the vicinity of the particle. Under a biaxial tension, however, σ^{mises} was found to increase by up to a factor of 5, while σ^h remained roughly constant. The authors interpreted this result as a proof of their theory that particle cavitation is a mechanism that triggers yielding in the matrix. The von Mises yield criterion was used for the underlying condition for yield in the matrix, which was modeled as isotropic linearly elastic. The authors also reported that the stress fields in the matrix are "more or less the same"

for particles made of rubber and of LDPE, under both loading conditions. Extending their model to a five-particle system, the authors used the finite element method to analyze the effect on the hydrostaic stresses felt by particles that neighbor a cavity. The model was formulated in two dimensions under plane strain conditions. Dijkstra et al. reported that those particles that lie in the same plane as the cavity that is oriented normal to the direction of tension, experience an increase in σ^h, wherase the particles lying in any other direction to the cavity experience a decrease in σ^h at a given macroscopic strain. From this, the authors concluded that the process of particle cavitation spreads along planes normal to the direction of tension; i.e. "cavitation zones grow in similar ways to crazes and cracks".

Borggreve et al. also studied the toughening mechanism in particle-modified glassy polymers. In their 1995 paper [17], the group presented experimental work on blends of PS with rubber particles, in which the contribution of crazing to the toughening of the blend was examined. Using small angle x-ray scattering, the authors observed craze formation and particle cavitation under loaded conditions. In notched Izod impact and tensile tests the blends' impact toughnesses and stress-strain responses were measured. It was reported that the amount of crazing decreased with increasing rubber content, whereas the impact toughness was found to increase at the same time. It was therefore concluded that the toughening was not due to crazing in any significant amount, but that a combination of particle cavitation and microscopic shear yielding in the matrix must be the main source of plastic energy dissipation. The authors also reported that the microstructure of the crazes was observed to be the same for rubber-modified and non-modified PS, and was independent of rubber type, rubber content and macroscopic strains the specimen underwent. Even the measured craze fibril diameters remained constant and comparable to those in a pure PS homopolymer. As a consequence of this result, the authors classified crazing in glassy polymers as a "damaging mechanism" that should be controlled in order to prevent premature fracture. The particle volume fraction, size and properties (moduli and cavitation strength), as well the adhesion between particle and matrix, were considered as the parameters to achieve this.

2.3.3 Bucknall, Lazzeri, Zhang et al.

Another group that has published numerous articles on the subject of toughening through particle-modification includes Bucknall, Lazzeri, Zhang and others. In their theory on the cause for the toughening of notch-sensitive polymers, the group [24, 23, 26, 25, 27] advances the idea that the expansion, interaction and eventual coalescence of voids, following cavitation of the rubber particles, plays a central role in the fracture behavior of many rubber-toughened polymers, including epoxy resins, polyamides (Nylon) and other craze-resistant polymers. The role of the voids is important in allowing the matrix polymer to reach high plastic strains within the zone of high triaxial stress in the vicinity of a crack tip, and hence the particle cavitation is a pre-condition for the toughening. The authors defend the theory of dilatation bands, which are band-like arrangements inside which the particles have preferentially cavitated. Using a continuum approach, Bucknall and co-workers emphasize the validity of their model by pointing out that the associated yield criterion is applicable to both plane strain and plane stress conditions.

In their 1993 article, Bucknall and Lazzeri [24] explained the observations of a critical inter-particle distance made by Wu and Borggreve et al. by means of their theory of dilatation bands. The authors assumed that most of the plastic deformation occurs inside dilatation bands within which the cavitated rubber particles expand to considerable size. Considering the ligament between two cavitated particles, now voids, the stress state is a combination of the shear stress and a mean stress acting on the dilatation bands. Both vary as a function of distance from the free surfaces of the closest cavities. At the center of the ligaments, the stress is highly triaxial, whereas the authors indicate that the normal stresses are "close to zero at the matrix-rubber boundary". The authors argue that the flow rate within the ligaments is influenced by the very rapid change in stress state between the particle surfaces. Therefore, the development of dilatation bands is said to account for the effect of the particle size on the brittle-to-tough transition in toughened Nylons. As with other explanations of the toughening mechanism that are based on stress arguments, the

theory of Bucknall and co-workers fails to explain the observation of the absolute length scale of the inter-particle distance. Their work does not show a connection between the micromechanism of the matrix polymer (yield) and the absolute stress levels that develop in the inter-particle ligaments. In the development of the theory on dilatation bands, the matrix properties are assumed to be isotropic.

Another issue of interest to the study of toughening mechanisms is the question of the sequence of matrix yield and particle cavitation. Bucknall and Lazzeri [2] investigated this question using tensile dilatometry on blends of rubber and Nylon-6. They reported that under simple tension, the particle cavitation occurred before matrix yield. Their results were confirmed by a number of other investigators who studied blends of rubber particles with matrix polymers as diverse as Nylon [16], epoxy [59] and PMMA [22]. Many investigators have concluded from this that particle cavitation is a pre-condition or even an trigger event for matrix yield [28]. A strong argument against this conclusion is the observations that, although certain particle-modified systems in which particles were not observed to cavitate at all or not in large numbers, exhibit less impact toughness than blends with massive cavitation or with voids, they do undergo sometimes substantial shear deformation. The connection between particle cavitation and matrix yield therefore need further investigation.

2.3.4 Kinloch, Huang, Guild et al.

Guild and Kinloch [41] studied rubber-modified epoxy polymers. In their study, they distinguished between two toughening mechanisms: localized shear yielding, or shear banding, and internal cavitation. The mechanism of shear yielding was observed at an orientation of 45^o to the direction of the maximum principal tensile stress. At the same orientation a large number of particles were observed to cavitate. Once the particles are cavitated they provide for additional plastic deformation of the matrix as the cavities grow. Consequently, the authors argued, the matrix volume that undergoes plastic yielding was increased due to the presence of cavitating particles, and the dissipation of plastic energy is higher than in pure epoxy. The two mechanisms, cavitation and shear yielding, are triggered by different types of stress concentrations

within the overall stress field of the blend. Using the results of a previous article by Huang and Kinloch [46], it was concluded that the initiation and growth of shear bands is only possible under plane-strain conditions. From this, the authors reasoned that internal cavitation or debonding of rubber particle is not expected to trigger additional shear banding in a rubber/epoxy system, but that its effect is limited to the additional yielding around the growing voids. A shortcoming of the theory proposed by Kinloch and co-workers is that the distinction between the matrix deformation termed "shear yielding" and that due to void growth is not qualified in terms of the underlying deformation mechanisms.

2.4 Discussion

The above discussion shows how complex the toughening process of polymers through particle-modification is. In order to fully understand it, aspects as diverse as the morphology of the matrix polymer, its deformation mechanism(s), the stress field effects due to stress concentration around particles and voids, and stress field overlap in multi-particle systems need to be considered. Additional factors include the effects of the mechanical properties of particle and matrix, the characteristics of the particle/matrix interface, as well as the conditions for and the nature of the particle cavitation event.

Many of the questions regarding the stress state in the blend are related to the mechanical properties of matrix and particle. Conversely, the deformation behavior of the matrix polymer depends on the stresses it is subjected to. The role of the particle adds to the complexity, since it too influences the stress state of the matrix, and the question of if and when it transitions from particle to cavity depends on the properties of the particle material, but also on the stress state of the particle, and hence the stress state of the matrix.

Several authors have reported that in the most common systems of rubber particle-toughened polymers, the influence of the particle on the stress state of the matrix was characterized by the absence of shear stresses [28, 42]; i.e. the stress state in

the particle was found to be nearly perfectly hydrostatic, and the tractions along the particle/matrix interface normal to the interface. Assuming that the particle can be modeled realistically as a fluid-filled cavity, the question of the material properties can be reduced to that of the matrix properties and the bulk modulus of rubber, except for the question of the conditions under which a particle transitions from particle to cavity. As was concluded after a review of the published literature on the subject of particle cavitation, a wide variety of particle cavitation criteria have been proposed and experimental findings reported. A review of these will be given in chapter 3.

The discussion of the works of Argon, Muratoglu and Lin has shown that it is beneficial to take into account the micromechanical deformation mechanisms and morphology when explaining the deformation behavior of the matrix polymer. In other words, the discussion of the toughening mechanism(s) must not be limited to considerations on the continuum level of the toughened blend. Hence it should be possible to model the behavior of a toughened blend by considering the micromechanical processes that govern the deformation behavior of the matrix polymer.

Combining both the micromechanical model of the matrix deformation behavior and the model of the particle as a fluid-filled cavity, a numerical study was undertaken with the goal of clarifying some of the questions about the toughening mechanisms in particle-modified polymers. Using the finite element method, two different plasticity models for the modeled matrix material were implemented, one representing a matrix polymer with a preferential orientation and the other an isotropic material. In our study, particular emphasis was given to the role of the particle and the effects of the particle cavitation event on the stress-strain response of the blend, and evolution of the plasticity in the matrix.

In the following chapter, a literature review will be presented with the purpose of clarifying what criteria should be chosen for the rubber particle cavitation event in our model.

Chapter 3

Cavitation Criteria for Rubber Particles

For a micromechanical model to capture correctly the influence of the rubber particle and of the cavitation event in a particle-toughened polymer system, a valid cavitation criterion needs to be established and numerically implemented. This chapter discusses some of the theoretical criteria that have been proposed in the literature, as well as experimental results and observations regarding particle cavitation strength and sizes limitations for cavitation to occur.

3.1 Introduction

There exist numerous ideas in the published literature on the effect the particle cavitation event has on particle-modified polymer systems. A popular notion is that the release of the tractions along the particle/matrix interface due to particle cavitation causes the stress state in the matrix in the vicinity of the particle to change and to induce yielding in the matrix [28, 29, 67]. For this mechanism to work, the stress state in the matrix under which the particle cavitation occurs must be such that the release of the interface tractions actually causes enough deviatoric stress for the matrix to yield. The particle therefore has to have a cavitation strength that is large enough to allow a build-up of stress in the matrix around the particle, but that is low enough

for the cavitation to occur before the stresses in the matrix reach a critical level at which the blend fails in a brittle manner, or at which other deformation mechanisms take over.

As the results presented in chapter 5 will show, the particles can influence the matrix plasticity only through their contribution to the stress state of the matrix surrounding the particle, and through the transition from particle to cavity. For the cavitation event to have any significance in the toughening, it must take place at a time during the matrix deformation when the release of tractions on the particle/matrix interface has an influence on the matrix plasticity.

The three issues related to the particle cavitation event that have emerged in the literature are:

- what is the critical stress state under which the particle cavitates,
- what is the minimal particle size for particle cavitation to occur inside a particle-modified blend,
- what theoretical cavitation criterion connects the cavitation strength and the size of a cavitating particle.

In this chapter a survey of the published literature will be given in order to clarify these questions. The published references include experimental observations of particle sizes at which particles cavitate (or don't cavitate), measurements of cavitation strengths and theoretical developments for energetic cavitation criteria.

Most authors agree that the shapes of the particles in particle-modified polymers can be approximated as spherical, in as much as they are made of materials like rubber, poly-ethylene, etc. Rubber is characterized by a Poisson's ratio close to 0.5, and hence its shear modulus is very small compared to its bulk modulus. Under the approximation of neglecting the shear stresses in the rubber particle altogether, the stress state in the particle is determined by the bulk modulus of the particle material and the volumetric strain the particle undergoes. The connection between the volumetric strain of an individual particle and the macroscopic volumetric strain

of the blend depends on the relative magnitudes of the materials' moduli and on the stress magnification effects that neighboring particles have on their neighbors. In most polymer systems that are modified with rubber particles, the bulk modulus of the matrix material is generally on the same order of magnitude as that of the particle.

To experimentally detect the particle cavitation events, some authors use tensile dilatometry. Other authors use the fact that the transparency to light of a blend changes as the included particles cavitate or decohere from the matrix.

In the following section the experimental results of cavitation pressures by Yerzley [34] and then Gent and Lindley [39] will be presented first. Then a number of theoretical criteria for rubber cavitation by Gent and Lindley [39], Ball [47] and Dompas and Goenickx [32, 31, 33] will be reviewed. A number of experimental observations of a critical (minimum) particle size for cavitation to occur will be reviewed.

3.2 Literature Review on Particle Cavitation Criteria

The first author to mention experimental observations related to the internal failure of rubber was Yerzley [34]. He observed a change in the load/deflection curve of neoprene specimens in tension, and attributed this 'yield point' to internal rupture. Motivated by Yerzley's conclusion, Gent and Lindley [39] performed their own experiments and were the first authors to propose a criterion for the cavitation of rubber spheres [39]. The authors estimated that all types of the rubbers they studied contained flaws on the order of 10 to $100\mu m$, which they regarded as pre-existing cavities. Assuming that these cavities behave like spherical voids inside infinitely thick spherical shells, the cavitation of the rubber sphere was approximated by the pre-existing cavity growing infinitely large. The stress state at which this happens is found to be a negative hydrostatic pressure that reaches a critical value, called the 'inflating pressure'. From previous developments, Gent and Lindley derived the expression for the hydrostatic

stress inside of a rubber cylinder, which is at a maximum along the axis of the cylinder. Assuming that the axis of the cylinder is also where the cracking occurs and where the crack that ultimately causes failure is initiated, the authors computed the theoretical cracking stress using an elastic stored-energy function and simple kinetic theory. When limiting their calculations to a neo-Hookean material with the microvoids being so large that surface energy terms can be neglected, the solution for the 'inflating pressure' reduces to the expression in equation 3.1.

$$P_{cr} = 2.5G \tag{3.1}$$

where G is the small strain shear modulus of the rubber. The 'inflating pressure' was assumed to be independent of the particle's size, which is not compatible with the observation that the assumed pre-existing microvoids are larger in size than the particles used in the toughening of typical polymer blends. Gent et al. performed experiements in which vulcanized rubber cylinders were bonded to plane metal end-pieces and then subjected to tensile loads. It was found that at relatively small loads internal flaws suddenly appeared which caused changes in the specimen's load-deflection curves, and in some cases failure. The authors' experimental results showed that the 'cracking stress', i.e., the stress at which the appearance of internal flaws was observed, was not uniform for all types of the vulcanized rubbers studied. It varied by a factor of more than 4 from the weakest to the toughest. The same large variation was observed in the 'average breaking stresses' which are the stresses at which the specimens failed. An interesting finding is the linear correlation between the cracking stress S' and the elastic modulus E of the rubbers that were used in the tests, as shown in equation 3.2.

$$S' = 0.55E + 0.049MPa \tag{3.2}$$

For a rubber material with an elastic modulus of $2MPa$ this translates into a cracking stress of $1.1MPa$. No experimental measurement of the hydrostatic stress state inside of the rubber at or close to the locations of 'cracking' was made.

Borggreve, Gaymans and Eichenwald [16] performed experiments on blends of

Nylon-6 and various types of rubber. Under uniaxial tension the cavitation strain was measured using tensile dilatometry. Particle sizes ranged from $0.3\mu m$ to $2.0\mu m$, and the particle volume fractions varied from 6.4% to 19.6%. It was found that the macroscopic strain at which the particles cavitate is independent of the particle size, from which the authors concluded that the particle strength is independent of the particle size. They also conluded that the stress concentration induced by neighboring particles does not act upon the rubber cavitation process. The findings of Borggreve et al. support the existence of a cavitation criterion that is independent of the particle size, such as Gent and Lindley's [39] criterion.

Stringfellow and Abeyaratne [4] verified the results of Gent and Lindley using finite element analysis. They found that the stress state on which Gent and Lindley based their criterion for rubber cavitation was a good approximation for the specimens they had used in their experiments, without being an exact solution. The cavitation criterion by Gent et al. is consequently a good approximation in the context of the experiments they performed.

Ball [47] expanded on the developments of Gent and Lindley by adopting the model of a large spherical solid of isotropic elastic material under tension in which a spherical cavity appears when certain energetic criteria are met. Assuming an appropriate stored-energy function that exists for large strains, he showed that at a certain critical value of surface traction or displacement, the solution to the elastic problem becomes unstable and bifurcates, i.e., it becomes energetically more favorable for the elastic body to nucleate a cavity rather than continue to deform homogeneously. Ball's results agree with Gent and Lindley's experiments. A general result of Ball's elastic solution to this bifurcation problem is that "an infinitesimal hole in a finite piece of material behaves like a finite hole in an infinite expanse of material". The solution accounts for the pressure inside of the cavity and the effect of surface energy e as shown in equation 3.3.

$$e(A) = KA^{n-1} \tag{3.3}$$

where A is the current surface area, K is the energy per unit area, and n is the space

dimension. However, when the surface energy of the cavity is taken into account in the analysis, Ball finds that the cavitation pressure tends toward infinity when the radius R_0 of the pre-existing cavity is reduced to zero:

$$R_0 \to 0 \implies P_{cr} \to \infty \tag{3.4}$$

This indicates that the surface energy can only be neglected if the initial microvoids are of a size that is larger than a certain critical size. If they are smaller than the critical size, or if there are no initial microvoids, then the surface energy needs to be taken into account. This also indicates a general trend that for small initial voids, the cavitation stress increases with decreasing void size.

Dompas and Goenickx [32] propose a criterion for internal cavitation of a rubber sphere, and find that there exists a minimum particle size for the cavitation to occur. Their calculations of new surface energy versus release of elastic strain energy are based on bulk modulus and surface energy. The surface energy is calculated from the chain scission energy of skeletal bonds, the mesh size of the network between the cross links, the crosslink density and the polymer backbone energy. Dompas et al. dismiss the idea that the cavitation event is the expansion of pre-existing cavities to infinite size. They propose that cavitation initiates at local inhomogeneities on a molecular scale, such as local differences in the crosslinking density of the rubber. The energy balance that governs the cavitation event required that the release of elastic strain energy be larger than the energy required for the creation of new or additional cavity surface:

$$U_{total} = U_{strain} + U_{surface} < 0. \tag{3.5}$$

The energetic form of the cavitation condition is then:

$$Cavitation\ when\ U_{strain} > U_{surface}. \tag{3.6}$$

The total energy balance as given by Dompas et al. is:

$$U_{total} = U_{strain} + U_{surface} = -\frac{1}{12}\Pi K_{rubber}\Delta^2 d_0^3 + (\gamma_r + \Gamma_{sc})\Pi\Delta^{2/3} d_0^2 < 0 \quad (3.7)$$

Where d_0 is the initial particle size, γ_r is the rubber surface energy, Γ_{sc} is the chain scission energy per unit area and Δ is the volumetric strain. The values used are $\gamma_r = 0.035 Jm^{-2}$, $\Gamma_{sc} = 0.035 Jm^{-2}$, $K_r = 2$ GPa. At a volumetric strain of 0.0128, which is assumed to be a typical strain at which the matrix yields, the plots of the strain, surface and total energies as a function of particle size are as shown in figure 3-1. The critical particle size for that volumetric strain is indicated by the vertical dashed line.

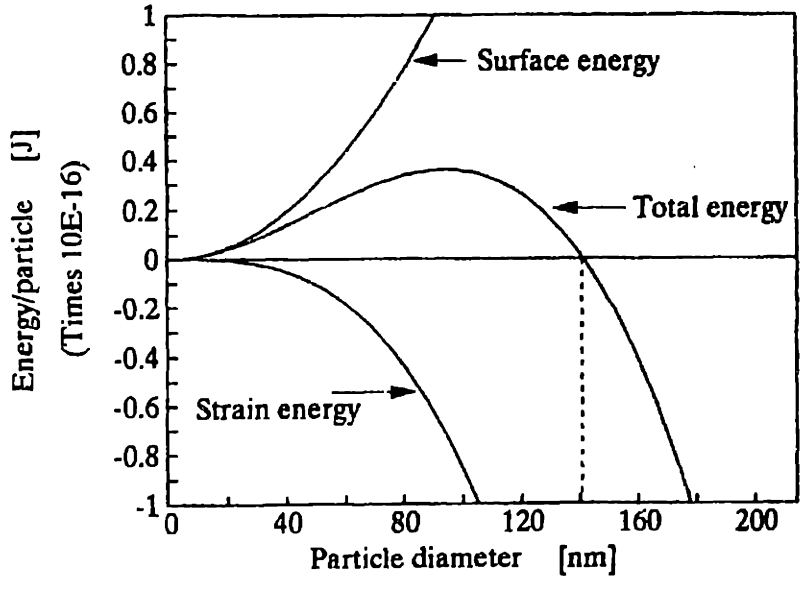

Figure 3-1: Strain energy, surface energy and total energy associated with internal rubber cavitation as function of particle diameter. After [32].

The graph shows that within the range of volumetric strains considered, the total energy for internal cavitation is negative for particles larger than $140nm$. Since the total energy is positive for particles smaller than $140nm$, these particles are not expected to cavitate at this strain.

Dompas et al. derive an equation for the critical (i.e. minimal) particle size d_0 as a function of the volumetric strain and the energy parameters previously defined, as

shown in equation 3.8.

$$d_0 = 12(\gamma_r + \Gamma_{sc})/K_r\Delta^{4/3} \tag{3.8}$$

Figure 3-2 shows the critical particle size as a function of volumetric strain.

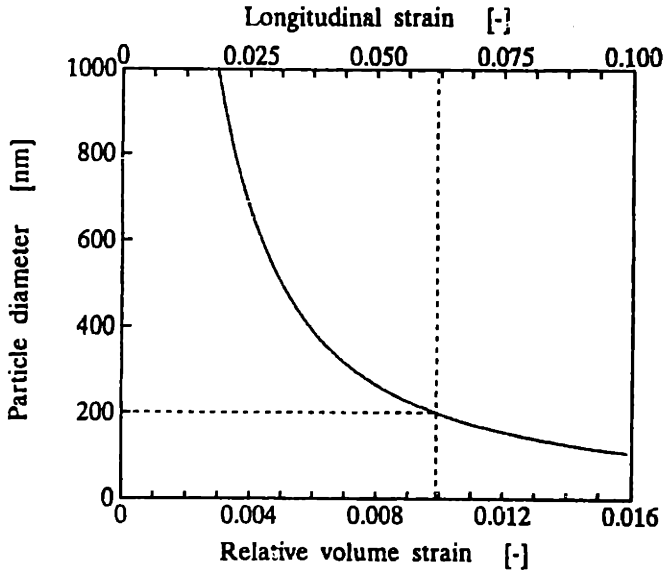

Figure 3-2: Relationship between the minimum particle diameter required for cavitation and the relaitve volume strain (Δ). The dotted lines are the critical conditions corresponding to a particle size of $200nm$ and a relative volume strain of 1%. After [32]

The results by Dompas et al. predict that large particles cavitate at an early stage of the deformation process, while smaller particles will cavitate at a later stage. A particle with a diameter of 0.2μm is expected to cavitate at approximately $-20MPa$ internal pressure, which is at a volumetric strain of 1.0%. A particle of $0.14\mu m$ diameter cavitates at an internal pressure of approximately $-25.6MPa$ at a volumetric strain of 1.28%. Dompas et al. make mention of the fact that the degree of cross-linking influences the cavitation strength of the particles by changing the chain scission and surface energies of the rubber.

Similar to the development of Dompas and Goenickx, a criterion for rubber particle cavitation was proposed by Lazzeri and Bucknall [24]. Their model is based on a large spherical rubber shell, inside of which is a small pre-existing cavity. However, contrary to the above approach, the particle diameter is assumed to remain constant

during the expansion of the cavtity.

This allows to limit the energy available for the expansion of the cavity to the strain energy that is pre-existing in the rubber shell and to avoid contributions from traction-displacement work done on the particle's outer boundary. Lazzeri and Bucknall limit the sources of energy contributions to the strain energy in the particle, the surface energy along the cavity boundary and the shear energy of the rubber as it stretches in order to grow the cavity. Equation 3.9 is the expression of the total energy of the rubber as a function of the cavity radius r, the particle radius R and the macroscopic volumetric strain Δ_{V0} of the particle.

$$U = \frac{2}{3}\pi K R^3 \left[\left(\Delta_{VO} - \frac{r^3}{R^3} \right)^2 + \frac{6\Gamma}{KR}\frac{r^2}{R^2} + \frac{3G\rho F(\lambda_f)}{K}\frac{r^3}{R^3} \right] \tag{3.9}$$

where K is the rubber bulk modulus, Γ is the surface energy, G is the rubber shear modulus, ρ is the ratio of the densities of the rubber phase before and after cavitation. The non-dimensional part of the shear strain energy function due to the stretching of the rubber to the maximum extension ratio is a function of λ_f, $F(\lambda_f)$.

The authors present their model in the form of a series of plots of $\frac{U}{U_0}$ as a function of $\frac{r}{R}$ for the outer particle radius ranging from 0.100 to $100\mu m$ which are shown in figure 3-3. The parameters used are $K = 2GPa$, $\Delta_{VO} = 0.4\%$, $\Gamma = 0.03Nm^{-1}$, $G = 0.4MPa$, $\rho = 1.0$, and $F(\lambda_f) = 1.0$.

Except for the small maximum at intermediate particle sizes and small $\frac{r}{R}$ ratios, the figure illustrates how only those particles exhibiting a minimum in potential energy are these that are $0.125\mu m$ in diameter or greater. For the particles of $0.100\mu m$ diameter the energetic minimum lies at an $\frac{r}{R}$ of zero which corresponds to the non-cavitated particle. From equation 3.9 it can be seen how in the development of Lazzeri and Bucknall the importance of surface energy term decreases with increasing particle size. However, the authors neglect the dissipation of energy due to the scission of rubber chains when the inside of the expanding cavity is stretched beyond the maximum stretching.

In a similar development as Lazzeri et al., Fond and Schirrer [35, 36] include in

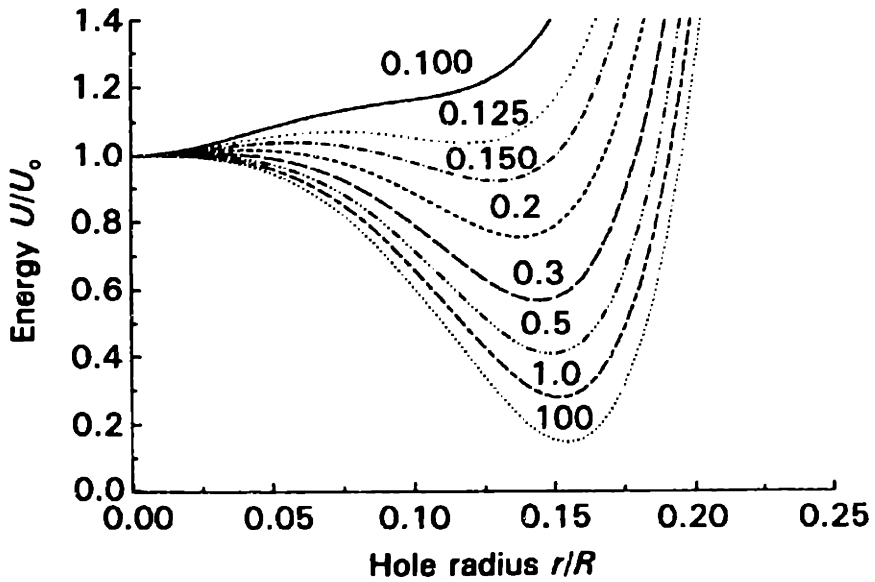

Figure 3-3: Calculated potential energy of a cavitated rubber particle as a function of the reduced radius of the void (r/R) for particles of radius R ranging from 0.1 to $100\mu m$. Values calculated at a fixed volume strain of 0.0004. After [24].

their calculations the initial cracking of the particle that leads to the formation of the initial void. The authors caution that it is not sufficient to explain the phenomenon of particle cavitation from a static and macroscopic point of view. They stress the importance of dynamic contributions of atomic forces, and that the microscopic fracture energies are unknown and cannot be measured. Pointing out that the creation of an internal void requires the advancement of internal cracks and that the continued crack propagation requires more and more volume dissipation, they expect the microscopic fracture energy to increase with the crack surface. The authors argue that the behavior of the particle in the vicinity of a pre-existing flaw cannot be predicted and is therefore a factor of inacuracy in their model. Fond and Schirrer conclude that, althought their model predicts that larger particles are easier to cavitate than smaller particles, there exists an energy barrier to the void initiation that is independent of particle size.

In a later paper Bucknall and co-workers [27] expanded on the criterion for rubber particle cavitation by including a term for strain energy of the matrix that is released during the particle cavitation event.

Dompas and Goenickx [31] performed real-time stress whitening experiments on blends of initially transparent poly(vinyl chloride) (PVC) with very small methyl methacrylate-butadiene-styrene graft co-polymer (MBS) core-shell particles. The particle sizes ranged from 0.08 to 0.26 μm. It was found that the onset of internal rubber cavitation in the blends during a tensile test depends on only the size of the rubber particles, and not on the core/shell ratio or the type of MBS used. The real-time stress-whitening experiments indicate that the resistance against cavitation increases with decreasing rubber particle size. Very small particles are unable to cavitate. This is confirmed by TEM and density measurements of the deformed specimens.

For their experiments, Dompas et al. used a tensile strain rate of $0.5\% min^{-1}$ and dumb-bell shaped speciments with cross-sections of $10x2mm^2$. Real-time stress whitening experiments were performed where a stablilized white light source focused on the specimens at an incident angle of 30^o relative to the CCD camera on the other side of the specimens. When cavitation occured, the light intensity at the camera increased dramatically because of the light scattered inside the specimens.

To understand the following results it is necessary to make a few definitions. The "average stress whitening" is defined as the intensity of scattering averaged over entire investigated area of specimen. The"percentage whitening" expresses how much of the specimen has undergone stress-whitening. The "cavitation strain" is the strain at which cavitation has occured in 50% of the investigated area of the specimen.

Figures 3-4 show the results of Dompas et al. for the tension tests up to 20% macroscopic axial strain for large and small PVC/MBS particles. It was noted that the stress-strain curves of all blends considered coincided with each other. The stress-strain curve is shown as the lower plot in figure 3-4. The figure at the top is a plot of percentage whitening versus macroscopic tensile strain and of average whitening versus tensile strain. The left ordinate corresponds to the percentage whitening and the right ordinate to the average whitening.

At the begining of the deformation, no stress-whitening has occurred and hence no light is scattered in the specimen. It appears transparent, and both the percentage whitening and the average whitening are zero. At strains of 4 - 8%, stress-whitening

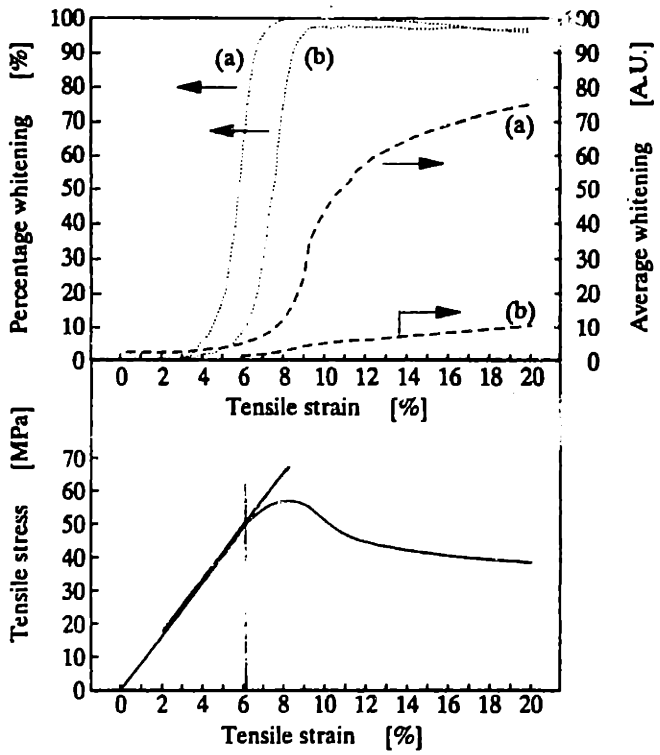

Figure 3-4: Examples of information obtained form stress-whitening experiments on PVC/MBS blends: average stress-whitening intensity, the percentage whitening and the tensile stress as a function of the tensile strain: (a) large particles, (b) small particles. The stress-strain response is the same for both particle sizes. From [31].

begins to appear homogeneously over the sampled area in the specimen. The authors observed that the percentage whitening usually approached 100% when the specimen was close to yield, which indicates that particle cavitation takes place before matrix yield. More importantly for the question of particle cavitation, the authors observed that the sharp increase in percentage whitening occurs earlier in samples with larger particles. This points toward a lower cavitation resistance for larger particles. The fact that the average whitening is higher in samples with larger particles is explained by the particles continuing to expand throughout the blend after their cavitation and hence providing more and more surface on which the incident light beam can be scattered. The degree of expansion of a particle was observed to increase with increasing particle size, which explains that the scattering is not a linear function of particle expansion. Examining the deformed specimens showed that the stress-

whitening was more pronounced in the shear bands than in the rest of the specimens.

Figure 3-5 shows another set of plots of percentage whitening as a function of tensile strain for blends with particles of 130, 165, 205 and 255nm in size. It can be seen very nicely how the particles with sizes of 205 and 220nm cavitate well before a strain of 6%, and hence before matrix yield, and how particles of 165nm in size cavitate during and after matrix yield. For these three particle sizes, the percentage whitening reaches at least close to 100%, which indicates that all particles in the investigated area of specimen cavitate. In blends with particles of 130nm the stress whitening occurs after the matrix yield and the percentage whitening reaches only 90%. This is interpreted as saying that not all particles cavitate. Since the particle sizes are likely to vary about the indicated sizes, the 10% of non-cavitating particles can be assumed to be those that are closer to the lower limit of the particle size distribution. Moreover the authors explain that in the case of blends with particles smaller than 150nm, the yielding of the matrix prevents the particles from reaching the volumetric strain necessary for their cavitation.

To confirm their conclusions Dompas et al. performed transmission electron microscopy. The specimens were cut into very thin sections parallel to the deformation direction in order to detect possible crazes in the material. The TEM micrographs showed that independently of the type of MBS used, 'small' particles ($d = 82nm$) had deformed by elongation only, whereas 'large' particles ($d = 255nm$) had deformed by elongation and cavitation.

In figure 3-6 Dompas et al. compare their experimental findings with the cavitation criterion they developed in their paper reviewed above [32]. In the figure, the particle diameter is plotted against longitudinal strain (top abscissa) and relative volumetric strain (bottom abscissa) at which a particle of that size is expected to cavitate (particle diameter measured on ordinate). Included in the figure is the theoretical result of the critical (i.e. minimal) particle size d_0 as a function of the volumetric strain and the energy parameters previously defined,

$$d_0 = 12(\gamma_r + \Gamma_{sc})/K_r\Delta^{4/3} \tag{3.10}$$

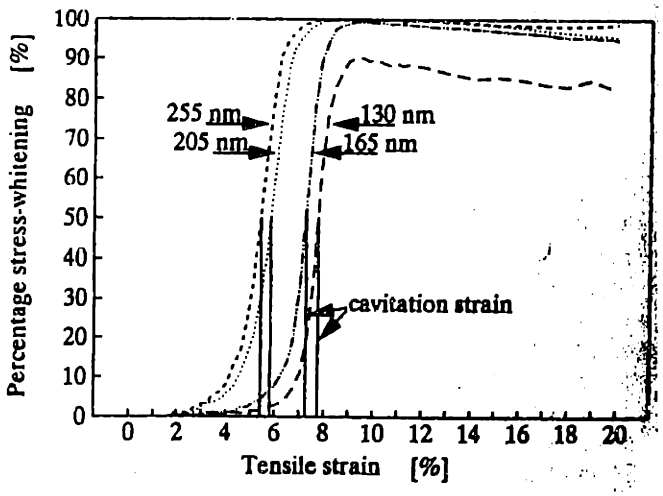

Figure 3-5: Comparison of the percentage whitening as a function of tensile strain for four different PVC/MBS blends. Rubber cavitation strains are indicated by the solid lines. From [31].

as the continuous line on the graph.

Within the limits of the range of particle sizes used in the experiments, the theoretical criterion proposed by the authors seems to be in a relatively good agreement with the experimental findings. The experimental findings indicate that the capacity of small particles (smaller than $150nm$) to cavitate at a given volumetric strain is actually less than predicted by the therory, i.e., the cavitation strength of small particles is somewhat higher than predicted. The general result, however, is that the cavitation strength of the particles seems indeed to be governed by the particle size.

Dijkstra, Van der Wal and Gaymans [29] performed experiments on Nylon-6 with particles of BR (poly(butadiene) rubber), EPDM (ethylene propylene copolymer rubber) and LDPE (low density polyethylene). The authors observed the changes in transpartency of the blends which occur when the particles cavitate and/or the matrix yield causes stress-whitening. In the case of particle cavitation, the incident light is scattered by means of the created internal free surface, and the transparency of the sample decreases. A laser beam was used as incident light and a photodiode was placed on the other side of the other side of the dumb-bell specimens to detect the transmitted light intensity. The blends were produced with a particle volume fraction of 23.5%. The weight-averaged sizes of the BR, EPDM and LDPE particles were 0.35,

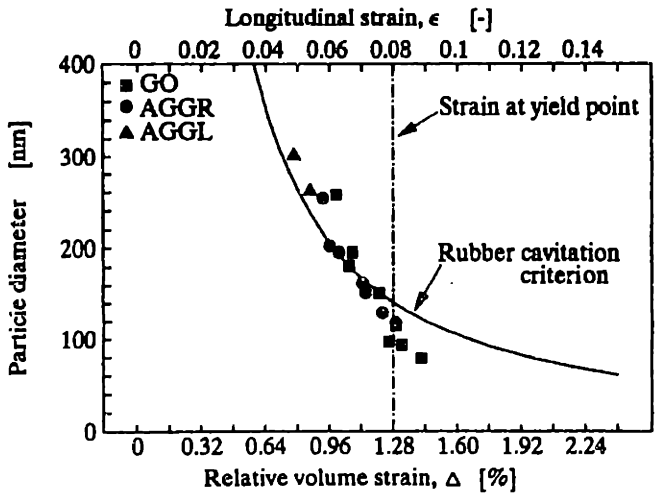

Figure 3-6: Relationship between the minimum particle diameter required for cavitation and the longitudinal strain ϵ or the volumetric strain Δ. The experimental data is obtained from analyses as shown in the plots of percentage whitening vs. strain. The continuous line is the theoretical result from equation 3.10. The material parameters used are described on page 52. From [31].

0.40 and $0.46\mu m$ respectively, which translates into inter-particle distances of 0.11, 0.12 and $0.14\mu m$ when Wu's formula for the interparticle distance is used [63]. All of the inter-particle distances are smaller than the critical inter-particle distance of $0.3\mu m$ identified by Wu. The macroscopic cavitation strengths, i.e. the macroscopically applied stress under which the particles in the blend were found to cavitate, were measured to be approximately $39MPa$ for BR, $48MPa$ for EPDM and $54MPa$ for LDPE at a strain rate of 0.001 per second. From the macroscopically applied stress the authors calculated the stresses acting in and around the particles. Together with the calculated thermal stresses due to the thermal expanion misfit between matrix and polymer, they obtained the values for the particle cavitation strength of $40.2MPa$ for particles of BR and $47.7MPa$ for those of LDPE. Unfortunately no value of the cavitation stress is given for the EPDM rubber particles.

When the results of Dijkstra et al. [29] are compared to the above theoretical criterion by Gent [39], the following results emerge for BR and LDPE. Gent's criterion predicts a value of 1 for the ratio of the cavitation stress divided by $2.5G$, where G is the shear modulus. For the experiments done by Dijkstra et al. [29] this ratio is

computed to be 0.04 for BR and 6.88 for LDPE particles [1]. This indicates that the criterion of Gent is not universally applicable. The authors indicate, however, that for their calculations they used properties from the published literature since they did not know the exact properties of the materials they used.

In another set of experiments Dijkstra, Van der Wal and Gaymans [29] studied blends of Nylon-6 and EPR (ethylene propylene rubber) under tension at varying strain rates. Dumb-bell shaped specimens with particle sizes of approximately 0.14, 0.25 and $0.32\mu m$ at fixed blending ratio of 20 wt% were prepared. Using Wu's formula for the inter-particle distance, it is found that under a volume fraction of 23.5% the particles used by Dijkstra et al. result in a inter-particle distances of 0.043, 0.077 and $0.10\mu m$ respectively, all of which are below the critical particle distance for Nylon-rubber blends identified by Wu [63]. The macroscopic cavitation strengths for these EPR particles were measured to be approximately $39MPa$ for $0.32\mu m$, $40MPa$ for $0.25\mu m$ and $53MPa$ for $0.14\mu m$ at the same strain rate as above. The trend of an increasing cavitation pressure with decreasing particle size is confirmed.

Dijkstra et al. [29] used transmission electron microscopy (TEM) to study blends of Nylon-6 with 15 vol% BR which were deformed under impact conditions with draw speeds of up to $1ms^{-1}$. The authors report that the micrographs of the deformed specimens show that voids are present only at the large particles, e.g., the particles of a size below $0.2\mu m$ have not cavitated. This finding seems to point toward a minimum size that a particle must exceed in order to undergo cavitation inside of a polymer blend.

Schwier, Argon and Cohen [12] performed tension tests on blends of Polystyrene (PS) matrices with very small Polybutadiene (PB) particles in order to observe the plastic behavior by crazing. The particle sizes ranged from 0.014 to $0.04\mu m$, and their volume fraction from 2.9% to 18%. The authors cast films with thicknesses ranging from 0.5 to $1.0mm$ out of which "dog bone" shaped specimens were cut out. The authors made a theoretical estimate of the residual stresses σ_{th} due to the thermal mismatch between particle and matrix. From Goodier [54] they obtained a

[1] For LDPE this would indicate a cavitation stress on the order of $17G$, which is not realistic.

stress concentration factor Ω for a spherical region of PB embedded in a surrounding medium having the average elastic properties of the overall composite. Using the thermal residual stresses and the stress concentration factor, the following expression for the the cavitation stress was developed:

$$\sigma_{cav,part}(PS/PB) = \sigma_{th} + [\sigma_\infty + 2(1 + \nu_{composite})(\sigma_m - \sigma_\infty)]\Omega \qquad (3.11)$$

where σ_m is the peak traction ahead of the cavitational process zone of a crazing polymer, and σ_∞ is the applied stress. In their calculations Schwier et al. used the following properties for the PS matrix: elastic modulus $E = 3.3GPa$, bulk modulus $K = 1.3GPa$ and Poisson's ratio $\nu = 0.33$. For the PB particle: $K = 1.8GPa$. They obtained $-60MPa$ the "intrinsic rubber cavitation strength" at room temperature and $-79MPa$ for a temperature of $-90°C$. Using Wu's formula, it is found that the inter-particle distances range from $6nm$ for the smallest particles at the highest volume fraction to $65nm$ for the largest particles at the lowest volume fraction. All inter-particle distances lied therefore below the critical value of $0.3\mu m$. In their calculations, Schwier et al. include the particle volume fraction, but not the particle size. The meaning of the "intrinsic cavitation strength" of the rubber particles is therefore somewhat limited. Since their experiments were performed using very small particles, the authors' findings confirm that very small particles do indeed require very high stresses to undergo cavitation.

Parker, Sue, Huang and Yee [44] examined stress-whitened zones in blends of polycarbonate (PC) and rubber under a pronounced triaxial stress state. Particles of approximately $600nm$ cavitated at significantly lower hydrostatic stress (tension) than particles of approximately $200nm$ size. The authors found that in blends with larger particles, the particle cavitation preceeded the shear yielding of the matrix by more tensile strain than was the case in blends with smaller particles.

Sultan and McGarry (after [32]) performed experiments on butadiene-co-acrylonitrile (CTBN) rubber particles suspended in a crosslinked epoxy matrix. When the blends contained particles with sizes of approximately $40nm$, the plastic deformation, frac-

ture toughness and mechanical properties of the blend in uniaxial and biaxial tension tests where observed to be very similar to that of the unmodified matrix material. When the particles were approximately $1200nm$ in diameter, the matrix yield occurred at lower stress levels, the fracture toughness increased dramatically, and stress-whitening of matrix material was observed, while scanning electron microscopy revealed cavity formation in particles. The results of Sultan et al. indicate that there exists a particle size below which the particles do not cavitate when the blend is subjected to uniaxial and biaxial tension. No information was available regarding the particle volume fraction and other conditions in the experiements.

Breuer, Haaf and Stabenow [20] examined methacrylate-butadiene-styrene (MBS) graft copolymer particles in PVC using transmission electron microscopy. At the chosen strain rate and particle volume fraction, the blends that contained particles with a diameter of $160nm$ or greater showed most particles cavitated. Blends with particle diameters of $80nm$ contained only very few cavities. The microscopy was done on the fractured specimens.

Morton, Cizmecioglu and Lhila [53] studied blends of PVC with polybutadiene particles (PB) ranging from 70 to $450nm$. A maximum in izod impact strength was observed when particles had a diameter in the range of 150 to $200nm$. The concentration of the rubber was indicated as 10%[2].

Oostenbrink et al. (1990, after [32]) studied a blend of Nylon-6 with maleic anhydride modified ethylene-co-propylene rubber (EPR-g-MA) and confirmed Wu's, Borggreve et al.'s discovery of a critical inter-particle distance. However, when the authors reduced the particle size to below $200nm$ (eventually down to $100nm$) the impact strength of the Nylon-6/EPR-g-MA blend decreased sharply with decresing particle size and approached that of unmodified semicrystalline Nylon-6. The decrease in toughening was attributed to the fact that the number of particles that cavitate decreases with the size of the particles. No information on the volume fractions and the conditions of the experiments is available.

Oshinski, Keskkula and Paul [56, 57] studied the toughening of Nylon-6 with

[2]The authors indicated "10 parts" as the concentration of the particles

particles made of tri-block co-polymers of the type styrene-(ethylene-co-butylene)-styrene (SEBS) and a maleic anhydride (MA) functionalized version of SEBS (SEBS-g-MA). By varying the composition of the particles, the authors controlled the particle sizes. The authors measured the Izod impact strength as a function of particle size for a fixed volume fraction of 80% Nylon and 20% rubber. It was found that when the particle size decreases below the optimal value of $250nm$, the impact toughness of the blend decreased. At particle sizes of $40nm$ the impact tougness had dropped by a factor of 5 from that at particle sizes of $250nm$. In all of these cases, the inter-particle distance was well below Wu's critical value of $300nm$. The reduced impact strength of the blends with the smaller particles seems to indicate that particles in these blends are less likely to cavitate, and hence the toughening mechanism of massive shear yielding of the matrix is somewhat prevented. In general, the authors state that particles made of a combination of SEBS and SEBS-g-MA were found to toughen the blend more than particles of SEBS-g-MA alone. At the maximum toughness of the blend the particles were $250nm$ in diameter and composed of 20% SEBS-g-MA and 80% SEBS. Unfortunately the authors have not made it clear whether the maximum toughness of the blend is due to the inter-particle distance at that particle volume fraction and size, or if it is due to the particle composition.

Wrotecki, Heim and Gaillard [38] studied blends of PMMA with butyl acrylate-co-styrene crosslinked copolymer (P(BA-co-St)) core-shell particles. The diameters of the soft cores of the particles ranged from 68 to $520nm$, the total diameter of the core-shell particles from 82 to $600nm$. The authors investigated the impact toughness of the blends at varying particle sizes. The observation that the blends with particles of $100nm$ or smaller diameters did not change the impact behavior of the matrix material was interpreted as indicating that the particles below this size did not cavitate.

In his 1992 paper [65], Wu reports that he observed a minimum particle size for the tougening of Nylon/rubber blends of $100nm$. Wu found the same minimum particle size for the toughening of PMMA.

3.3 Conclusion

Summarizing the above, the majority of authors reported a dependence of the particle cavitation strength on the particle size. The range of reported particle cavitation includes such high values as $-60MPa$ at room temperature and $-79MPa$ at $-90°C$ for particle sizes ranging from 0.014 to $0.04\mu m$ as reported by Schwier et al. [12], and such low values as the "cracking stress" of Gent and Lindley [39] which is on the order of a few MPa. A dependence of the cavitation strength on the type of rubber the particle is made of was pointed out by several authors.

Since our numerical simulations were intended to yield insight into the effects of particle cavitation on the toughening mechanisms in polymers, an appropriate range of cavitation strengths had to be chosen. It was decided to take the two values of $40MPa$ and $60MPa$ as useful cavitation strengths for our micromechanical model, as discussed in the next chapter.

Only the theoretical cavitation criterion of Gent and Lindley [39] and the experiments of Borggreve, Gaymans and Eichenwald [16] point toward a cavitation strength of particles that is independent of the particle size. The authors who proposed a cavitation criterion that includes the size of the particle are Ball [47] and Dompas and Goenickx [32]. The latter group's work includes a dependence of the cavitation strength on molecular parameters. Among the authors who observed that cavitation strength does depend on particle size and/or that a minimum particle size exists for cavitation to occur, are Dompas and Goenickx [31], Dijkstra, Van der Wal and Gaymans [29], Schwier, Argon and Cohen [12], Parker, Sue, Huang and Yee [44], Sultan and McGarry (after [32]), Breuer et al. [20], Morton et al. [53] and Oshinski et al. [56, 57]. For the polymer blends of PVC, PMMA and Nylon matrices with rubber particles, a universal range for the critical particle size of 100 - $200nm$ emerges from the experiments reviewed above. Below this size, particles are observed not to cavitate when inside a polymer matrix, which is in good agreement with the cavitation criteria of Ball [47] and Dompas et al. [31].

One issue that has not been addressed in this review is whether the assumption

of the spherical shape of the rubber particles is realistic. From the micrographs of particle-modified polymers that were presented in a number of publications, it can be seen that the particles are certainly not perfectly spherical in shape, but that for many of the blends it seems a reasonable approximation. Another open question is how the processing conditions or the composition of the rubber affect the properties of the rubber particles, i.e. whether they are a factor in the cavitation strength of the particles and hence in the toughening of the blend. The results that Oshinski, Keskkula and Paul [56] reported in their experiements do not answer the question whether the maximum in blend toughness they observed was due to the particle composition or simply to the inter-particle distance at that particle volume fraction and size.

Chapter 4

Micromechanical Model

In order to clarify some of the theories on the toughening of polymers that were reviewed in chapter 2, a more detailed understanding of the influence of the particle in the deformation response of the blended heterogenous polymer is required. Toward that end, this chapter discusses the development of micromechanical models which can explore the interactions between the particles and the matrix during various forms of loading conditions. The models are formulated using the finite element method. In particular, the effects of the following parameters are of interest in our study:

- the constitutive response of the matrix;
- the constitutive response of the particle; in particular, the cavitation strength;
- the level of triaxial loading condition.

The outcome of the simulations was hoped to bring some insight into the above parameters' influence on:

- onset, distribution, magnitudes and evolution of matrix plasticity;
- particle pressure and cavitation;
- macroscopic stress-strain response of the model;
- macroscopic strain evolution of the model.

A general introduction will first be presented below, including the concept of the unit cell. Then the boundary conditions, the constitutive laws for the materials and the loading conditions will be introduced. Finally, the methods of data reduction and the computer software and hardware that is used will be discussed.

4.1 Introduction

Several authors [68, 21, 5, 66, 45, 19, 28] have used finite element analysis to investigate the mechanical response of heterogeneous polymer systems. It is customary in such analyses to assume a periodic arrangement of the particles (e.g. simple cubic or body-centered cubic) inside of a matrix medium that is large compared to the size of the particles. The commonly followed approach is to define a representative volume element or 'unit cell' that each consists of a particle surrounded by matrix polymer. For the unit cell to fill space and to be easily 'stackable', it has to have a suitable shape, such as that of a cylinder with a hexagonal base. See figure 4-1 below for a schematic of the regular array and the basic unit cell.

The unit cell is assumed to be a model of the heterogeneous (macroscopic) polymer system, so that by studying its deformation response, an understanding of the response of the macroscopic continuum can be obtained. The stresses and strains that at the level of the unit cell are macroscopic, are in fact volume-averaged stresses and strains of the modeled macroscopic system. The deformation processes in the unit cell are thought of as the microscopic processes that on average are occurring in the macroscopic system.

One limitation of this approach is that the introduction of periodic boundary conditions, which capture the preassumed distribution of particles in the matrix, act to limit the inter-particle effects, such as plastic flow across boundaries or the overlap of stresses due to neighboring particles to be those of the specific arrangement of particles modelled. Other particle distributions will produce different inter-particle interactions which can be captured by alternative boundary conditions and/or multi-particle cell models.

Performing a finite element analysis of a three-dimensional array of unit cells requires considerable computational resources. It was therefore decided to follow the approach of, for example, Tvergaard [68] and to limit the analysis to a two-dimensional axisymmetric model. Consequently, the unit cell was simplified to a cylinder with a circular base, and the particle is a sphere at the center of the unit cell. The choice of such a geometry proved to be quite useful for modelling the anisotropy of a semi-crystalline matrix polymer, because some of the standard features in the employed finite element software could conveniently be made use of. Also, the axisymmetry of the model allowed to limit the analysis to a two-dimensional one-quarter section of the unit cell, as shown in figure 4-1.

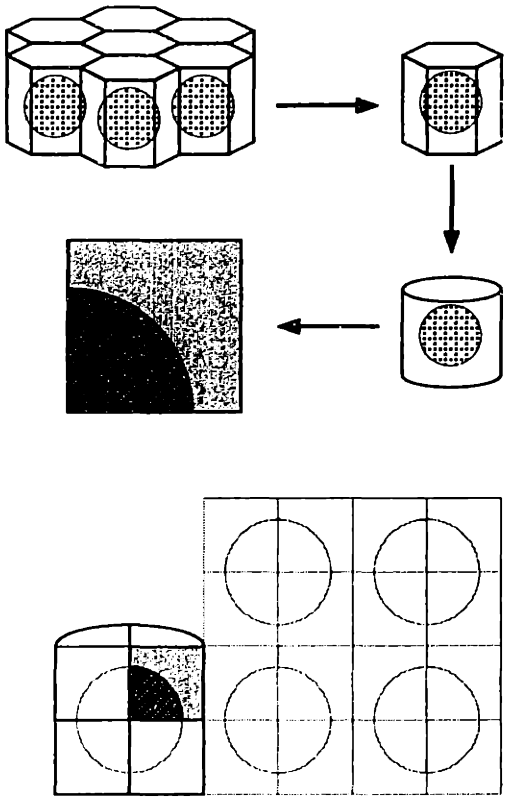

Figure 4-1: Development of the cylindrical unit cell from a regular array of particles inside a representative volume element whose shape is a cylinder with hexagonal base.

The formulation of the model and its implementation will be discussed in the sections below, which are:

- geometry of unit cell and particle;

- geometric boundary conditions;
- constituent material behaviors;
- loading conditions;
- thermal pre-loading;
- data reduction;
- software and hardware.

4.2 Geometry of Unit Cell and Particle

Figure 4-2 shows a schematic of the quarter-segment of the unit cell that was used in the finite element analysis.

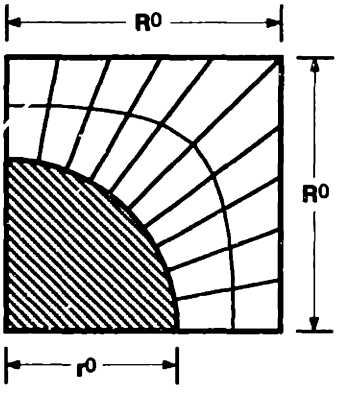

Figure 4-2: Schematic of the quarter-segment of the unit cell that was used in the finite element simulations. Shown are the initial radius R^0 of the unit cell, and the initial radius r^0 of the particle.

The dimensions of the undeformed unit cell's quarter segment are an initial height and width of R^0. The cylindrical unit cell is therefore of height and diameter $2R^0$. The particle or void has an initial radius r^0, and is located along the axis of the cylindrical unit cell. The particle volume fraction is then given by equation 4.1

$$\Phi = \frac{2}{3}\left(\frac{r^0}{R^0}\right)^3 \tag{4.1}$$

During the course of the deformation, the geometry and hence the volume fraction changes because of the different load-bearing capacities of matrix and particle or cavity and the different loading conditions. Small changes in the particle volume fraction are also due to the thermal misfit between particle and matrix, as discussed below.

Figure 4-3 shows the undeformed mesh for the particle volume fraction $\Phi = 25\%$, and figure 4-4 shows an example of a mesh that was deformed under tension. In order to illustrate the evolution of the unit cell, the deformed and undeformed meshes are superposed in figure 4-5. The deformed mesh is shown in a lighter grey tone, whereas the undeformed mesh is drawn in black.

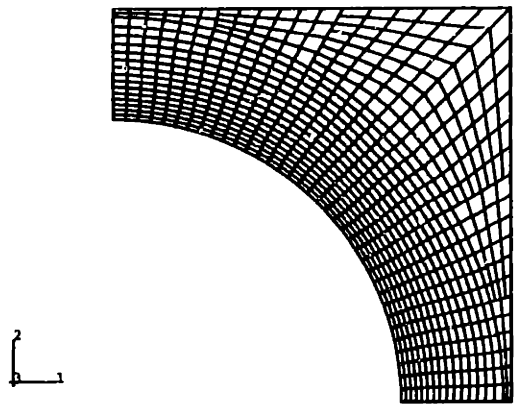

Figure 4-3: The undeformed mesh. $\Phi = 25\%$.

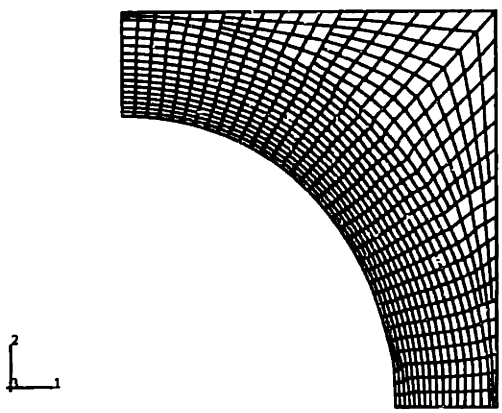

Figure 4-4: Example of a deformed mesh.

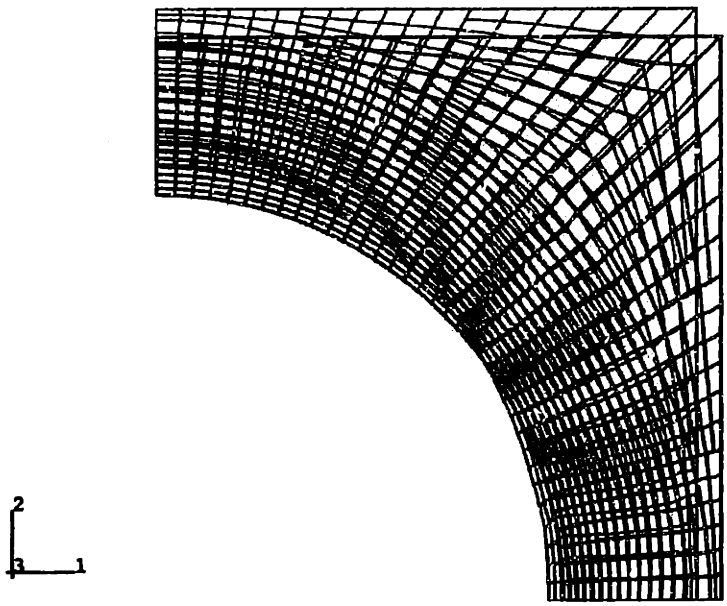

Figure 4-5: Example of an undeformed (black) and a deformed (grey) meshes. Φ = 25%. Note how the mesh boundaries match at the vertical mid-plane of symmetry (bottom) and the axis of symmetry (left).

4.3 Geometric Boundary Conditions

The geometric boundary conditions have to follow the axisymmetry of the unit cell. They prescribe the shape of the unit cell to remain that of a circular cylinder throughout the deformation. The top and bottom of the unit cell have to remain horizontal, and the lateral walls vertical. This is to guarantee the spatial consistency of the unit cell.

The boundary conditions of the quarter-segment of the unit cell are the parallel displacement of all nodes on a given segment of the unit cell boundary. As seen in figure 4-6, on the vertical boundary D, all nodes must follow the same displacement in the global 1-direction, whereas the displacements in the 2-direction are free except for the top-most and bottom-most nodes, which are part of two boundary segments and therefore must satisfy the requirements for both segments they are part of. On boundary C, all nodes must displace by the same amount in the 2-direction, with the exception of the left-most and right-most nodes. The displacements of the nodes on boundaries A and B are limited to be along the respective segments, i.e., the nodes on segment A can move in the 1-direction but not in the 2-direction, and the nodes on

segment B cannot move in the 1-direction. Referring back to figure 4-5 it can be seen

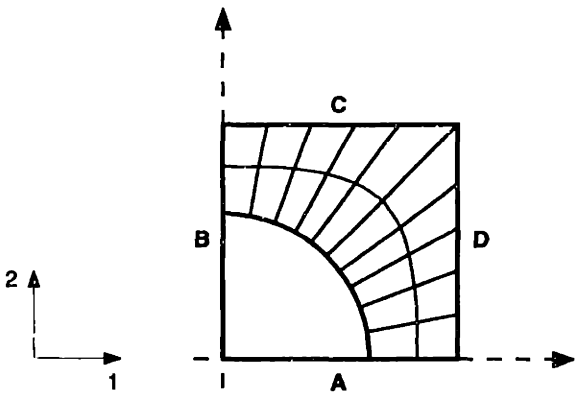

Figure 4-6: Boundary conditions of the 2-D quarter segment of the axiasymmetric unit cell.

how the axial boundary (left in the figure) and the bottom boundary are constrained in the 1- and 2-directions, respectively. The lateral boundary (on the right) moves freely in the 1-direction, but is constrained to remain vertical. The top boundary is constrained to remain horizontal, as it is displaced.

4.4 Material Behavior

The material models used in the simulations were intended to match the experimentally observed deformation behavior of two types of systems:

- Cases A & B[1] : rubber-toughened semi-crystalline Nylon-6 in which the interparticle distance ID is smaller than or equal to the critical value ID_{cr} as established by Wu [62]: $ID \leq ID_{cr}$;
- Cases C & D: rubber-toughened semi-crystalline Nylon-6 with $ID > ID_{cr}$, or any other rubber/polymer system where the matrix polymer is predominantly glassy and/or without significant orientation effects in its plastic response.

In cases A & B the plastic response of the matrix polymer is dominated by a preferentially crystallographically oriented material. In cases C & D its matrix plastic

[1]The 'numbering' of these cases is related to the schematic in figure 4-21 which will be discussed below.

response is dominated by the behavior of the isotropic bulk semi-crystalline material. Consequently the above cases translate into the following framework:

- Cases A & B: unit cells in which the matrix plasticity is anisotropic non-hardening;
- Cases C & D: unit cells in which the matrix plasticity is isotropic hardening.

Both the isotropic and anisotropic matrices were modeled using 710 eight-node isoparametric quadrilateral axisymmetric elements as provided in the HKS ABAQUS software under the name CAX8. A typical mesh is shown in figure 4-3. The rubber particle was modeled using a user-programmed element, as explained below.

4.4.1 The Isotropic Matrix

The isotropic matrix is intended as a model of the bulk isotropic semi-crystalline polymer. The material description is therefore chosen to be a linearly elastic isotropic solid with elastic modulus $E_m = 4.49GPa$ and Poisson's ratio $\nu_m = 0.33$. The plastic behavior of the material was modeled as an isotropic hardening solid after data obtained from G'Sell et al. [40]. Figure 4-7 shows a plot of yield stress as a function of strain for both G'Sell's data and the piecewise linear approximation used in the simulations. The initical yield stress σ^y is taken as $55MPa$. No rate dependencies were used.

4.4.2 The Anisotropic Matrix

The anisotropic matrix is thought of as a model for the response of either a semi-crystalline polymer whose plastic response is dominated by its crystalline phase, or any other polymer type that exhibits a high degree of anisotropy with easy shear on the slip system parallel to the particle/matrix interface.

Tzika [58] showed that it is possible to characterize the plastic anisotropy of the crystalline part of Nylon-6 using the Hill plasticity model [1]. In her development, she used the model of an intrinsically itotropic poly-crystalline material whose texture

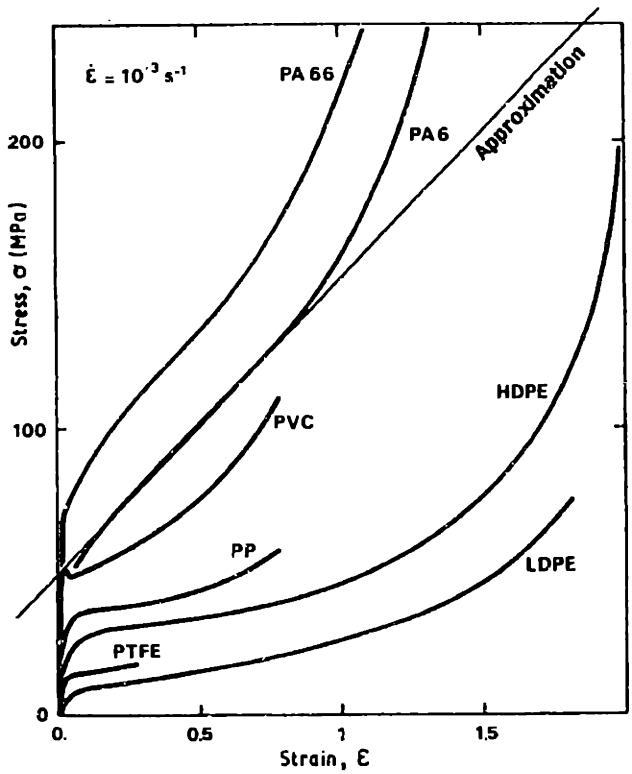

Figure 4-7: Stress-strain plots for various ploymers, among which Nylon-6 (PA6) and the linear approximation used in the simulations. G'Sell[40].

evolution is followed during uniaxial compression. The resulting transversely isotropic material properties matched the experimental data of Lin [51].

The Hill yield criterion [1] is expressed in terms of the corresponding potential function, which is obtained by weighting the individual stress components, as shown in equation 4.2:

$$f(\sigma) = \sqrt{F(\sigma_{22} - \sigma_{33})^2 + G(\sigma_{33} - \sigma_{11})^2 + H(\sigma_{11} - \sigma_{22})^2 + 2L\sigma_{23}^2 + 2M\sigma_{31}^2 + 2N\sigma_{12}^2} \tag{4.2}$$

where F, G, H, L, M and N are the weighting constants. They are obtained experimentally, by straining the specimens along the directions of anisotropy. The weighting constants are defined as indicated in equation 4.3:

$$\left\{\begin{array}{r} F = \frac{(\sigma^0)^2}{2}\left(\frac{1}{\bar{\sigma}_{22}^2}+\frac{1}{\bar{\sigma}_{33}^2}-\frac{1}{\bar{\sigma}_{11}^2}\right) = \frac{1}{2}\left(\frac{1}{H_{22}^2}+\frac{1}{H_{33}^2}-\frac{1}{H_{11}^2}\right) \\ G = \frac{(\sigma^0)^2}{2}\left(\frac{1}{\bar{\sigma}_{33}^2}+\frac{1}{\bar{\sigma}_{11}^2}-\frac{1}{\bar{\sigma}_{22}^2}\right) = \frac{1}{2}\left(\frac{1}{H_{33}^2}+\frac{1}{H_{11}^2}-\frac{1}{H_{22}^2}\right) \\ H = \frac{(\sigma^0)^2}{2}\left(\frac{1}{\bar{\sigma}_{11}^2}+\frac{1}{\bar{\sigma}_{22}^2}-\frac{1}{\bar{\sigma}_{33}^2}\right) = \frac{1}{2}\left(\frac{1}{H_{11}^2}+\frac{1}{H_{22}^2}-\frac{1}{H_{33}^2}\right) \\ L = \frac{2}{3}\left(\frac{\tau^0}{\bar{\sigma}_{23}}\right) = \frac{3}{2R_{23}^2} \\ M = \frac{2}{3}\left(\frac{\tau^0}{\bar{\sigma}_{13}}\right) = \frac{3}{2R_{13}^2} \\ N = \frac{2}{3}\left(\frac{\tau^0}{\bar{\sigma}_{12}}\right) = \frac{3}{2R_{12}^2} \end{array}\right\} \tag{4.3}$$

Each $\bar{\sigma}_{ij}$ is the measured yield stress value when σ_{ij} is applied as the only non-zero stress component. σ^0 is the reference yield stress, and τ^0, the reference yield stress in shear. They are related through:

$$\tau^0 = \frac{\sigma^0}{\sqrt{3}} \tag{4.4}$$

The Hill coefficients, or anisotropic yield stress ratios H_{ij}, are given in equation 4.5:

$$\left\{\begin{array}{lll} H_{11} = \frac{\bar{\sigma}_{11}}{\sigma^0} & H_{22} = \frac{\bar{\sigma}_{22}}{\sigma^0} & H_{33} = \frac{\bar{\sigma}_{33}}{\sigma^0} \\ H_{12} = \frac{\bar{\sigma}_{12}}{\sigma^0} & H_{13} = \frac{\bar{\sigma}_{13}}{\sigma^0} & H_{23} = \frac{\bar{\sigma}_{23}}{\sigma^0} \end{array}\right\} \tag{4.5}$$

The material model for the anisotropic matrix was implemented using the *POTENTIAL option in the definition of the matrix plasticity of the ABAQUS input deck (*PLASTIC). The Hill coefficients were taken from Tzika [58] as shown in equation 4.6:

$$\left\{\begin{array}{lll} H_{11} = 3.0 & H_{22} = 2.2 & H_{33} = 2.2 \\ H_{12} = 0.7 & H_{13} = 0.7 & H_{23} = 1.0 \end{array}\right\} \tag{4.6}$$

The equality between the coefficients for the in-plane normal deformations, H_{22} and H_{33}, as well as between the coefficients for shear on a plane normal to the 1-direction, H_{12} and H_{13}, indicate the transverse symmetry of the material. Issues regarding the limitations in the use of the Hill plasticity model are discussed below.

The anisotropy of the matrix plasticity is defined according to a local coordinate system, which is initially spherical, so that the local 1-direction corresponds to the radial direction, and the local 2-direction corresponds to the tangential direction in

the undeformed configuration. In the deformed configuration the local directions are averaged over the element boundary orientations.

Figures 4-9 and 4-10 show element 820 in the undeformed and the deformed configurations, respectively. Figure 4-8 shows the entire matrix mesh, and where the element 820 is located in it.

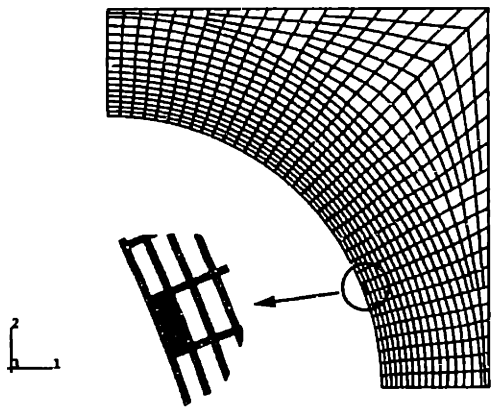

Figure 4-8: Schematic showing where in the matrix mesh the element 820 is located.

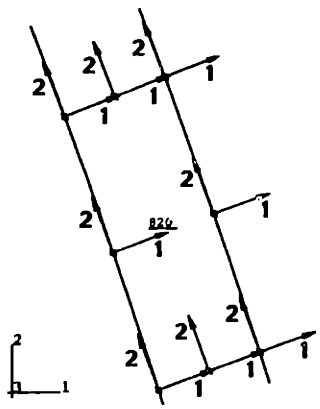

Figure 4-9: Element 820 in its undeformed configuration. Global and local directions.

The global 1- and 2-directions are indicated by the coordinate system in the lower left-hand corner of the three figures. The local directions are indicated by the arrows labeled "1" and "2" that emanate from each of the mesh nodes in figures 4-9 and 4-10. In both the local and the global coordinate systems, the 3-direction is normal to the plane of the paper.

As can be seen from the figures, the local directions initially follow a spherical arrangement, i.e., they are radial and tangential in figure 4-9 and co-incide with the

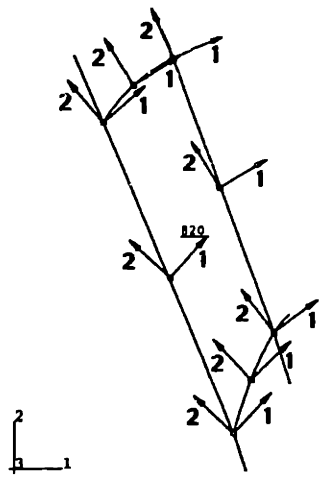

Figure 4-10: Element 820 in its deformed configuration. Global and local directions.

orientations of the element boundaries which have themselves been defined according to the spherical geometry of the model's particle/matrix interface. As the mesh and elements deform during the simulation, the local directions follow the orientation of the element boundaries, as seen in figure 4-10 where the local directions continue to be perpendicular to each other at each element node, but are found to be at an average direction relative to the element boundaries.

4.4.3 The Rubber Particle

There is general agreement in the literature [41, 37, 39, 44, 32] that the deviatoric stress within a rubber particle inside a polymer matrix is negligeable in the sense that it provides little influence on the behavior of the composite; i.e., the stress state is nearly perfectly hydrostatic. This is due to the very low shear modulus of the rubber particle relative to that of the matrix, and relative to its own bulk modulus. In preliminary studies this was confirmed using the "8-chain" constitutive model for rubber as proposed by Arruda and Boyce [14].

Guild, Young and Lovell [42] performed a two-dimensional finite element analysis of a single particle/matrix system modelled after rubber in PMMA. Their choice of finite element mesh and the types of elements was similar to those in the present work. However, their analysis was limited to isotropic elastic materials, and the

deformation process was simple tension. They confirmed that the shear stresses in the rubber particle are negligeable for the Poisson's ratio of the rubber ν_r ranging from 0.490 to 0.49992, and the particle volume fraction from 0% to 30%.

Similarly, Dijkstra and Ten Bolscher [28] reported that the stress state inside a particle inclusion shows little sensitivity to a variation of the shear modulus if the inclusion's Poisson's ratio is close to 0.5. The result was obtained from an analytical solution to a particle inside an infinite cylindrical medium under simple tension.

The rubber particle was therefore modeled as a compressible fluid cavity. It is characterized by a constant hydrostatic stress throughout the cavity and the absence of shear stresses. The tractions along the particle-matrix interface are constant everywhere and normal to the interface.

The hydrostatic stress, or pressure[2], is a linear function of the volumetric strain Ψ and the bulk modulus K:

$$P = -K\Psi = -K\left(\frac{V}{V_0} - 1\right) \tag{4.7}$$

where V_0 is the volume of the undeformed and V is the volume of the deformed rubber particle.

In order to simulate a particle cavitation event, a constitutive model of the behavior of the rubber up to a modeled cavitation event needed to be developed and then implemented using a "user element". The details of this implementation are discussed in appendix B.

The idea of the particle cavitation model is based on the observations and theoretical developments presented in chapter 3 "Particle Cavitation Criteria". When the particle reaches a critical volumetric strain Ψ_{cr} and the stress state inside the particle reaches a critical level, P_{cr}, then the particle is assumed to fail in a more-or-less catastrophic fashion. During the cavitation event, the load-bearing capacity of the particle drops to zero, which causes the tractions at the particle-matrix interface to

[2]Hydrostatic stress σ^h and pressure P are in fact defined with opposite signs, i.e. $\sigma^h = -P$. The sign convention is not of great importance, since the stress state of the particle in the blend is that of hydrostatic tension because of the macroscopically applied tensile stress state.

vanish.[3]

One way to implement this is to drop the bulk modulus K of the particle to zero when the criterion for cavitation is satisfied. This is shown in equation 4.8,

$$P = \begin{cases} -K\Psi & \text{if } \Psi < \Psi_{cr} \\ 0 & \text{if } \Psi \geq \Psi_{cr} \end{cases} \tag{4.8}$$

and schematically shown in figure 4-11:

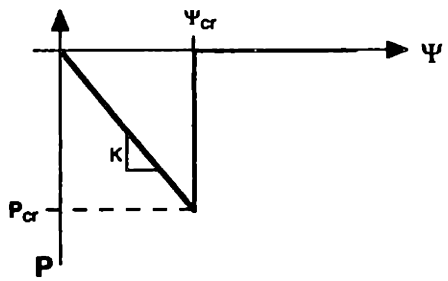

Figure 4-11: Schematic of the simple cavitation implementation. The pressure P is reduced to zero when the volumetric strain Ψ reaches a critical value Ψ_{cr}.

This method proved to be useful for the simulations in which the unit cell was subjected to low levels of the triaxial loading condition Σ. In these cases the finite element software successfully found displacement fields that satisfied the model across the dramatic change of the disappearing tractions at the particle-matrix interface.

In simulations with higher levels of triaxiality, the sudden drop of the bulk modulus proved to be too much of a discontinuity for the simulation to continue across the cavitation event. Therefore a force-relaxation algorithm needed to be developed and implemented, in which the tractions are decreased to zero over a finite increment $\Delta\varepsilon_{zz,cav}$ in the axial displacement of the unit cell. Equation 4.9 and the schematic in

[3]In reality the process of rubber failure is quite complex, involving a mix of tearing and rupturing with considerable dynamic effects.

figure 4-12 illustrate the sequence of events and the corresponding parameters.

$$P = \begin{cases} -K\Psi & \text{if } \Psi < \Psi_{cr} \\ -K\Psi\left(\frac{\varepsilon_{zz,cav}-\varepsilon_{zz}}{\Delta\varepsilon_{zz,cav}}+1\right) & \text{if } \Psi \geq \Psi_{cr} \text{ and } \varepsilon_{zz} < (\varepsilon_{zz,cav}+\Delta\varepsilon_{zz,cav}) \\ 0 & \text{if } \Psi \geq \Psi_{cr} \text{ and } \varepsilon_{zz} \geq (\varepsilon_{zz,cav}+\Delta\varepsilon_{zz,cav}) \end{cases} \tag{4.9}$$

Before the volumetric strain of the particle Ψ reaches the critical value Ψ_{cr}, the particle pressure is simply the negative product of the bulk modulus K and the current volumetric strain Ψ. When Ψ reaches the critical value Ψ_{cr} the current macroscopic axial strain $\varepsilon_{zz,cav}$ is recorded, and subsequently the pressure P is scaled down linearly over an interval $\Delta\varepsilon_{zz}$. In other words, for axial strains between $\varepsilon_{zz,cav}$ and $(\varepsilon_{zz,cav} + \Delta\varepsilon_{zz,var})$, the particle pressure is a function of the current Ψ and ε_{zz}. Ψ may be evolving during $\varepsilon_{zz,cav} \leq \varepsilon_{zz} \leq (\varepsilon_{zz,cav} + \Delta\varepsilon_{cav}$

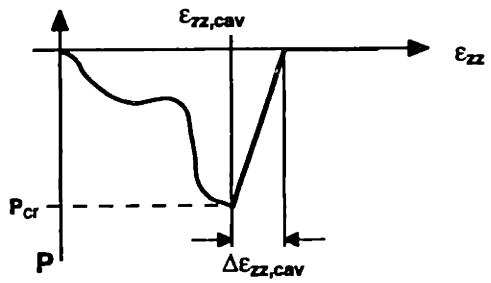

Figure 4-12: Schematic of the force-relaxation algorithm for particle cavitation. Once the volumetric strain Ψ has reached a critical value Ψ_{cr}, the pressure is reduced to zero over a non-zero interval of ε_{zz}.

The implementation was successful and the details are discussed in appendix B.

Relative to the particle consitutive model, the undertaken simulations can be categorized in the following way[4]:

- Cases A & C: unit cells with solid (non-cavitating) particles;
- Cases B & D: unit cells with cavities.

A cavitation event takes a simulation from either case A to case B, or from case C to case D. As will be discussed below, this categorization is well-justified when

[4]Again, this categorization is in regards to figure 4-21 on page 94, which is discussed below.

considering the matrix plasticity and stress-strain responses of the relevant unit cells. Depending on the chosen particle cavitation strength, the transition from cases A or C to cases B or D occurs at different levels of macroscopic axial strain ε_{zz}.

4.5 Loading Conditions

After describing the geometry, symmetry and material properties of the cell, the model is ready for loading. The loading consists of two basic steps: (i) the initial residual stresses due to cooling from melting temperature to useage temperature are simulated by a thermal contraction, and (ii) the macroscopic loading conditions, which consist of uniaxial tension accomplished by axially displacing the top boundary, with varying levels of superposed lateral pressure to simulate a range in triaxiality. The thermal contraction step is discussed in section 4.5.1 and the macroscopic loading is discussed in section 4.5.2.

4.5.1 Thermal Contraction

In this section it is explained how the matrix polymer's thermal response is modelled after that of semi-crystalline Nylon-6, where the processing temperature lies above the melting temperature T_m, and the useage temperature T_r lies below the glass-transition temperature T_g [53, 60][5].

Problem Description

Many rubber particle/polymer matrix blends are produced by hot extrusion where the mixed components are heated to a temperature that lies above the matrix polymer's glass-transition temperature T_g, and in the case of crystalline or semi-crystalline polymers, above the melting temperature T_m. Then a blending process takes place in the extruder after which the blend is cooled down to room temperature T_r. The term "room temperature" is used synonymous with the temperature at which the blend is

[5]The crystallization part is relevant only for matrix polymers whose useage temperature T_r lies below the crystallization temperature T_m.

used in its final application or at which experiments were performed, i.e. the usage temperature.

Due to the different thermal expansion coefficients of the rubber and the matrix polymer, and, in the case of crystalline or semi-crystalline polymers, due to the change in volume during the crystallization phase-transformation of the matrix polymer, particle-matrix blends exhibit residual thermal stresses at the end of the blending and cooling process. In order to introduce these residual stresses into the model, it is subjected to a cooling step of magnitude ΔT before the deformation begins, thereby generating a state of stress as assumed to exist in real systems. The magnitude of ΔT has to be estimated.

No in-situ measurements of the misfit stresses have been reported in the published literature. Those authors who take into account residual stresses depend on calculations in conjunction with measurements of the thermal and mechanical properties the pure components in either bulk or thin films.

The underlying assumption for the calculations is that the bonding between particle and matrix is sufficiently good to sustain the traction forces at the particle/matrix interface resulting from the residual stresses. The assumption of compatibility between particle and matrix is necessary for computation of the stresses. From a mechanics point of view, it is the difference between the materials' free thermal expansion characteristics and compatibility requirement that results in residual stresses.

In the calculations it is necessary to distinguish between (i) the stresses due to the crystallization volume change[6], (ii) the thermal stresses due to cooling from the matrix polymer's melting temperature T_m to its glass-transition temperature T_g, and (iii) the thermal stresses due to cooling from T_g to room temperature T_r (or service temperature). Figure 4-13 shows the volume as a function of temperature for the modelled material.

Thermal strains above T_m are generally ignored under the assumption that the matrix polymer exhibits so little viscosity in its liquid state that the stress relaxation above T_m is very fast compared to its cooling rate. Table 4.1 shows the thermal

[6]only in the case of semi-crystalline polymers

expansion coefficients of Nylon above and below T_g. The elastic properties of Nylon also change with temperature, but can for our purposes be taken as approximately constant within each domain. The elastic properties of the rubber are assumed as approximately constant for the range of T_r to T_m of the matrix polymer. The thermal expansion coefficient of the rubber particle is assumed to be constant, as seen from figure 4-14.

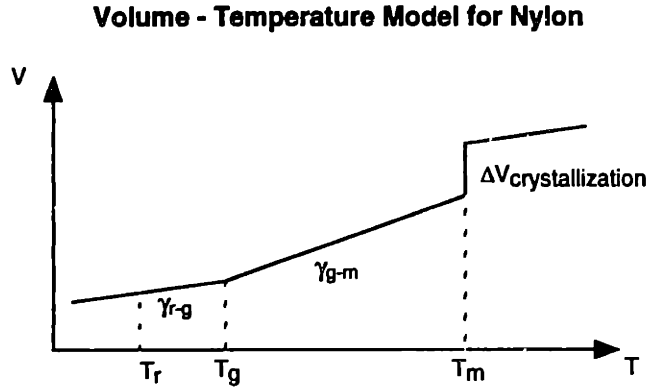

Figure 4-13: Volume as a function of temperature in Nylon. After[60, 55]

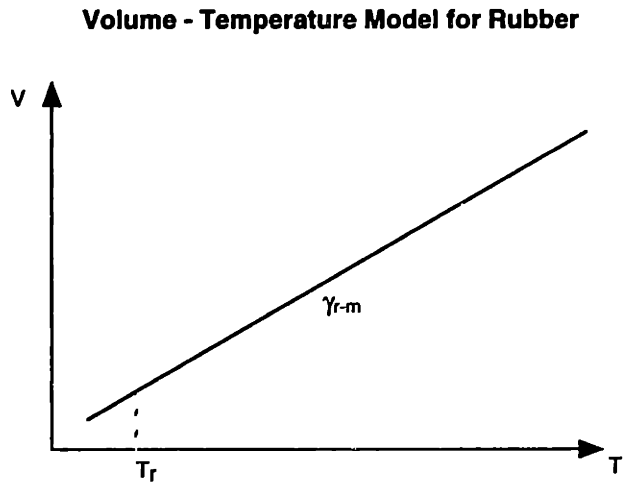

Figure 4-14: Volume as a function of temperature in rubber. After[50]

To compute the residual stresses we considered the elastic solution for a sphere surrounded by a concentric shell of infinite radius. Following the development of Nguyen and Boyce [55, 18], the sphere and shell were subjected to volumetric strains corresponding to crystallization and cooling. The stresses required to satisfy compatibility along the particle/matrix interface are the residual stresses to be calculated.

Equation 4.10 is taken from Nguyen and Boyce [55] and gives the resulting stress in terms of the thermal expansion coefficients, elastic moduli and Poisson's ratios of particle and matrix, as well as the crystallization volume change of the matrix.

$$\sigma = \frac{K_p(\gamma_{m,a} - \gamma_p)(T_g - T_m)}{1 + \frac{K_p}{K_{m,a}(1-c)}\frac{1+\nu_{m,a}}{2(1-2\nu_{m,a})} + c} + \frac{K_p(\gamma_{m,b} - \gamma_p)(T_r - T_g)}{1 + \frac{K_p}{K_{m,b}(1-c)}\frac{1+\nu_{m,b}}{2(1-2\nu_{m,b})} + c} \tag{4.10}$$

The subscript a identifies the properties that are valid in the temperature range from T_m to T_g, and the subscript b identifies the properties for the range from T_g to T_r. K_p is the bulk modulus of the particle, K_m the bulk modulus of the matrix, c the particle volume fraction, and ν_m the Poisson's ratio of the matrix material.

Dijkstra, Van Der Wal and Gaymans [29] made the assumption that the stress relaxation above T_g is so rapid that the residual stress can be calculated for the range from T_g to T_r only. Their calculation therefore reduced to:

$$\sigma_{thermal} = 3K_{part}\Delta T(\alpha_{part} - \alpha_{matrix}) \tag{4.11}$$

The temperature difference considered is $\Delta T = T_r - T_g = -40°K$. Using data from the published literature [29], they obtained the following results for the residual stresses:

$\sigma_{thermal}$ (Nylon-6 / BR) = 20.1 MPa

$\sigma_{thermal}$ (Nylon-6 / LDPE) = 15.5 MPa

It seems, however, that Dijkstra et al. based their assumption of complete relaxation above T_g on the view that in that regime, the mechanical response of Nylon is dominated by its amorphous part. Referring to the matrix properties presented below (table 4.1), it appears that the mechanical response of the Nylon's crystalline part cannot be ignored. The crystalline domains, however, are not expected to undergo any significant amount of stress relaxation, so that the thermal stresses are expected to be higher than those proposed by Dijkastra et al. Another source of confusion may be the choice of temperatures to base the computation of thermal stresses on. Dijkstra et al. chose the glass-transition temperature to be $T_g = 60°C$. Other sources

[55, 60] indicate other values.

Solution and Results

The mechanical properties for both rubber particle and matrix polymer were assumed to be linearly isotropic, and were taken from [60, 50] as listed in table 4.1. The data for the crystallization volume change, the temperatures and the thermal expansion coefficients of the rubber and the matrix polymer were taken from [60] and are also listed in Table 4.1. At T_g the elastic modulus of Nylon increases by a factor of 8, its Poisson's ratio drops from 0.46 to 0.33, and the bulk modulus doubles. This is due to the now reduced mobility of the polymer chains in the amorphous part of the Nylon, caused by the transformation of the rubbery regions into glassy regions.

Properties of Nylon			
Property	Nylon below T_g	Nylon above T_g	Rubber
Volumetric thermal expansion coefficient (1/deg K)	0.00027	0.00042	0.00075
Poisson's ratio	0.33	0.46	0.50
Bulk modulus (MPa)	4400	2200	2000
Elastic Modulus (MPa)	4488	528	n / a

Table 4.1: Properties of Nylon in the temperatures regimes above and below T_g. Properties of rubber. From[60, 50]

The volumetric strain of the Nylon due to the crystallization phase transformation was 0.02 - 0.03. The volume fraction of the crystalline Nylon was assumed to be 50%. The relevant temperatures are $T_r = 20°C$, $T_g = 40°C$ and $T_m = 220°C$. Note that the crystallization volume change of the matrix polymer results in a compressive stress state in the particle, whereas the effect of the cooling is a tensile stress state. The boundary conditions during the cooling were the same as the geometric boundary conditions discussed above.

Some difficulties were encountered when the computation of the misfit stresses was attempted in three separate steps for the crystallization and cooling. Therefore it was decided to compute an "effective ΔT" that generates the same stress state in the particle within a single cooling step as the particle would experience after the

Residual Stresses					
Case	Vol. strain of crystallization	Stress due to cooling from T_m to T_g	Stress due to cooling from T_g to T_r	Total stress in particle	Effective ΔT
1	0	-12.78	-10.16	-22.94	-45.15
2	-0.02	-8.48	-10.16	-18.64	-36.68
3	-0.03	-6.33	-10.16	-16.49	-32.45

Table 4.2: Residual stresses due to cooling and matrix crystallization.

succession of matrix crystallization, cooling from T_m to T_g and cooling from T_g to T_r. This effective ΔT was computed using the properties of the matrix polymer between T_r and T_g. The effective ΔT is listed in the last column of table 4.2 for the range of considered temperatures and for three levels of crystallization volume change.

The results for the residual stresses in the case of a matrix with isotropic thermal properties are listed in table 4.2. The total stress in the particle (column 5) is the sum of the stresses due to matrix crystallization, cooling from T_m to T_g, and cooling from T_g to T_r, respectively.

Case 1 with of zero crystallization volume change corresponds to the case where the thermal stresses are thought to be generated only by the strains due to thermal contraction from T_m to T_r. In cases 2 and 3 the crystallization volume change is taken into account for the determination of the residual stresses. It is to be noted that the residual stresses in both the isotropic and anisotropic unit cells are the same because the matrix does not yield under the residual stresses.

Because of the fact that the simulations were done using a spherical particle surrounded by the cylindrical unit cell with circular base instead of two concentric shells/spheres as in the theoretical computations, the amount of cooling needed to be adjusted so that in this geometry and for different volume fractions the negative pressure experienced by the particle at the end of the cooling step corresponds to that caused by the computed effective ΔT.

Implementation The thermal response of the matrix polymer was modeled using standard options of the ABAQUS finite element software by specifying the mate-

rial's linear thermal expansion coefficient in the *EXPANSION option of the *SOLID SECTION part of the "input deck"[7]. For more details see Appendix B.

The particle is modeled as a fluid cavity with temperature-independent bulk elastic properties. Therefore the thermal strain can be simulated by reducing the reference volume of the particle with the decreasing temperature. The constitutive equation for the fluid cavity is then:

$$P = -K\left(\frac{V}{V_0'} - 1\right) \tag{4.12}$$

The current reference volume V_0' changes with temperature as

$$V_0' = V_0\left(1 + \alpha a \Delta T\right)^3 \tag{4.13}$$

In the algorithm of the user subroutine for the particle the current reference volume V_0' is first computed according to equation 4.13. Then the elastic response of the particle is determined by use of equation 4.12 using the current reference volume V_0'.

4.5.2 Macroscopic Loading Conditions

Uniaxial Tension

The loading condition of uniaxial tension in the axial or z-direction is achieved by displacing the top boundary of the unit cell in the z-direction. Because the geometric boundary conditions (section 4.3) constrain the unit cell's bottom boundary to remain undisplaced in the z-direction, a z-displacement of the unit cell's top results in a state of simple tension. Figure 4-15 shows a schematic of the unit cell with its top boundary being displaced.

Triaxial Loading

Whereas the geometric boundary conditions in section 4.3 are there to maintain the geometric integrity of the unit cell, the loading conditions are intended to reproduce the stress state that exists in the vicinity of a crack or notch tip, i.e., to capture the

[7] i.e., the input code of the finite element software.

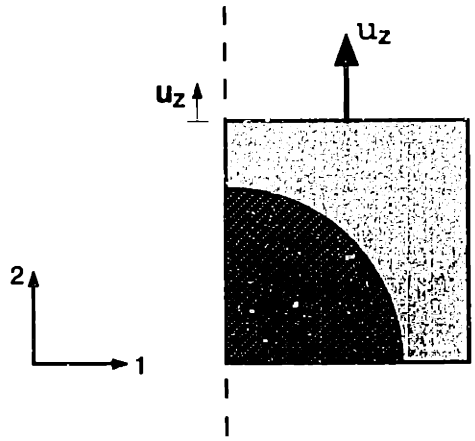

Figure 4-15: Schematic of the unit cell subjected to simple tension.

extreme conditions of high strain rates and notch effects in a simple test.

Problem Description Most data on the fracture behavior of polymers in the published literature has been measured under impact loading conditions, such as in a notched Izod impact test[8]. The stress state at the tip of a notch (or crack) has been described by McClintock, Johnson, Rice and others [48, 3, 61] in the context of elastic-plastic fracture analysis. Li, Li and Yee [52] experimentally confirmed the validity of slip line theory in the vicinity of a semi-circular notch in rubber-modified epoxy.

The slip line theory generally assumes plane strain conditions. The region of extensive plastic deformation in front of the advancing crack is divided into a "root" and a "core" region. The size of the root region in the case of a fully rounded crack is described by Johnson and Rice [48] as being on the order of $\frac{\sigma_0}{E}$ "times the maxiumum extent of the plastic zone", where σ_0 is the tensile yield stress and E is the elastic modulus. If the rounded crack's opening equals some δ_t then the distance over which the root region extends ahead of the crack tip is approximately $1.9\delta_t$. Figure 4-16

[8]The motivation for this choice seems to lie in the reproduceablility of the results and the simple interpretation of the results in terms of energy dissipation. The introduction of a notch rather than a crack is a way to avoid potential errors that could prevent the results of different experiments from being compared with eachother, all the while the notch is a reasonable approximation of a crack. From conversations with Professor Ali Argon.

shows the geometry of Johnson and Rice's version of the crack tip region. Note that region "D" is the root region and "B" is the core region.

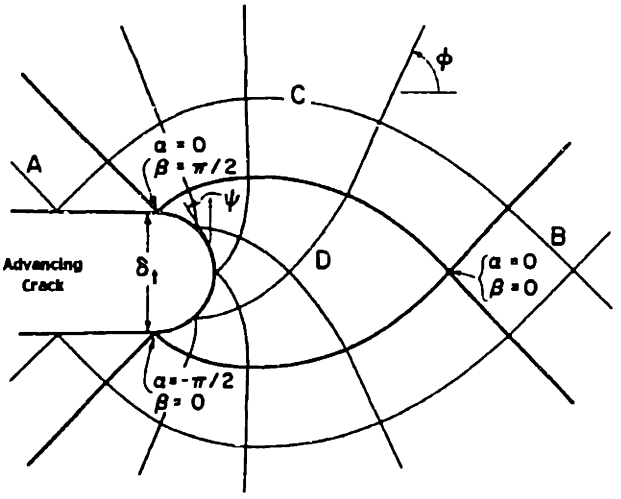

Figure 4-16: Blunted crack tip and surrounding flow field, after[48].

McClintock [3] assumes a slightly different shape of the notch as shown in figure 4-17. The expressions for the stress state in the core region and the root region of the

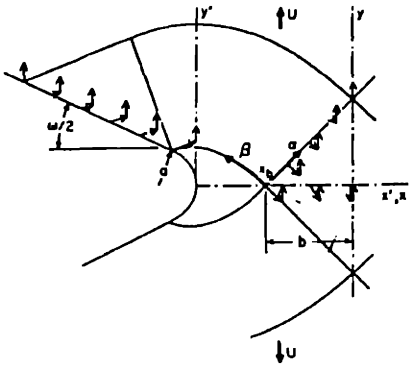

Figure 4-17: Flow field for a blunted notch, after[3].

advancing crack are given in equations 4.14 and 4.15 respectively [3].

$$\sigma^{core}_{xx,yy,zz} = 2k\left[\left(0,1,\frac{1}{2}\right) + \frac{\pi}{2} - \frac{\omega}{2}\right] \tag{4.14}$$

$$\sigma^{root}_{xx,yy,zz} = 2k\left[\left(0,1,\frac{1}{2}\right) + \ln\left(1 + \frac{x'}{a}\right)\right] \tag{4.15}$$

where k is the yield strength in shear, $\frac{\omega}{2}$ is the semi-angle of the crack opening, a is the radius of the rounded crack tip and x' is the distance from the crack tip in the plane of the advancing crack[9].

Solution In order to characterize the stress state in the vicinity of a crack or notch tip by means of a single parameter, a 'triaxiality ratio' Σ is defined as the ratio of the hydrostatic stress and the von Mises equivalent stres. For the loading condition of tension with a superposed lateral pressure, the triaxiality ratio is given by equation 4.16.

$$\Sigma = \frac{\sigma_{zz} + 2\sigma_{rr}}{3\left(\sigma_{zz} - \sigma_{rr}\right)} \tag{4.16}$$

As an example, when it is desired to subject the unit cell to a state of simple tension, the laterally applied stress σ_{rr} is zero. The corresponding triaxiality ratio Σ is 0.33. A loading condition with a triaxiality $\Sigma = 1.33$ corresponds to a case where the laterally applied stress σ_{rr} is one-half the axially applied stress σ_{zz}.

The stress state close to a crack or notch tip according to McClintock [3] (equations 4.15 and 4.14) translates into the values of the triaxiality ratio Σ as shown in figure 4-19 for the root region and figure 4-18 for the core region. For the core region the triaxiality of the stress state is found to increase with decreasing notch opening angle ω. For a fully closed notch ($\omega = 0$) the triaxiality ratio in the core region is found to be 2.4.

In our simulations, the triaxiality was varied from $\Sigma = 0$ for simple tension to $\Sigma = 2.33$ for a high-triaxiality state of stress which is comparable to that of fully closed notch in the analysis of McClintock[10].

---

[9] In fact, a rather complete theory exists on the conditions of crack propagation and fracture in ductile materials, even though the applicability of the theory is limited to certain materials, in particular those materials in which cavities are pre-existing. According to this theory, the crack is expected to propagate if the plastic strain at the crack tip exceeds a certain critical value; i.e. a critical combination of stresses and strains is required. The plastic strain at the crack tip is measured through the parameter of the crack tip opening displacement, or equivalently is expressed in the form of the J-integral.

[10] In terms of the schematic in figure 4-21 on page 94 the variation of the triaxiality Σ is thought of as occurring within each sector A, B, C or D.

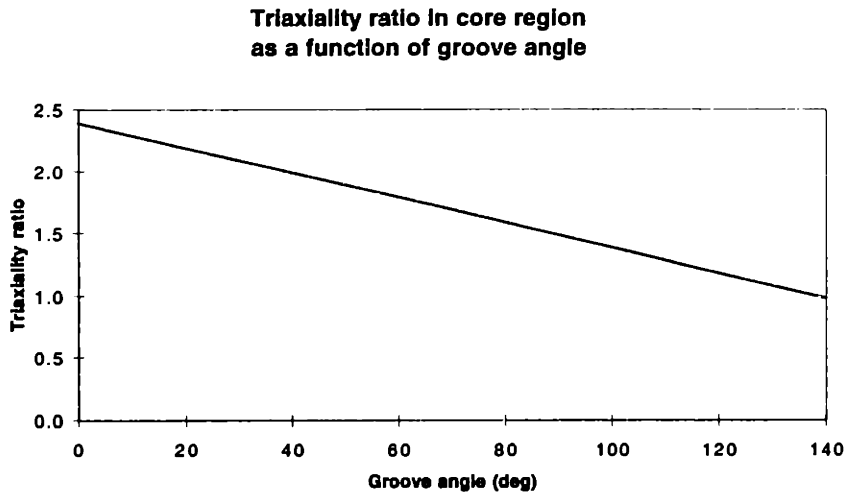

Figure 4-18: Triaxiality ratio in core region as function of groove angle, after [48].

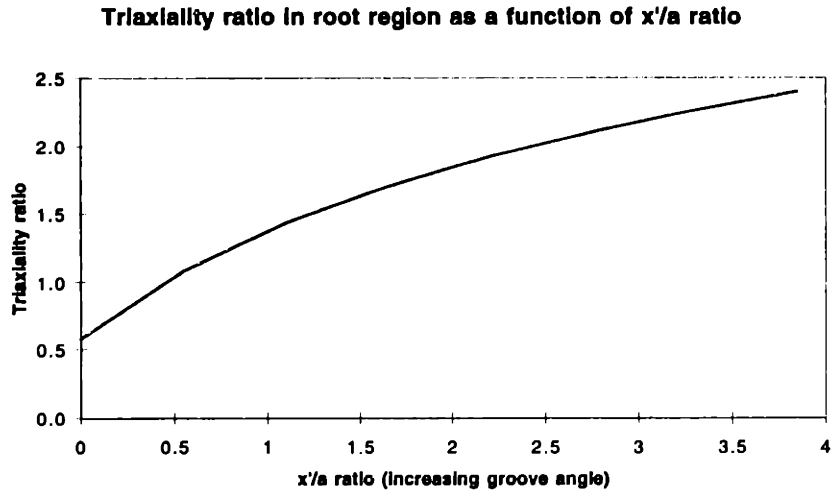

Figure 4-19: Triaxiality ratio in root region as function of x'/a, after [48].

Implementation The simulations are displacement-controlled, i.e. the evolution of the displacement at the top of the unit cell is prescribed by the macroscopic axial displacement u_z^{top}. In order to generate the desired stress state in the unit cell, however, it is necessary to displace the lateral boundary by the correct amount u_r^{lat}. Since the mechanical response of the unit cell cannot be known ahead of time, it is not possible to know the displacement history of both the top and the lateral boundary in advance. The problem was solved with the following procedure.

For a given lateral displacement of the unit cell's lateral boundary, u_r^{lat}, the macroscopic axial true stress σ_{zz} can be computed by dividing the current total axial reaction

force F_z^{top} by the current cross-sectional area of the unit cell (boundary segment C of figure 4-6), as shown in equation 4.17:

$$\sigma_{zz} = \frac{F_z^{top}}{\pi(R^0 + u_r^{lat})^2} \tag{4.17}$$

Figure 4-20 shows a schematic of the unit cell subjected to axial tension and a laterally applied distributed load. To generate a desired macroscopic triaxial stress state in

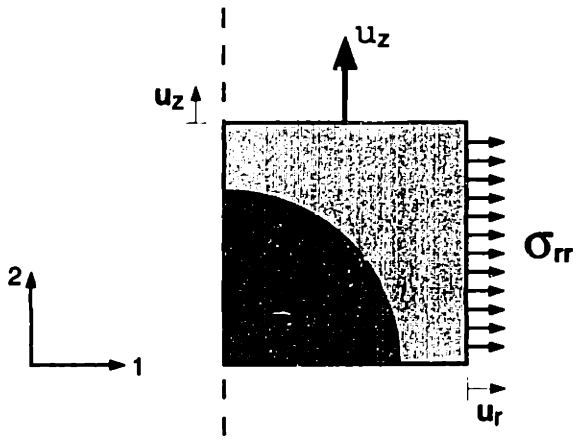

Figure 4-20: Schematic of the unit cell under triaxial loading: subjected to axial tension by means of displacement u_z of the top boundary, and to a laterally applied distributed load σ_{rr}.

the unit cell, an appropriate stress σ_{rr} has to be applied to the lateral boundary of the unit cell (boundary segment D in figure 4-6). Equation 4.16 can be rewritten into an expression that expresses σ_{rr} as a function of Σ and σ_{zz} (equation 4.18):

$$\sigma_{rr} = \sigma_{zz}\frac{3\Sigma - 1}{3\Sigma + 2} \tag{4.18}$$

The laterally applied load is computed inside of a user subroutine UEL (UEL2) and passed back to the finite element software through a DLOAD subroutine in order to be applied as a distributed load on the element boundaries along the lateral boundary of the unit cell. See appendix B for details.

4.6 Data Reduction

The finite element calculations yielded the following data relative to the unit cell and particle:

- axial displacement of the top boundary u_z^{top};
- radial displacement of the lateral boundary u_r^{lat};
- axial reaction force at the top boundary F_z^{top};
- particle pressure P;
- particle volume V_p.

The data was reduced using the following relations. Equation 4.17 gives the expression for the axial true strain σ_{zz} as function of F_z^{top} and u_r^{lat}. The macroscopic axial true strain ε_{zz} or ε_2 was obtained using equation 4.19:

$$\varepsilon_{zz} = \ln \frac{R^{0\prime} + u_z^{top}}{R^0} \tag{4.19}$$

where $R^{0\prime}$ is the radius of the unit cell at the end of the cooling step. The macroscopic radial true strain ε_{rr} or ε_1 was computed as in equation 4.20:

$$\varepsilon_{rr} = \ln \left(\frac{R^{0\prime} + u_r^{lat}}{R^{0\prime}} \right) \tag{4.20}$$

The volumetric strain of the unit cell, Ψ_c, is given in equation 4.21:

$$\Psi_c = \frac{(R^{0\prime} + u_r^{lat})^2 (R^{0\prime} + u_z^{top})}{(R^{0\prime})^3} - 1 \tag{4.21}$$

The volumetric strain of the particle, Ψ_p, is computed from the initial particle volume V_p^0 and the current particle volume V_p:

$$\Psi_p = \frac{V_p}{V_p^0} - 1 \tag{4.22}$$

All macroscopic strains ε_{zz} and ε_{rr} are expressed relative to the geometry at the end of the cooling step, i.e., the strains due to the thermal misfits are not taken into account.

Reaction forces and nodal displacements were stored in the ABAQUS .fil files. Using ABAQUS Post, the data was written to text files using xy-print commands inside ABAQUS Post scripts. The data was then processed using MathWorks Matlab scripts. The pressure and volume data of the particle were written to the .dat file from where they were extracted using FORTRAN and Matlab scripts. All contour plots were generated using ABAQUS Post.

4.7 Software and Hardware Used

All simulations were performed using the HKS finite element analysis package 'ABAQUS' versions 5.5 and 5.6 on Hewlett-Packard workstations running HP-UX version 9 and 10. For the implementation of the rubber particle, the triaxial loading condition and the user variables, user subroutines were written in FORTRAN 77. The results were interpreted using Matlab by The MathWorks versions 4 and 5, and FORTRAN 77 programs. Most of the FORTRAN codes and some of the Matlab scripts can be found in the appendices B, C andD.

4.8 Procedure

In order to make the distinction between the different cases easier to the reader, the schematic in figure 4-21 is introduced. As introduced above, the simulations are categorized according to three parameters: matrix properties, particle cavitation strength and triaxiality ratio.

Unit cells with anisotropic matrices are found in the upper half of the schematic in figure 4-21, corresponding to cases A and B. Those with isotropic matrices correspond to cases C and D. The left half of the schematic corresponds to the simulations in which the particle is coherent (cases A and C), whereas cases B and D are represen-

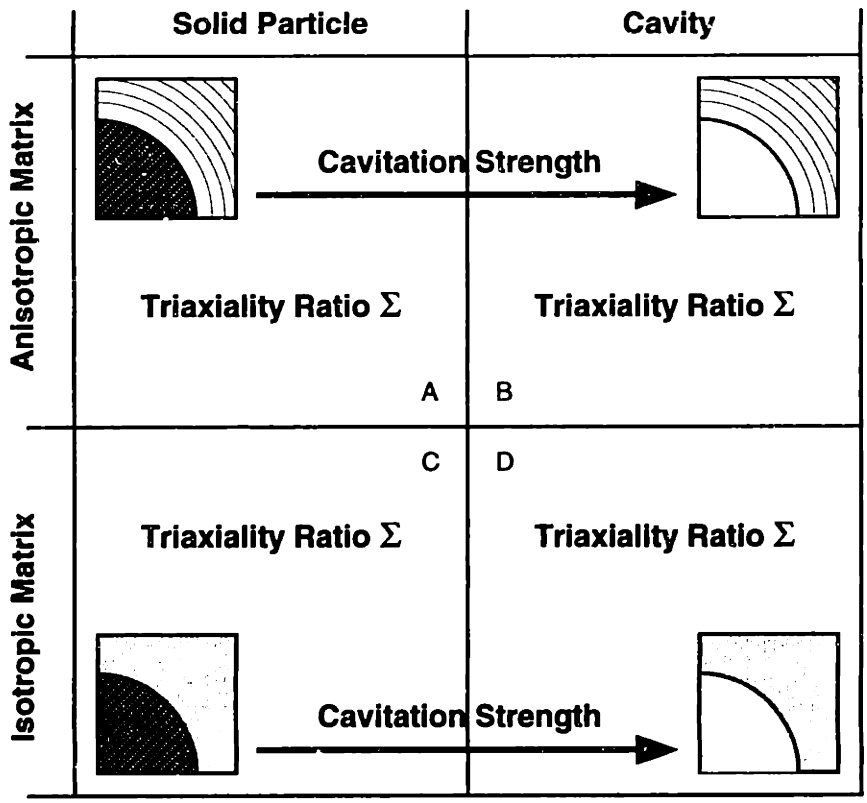

Figure 4-21: Schematic representation of the numerical study.

tative of unit cells with cavities. A particle cavitation event takes a simulation from either case A to case B, or from case C to case D. In a simulation where a particle does not cavitate, is thought of as 'remaining' within its initial case, either A or C. The axial strains at which this cavitation event takes place depends on the particle cavitation strength and the loading conditions. The different levels of triaxial stress state that are imposed on the unit cell, applies to each one of the above cases; it is thought of as being a parameter 'within each case'.

In the following chapter, the results of the numerical simulations will be presented and discussed. The reader is invited to refer back to figure 4-21 in order keep the "big picture" of the simulations in mind.

Chapter 5

Results

5.1 Introduction

In this chapter the results of the numerical simulations for the rubber-toughened nylon will be presented. In order to illustrate the types of results obtained from the numerical simulations, two typical examples will be discussed. In a "walk-through" of the example simulations, the various plots and contour plots will be explained and the connections between them discussed.

The first example is that of an isotropic matrix with a cavity, subjected to uniaxial tension. The second example is somewhat more complex, as it comprizes a cavitating particle inside an anisotropic matrix under a stress state of high triaxiality.

Following the examples, the effects of the following parameters will be discussed, as previously announced (see page 65):

- triaxial loading condition ($\Sigma = 0.33, 0.66, 1.33$, and 2.33);
- particle cavitation strength (P_{cr});
- matrix properties (anisotropic, isotropic).

The reader is invited to refer to the schematic in figure 4-21 on page 94 for the purpose of keeping the big picture of the overall study in mind.

5.2 Uniaxial Tension of Bulk Nylon with a Pre-Existing Cavity

5.2.1 Introduction

The simulation chosen as a simple example is "25iso-00-45-033", which stands for a particle volume fraction of 25% ("25") inside of an isotropic matrix ("iso"), the cavitation strength of the "particle" is $P_{cr} = 0MPa$ ("00") and hence a cavity, the pre-cooling is $\Delta T = -45^{o}K$ ("45") and the triaxiality is $\Sigma = 0.33$ ("033")[1]. The finite element and material parameters listed in table 5.1 characterize this simulation.

Parameter	Symbol	Value
Volume fraction of the particle	Φ	25%
Triaxiality ratio	Σ	0.33
Material model of the matrix		isotropic
Young's modulus of matrix	E_m	$4488MPa$
Poisson's ratio of the matrix	ν_m	0.33
Yield Stress (reference)	σ_y	$55MPa$

Table 5.1: 25iso-00-45-033: Charateristic Parameters.

The graphs and contours listed in table 5.2 will be used in the explanation below.

In this simulation, the isotropic matrix surrounds a pre-existing cavity. Subjected to uniaxial tension in the global 2-direction, the unit cell and the corresponding mesh will first deform elastically and then plastically.

The evolution of the finite element mesh will be introduced below, followed by a discussion of the stress state in the matrix and its plastic deformation. Next, the macroscopic stress-strain response of the unit cell and the evolution of the volumetric strain of the cavity will be discussed.

In the discussion below, the cooling step that the model undergoes is ignored. This is because without a particle present, no thermal stresses develop in the matrix.

[1]See appendix A for explanations of this code and the meaning of the variables used here.

Figure number(s)	Contents
Figures 5-1a - 5-1f	Undeformed mesh at the start of the simulation, deformed mesh at different stages of the deformation.
Figures 5-2a - 5-2f	Contour plots of the stress components Sij in the unit cell.
Figure 5-4a	Macroscopic true axial stress σ_{zz} as function of macroscopic true axial strain ε_{zz}.
Figure 5-4b	Volumetric strain of the unit cell Ψ_c as function of macroscopic true axial strain ε_{zz}.
Figure 5-3	Evolution of the unit cell in macroscopic true strain space: ε_{zz} vs ε_{rr}.
Figures 5-5a - 5-5f	Contour plots of the equivalent plastic strain ε^p_{equiv}.

Table 5.2: 25iso-00-45-033: Overview of graphs and contour plots.

5.2.2 Evolution of the Finite Element Mesh

Figures 5-1a-f show the finite element mesh used for the chosen particle volume fraction of 25%. The mesh is displayed at various points in the simulation, and the current and undeformed meshes are superposed. The displaced mesh can be recognized by that it vertically extends further up than the undeformed mesh.

5.2.3 Evolution of the Stress State

In this section the evolution of the stress state in the matrix will be studied by examining contour plots of the stress components $S11, S22, S33, S12$ in the matrix. The stress components are expressed relative to the global coordinate system shown in the lower left-hand corner of the plots.

The evolution of the stress components will be examined under the macroscopic axial strain ε_{zz} increasing from 0% to 5.5%. Figures 5-2a-f show the contour plots of the stress components at these strains.

To better understand the contour plots of stress components, the reader is invited to compare them to the contour plots of equivalent plastic strain (figures 5-5a-f) below.

The matrix yields at $\varepsilon^y_{zz} = 1.4\%$, so that the first contour plot, figure 5-2a at $\varepsilon_{zz} = 1.5\%$ is plotted just after the yield point. The shape of the stress contours is dominated

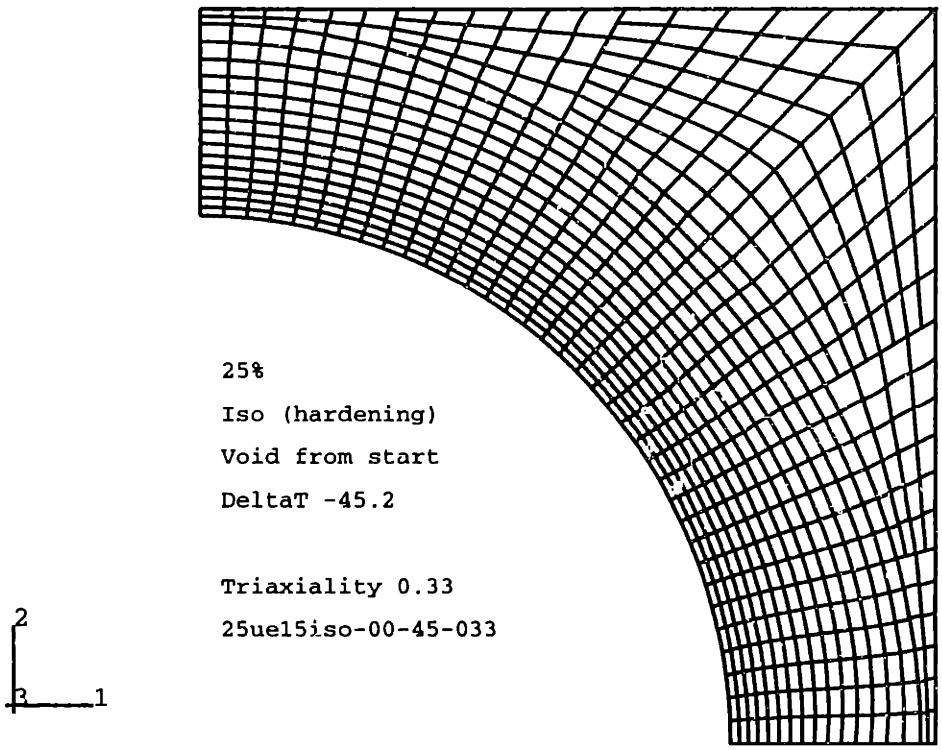

Figure 5-1a: 25iso-00-45-033: Undeformed mesh at start of simulation. $\varepsilon_{zz} = 0$.

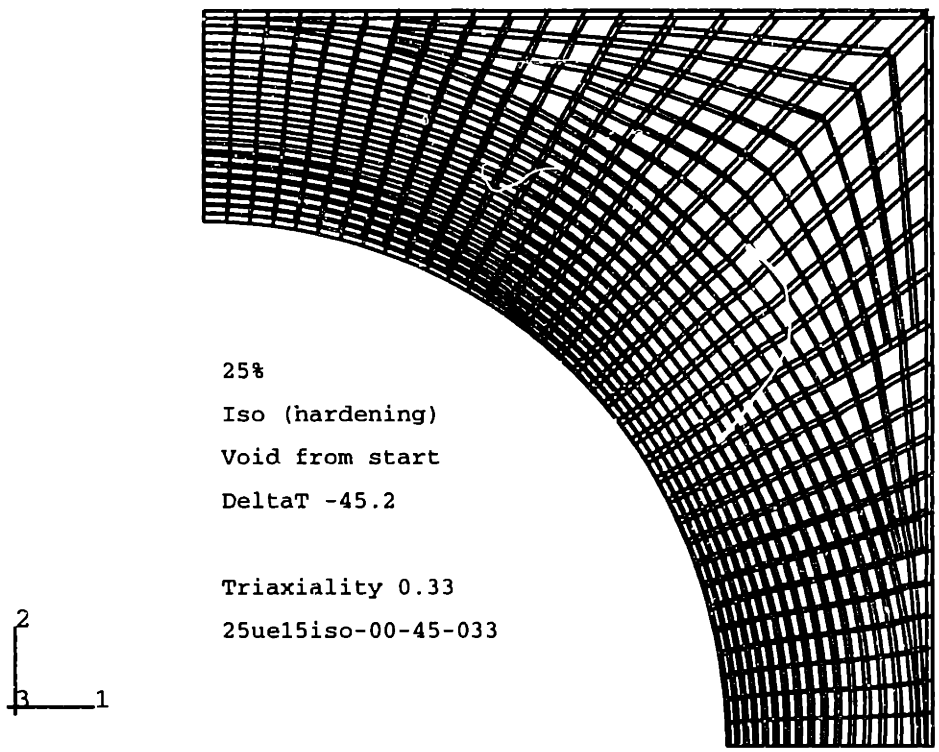

Figure 5-1b: 25iso-00-45-033: Deformed and undeformed meshes at $\varepsilon_{zz} = 1.5\%$.

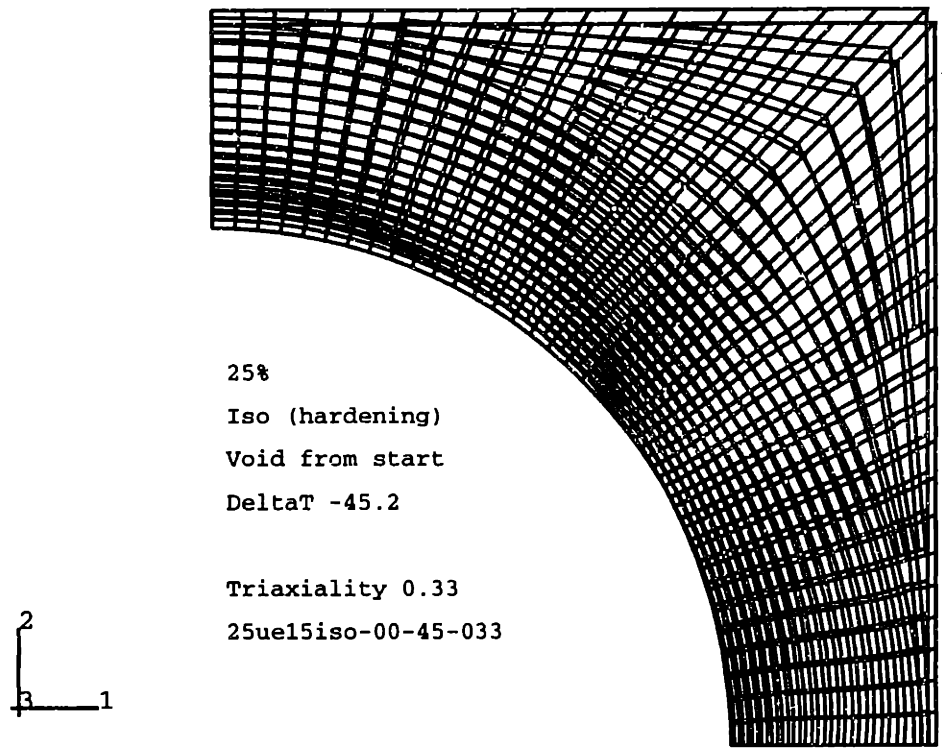

Figure 5-1c: 25iso-00-45-033: Deformed and undeformed meshes at $\varepsilon_{zz} = 2.5\%$.

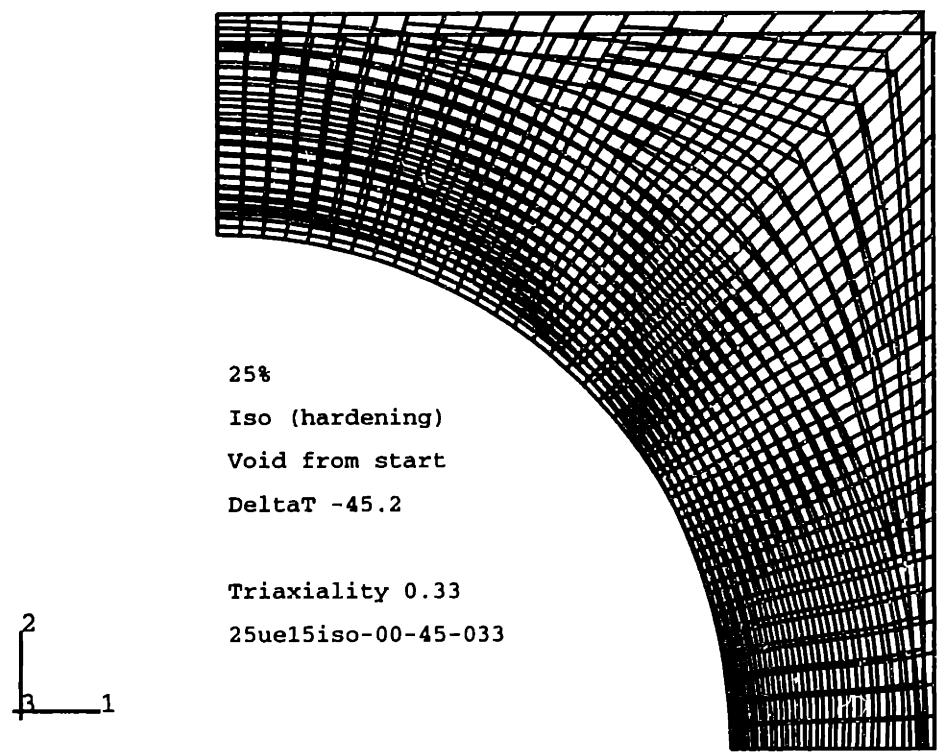

Figure 5-1d: 25iso-00-45-033: Deformed and undeformed meshes at $\varepsilon_{zz} = 3.5\%$.

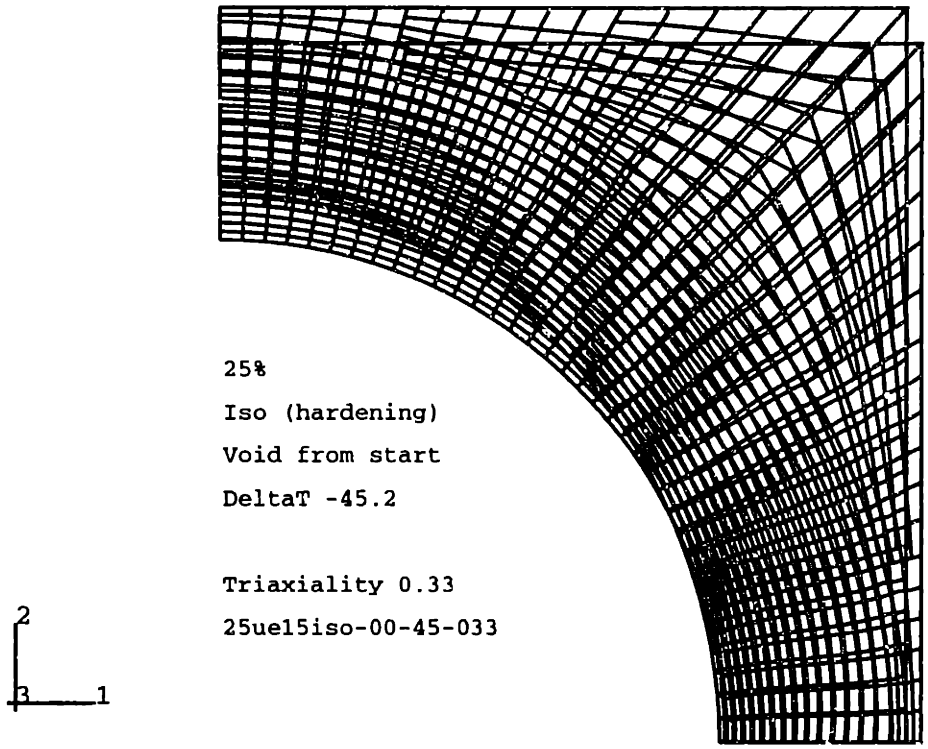

Figure 5-1e: 25iso-00-45-033: Deformed and undeformed meshes at $\varepsilon_{zz} = 4.5\%$.

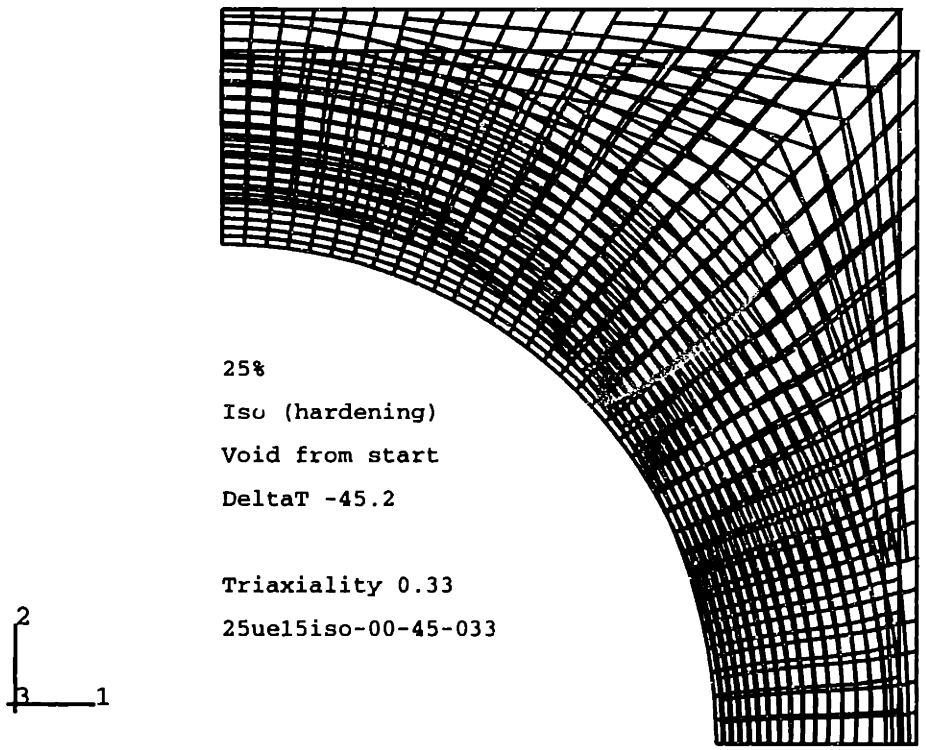

Figure 5-1f: 25iso-00-45-033: Deformed and undeformed meshes at $\varepsilon_{zz} = 5.5\%$

by the geometry of the unit cell, i.e. the free surface at the cavity/matrix interface and the geometric boundary conditions, because little plastic flow has occurred at that point. The magnitudes of the normal stress components vary between $-21MPa$ and $+75MPa$ according to their position in the matrix. $S12$ varies between $-24MPa$ and $+5MPa$, its maximum coinciding with the plastic region near cavity surface. At $\varepsilon_{zz} = 2.5\%$, all stress components have increased as the matrix undergoes further yielding. 12 has increased to -27 and $+11MPa$ and $S22$ to $+82MPa$. The region of maxium $S22$ does no longer cover the entire matrix ligament near the cavity equator, as more and more of the axial load appears to be carried by a combination of $S22$ and the radial tension provided by the region connecting the yield area at the cavity surface and the lower right-hand corner of the unit cell in which $S11$ is at its tensile maxium. This region can be seen to evolve as ε_{zz} increases to 6.5%.

As the matrix begins to deform plastically, its stress state becomes increasingly characterized by the patterns of the matrix plasticity. Therefore, the reader is invited to compare the discussion of the stress state with section 5.2.5 where the evolution of the matrix plasticity is discussed.

5.2.4 Macroscopic Strain History

Figure 5-3 shows a plot of the macroscopic strain of the unit cell in the global 2-direction, ε_{zz}, as a function of the strain in the global 1-direction, ε_{rr}.

Starting along a slope of $\frac{\varepsilon_{zz}}{\varepsilon_{rr}} = -3.6$, the unit cell first deforms elastically. At $\varepsilon_{zz} = 1.4\%$ and $\varepsilon_{rr} = 0.4\%$, the matrix undergoes yielding, which can be detected by the change of slope at those strains. After yielding, the strain-space evolution of the matrix continues along a constant slope of $\frac{\varepsilon_{zz}}{\varepsilon_{rr}} = -2.7$.

The unit cell's strain space evolution allows to draw conclusions about the volumetric strain and the relative shape changes the cell undergoes. In this example, the unit cell clearly becomes "thinner" as it elongates under the applied tension. Since the slope of ε_{zz} relative to ε_{rr} is always smaller than -1, the unit cell must be creating additional volume as a result of the deformation process. This is confirmed by the plot of cell volumetric strain Ψ_c as a function of ε_{zz} shown in figure 5-4b below. The

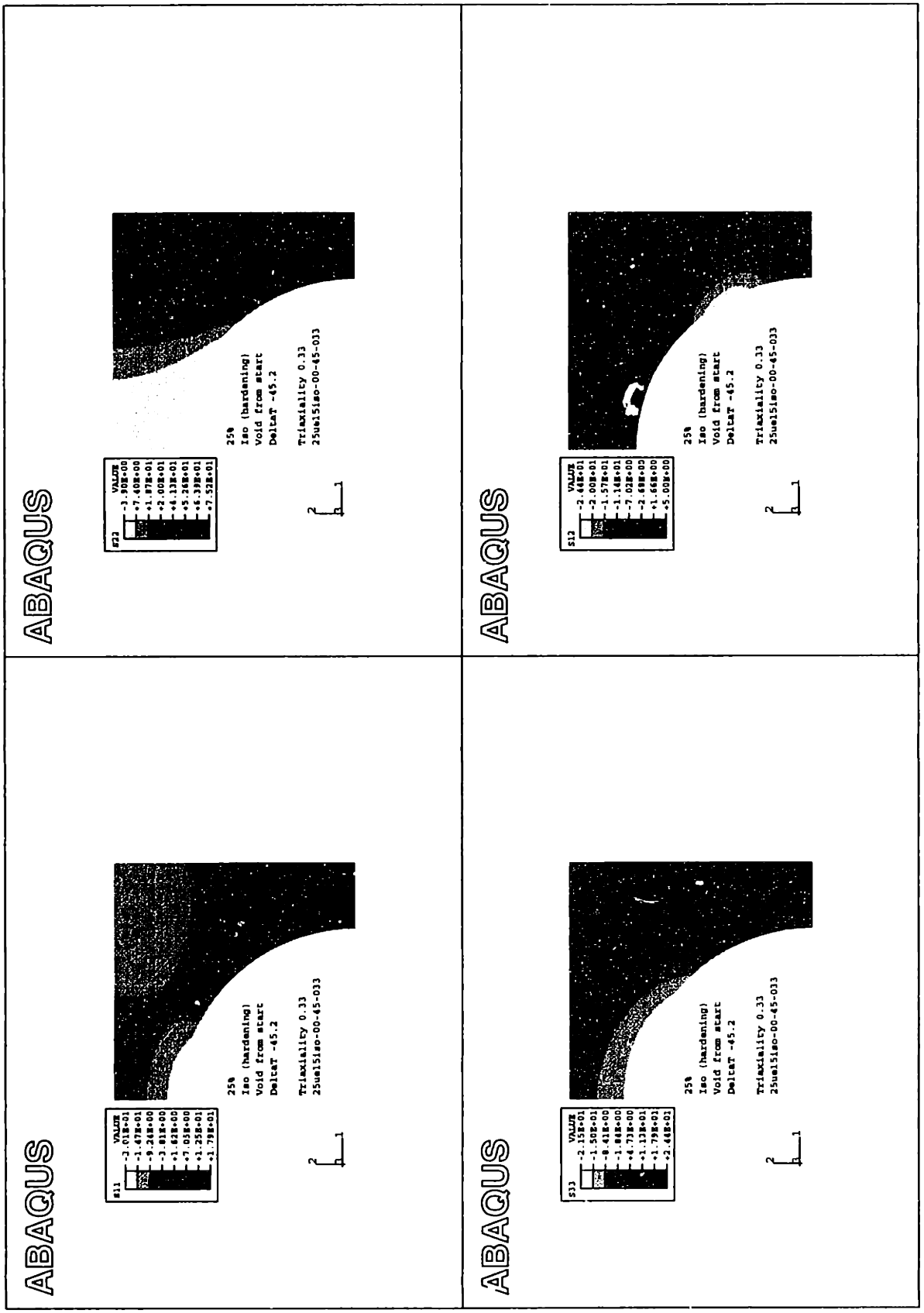

Figure 5-2a: 25iso-00-45-033: Stress components at $\varepsilon_{zz} = 1.5$.

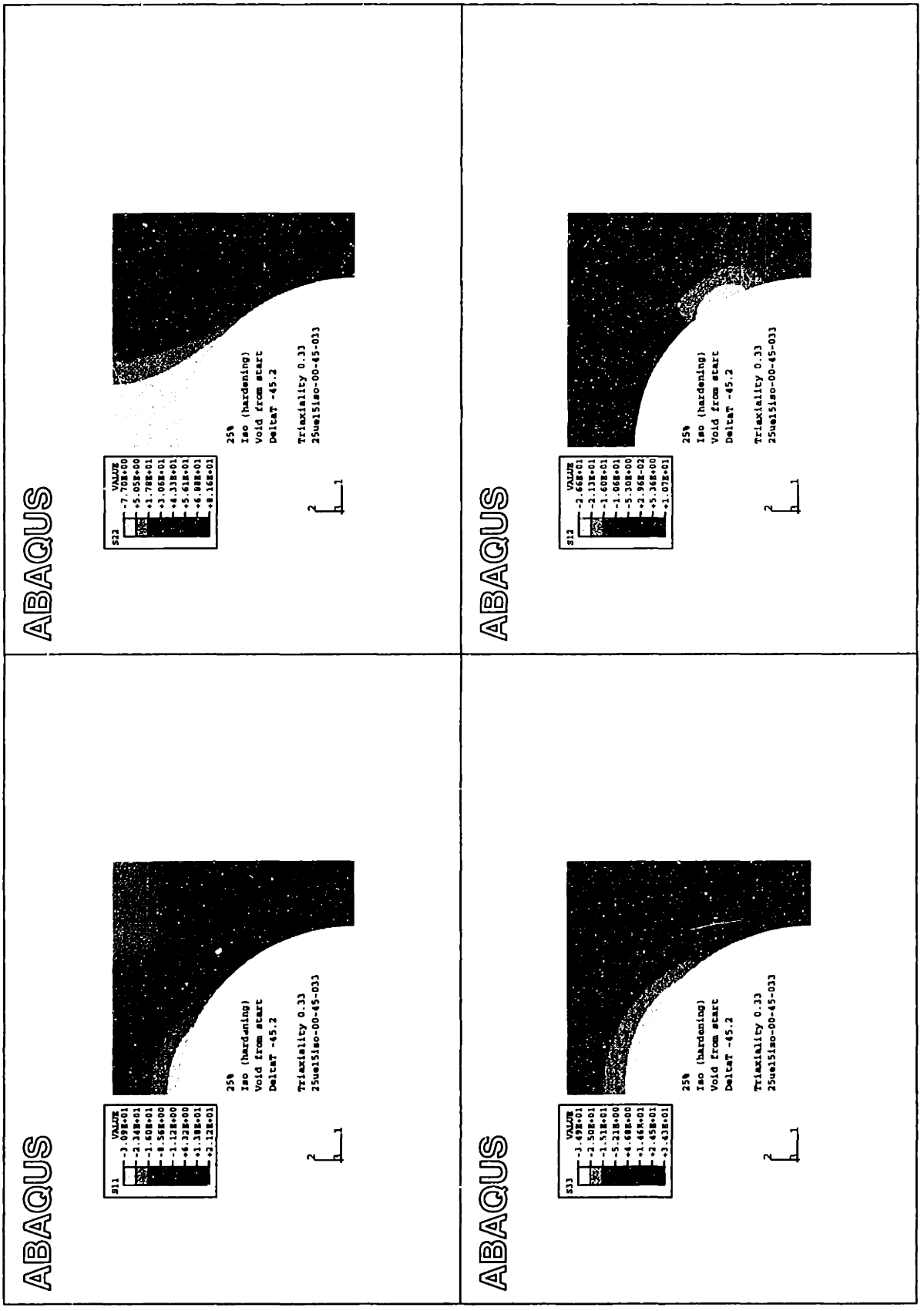

Figure 5-2b: 25iso-00-45-033: Stress components at $\varepsilon_{zz} = 2.5\%$.

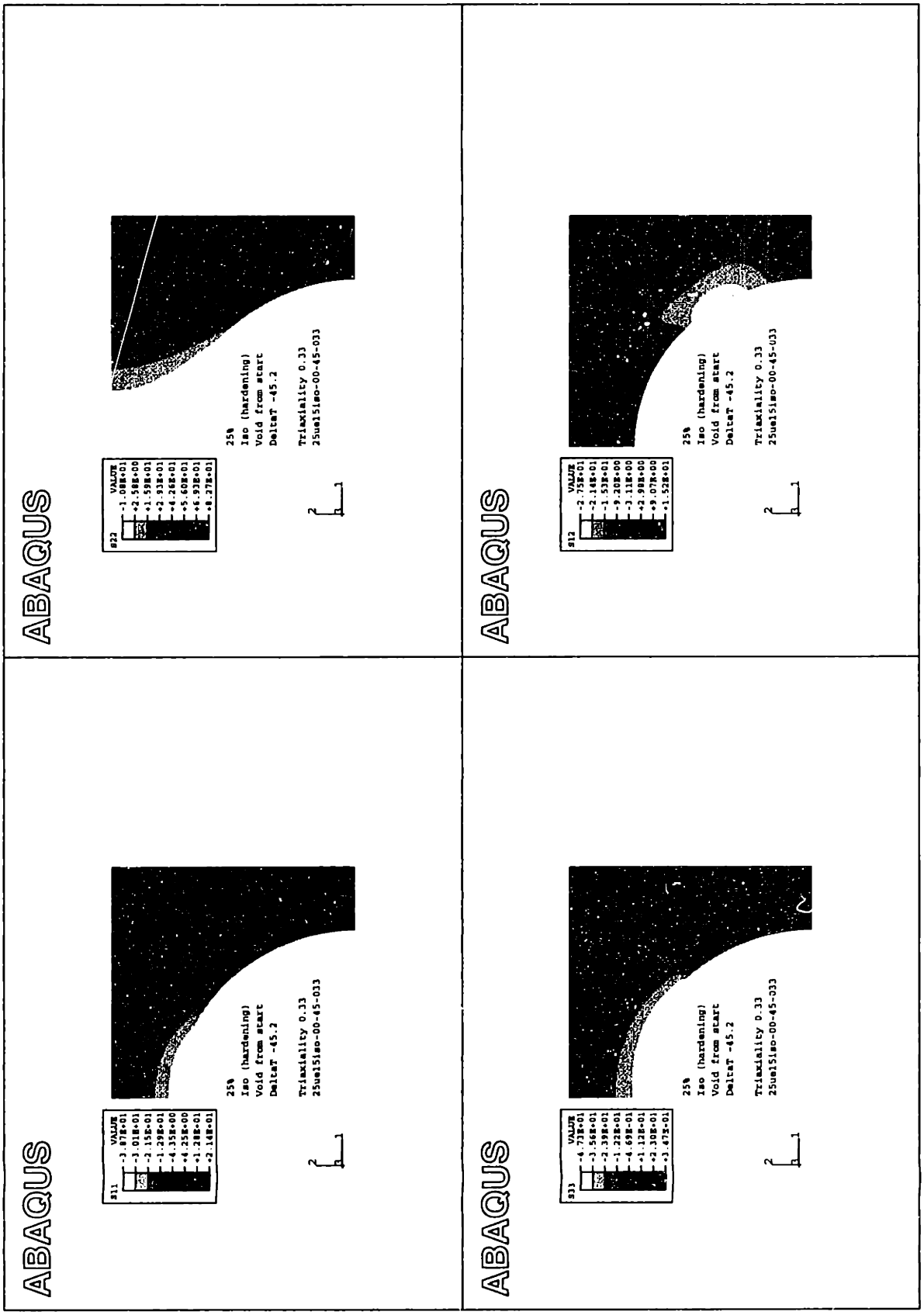

Figure 5-2c: 25iso-00-45-033: Stress components at $\varepsilon_{zz} = 3.5\%$.

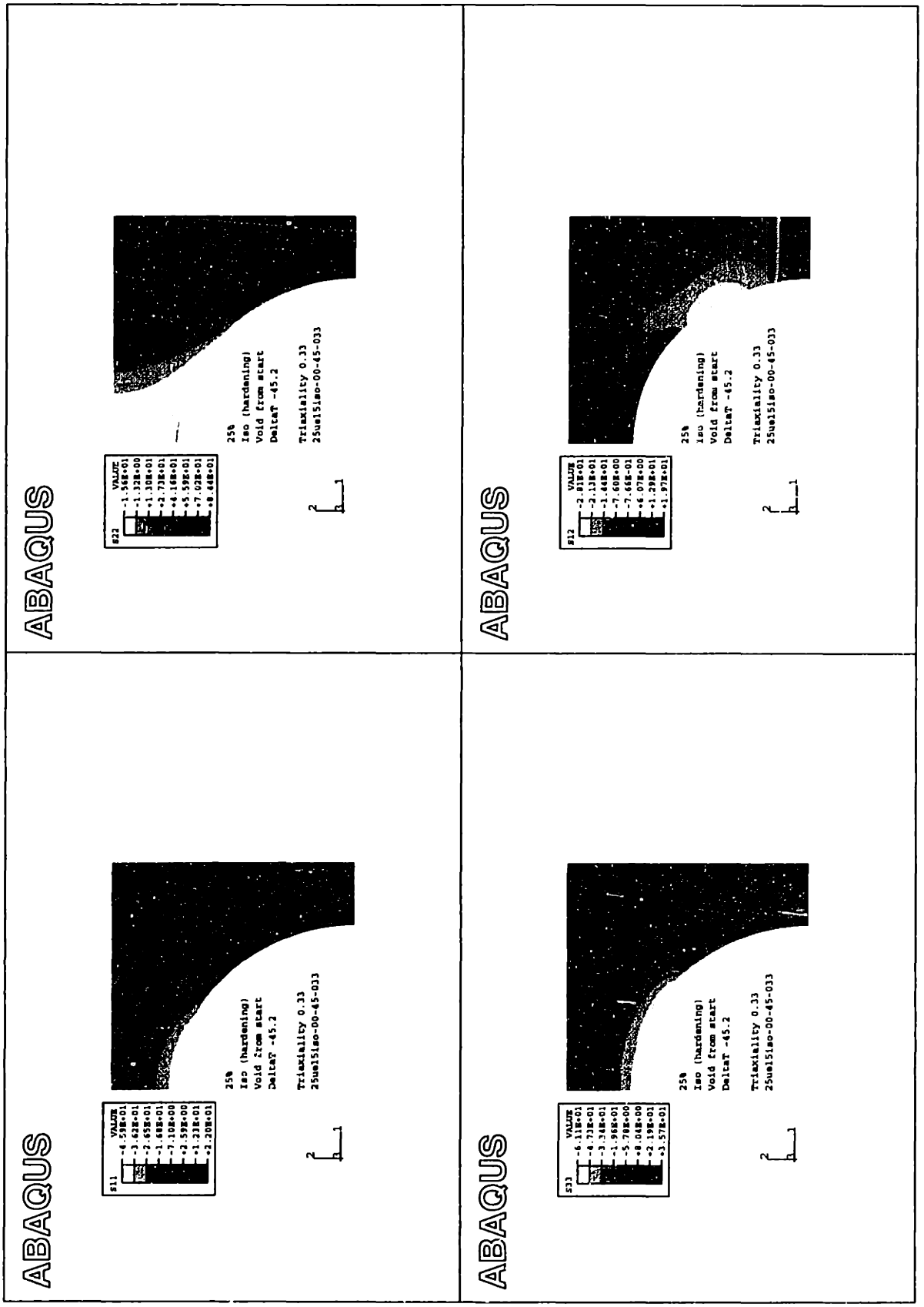

Figure 5-2d: 25iso-00-45-033: Stress components at $\varepsilon_{zz} = 4.5\%$.

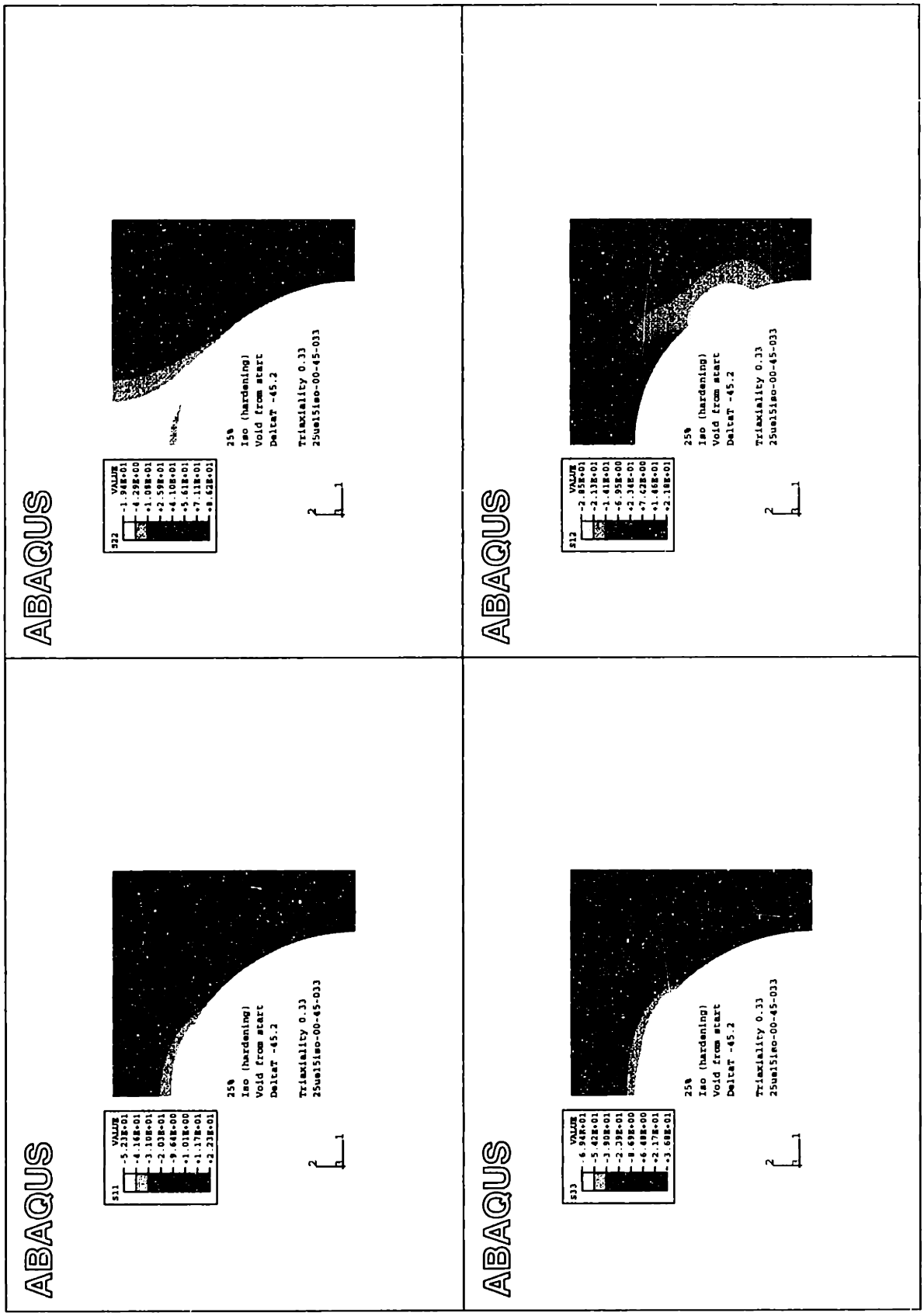

Figure 5-2e: 25iso-00-45-033: Stress components at $\varepsilon_{zz} = 5.5\%$.

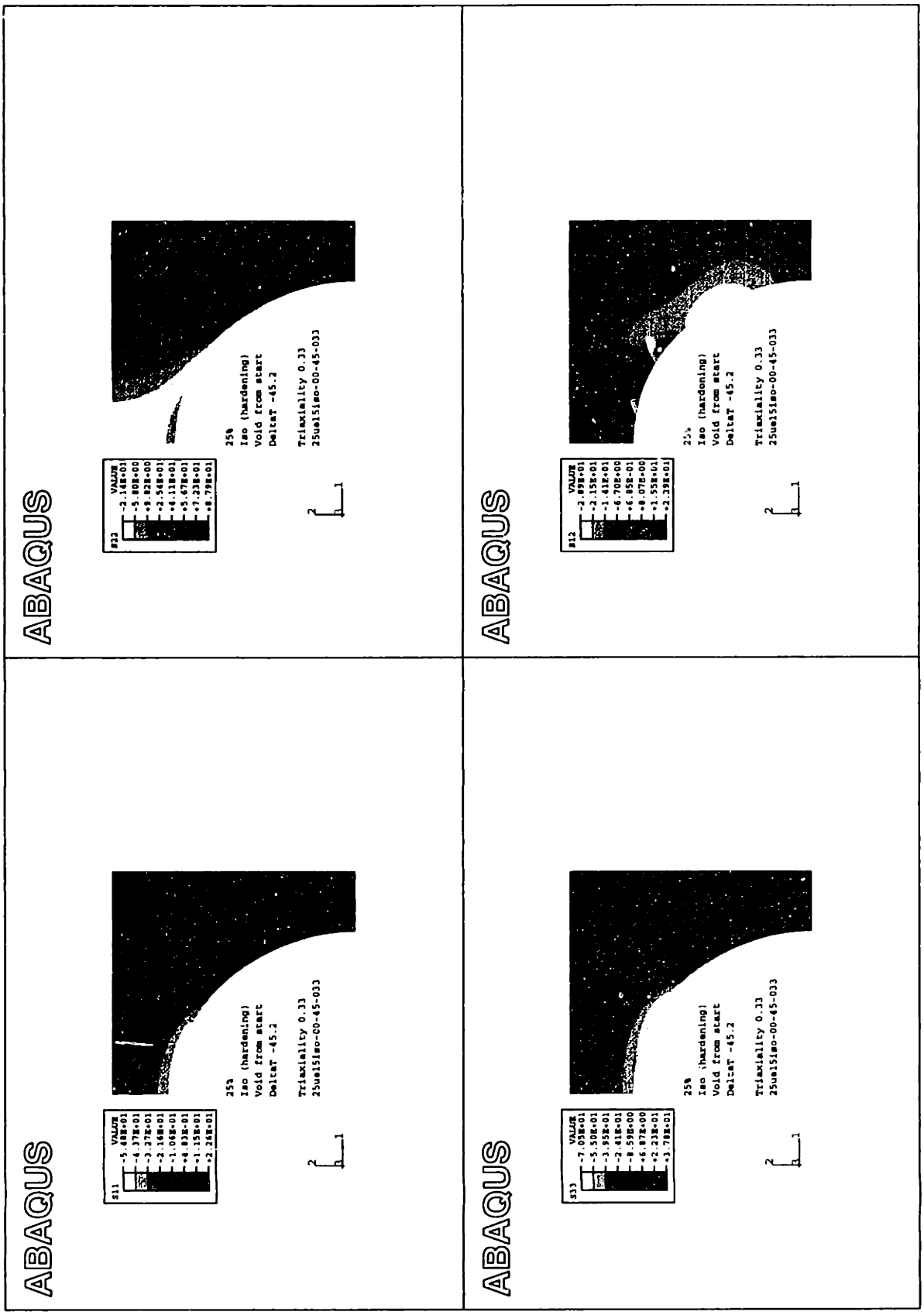

Figure 5-2f: 25iso-00-45-033: Stress components at $\varepsilon_{zz} = 6.5\%$.

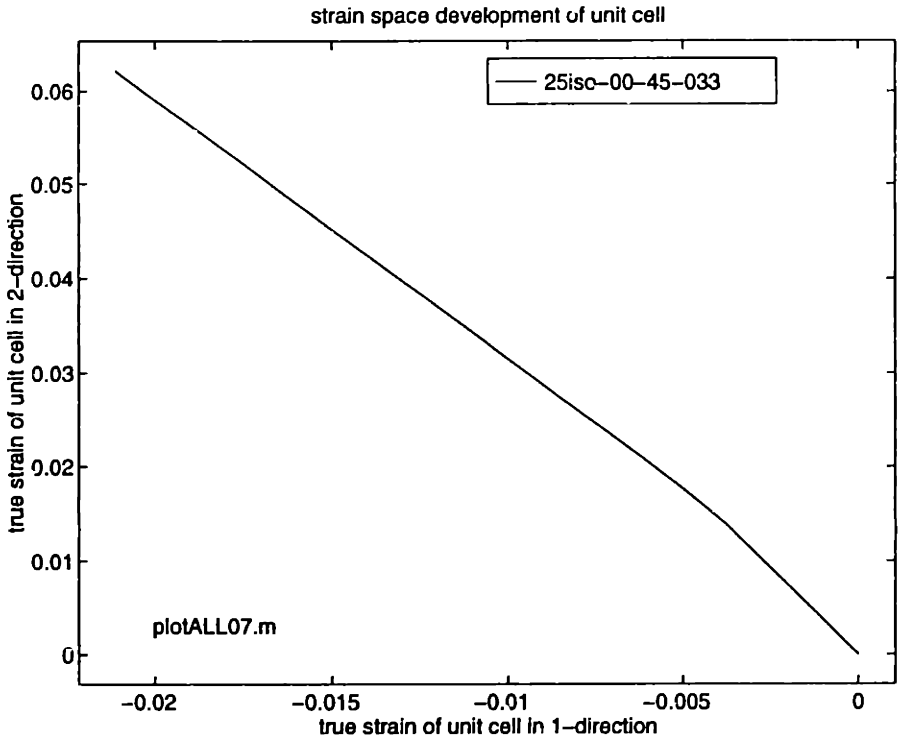

Figure 5-3: 25iso-00-45-033: Strain space evolution: ε_{zz} as function of ε_{rr}.

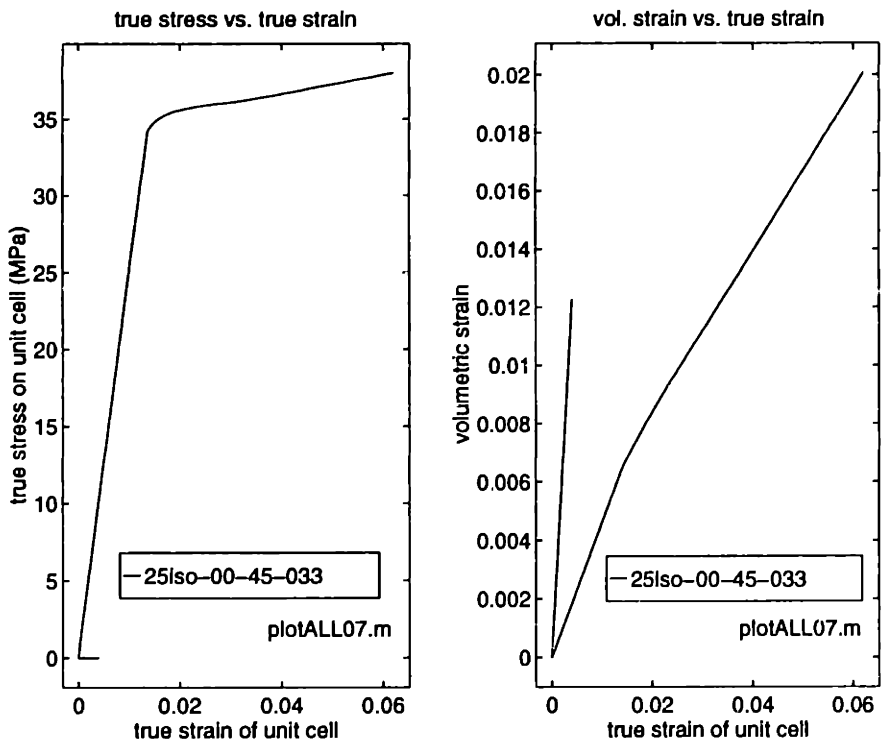

Figure 5-4: 25iso-00-45-033: (a) macroscopic axial true stress σ_{zz} and (b) cell volumetric strain Ψ_c as functions of macroscopic axial true strain ε_{zz}.

plot of Ψ_c as function of ε_{zz} follows the same trends as the plot of ε_{zz} as function of ε_{rr}: during the elastic deformation it follows a constant slope, which, after matrix yield at ε_{zz}^{y}, decreases somewhat. At $\varepsilon_{zz} = 6\%$ the volumetric strain of the unit cell has reached 2%.

5.2.5 Evolution of the Equivalent Plastic Strain

In order to illustrate the evolution of the plastic deformation in the matrix, contour plots of the equivalent plastic strain measure ε_{equiv}^{p} (PEEQ) are examined. Figures 5-5a-f show the matrix plasticity at ε_{zz} ranging from 0 to 6.5%.

Figure 5-5a shows the contour plot of ε_{equiv}^{p} at $\varepsilon_{zz} = 1.5\%$, which is close to the yield point at $\varepsilon_{zz}^{y} = 1.4\%$. From the figure it can be seen that the highest levels of ε_{equiv}^{p} are found at the internal free surface near the cavity equator, which is where the matrix first yielded due to the stress concentration effect at the equator. After the plasticity initiated there, it spread radially outward through the net section of the matrix ligament. At $\varepsilon_{zz} = 1.5\%$, ε_{equiv}^{p} has reached a maximum of 1.4%.

Once the net-section of the unit cell has undergone yield, the plastic zone spreads axially. The straight boundary conditions require for some plastic flow throughout the lateral height of the unit cell, for it to accommodate the axial elongation. This is seen in figure 5-5b-e, where the plastic zone is seen to extend into the upper right-hand corner and to intensify in the region between cavity surface and the corner, as well as along the equatorial ligament. At $\varepsilon_{zz} = 2.5\%\varepsilon_{equiv}^{p}$ has reached a maxium of 3.3%, at $\varepsilon_{zz} = 6.5\%$, it has a maxium of 9.8%.

5.2.6 Macroscopic Stress-Strain Response

Figure 5-4a is a plot of the macroscopic axial stress σ_{zz} as function of macroscopic axial strain ε_{zz} of the unit cell.

Starting along a slope of $\frac{\sigma_{zz}}{\varepsilon_{zz}} = 2.7GPa$, σ_{zz} increases to $34MPa$ at the yield point of $\varepsilon_{zz}^{y} = 1.4\%$. After matrix yield, the slope of the stress-strain curve decreases to $66MPa$. It can be seen that after yield, σ_{zz} increase with ε_{zz} in a non-linear way.

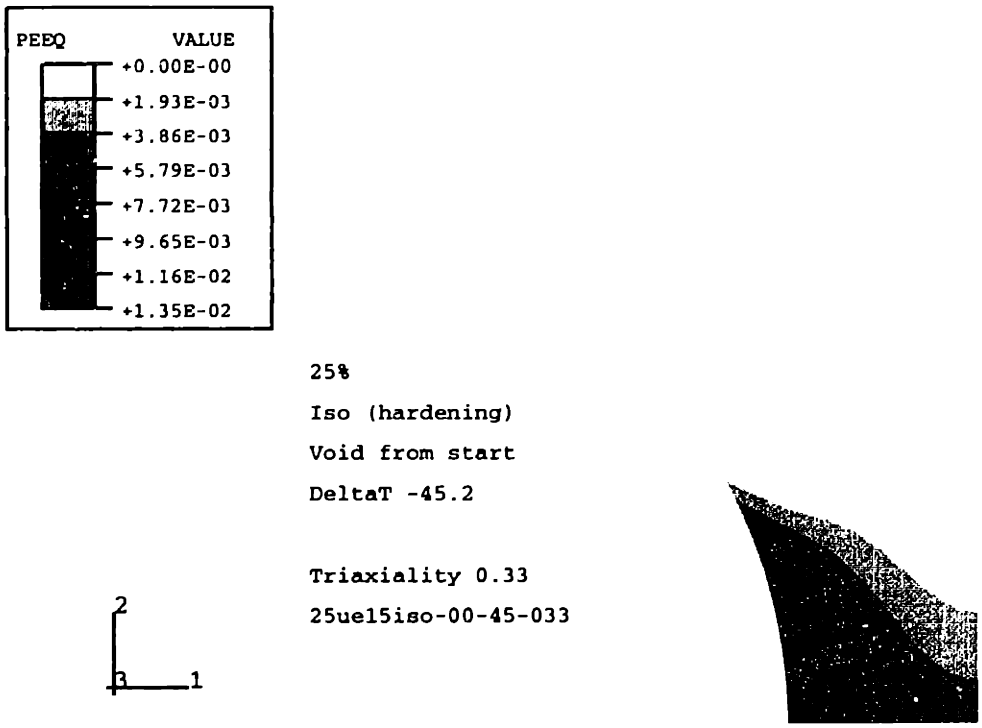

Figure 5-5a: 25iso-00-45-033: Contour Plots of the equivalent plastic strain ε^p_{equiv} at $\varepsilon_{zz} = 1.5\%$.

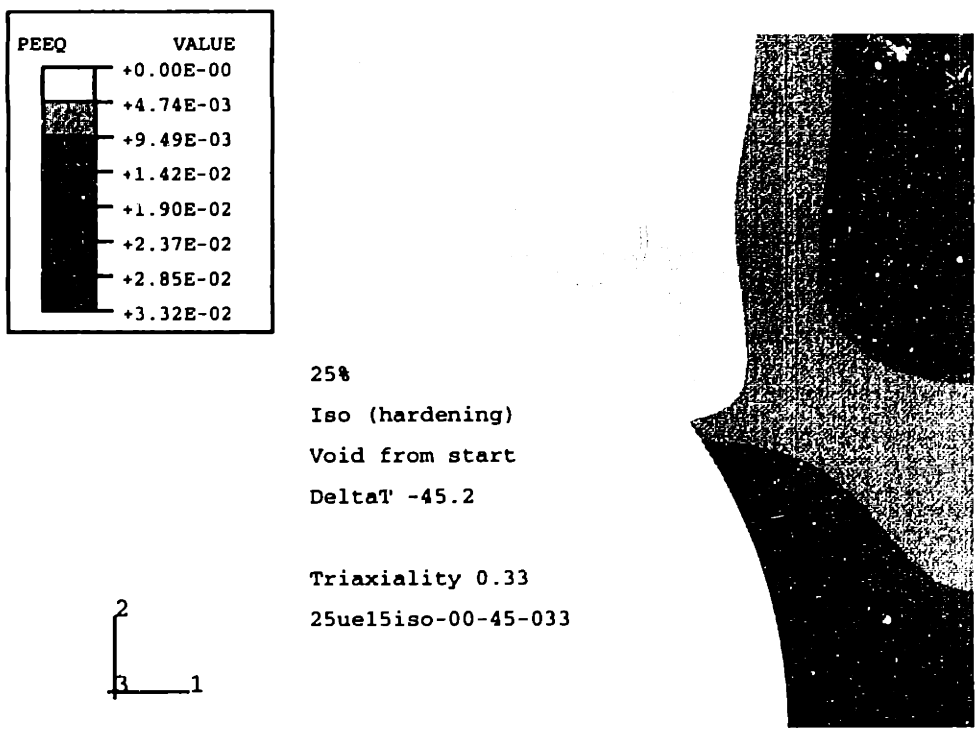

Figure 5-5b: 25iso-00-45-033: Contour Plots of the equivalent plastic strain ε^p_{equiv} at $\varepsilon_{zz} = 2.5\%$.

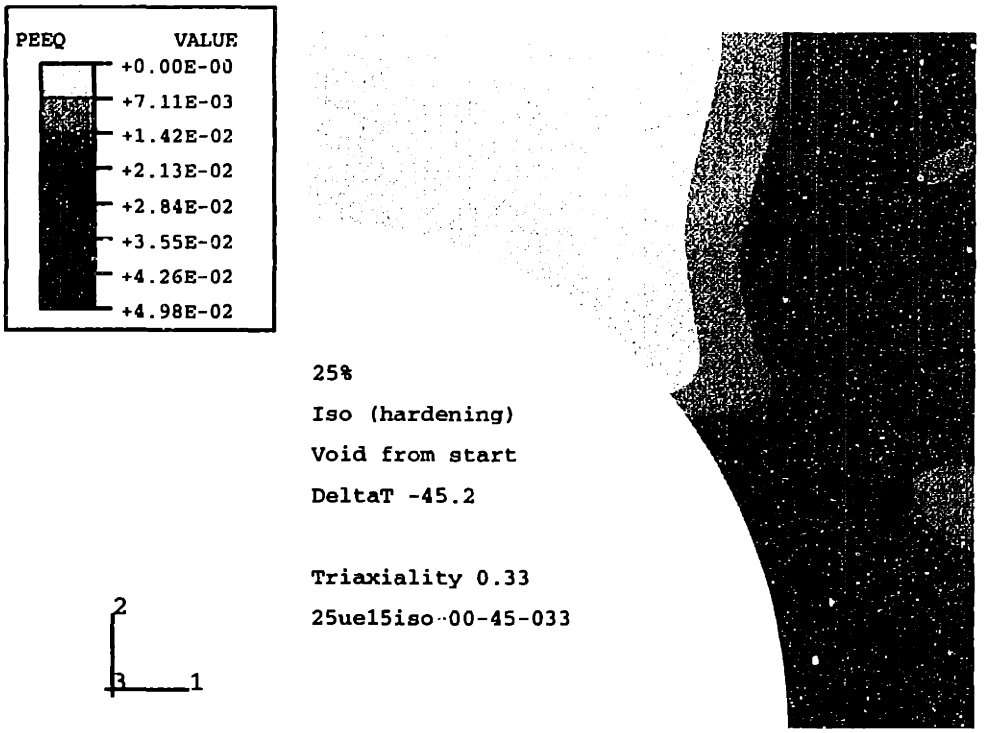

Figure 5-5c: 25iso-00-45-033: Contour Plots of the equivalent plastic strain ε^p_{equiv} at $\varepsilon_{zz} = 3.5\%$.

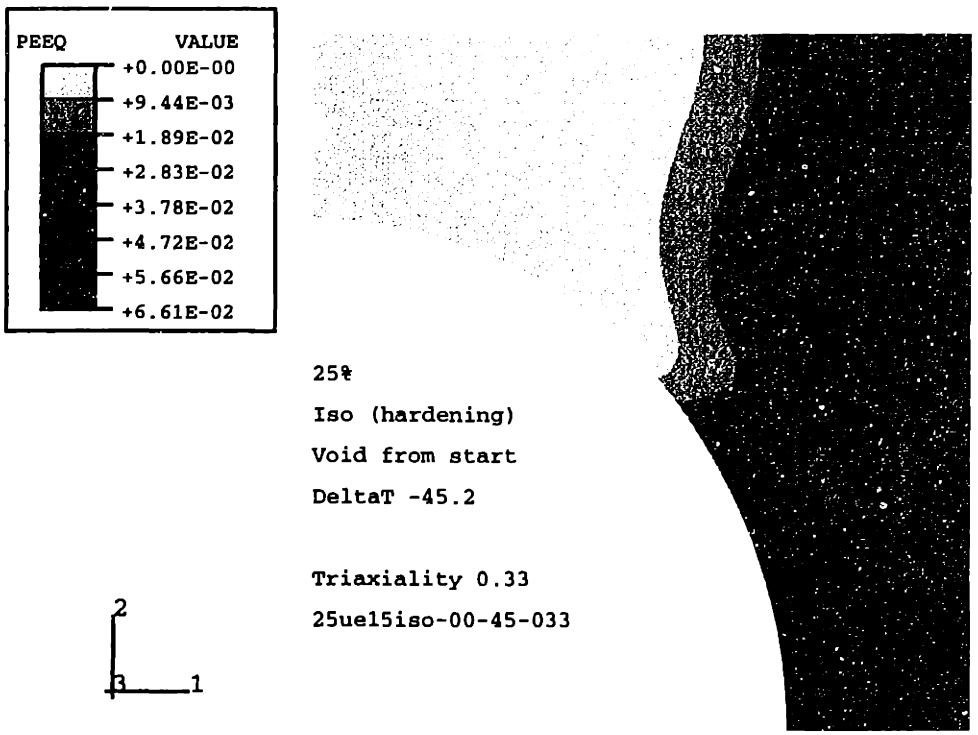

Figure 5-5d: 25iso-00-45-033: Contour Plots of the equivalent plastic strain ε^p_{equiv} at $\varepsilon_{zz} = 4.5\%$.

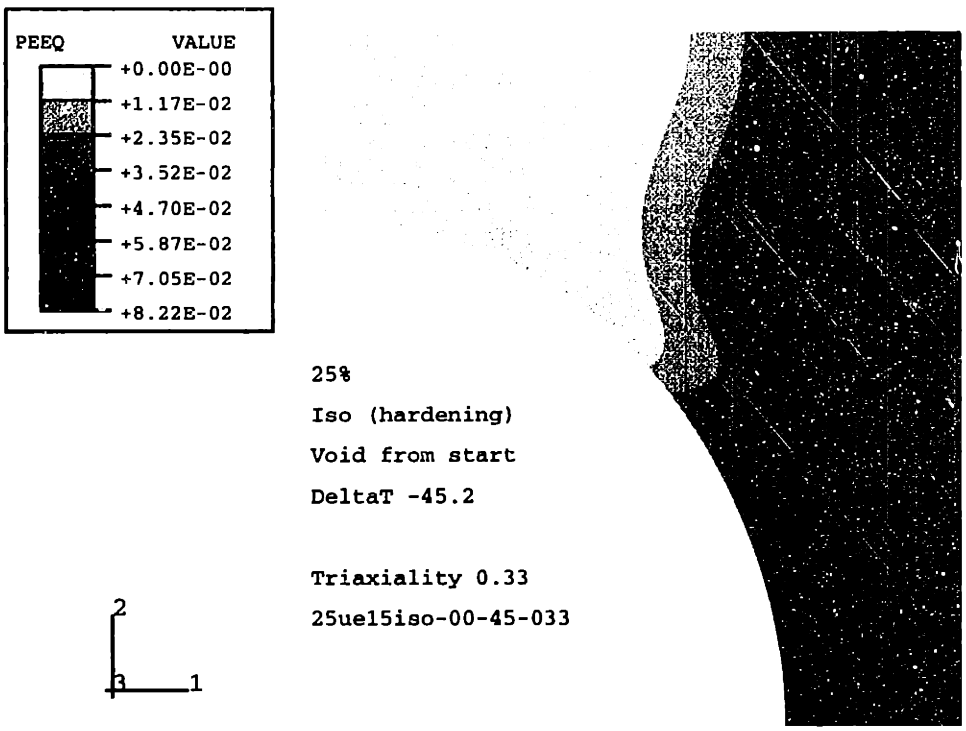

Figure 5-5e: 25iso-00-45-033: Contour Plots of the equivalent plastic strain ε^p_{equiv} at $\varepsilon_{zz} = 5.5\%$.

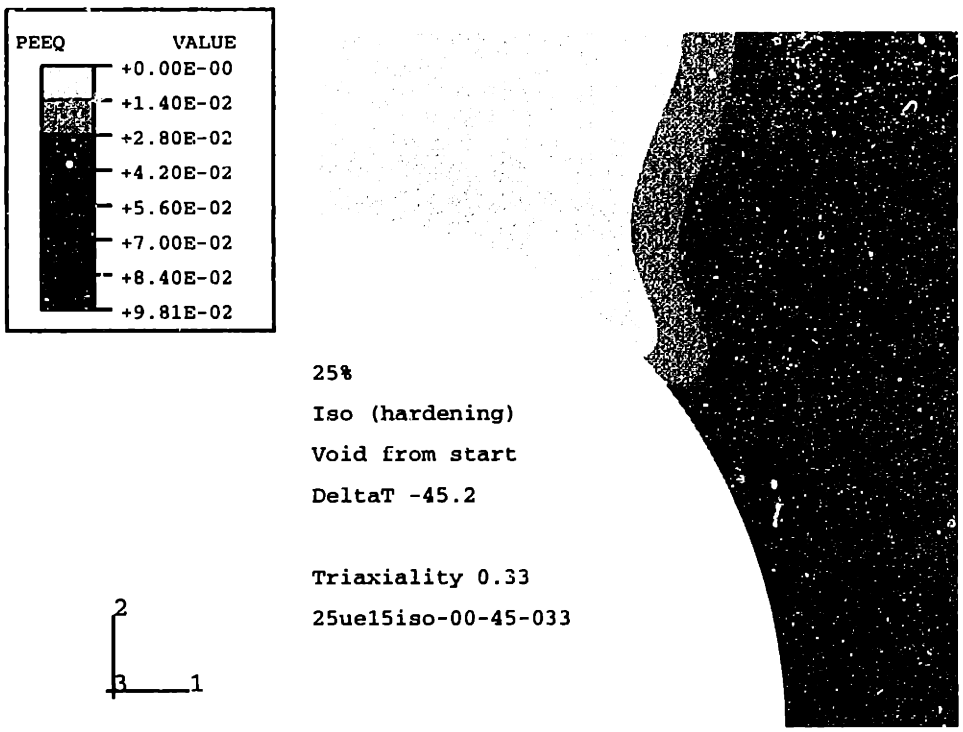

Figure 5-5f: 25iso-00-45-033: Contour Plots of the equivalent plastic strain ε^p_{equiv} at $\varepsilon_{zz} = 6.5\%$.

From about 3% axial strain on, a slight tendency to harden can be seen.

Following the relatively simple example of the simulation with an isotropic matrix and a cavity under simple tension, a more complex example will be introduced in order to illustrate some more types of data obtained from the simulations.

5.3 Example of a More Involved Simulation: "25ani-60-45-133"

5.3.1 Introduction

The simulation chosen as second example is "25ani-60-45-133" (see appendix A for an explanation of this code) which is a somewhat more involved simulation when compared to the previous example. Here, the matrix properties are anisotropic, the particle cavitates and the applied stress state is no longer simple tension, but triaxial. The finite element and material parameters listed in table 5.3 characterize this simulation.

Parameter	Symbol	Value
Volume fraction of the particle	Φ	25%
Bulk modulus of the particle	K	2000 MPa
Cavitation strength of the particle	P_{cr}	-60 MPa
Triaxiality ratio	Σ	1.33
Material model of the matrix		anisotropic
Young's modulus of matrix	E_m	$4488MPA$
Poisson's ratio of the matrix	ν_m	0.33
Yield Stress (reference)	σ_y	$55MPa$
Hill Ratios for Anisotropic Yielding	H	3.0, 2.2, 2.2, 0.7, 0.7, 1.0
Amount of equivalent cooling	ΔT	$-45.3K$

Table 5.3: 25ani-60-45-133: Charateristic Parameters.

The graphs and contours listed in table 5.4 will be used in the explanation below.

All contour plots, such as for stresses, strains and plastic strains, are plotted for the local coordinate system. The global coordinate system is such that the macroscopic 1-direction is horizontal in the contour plots, as in Figure 5-6a. The global 1-direction is also called r-direction or radial direction. The global 2-direction is parallel to the vertical direction in the contour plots. It is also called "axial direction" or global z-direction. The global 3-direction is the out-of-paper direction.

In the simulations with anisotropic matrices the local coordinate system is defined as a spherical coordinate system about the (0,0) point which is also the center of the particle. The local 1-direction is therefore pointing radially outward from the center

Figure number(s)	Contents
Figures 5-6a - 5-6g	Undeformed mesh at the start of the simulation, mesh at the end of the cooling step, deformed mesh at different stages of the deformation.
Figures 5-7a - 5-7h	Contour plots of the stress components $S11, S22, S33$ and $S12$ in the unit cell.
Figure 5-11a	Macroscopic true axial stress σ_{zz} as function of macroscopic true axial strain ε_{zz}.
Figure 5-11b	Volumetric strain of the unit cell Ψ_c as function of macroscopic true axial strain ε_{zz}.
Figure 5-13a	Pressure in the particle P as function of macroscopic true axial strain ε_{zz}.
Figure 5-13b	Volumetric strain of the particle/cavity $\|Psi_p$ as function macroscopic true axial strain ε_{zz}.
Figure 5-8	Evolution of the unit cell in macroscopic true strain space. ε_{zz} as function of ε_{rr}.
Figures 5-9a - 5-9g	Contour plots of the equivalent plastic strain ε^p_{equiv} (PEEQ) in the unit cell.
Figures 5-10a - 5-10g	Contour plots of plastic strain components $PE11, PE22, PE33, PE12$.

Table 5.4: 25ani-60-45-133: Overview of graphs and contour plots.

point. The local 2-direction is in the plane of the shown section of the unit cell, normal to the local 1-direction. It is the tangential in-plane direction. The local 3-direction is normal to the local 1- and 2-directions; i.e., it is the tangential direction normal to section of the unit cell shown.

Although not shown, the particle is situated in the lower left-hand corner of the mesh. It is not shown on the contour plots because ABAQUS does not display user-programmed elements.

Because of the model's axial symmetry, there are no 23- or 31-shear stresses. Whenever a shear stress is referred to, the 12-shear stress σ_{12} is meant.

The chronological sequence in the chosen simulation is as follows: cooling, elastic deformation, matrix yield, plastic deformation, particle cavitation, continued plastic deformation.

Situating the second example simulation in terms of the schematic in figure 4-21 on page 94, we find that "25ani-60-45-133" starts out in sector A with a coherent particle, an anisotropic matrix and $\Sigma = 1.33$. When the particle cavitates, the simulation

changes into sector B.

For comparison, the previous example ("25iso-00-45-033") with an isotropic matrix under simple tension and surrounding a cavity would be situated in sector D from beginning to end of the simulation.

5.3.2 Evolution of the Finite Element Mesh

Figures 5-6a through 5-6g show the finite element mesh used for the chosen particle volume fraction of 25%. The meshes are displayed at various points in the simulation, and the current and undeformed meshes are superposed.

Figure 5-6b shows the mesh at the end of the cooling and before deformation. At this point, the undeformed mesh extends further than the deformed mesh, both axially and radially.

In figure 5-6c the top of the unit cell has been displaced by an amount that corresponds to an axial true strain of $\varepsilon_{zz} = 1.5\%$, and now extends further in the global 2-direction than that of the undeformed mesh.

As the deformation continues, it can be seen how some of the mesh elements begin to deform noticeably. Referring to figure 5-6g, which shows the meshes at $\varepsilon_{zz} = 5.5\%$, the elements along the particle/matrix or cavity/matrix interface near the particle or cavity equator have deformed in shear along a plane parallel to the interface, which can be recognized by the "wavyness" of the mesh there.

5.3.3 Evolution of the Stress State

In this section the evolution of the stress state in the matrix will be studied by examining the contour plots of the 11−, 22−, 33− and 12−stress components of the matrix. In the unit cell with anisotropic matrix, the stress components are measured relative to the local coordinate system, as discussed in section 4.4.2.

The evolution of the stress components will be examined at the following instances of the deformation, identified by the macroscopic axial strain ε_{zz} and some by specific events:

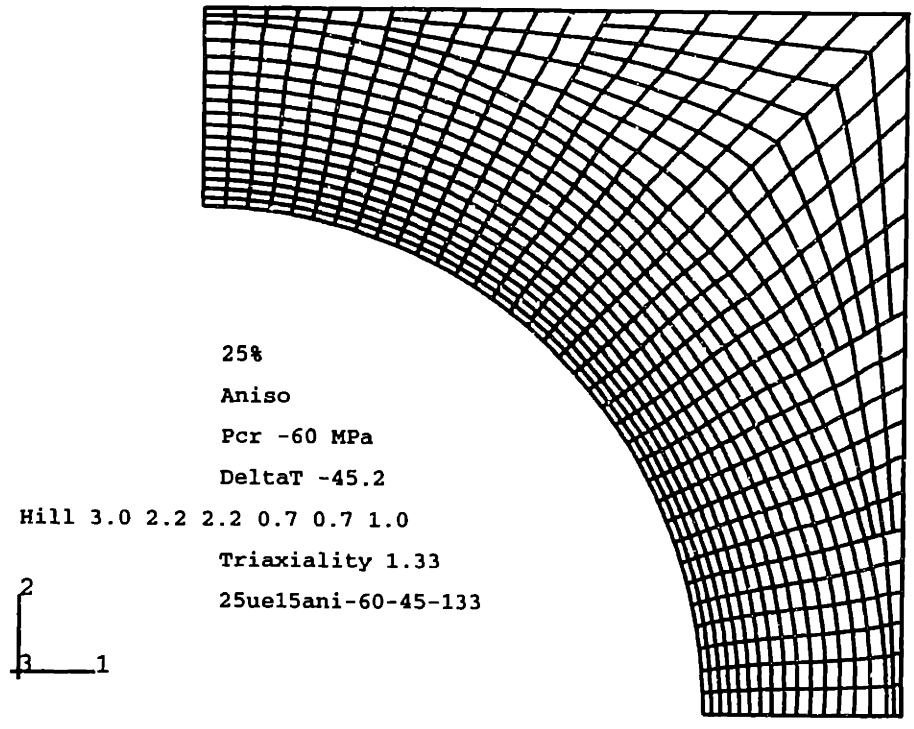

Figure 5-6a: 25ani-60-45-133: Undeformed mesh at start of simulation.

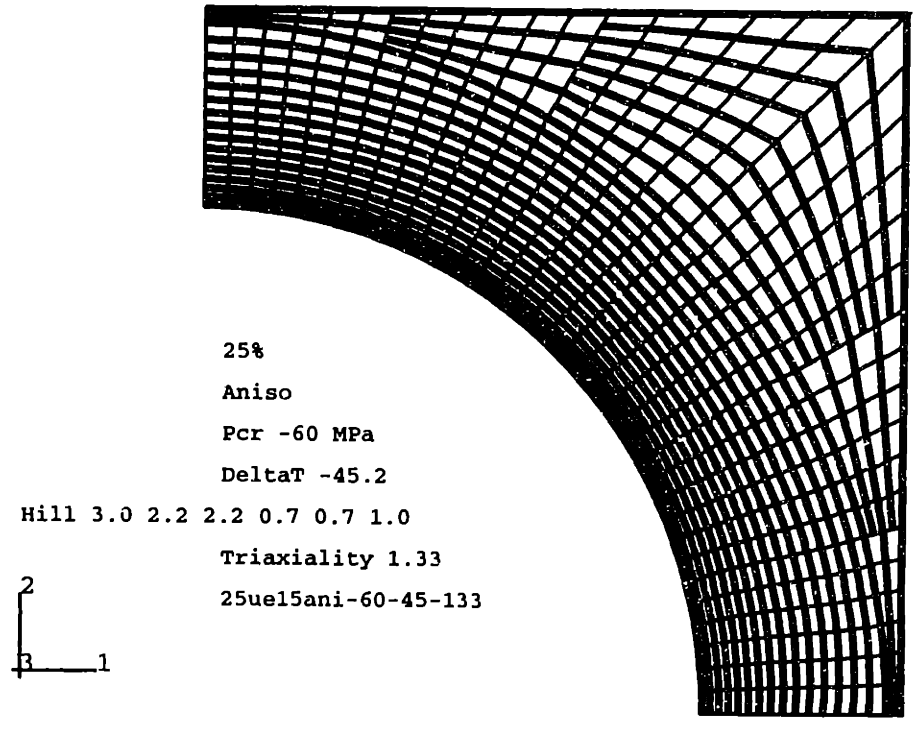

Figure 5-6b: 25ani-60-45-133: Deformed and undeformed meshes after completion of cooling. $\varepsilon_{zz} = 0$.

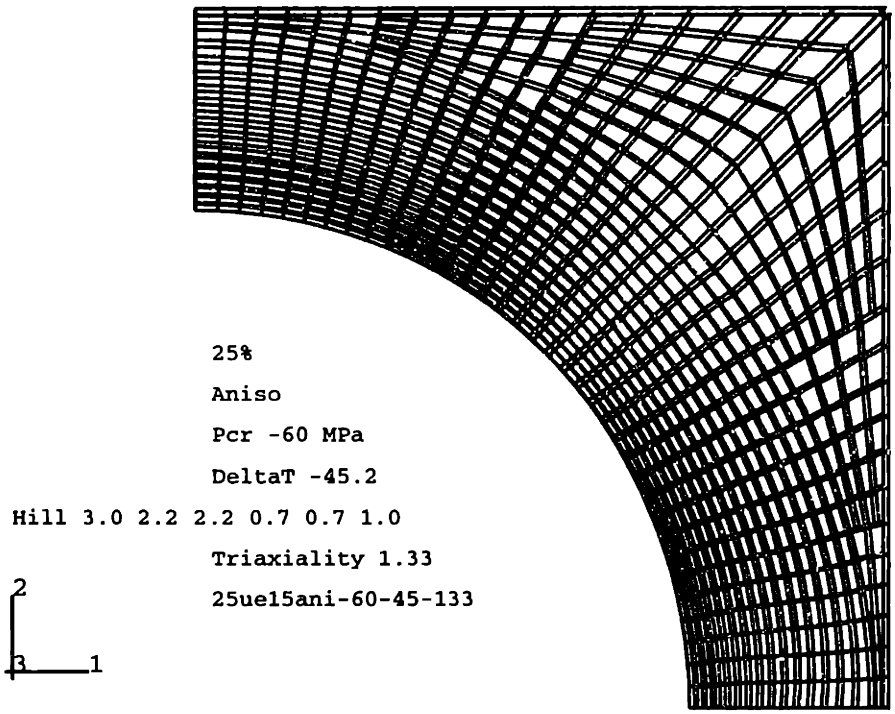

Figure 5-6c: 25ani-60-45-133: Deformed and undeformed meshes at $\varepsilon_{zz} = 1.5\%$.

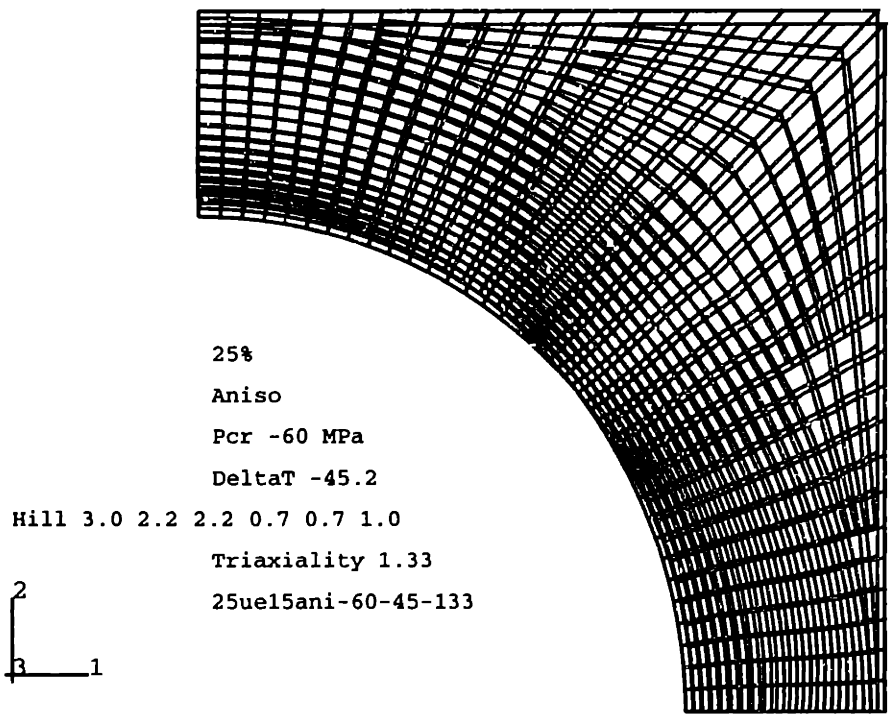

Figure 5-6d: 25ani-60-45-133: Deformed and undeformed meshes at $\varepsilon_{zz} = 2.5\%$.

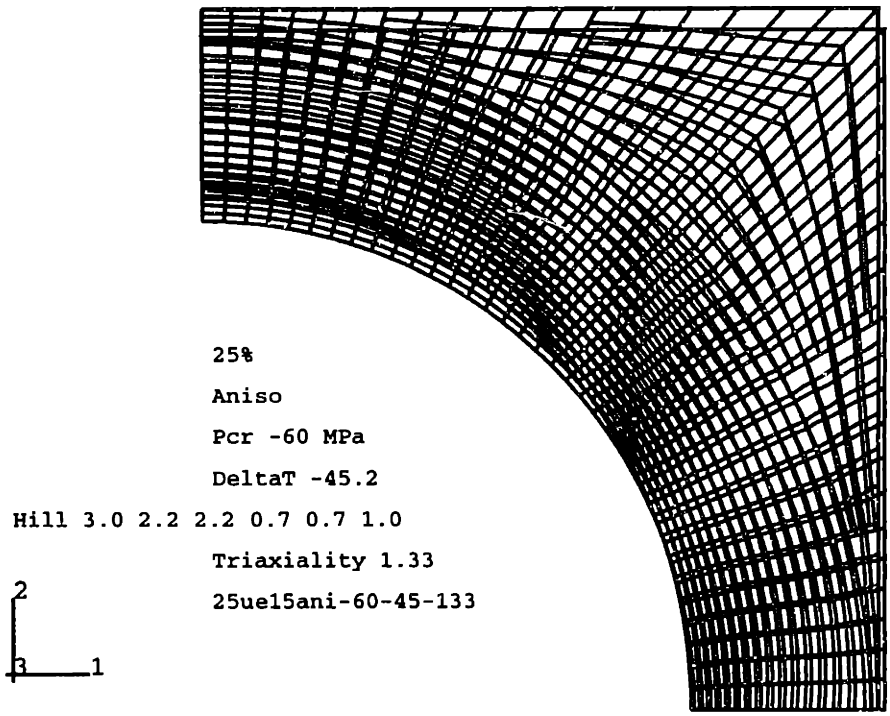

Figure 5-6e: 25ani-60-45-133: Deformed and undeformed meshes at $\varepsilon_{zz} = 3.5\%$.

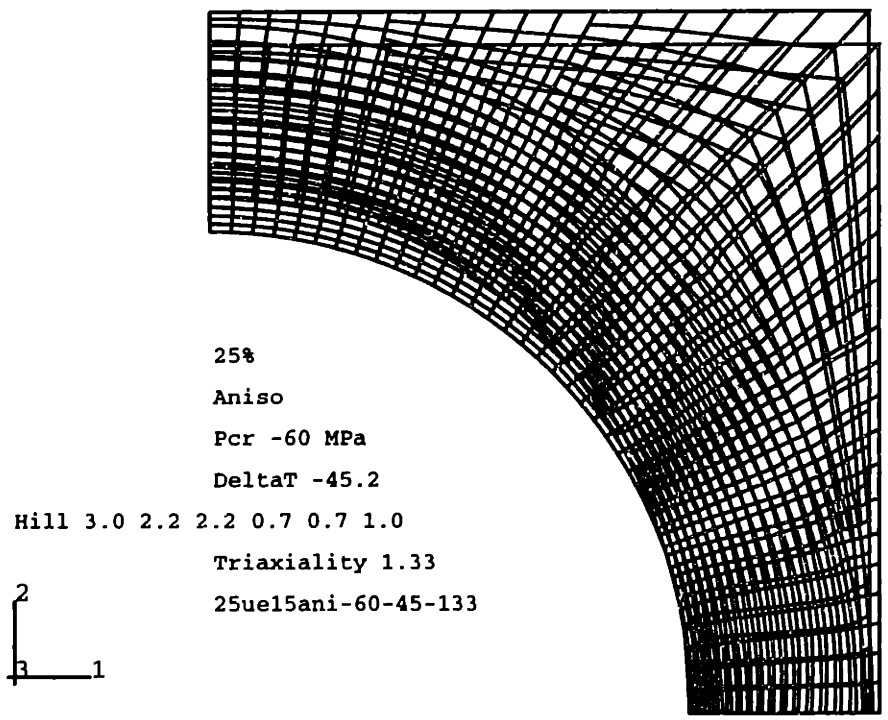

Figure 5-6f: 25ani-60-45-133: Deformed and undeformed meshes at $\varepsilon_{zz} = 4.5\%$.

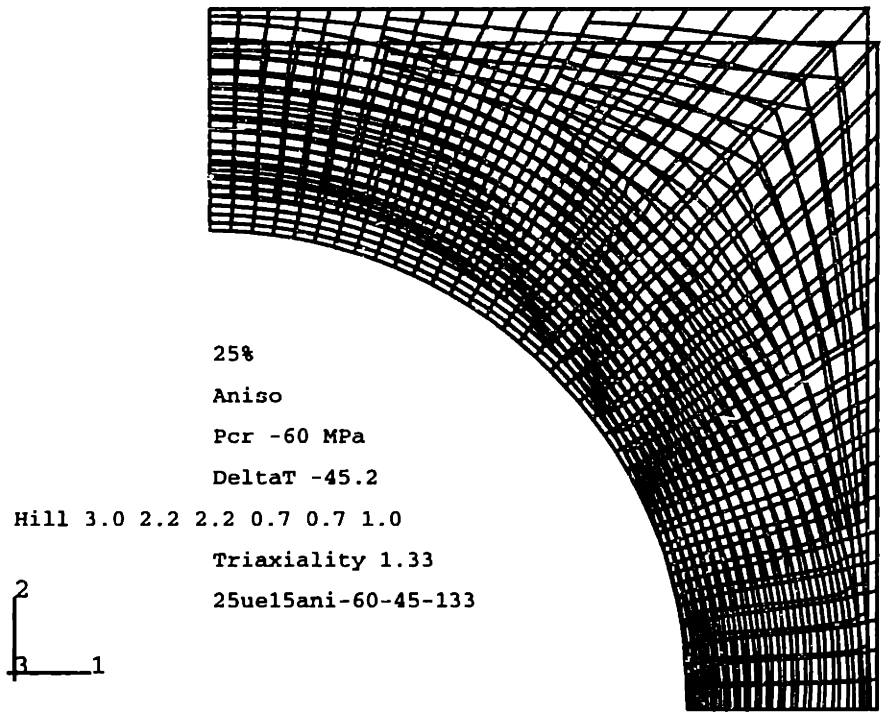

Figure 5-6g: 25ani-60-45-133: Deformed and undeformed meshes at $\varepsilon_{zz} = 5.5\%$

- At the end of the cooling step (crystallization and thermal residual stresses), $\varepsilon_{zz} = 0$;
- Just after matrix yield, $\varepsilon_{zz} = 1.5\%$ and $\varepsilon_{zz} = 2.5\%$;
- Just before and just after particle cavitation, $\varepsilon_{zz} = 2.8\%$;
- Further evolution after particle cavitation, $\varepsilon_{zz} = 3.5\%, 4.5\%, 5.5\%$.

As the matrix deforms plastically, its stress state becomes increasingly characterized by the patterns of the matrix plasticity. Therefore the reader is invited to compare the discussion of the stress state with section 5.3.5 where the evolution of the matrix plasticity is discussed.

Residual Stresses due to Matrix Crystallization and Thermal Misfit

In the first step of the simulation the model is subjected to cooling by an amount $\Delta T_{effective}$ as discussed in chapter 4.

In the case of the chosen simulation, the stresses generated by the matrix crystallization and thermal misfit are not large enough to cause the matrix to yield or the particle to cavitate. Therefore, at the end of the cooling step, the matrix is fully elastic and the particle is coherent (solid). The strains are therefore proportional to the stress contours, scaled by the isotropic moduli of particle and matrix material.

Figure 5-7a shows the contour plots of the $S11$, $S22$, $S33$, $S12$ at the end of the cooling step.

The general stress state of the unit cell at the end of the cooling step is that of tension in the 1-direction, and compression in the 2- and 3-directions. The zone of compression in the 1-direction in the upper right-hand corner is attributed to the geometry of the unit cell. The shear stress ($S12$) in the unit cell ranges from -5MPa to +6MPa. Its maxima are at the top and lateral boundaries of the unit cell. No specific pattern emerges from the contours.

Along the particle-matrix interface, the tension in the 1-direction ($S11$) is of a nearly constant magnitude due to the uniform stress state inside the particle. $S11$ ranges from approximately 16 to 19MPa[2]. The compressive 22- and 33-stresses range from 11 to 27MPa and from 15 to 24MPa respectively along the particle-matrix interface, with maxima at the equator and pole, and minima at approximately 35^o to 45^o measured from the horizontal. At this point, the particle is in a state of hydrostatic tension of $\sigma^h = -P = 17MPa$ which is not enough for cavitation to occur.

Stress State at Yield

At a macroscopic axial strain of $\varepsilon_{zz} = 1.1\%$ the matrix yields, whereas the particle is still coherent. Figure 5-7b shows contour plots of the stresses in the matrix at $\varepsilon_{zz} = 1.5\%$, which is not exactly the stress state at matrix yield, but an indication of it can be obtained from the stress state at the beginning of the deformation (figure 5-7a) and the stress state at $\varepsilon_{zz} = 1.5\%$.

[2]The variation displayed in the contour plots is an artifact of the way in which the stress information is conveyed through the contour plots.

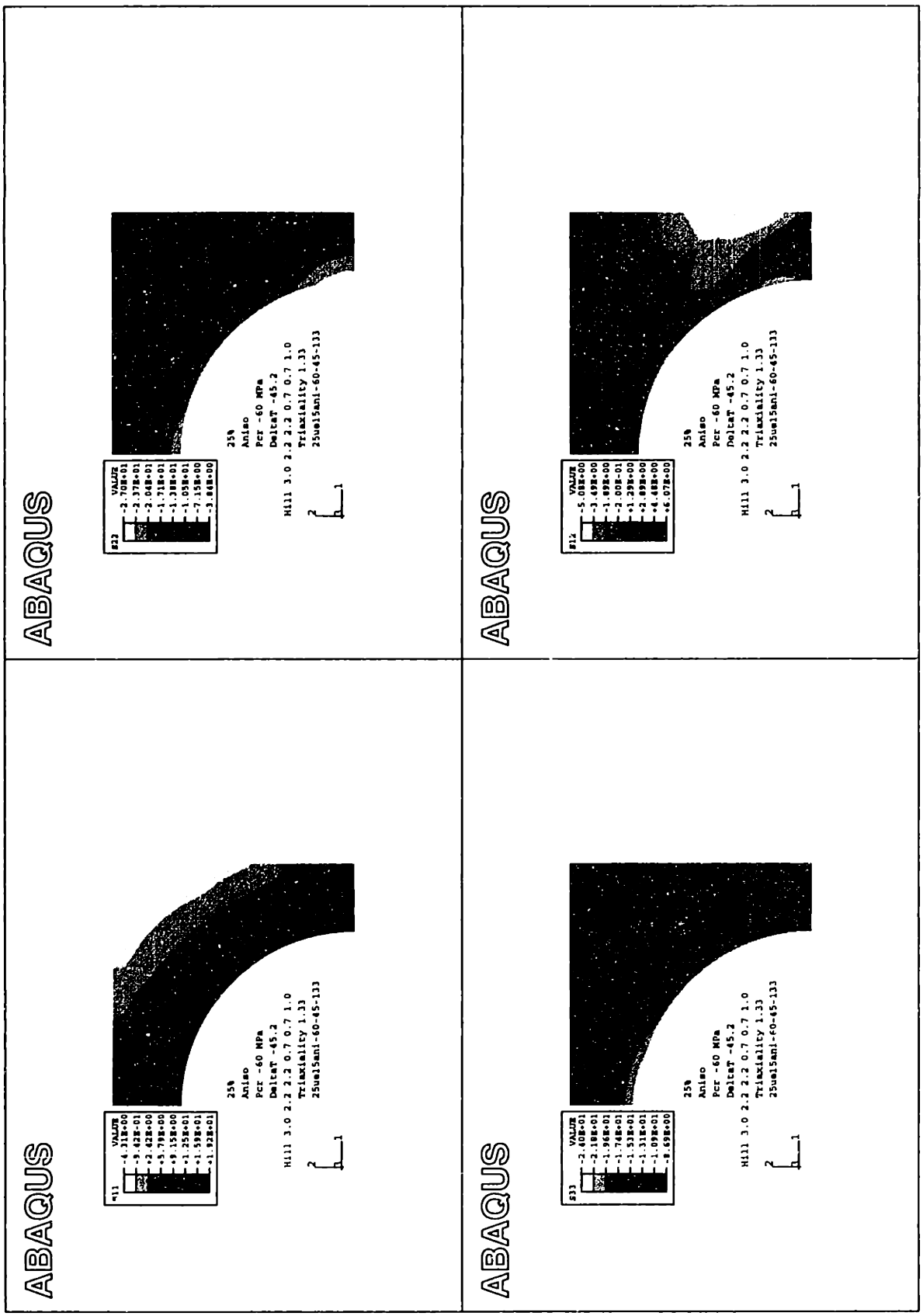

Figure 5-7a: 25ani-60-45-133: Stress components after completion of cooling. $\varepsilon_{zz} = 0$.

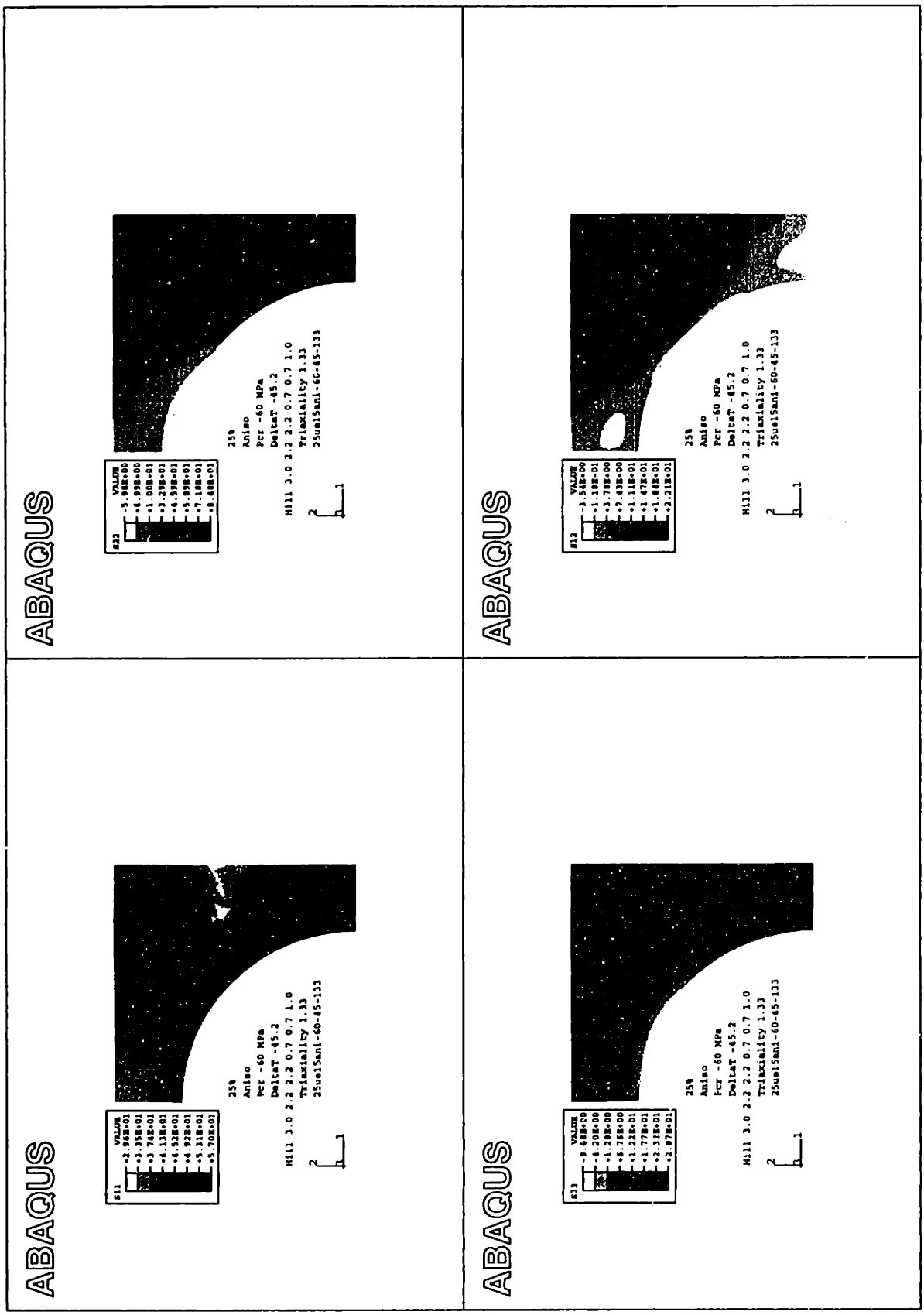

Figure 5-7b: 25ani-60-45-133: Stress components at $\varepsilon_{zz} = 1.5\%$.

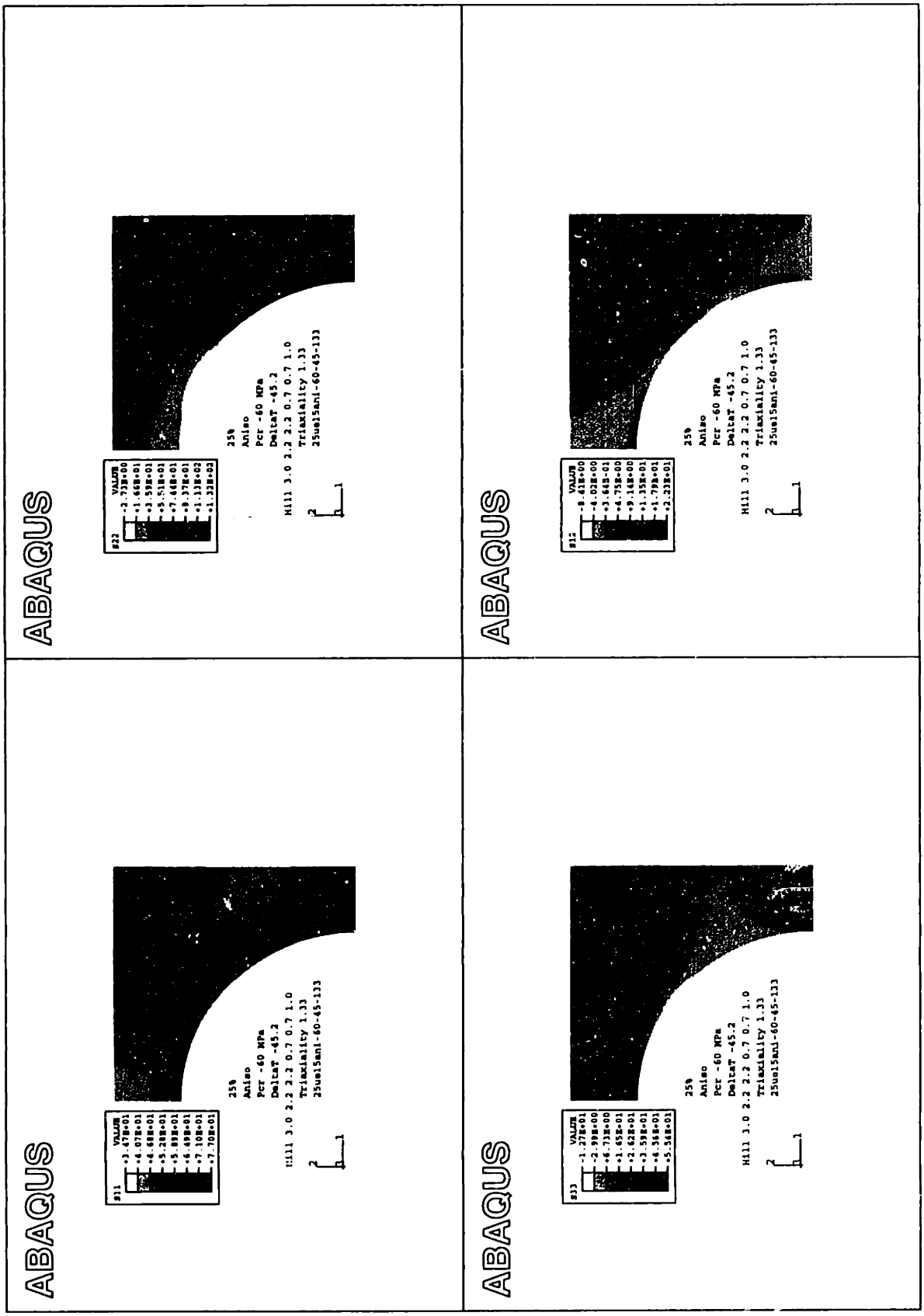

Figure 5-7c: 25ani-60-45-133: Stress components at $\varepsilon_{zz} = 2.5\%$.

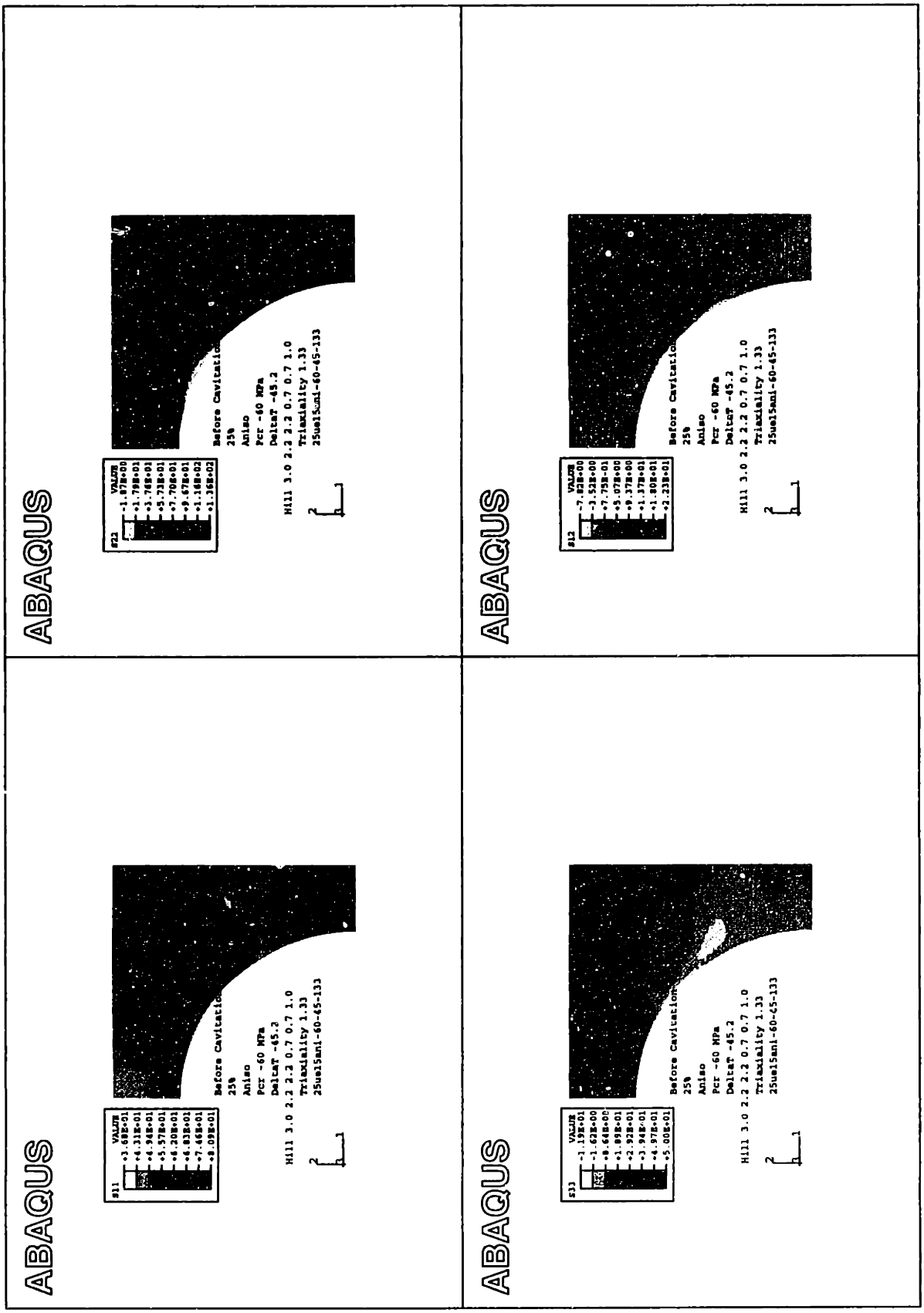

Figure 5-7d: 25ani-60-45-133: Stress components just before cavitation. $\varepsilon_{zz} = 2.81\%$.

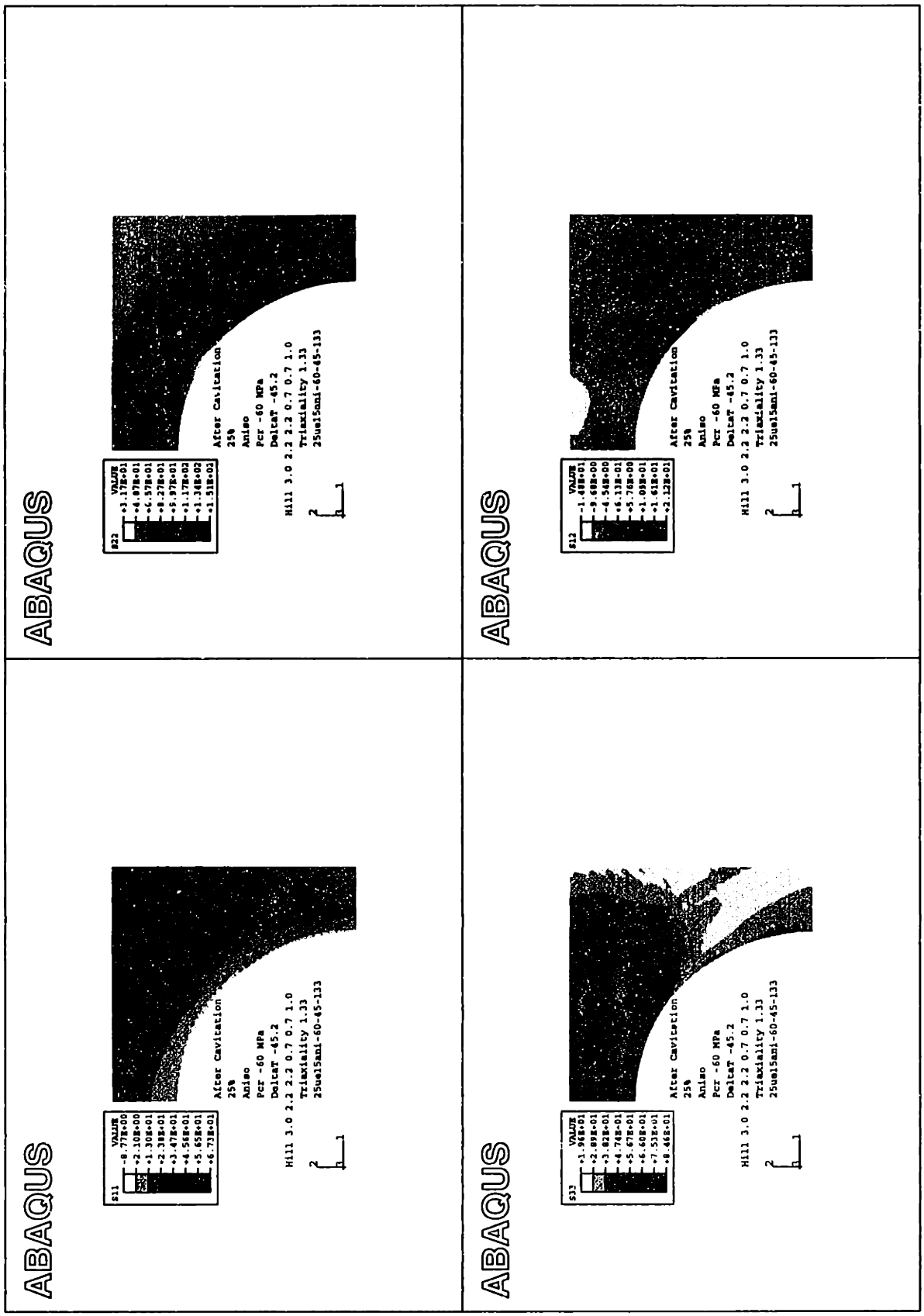

Figure 5-7e: 25ani-60-45-133: Stress components just after cavitation. $\varepsilon_{zz} = 2.82\%$.

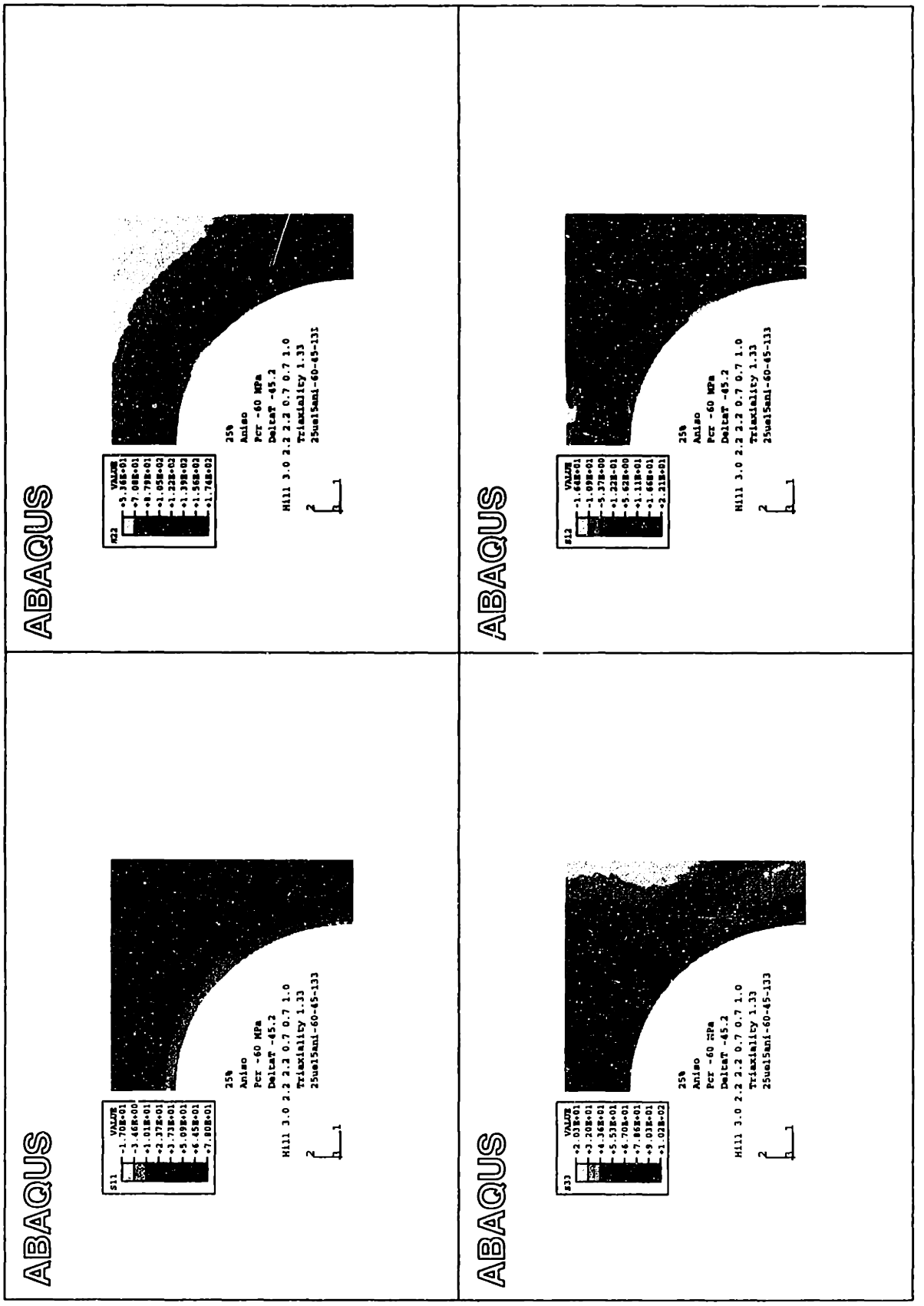

Figure 5-7f: 25ani-60-45-133: Stress components at $\varepsilon_{zz} = 3.5\%$.

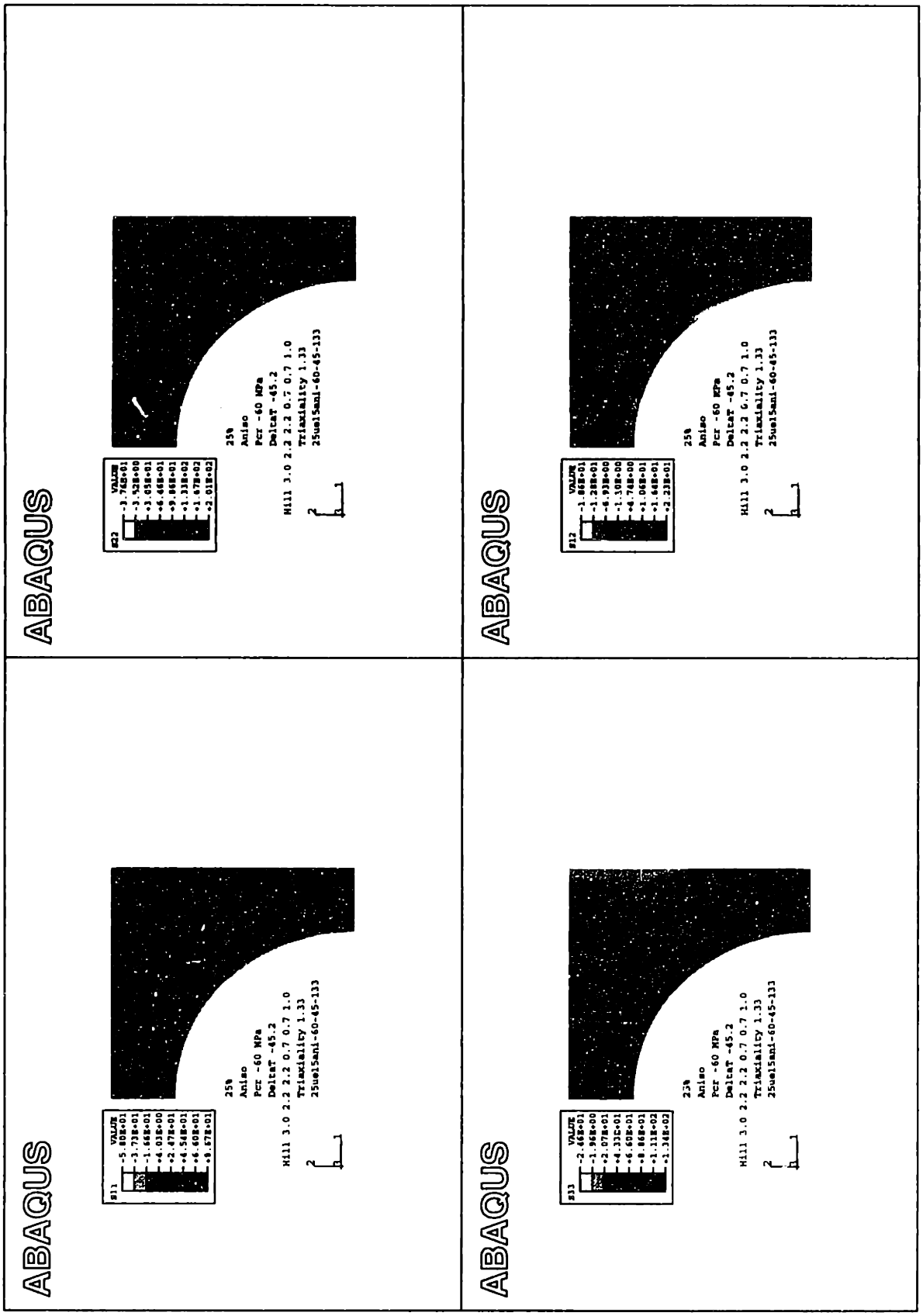

Figure 5-7g: 25ani-60-45-133: Stress components at $\varepsilon_{zz} = 4.5\%$.

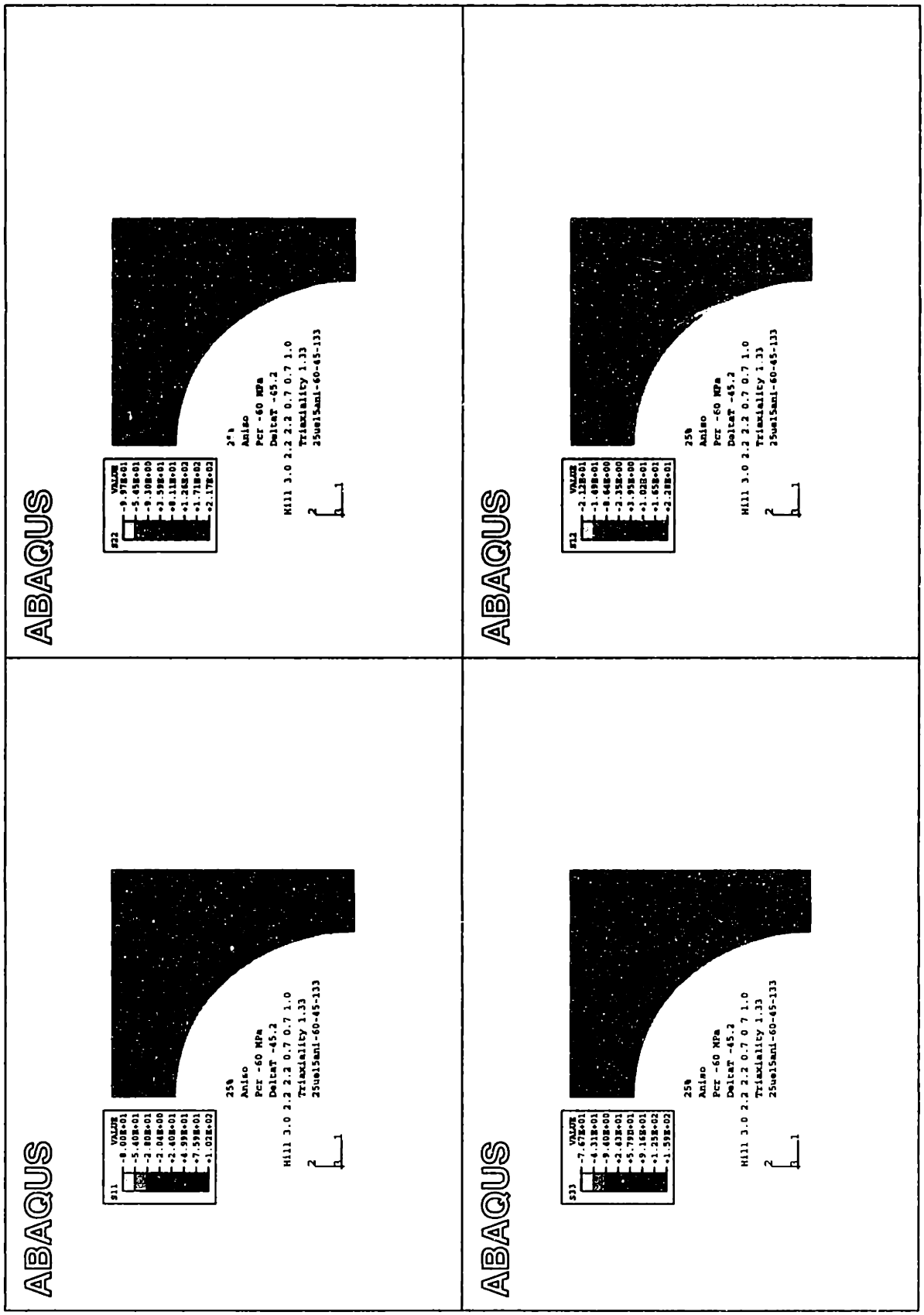

Figure 5-7h: 25ani-60-45-133: Stress components at $\varepsilon_{zz} = 5.5\%$.

Referring to figure 5-7b, $S11$ is found to have increased to a maximum of $57MPa$. Along the particle/matrix interface it ranges from 49 to $53MPa$. $S22$ displays a maximum near the particle equator due to stress concentration effect of the particle. $S33$ is found to be relatively moderate with a maximum of $29MPa$. More interestingly, $S12$ is found to have its highest values in an area in the upper right-hand corner of the unit cell, along the diagonal. This is indeed where the matrix is found to yield first in the present simulation. Since the particle does not support any shear stresses, $S12$ is found to remain very low near the particle/matrix interface[3].

The overall stress state at this point of the simulation seems to be characterized mainly by the high 22-tension near the particle equator, which is due to the macroscopic stress state of tension in the global 2-direction and the hoop stresses due to the thermal misfit between particle and matrix. Interestingly, the stress normal to the particle/matrix interface, $S11$, has increased by a factor of 2.5 from the stresses at the end of the cooling step, whereas $S22$ has increased from very small values to over $80MPa$. It appears that the matrix ligament near the particle equator experiences the stress concentration of the axial load due to the presence of the partice.

Studying the stresses at $\varepsilon_{zz} = 2.5\%$ (figure 5-7c), it is found that the previously observed trends have continued. $S22$ has increased to over $130MPa$, whereas $S11$ has reached only $77MPa$. $S33$ has cought up and has reached a maximum of $55MPa$, apperently now carrying a hoop stress in the upper part of the unit cell due to the occured matrix yield along the diagonal. $S12$ remains at $22MPa$ due to the low shear resistance of the anisotropic matrix.

Stress State before and after Particle Cavitation

Figures 5-7d and 5-7e are contour plots of the local stress state at $\varepsilon_{zz} = 2.81\%$ and 2.82%; i.e., just before and just after the particle cavitation in the case of the "25ani-60-45-133" simulation. As above, all 3 normal stress components and the 12-shear stresses are depicted in the local coordinate system.

[3]Again, the displayed non-zero value of $S12$ along the interface is an artifact of the contour plots.

Before cavitation, the particle behaves like a fluid cavity and its stress state is constant throughout. The particle supports loads that are normal to its interface with the matrix, which causes the stress normal to this interface, i.e. the normal stress in the local 1-direction ($S11$), to be constant along the interface. Figure 5-7d shows this stress as $60.4MPa$, which is equal to the cavitation strength of the particle chosen for this simulation, within the precision of the numerical solutions. The normal stresses in the 2- and 3- directions (S22 and S33) vary according to the geometry of the unit cell. As previously, $S22$ dominates near the particle equator. The zone in which $S12$ is close to the 12-yield stress, has further extended, which correlates with the general yielding in the upper right-hand corner of the unit cell (see below).

Just after the particle cavitation (figure 5-7e), $S11$ has dropped to zero along the newly created free surface of the cavity. Throughout the matrix, however, $S11$ is still at levels of up to $67MPa$. $S22$ still displays a maximum near the cavity equator with $151MPa$, and $S33$ has increased to $85MPa$ in an area that now extends throughout the top ligament of the unit cell. The most interesting change in the stress state is observed in the 12-shear stress: the zone of maximum $S12$ has moved from the rather extended area along the cell diagonal to an area along the lateral boundary. This perfectly correlates with the findings about the evolution of the matrix plasticity as described below. As expected, $S12$ continues to be zero along the particle interface, within the accuracy of the contour plots.

Further Evolution of Stress State

As the simulation continues (figures 5-7f through 5-7h), the plastic zone continues to spread out (see below), which correlates with the spreading of the zone in which $S12$ is on the order of $22MPa$. A small zone of very high shear stresses has formed near the cavity equator, which is due to the local plastic straining and re-orientation of the matrix material at that location. $S22$ continues to increase and reaches over $210MPa$ at $\epsilon_{zz} = 5.5\%$, however, its maximum evolves along one of the shear bands mid-way along the cell diagonal (see below). The stress state of the matrix becomes

increasingly dominated by the formation and evolution of the shear bands in which much of the matrix plasticity is localized.

5.3.4 Macroscopic Strain History

After the completion of the cooling step, the simulation continues with the displacement of the top of the unit cell and the application of a distributed load at the lateral boundary. More details on this are given in section 4.5.2.

The macroscopic strain history that corresponds to the chosen triaxial stress state, the chosen volume fraction and the material properties used, can be found from the simulations. Figure 5-8 shows a plot of the strain of the unit cell in the global 2-direction ε_{zz} as a function of the strain in the global 1-direction ε_{rr}. The data

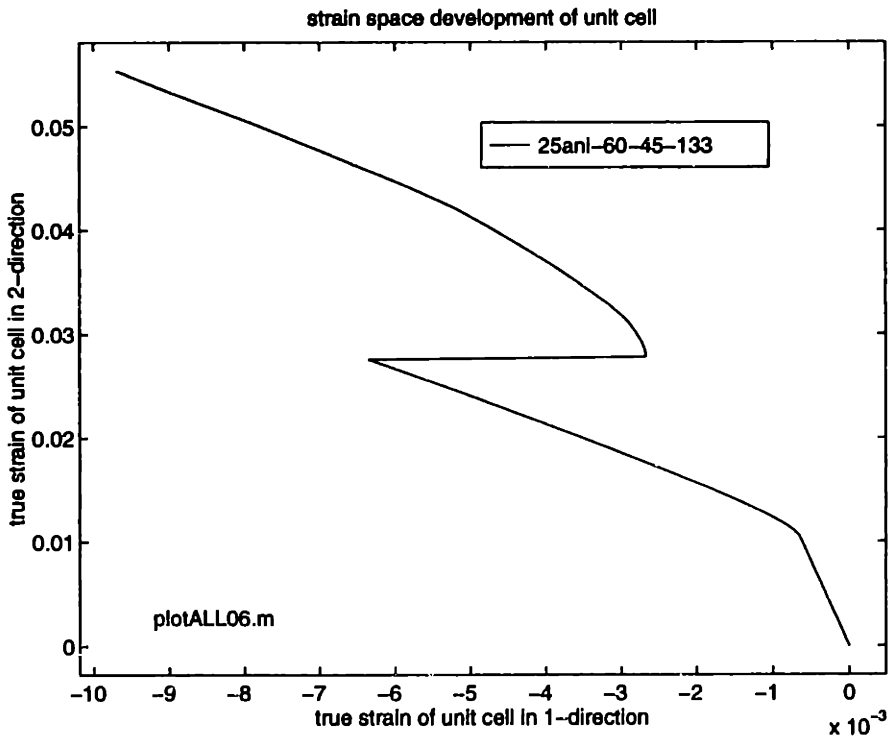

Figure 5-8: 25ani-60-45-133: Strain space evolution: ε_{zz} as function of ε_{rr}.

displayed only from the starts of the deformation part of the simulation on; i.e., the data corresponding to the cooling step is not displayed.

Starting from the point in strain space that corresponds to the undeformed unit cell, the strains increase linearly along a line with a slope of -15. At a radial strain of

$\varepsilon_{rr} = -0.08\%$ in the 1-direction and an axial strain of $\varepsilon_{zz} = +1.1\%$ in the 2-direction, the slope gradually changes to -2.7. This change of slope corresponds to the yielding of the matrix. At this point, the deformation of the matrix changes from completely elastic to partly elastic and partly plastic.

At $\varepsilon_{rr} = -0.62\%$ and $\varepsilon_{zz} = 2.7\%$, the pressure in the particle reaches the critical value, and the cavitation of the particle begins. The cavitation corresponds to the ("horizontal") line between $\varepsilon_{rr} = -0.62\%$ and $\varepsilon_{r} = -0.27\%$ at very little change in ε_{zz}. During the cavitation a small increase of approximately 0.1% in ε_{zz} is observed, which is due to the way in which the cavitation force-relaxation algorithm is implemented. See appendix C for details.

The deformation then continues along a slope, that gradually reduces to the previously observed slope of -2.7.

5.3.5 Plastic Deformation of Matrix

In order to illustrate the evolution of the plastic deformation of the matrix, the equivalent plastic strain measure ε^{p}_{equiv} (PEEQ) will first be considered in contour plots, followed by the individual plastic strain components ε^{p}_{11}, ε^{p}_{22}, ε^{p}_{33} and ε^{p}_{12}.

Evolution of the Equivalent Plastic Strain

After completing the cooling step, the simulation is continued with the displacement of the top of the unit cell and the application of a distributed load at its lateral boundary.

As the macroscopic axial strain ε_{zz} reaches 1.1%, the matrix begins to yield in the upper right-hand corner of the unit cell due to the shear stresses present here, as shown in figure 5-7b, in combination with the lower shear resistance to plastic deformation by shear (anisotropic response of the material). Figure 5-9a shows the contours of the equivalent plastic strain ε^{p}_{equiv} at $\varepsilon_{zz} = 1.5\%$. ε^{p}_{equiv} is maximum along the diagonal line from the cell center to the upper-right-hand corner of the unit cell. The highest levels of plastic deformation are located in the corner area and at a shear

band that can be identified by its orientation normal to the diagonal at approximately half the distance from the interface to the corner. In these areas, ε^p_{equiv} reaches levels of 0.7%.

Figure 5-9b shows the contour of ε^p_{equiv} at $\varepsilon_{zz} = 2.5\%$. At this strain level, the particle has not cavitated yet. The plastic strains in the unit cell have intensified to a level of up to 2%, while their spatial distribution has qualitatively not changed much. The yielded region of the unit cell has spread out further, both along the diagonal and normal to it, but tends to spread out more downward, toward the lateral boundary. Most of the unit cell along the diagonal has yielded. The first shear band has intensified and now displays the highest values of ε^p_{equiv} observed at this strain.

At a $\varepsilon_{zz} = 2.8\%$ the pressure in the particle reaches its cavitation strength, and the particle cavitates. Figures 5-9c and 5-9d show the plastic strains in the unit cell just before ($\varepsilon_{zz} = 2.81\%$) and just after ($\varepsilon_{zz} = 2.82\%$) the particle cavitation. Comparing the contour plots of ε^p_{equiv} just before cavitation with the previous contour plot at $\varepsilon_{zz} = 2.5\%$, it can be seen that the observed spatial distribution of plastic strain has not changed much. But note that this is accumulated plastic strain. The maximum ε^p_{equiv} is now 2.3%. However, the matrix has developed another area of yield along the particle-matrix interface.

The distribution and magnitudes of ε^p_{equiv} are very similar before and after cavitation. However, the small plastic zone at the particle-matrix interface spreads out along the interface and reaches levels of plastic strain that are comparable in magnitude to those in the shear band and corner. The explanation for the additional plasticity along the interface lies in the relief of normal stress along the interface which turns into a free surface upon the particle cavitation. Due to the stress relief, the matrix moves radially outward and locally undergoes additional yield along the interface or free surface. A factor not to be neglected in this explanation is the way in which the particle cavitation is implemented. During the cavitation event, the macroscopic stress state of the unit cell is artificially corrected to match the desired triaxiality by increasing the laterally applied distributed stress. This causes the lat-

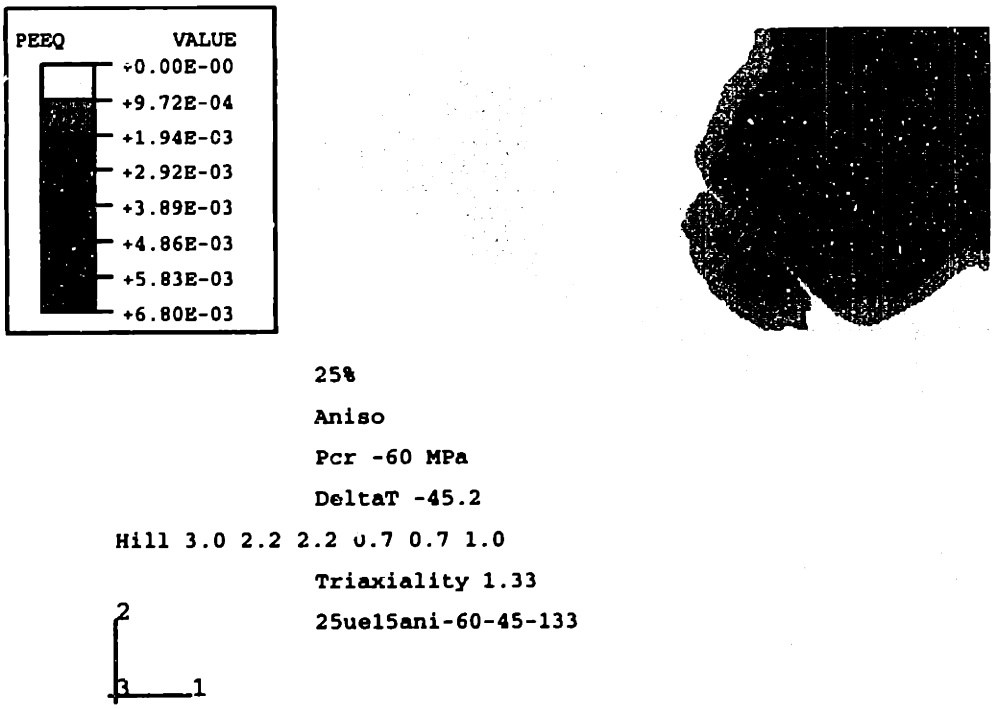

Figure 5-9a: 25ani-60-45-133: Contour plots of ε^p_{equiv} at $varepsilon_{zz} = 1.5\%$.

eral boundary to move outward while the top of the unit cell remains fix. This causes the 22-stresses to increase considerably along the now free surface near the cavity equator, and plastic straining in the 22-direction results.

Figure 5-9e shows the plastic strains in the unit cell at 3.5% macroscopic strain. The distribution of the plastic strains has changed dramatically from that at 2.3%. The magnitudes reach 8.4% in the shear band along the free surface, and 6% in the shear band across the diagonal. Most importantly, the plastic strains have localized in the two shear bands. Everywhere else in the unit cell, ε^p_{equiv} remains below 2.5%.

At $\varepsilon_{zz} = 4.5\%$ and $\varepsilon_{zz} = 5.5\%$ (figures 5-9f and 5-9g, respectively) the localization of plasticity is even more pronounced. At $\varepsilon_{zz} = 5.5\%$, ε^p_{equiv} reaches levels of over 40% in the highly localized plastic zone along the lower free surface and over 20% in the shear bands, whereas it remains below 2.5% everywhere else. At $\varepsilon_{zz} = 5.5\%$, a third shear band has developed, situated half-way between the first shear band and the free surface.

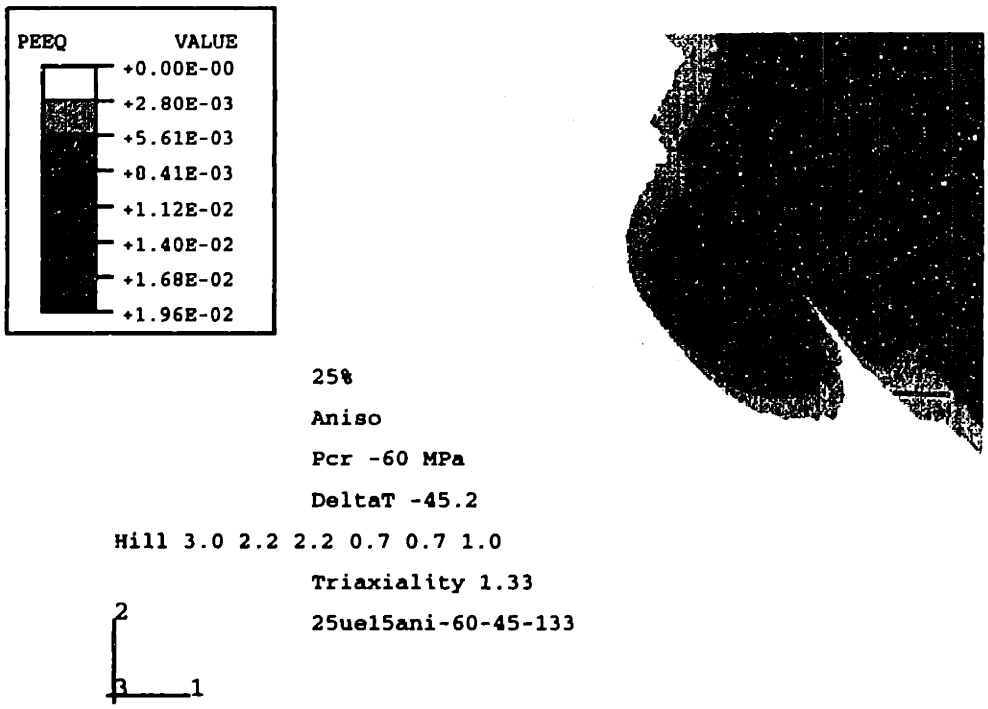

Figure 5-9b: 25ani-60-45-133: Contour plots of ε^{p}_{equiv} at $varepsilon_{zz} = 2.5\%$.

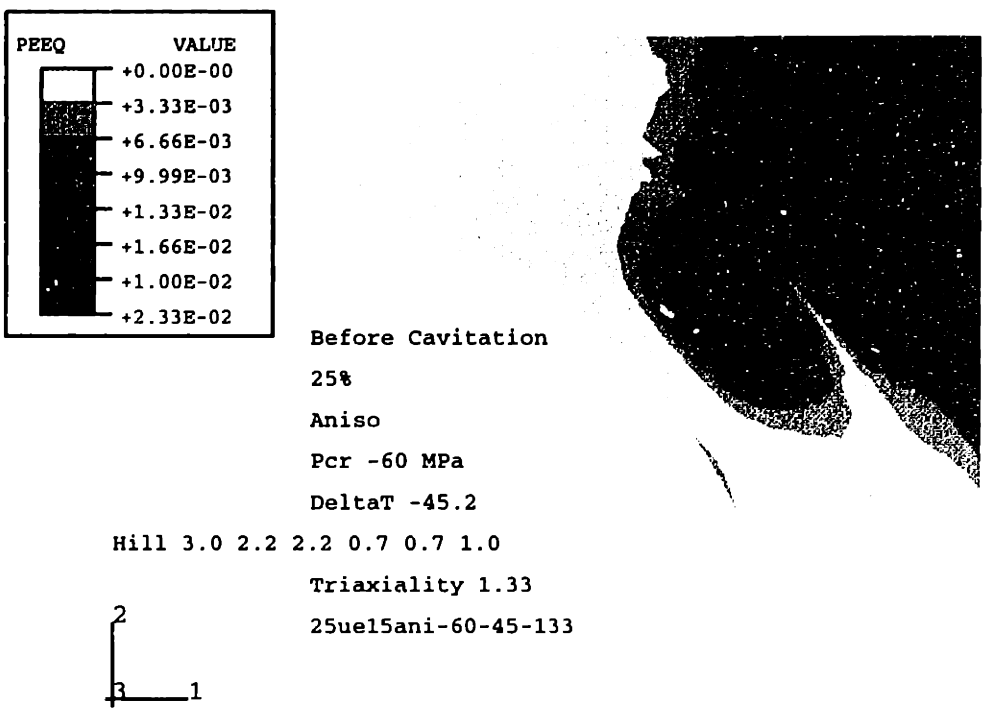

Figure 5-9c: 25ani-60-45-133: PEEQ just before cavitation. $varepsilon_{zz} = 2.81\%$.

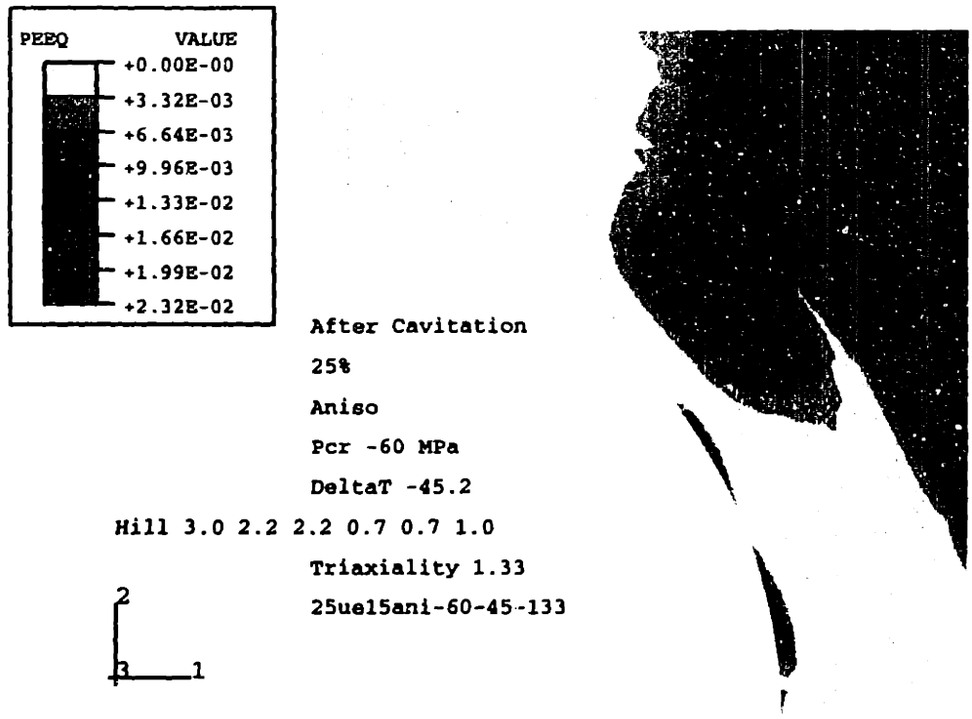

Figure 5-9d: 25ani-60-45-133: PEEQ just after cavitation. $varepsilon_{zz} = 2.82\%$.

Plastic Strain Components

Figures 5-10a through 5-10g show the contour plots of the plastic strain components at macroscopic axial strains ε_{zz} of 1.5% to 5.5%. From these plots it is obvious that the plastic deformation in the matrix is dominated by the plastic 12-shear strain ε_{12}^{p}. At $\varepsilon_{zz} = 2.8\%$ (figure 5-10c), for example, ε_{12}^{p} has reached up to 5.6%, whereas the plastic normal strains is the 1-, 2- and 3-directions are at most 0.07%, 0.3% and 0.3%, a difference of more than an order of magnitude. This trend is continued throughout the simulations for anisotropic matrix materials.

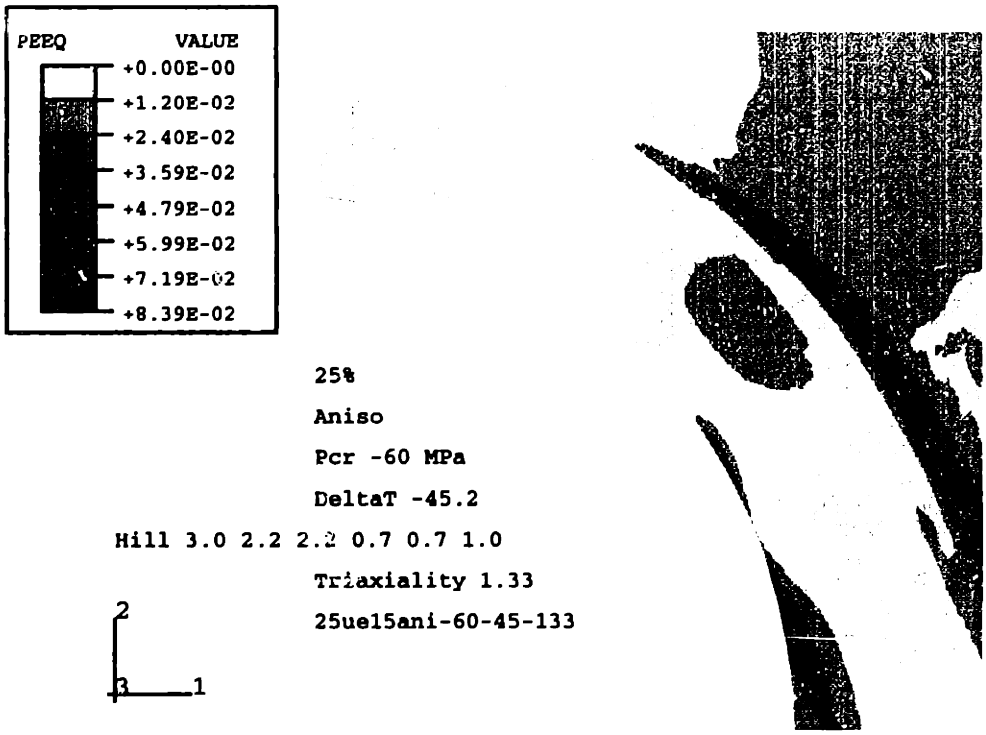

Figure 5-9e: 25ani-60-45-133: Contour plots of ε^{p}_{equiv} at $varepsilon_{zz} = 3.5\%$.

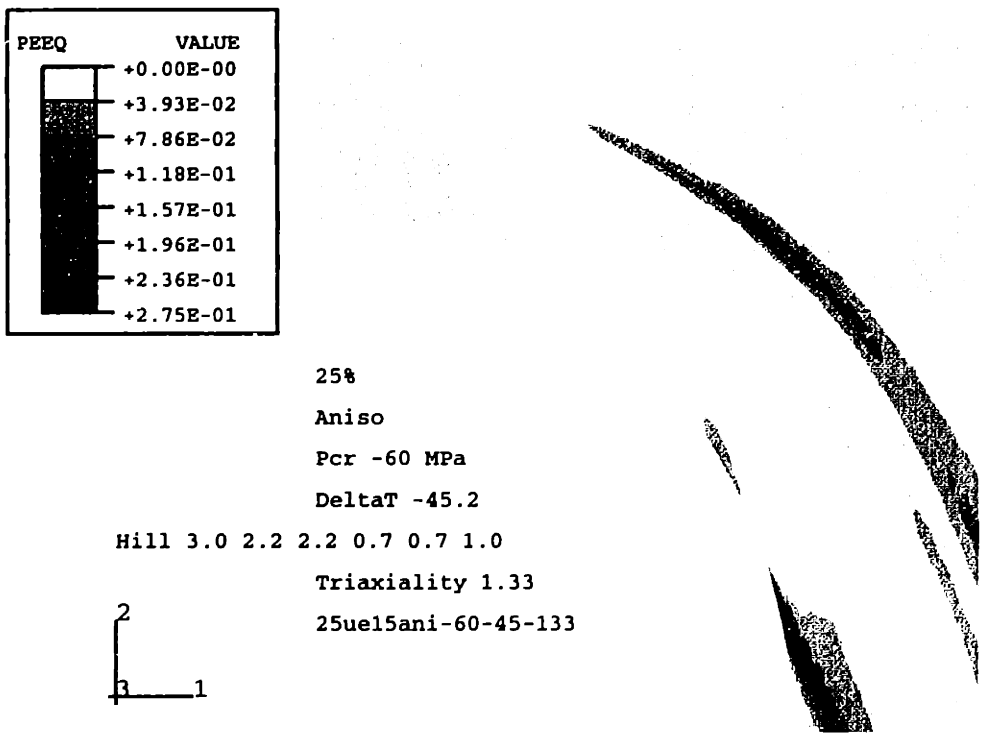

Figure 5-9f: 25ani-60-45-133: Contour plots of ε^{p}_{equiv} at $varepsilon_{zz} = 4.5\%$.

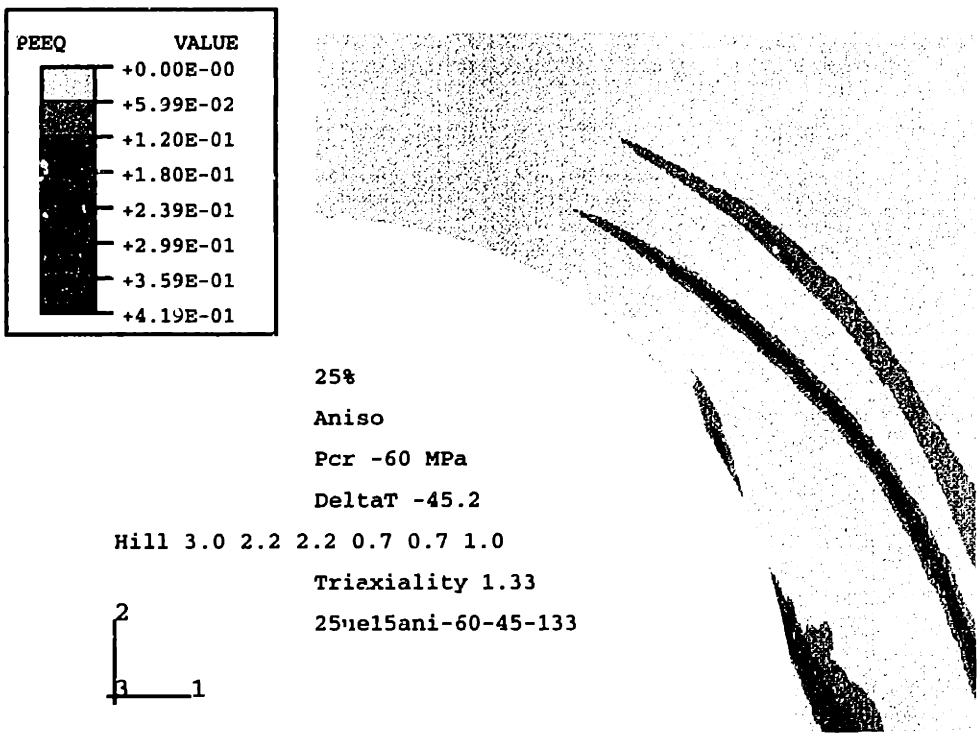

Figure 5-9g: 25ani-60-45-133: Contour plots of ε^{p}_{equiv} at $varepsilon_{zz} = 5.5\%$.

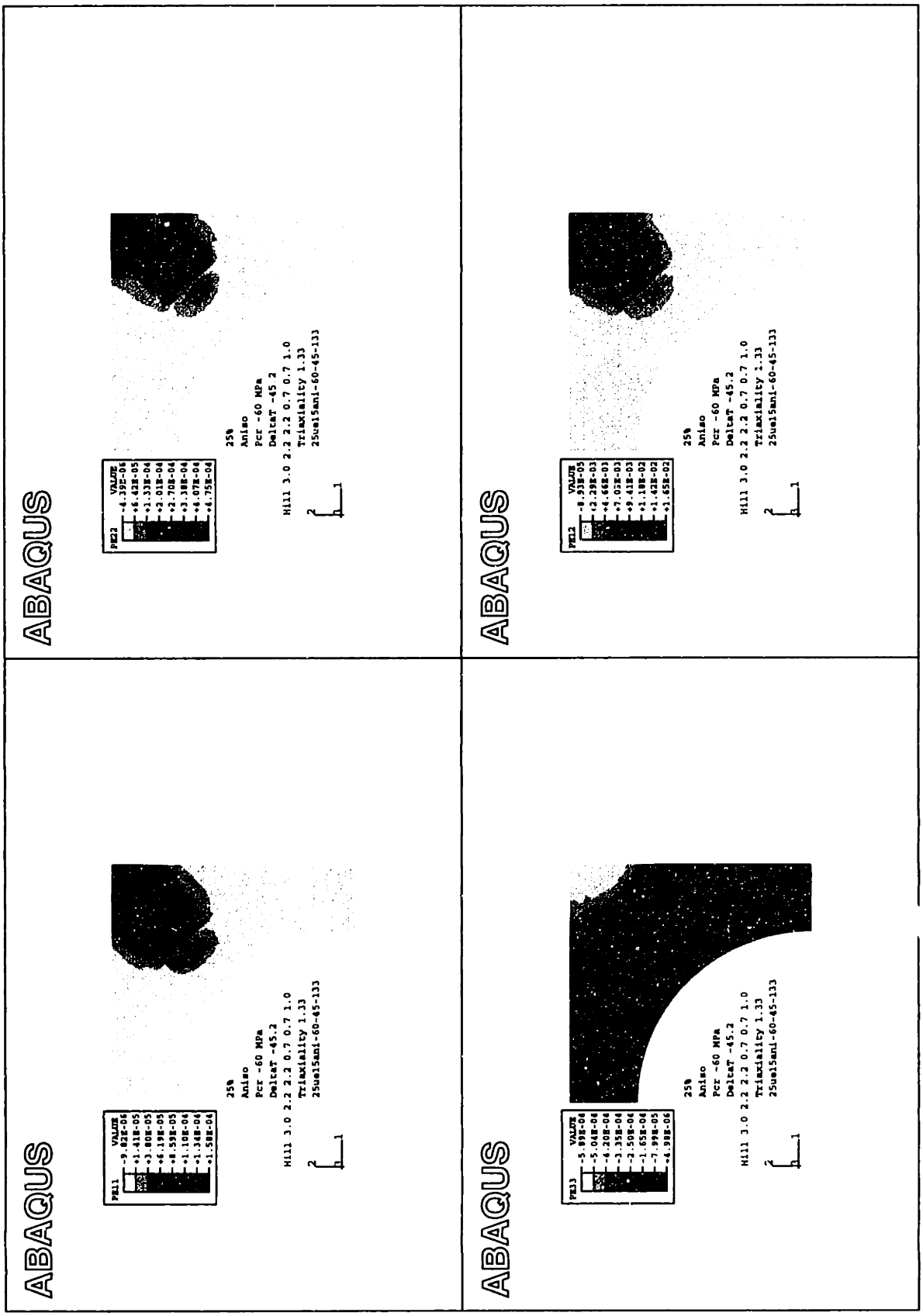

Figure 5-10a: 25ani-60-45-133: Plastic strain components at $\varepsilon_{zz} = 1.5\%$.

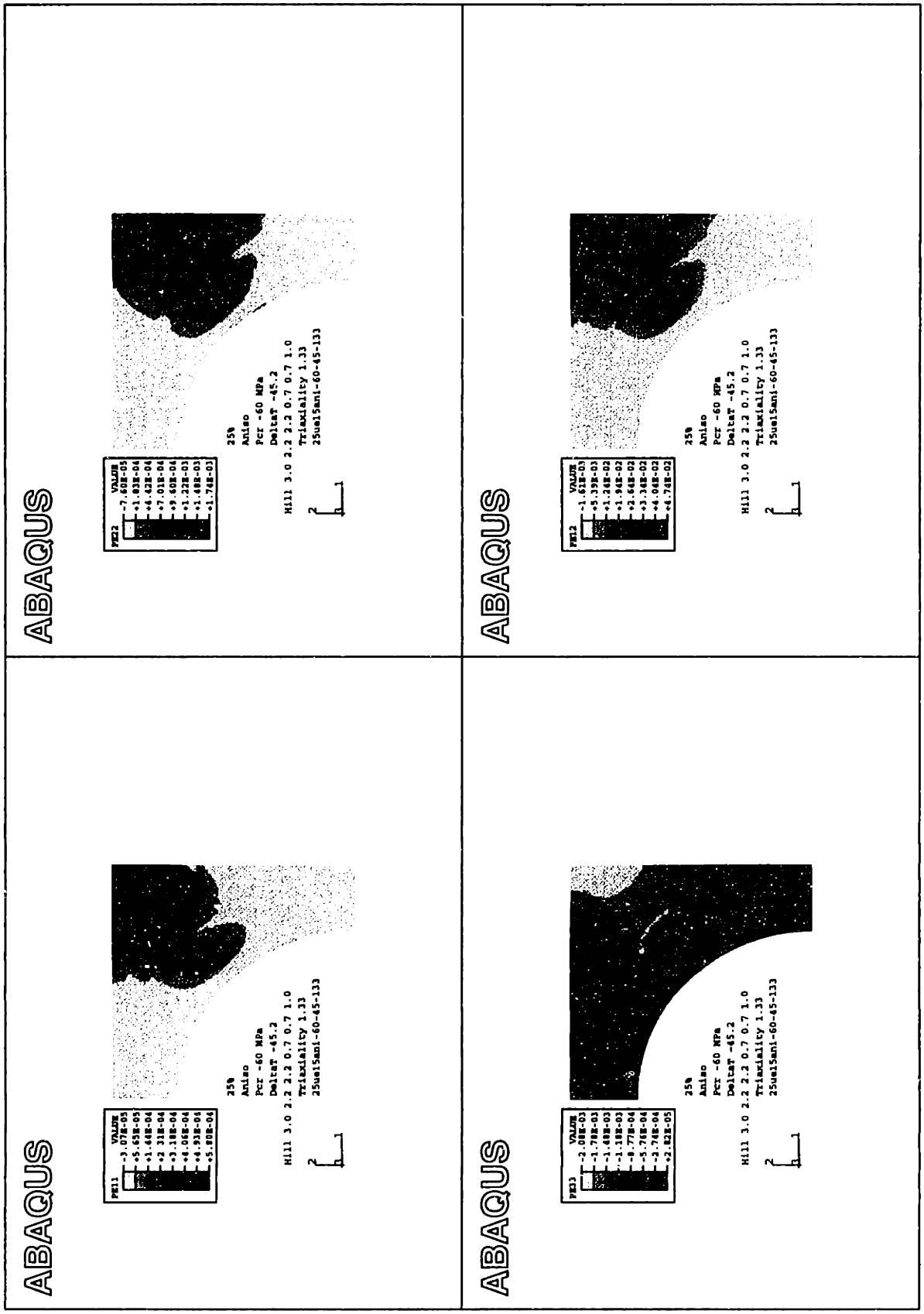

Figure 5-10b: 25ani-60-45-133: Plastic strain components at $\varepsilon_{zz} = 2.5\%$.

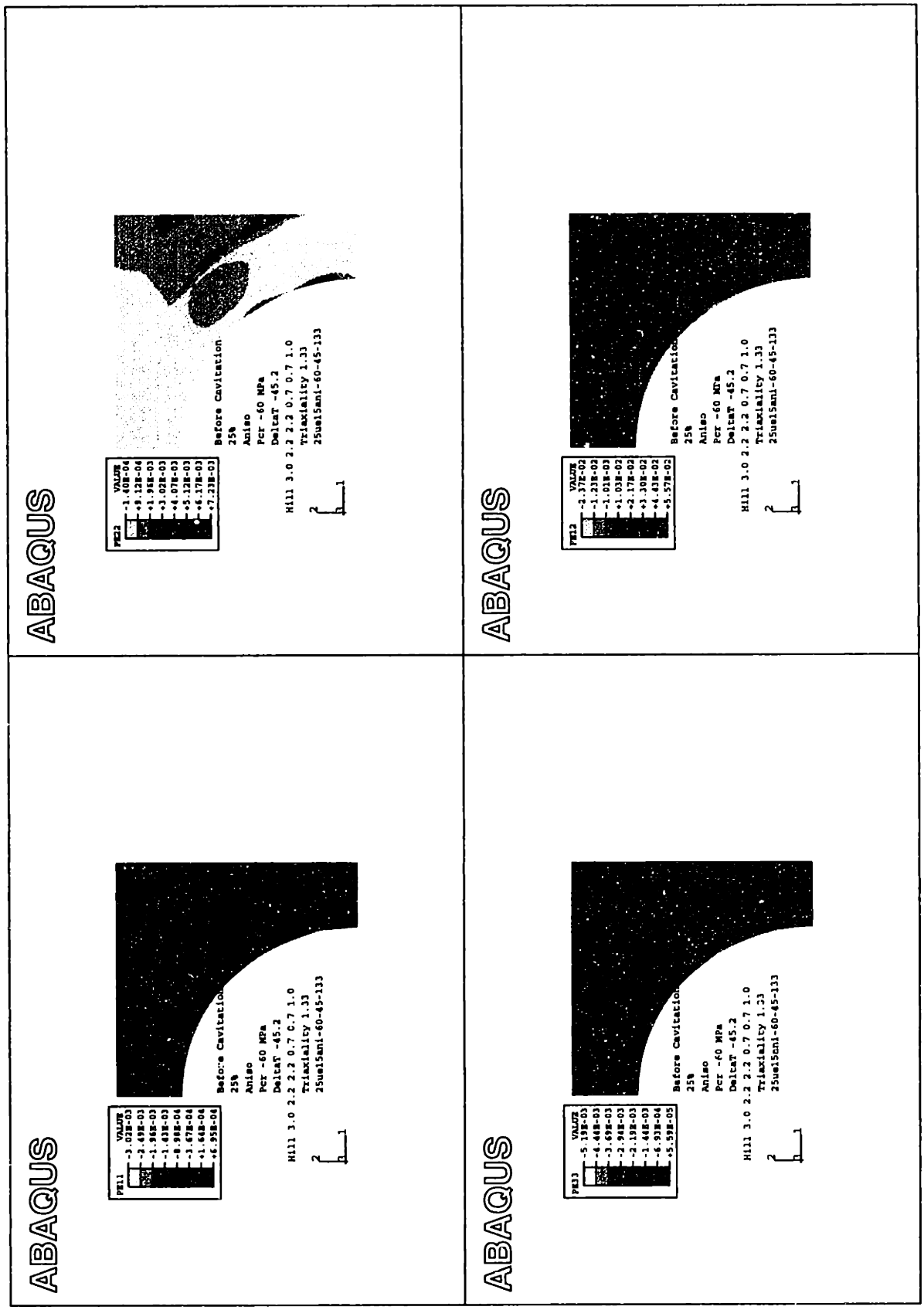

Figure 5-10c: 25ani-60-45-133: Plastic strain components just before cavitation. $\varepsilon_{zz} = 2.81\%$.

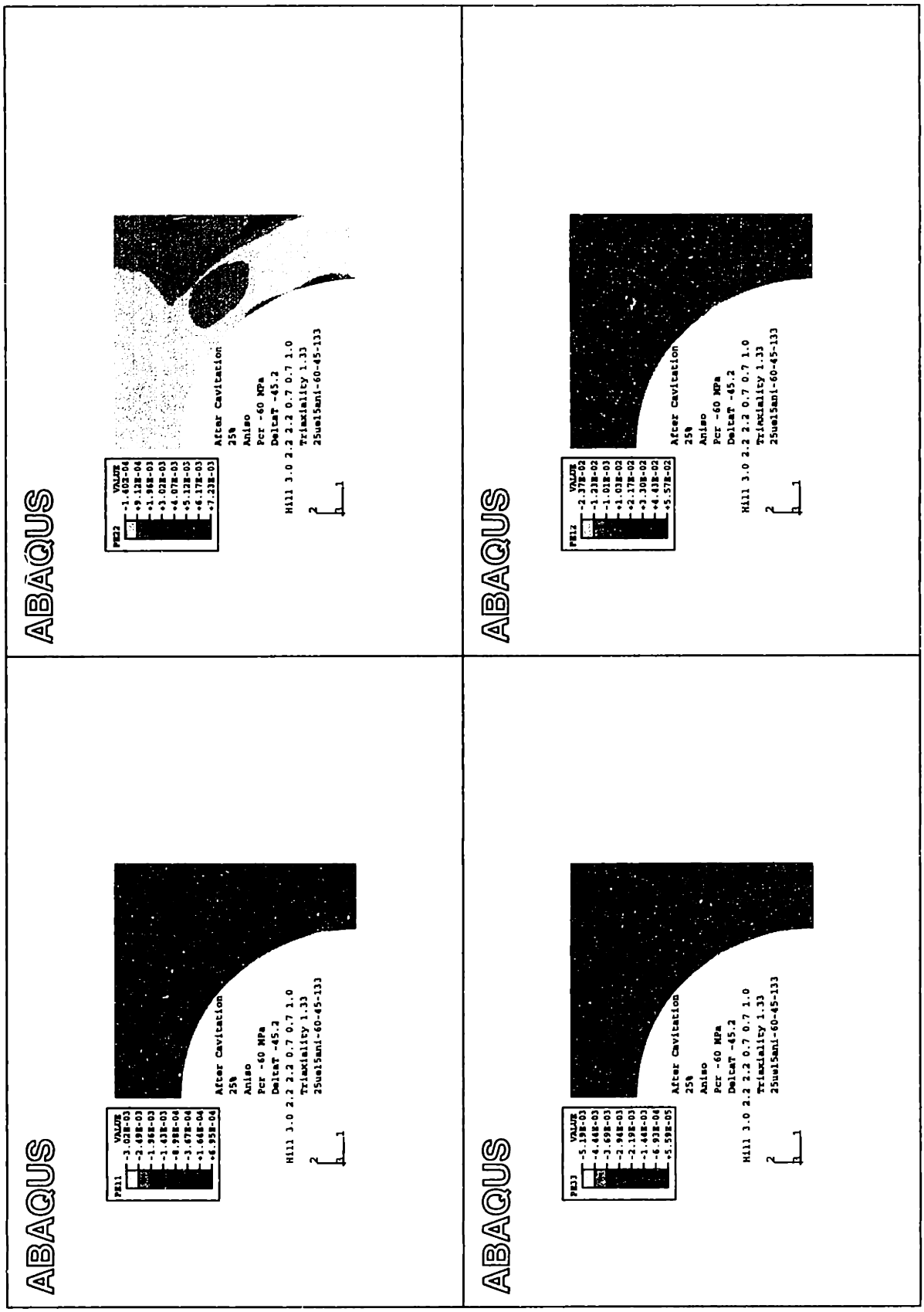

Figure 5-10d: 25ani-60-45-133: Plastic strain components just after cavitation. $\varepsilon_{zz} = 2.82\%$.

5.3.6 Macroscopic Stress-Stain Response

Figure 5-11a is a plot of macroscopic axial stress σ_{zz} versus macroscopic axial strain ε_{zz} of the unit cell. The origin of the stress-strain plot has been chosen such that the unit cell reaches zero strain and zero stress at the end of the cooling step; i.e., the macroscopic deformation begins at $\varepsilon_{zz} = 0$ and $\sigma_{zz} = 0$. On the stress-strain plot this is reflected by the short horizontal line (at $\sigma_{zz} = 0$) between $\varepsilon_{zz} = 0$ and $\varepsilon_{zz} = 0.56\%$.

After the cooling, the deformation of the unit cell begins with the axial displacement of its top and distributed loading of its lateral boundary. The macroscopic stress-strain curve of the initially elastic matrix with solid particle follows an apparent slope of approximately $4.6GPa$. At $\varepsilon_{zz} = 1.5\%$, the matrix begins to yield and the slope of the stress-strain curve changes to $1.5GPa$. At $\varepsilon_{zz} = 2.8\%$ the particle cavitates causing σ_{zz} to drop from $80MPa$ to $60MPa$. Upon further straining, the unit cell hardens again, reaching a peak macroscopic axial stress of $\sigma_{zz} = 79MPa$ at $\varepsilon_{zz} = 5.5\%$ strain. Subsequently, the load-bearing capacity of the unit cell declines and σ_{zz} drops steadily.

Because of the laterally applied load, the apparent stiffness of the unit cell's elastic stress-strain curve appears to be higher than the actual strength of the unit cell. The laterally applied load adds in fact a hydrostatic component to the macroscopic stress state of the unit cell, which depends on the triaxiality ratio Σ. Figure 5-12 shows a plot of the unit cell's macroscopic deviatoric true axial stress $\hat{\sigma}_{zz}$ as function of ε_{zz}. The slope of the stress-strain curve of the unit cell is found to be $1.6GPa$ when it is computed from the deviatoric stress $\hat{\sigma}_{zz}$ as function of ε_{zz}. The peak deviatoric stress is found to be $\hat{\sigma}_{zz}^{max} = 27MPa$. See page 156 for more details on the connection between $\hat{sigma}_{zz}$, σ_{zz} and Σ.

When comparing figure 5-12 with the ε^p_{equiv}-contours (figures 5-9a-f), the decrease in the slope of σ_{zz} vs. ε_{zz} can be related to the increased localization of ε^p_{equiv} in the shear bands along the cavity surfcaca as seen at $\varepsilon_{zz} \geq 3.5\%$. Furthermore, the drop in σ_{zz} starting at $\varepsilon_{zz} \simeq 5\%$ coincides with the emergence of an additional shear band (figure 5-9g).

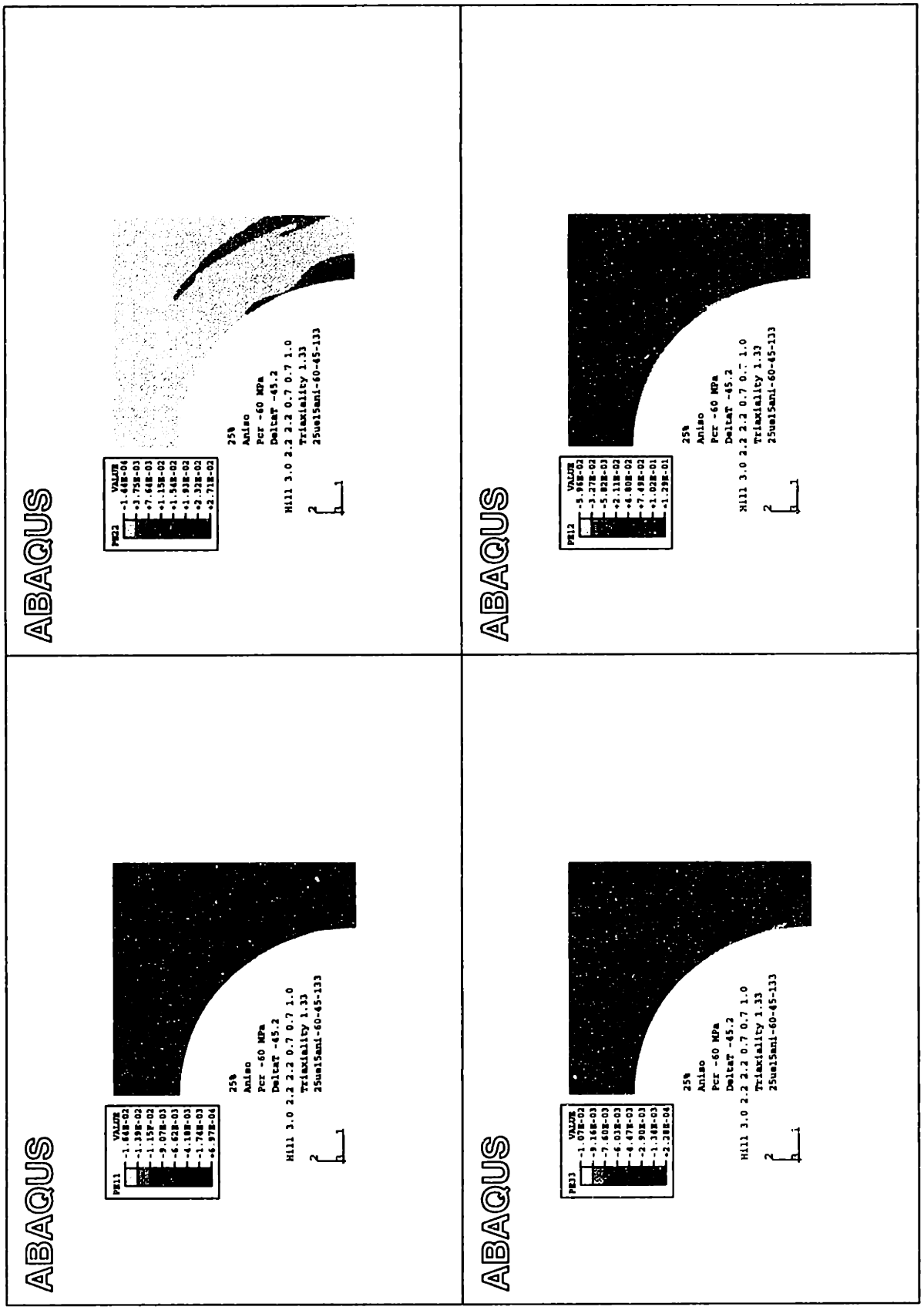

Figure 5-10e: 25ani-60-45-133: Plastic strain components at $\epsilon_{zz} = 3.5\%$.

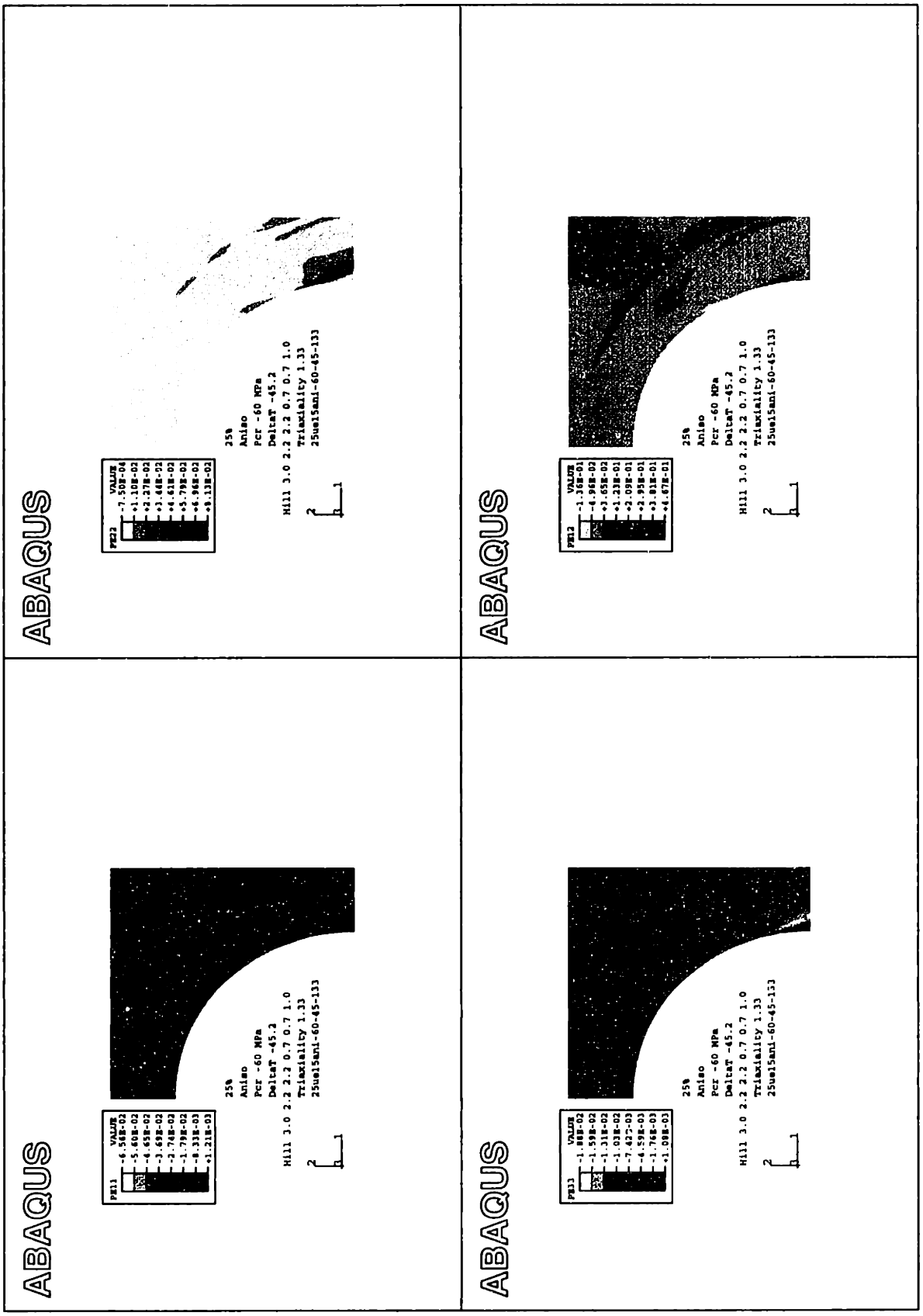

Figure 5-10f: 25ani-60-45-133: Plastic strain components at $\varepsilon_{zz} = 4.5\%$.

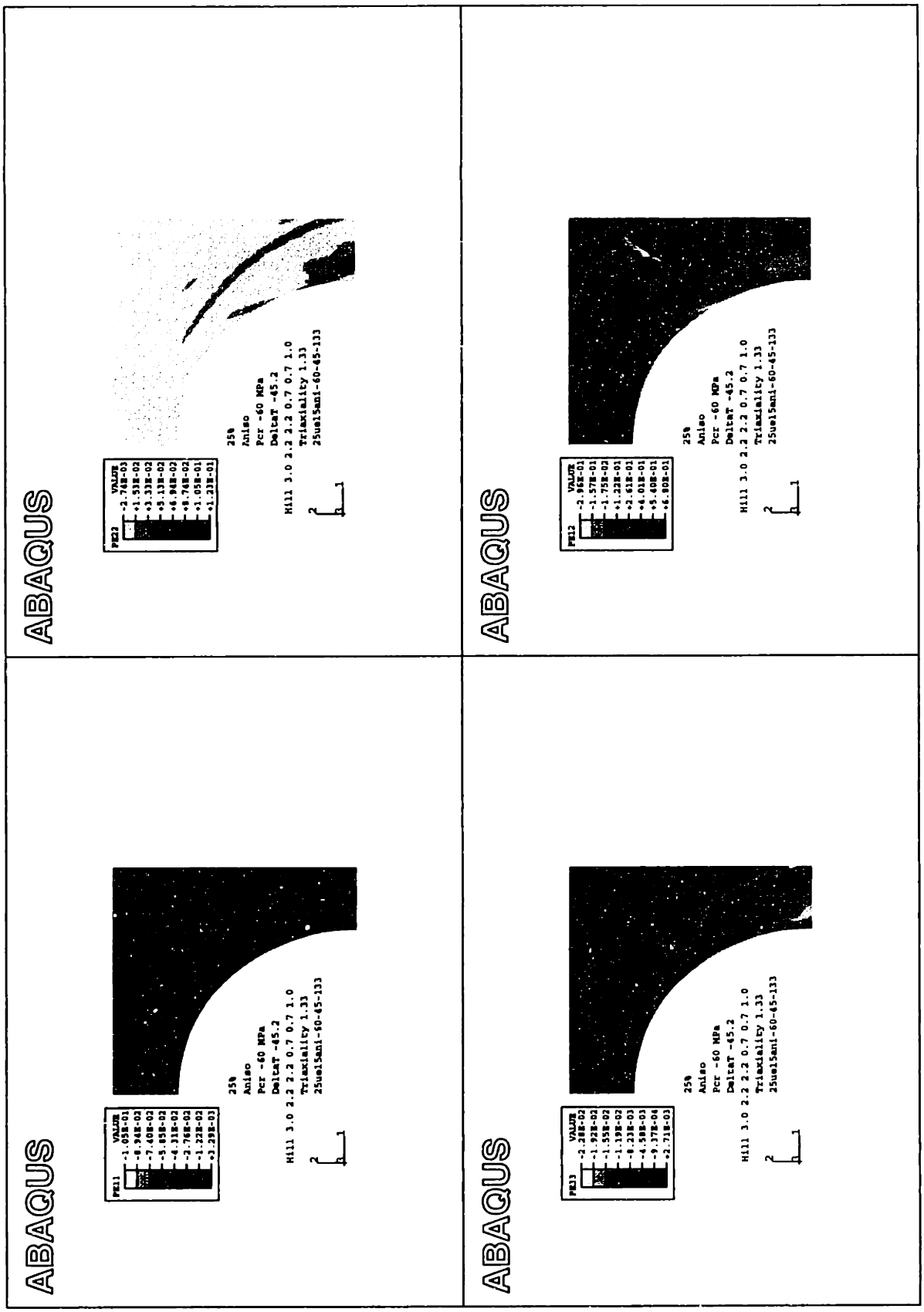

Figure 5-10g: 25ani-60-45-133: Plastic strain components at $\varepsilon_{zz} = 5.5\%$.

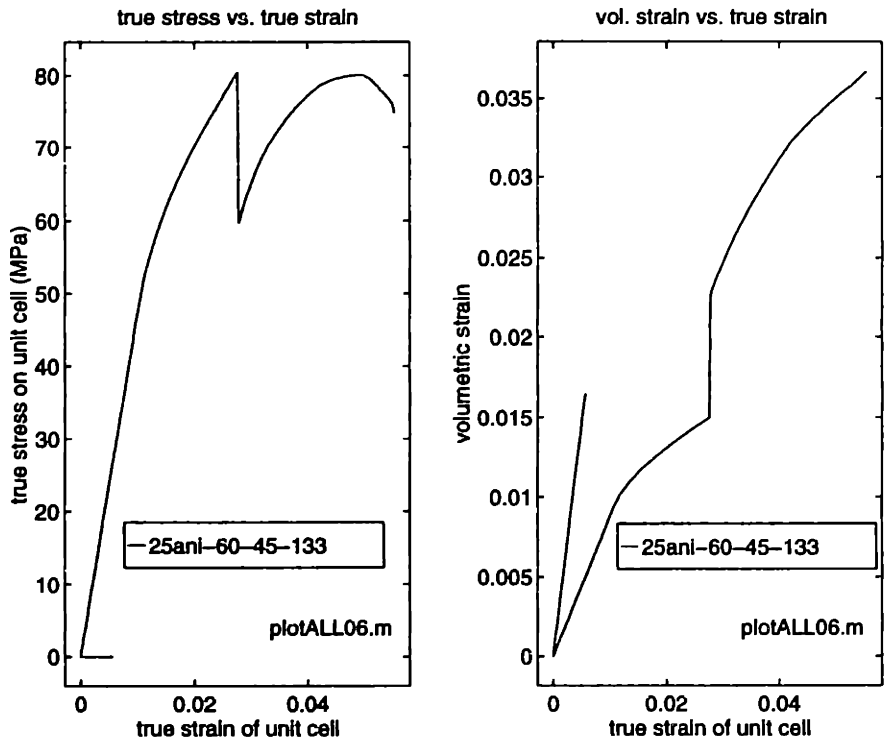

Figure 5-11: 25ani-60-45-133: Macroscopic stress σ_{zz} and volumetric strain Ψ_m of the unit cell as functions of macroscopic axial true strain ε_{zz}.

5.3.7 Volumetric Strain History of the Unit Cell

Figure 5-11b shows the unit cell's volumetric strain plotted against the macroscopic axial strain of the unit cell.

For the same reasons as above, the cooling step at the start of the simulation can be identified by the line starting at an axial strain of $\varepsilon_{zz} = 0.56\%$ and a volumetric strain of $\Psi_m = 1.7\%$, and ending at both strain measures being zero.

During the elastic part of the deformation, the unit cell follows an initial slope of 0.9 up to the yield point at $\varepsilon_{zz} = 1.5\%$. From yield until the particle cavitation at $\varepsilon_{zz} = 2.8\%$, the volumetric strain increases with a slope $\frac{\Psi_m}{\varepsilon_{zz}}$ 0.26 and 0.31. The increase in Ψ_m due to particle cavitation is 0.8%. After particle cavitation the Ψ_m follows an initial slope of 0.9 that gradually decreases to a slope of 0.31 over the next 2% of axial strain.

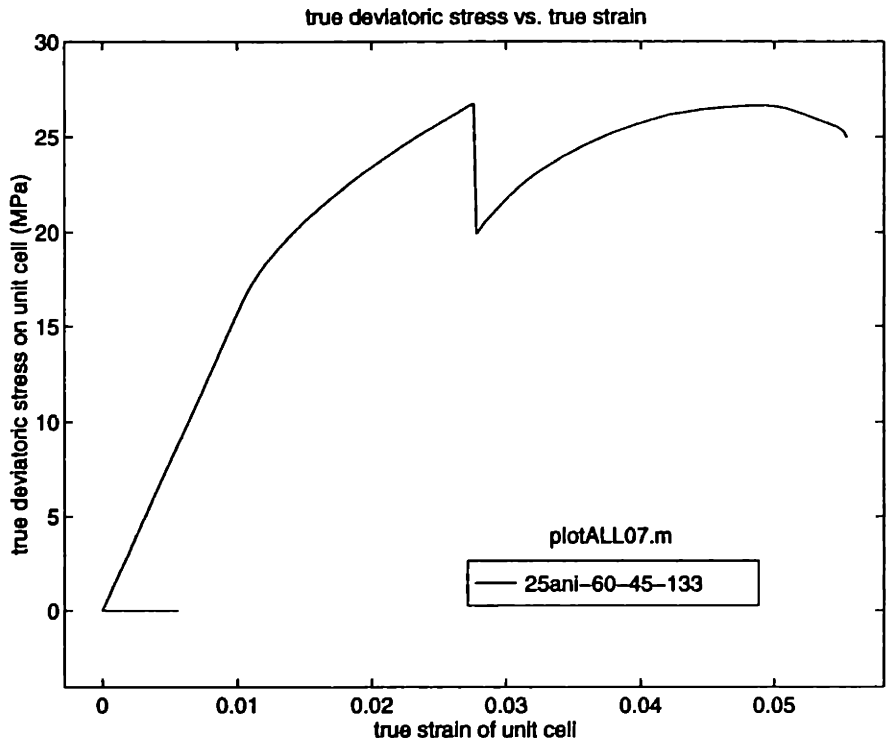

Figure 5-12: 25ani-60-45-133: Macroscopic deviatoric true stress $\hat{\sigma}_{zz}$ as function of macroscopic true axial strain ε_{zz}.

5.3.8 Evolution of the Pressure in the Particle

Figure 5-13a shows a plot of pressure P in the particle as a function of axial true macroscopic strain ε_{zz} of the unit cell. From an initial macroscopic axial true strain of $\varepsilon_{zz} = 0.5\%$ the particle pressure decreases from zero to -18.6 MPa at $\varepsilon_{zz} = 0$. This initial built-up of pressure is due to matrix crystallization and thermal misfit between particle and matrix as discussed above.

The elastic part of the deformation between $\varepsilon_{zz} = 0$ and $\varepsilon_{zz} = 1.0\%$ is reflected in a linear increase of negative particle pressure along a slope of approximately $-2.3GPa$. After matrix yield the particle pressure follows a slope of $-0.7GPa$. At $-60MPa$, the particle cavitates and the pressure is linearly decreased to zero over a $\Delta\varepsilon_{zz}^{cavitation} = 0.01\%$. After completion of the cavitation event, the particle pressure remains zero for the rest of the simulation.

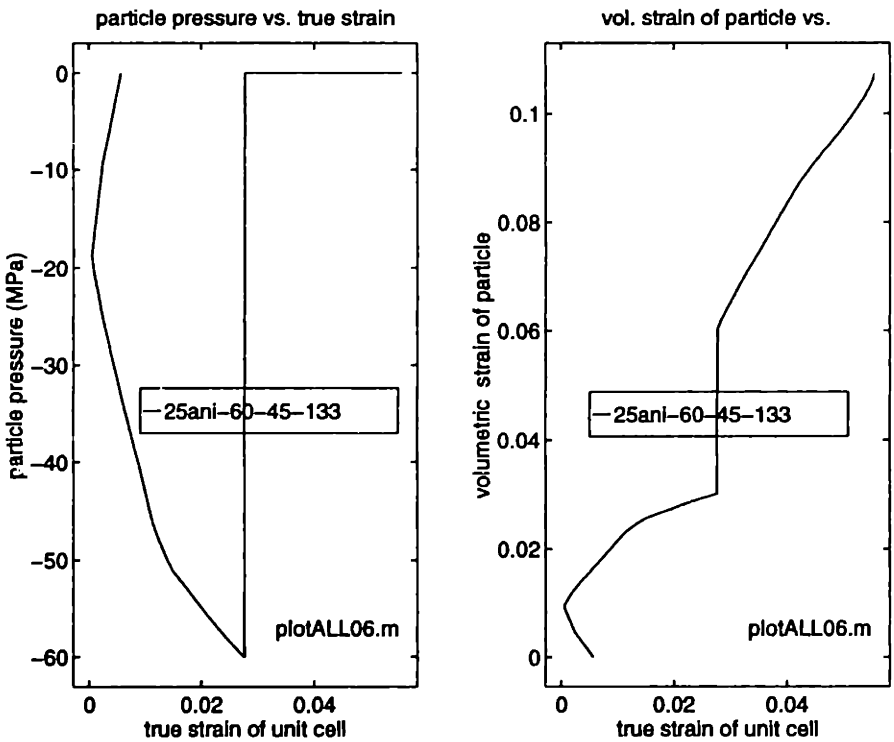

Figure 5-13: 25ani-60-45-133: Particle pressure P and volumetric strain $\Psi_{p/c}$ of the particle as functions of macroscopic axial true strain ε_{zz}.

5.3.9 Volumetric Strain in the Particle and Cavity

Figure 5-13b is a plot of the particle's volumetric strain Ψ_p as a function of axial true macroscopic strain ε_{zz} of the unit cell. After the particle has cavitated, the volumetric strain continues to be recorded, now corresponding to the volumetric strain Ψ_c of the growing cavity.

Again, the cooling step is visible as the increase of Ψ_p from zero to 0.9% between $\varepsilon_{zz} = 0.56\%$ and $\varepsilon_{zz} = 0$. During the elastic and plastic parts of the simulation, the Ψ_p follows first a slope of 1.2 and then a slope of 0.35. During the transition from fluid-filled cavity to hollow cavity Ψ_p increases by 3% to approximately 6%. After the cavitation event, Ψ_c increases along a slope of approximately 1.75.

In the following sections the same type of information on a series of simulations is presented, while discussing the effects of varying a number of extrinsic and intrinsic parameters. Starting with the effect of varying the triaxiality of the applied macro-

scopic stress state, then examining the effect of the particle cavitation strength and finally the effects of the matrix properties will be studied.

Referring back to figure 4-21 on page 94, the two simulations fit into the schematic as follows. The first example, involving an isotropic matrix under simple tension with a pre-existing cavity is situated in sector D in the schematic. The more involved simulation of the second example (anisotropic matrix, high triaxiality and cavitating particle) started out in sector A and, upon the particle cavitation event, transtitioned into sector B.

The results presented below will first examine the effect of varying the triaxiality ratio Σ on simulations corresponding to each of the sectors; i.e. what influence does Σ have on the matrix plasticity, particle pressure etc. on simulations corresponding to sectors A, B, C or D. Next the effect of varying the particle pressure will be studied, which corresponds to the effects that a transition from sector A to sector B, or from C to D has on the matrix plasticity etc. when it occurs at different critical particle pressures P_{cr}. Finally, the effects of the matrix properties on the same parameters will be examined, which corresponds to a comparison between cases A and C, and between B and D.

5.4 Effect of Varying the Triaxial Stress State Σ

5.4.1 Introduction

In order to study the effect of varying loading conditions on the unit cell, a series of simulations with different triaxiality ratios were undertaken. The triaxiality ratios chosen were $\Sigma = 0.33$, 0.66, 1.33 and 2.33 which correspond to a ratio of applied radial stress to applied axial stress $\frac{\sigma_{rr}}{\sigma_{zz}}$ of 0, $\frac{1}{4}$, $\frac{1}{2}$ and $\frac{2}{3}$, respectively.

Within the variation of the triaxiality, 4 cases of unit cells were studied. They are characterized by having either an anisotropic or an isotropic matrix, and they include either a non-cavitating particle acting like a fluid-filled cavity, or a hollow cavity. In section 4.5.2 the circumstances under which the above cases are representative of a rubber-nylon system are discussed.

Referring to figure 4-21 on page 94, each of those cases corresponds to one of the sectors A, B, C and D of the schematic. It is within each sector that the triaxiality is varied.

5.4.2 Effect of Varying Σ on Particle Pressure and Particle Cavitation

Figures 5-14a and 5-15a are plots of the pressures in the particles as a function of true macroscopic axial strain of the unit cell at four triaxiality ratios. In the chosen simulations the particles are not allowed to cavitate. The matrix is anisotropic in figure 5-14a and isotropic in figure 5-15a. (The corresponding job names are "25ani-nv-45-xxx" and "25iso-nv-45-xxx". See appendix A for an explanation)

General Trends

The higher the triaxiality of the applied stress state, the higher are the negative pressures the particles experience in all cases. Figures 5-14a and 5-15a can be used to read off whether a particle with a given cavitation strength cavitates under given triaxial loading conditions, and, if yes, at what level of macroscopic axial strain.

A general trend for unit cells with both anisotropic and isotropic matrix properties is that at a given macroscopic axial strain, the negative pressure experienced by the particle increases with increasing triaxiality ratio. This means that the higher the triaxiality ratio, the lower the axial strain level at which the cavitation of a particle with given cavitation strength occurs.

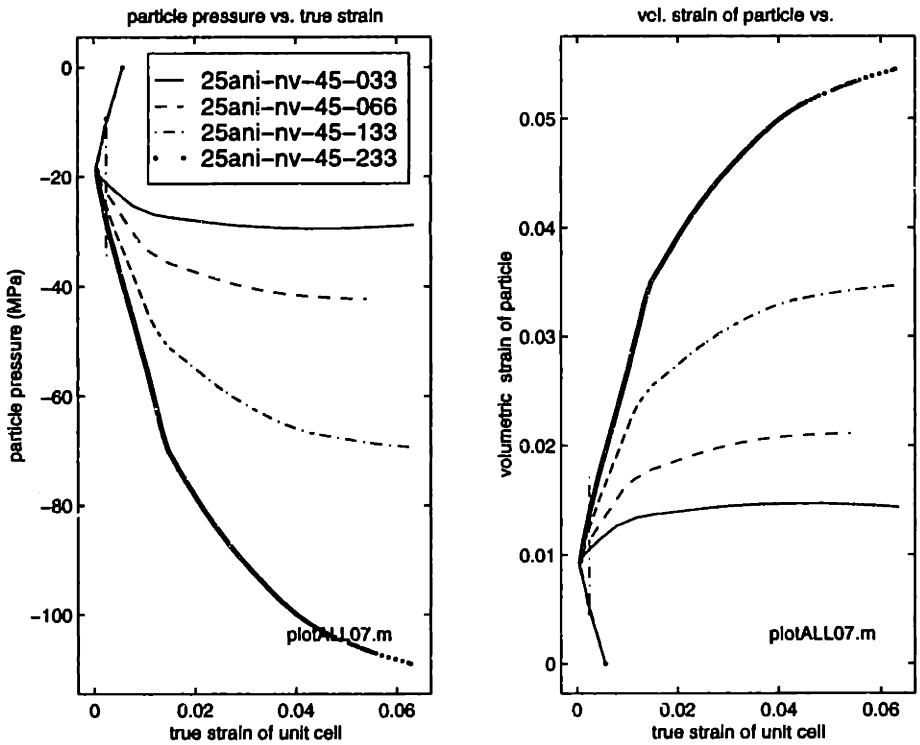

Figure 5-14: (a) particle pressure P and (b) particle volumetric strain Ψ as functions of macroscopic axial true strain ε_{zz}. Anisotropic matrix.

Anisotropic Matrix

In the anisotropic case, all particles experience a monotonic increase in negative pressure from the initial pressurization during the cooling step on. Within the first 6% of macroscopic axial strain ε_{zz}, the pressures do not reach a peak. Only in the cases of $\Sigma = 0.33$ and 0.66, the pressure levels out at $\varepsilon_{zz} = 4.5\%$ and 5.5% respectively.

A change in slope can be identified at strains between approximately 0.8% ($\Sigma = 0.33$) and 1.4% ($\Sigma = 2.33$). This corresponds to matrix yielding in the case of the noncavitating particle.

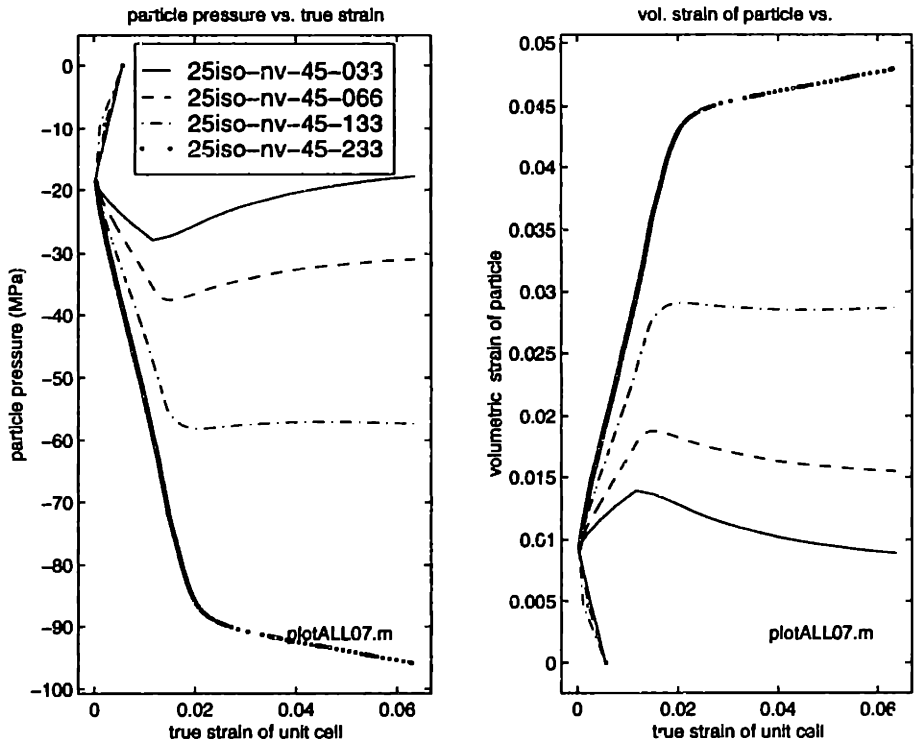

Figure 5-15: (a) particle pressure P and (b) particle volumetric strain Ψ as functions of macroscopic axial true strain ε_{zz}. Isotropic matrix with non-cavitating particle.

In order to quantify the increase in particle pressure as a consequence of the laterally applied stress, the ratio of particle pressure at some Σ, P^{Σ} to that of the particle pressure in simple tension $P^{0.33}$ at a given axial strain is calculated as $\frac{P^{\Sigma}}{P^{0.33}}$. For the particle at $\Sigma = 0.66$, the ratio is on the order of $\frac{P^{0.66}}{P^{0.33}} = 1.4$ for $\varepsilon_{zz} \leq 6\%$. For the $\Sigma = 1.33$, the ratio increases from $\frac{P^{1.33}}{P^{0.33}} = 2.0$ at $\varepsilon_{zz} = 2\%$ to $\frac{P^{1.33}}{P^{0.33}} = 2.3$ at $\varepsilon_{zz} = 6\%$ strain. For $\Sigma = 2.33$ the ratio is $\frac{P^{2.33}}{P^{0.33}} = 2.8$ at $\varepsilon_{zz} = 2.\%$ and increases to $\frac{P^{2.33}}{P^{0.33}} = 3.6$ at $\varepsilon = 6\%$.

Particles with cavitation strengths exceeding $-29MPa$ are expected not to fail in simple tension. For $\Sigma = 0.66$ the maximum cavitation strength for cavitation to occur is $-42MPa$, and for $\Sigma = 1.33$ it is $-69MPa$. Under highly triaxial loading conditions ($\Sigma = 2.33$) even particles with cavitation strengths exceeding $-100MPa$ are expected to cavitate at axial strains of up to 4%.

In the case of the triaxiality being between $\Sigma = 0.33$ and $\Sigma = 1.33$, all simulations with particles whose cavitation strength exceeds the indicated maximum cavitation strength are not expected to cavitate, and can therefore be meaningfully simplified

by simulations with a non-cavitating fluid cavity.

Isotropic Matrix

In the unit cell with isotropic matrix properties the matrix yields at axial strains between approximately $\varepsilon_{zz} = 1.2\%$ in simple tension and $\varepsilon_{zz} = 2.0\%$ in the case of $\Sigma = 2.33$, as seen in figure 5-15a.

With Σ between 0.33 and 1.33, the negative particle pressure increases monotonically only up to matrix yield. It then decreases and, at least in the case of $\Sigma = 1.33$, starts to increase again at axial strains of the order of 5%. For the case of $\Sigma = 2.33$, the particle pressure does not reach a peak within the $\varepsilon_{zz} \leq 6\%$, but it changes its slope at matrix yield.

Computing the ratio of particle pressures at different triaxialities to that of simple tension as above, $\frac{P^{\Sigma}}{P^{0.33}}$, it is found to increase from $\frac{P^{0.66}}{P^{0.33}} = 1.4$ at $\varepsilon_{zz} = 2\%$ to $\frac{P^{\Sigma}}{P^{0.33}} = 1.7$ at $\varepsilon_{zz} = 6\%$ in the case of $\Sigma = 0.66$. Under $\Sigma = 1.33$, $\frac{P^{1.33}}{P^{0.33}}$ increases from $\frac{P^{1.33}}{P^{0.33}} = 2.2$ to $\frac{P^{1.33}}{P^{0.33}} = 3.2$ at ε_{zz} between 2% and 6%. In the case of high triaxiality ($\Sigma = 2.33$) the ratio increases from $\frac{P^{2.33}}{P^{0.33}} = 3.3$ at $\varepsilon_{zz} = 2\%$ to $\frac{P^{2.33}}{P^{0.33}} = 5.3$ at $\varepsilon_{zz} = 6\%$.

For cavitation to occur within the first 5% of axial strain, the particles' cavitation strengths must not exceed $-28MPA$ under simple tension, $-38MPa$ for $\Sigma = 0.66$, and $-58MPa$ for $\Sigma = 1.33$. In the case of $\Sigma = 2.33$ a particle with a cavitation strength of $-90MPa$ can be expected to cavitate within $\varepsilon_{zz} \leq 2.5\%$, and a particle with $-95MPa$ cavitation strength within $\varepsilon_{zz} \leq 6\%$.

Summary

The particles inside an anisotropic matrix experience a monotonic increase of negative pressure with macroscopic axial strain. In the case of an isotopic matrix this is only the case at low triaxiality ratios. At low Σ the particle inside an isotropic matrix experiences a peak negative pressure at matrix yield with a subsequent drop in pressure. It seems that the isotropic matrix is capable of "plastically flowing around the particle" after yield, thereby decreasing ($\Sigma \leq 0.66$), not changing ($\Sigma = 1.33$) or only very slightly increasing ($\Sigma = 2.33$) the load that is transferred onto the particle.

In the anisotropic matrix, on the other hand, this load transfer seems to be somewhat more continuously increasing as the unit cells is strained. In the discussions below it will be shown that this phenomenon can be explained with the "shell model" for the anisotropic matrix.

The ratio of particle pressures at different triaxialities to that of simple tension, $\frac{P^{\Sigma}}{P^{0.33}}$, is generally higher in the isotropic unit cell than in the anisotropic. Due to the drop in negative pressure at low triaxiality and a continued increase at high Σ, the $\frac{P^{\Sigma}}{P^{0.33}}$ reaches values of up to 5.3 at $\varepsilon_{zz} = 6\%$ in the isotropic matrix at high $\Sigma = 2.33$, whereas it is only $\frac{P^{\Sigma}}{P^{0.33}} = 3.6$ in the anisotropic unit cell at the same strain and same triaxiality. Again, this seems to be an indication that the anisotropic matrix carries macroscopically applied load very differently from the isotropic matrix.

5.4.3 Effect of Varying Σ on the Macroscopic Stress-Strain Response of Unit Cells with Non-Cavitating Particles

Figures 5-16a and 5-18a are plots of the macroscopic true axial stress σ_{zz} as a function of the macroscopic true axial strain ε_{zz} of the unit cell. Figure 5-16a is for the unit cell with anisotropic matrix properties, and figure 5-18a for isotropic matrix properties, both with non-cavitating particles.

Figures 5-17 and 5-19 are plots of the macroscopic deviatoric true axial stress $\hat{\sigma}_{zz}$ as a function of ε_{zz}. Figure 5-17 is for the unit cell with anisotropic matrix properties, and figure 5-19 for isotropic matrix properties, both with non-cavitating particles.

The choice to plot the deviatoric stress $\hat{\sigma}_{zz}$ as function of ε_{zz} is motivated by the observation that the laterally applied stress σ_{rr} effectively adds a hydrostatic component σ^h to the axial stress, which is itself a reaction to the axial displacement of the unit cell's top boundary. Since σ_{rr} depends on the desired triaxiality ratio Σ, the deviatoric and hydrostatic parts of the stress state also depend on the Σ.

Decomposing the total stress state into its deviatoric and hydrostatic part at

different triaxiality ratios, we obtain:

$$\hat{\sigma}_{zz} = \sigma_{zz} - \sigma^h \tag{5.1}$$

$$\sigma^h = \frac{1}{3}(\sigma_{zz} + 2\sigma_{rr}) \tag{5.2}$$

From equation 4.16 we get

$$\sigma_{rr} = \frac{3\Sigma - 1}{(3\Sigma + 2)\,\sigma_z}, \tag{5.3}$$

so that the following expression give the macroscopic deviatoric true axial stress as a function of Σ and σ_{zz}:

$$\hat{\sigma}_{zz} = \frac{2}{3\Sigma + 2}\,\sigma_{zz} \tag{5.4}$$

General Trends

During the first part of the deformation the matrix is completely elastic. This translates into a linear increase of the stress-strain curve, as seen in figures 5-16a and 5-18a. The slope of these curves increases with increasing triaxiality ratio because of the added hydrostatic component that the increase in Σ adds according to equation 5.4. The slope of the stress-strain curves changes with the onset of plastic deformation in the matrix.

Anisotropic Matrix

Examining figure 5-16a , the slope of the macroscopic true stress-true strain curve of the anisotropic unit cells increases in the elastic part of the deformation from approximately $2.6GPa$ for simple tension to $5.8GPa$ at $\Sigma = 2.33$.

The macroscopic axial true strains at which the matrix yields increase with increasing Σ if the stress state is different from simple tension. For triaxialities of 0.33, 0.66, 1.33 and 2.33 the yield strains σ^y_{zz} are 0.8%, 0.9%, 1.0% and 1.4% respectively.

After yielding, σ_{zz} continues to increase along an initially elevated slope that gradually decreases. The stress-strain curves seem to level off at strain levels between

5% and 6%. In simple tension the slope of the stress-strain curve after yield is initially $0.9GPa$ and decreases to $0.1GPa$ at $\varepsilon_{zz} = 6\%$. Under high triaxiality this slope is first $3GPa$ and then decreases to $0.3GPa$ at $\varepsilon = 6\%$.

The anisotropic matrix exhibits substantial hardening during its plastic deformation. The increase in σ_{zz} between $\varepsilon_{zz} = \varepsilon^y_{zz}$ and $\varepsilon_{zz} = 6\%$ ranges from 50% of the yield stress σ^y_{zz} for the case of simple tension to 75% of σ^y_{zz} in the case of $\Sigma = 2.33$.

Comparing the axial stresses of the simulations under different triaxialities but at the same strain levels, it is found that σ_{zz} of the unit cell scales according to some function of the triaxiality ratio. Figure 5-17 shows the deviatoric axial stress $\hat{\sigma}_{zz}$ plotted against ε_{zz}. For $\varepsilon_{zz} \geq 4\%$ or $\geq 5\%$, the curves of $\hat{\sigma}_{zz}$ collapse onto each other. It seems that the initial differences are due to the effects of the matrix yielding being delayed with increasing levels of triaxiality. This effect vanishes after a few percent of axial straining after the initial yield.

The difference in σ^y_{zz} is due to the different levels of hydrostatic stress present in the matrix, and the corresponding hydrostatic strain ε^h. These hydrostatic stress components increase with triaxiality ratio, and hence the higher the triaxiality, the higher the hydrostatic strain ε^h and the apparent yield strain ε_{zz}. Again only the case of simple tension does not follow this trend.

Isotropic Matrix

Examining figure 5-18a , the slopes of the macroscopic stress-strain curves during the elastic part of the deformation are found to be the same as in the anisotropic case. This has to be the case because the "anisotropy unit cell" is elastically isotropic and anisotropic only in the plastic regime.

The yield strains are approximately $\varepsilon^y_{zz} = 1.2\%$, 1.3%, 1.5% and 1.7% for $\Sigma = 0.33$, 0.66, 1.33 and 2.33, respectively.

The axial stress σ_{zz} in the isotropic unit cell exhibits a dramatic change in slope after matrix yield. In the case of simple tension the slope after yield is approximately $80MPa$, whereas that in the case of $\Sigma = 2.33$ is approximately $120MPa$. A slight hardening can be noticed in the cases of high triaxiality, e.g. $\Sigma = 1.33$ and 2.33.

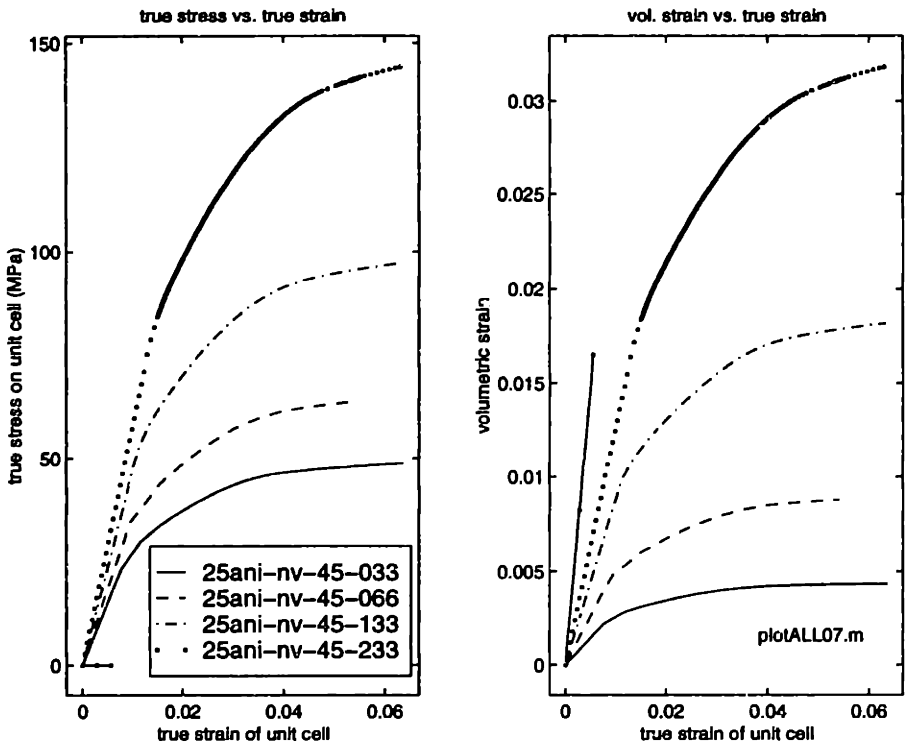

Figure 5-16: (a) macroscopic true axial stress σ_{zz} and (b) volumetric strain Ψ_m as functions of macroscopic axial true strain ε_{zz}. Anisotropic matrix with non-cavitating particle.

At $\varepsilon_{zz} = 6\%$, the axial stress σ_{zz} in the isotropic unit cell has increased by an amount that is on the order of $0.1\sigma^y_{zz}$. The isotropic matricies do not seem to be able to harden under plastic deformation, although the material model used for the isotropic matrix includes isotropic hardening.

The same trends for the relative stress levels between the unit cells under different triaxial stress states observed in the case of the anisotropic matrix with non-cavitating particle can be found in the isotropic unit cell. The axial stress scales with some function of triaxiality.

Figure 5-19 shows $\hat{\sigma}_{zz}$ as function of ε_{zz}. The same observations as in the anistropic matrices can be made here, but to a larger extent: all curves of $\hat{\sigma}_{zz}$ versus ε_{zz} collapse onto each other from approximately $\varepsilon_{zz} \simeq 2.5\%$ on. The effect of differences in yield strain ε^y_{zz} seem to have an effect only at the beginning of the deformation. After $\varepsilon_{zz} \simeq 2.5\%$ the differences in $\hat{\sigma}_{zz}$ vanish and the curves are very similar.

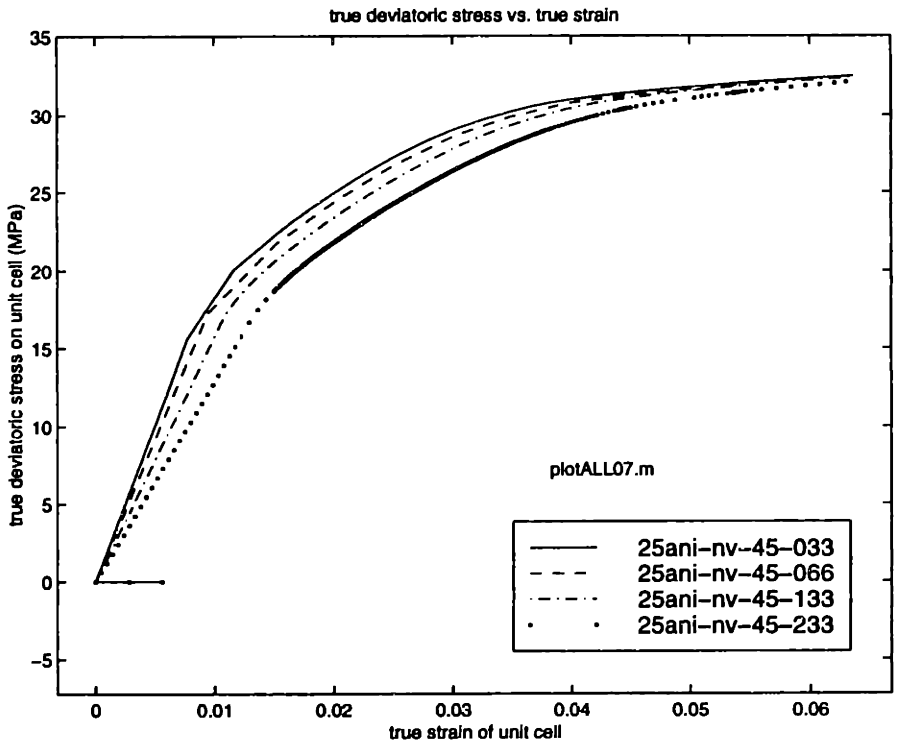

Figure 5-17: Macroscopic true deviatoric axial stress $\hat{\sigma}_{zz}$ as function of macroscopic axial true strain ε_{zz}. Anisotropic matrix with non-cavitating particle.

Summary

Contrary to the isotropic unit cell, the anisotropic unit cell is capable of substantial strain hardening. This seems to indicate that the plastic anisotropy allows for a reorientation of the material texture, resulting in a stiffer stress-strain response under plastic deformation. However, the limitations of the Hill plasticity model and the observed rigid particle rotation, indicate that if a true crystal plasticity model had been chosen, then the re-orientation of the material texture based on plastic spin would have allowed for a continued availablility of the easy shear slip systems, and would have resulted in less strain hardeing of the matrix.

The anisotropic matrix yields at lower levels of macroscopic axial strain than the isotropic matrix. This is caused by the lower shear resistance of the anisotropic matrix as determined by the corresponding Hill coefficient $H_{12} = 0.7$. In both anisotropic and isotropic unit cells, the yield strain increases with increasing triaxiality. Exceptions to this trend are the cases of uniaxial tension, which have yield strains comparable

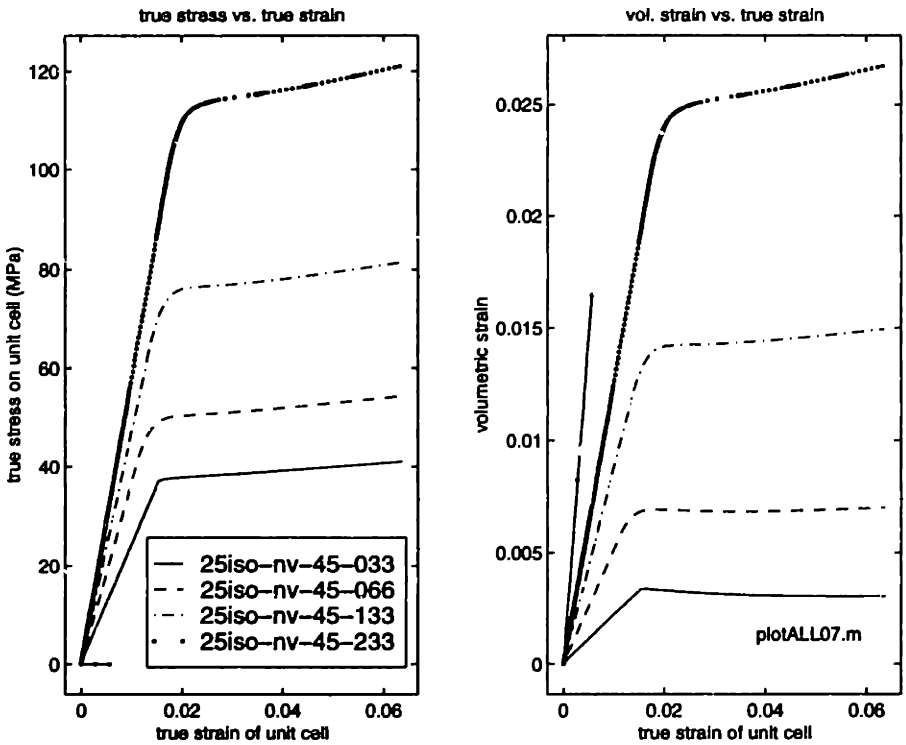

Figure 5-18: (a) macroscopic true axial stress σ_{zz} and (b) cell volumetric strain Ψ as functions of macroscopic axial true strain ε_{zz}. Isotropic matrix with non-cavitating particle.

to that of $\Sigma = 1.33$.

The macroscopic true axial stress is found to scale with the level of triaxiality. In both, anisotropic and isotropic matrices, the curves of $\hat{\sigma}_{zz}$ vs. ε_{zz} collapse onto each other after some intitial differences due to the initial matrix yield are overcome.

5.4.4 Effect of Varying Σ on the Macroscopic Stress-Strain Response of Unit Cells with Pre-Existing Cavities

As above, stress-strain plots for both anisotropic and isotropic matrices at varying triaxiality ratios will be used in this section. The key feature is here that the "particles" are set to have zero bulk modulus and thus behave like cavities from the start of the deformation.

Figures 5-20a and 5-22a are plots of the macroscopic true axial stress σ_{zz} as a function of the macroscopic true axial strain ε_{zz} of the unit cell. Figure 5-20a is

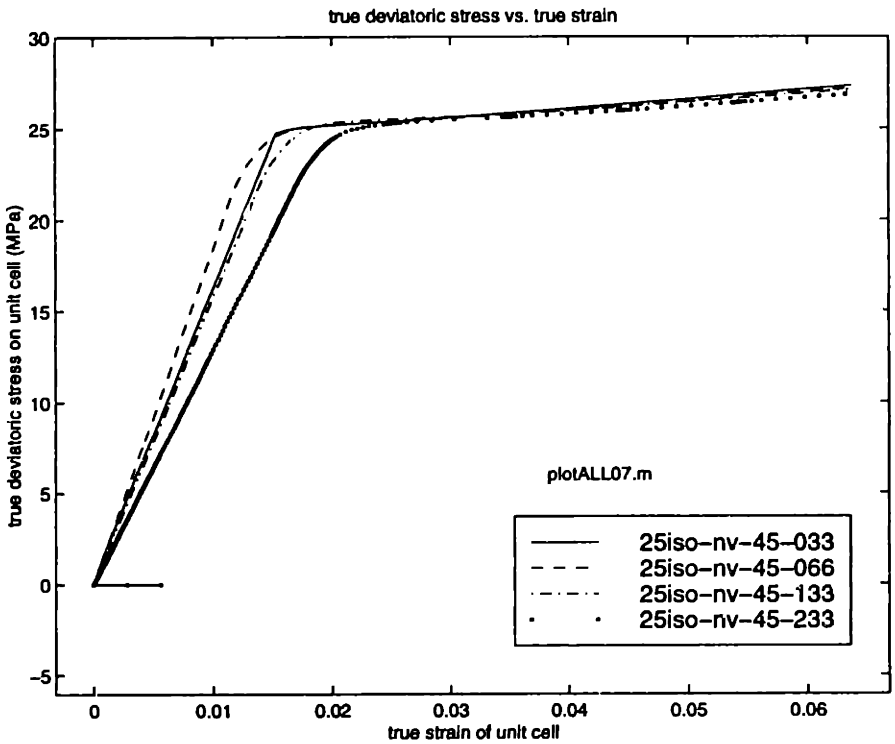

Figure 5-19: Macroscopic true deviatoric stress $\hat{\sigma}_{zz}$ as function of macroscopic axial true strain ε_{zz}. Isotropic matrix with non-cavitating particle.

for the unit cell with anisotropic matrix properties, and figure 5-22a for that with isotropic matrix properties, both with a pre-existing cavity.

Figures 5-21 and 5-23 are plots of the macroscopic deviatoric true axial stress $\hat{\sigma}_{zz}$ as a function of ε_{zz}. Figure 5-21 is for the unit cell with anisotropic matrix properties, and figure 5-23 for that with isotropic matrix properties, both with pre-existing cavities.

General Trends

As above, σ_{zz} is found to increase with Σ at a given ε_{zz}. The negative axial strain due to cooling process is less than that of the simulations with coherent particles at the start of the simulation. This is because of the rubber particle having a higher thermal expansion coefficient than the polyamide matrix. Hence the macroscopic thermal stresses as measured by the displacement of the unit cell boundaries at the end of the cooling step are less in the absence of a particle. For the interpretation of

the data they have little significance.

Anisotropic Matrix

During the elastic part of the deformation, the slopes of the stress-strain curves are found to vary from $2.8GPa$ for simple tension to $4.4GPa$ for $\Sigma = 2.33$.

Matrix yield is found to occur at axial strain levels of $\varepsilon_{zz}^{y} = 0.9\%$, 1.0%, 1.1% and 1.3% for $\Sigma = 0.33$, 0.66, 1.33 and 2.33.

After matrix yield the stresses in the low-triaxiality simulations ($\Sigma = 0.33$ and 0.66) continue to increase monotonically. The increase in σ_{zz} between $\varepsilon_{zz} = \varepsilon_{zz}^{y}$ and $\varepsilon_{zz} = 6\%$ is of the order of 70%.

In the cases of $\Sigma = 1.33$ and 2.33, the σ_{zz} reaches a peak and then drops with increasing ε_{zz}. Under 2.33 triaxiality, the σ_{zz} reaches a peak of $87MPa$ at $\varepsilon_{zz} \simeq 2.8\%$ and then drops to levels below the yield stress of $61MPa$. The 1.33 triaxiality unit cell reaches a stress peak of $80MPa$ at approximately $\varepsilon_{zz} \simeq 5.5\%$.

In the case of the anisotropic matrix with a hollow cavity the attempt at finding a scaling dependency of the axial stresses on the applied triaxiality is less successful. As can be seen from figure 5-21, the curves of $\hat{\sigma}_{zz}$ as functions of ε_{zz} do not collapse onto one curve, as was observable in the unit cell with a non-cavitating particle. This is explained by that fact that the unit cell cannot stiffen as much if it does not have the fluid-filled cavity at its disposal for a "redirection" of the laterally applied stresses. In fact, when comparing the ε_{equiv}^{p}-plots of the cells with cavities (e.g. figures 5-35a-f) with those of the cells with non-cavitating particels (e.g. figures 5-27a-f), it can be seen how the degree of plastic localization is dramatically increased in the cases with non-cavitating particles. Clearly, the presence of the particle introduces additional constraints in the deformation of the matrix that prevents the relative similatity that is observed in the cases with cavities from occurring in the cases with particles.

Isotropic Matrix

Again the slopes of the axial stress-strain curves exhibit a positive dependency on Σ for the elastic part of the simulation. The yield strains are decreasing with in-

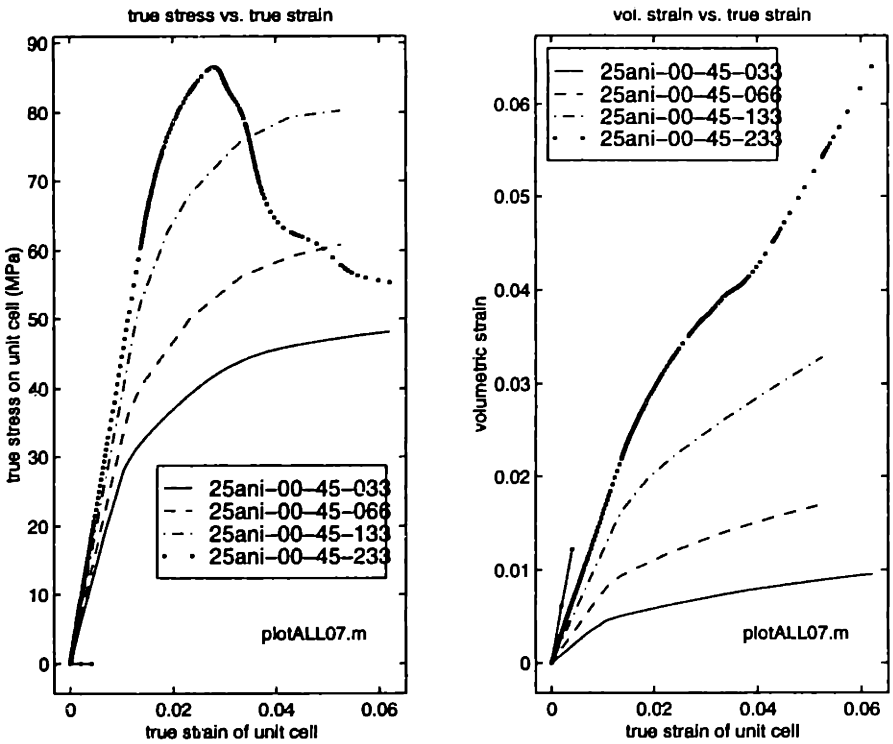

Figure 5-20: (a) macroscopic true axial stress σ_{zz} and (b) cell volumetric strain Ψ_m as functions of macroscopic axial true strain ε_{zz}. Anisotropic matrix with pre-existing cavity.

creasing triaxiality: $\varepsilon_{zz}^y = 1.3\%$, 1.1%, 1.0%, and 0.8% for $\Sigma = 0.33$, 0.66, 1.33, 2.33, respectively.

The yield stresses are very close together. $\Sigma = 0.33$, 0.66, 1.33, 2.33 they are $\sigma_{zz}^y = 34MPa$, $35MPa$, $36MPa$ and $37MPa$, respectively.

After matrix yield the unit cell displays some strain hardening. The increase in σ_{zz} between $\varepsilon_{zz} = \varepsilon_{zz}^y$ and $\varepsilon_{zz} = 6\%$ is of the order of $0.2\sigma_{zz}^y$.

The more remarkable feature of the simulations with a pre-existing cavity inside of an isotropic matrix is that the macroscopic stress-strain curves for triaxialities of 0.66, 1.33 and 2.33 are very similar for axial strain levels of 2% and more. Only the unit cell under simple tension remains some $5MPa$ below the stress levels of the higher triaxialities.

As in the case of the anisotropic matrix with a cavity, the attempt at identifying a scaling dependency of the deviatoric macroscopic stresses on the level of triaxiality was not successful as can be seen from figure 5-23.

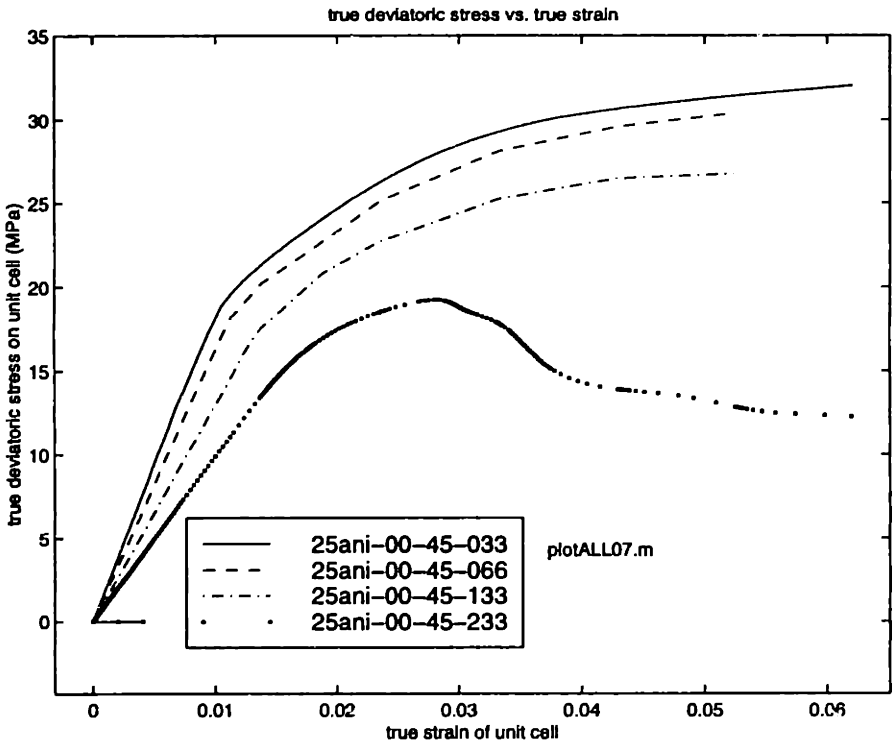

Figure 5-21: Macroscopic deviatoric true axial stress $\hat{\sigma}_{zz}$ as function of macroscopic axial true strain ε_{zz}. Anisotropic matrix with pre-existing cavity.

Summary

Whereas the yield strains ε_{zz}^{y} are found to increase as a function of Σ in the case of the anisotropic matrix, they show a negative dependency on Σ in the case of the isotropic matrix.

In the anisotropic matrix, σ_{zz} is found to increase with Σ, with the only exception being the case of $\Sigma = 2.33$ exhibiting a drop in σ_{zz} after a peak at $\varepsilon_{zz} = 2.8\%$. The macroscopic axial true strain of the isotropic unit cell shows very little dependence on Σ: the plots of σ_{zz} vs. ε_{zz} are nearly equal for $\Sigma = 0.66$, 1.33 and 2.33, for $\varepsilon_{zz} \geq 2\%$.

The anisotropic unit cell displays considerable strain hardening, whereas the stress-strain response of the isotropic unit cell exhibits a near-plateau after yield at all Σ.

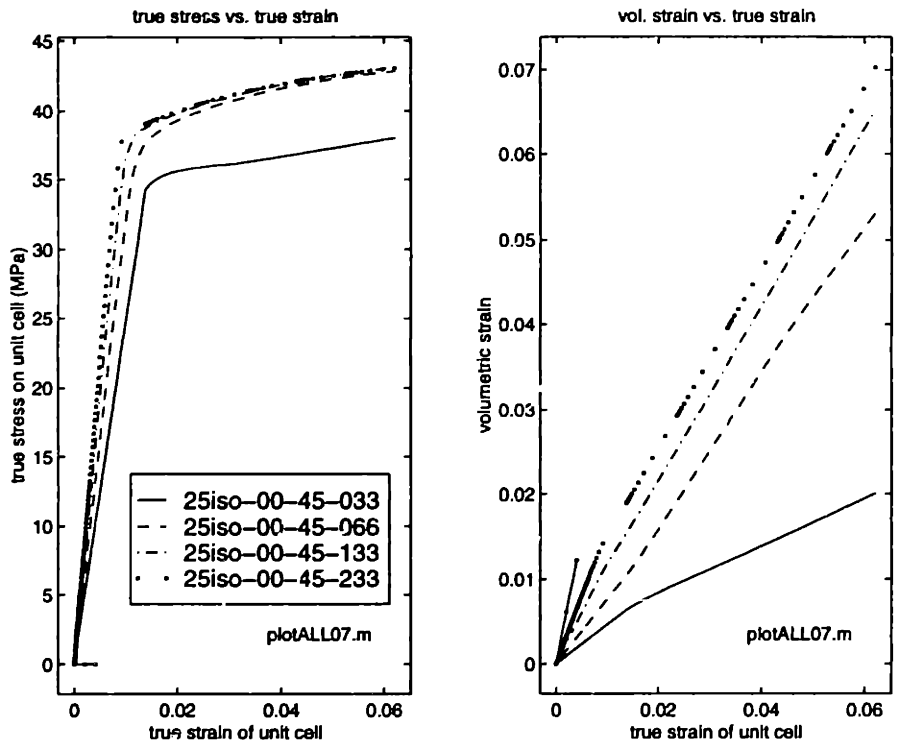

Figure 5-22: (a) macroscopic true axial stress σ_{zz} and (b) cell volumetric strain Ψ as functions of macroscopic axial true strain ε_{zz}. Anisotropic matrix with pre-existing cavity.

5.4.5 Effect of Varying Σ on the Matrix Plasticity of Unit Cells with Non-Cavitating Particles

The purpose of this section is to identify the effects of varying the triaxiality ratio Σ of the applied stresses on the distribution, evolution and magnitudes of the matrix plasticity in the case of non-cavitating particles.

Figures 5-24a through 5-31e are contour plots of the equivalent plastic strain measure ε^p_{equiv} (PEEQ) of the anisotropic and isotropic unit cells with non-cavitating particles at macroscopic axial true strains ε_{zz} = 1.5%, 2.5%, 3.5%, 4.5%, 5.5% and 6.5%.

Anisotropic Matrix

Examining figures 5-24a through 5-27f it can be seen that in the case of anisotropic matrices with non-cavitating particles, the evolution of the matrix plasticity is very

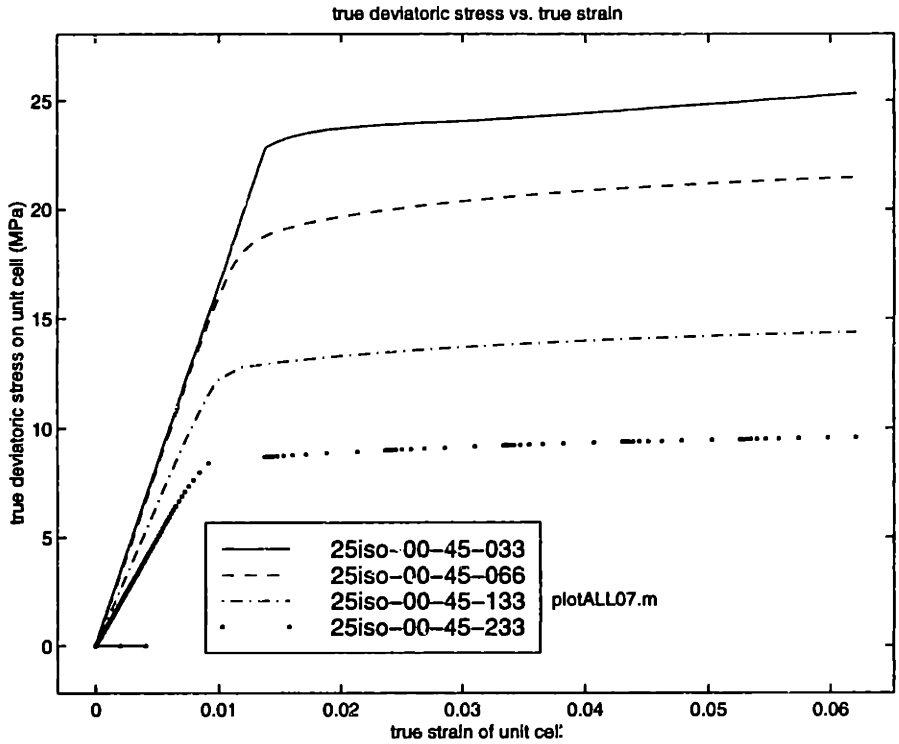

Figure 5-23: Macroscopic true deviatoric stress $\hat{\sigma}_{zz}$ as function of macroscopic axial true strain ε_{zz}. Isotropic matrix with pre-existing cavity.

similar for all triaxialities studied at axial strains of up to 6.5%.

The onset of plastic deformation is always in the upper right-hand corner of the unit cell. At $\varepsilon_{zz} = 1\%$ to 2% a shear band develops at a location approximately halfway between the particle-matrix interface and the corner of the unit cell, and the plastic zone along the diagonal spreads out. At some $\varepsilon_{zz} = 2\%$ to 3%, the matrix yields at the particle-matrix interface and the previously mentioned shear band intensifies.

At $\varepsilon_{zz} \lesssim 3\%$ the maximum levels of ε^p_{equiv} are higher under low triaxialities. This trend is reversed from $\varepsilon_{zz} \simeq 5\%$ on, where the unit cells under high Σ exhibit higher levels of ε^p_{equiv}. However, at all strains examined the levels of ε^p_{equiv} remain close to each other at all triaxialities. At $\varepsilon_{zz} = 6.5\%$ the maximum ε^p_{equiv} found in simple tension is 9.1%, wherease that of $\Sigma = 2.33$ triaxiality is 9.6%.

The yield strain ε^y_{zz} is found to increase with increasing Σ. The explanation lies in the fact that the higher levels of laterally applied stresses at high Σ cause the deviatoric component of the macroscopic stress $\hat{\sigma}_{zz}$ to be smaller at a given axial

strain ε_{zz} relative to the total macroscopic axial stress σ_{zz}. Also, the increased σ^h causes a larger hydrostatic elastic strain component throughout the matrix.

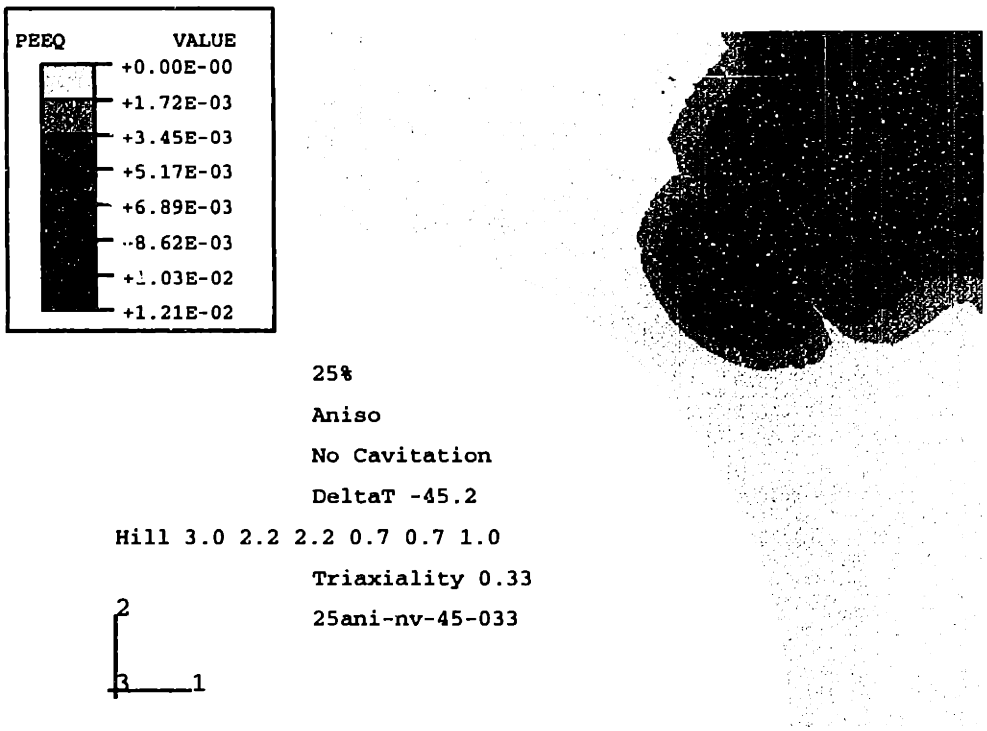

Figure 5-24a: 25ani-nv-45-033: Equivalent plastic strain ε^p_{equiv} at $\varepsilon_{zz} = 1.5\%$. Anisotropic matrix with non-cavitating particle.

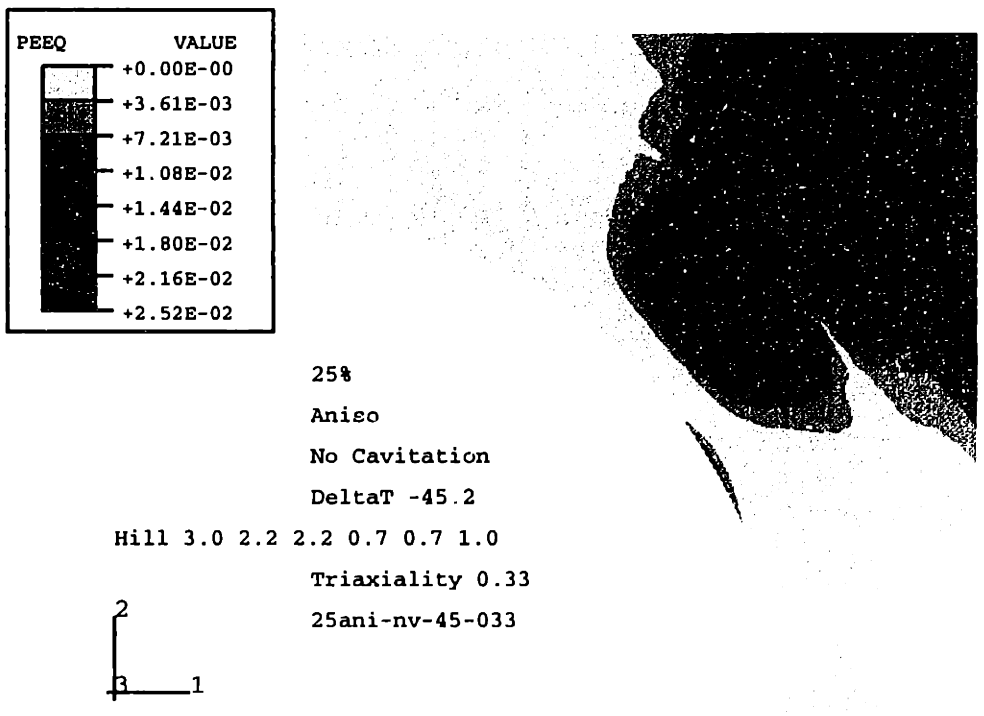

Figure 5-24b: 25ani-nv-45-033: Equivalent plastic strain ε^p_{equiv} at $\varepsilon_{zz} = 2.5\%$. Anisotropic matrix with non-cavitating particle.

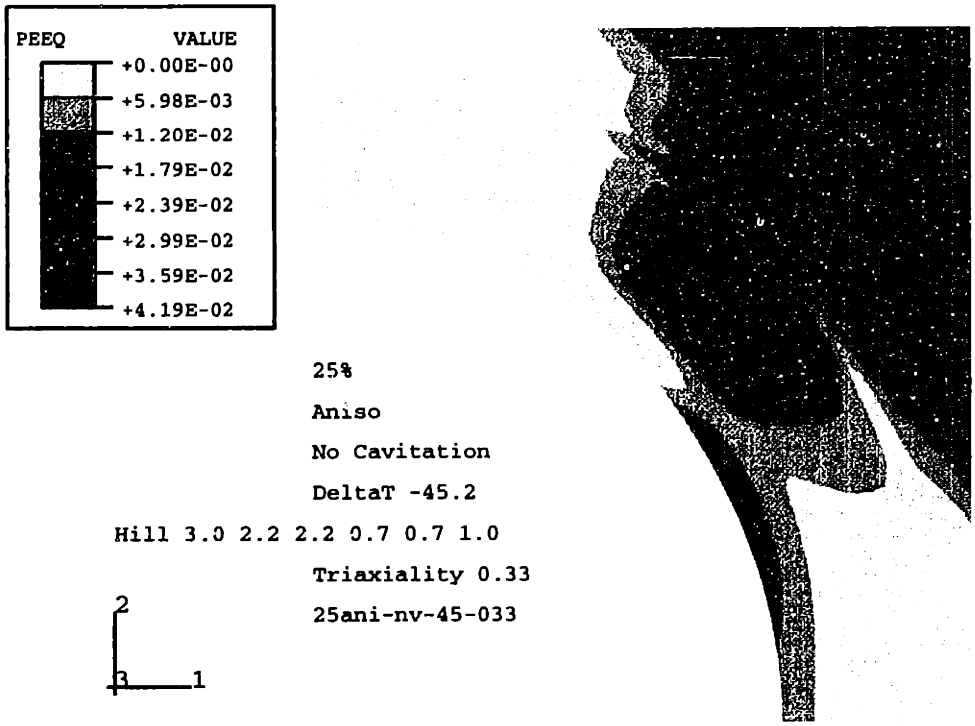

Figure 5-24c: 25ani-nv-45-033: Equivalent plastic strain ε^p_{equiv} at $\varepsilon_{zz} = 3.5\%$. Anisotropic matrix with non-cavitating particle.

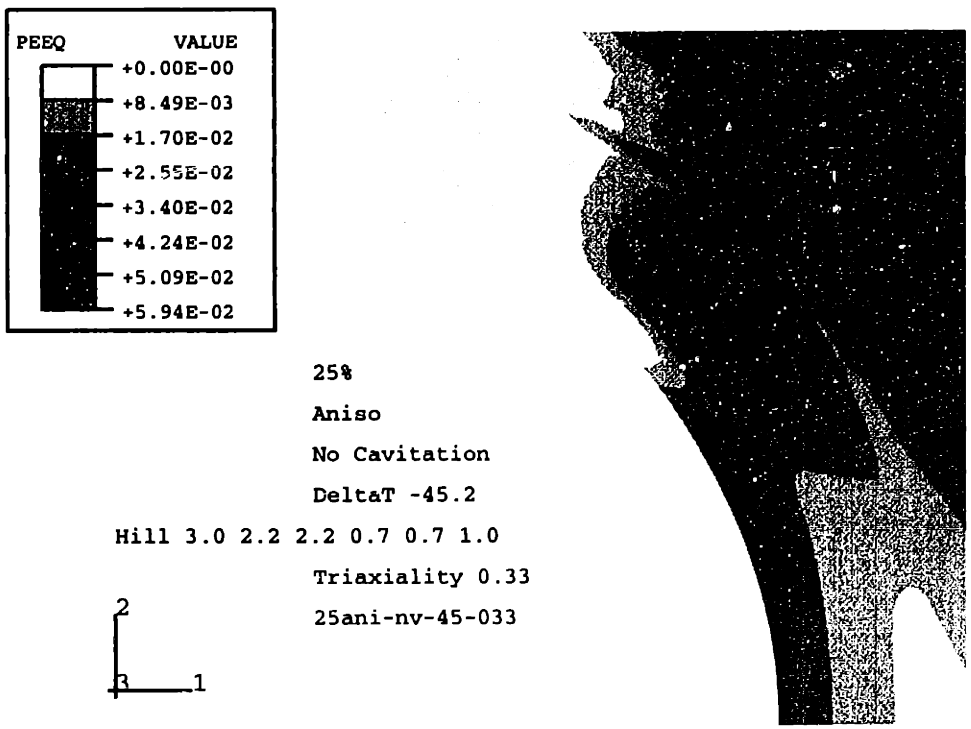

Figure 5-24d: 25ani-nv-45-033: Equivalent plastic strain ε^p_{equiv} at $\varepsilon_{zz} = 4.5\%$. Anisotropic matrix with non-cavitating particle.

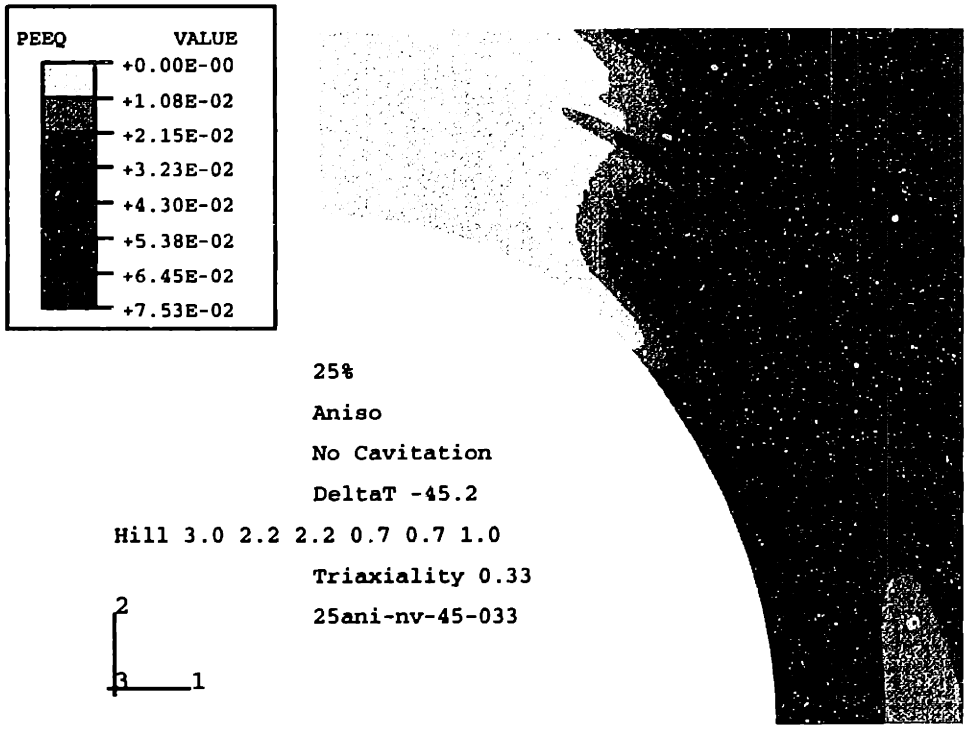

Figure 5-24e: 25ani-nv-45-033: Equivalent plastic strain ε^p_{equiv} at $\varepsilon_{zz} = 5.5\%$. Anisotropic matrix with non-cavitating particle.

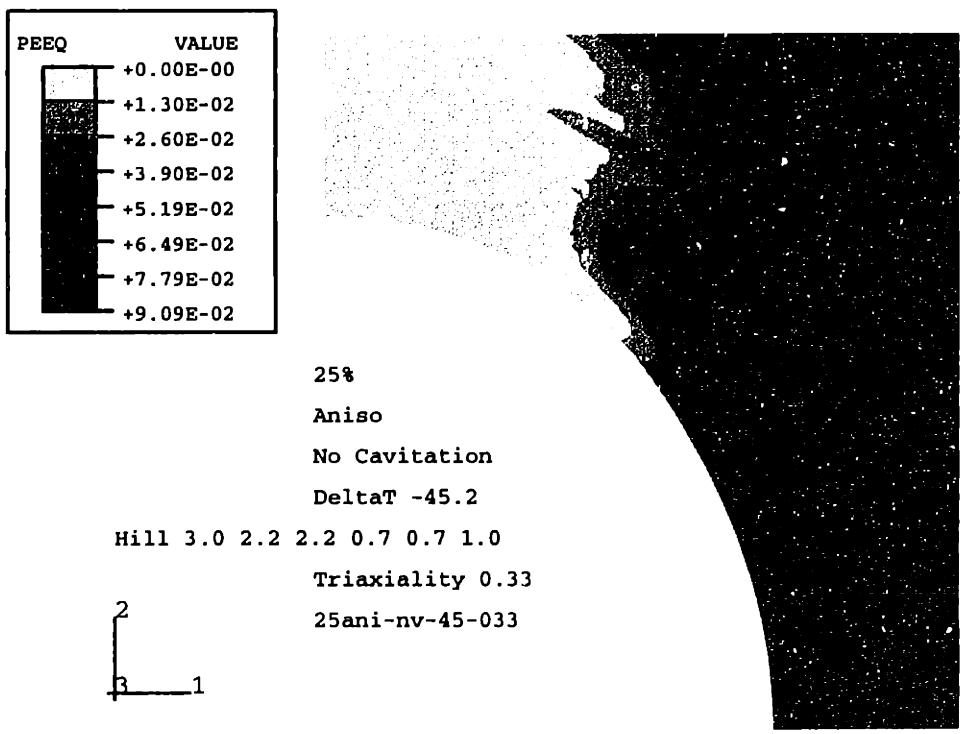

Figure 5-24f: 25ani-nv-45-033: Equivalent plastic strain ε^p_{equiv} at $\varepsilon_{zz} = 6.5\%$. Anisotropic matrix with non-cavitating particle.

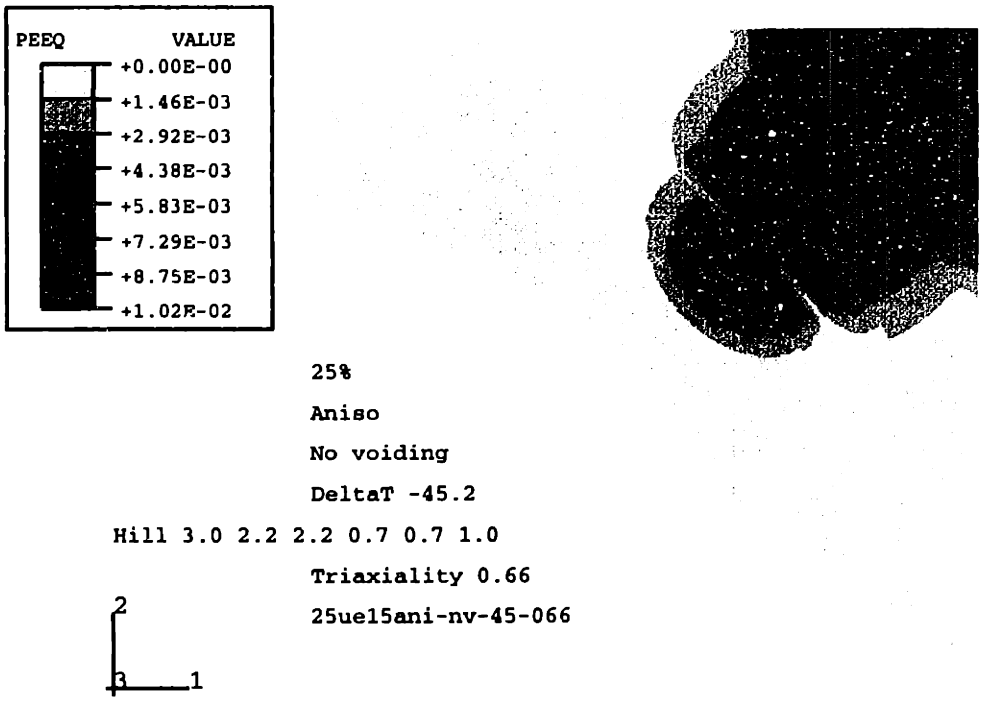

Figure 5-25a: 25ani-nv-45-066: Equivalent plastic strain ε^p_{equiv} at $\varepsilon_{zz} = 1.5\%$. Anisotropic matrix with non-cavitating particle.

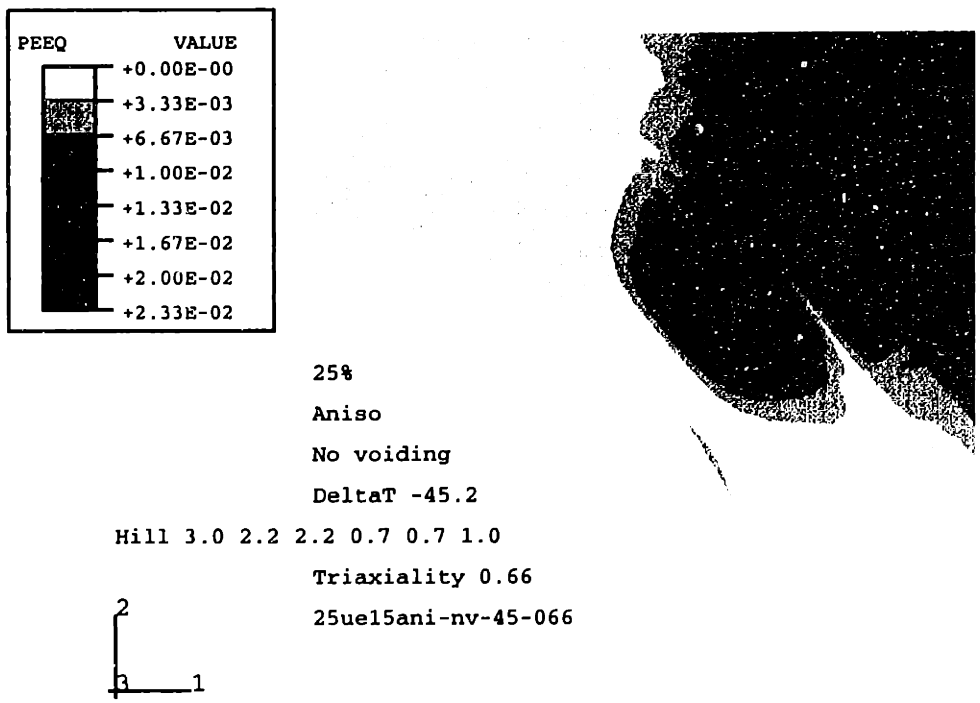

Figure 5-25b: 25ani-nv-45-066: Equivalent plastic strain ε^p_{equiv} at $\varepsilon_{zz} = 2.5\%$. Anisotropic matrix with non-cavitating particle.

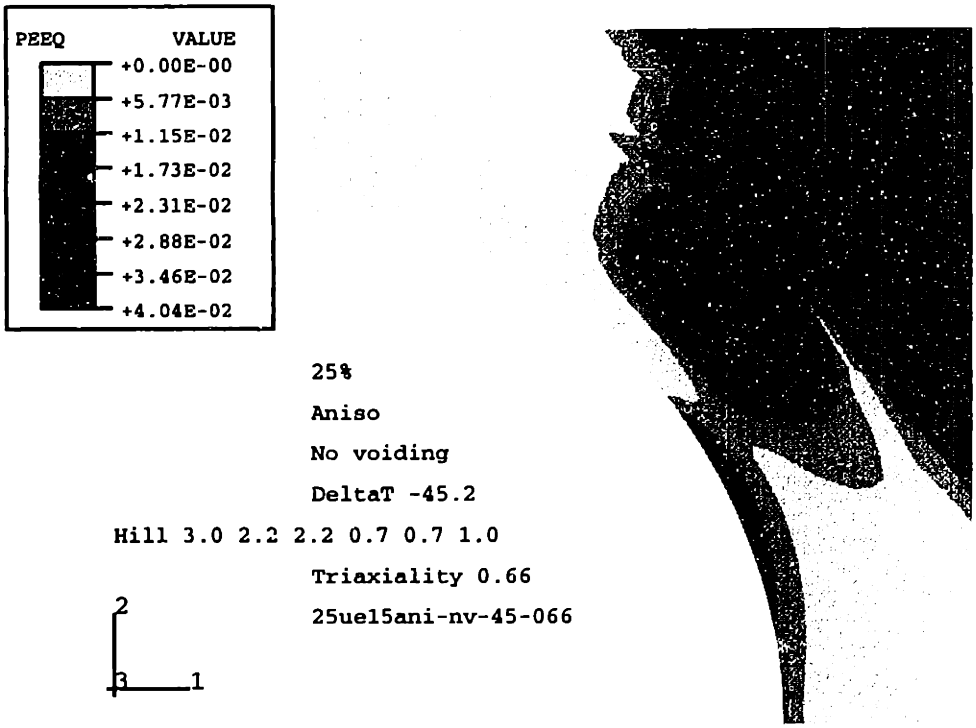

Figure 5-25c: 25ani-nv-45-066: Equivalent plastic strain ε^p_{equiv} at $\varepsilon_{zz} = 3.5\%$. Anisotropic matrix with non-cavitating particle.

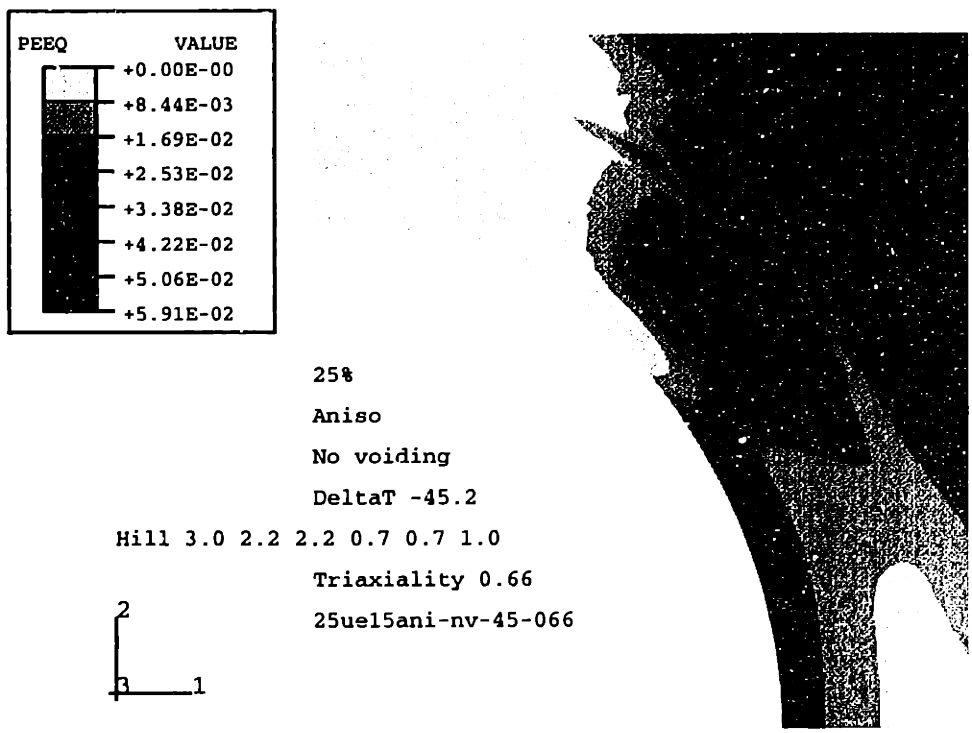

Figure 5-25d: 25ani-nv-45-066: Equivalent plastic strain ε^p_{equiv} at $\varepsilon_{zz} = 4.5\%$. Anisotropic matrix with non-cavitating particle.

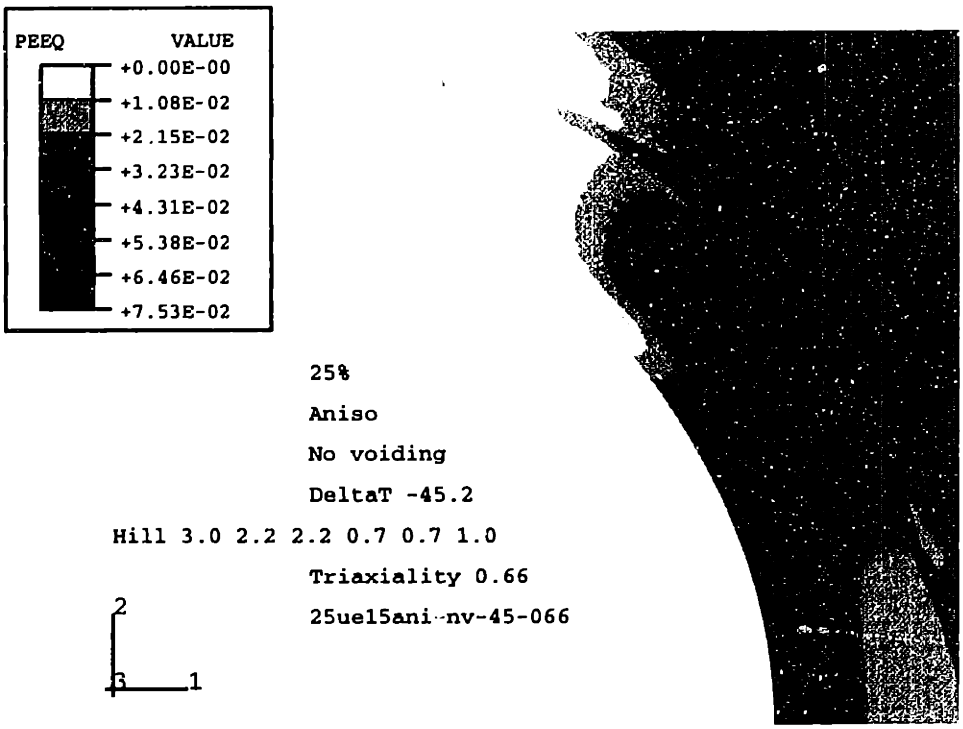

Figure 5-25e: 25ani-nv-45-066: Equivalent plastic strain ε^p_{equiv} at $\varepsilon_{zz} = 5.5\%$. Anisotropic matrix with non-cavitating particle.

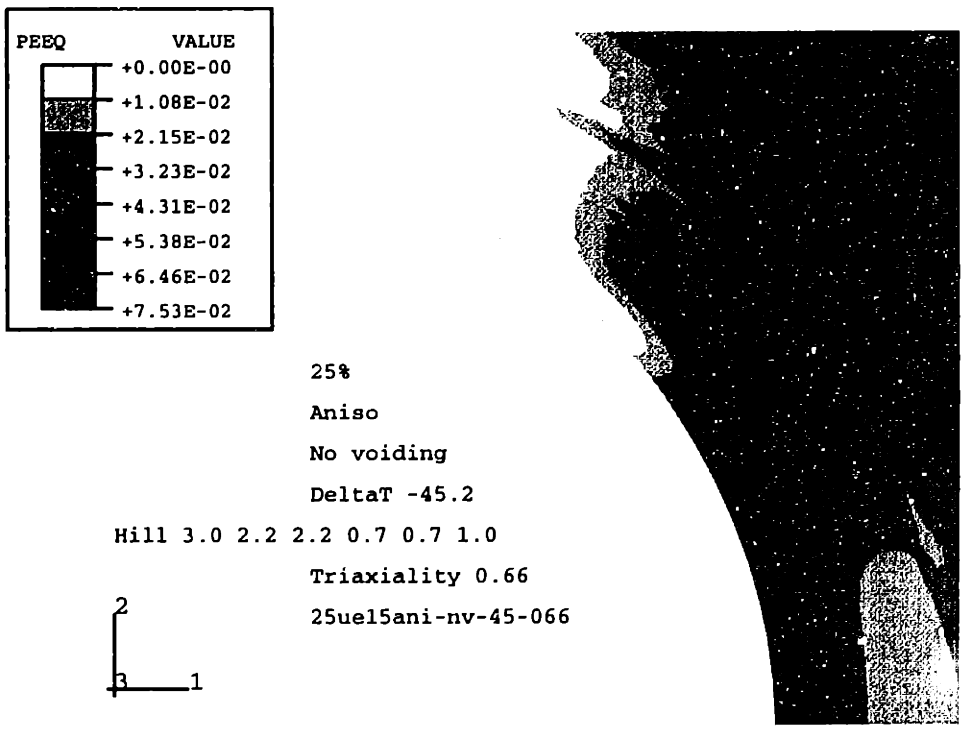

Figure 5-25f: 25ani-nv-45-066: Equivalent plastic strain ε^p_{equiv} at $\varepsilon_{zz} = 6.5\%$. Anisotropic matrix with non-cavitating particle.

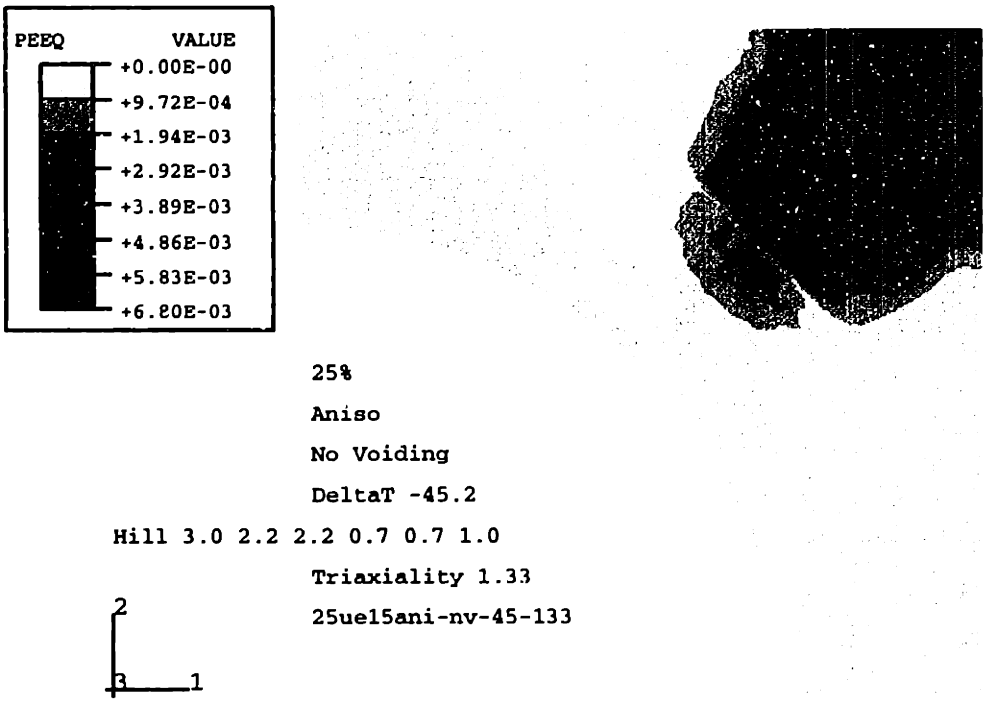

Figure 5-26a: 25ani-nv-45-133: Equivalent plastic strain ε^p_{equiv} at $\varepsilon_{zz} = 1.5\%$. Anisotropic matrix with non-cavitating particle.

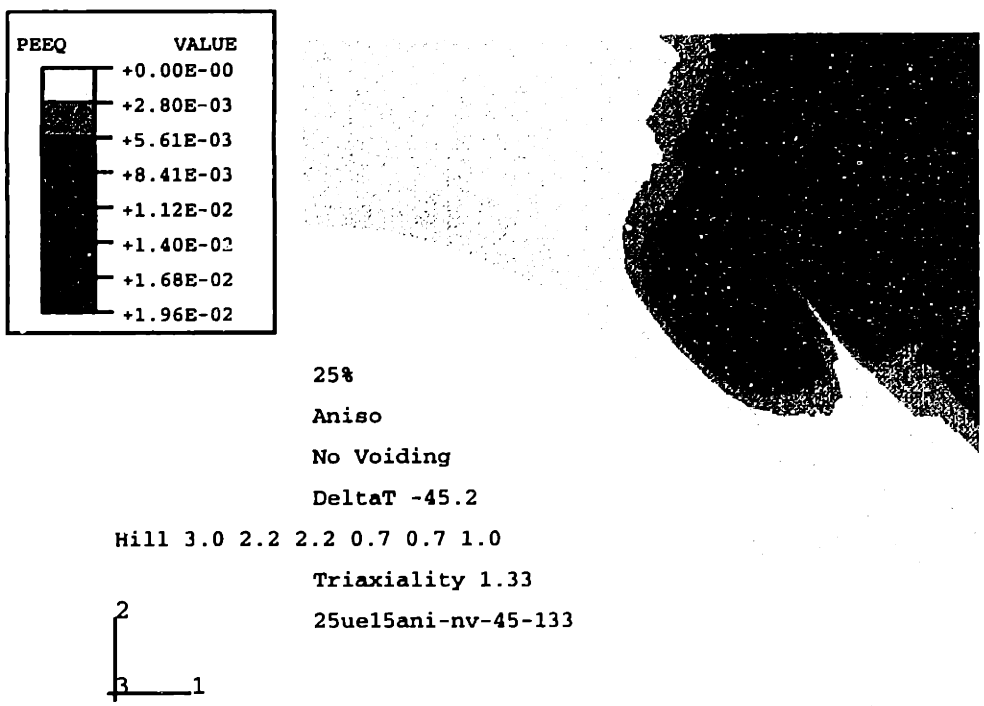

Figure 5-26b: 25ani-nv-45-133: Equivalent plastic strain ε^p_{equiv} at $\varepsilon_{zz} = 2.5\%$. Anisotropic matrix with non-cavitating particle.

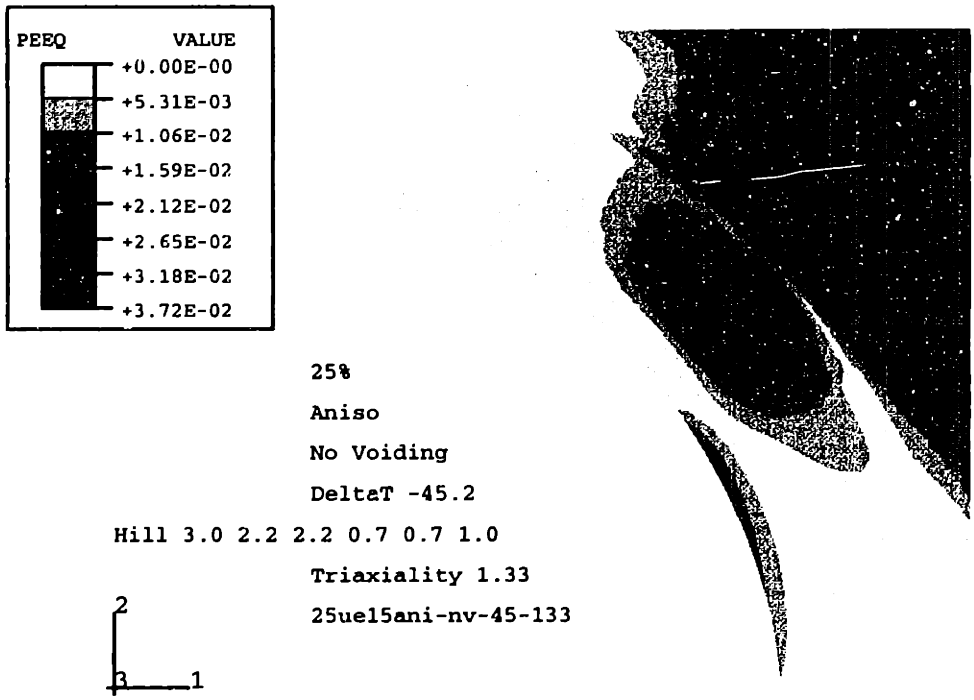

Figure 5-26c: 25ani-nv-45-133: Equivalent plastic strain ε^p_{equiv} at $\varepsilon_{zz} = 3.5\%$. Anisotropic matrix with non-cavitating particle.

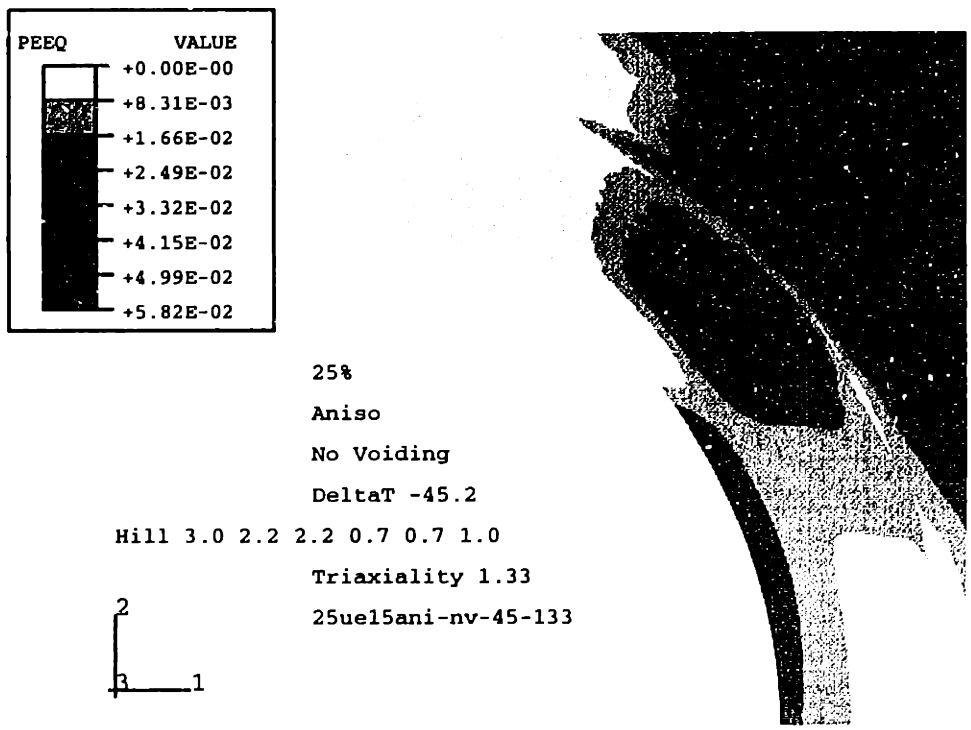

Figure 5-26d: 25ani-nv-45-133: Equivalent plastic strain ε^p_{equiv} at $\varepsilon_{zz} = 4.5\%$. Anisotropic matrix with non-cavitating particle.

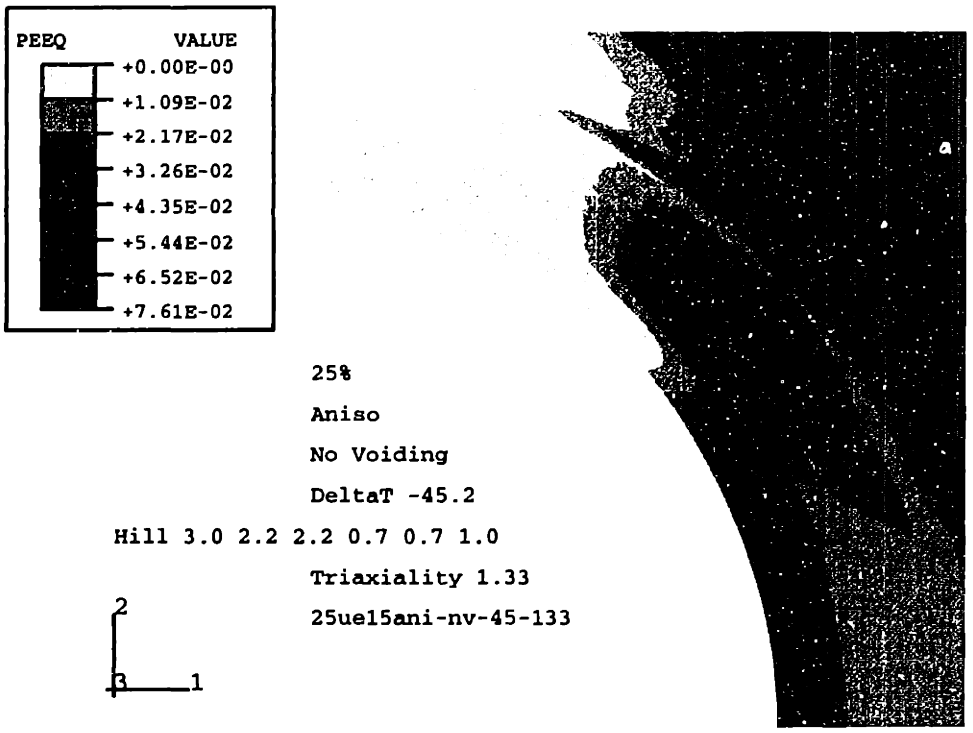

Figure 5-26e: 25ani-nv-45-133: Equivalent plastic strain ε^p_{equiv} at $\varepsilon_{zz} = 5.5\%$. Anisotropic matrix with non-cavitating particle.

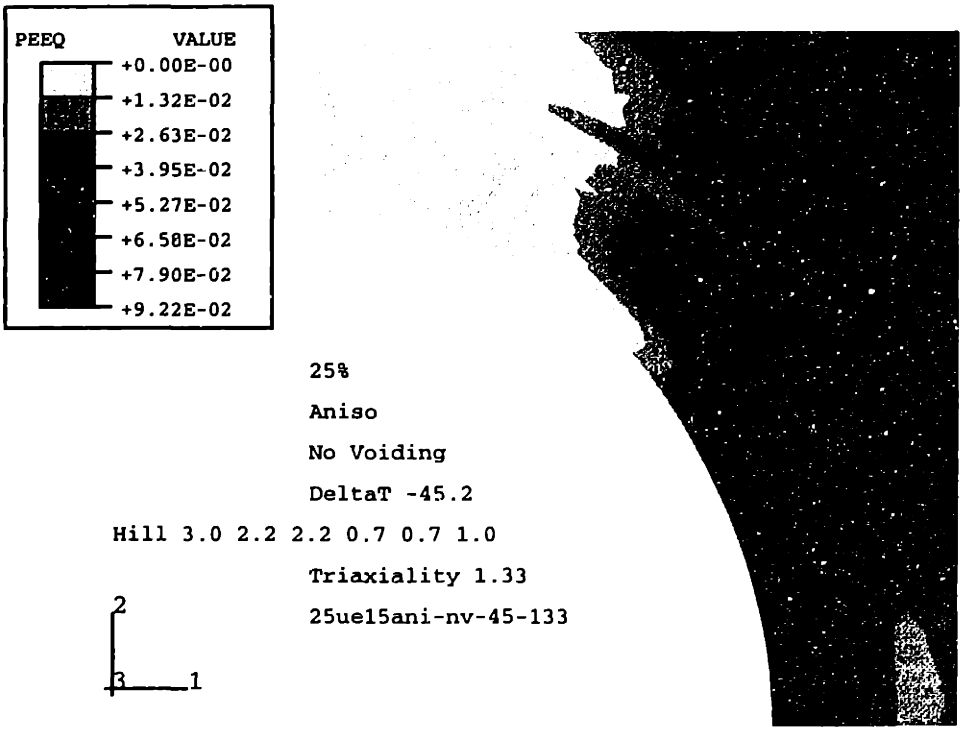

Figure 5-26f: 25ani-nv-45-133: Equivalent plastic strain ε^p_{equiv} at $\varepsilon_{zz} = 6.5\%$. Anisotropic matrix with non-cavitating particle.

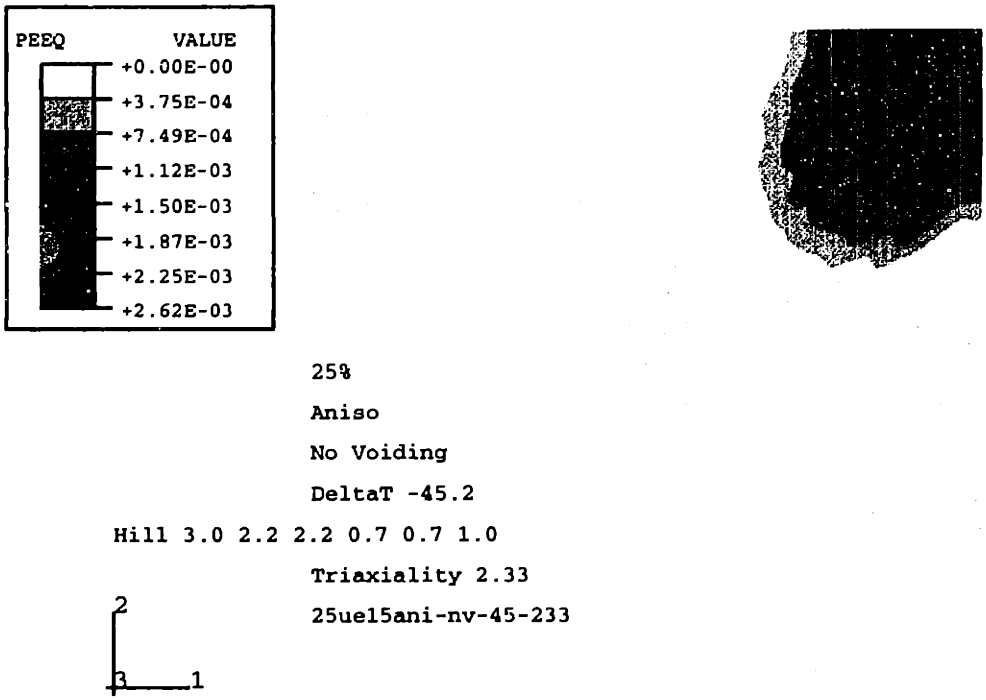

Figure 5-27a: 25ani-nv-45-233: Equivalent plastic strain ε^p_{equiv} at $\varepsilon_{zz} = 1.5\%$. Anisotropic matrix with non-cavitating particle.

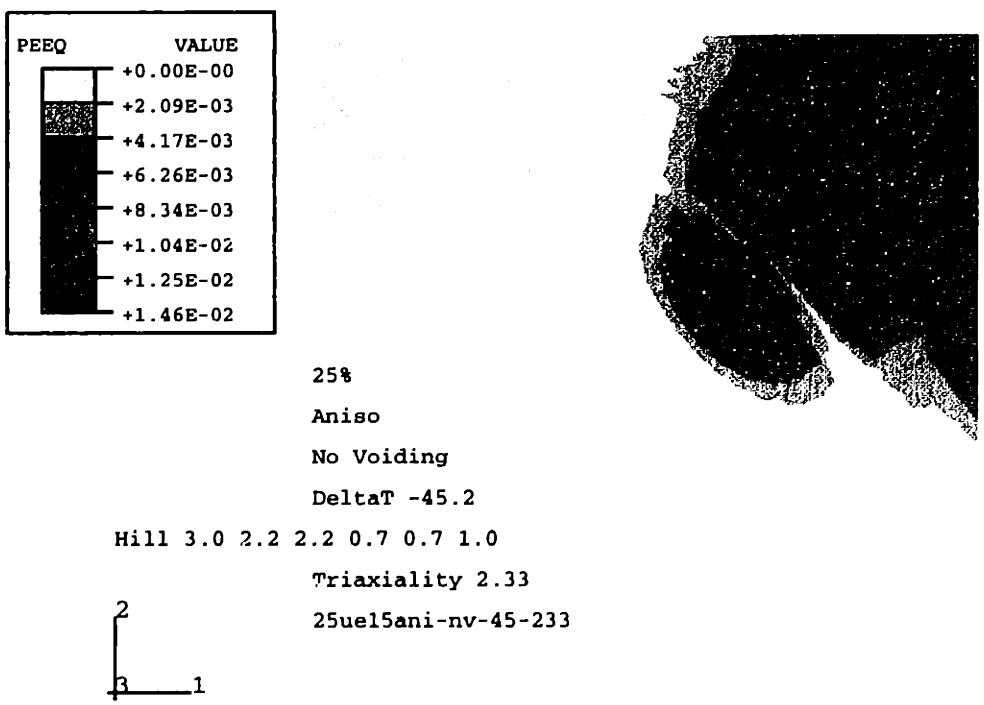

Figure 5-27b: 25ani-nv-45-233: Equivalent plastic strain ε^p_{equiv} at $\varepsilon_{zz} = 2.5\%$. Anisotropic matrix with non-cavitating particle.

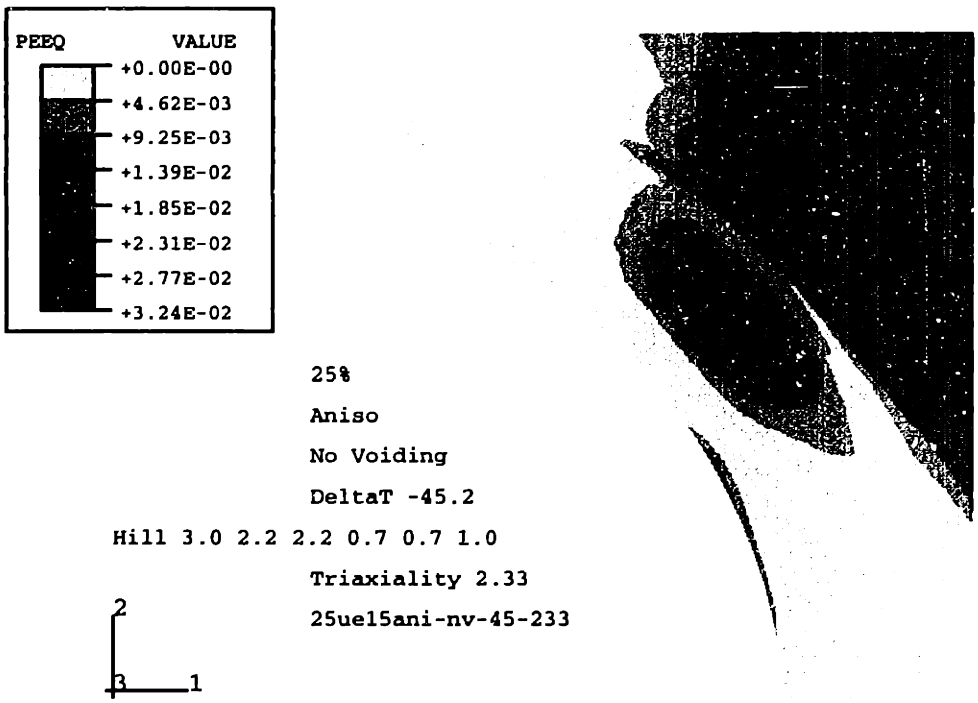

Figure 5-27c: 25ani-nv-45-233: Equivalent plastic strain ε^p_{equiv} at $\varepsilon_{zz} = 3.5\%$. Anisotropic matrix with non-cavitating particle.

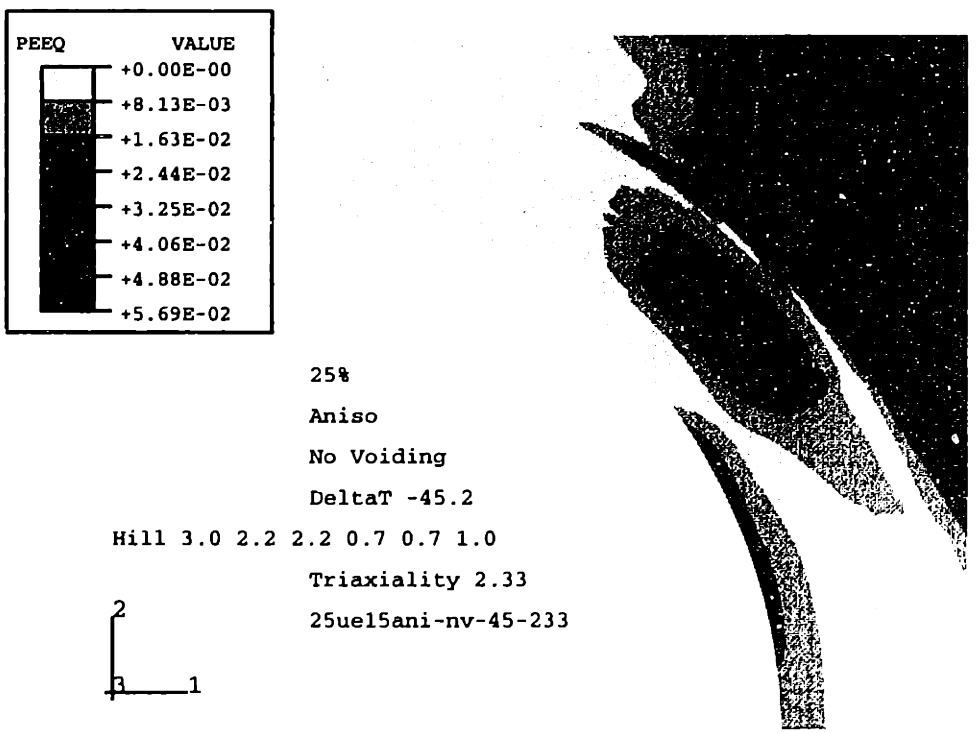

Figure 5-27d: 25ani-nv-45-233: Equivalent plastic strain ε^p_{equiv} at $\varepsilon_{zz} = 4.5\%$. Anisotropic matrix with non-cavitating particle.

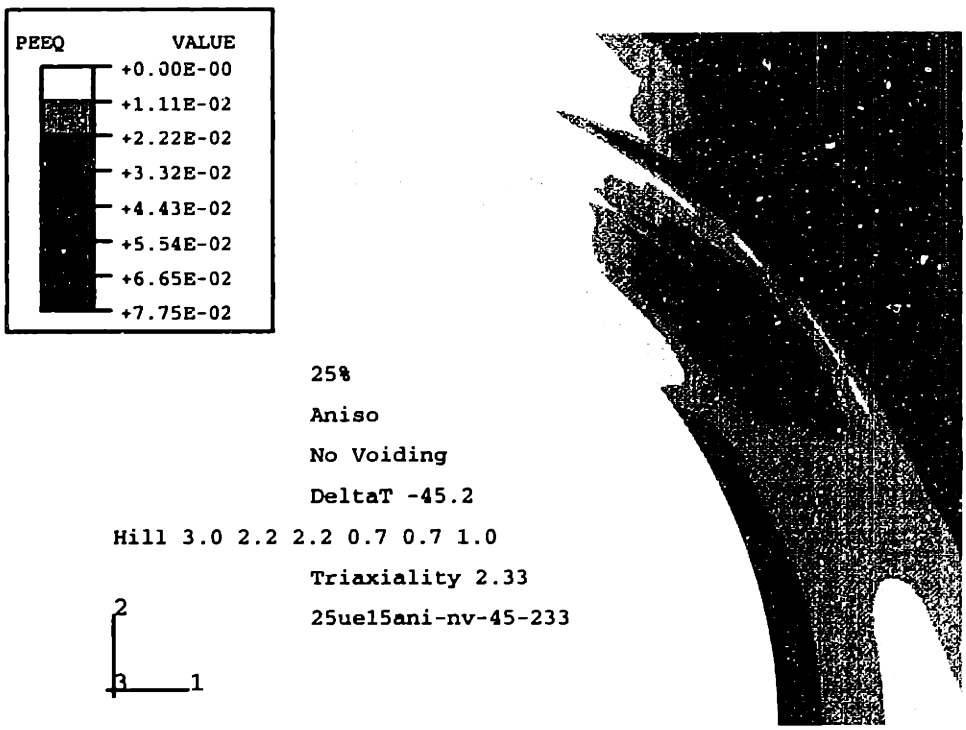

Figure 5-27e: 25ani-nv-45-233: Equivalent plastic strain ε^p_{equiv} at $\varepsilon_{zz} = 5.5\%$. Anisotropic matrix with non-cavitating particle.

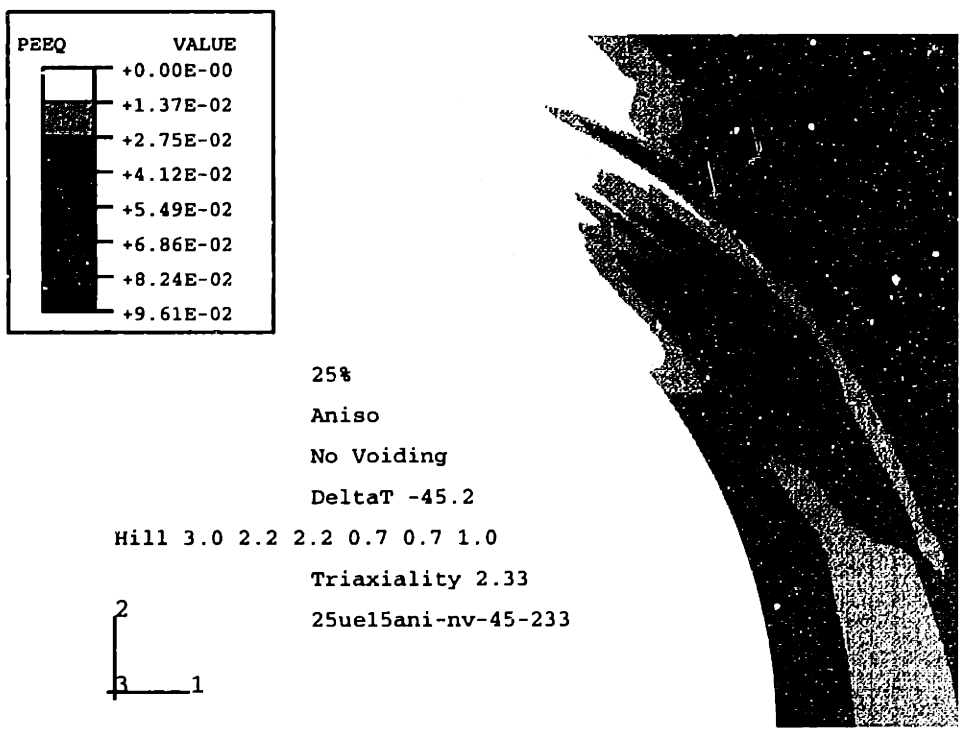

Figure 5-27f: 25ani-nv-45-233: Equivalent plastic strain ε^p_{equiv} at $\varepsilon_{zz} = 6.5\%$. Anisotropic matrix with non-cavitating particle.

Isotropic Matrix

Referring to the contour plots of ε^p_{equiv} in figures 5-28a through 5-31e.

The onset of plasticity is found to be somewhat different in simple tension than what it is under $\Sigma = 2.33$. Both show the same plastic zone in the upper right-hand corner, but the unit cell under simple tension has most strongly deformed plastically at the pole of the particle, whereas the cell under $\Sigma = 2.33$ has deformed plastically most prominently at the particle equator.

As seen above, the unit cell with $\Sigma = 2.33$ yields at $\varepsilon^y_{zz} = 1.7\%$, whereas that under simple tension yields at $\varepsilon^y_{zz} = 1.2\%$.

At $\varepsilon_{zz} \geq 4.5\%$, the contour plots of ε^p_{equiv} at all triaxialities resemble each other more and more. The lower Σ, the more plastic deformation occurs at the particle pole. The levels of ε^p_{equiv} are always higher for lower $|Sigma$, but their maximum difference decreases to only 15% at $\varepsilon_{zz} = 6.5\%$.

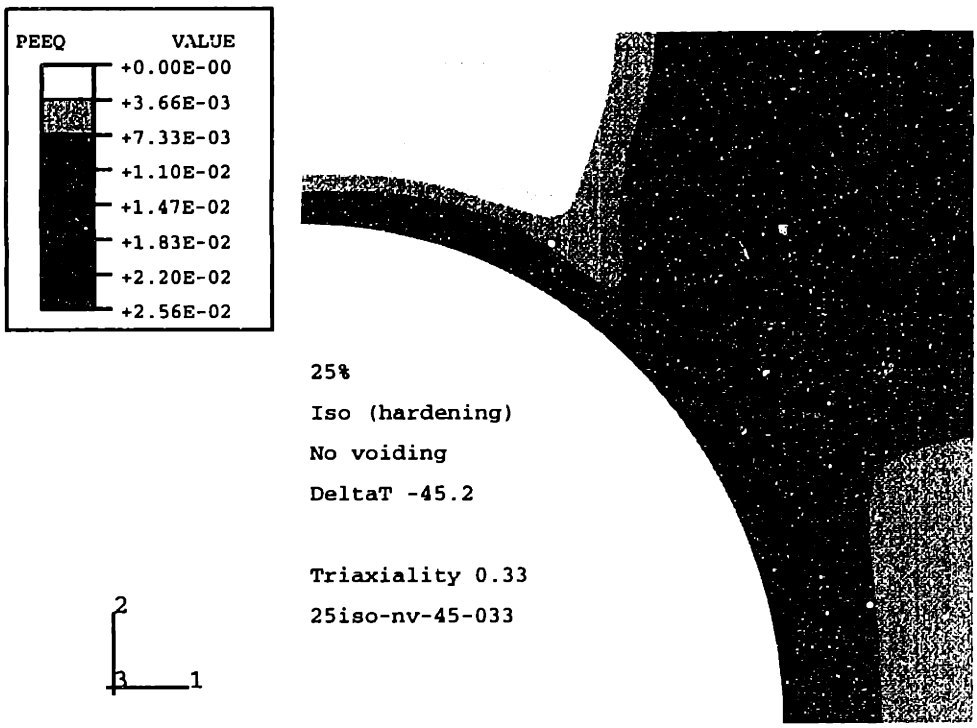

Figure 5-28a: 25iso-nv-45-033: Equivalent plastic strain ε^p_{equiv} at $\varepsilon_{zz} = 2.5\%$. Isotropic matrix with non-cavitating particle.

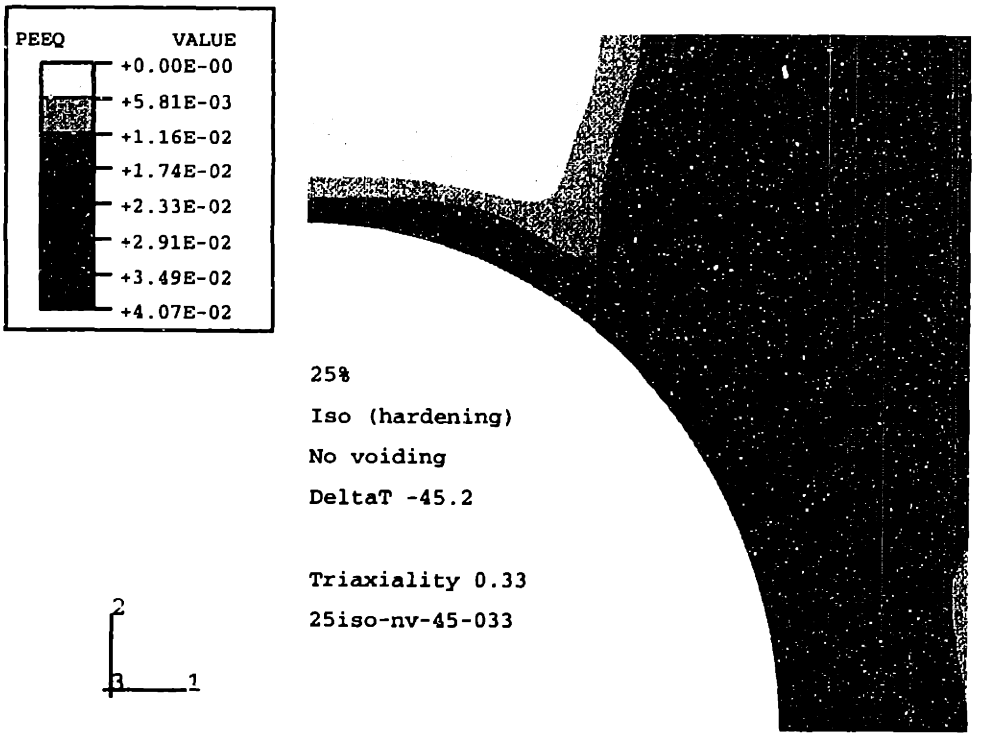

Figure 5-28b: 25iso-nv-45-033: Equivalent plastic strain ε^p_{equiv} at $\varepsilon_{zz} = 3.5\%$. Isotropic matrix with non-cavitating particle.

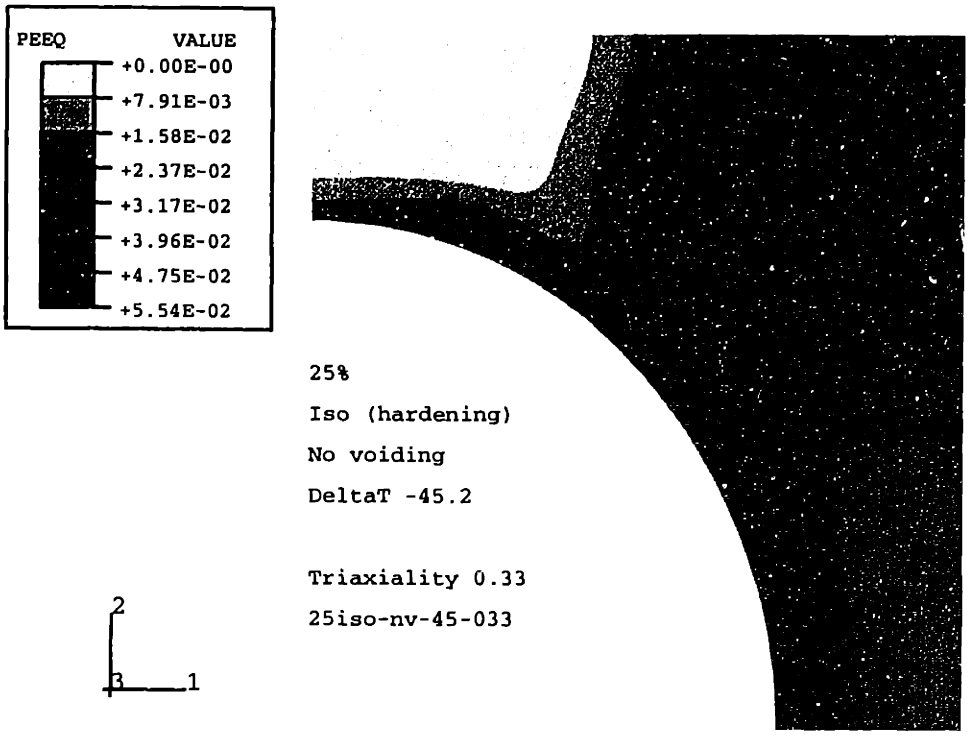

Figure 5-28c: 25iso-nv-45-033: Equivalent plastic strain ε^p_{equiv} at $\varepsilon_{zz} = 4.5\%$. Isotropic matrix with non-cavitating particle.

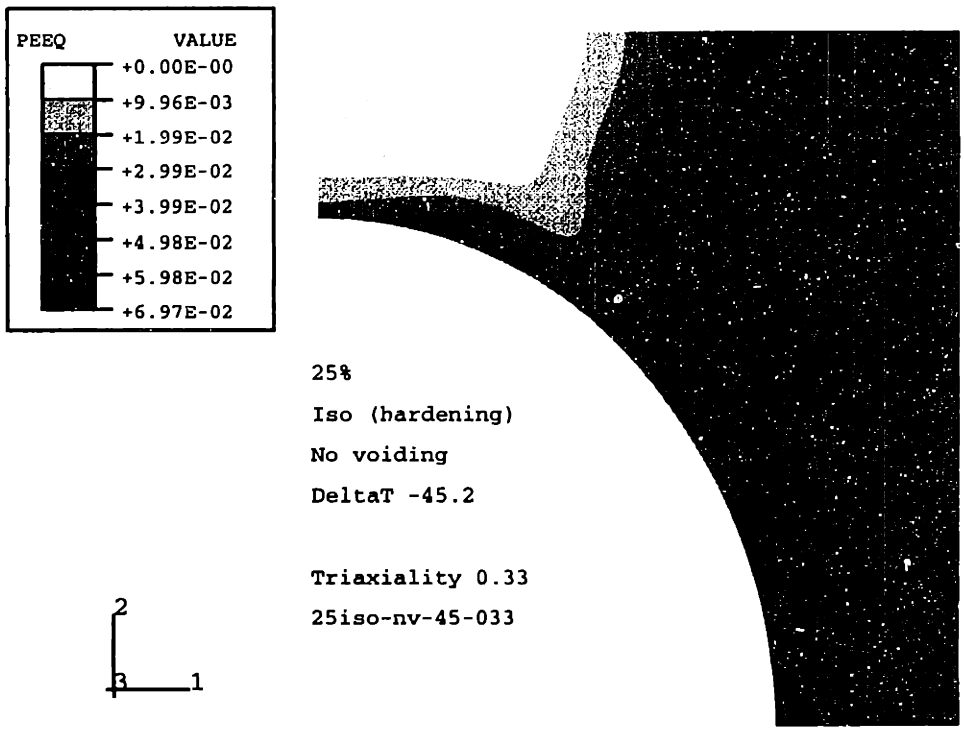

Figure 5-28d: 25iso-nv-45-033: Equivalent plastic strain ε^p_{equiv} at $\varepsilon_{zz} = 5.5\%$. Isotropic matrix with non-cavitating particle.

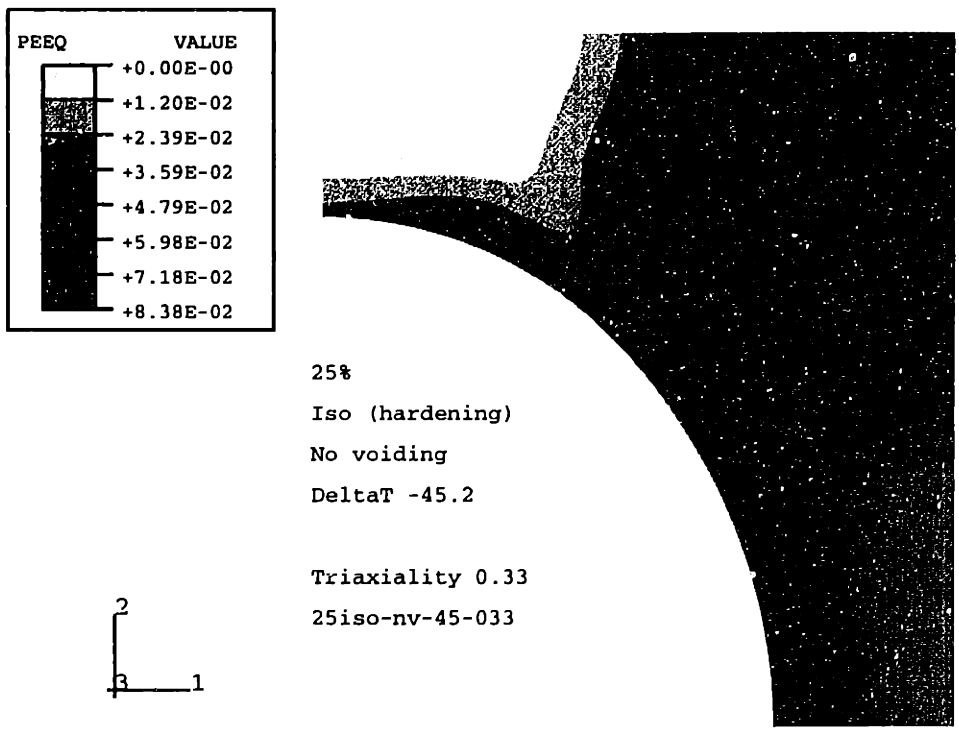

Figure 5-28e: 25iso-nv-45-033: Equivalent plastic strain ε^p_{equiv} at $\varepsilon_{zz} = 6.5\%$. Isotropic matrix with non-cavitating particle.

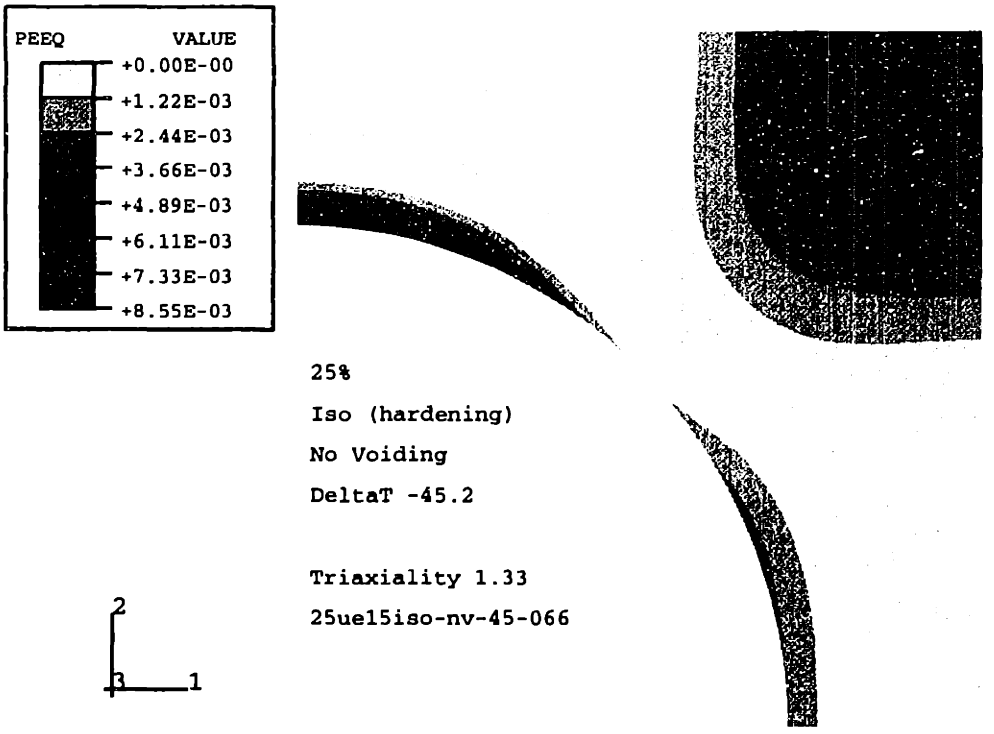

Figure 5-29a: 25iso-nv-45-066: Equivalent plastic strain ε^p_{equiv} at $\varepsilon_{zz} = 1.5\%$. Isotropic matrix with non-cavitating particle.

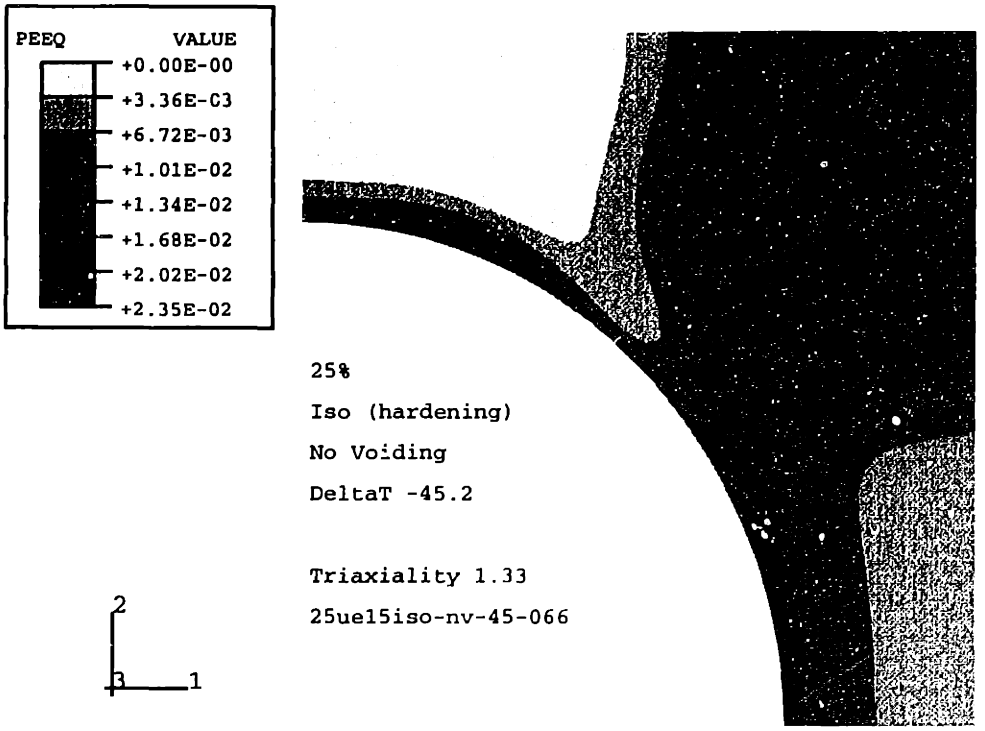

Figure 5-29b: 25iso-nv-45-066: Equivalent plastic strain ε^p_{equiv} at $\varepsilon_{zz} = 2.5\%$. Isotropic matrix with non-cavitating particle.

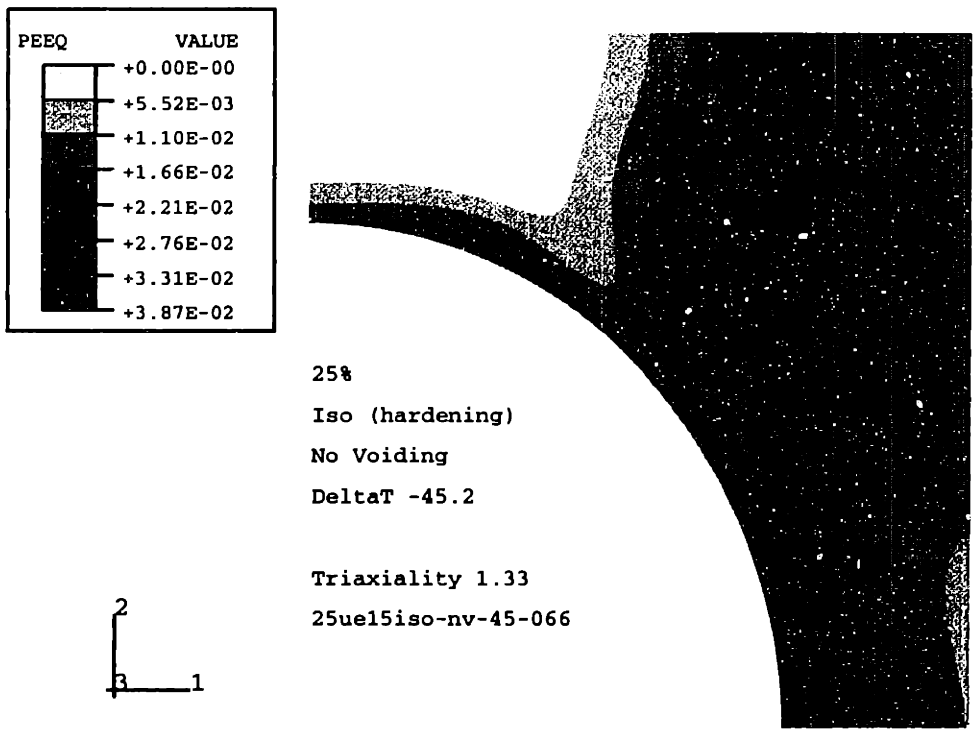

Figure 5-29c: 25iso-nv-45-066: Equivalent plastic strain ε^p_{equiv} at $\varepsilon_{zz} = 3.5\%$. Isotropic matrix with non-cavitating particle.

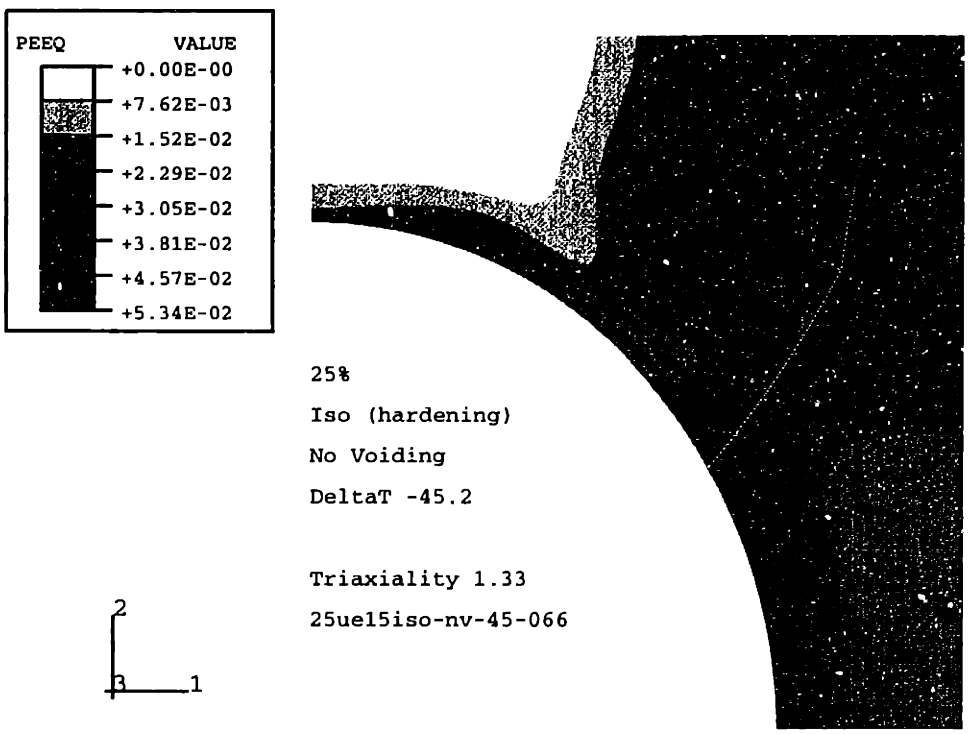

Figure 5-29d: 25iso-nv-45-066: Equivalent plastic strain ε^p_{equiv} at $\varepsilon_{zz} = 4.5\%$. Isotropic matrix with non-cavitating particle.

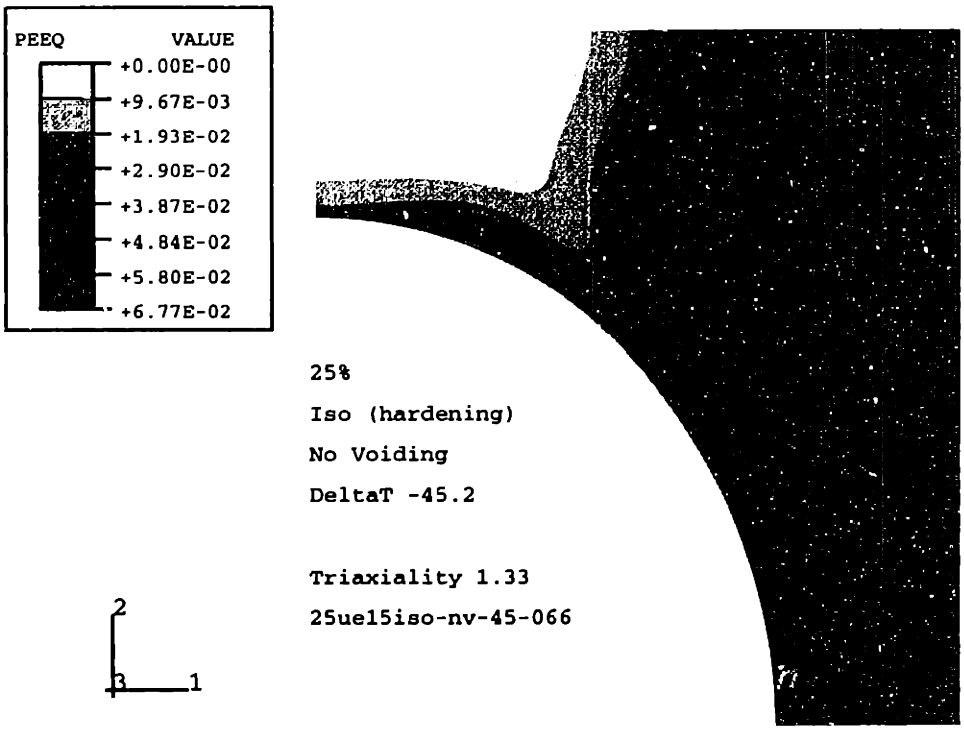

Figure 5-29e: 25iso-nv-45-066: Equivalent plastic strain ε^p_{equiv} at $\varepsilon_{zz} = 5.5\%$. Isotropic matrix with non-cavitating particle.

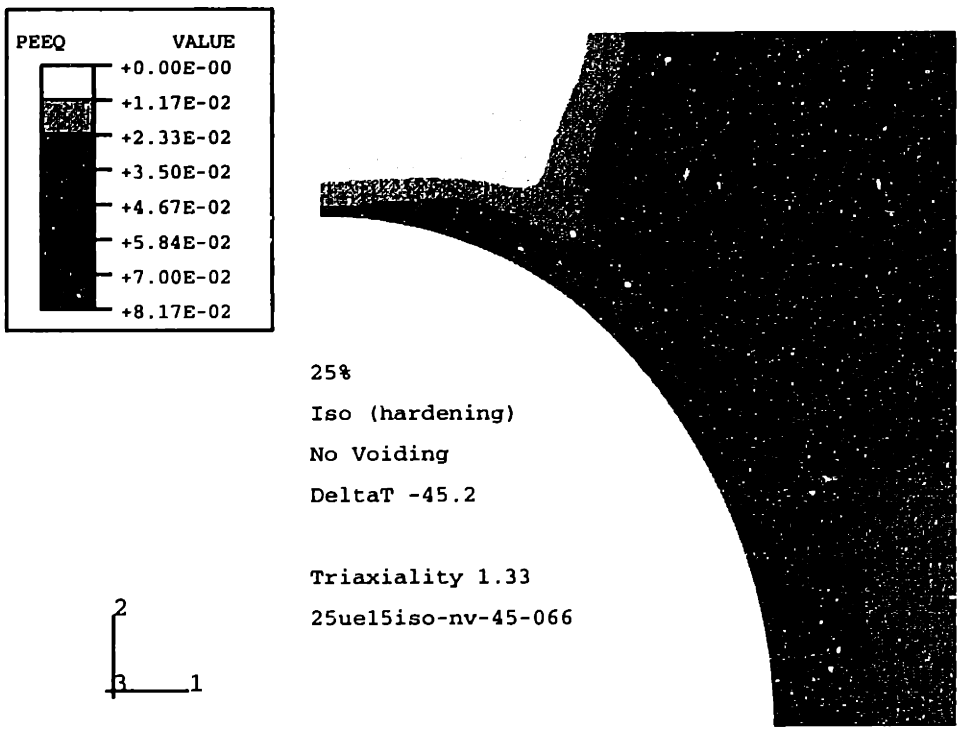

Figure 5-29f: 25iso-nv-45-066: Equivalent plastic strain ε^p_{equiv} at $\varepsilon_{zz} = 6.5\%$. Isotropic matrix with non-cavitating particle.

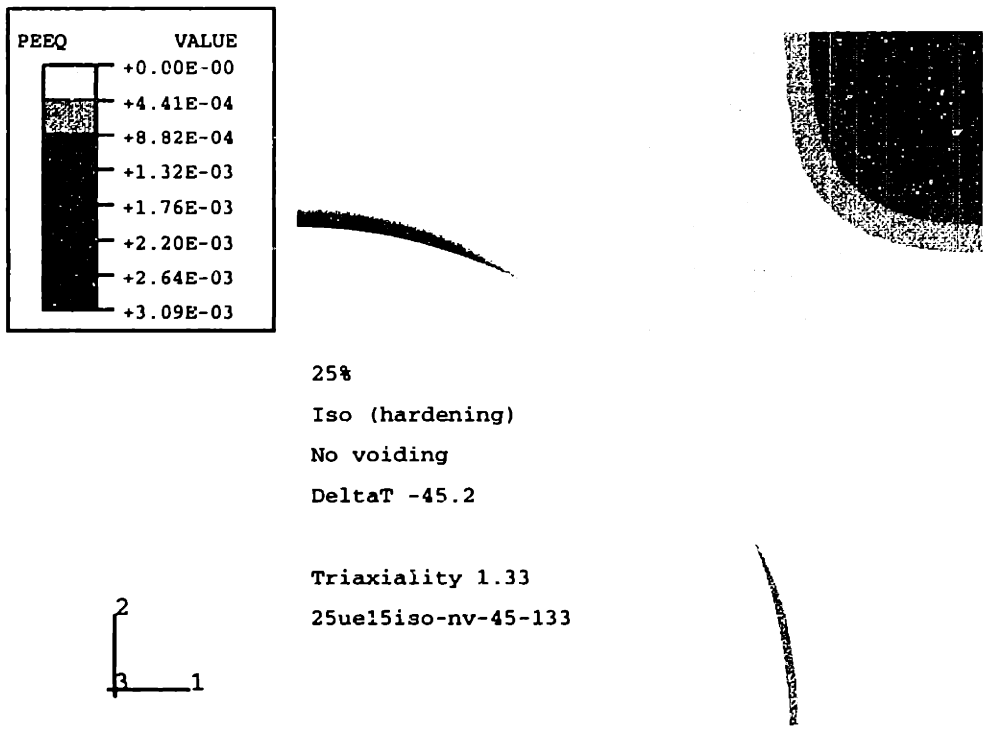

Figure 5-30a: 25iso-nv-45-133: Equivalent plastic strain ε^p_{equiv} at $\varepsilon_{zz} = 1.5\%$. Isotropic matrix with non-cavitating particle.

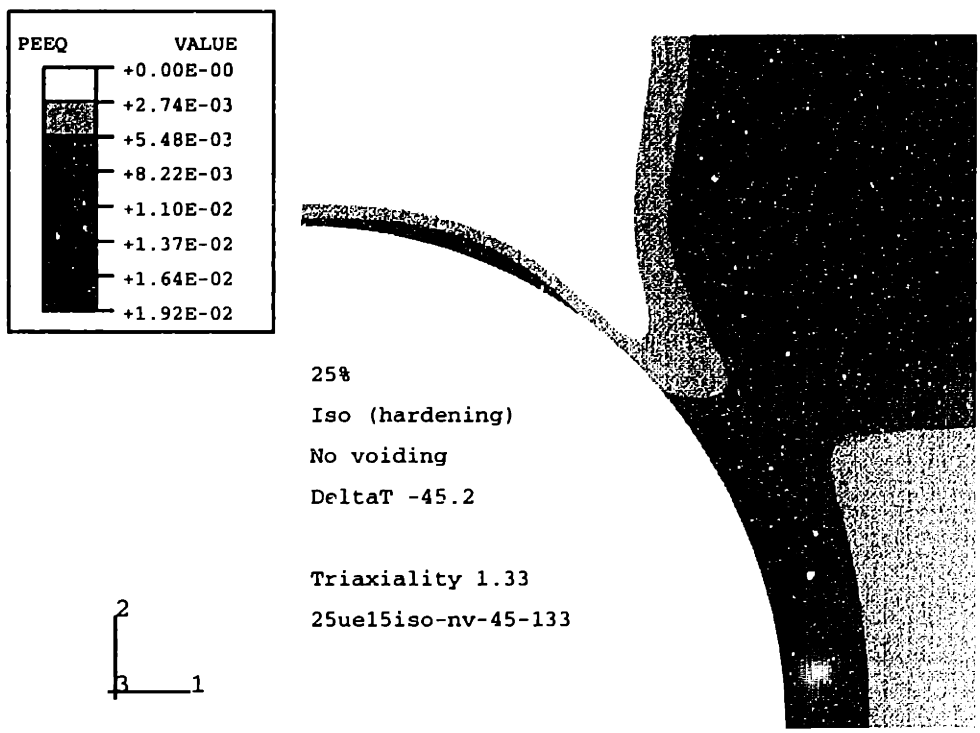

Figure 5-30b: 25iso-nv-45-133: Equivalent plastic strain ε^p_{equiv} at $\varepsilon_{zz} = 2.5\%$. Isotropic matrix with non-cavitating particle.

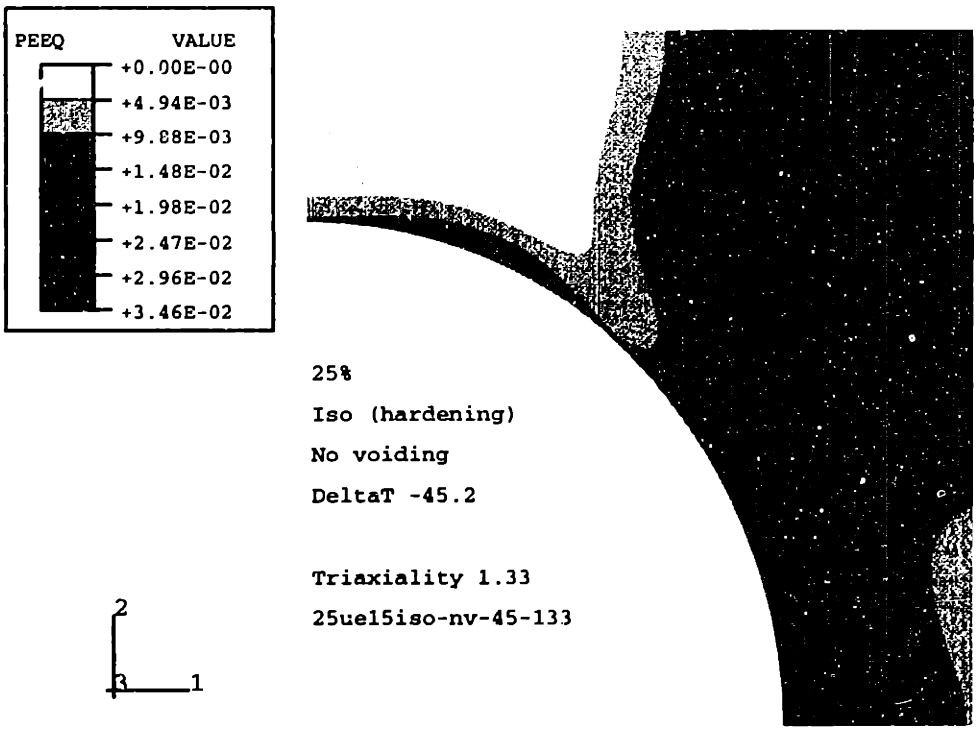

Figure 5-30c: 25iso-nv-45-133: Equivalent plastic strain ε^p_{equiv} at $\varepsilon_{zz} = 3.5\%$. Isotropic matrix with non-cavitating particle.

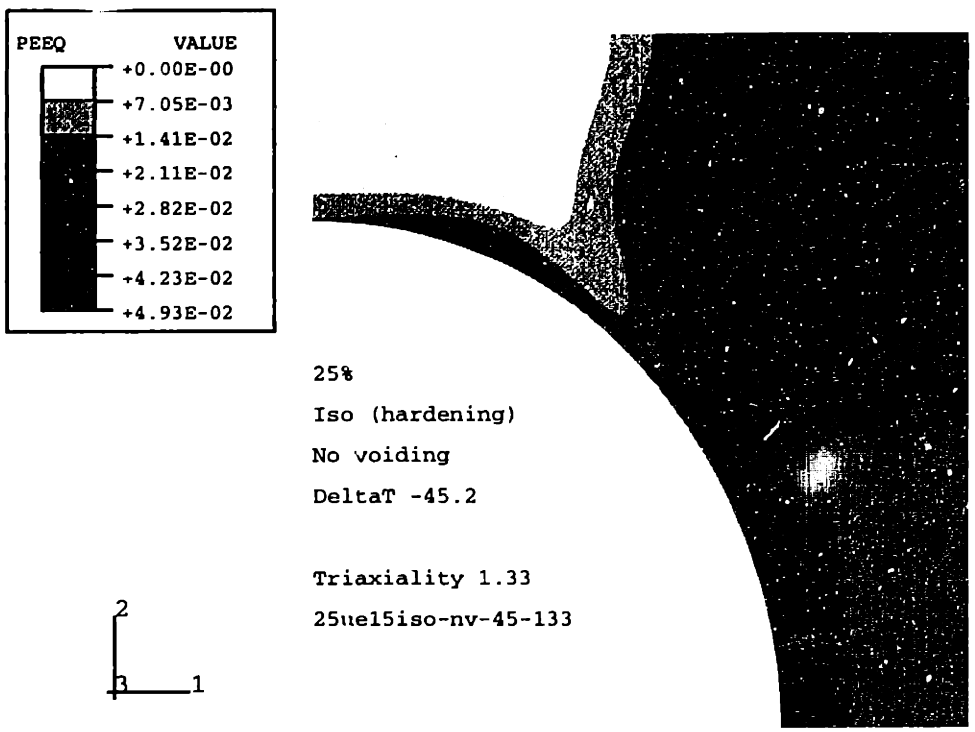

Figure 5-30d: 25iso-nv-45-133. Equivalent plastic strain ε^p_{equiv} at $\varepsilon_{zz} = 4.5\%$. Isotropic matrix with non-cavitating particle.

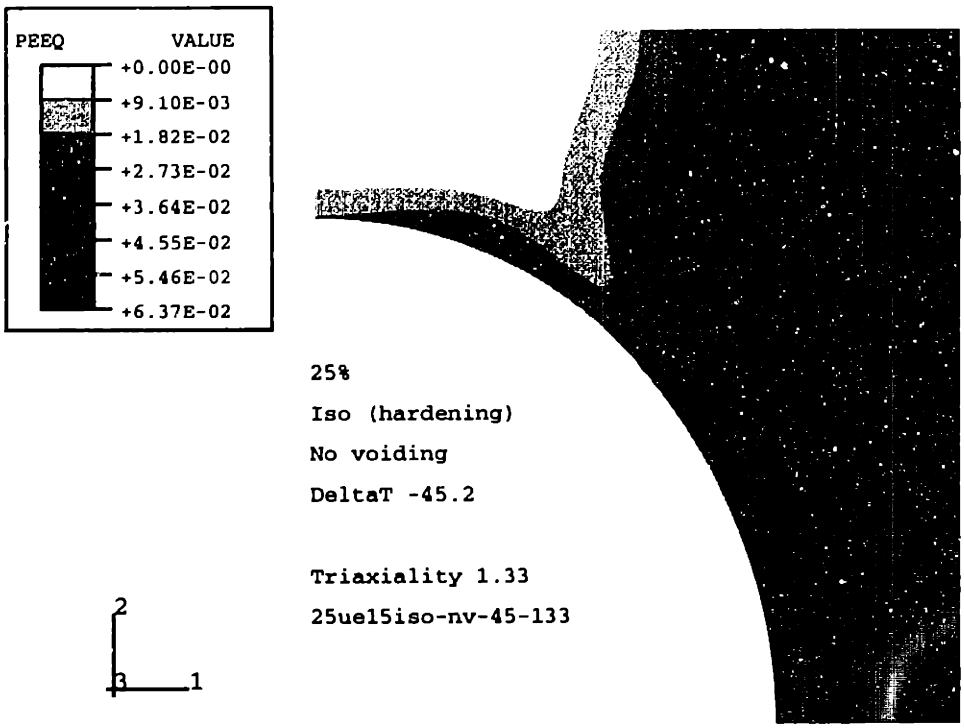

Figure 5-30e: 25iso-nv-45-133: Equivalent plastic strain ε^p_{equiv} at $\varepsilon_{zz} = 5.5\%$. Isotropic matrix with non-cavitating particle.

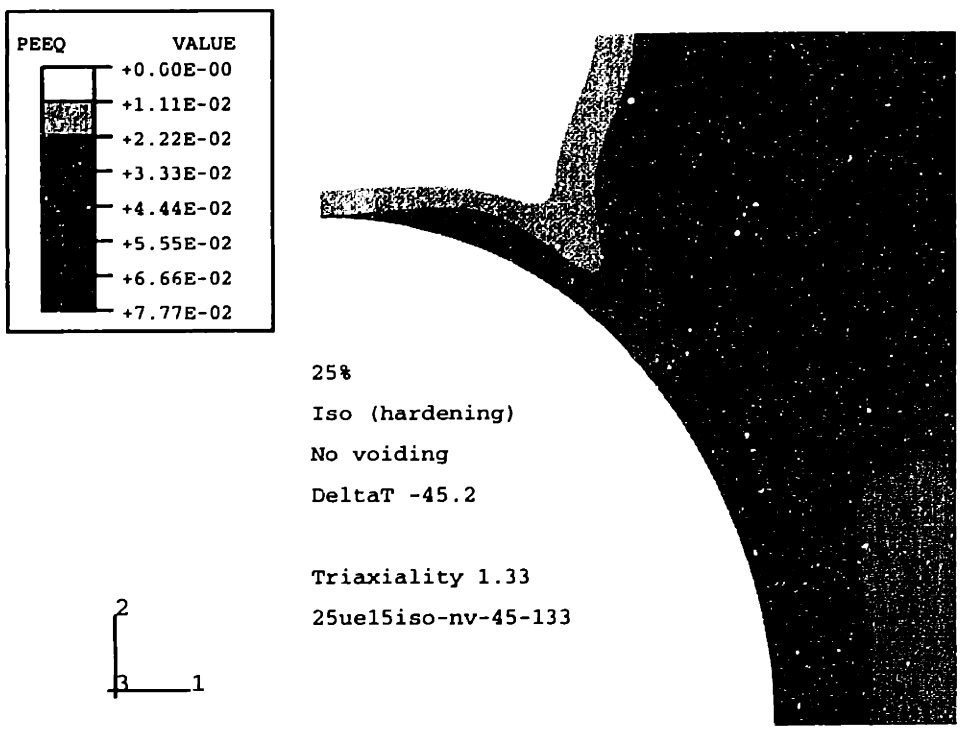

Figure 5-30f: 25iso-nv-45-133: Equivalent plastic strain ε^p_{equiv} at $\varepsilon_{zz} = 6.5\%$. Isotropic matrix with non-cavitating particle.

Summary

The plasticity in both, anisotropic and isotropic matrices with coherent particles exhibits little sensitivity to the level of the applied triaxial stress state, relative to the distribution and magnitudes of ε^p_{equiv}. Only in the isotropic matrix at very low strains the plasticity differs between cases of different Σ, which seems to be related to the increasing ϵ^y_{zz} with increasing Σ.

5.4.6 Effect of Varying Σ on the Matrix Plasticity of Unit Cells with Pre-Existing Cavities

Purpose of this section is it to identify the effects of varying the triaxiality on the distribution, evolution and magnitudes of the plasticity in the matrix for the case of unit cells with pre-existing cavities.

Figures 5-32a through 5-39f are contour plots of ε^p_{equiv} of the anisotropic and isotropic unit cells with pre-existing cavities at ε_{zz} = 1.5%, 2.5%, 3.5%, 4.5%, 5.5% and 6.5%.

Anisotropic Matrix

In the case of uniaxial tension, the onset of matrix plasticity is found to be located along the same patterns as was previously found for the case of the non-cavitating particle. Considering figure 5-32a, most of the plasticity is found in the upper right-hand corner of the unit cell and a shear band begins to form. From ε_{zz} = 2.5% on, the evolution of the matrix plasticity changes quickly to that typical for the cells with cavities (figures 5-32b-f). The previously noted shear band begins to dominate, the plastic zone along the particle/matrix interface close to the particle equator emerges, and the plastic zone spreads out mostly toward the lateral boundary and the lower parts of the matrix. The matrix plasticity concentrates more and more in the shear band. At ε_{zz} = 2.5%, ε^p_{equiv} reaches levels of up to 2.8% in the shear band, whereas ε^p_{equiv} is limited to levels below 2% elsewhere. At ε_{zz} = 6.5%, ε^p_{equiv} reaches 11% in the shear band, 7.9% in the plastic zone near the particle equator and 6.3% elsewhere.

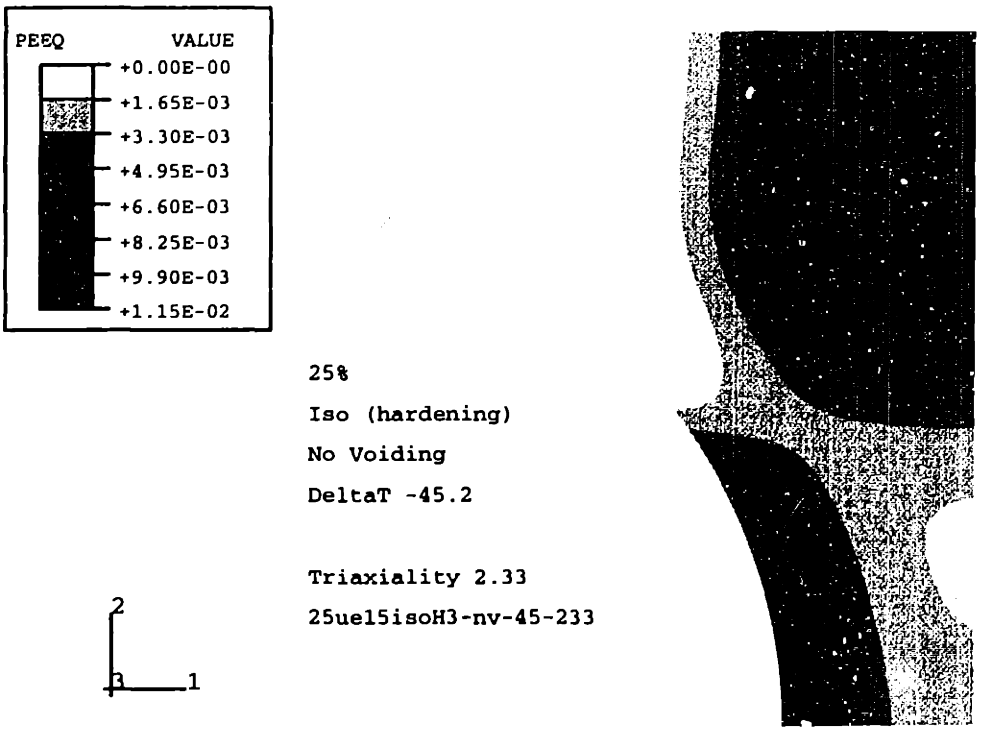

Figure 5-31a: 25iso-nv-45-233: Equivalent plastic strain ε^p_{equiv} at $\varepsilon_{zz} = 2.5\%$. Isotropic matrix with non-cavitating particle.

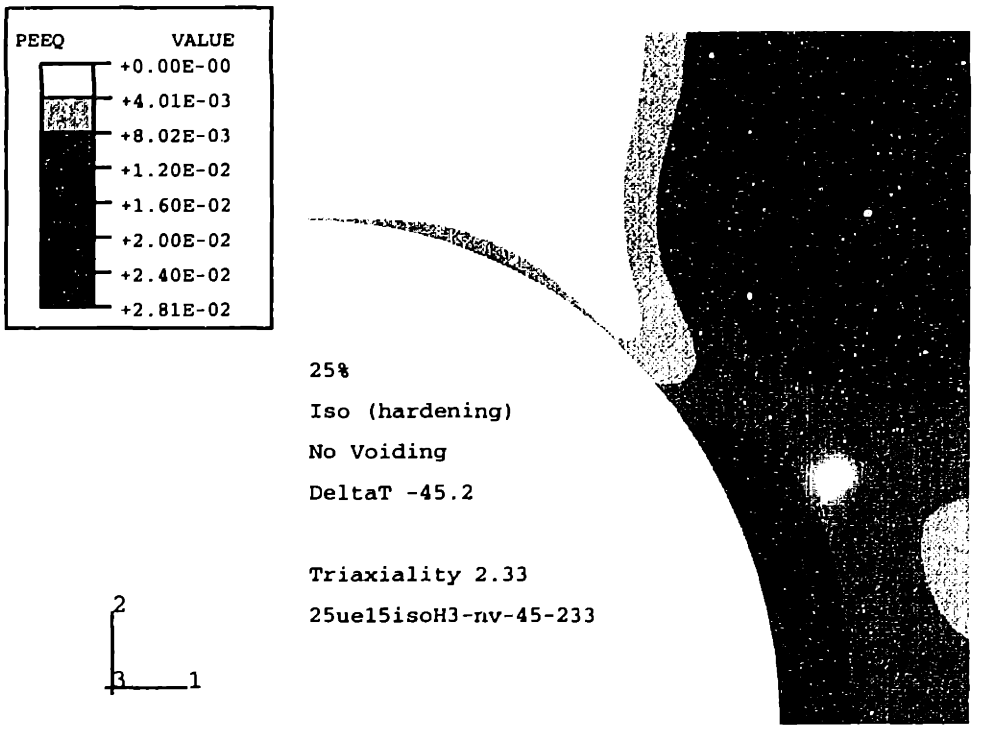

Figure 5-31b: 25iso-nv-45-233: Equivalent plastic strain ε^p_{equiv} at $\varepsilon_{zz} = 3.5\%$. Isotropic matrix with non-cavitating particle.

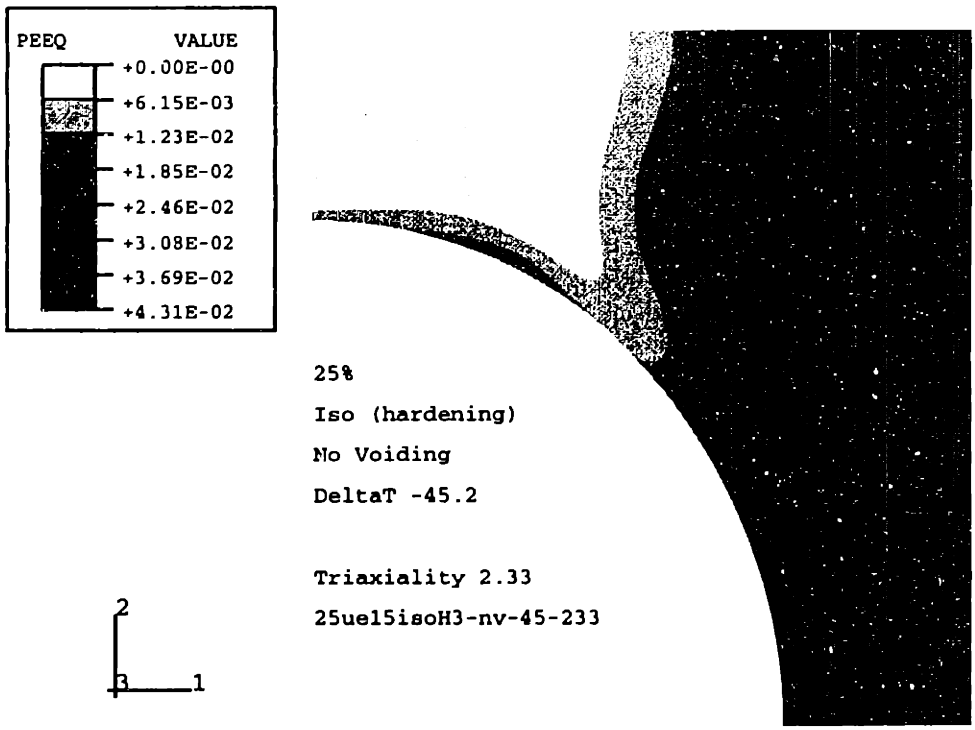

Figure 5-31c: 25iso-nv-45-233: Equivalent plastic strain ε^p_{equiv} at $\varepsilon_{zz} = 4.5\%$. Isotropic matrix with non-cavitating particle.

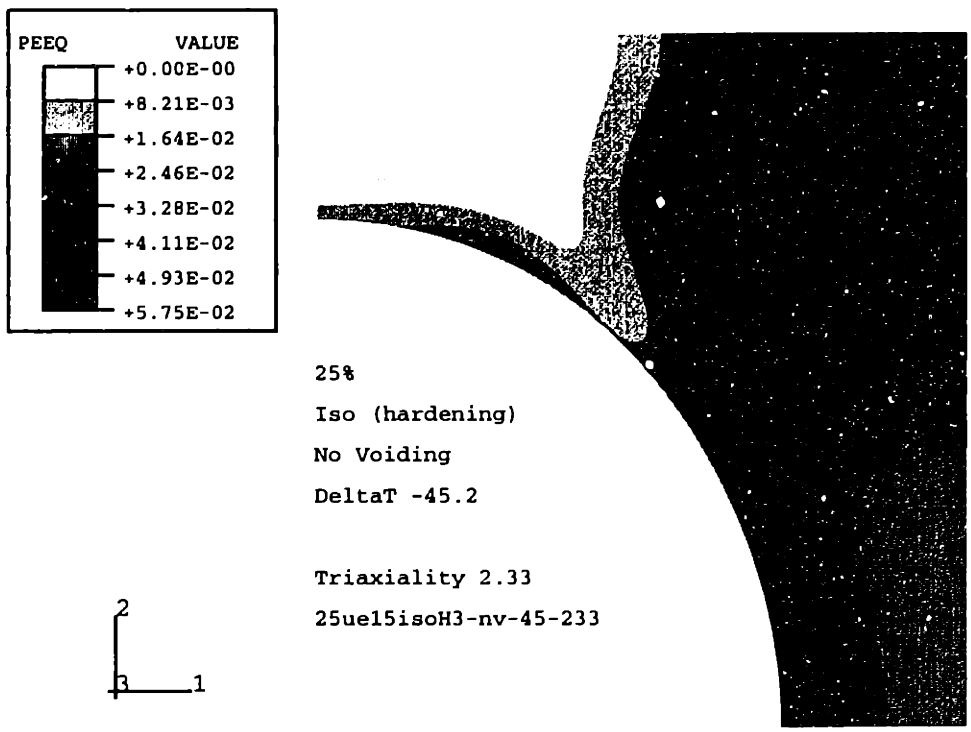

Figure 5-31d: 25iso-nv-45-233: Equivalent plastic strain ε^p_{equiv} at $\varepsilon_{zz} = 5.5\%$. Isotropic matrix with non-cavitating particle.

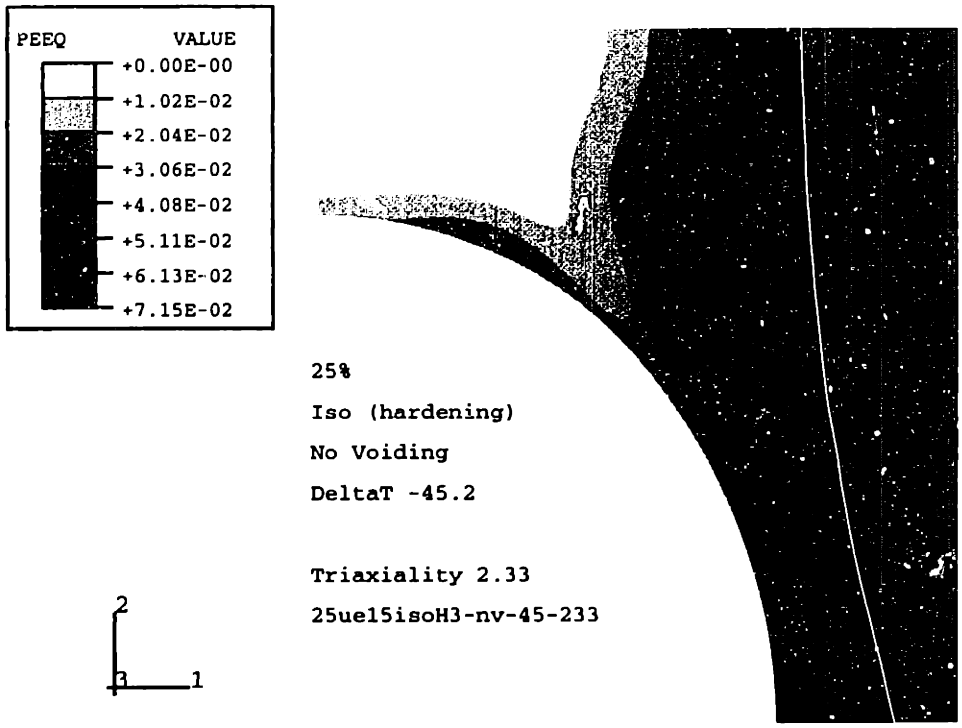

Figure 5-31e: 25iso-nv-45-233: Equivalent plastic strain ε^p_{equiv} at $\varepsilon_{zz} = 6.5\%$. Isotropic matrix with non-cavitating particle.

With increasing triaxiality the onset of plasticity shifts toward regions close to the lateral boundary and the concentration of plastic deformation becomes more and more pronounced.

Considering Figures 5-35a-f where $\Sigma = 2.33$, it can be seen how the matrix yield is limited to a small region at the lateral boundary. This region is located where the previously discussed shear band extends to the lateral boundary at higher axial strain.

To better illustrate the very localized plasticity, the contour levels of ε^p_{equiv} have been limited to 7.5% in figures 5-36a-f. The contour levels are therefore 0, 1.25%, 2.50%, 3.75%, 5.00%, 6.25% and 7.50%, and all levels of ε^p_{equiv} exceeding 7.50% are filled with the darkest shade. Following the evolution of the matrix plasticity, it can be seen how very high levels of ε^p_{equiv} are generated at relatively modest axial strain. At $\varepsilon_{zz} = 2.5\%$, ε^p_{equiv} reaches 23% in two regions: the previously discussed shear band ("shear band I") and the second shear band that has formed close to the particle equator ("shear band II"). Everywhere else in the matrix ε^p_{equiv} remains below 1.25%

at that axial strain. At $\varepsilon_{zz} = 3.5\%$ two more shear band emerge. "Shear band III" is parallel to shear band I starting at the lateral boundary. "Shear band IV" starts at shear band II close to the particle equator and extends vertically upward slightly curving toward the particle. In some parts of these shear bands ε^p_{equiv} reaches over 200%. Another plastic region spreads out laterally from the particle equator. At $\varepsilon_{zz} = 4.5\%$, the zones with $\varepsilon^p_{equiv} = 7.5\%$ or higher, spread out further, except in shear band I. Shear bands III and IV connect and the plastic zone at the equator has further spread out laterally. This trend continues as ε_{zz} increases to 6.5%. The inhomogeneous deformation of the cavity surface that can be seen near the cavity equator will be discussed below.

Comparing the contour plots of ε^p_{equiv} to the stress-strain plots in figure 5-20, it can be seen how the changes in the stress-strain plots can be related to the patterns of contour plots of ε^p_{equiv}. In the case of $\Sigma = 0.33$, it can be seen how between $\varepsilon_{zz} = 0$ and 3.5% the contour plots of ε^p_{equiv} evolve from an initially relatively spread-out yielding zone in the upper right-hand corner to the pattern of localized plasticity. This corresponds to the departure from linearity on the stress-strain plots and the decreasing hardening of the anisotropic matrix. When $\varepsilon_{zz} > 3.5\%$, the plots are not very different from each other; i.e., the distribution and relative magnitudes of ε^p_{equiv} are very similar between the plots and do not evolve much, only the absolute magnitudes of ε^p_{equiv} keep increasing with ε_{zz}. On the stress-strain plot this corresponds to the very light increase or near-plateau in σ_{zz} with increasing ε_{zz}. In the case of $\Sigma = 2.33$ (figures 5-36a-f), additional shear bands can be seen to emerge as the axial stress begins to drop at $\varepsilon_{zz} > 2.8\%$. These observations suggest that the deformation of the anisotropic matrix can be divided in to three phases:

- $\varepsilon_{zz} \leq \varepsilon^y_{zz}$: elastic deformation up to yield;
- $\varepsilon_{zz} > \varepsilon^y_{zz}$ and $\sigma_{zz} < \sigma^{max}_{zz}$: yielding in a spread-out region and subsequent localization;
- $\varepsilon_{zz} > \varepsilon^y_{zz}$ and $\sigma_{zz} > \sigma^{max}_{zz}$: appearance of additional shear bands and load drop.

Because of the anisotropy and the geometric constraints of the unit cell, the additional

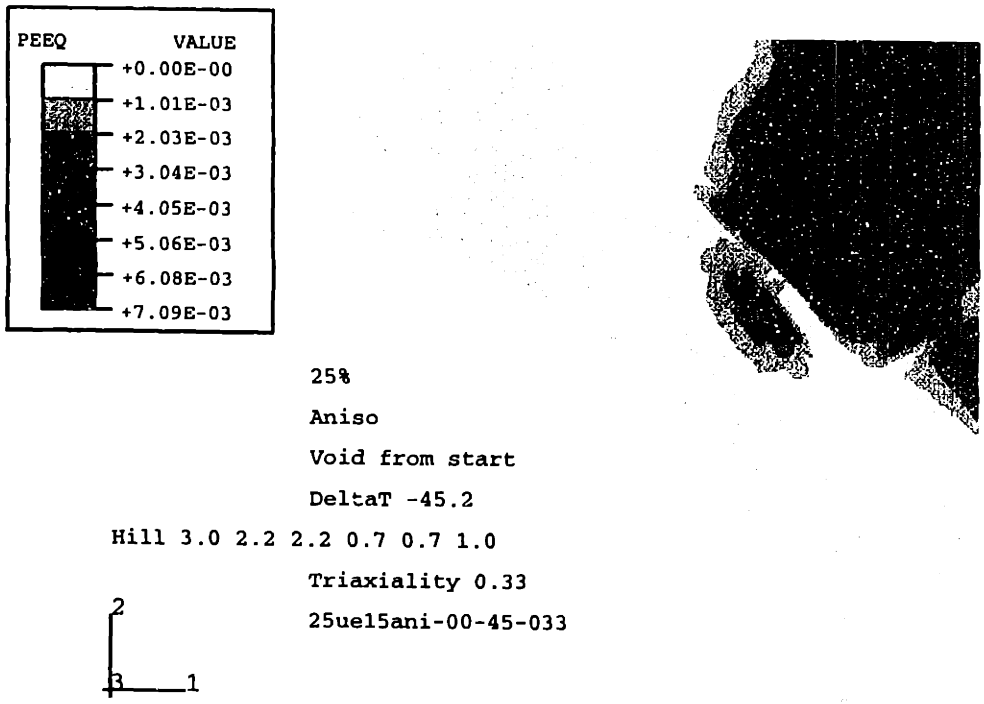

Figure 5-32a: 25ani-00-45-033: Contour plots of ε^{p}_{equiv} at $\varepsilon_{zz} = 1.5\%$.

shear bands appear to be necessary for the anisotropic matrix to be able to undergo additional plastic deformation.

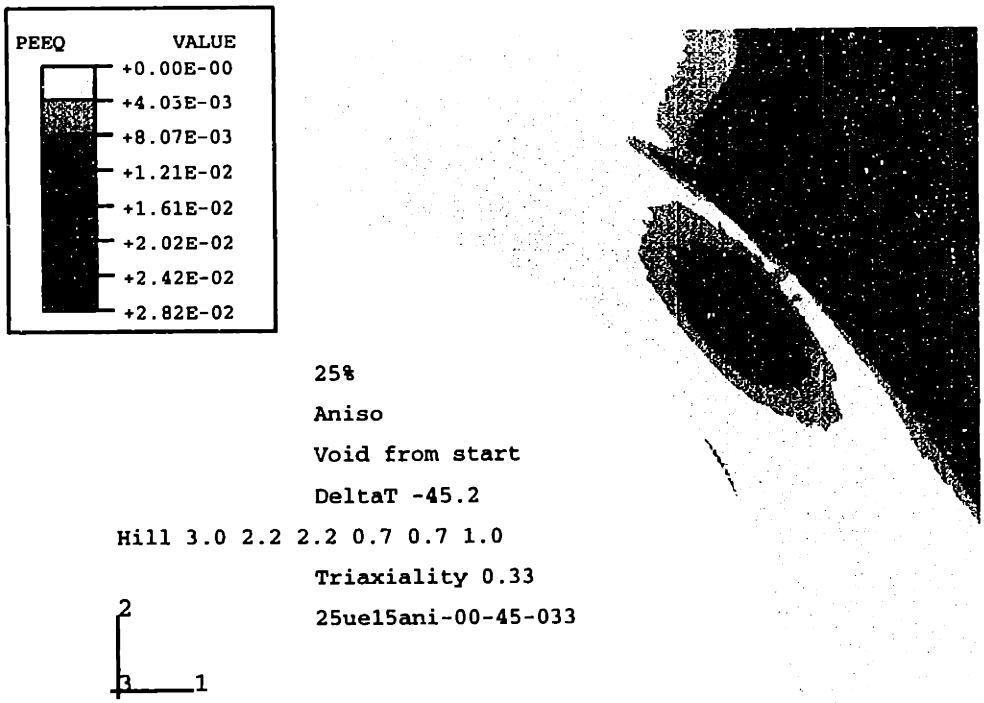

Figure 5-32b: 25ani-00-45-033: Contour plots of ε^p_{equiv} at $\varepsilon_{zz} = 2.5\%$.

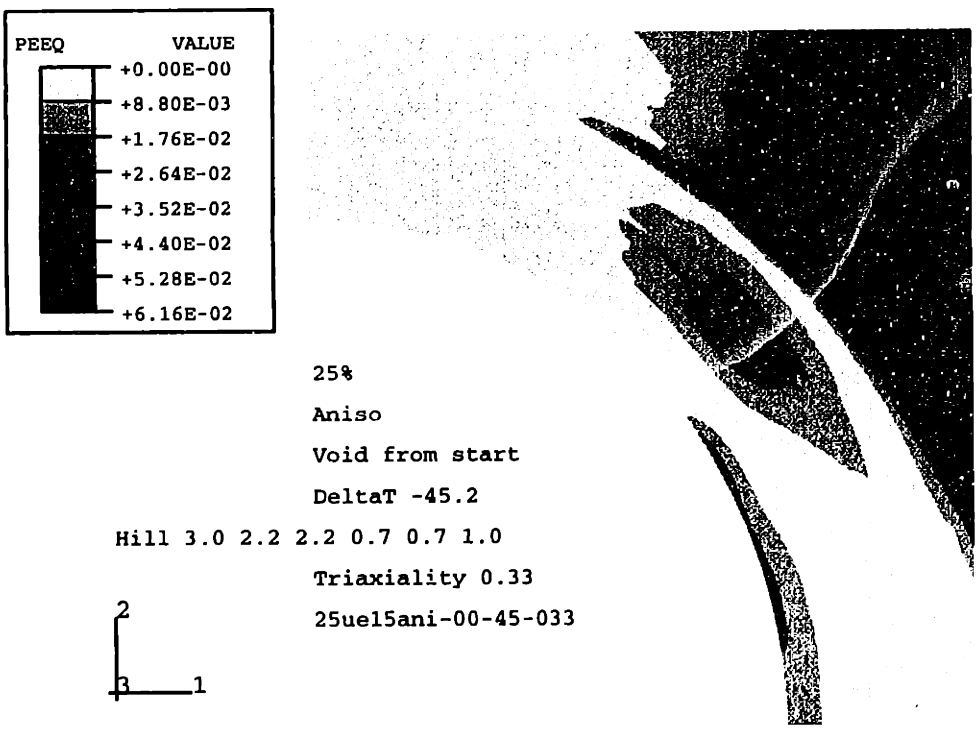

Figure 5-32c: 25ani-00-45-033: Contour plots of ε^p_{equiv} at $\varepsilon_{zz} = 3.5\%$.

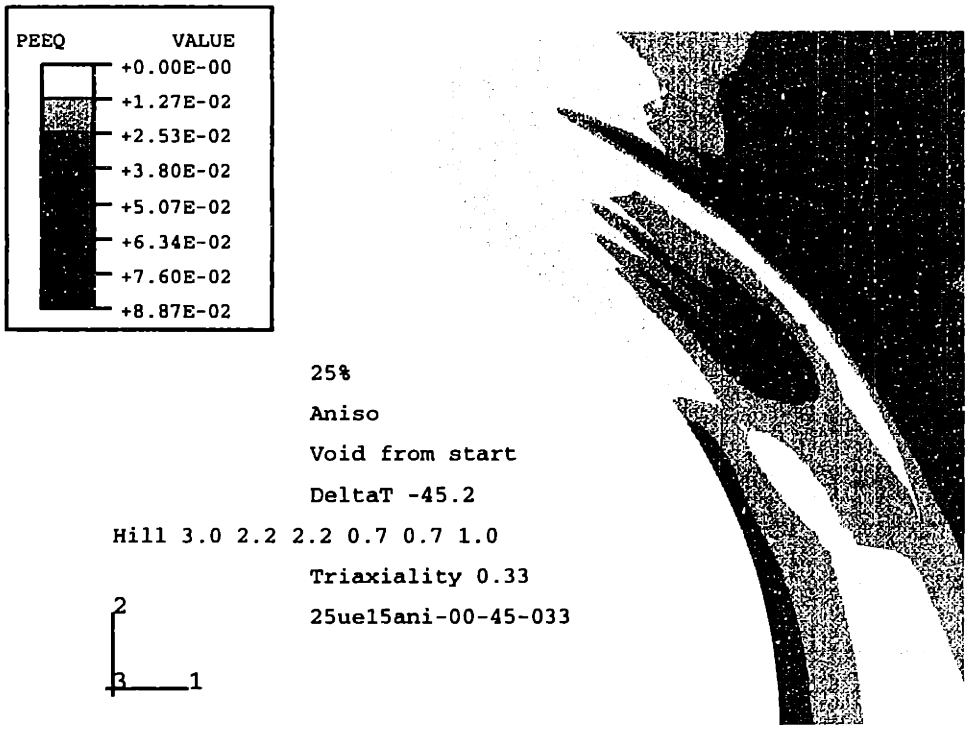

Figure 5-32d: 25ani-00-45-033: Contour plots of ε^p_{equiv} at $\varepsilon_{zz} = 4.5\%$.

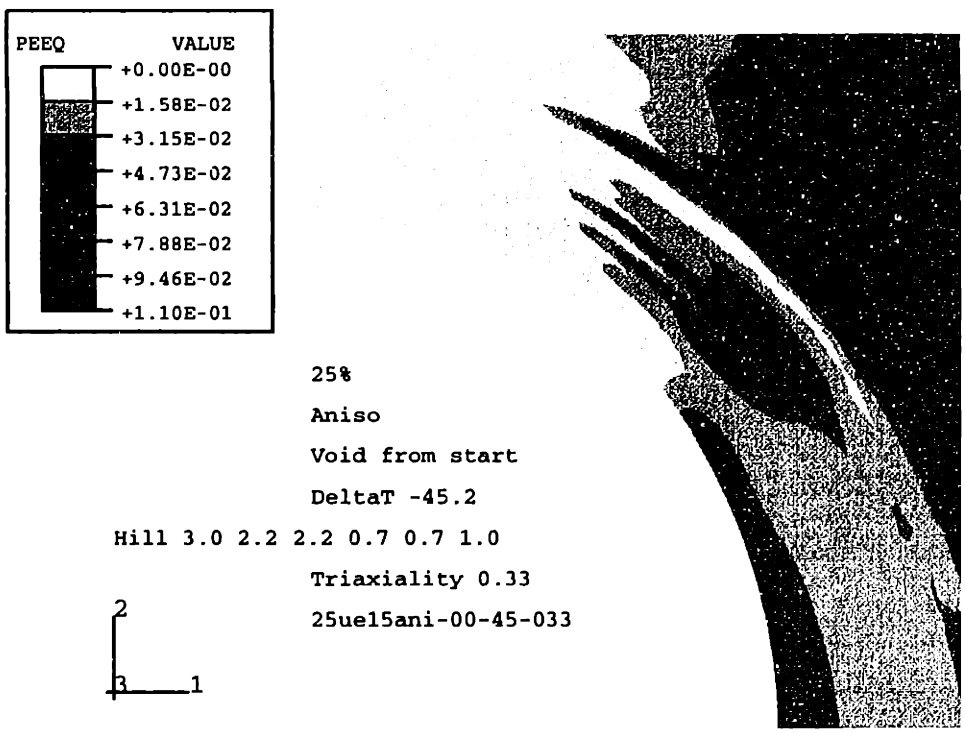

Figure 5-32e: 25ani-00-45-033: Contour plots of ε^p_{equiv} at $\varepsilon_{zz} = 5.5\%$.

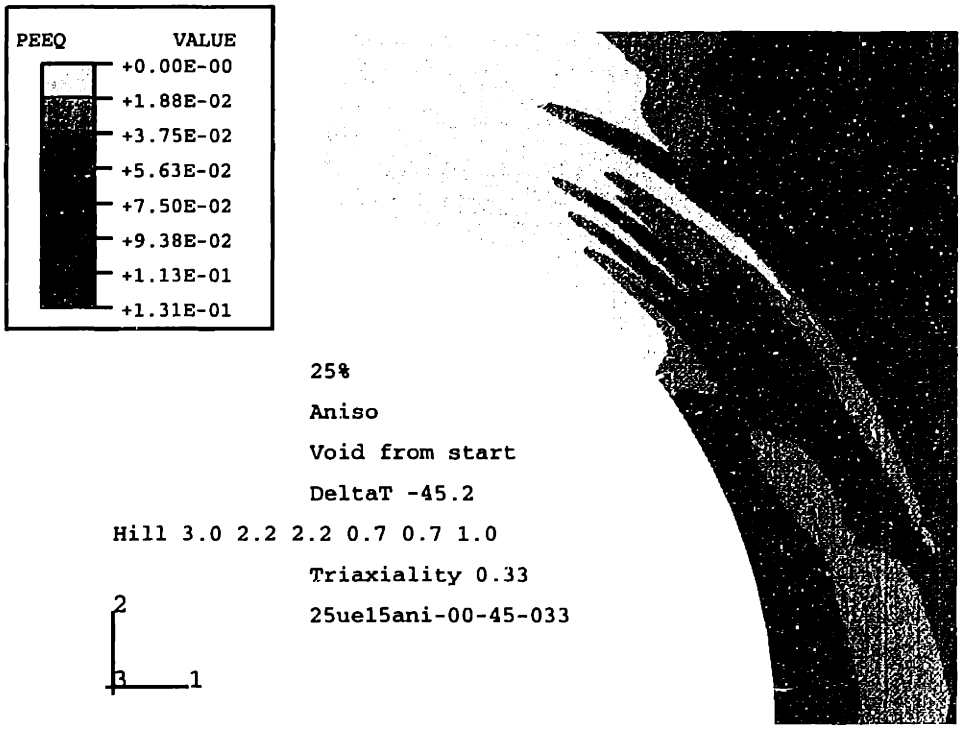

Figure 5-32f: 25ani-00-45-033: Contour plots of ε^{p}_{equiv} at $\varepsilon_{zz} = 6.5\%$.

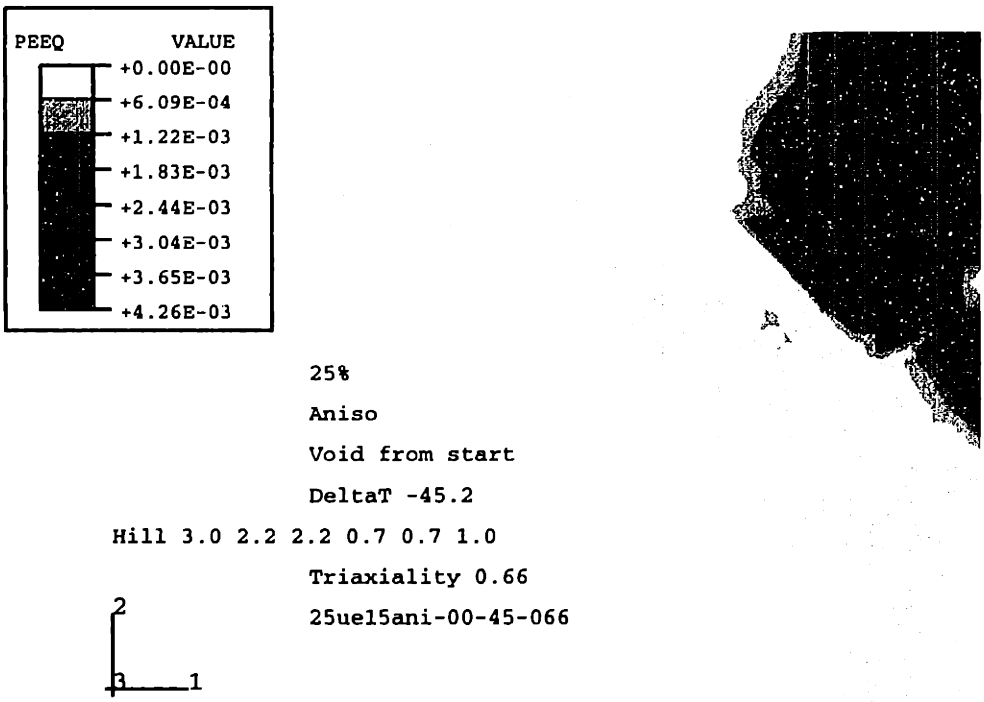

Figure 5-33a: 25ani-00-45-066: Contour plots of ε^p_{equiv} at $\varepsilon_{zz} = 1.5\%$.

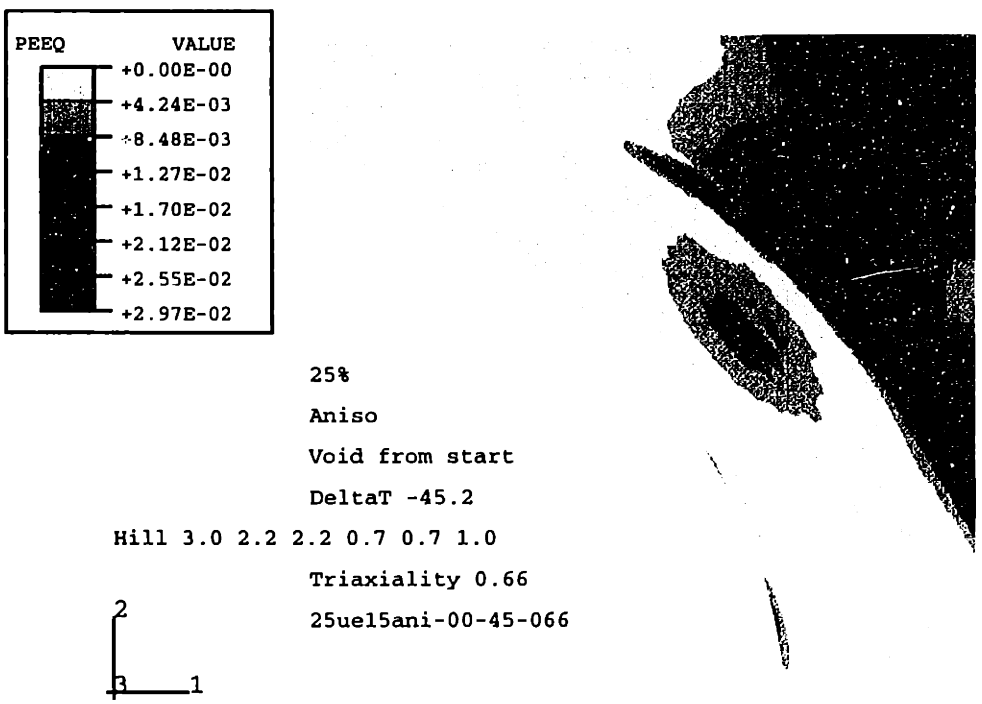

Figure 5-33b: 25ani-00-45-066: Contour plots of ε^p_{equiv} at $\varepsilon_{zz} = 2.5\%$.

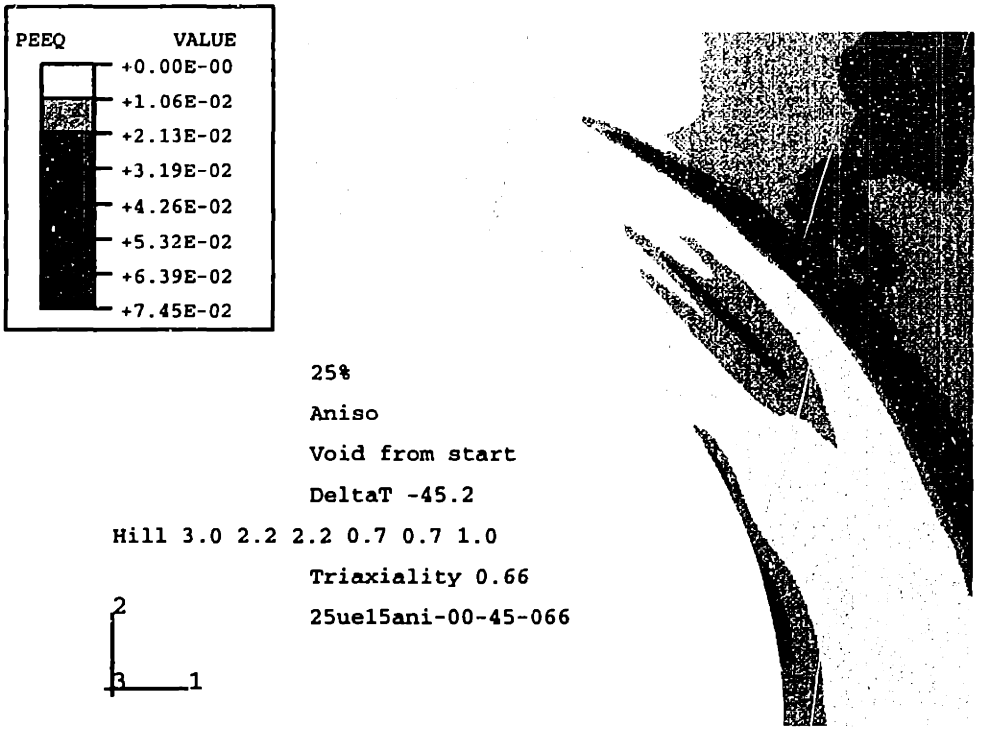

Figure 5-33c: 25ani-00-45-066: Contour plots of ε^p_{equiv} at $\varepsilon_{zz} = 3.5\%$.

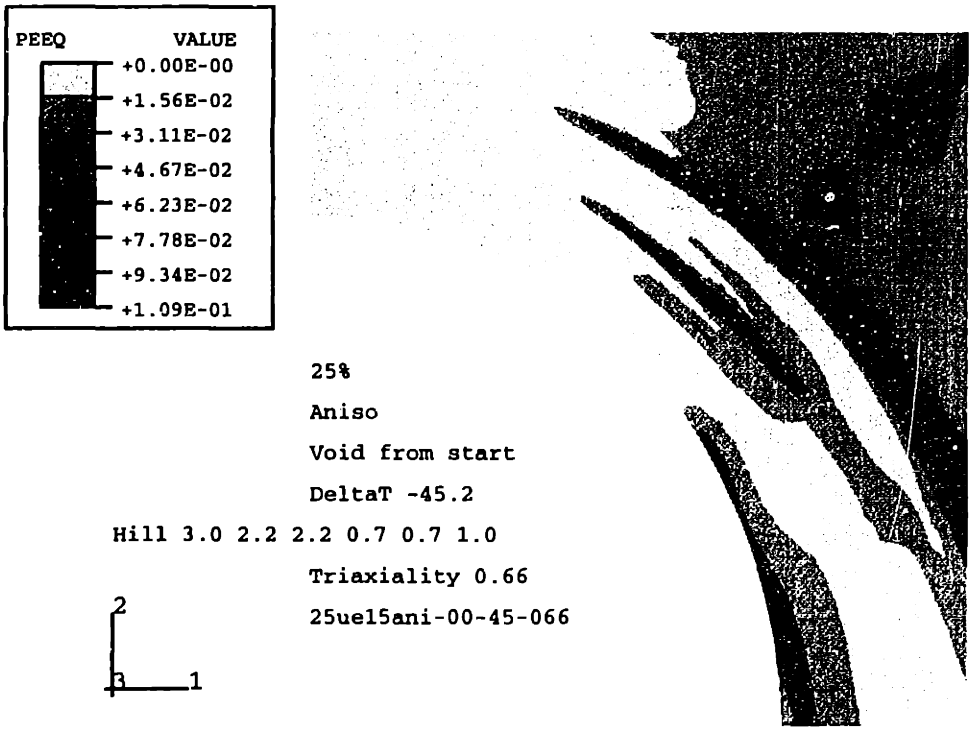

Figure 5-33d: 25ani-00-45-066: Contour plots of ε^p_{equiv} at $\varepsilon_{zz} = 4.5\%$.

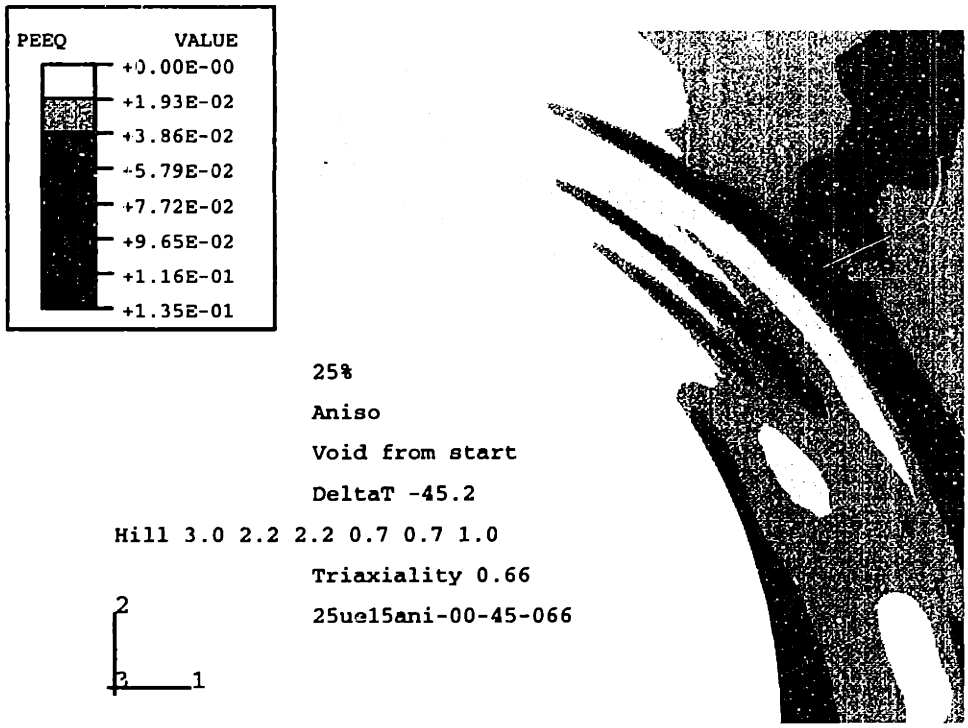

Figure 5-33e: 25ani-00-45-066: Contour plots of ε^p_{equiv} at $\varepsilon_{zz} = 5.5\%$.

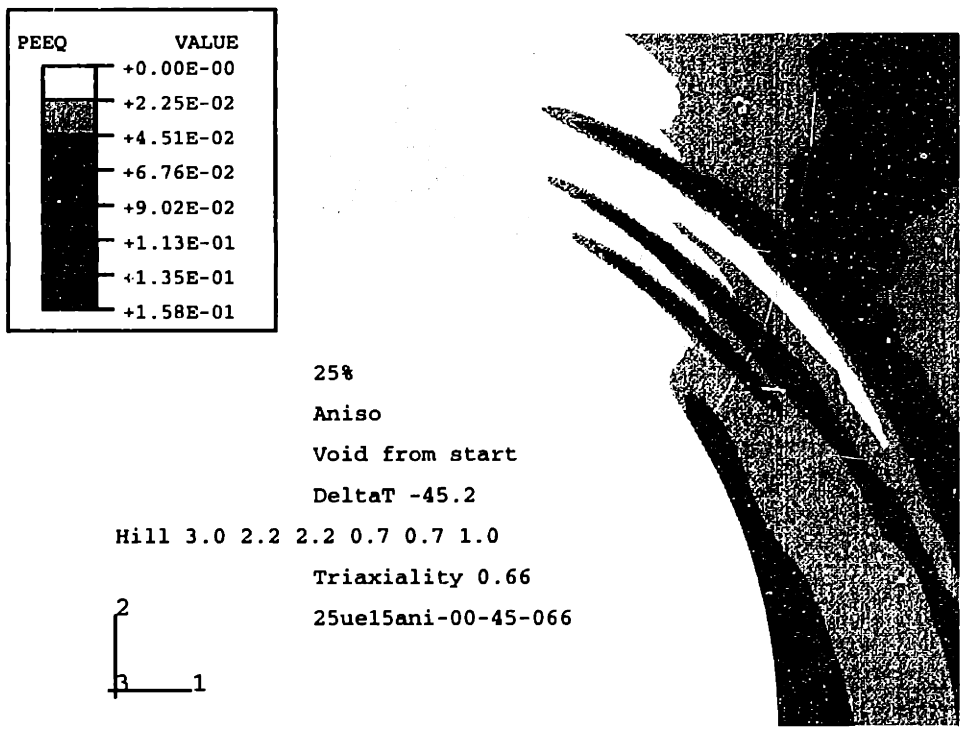

Figure 5-33f: 25ani-00-45-066: Contour plots of ε^p_{equiv} at $\varepsilon_{zz} = 6.5\%$.

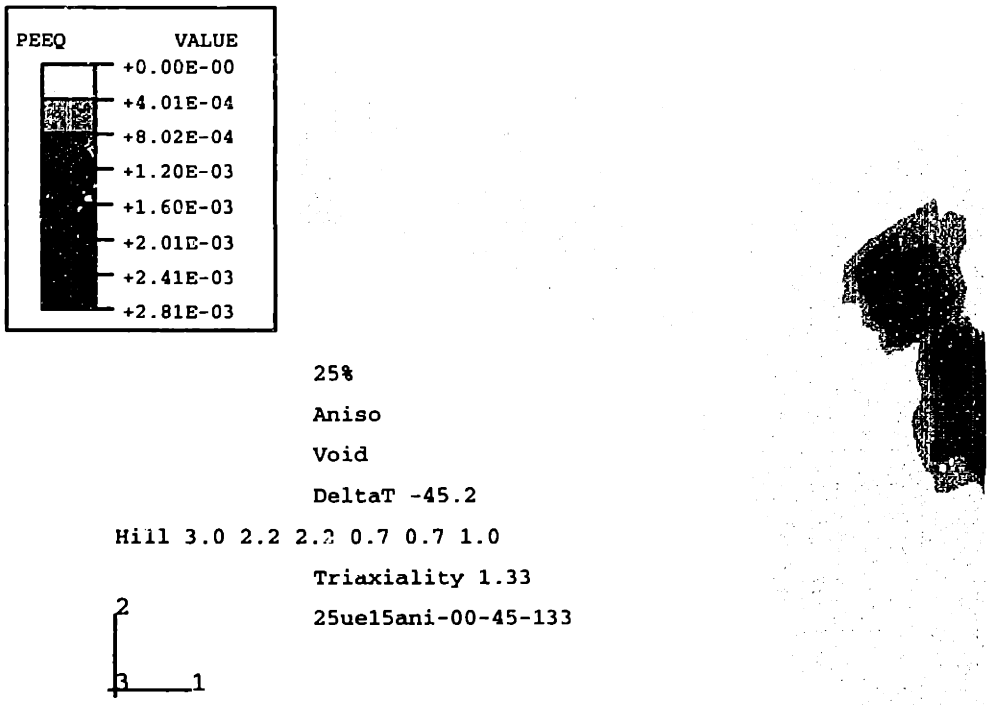

Figure 5-34a: 25ani-00-45-133: Contour plots of ε^p_{equiv} at $\varepsilon_{zz} = 1.5\%$.

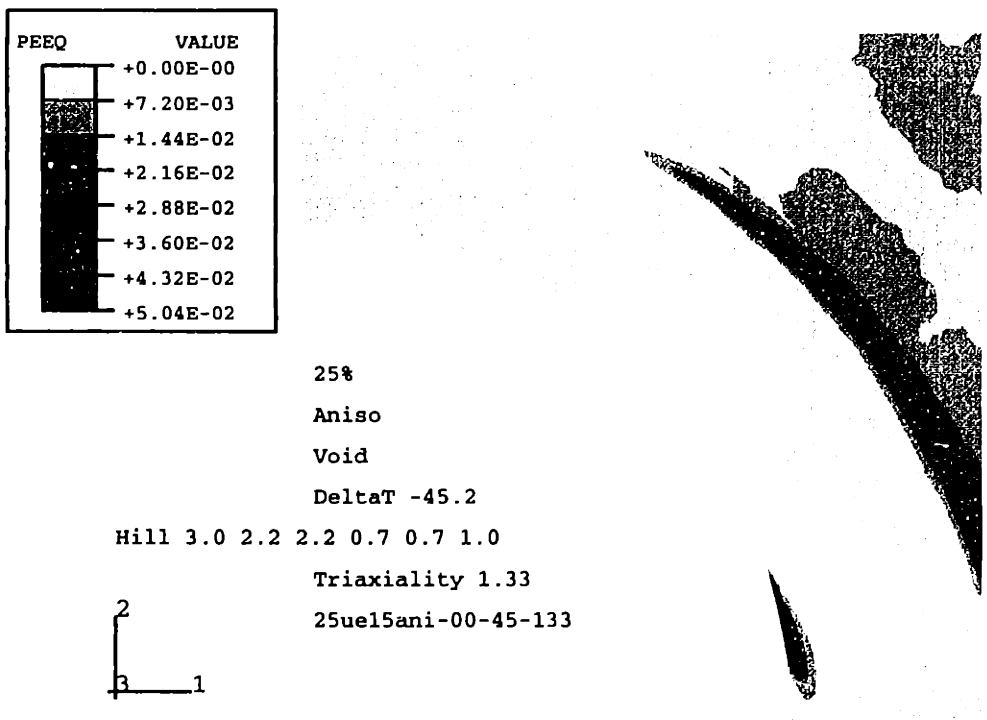

Figure 5-34b: 25ani-00-45-133: Contour plots of ε^p_{equiv} at $\varepsilon_{zz} = 2.5\%$.

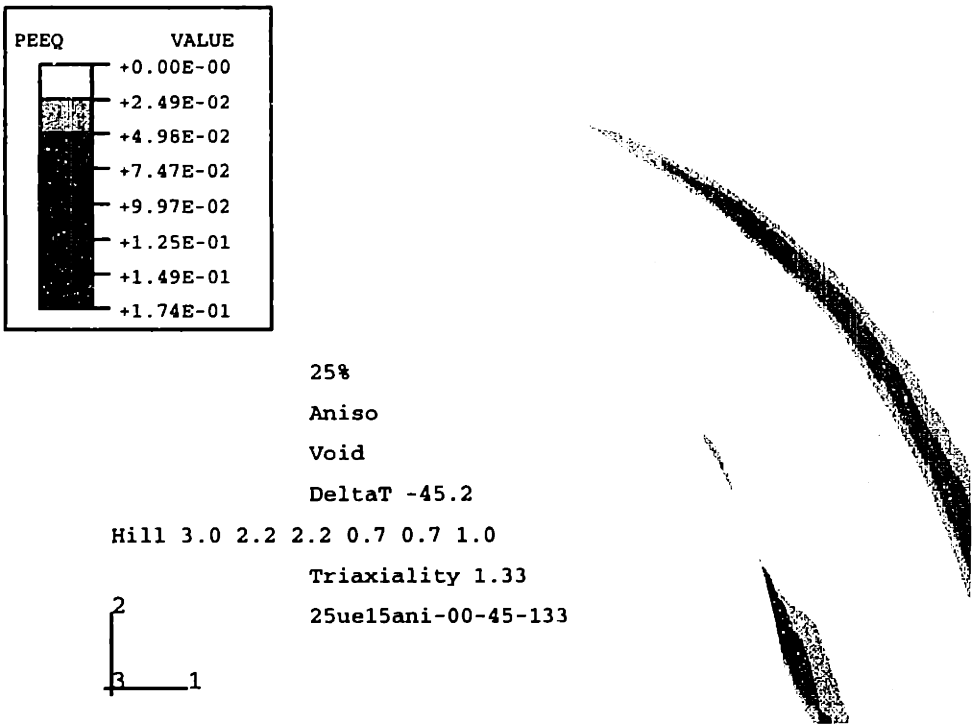

Figure 5-34c: 25ani-00-45-133: Contour plots of ε^p_{equiv} at $\varepsilon_{zz} = 3.5\%$.

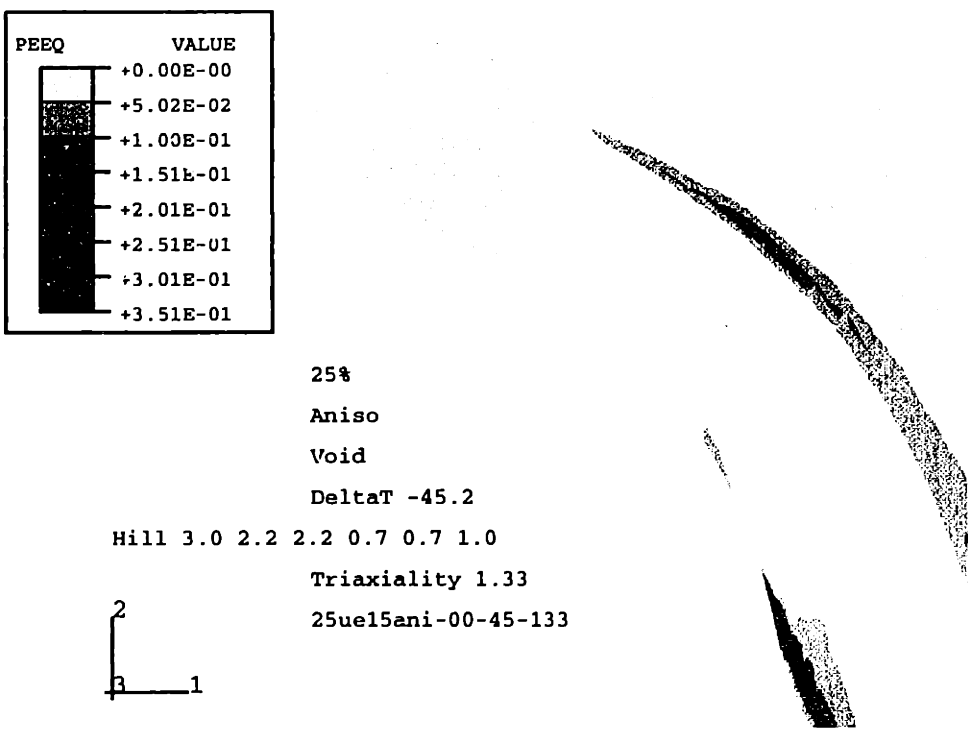

Figure 5-34d: 25ani-00-45-133: Contour plots of ε^p_{equiv} at $\varepsilon_{zz} = 4.5\%$.

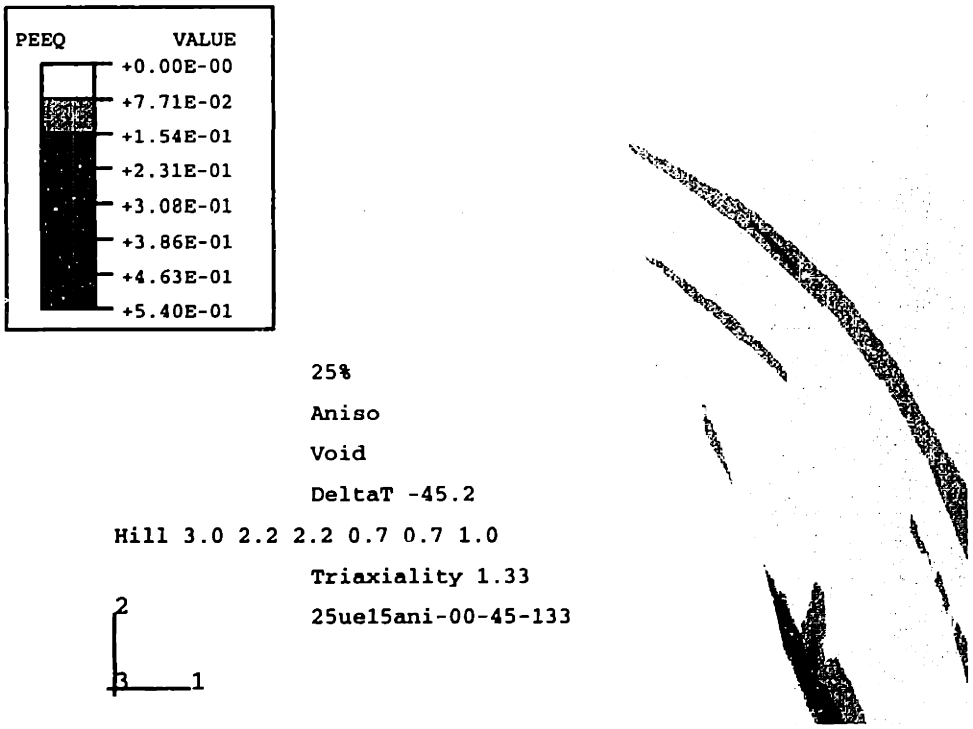

Figure 5-34e: 25ani-00-45-133: Contour plots of ε^p_{equiv} at $\varepsilon_{zz} = 5.5\%$.

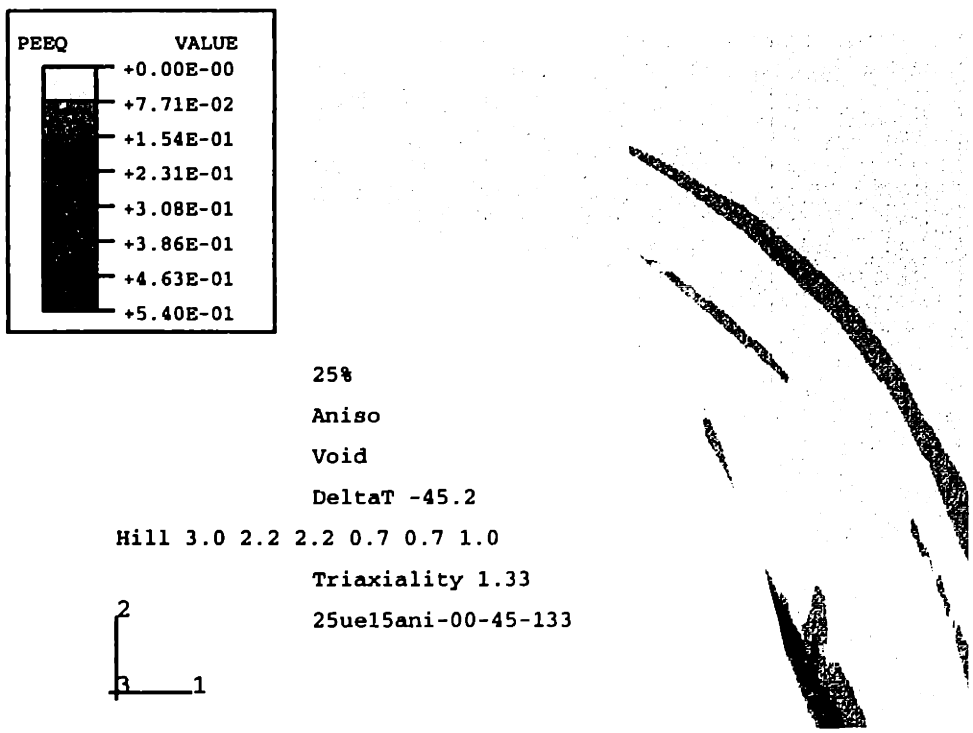

Figure 5-34f: 25ani-00-45-133: Contour plots of ε^p_{equiv} at $\varepsilon_{zz} = 6.5\%$.

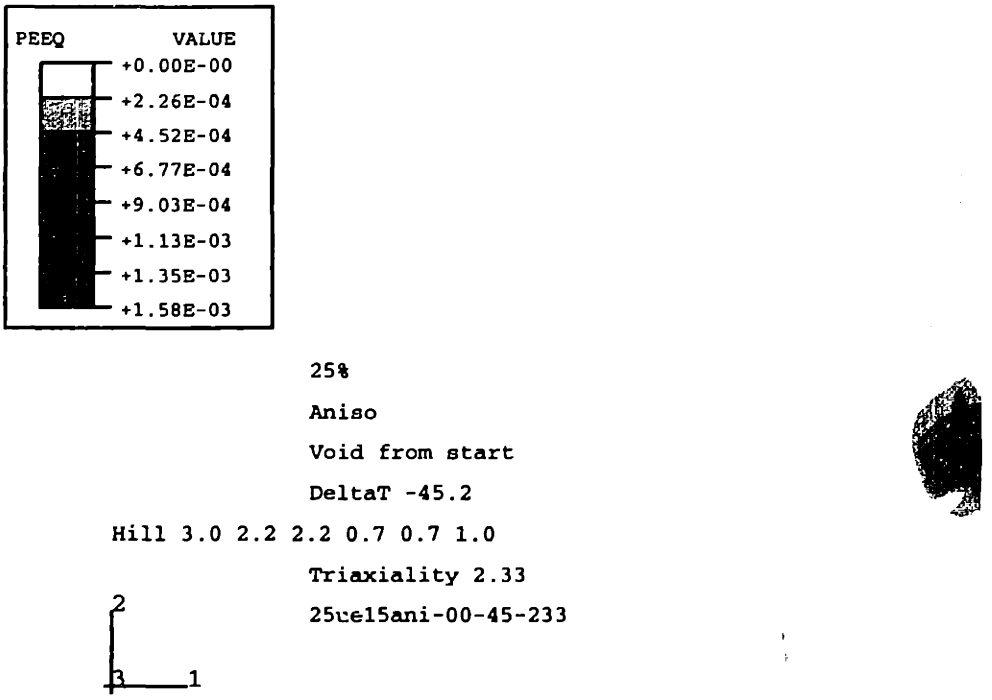

Figure 5-35a: 25ani-00-45-233: Contour plots of ε^p_{equiv} at $\varepsilon_{zz} = 1.5\%$.

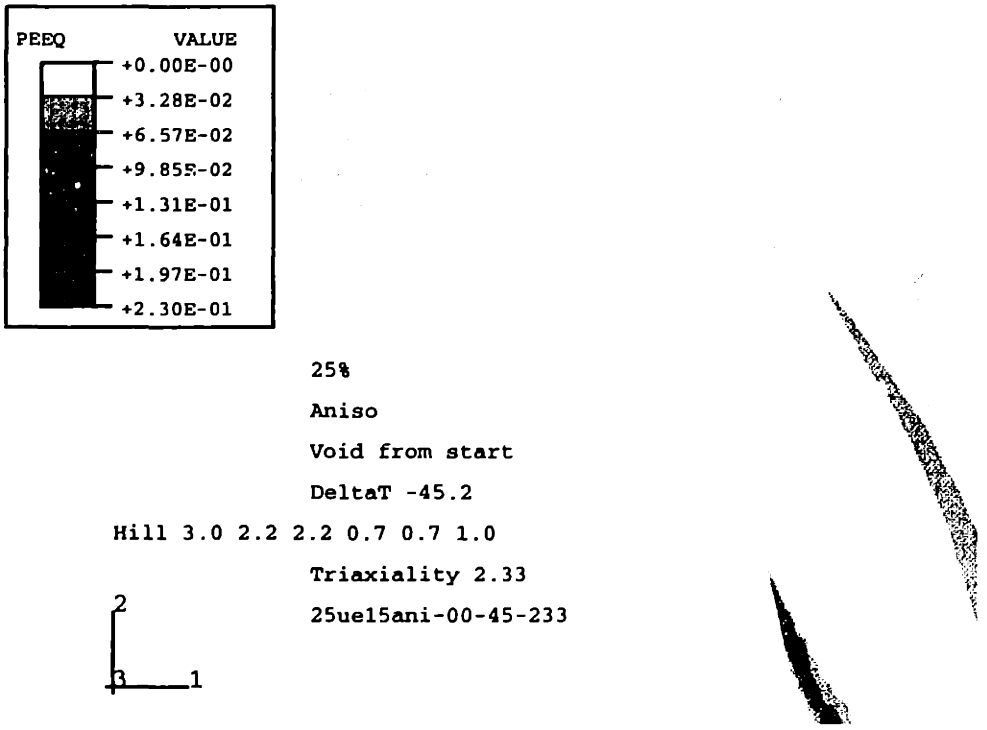

Figure 5-35b: 25ani-00-45-233: Contour plots of ε^p_{equiv} at $\varepsilon_{zz} = 2.5\%$.

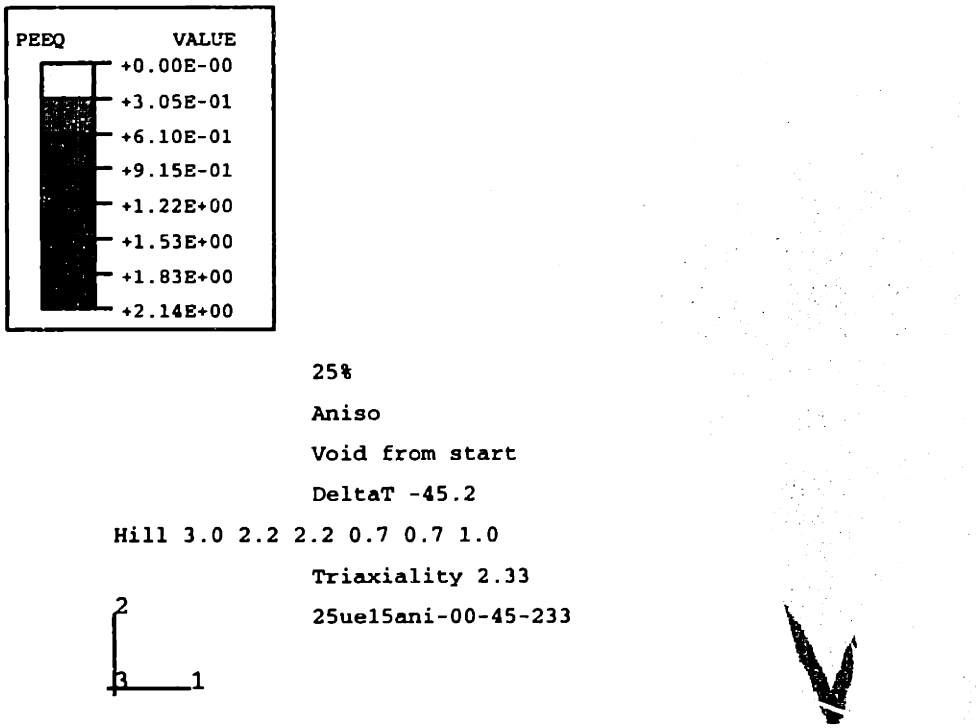

Figure 5-35c: 25ani-00-45-233: Contour plots of ε^{p}_{equiv} at $\varepsilon_{zz} = 3.5\%$.

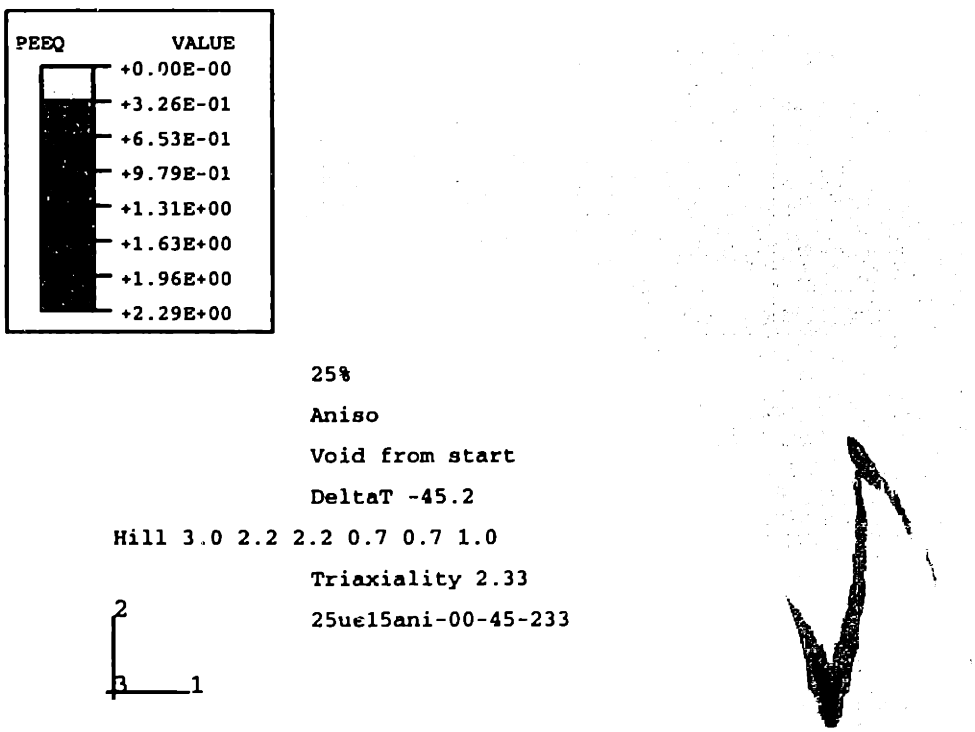

Figure 5-35d: 25ani-00-45-233: Contour plots of ε^{p}_{equiv} at $\varepsilon_{zz} = 4.5\%$.

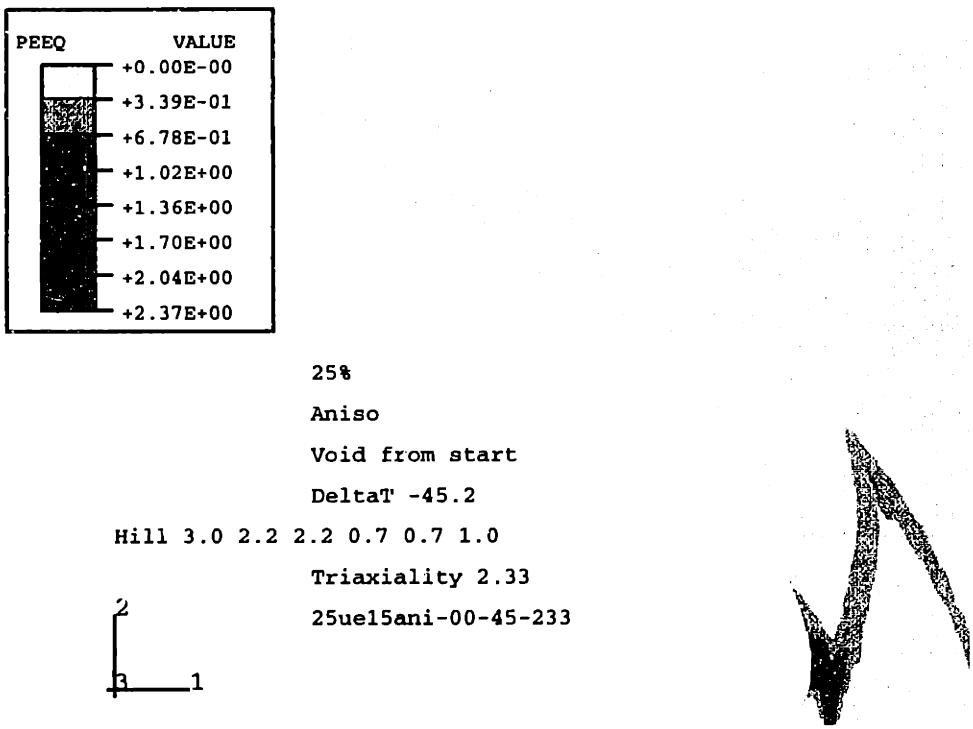

Figure 5-35e: 25ani-00-45-233: Contour plots of ε^p_{equiv} at $\varepsilon_{zz} = 5.5\%$.

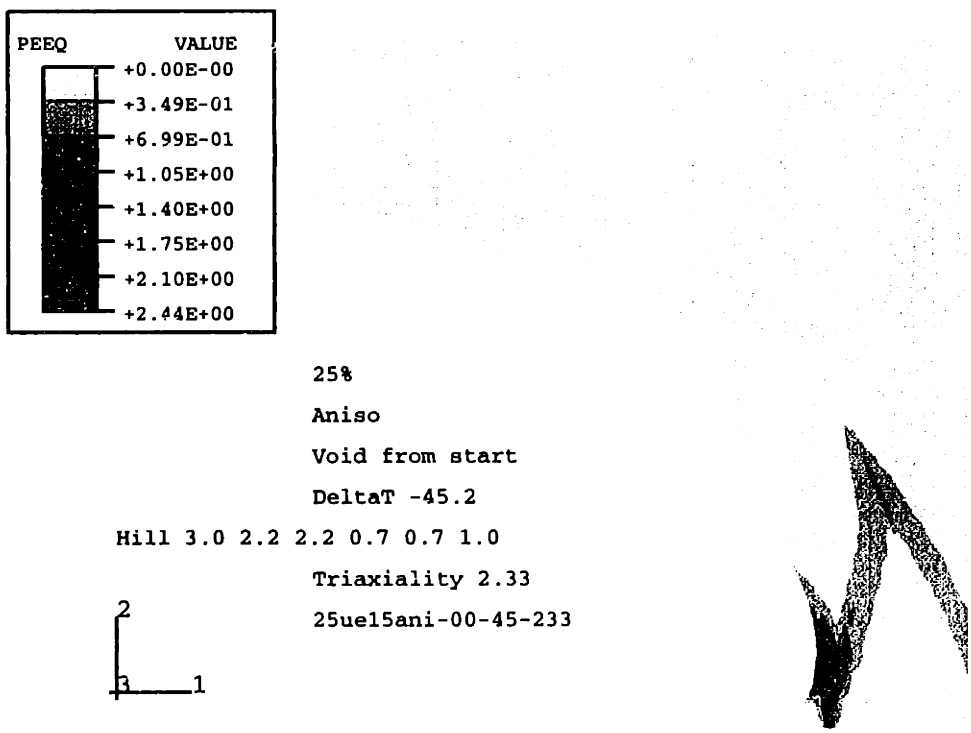

Figure 5-35f: 25ani-00-45-233: Contour plots of ε^p_{equiv} at $\varepsilon_{zz} = 6.5\%$.

Isotropic Matrix

Figures 5-5a through 5-39f on pages 110 through 223 reveal how both the onset and evolution of plasticity in the isotropic unit cells with a cavity are fundamentally different from those with a non-cavitating particle. For all triaxialities the matrix yields close to the particle equator. At low triaxiality the yield occurs at the cavity surface, and at higher Σ, the matrix yields at both the free surface and the lower right-hand corner of the unit cell. At $\varepsilon_{zz} = 1.5\%$, ε^p_{equiv} reaches levels of 1.4% in the case of uniaxial tension, and 4.6% under $\Sigma = 2.33$.

In the case of uniaxial tension, the evolution of plasticity is somewhat different from that of the $\Sigma = 0.66$ to 2.33. After the initial yielding the plastic zone intensifies and spreads from the cavity surface. From $\varepsilon_{zz} = 2.5\%$ on, the upper right-hand corner of the matrix also deforms plastically, so that the entire right-hand side of the matrix undergoes plastic deformation. ε^p_{equiv} reaches levels of 9.8% at an axial strain of 6.5%.

The addition of a laterally stress changes the evolution of matrix plasticity such that all of it is concentrated in the lower part of the matrix. Highest levels of ε^p_{equiv} are found at the cavity surface and in the lower right-hand corner of the matrix. The levels of ε^p_{equiv} that develop at $\varepsilon_{zz} = 6.5\%$ are on the order of 27% for $\Sigma = 0.66$, and up to 35% for $\Sigma = 2.33$.

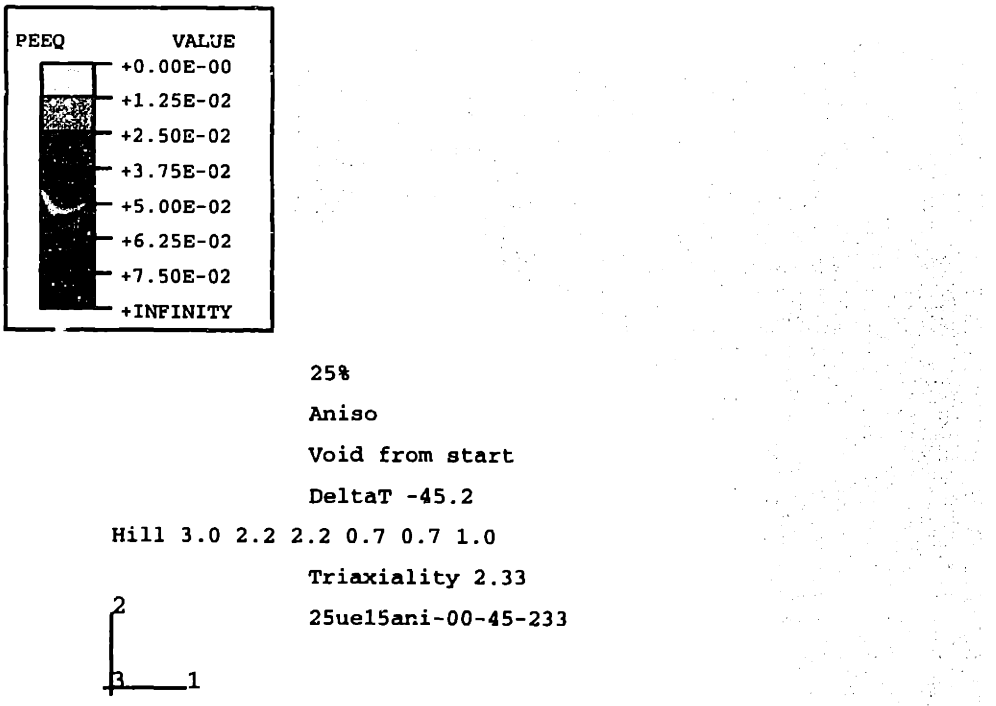

Figure 5-36a: 25ani-00-45-233: Contour plots of ε^p_{equiv} at $\varepsilon_{zz} = 1.5\%$. Cmax = 7.5%.

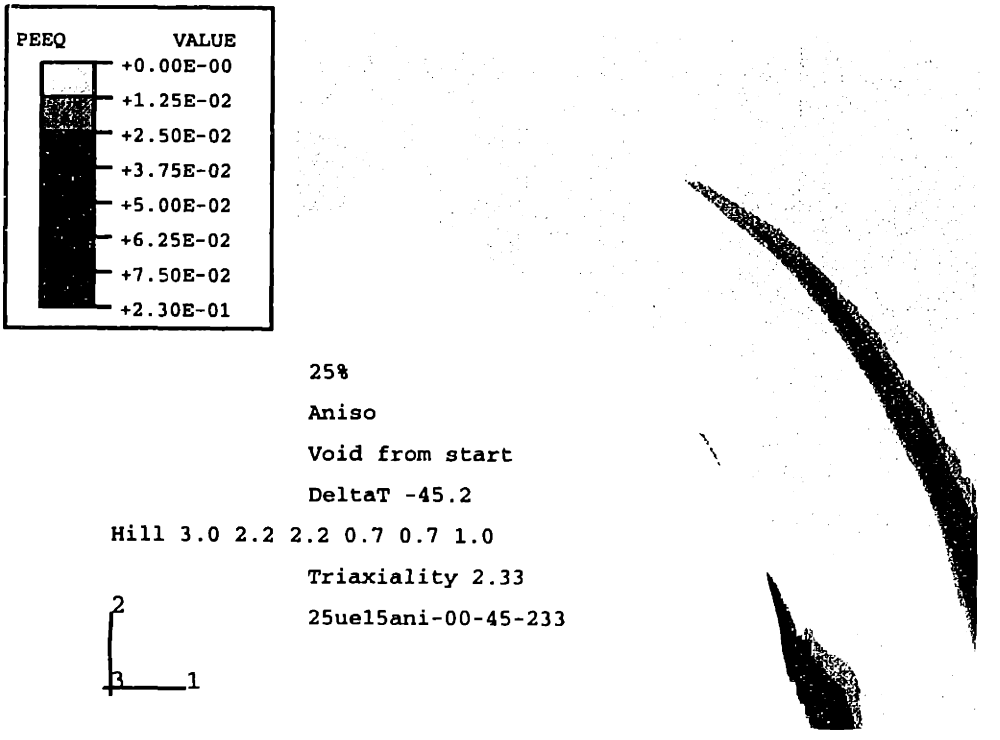

Figure 5-36b: 25ani-00-45-233: Contour plots of ε^p_{equiv} at $\varepsilon_{zz} = 2.5\%$. Cmax = 7.5%.

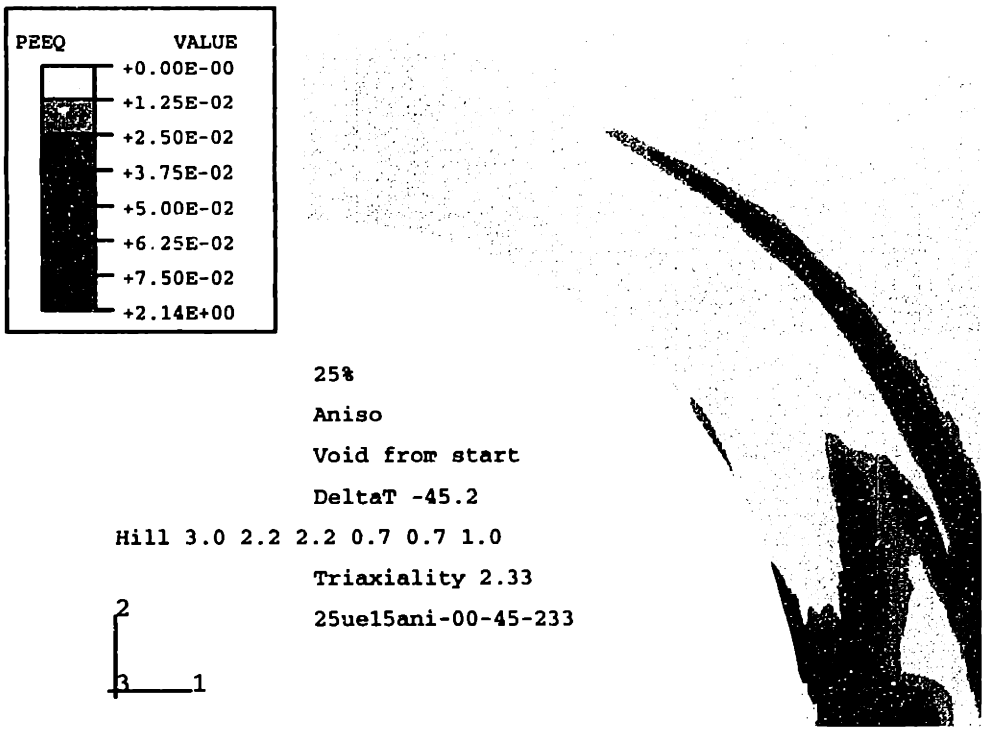

Figure 5-36c: 25ani-00-45-233: Contour plots of ε^p_{equiv} at $\varepsilon_{zz} = 3.5\%$. Cmax = 7.5%.

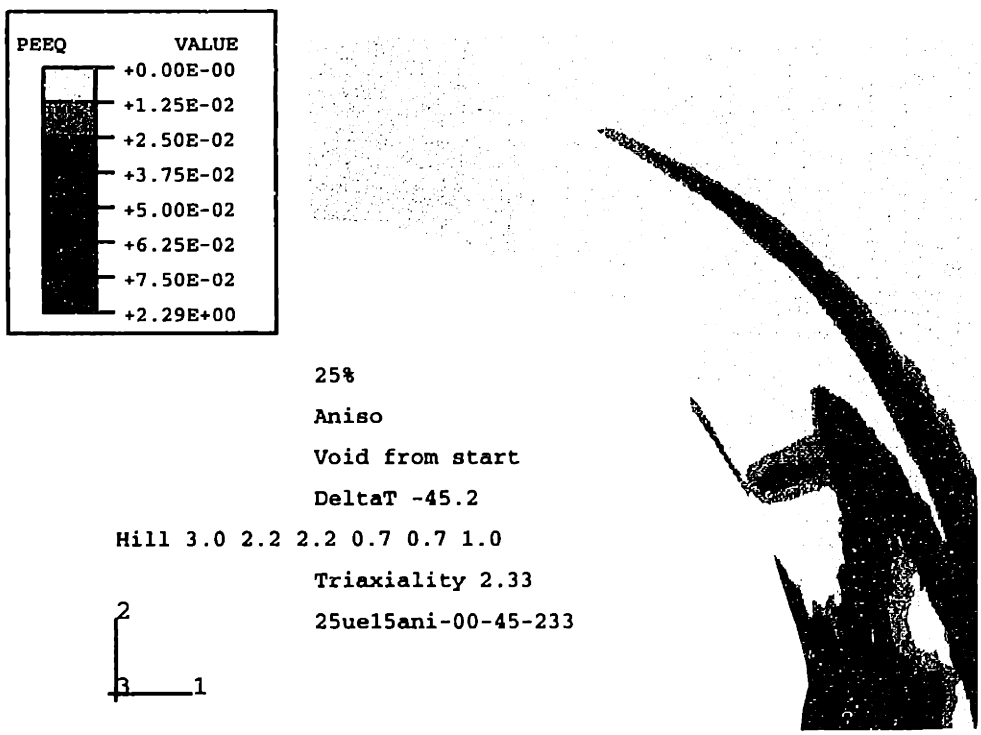

Figure 5-36d: 25ani-00-45-233: Contour plots of ε^p_{equiv} at $\varepsilon_{zz} = 4.5\%$. Cmax = 7.5%.

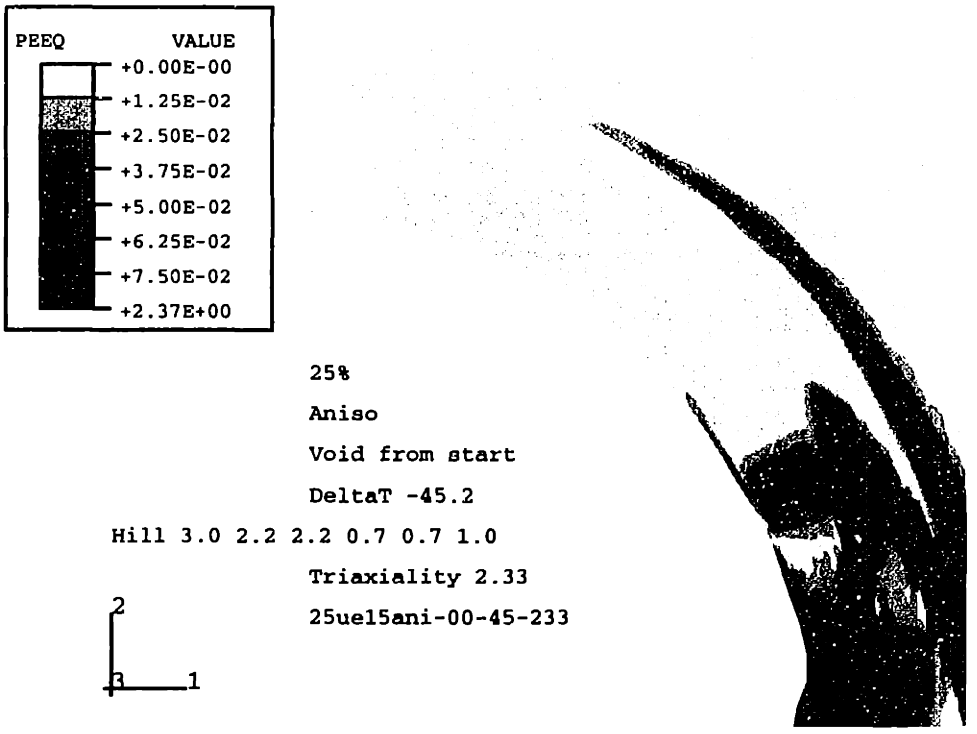

Figure 5-36e: 25ani-00-45-233: Contour plots of ε^p_{equiv} at $\varepsilon_{zz} = 5.5\%$. Cmax = 7.5%.

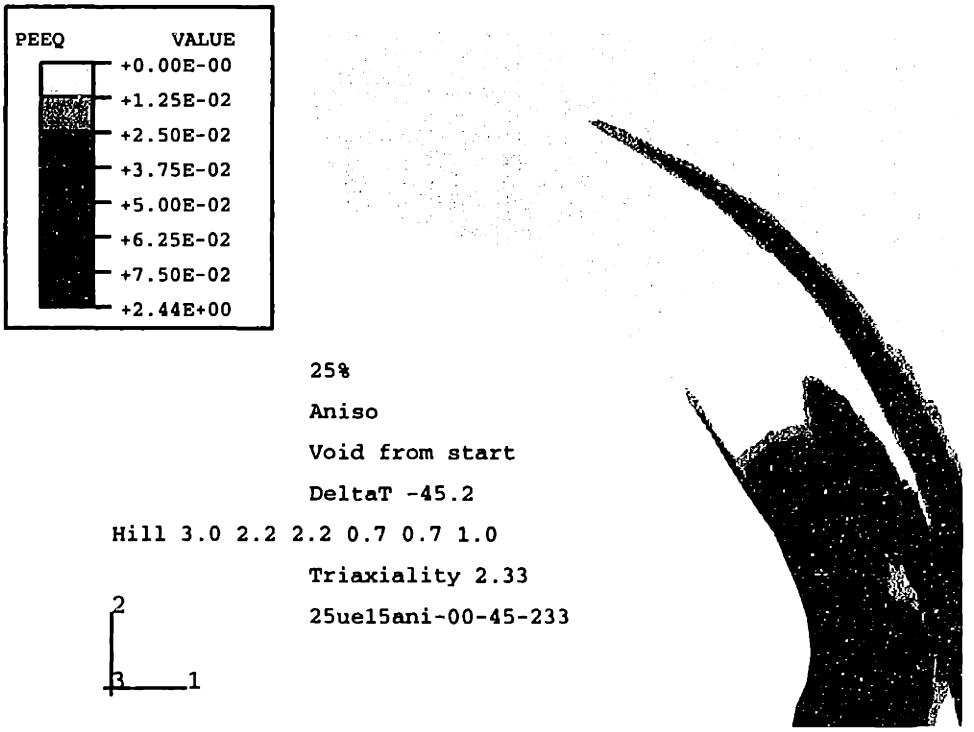

Figure 5-36f: 25ani-00-45-233: Contour plots of ε^p_{equiv} at $\varepsilon_{zz} = 6.5\%$. Cmax = 7.5%.

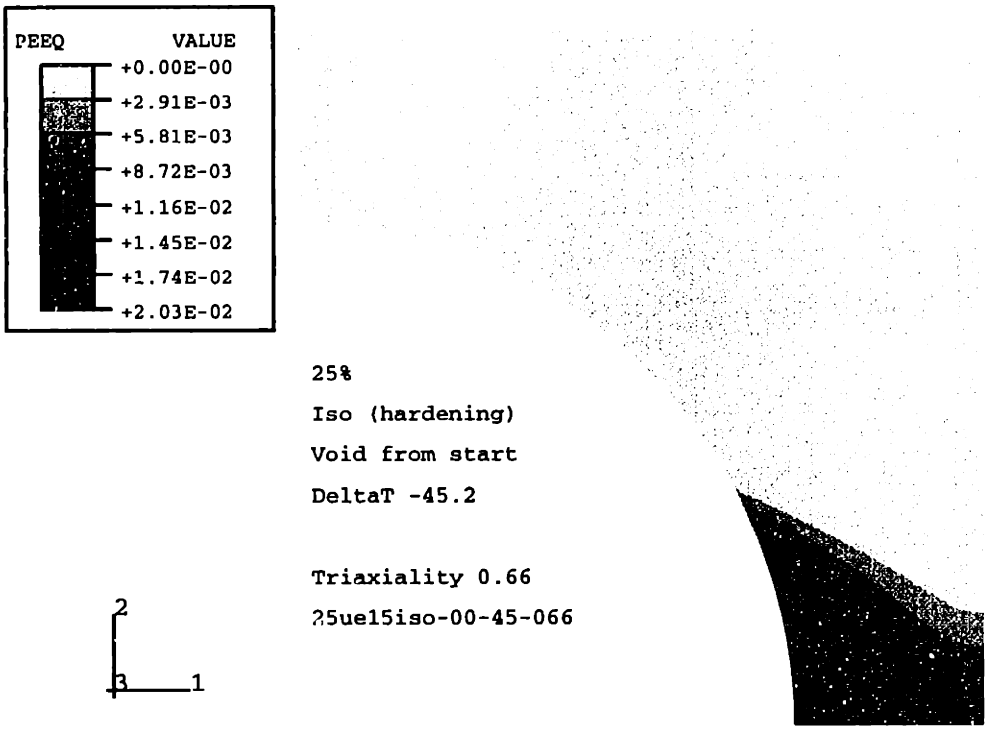

Figure 5-37a: 25iso-00-45-066: Contour plots of ε^p_{equiv} at $\varepsilon_{zz} = 1.5\%$.

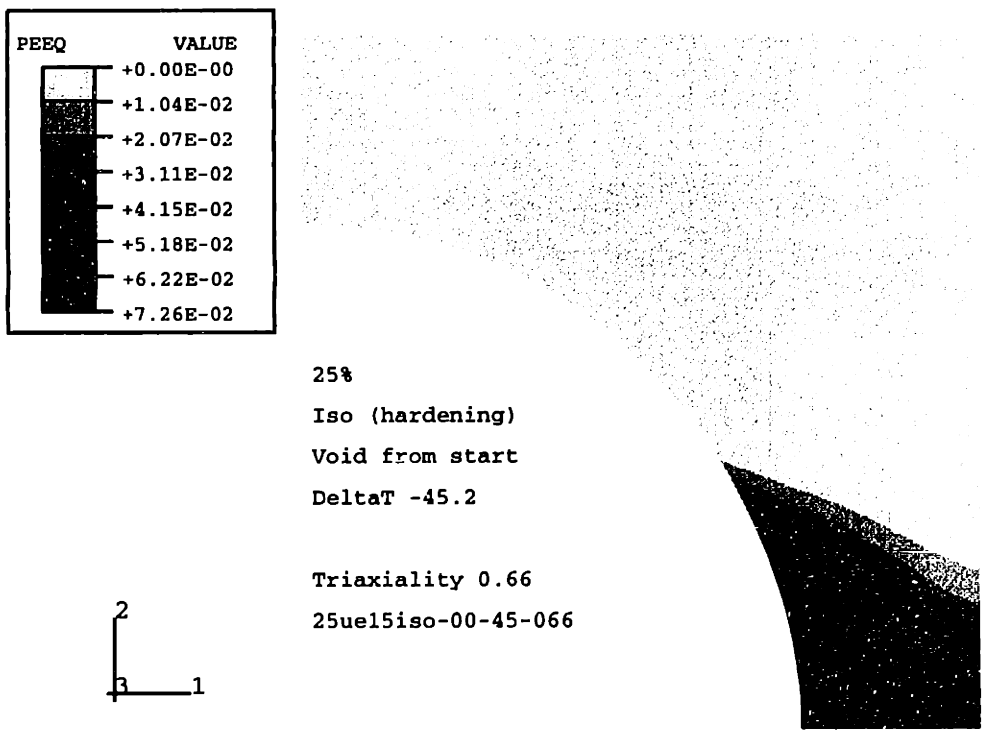

Figure 5-37b: 25iso-00-45-066: Contour plots of ε^p_{equiv} at $\varepsilon_{zz} = 2.5\%$.

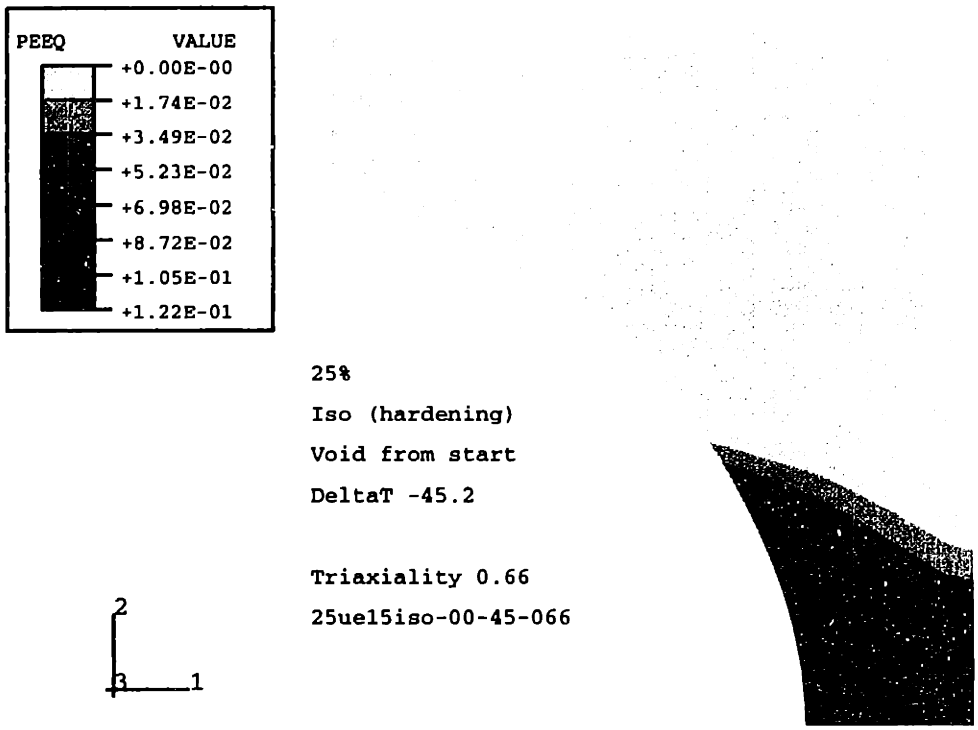

Figure 5-37c: 25iso-00-45-066: Contour plots of ε^p_{equiv} at $\varepsilon_{zz} = 3.5\%$.

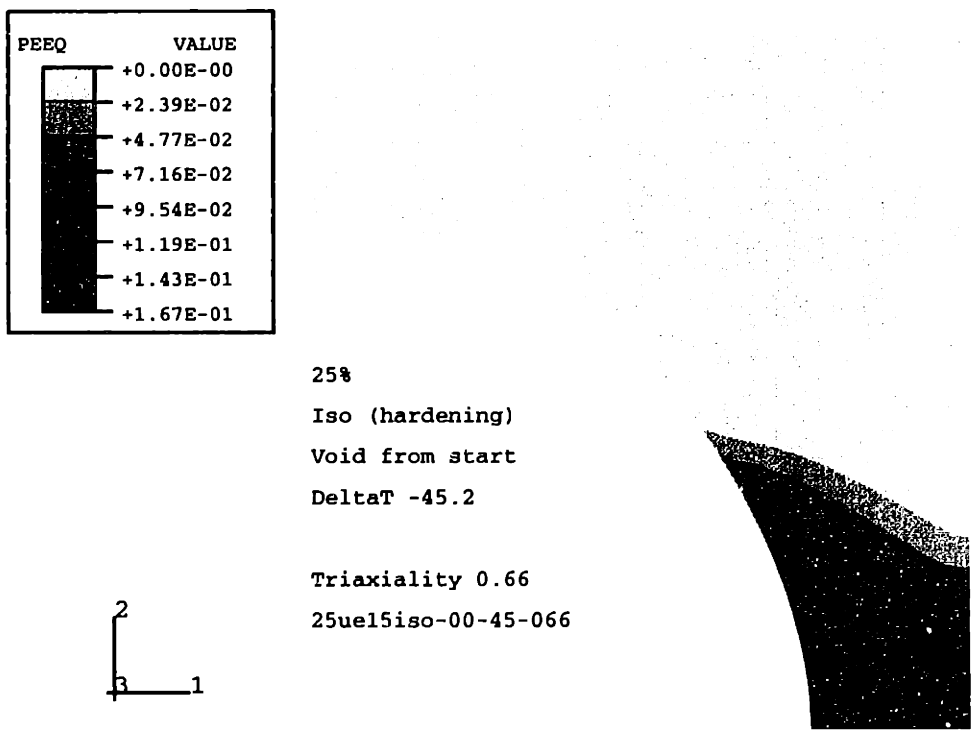

Figure 5-37d: 25iso-00-45-066: Contour plots of ε^p_{equiv} at $\varepsilon_{zz} = 4.5\%$.

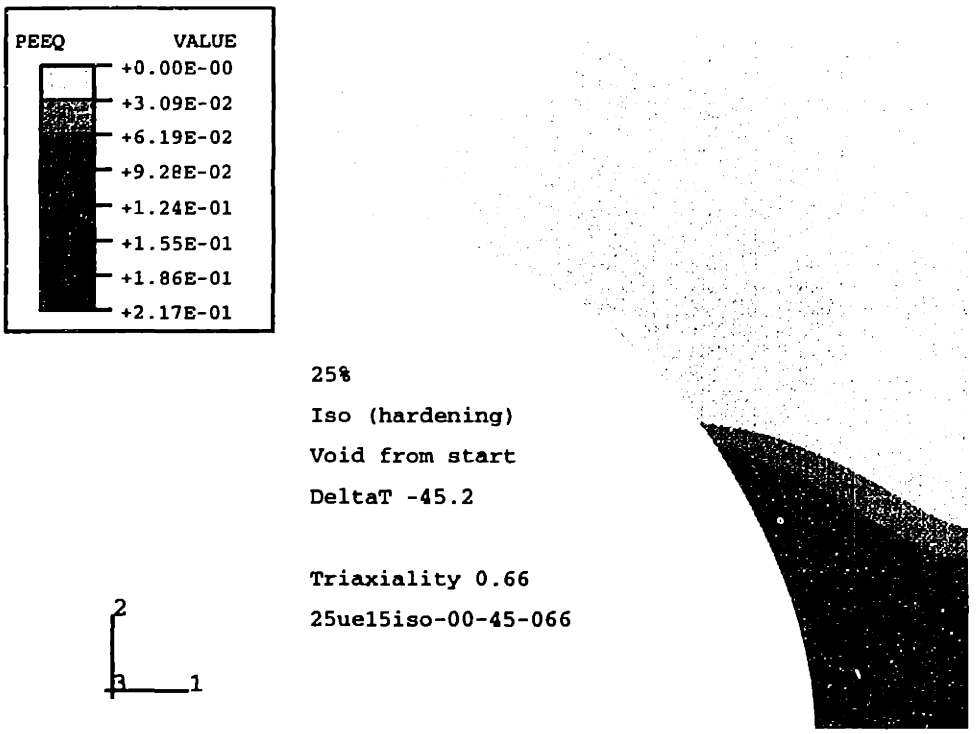

Figure 5-37e: 25iso-00-45-066: Contour plots of ε^p_{equiv} at $\varepsilon_{zz} = 5.5\%$.

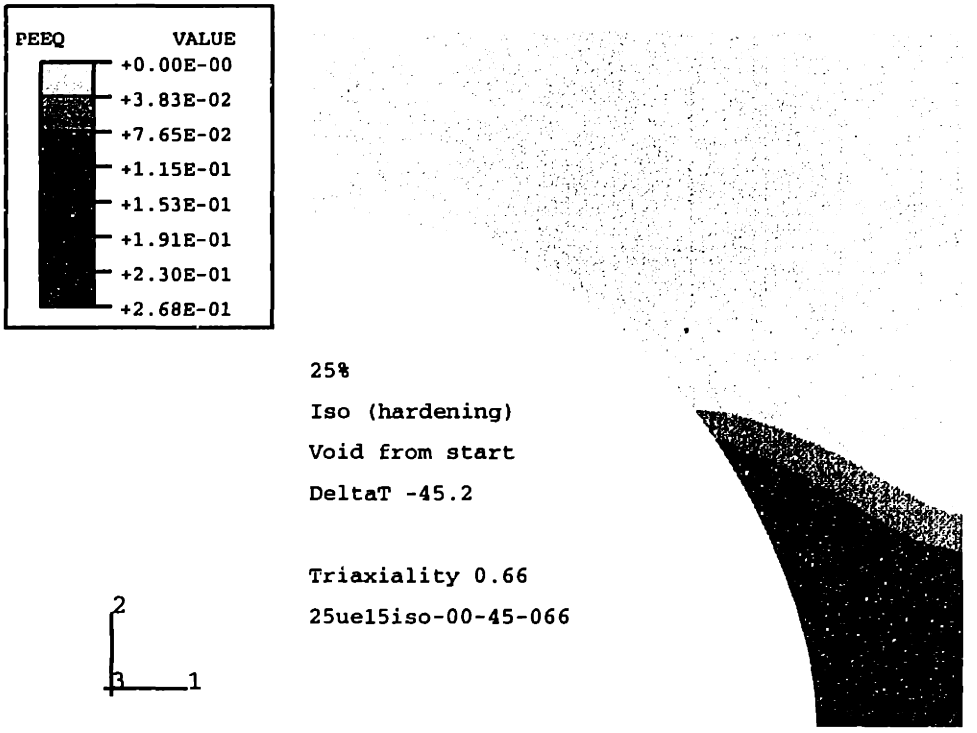

Figure 5-37f: 25iso-00-45-066: Contour plots of ε^p_{equiv} at $\varepsilon_{zz} = 6.5\%$.

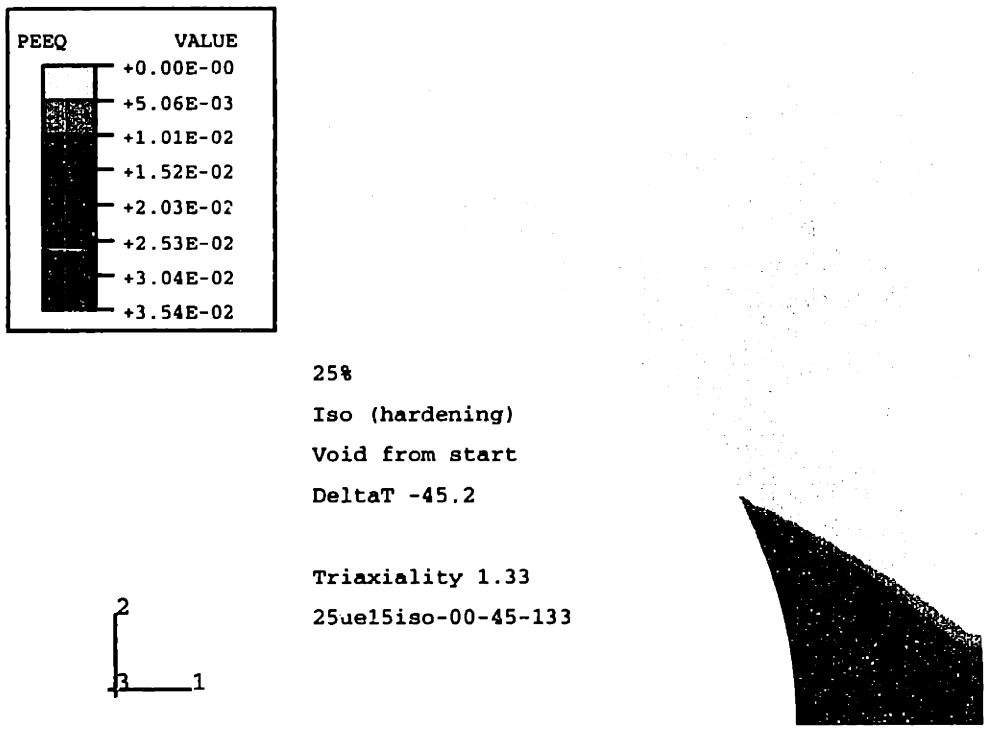

Figure 5-38a: 25iso-00-45-133: Contour plots of ε^{p}_{equiv} at $\varepsilon_{zz} = 1.5\%$.

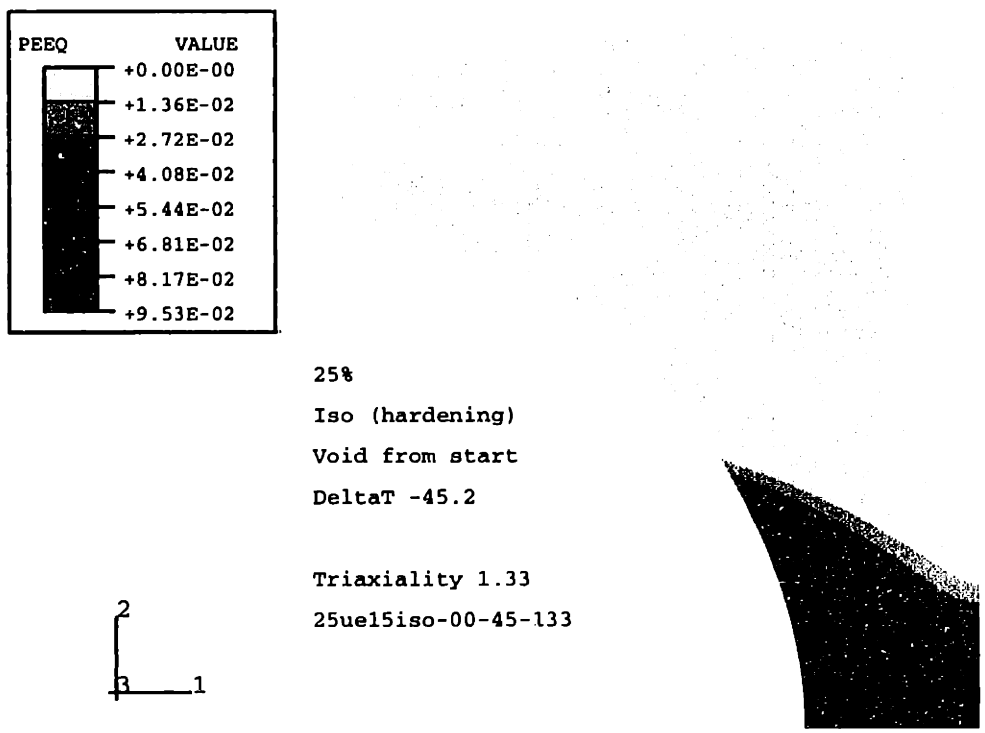

Figure 5-38b: 25iso-00-45-133: Contour plots of ε^{p}_{equiv} at $\varepsilon_{zz} = 2.5\%$.

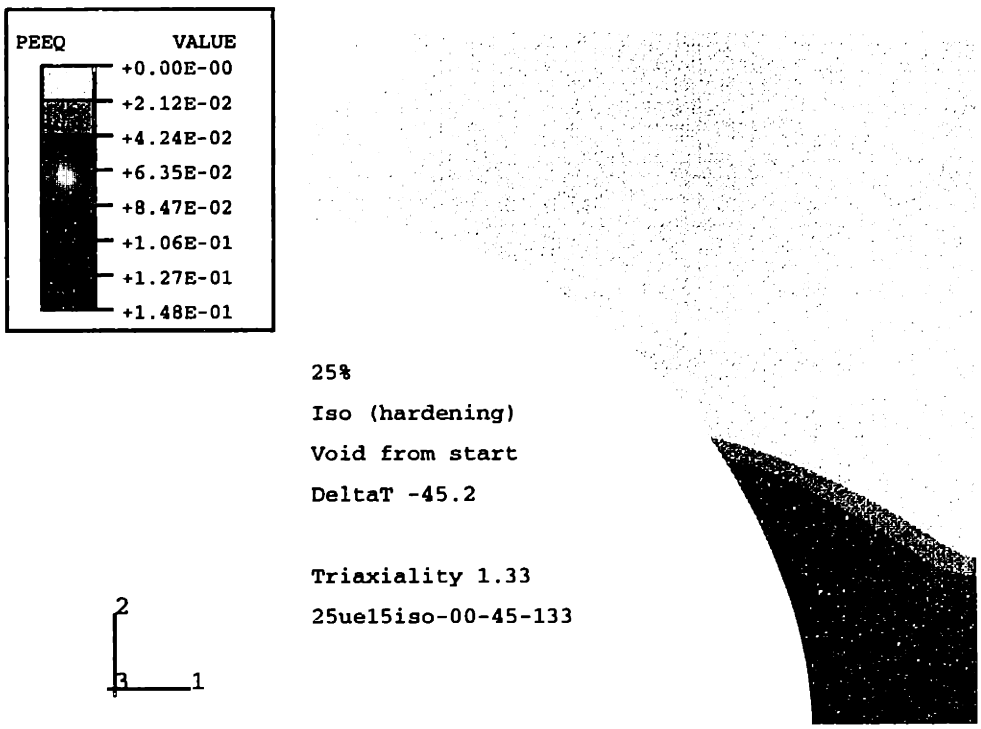

Figure 5-38c: 25iso-00-45-133: Contour plots of ε^{p}_{equiv} at $\varepsilon_{zz} = 3.5\%$.

Summary

With the exception of uniaxial tension, all isotropic unit cells with a pre-existing cavity exhibit a concentration of plastic deformation along the lower bondary of the unit cell. The equivalent plastic strains are up to 35%.

The anisotropic unit cells with cavities exhibit a strong locallization of plastic deformation with little plasticity elsewhere. Several shear bands emerge. ε^p_{equiv} reaches levels of over 200% at relatively low axial strains.

In unit cells with both types of matrices, the cases of uniaxial tension differ somewhat from the cases of $\Sigma = 0.66$, 1.33 and 2.33. In simple tension the matrix yields in the upper right-hand corner of the unit cell and the localization of plasticity is not as pronounced as in the other cases.

5.4.7 Effect of Varying Σ on the Yield Point

The macroscopic axial true strain ε^y_{zz} at which the matrix yields, ε^y_{zz} can be read off either from the stress-strain plots (e.g. figure 5-11 etc.) or the plots of the unit cell's strain space evolution (e.g. figure 5-8 etc.). The relevant data has been summarized in tables 5.6 and 5.5 below.

Anisotropic Matrix

Figure 5-40 shows a plot of the yield strain ε^y_{zz} as a function of the triaxiality ratio Σ for both an anisotropic matrix with a cavity and one with a coherent particle.

The general trend is clearly an increasing ε^y_{zz} with increasing Σ for both curves. In an anisotropic unit cell with a cavity, ε^y_{zz} increases from 0.9% under uniaxial tension to 1.4% when Σ is 2.33. With a coherent particle present, the yield strains increase from 0.8% to 1.3% for the same increase in Σ. A rough linear approximation for both unit cells is:

$$\varepsilon^y_{zz} \simeq 0.25\,\Sigma \tag{5.5}$$

Similarly, the plots of σ^y_{zz} as function of Σ in figure 5-41 shows a positive correlation between the yield stress and the triaxiality ratio. With a cavity present, σ^y_{zz} increased

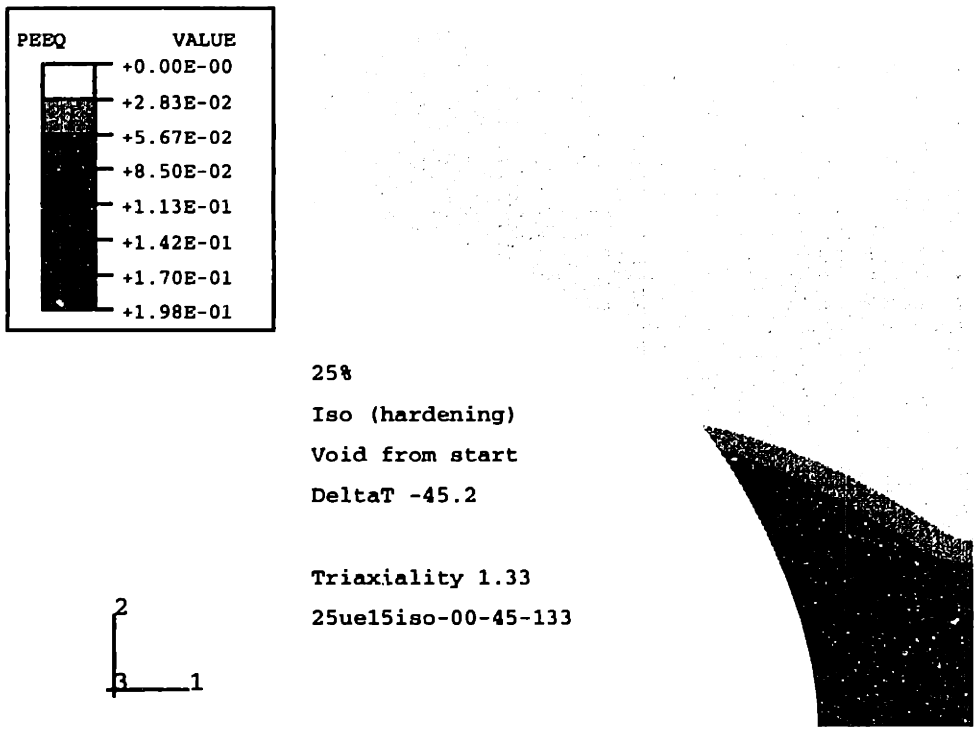

Figure 5-38d: 25iso-00-45-133: Contour plots of ε^p_{equiv} at $\varepsilon_{zz} = 4.5\%$.

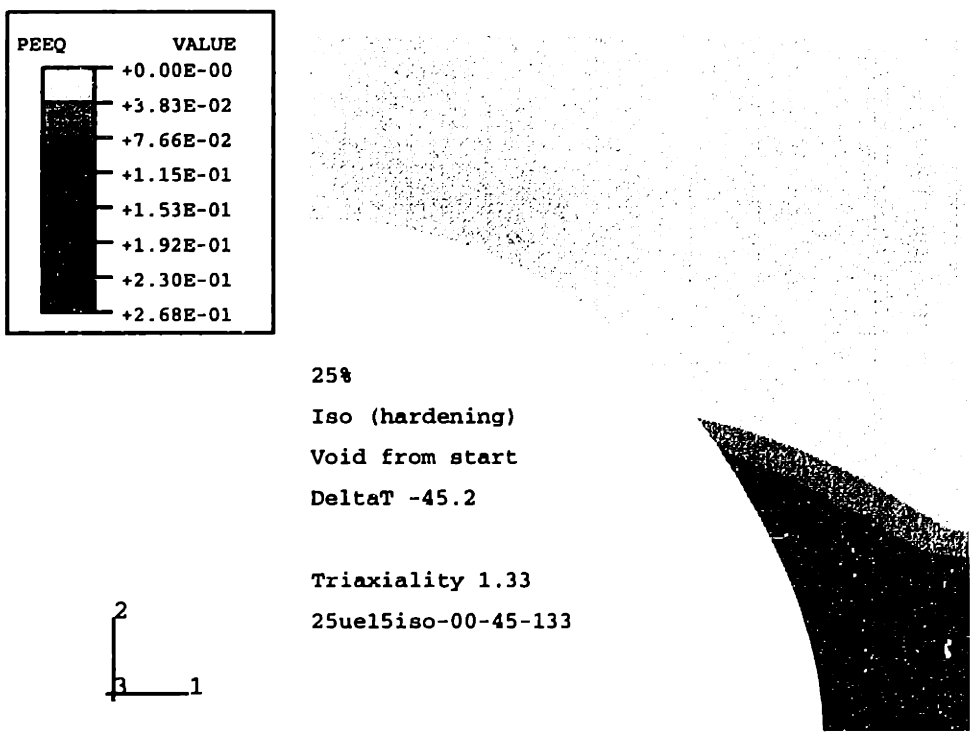

Figure 5-38e: 25iso-00-45-133: Contour plots of ε^p_{equiv} at $\varepsilon_{zz} = 5.5\%$.

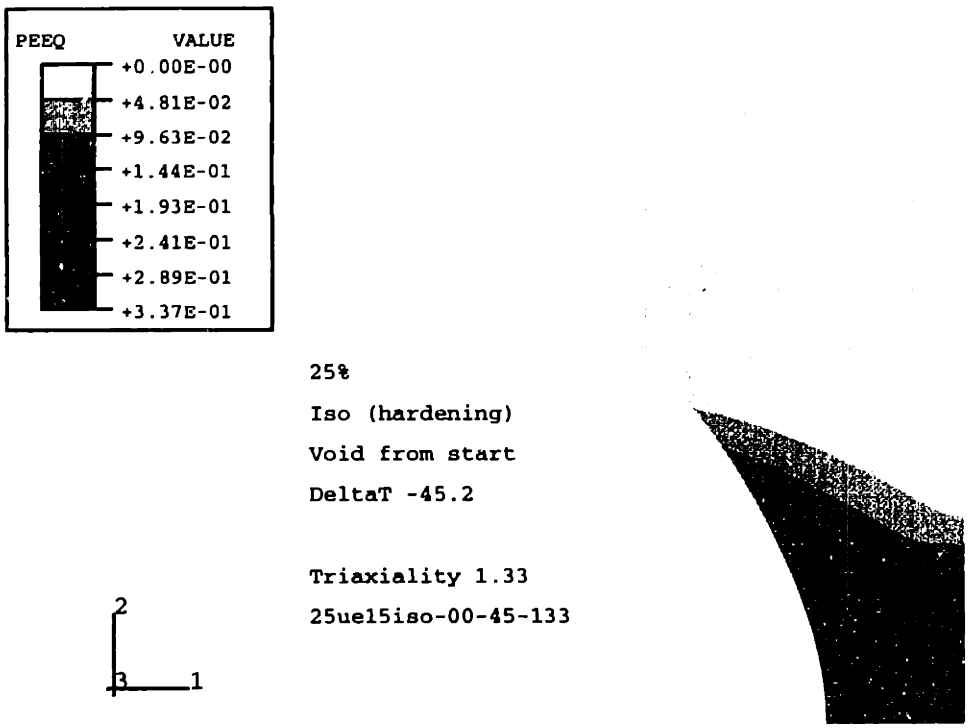

Figure 5-38f: 25iso-00-45-133: Contour plots of ε^p_{equiv} at $\varepsilon_{zz} = 6.5\%$.

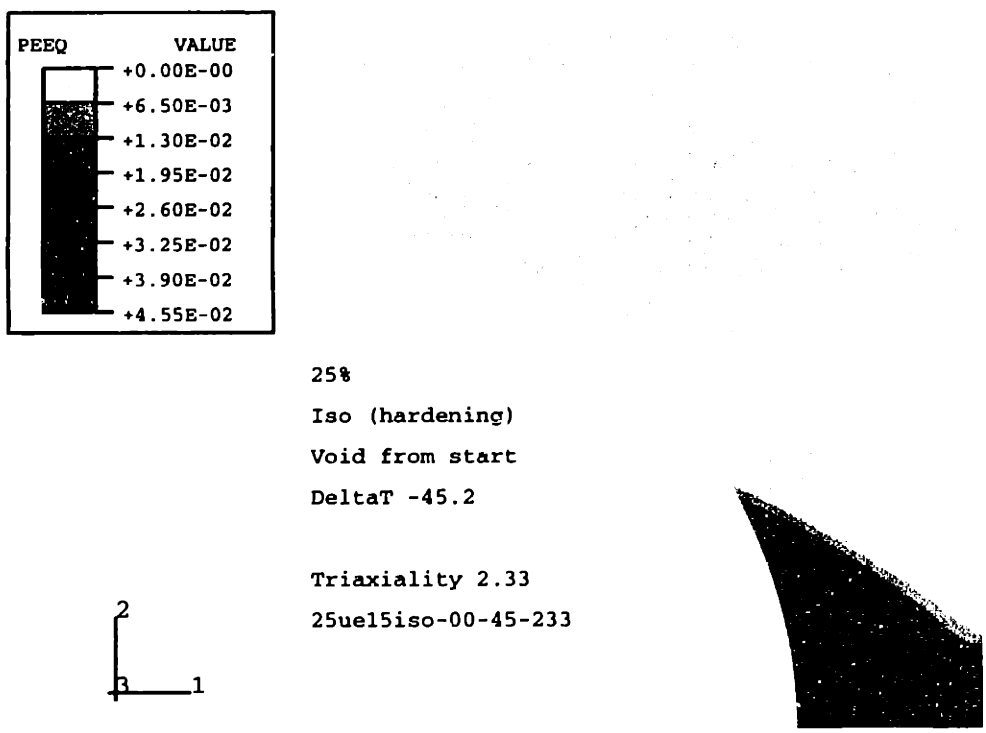

Figure 5-39a: 25iso-00-45-233: Contour plots of ε^p_{equiv} at $\varepsilon_{zz} = 1.5\%$.

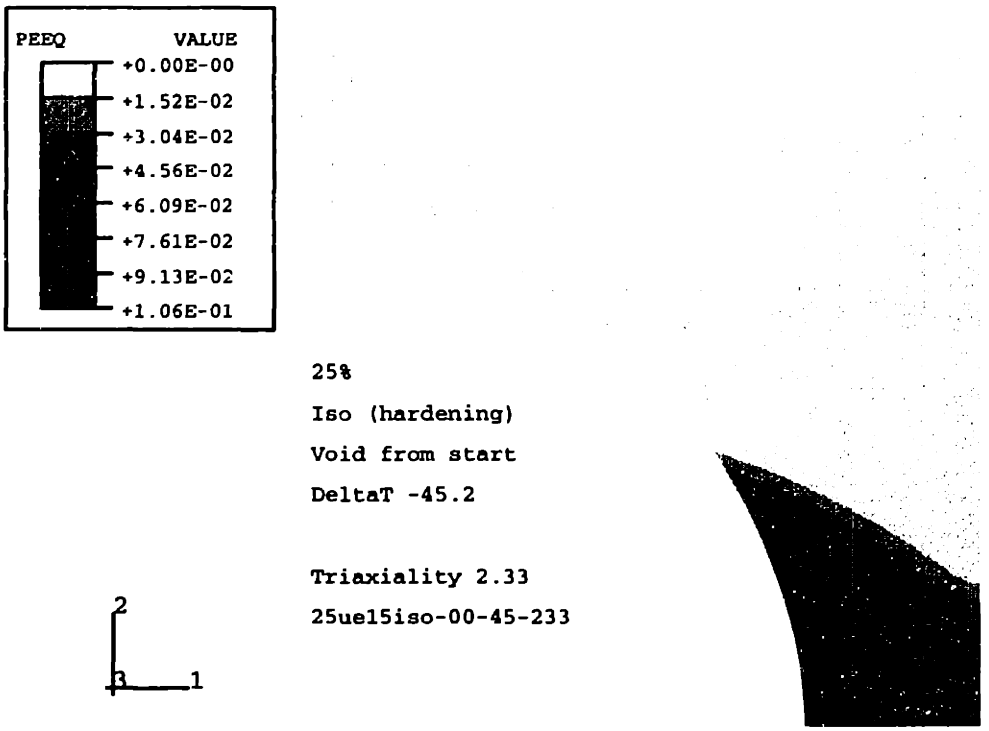

Figure 5-39b: 25iso-00-45-233: Contour plots of ε^p_{equiv} at $\varepsilon_{zz} = 2.5\%$.

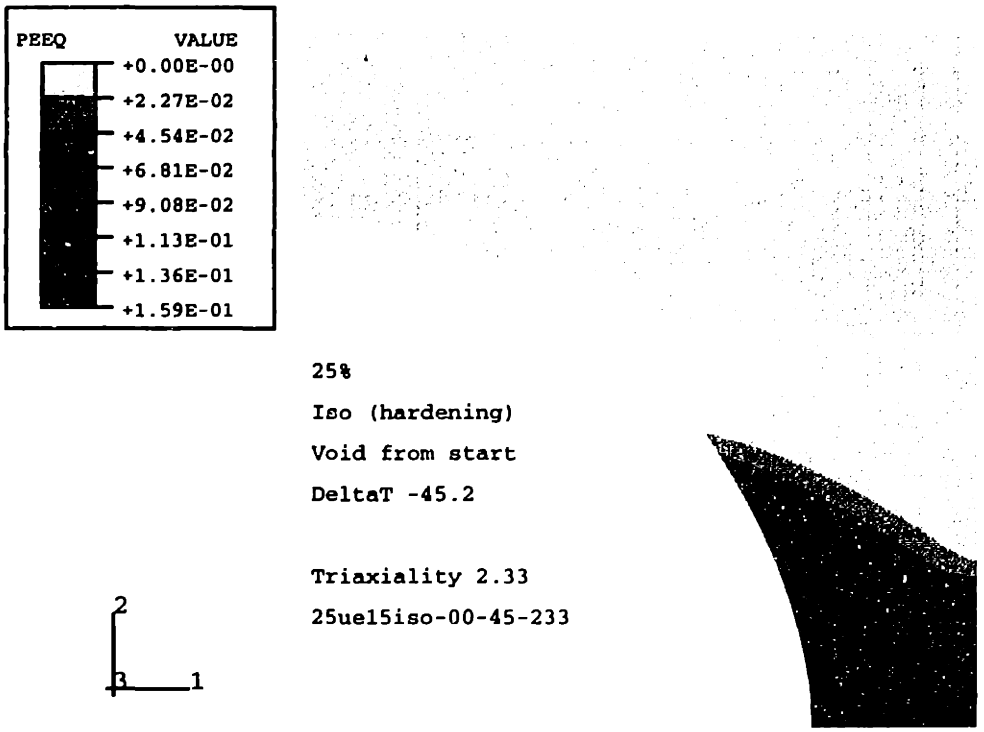

Figure 5-39c: 25iso-00-45-233: Contour plots of ε^p_{equiv} at $\varepsilon_{zz} = 3.5\%$.

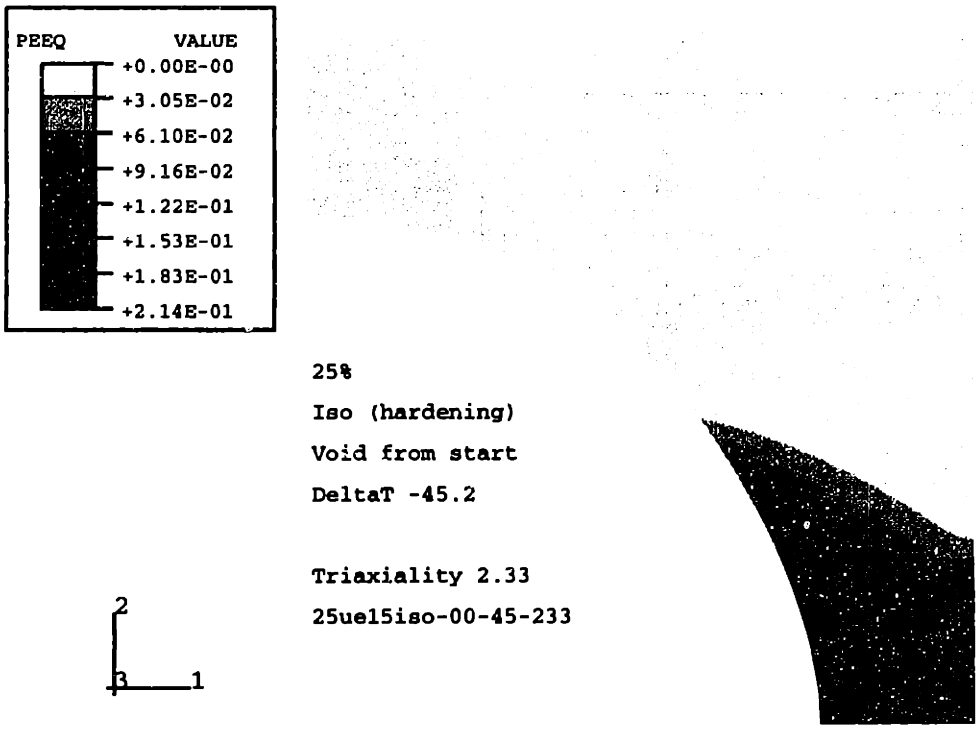

Figure 5-39d: 25iso-00-45-233: Contour plots of ε^p_{equiv} at $\varepsilon_{zz} = 4.5\%$.

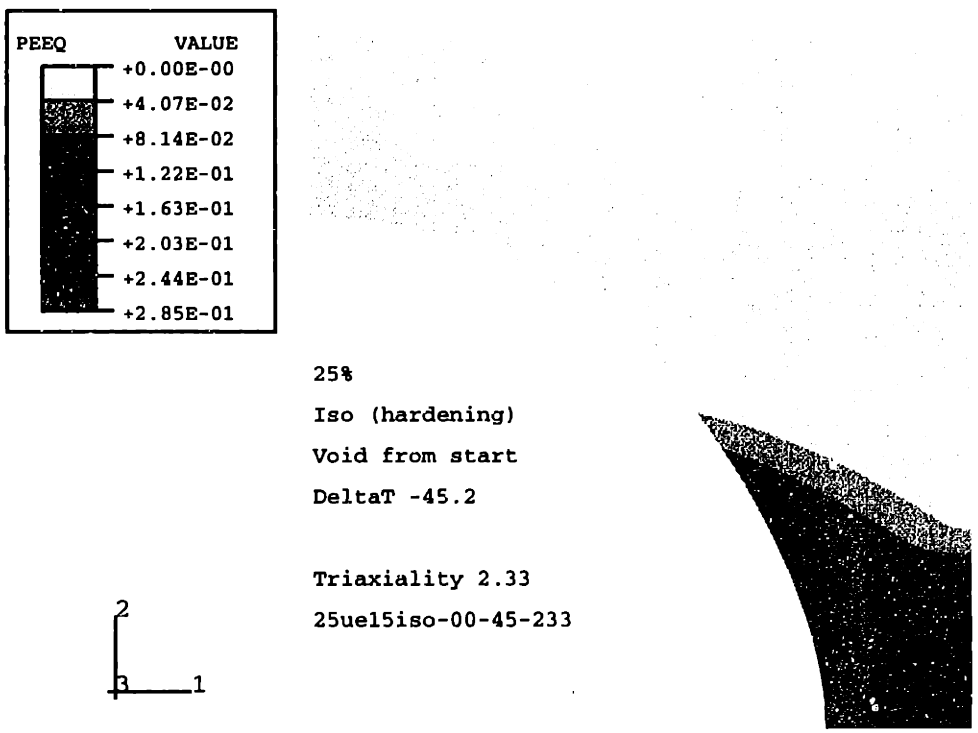

Figure 5-39c: 25iso-00-45-233: Contour plots of ε^p_{equiv} at $\varepsilon_{zz} = 5.5\%$.

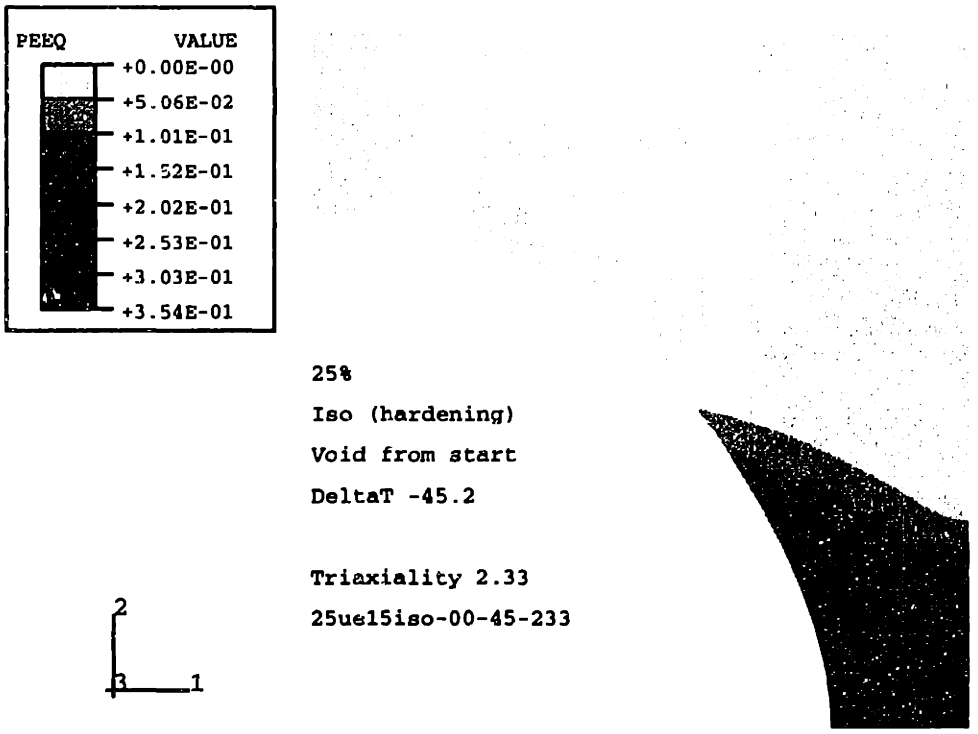

Figure 5-39f: 25iso-00-45-233: Contour plots of ε^{p}_{equiv} at $\varepsilon_{zz} = 6.5\%$.

from $25MPa$ under simple tension to $61MPa$ when Σ is 2.33. σ^{y}_{zz} of a unit with a coherent particle was found to increase from $23MPa$ to $76MPa$ for the same range in Σ. A rough linear approximation is:

$$\sigma^{y}_{zz} \simeq 17\,\Sigma\,(MPa) \tag{5.6}$$

From these results, it seems that the additional hydrostatic stress component due to the increase in Σ causes the deviatoric stresses in the matrix to decrease and to delay matrix yielding. This conclusion, however, is not without ambiguity, since the stress deviator is not directly applicable to the yield criterion in the anisotropic matrix.

Isotropic Matrix

In the isotropic matrix the cases of matrices with cavities and those with particles are very similar under simple tension, but quite different under higher triaxiality.

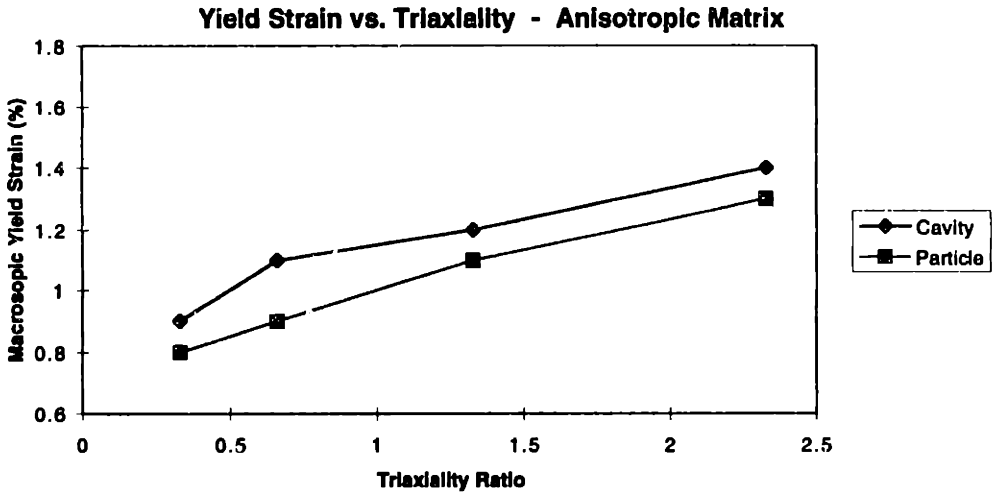

Figure 5-40: Macroscopic true axial strain at yield ε_{zz}^{y} as function of triaxiality Σ. Anisotropic matrix with pre-existing cavity ("Cavity") and non-cavitating particle ("Particle").

Considering the plots of ε_{zz}^{y} and σ_{zz}^{y} vs. Σ in figures 5-43 and 5-42. In the case of the unit cell with a cavity, σ_{zz}^{y} is found to be quite insensitive to a variation in Σ with a negligeable increases from $34MPa$ to $37MPa$, whereas ε_{zz}^{y} is observed to decrease from 1.4% ($\Sigma = 0.33$) to 0.8% ($\Sigma = 2.33$). The result seems to indicate that the added hydrostatic stress due to increasing Σ adds to the local stress deviator, causing ε_{zz}^{y} to drop, while it is not transmitted to the macroscopic stresses in the global 1-direction.

The case of a cell with a coherent particle is quite different. There, both ε_{zz}^{y} and σ_{zz}^{y} increase with increasing Σ, with the exception of ε_{zz}^{y} under uniaxial tension. σ_{zz}^{y} first drops from $37MPa$ to $33MPa$ ($\Sigma = 0.66$) and then increases to $102MPa$ at $\Sigma = 2.33$, whereas ε_{zz}^{y} drops from 1.5% to 1.2% and then increases to 1.7%. The increase in both ε_{zz}^{y} and σ_{zz}^{y} seems plausibly explained with the increase in σ^{h} as Σ increases, since with the particle present, σ^{h} can act throughout the unit cell, thereby unifying the stress state compared to that of the cell with cavity, lowering the stress deviator, and consequently delaying the yield event.

Summary

The general trend for the effect that varying Σ has on ε_{zz}^{p} and σ_{zz}^{y} is the increase of ε_{zz}^{y} with increasing Σ. The only exception to this trend is the simulation with an

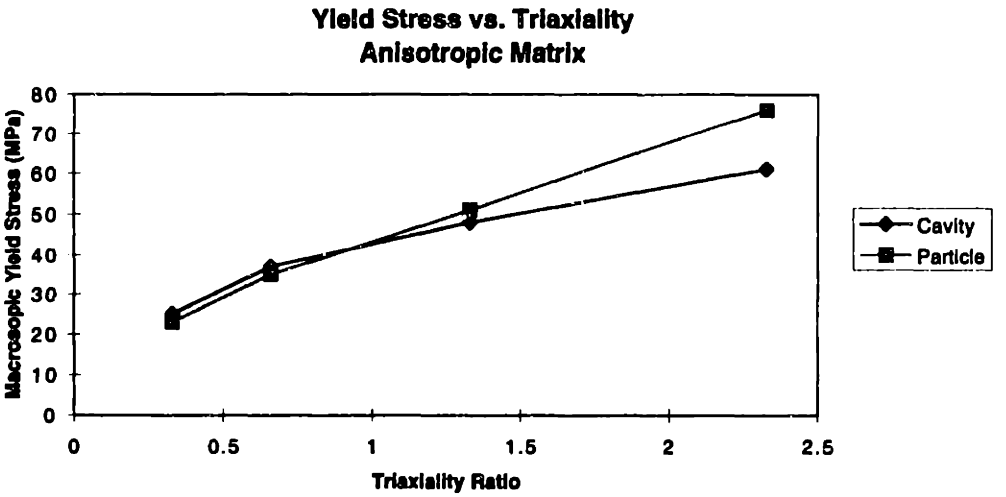

Figure 5-41: Macroscopic true axial stress at yield σ_{zz}^{y} as function of triaxiality Σ. Anisotropic matrix with pre-existing cavity ("Cavity") and non-cavitating particle ("Particle").

Yield Point of Unit Cells with Cavity ("00")				
	Anisotropic Matrix		Isotropic Matrix	
Σ	ε_{zz}^{y} (%)	σ_{zz}^{y} (MPa)	ε_{zz}^{y} (%)	σ_{zz}^{y} (MPa)
0.33	0.9	25	1.4	34
0.66	1.1	37	1.0	35
1.33	1.2	48	0.9	36
2.33	1.4	61	0.8	37

Table 5.5: Macroscopic axial yield stress σ_{zz}^{y} and macroscopic axial yield strain ε_{zz}^{y} as function of triaxiality Σ. Anisotropic and isotropic matrices with cavity.

isotropic matrix surrounding a hollow cavity where the yield strain decreases with increasing triaxiality.

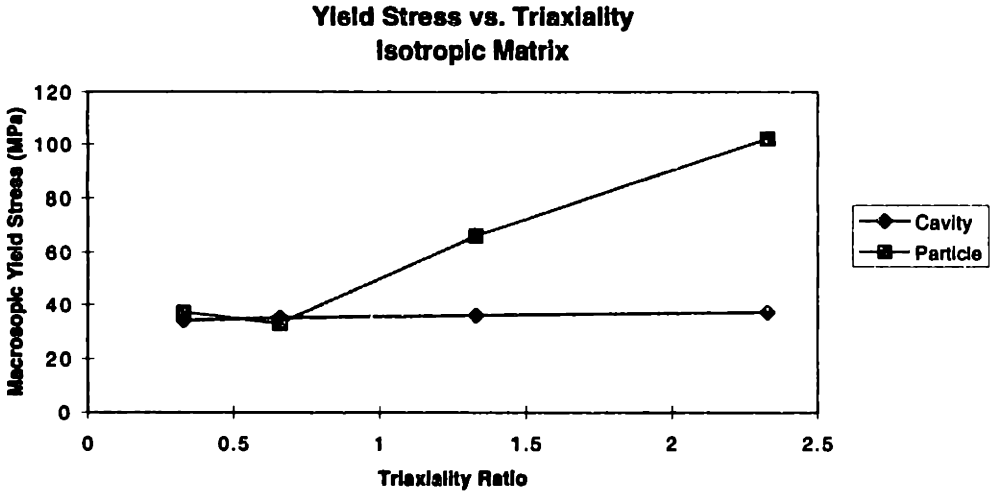

Figure 5-42: Macroscopic true axial stress at yield σ^y_{zz} as function of triaxiality Σ. Isotropic matrix with pre-existing cavity ("Cavity") and non-cavitating particle ("Particle").

Yield Point of Unit Cells with Non-Cavitating Particle ("nv")				
	Anisotropic Matrix		Isotropic Matrix	
Σ	ε^y_{zz} (%)	σ^y_{zz} (MPa)	ε^y_{zz} (%)	σ^y_{zz} (MPa)
0.33	0.8	23	1.5	37
0.66	0.9	35	1.2	33
1.33	1.1	51	1.4	66
2.33	1.3	76	1.7	102

Table 5.6: Macroscopic axial yield stress σ^y_{zz} and macroscopic axial yield strain ε^y_{zz} as function of triaxiality Σ. Asnisotropic and isotropic matrices with coherent particle.

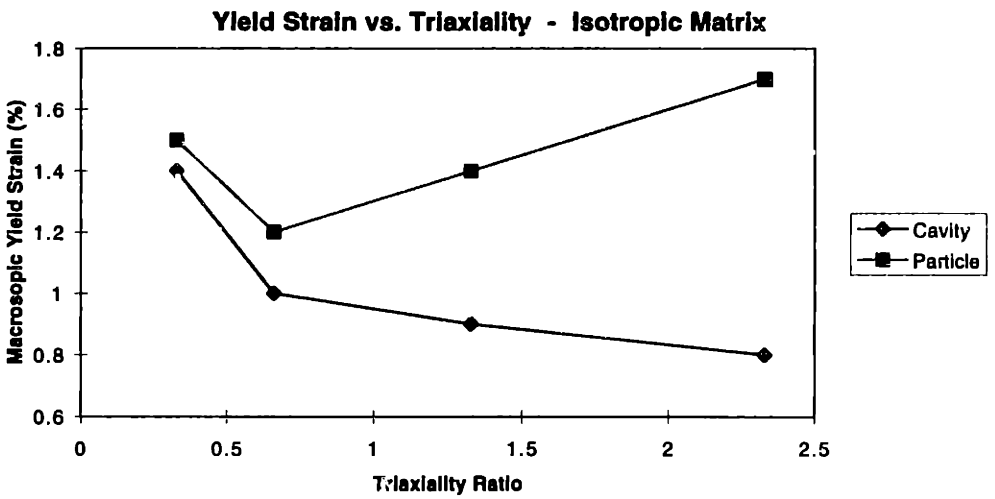

Figure 5-43: Macroscopic true axial strain at yield ε^y_{zz} as function of triaxiality Σ. Isotropic matrix with pre-existing cavity ("Cavity") and non-cavitating particle ("Particle").

5.5 Effect of Varying the Cavitation Strength of the Particle P_{cr}

5.5.1 Introduction

The cavitation strength of the particle determines at what levels of macroscopic stresses and strains the particle cavitates. As discussed above, various authors in the literature do not agree on a precise value for the cavitation strength of a rubber particle of a given size.

In order to study the effect of cavitation strength on the macroscopic stress-strain response of the unit cell and on matrix plasticity, the particle strengths are set to 0, -40MPa, -60MPa and infinity in a series of simulations. A cavitation strength of 0 corresponds to a hollow cavity and that of infinity corresponds to a non-cavitating particle. Unit cells with both anisotropic and isotropic matrix properties and at varying levels of triaxiality are examined.

As indicated in section 5.4, in some simulations the pressure that particles experience do not reach the critical values of -40MPa or -60MPa within the 6.5% of axial strain to which the unit cells are strained in the simulations. For example the particle in the unit cell under uniaxial tension reaches -29MPa in the anisotropic case and -28MPa in the isotropic case. Therefore in the case of simple tension only the two extreme case are studied: hollow cavity and non-cavitating particle. Cavitation strengths of less than -29 or -28MPa are assumed to be meaningfully approximated by the hollow cavity. A similar situation presents itself for 0.66 triaxiality where the critical pressure of -40MPa is reached only in the anisotropic matrix. For 1.33 and 2.33 triaxialities all critical pressures are reached by the particles, except that of -60MPa in the isotropic matrix under 1.33 triaxiality so that -55MPa is substituted in order to have comparative data.

5.5.2 Effect of Varying P_{cr} on the Macroscopic Stress-Strain Response of the Unit Cell

Figures 5-44a through 5-51a are plots of macroscopic axial true stress as a function macroscopic axial true strain. Each graph is plotted for one triaxiality and represents data of either the anistropic or the isotropic matrix.

Anisotropic Matrix

Figure 5-44a shows stress-strain plots of the anisotropic unit cell with both a hollow cavity ("00") and a non-cavitating particle ("nv") at a triaxiality of 0.33 (unixial tension). The stress-strain curves for particles and cavity are nearly identical within the given range of axial strain. From $\varepsilon_{zz} = 3\%$ on, the unit cell with the non-cavitating particle reaches a slightly higher stress than that with the hollow cavity. The difference remains smaller than 5%.

Considering now the cases of $\Sigma = 0.66$ with a cavity, a particle cavitating at a pressure of $P_{cr} = -40MPa$ ("40") and a non-cavitating particle. The corresponding stress-strain curves are shown in figure 5-45a. The difference between the macroscopic stresses in the simulations with the non-cavitating particle and the cavity is less than 10% for $\varepsilon_{zz} \leq 6\%$. Up to particle cavitation the unit cell with the cavitating particle follows the stress-strain curve of that of the non-cavitating particle. At $\varepsilon_{zz} = 3\%$, the particle cavitates and σ_{zz} carried by the unit cell drops from $57MPa$ to $49MPa$. After the particle cavitation, the macroscopic axial stress rises again sharply and at $\varepsilon_{zz} = 4\%$, it reaches that of the unit cell with a hollow cavity.

Figure 5-46a shows the stress-strain curves of the anisotropic unit cells with particles cavitating at $P_{cr} = -40MPa$ and $-60MPa$ as well as the non-cavitating particle and the pre-existing cavity under $\Sigma = 1.33$. The same trends as those previously observed are confirmed here. The difference in σ_{zz} between the non-cavitating particle and cavitating particles or cavities has increased to an order of 20% within the range of axial strains considered. The stresses of both cavitating particles are found to approach that of the cavity after particle cavitation. The difference in σ_{zz} between

the unit cell with the particle cavitating at $-40MPa$ and $\varepsilon_{zz} = 0.8\%$ and the unit cell with the pre-existing cavity after particle cavitation is in the order of $6MPa$ or 10%. This difference vanishes at $\varepsilon_{zz} = 4\%$.

σ_{zz} of the unit cell under 2.33 triaxiality exhibits a peak at $\varepsilon_{zz} = 2.8\%$ and subsequent drops-off for all cavitating particles and the hollow cavity. Figure 5-47a shows the same set of data as the previous figures, but for $\Sigma = 2.33$. The difference in stress between the unit cell with a cavitating particle or a cavity and that with a non-cavitating particle reaches $28MPa$ or 35% at the stress peak and $88MPa$ or 160% at $\varepsilon_{zz} = 6\%$. The difference between σ_{zz} due to the pre-existing cavity and that due to cavitating particles is below 10%. Again, from axial strains of 4% on, the stress curves of the cavitating particles merge with that of the pre-existing cavity.

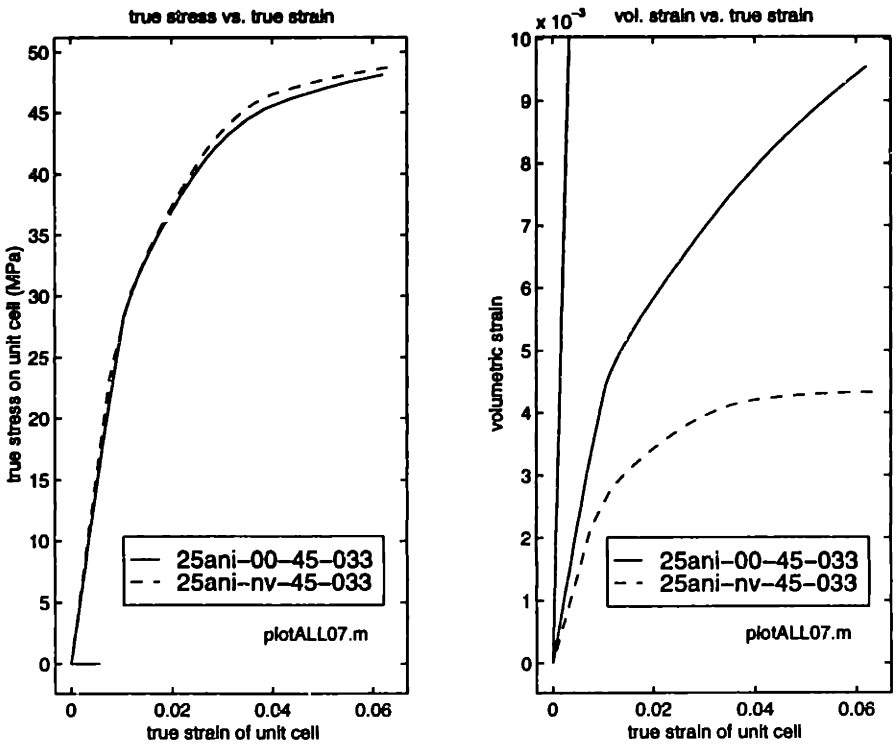

Figure 5-44: (a) macroscopic true axial stress σ_{zz} and (b) cell volumetric strain Ψ as functions of macroscopic axial true strain ε_{zz}. Anisotropic matrix. $\Sigma = 0.33$.

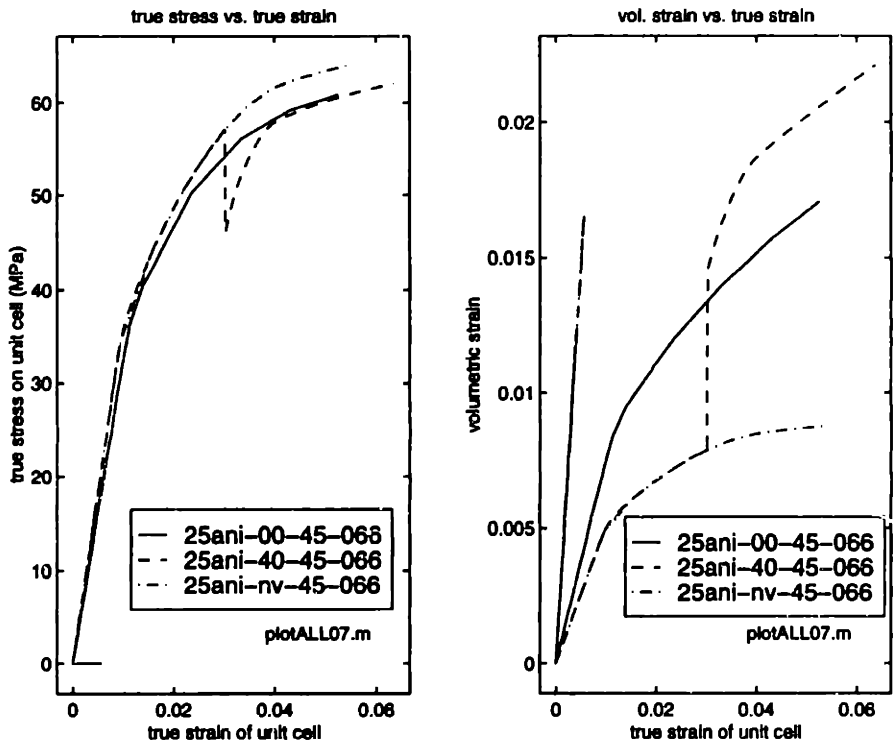

Figure 5-45: (a) macroscopic true axial stress σ_{zz} and (b) cell volumetric strain Ψ as functions of macroscopic axial true strain ε_{zz}. Anisotropic matrix. $\Sigma = 0.66$.

Isotropic Matrix

In figures 5-48a - 5-51a the same sequence of graphs is presented for the isotropic matrix as previously presented for the anisotropic matrix.

In figure 5-48a the stress-strain plots for an isotropic unit cell with a pre-existing cavity ("00") and a non-cavitating particle ("nv") under simple tension ($\Sigma = 0.33$) are shown. Within the strain levels considered, the difference between the stresses of the two unit cells after matrix yield is found to be on the order of 7% or $3MPa$.

In the case of $\Sigma = 0.66$, this difference increases to 28% or $11MPa$. Figure 5-49a shows the stress-strain plots for the same cases as above, but at $\Sigma = 0.66$.

The particles inside the unit cell under $\Sigma = 1.33$ reach the critical pressures and a cavitation event is initiated. The stress-strain plots in figure 5-50a are for a pre-existing cavity, particles cavitating at $-40MPa$ and $-55MPa$ and a non-cavitating particle. The particle with $P_{cr} = -40MPa$ cavitates at an $\varepsilon_{zz} = 0.9\%$. Due to the particle cavitation, σ_{zz} drops from $38MPa$ to $28MPa$. It then climbs back up to join

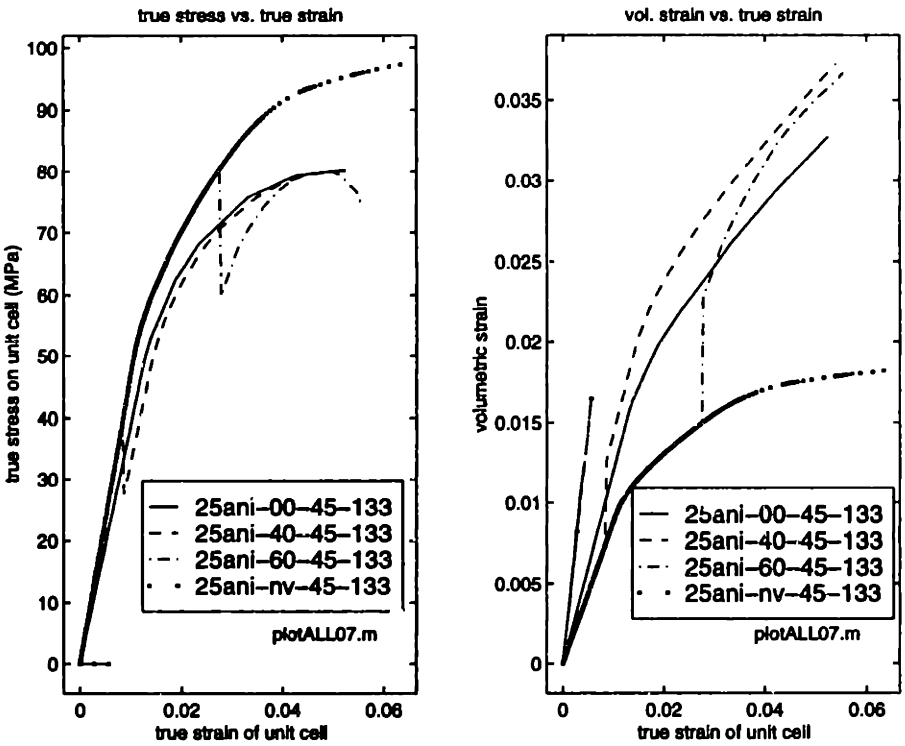

Figure 5-46: (a) macroscopic true axial stress σ_{zz} and (b) cell volumetric strain Ψ as functions of macroscopic axial true strain ε_{zz}. Anisotropic matrix. $\Sigma = 1.33$.

the stress curve of the unit cell with the hollow cavity. At an $\varepsilon_{zz} = 2\%$ they are nearly identical. The particle with $P_{cr} = -60MPa$ reaches that pressure at approximately $\varepsilon_{zz} = 1.4\%$. The subsequent drop in macroscopic stress from $67MPa$ to $38MPa$ is not big enough to let the stress curve drop below that of the pre-existing cavity. By the time ε_{zz} reaches 2% the curve of the case with $P_{cr} = -60MPa$ and that of the pre-existing cavity are undistinguishable. The difference between the stresses supported by the unit cell with a pre-existing cavity and that with a non-cavitating particle lies above 85% or $36MPa$ at $\varepsilon_{zz} = 6.5\%$.

The same trends are observed in the case of $\Sigma = 2.33$ (figure 5-51a). After the particle with $P_{cr} = -40MPa$ cavitates at $\varepsilon_{zz} = 0.6\%$ and $\sigma = 33MPa$, the macroscopic stress across the unit cell drops to $22MPa$ before sharply increasing again and merging with the stress-strain curve of the unit cell with the pre-existing cavity after an additional 1.5% of axial strain. The same is true for the unit cell with the particle with $P_{cr} = -60MPa$. With this particle the cavitation occurs at approximately $\varepsilon_{zz} = 1.2\%$ and $\sigma_{zz} = 67MPa$, the stress drops to $38MPa$ and merges

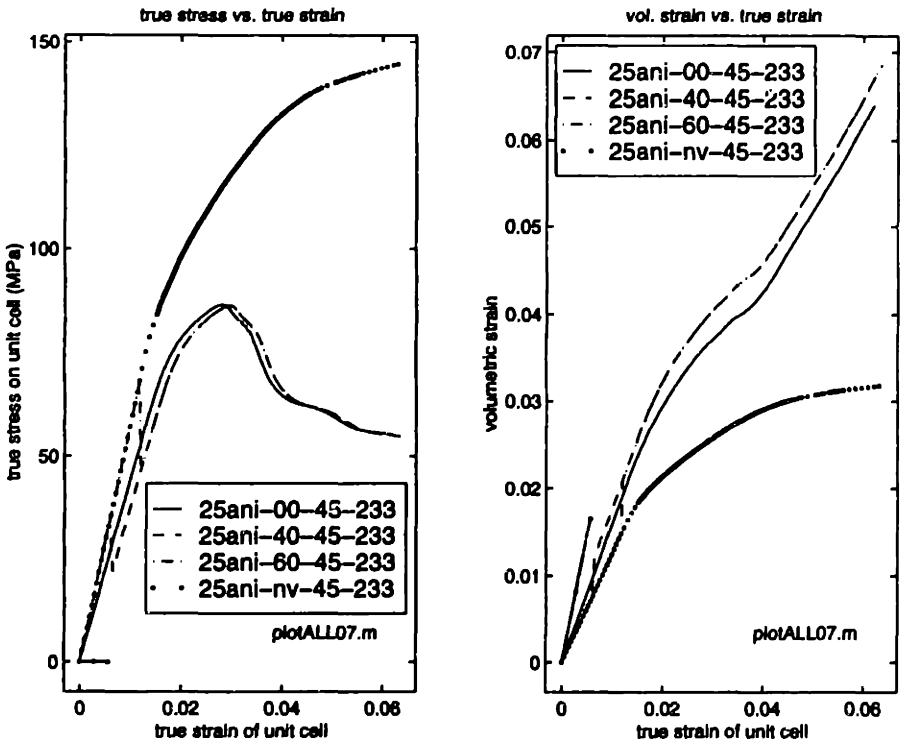

Figure 5-47: (a) macroscopic true axial stress σ_{zz} and (b) cell volumetric strain Ψ as functions of macroscopic axial true strain ε_{zz}. Anisotropic matrix. $\Sigma = 2.33$.

with that of the pre-existing cavity-case after an additional 1.5% axial strain. The difference between the stresses supported by the unit cell with a pre-existing cavity and that with a non-cavitating particle lies above 180% or $75MPa$ at $\varepsilon_{zz} = 6.5\%$.

Summary

As the previous discussion of the unit cell's macroscopic stress-strain response reveals, both isotropic and anisotropic simulations can be grouped into two categories:

- simulations where the particle cavitates or is a cavity from the start,
- simulations where the particle does not cavitate.

The differences between the stress-strain curves of unit cells where the particle cavitates and those where it is a cavity from the start are very small after the effects of the cavitation event subside.

If the particle cavitation occurs before yield, the unit cell's macroscopic stress-strain response is that of a unit cell with a pre-existing cavity. If the matrix yields

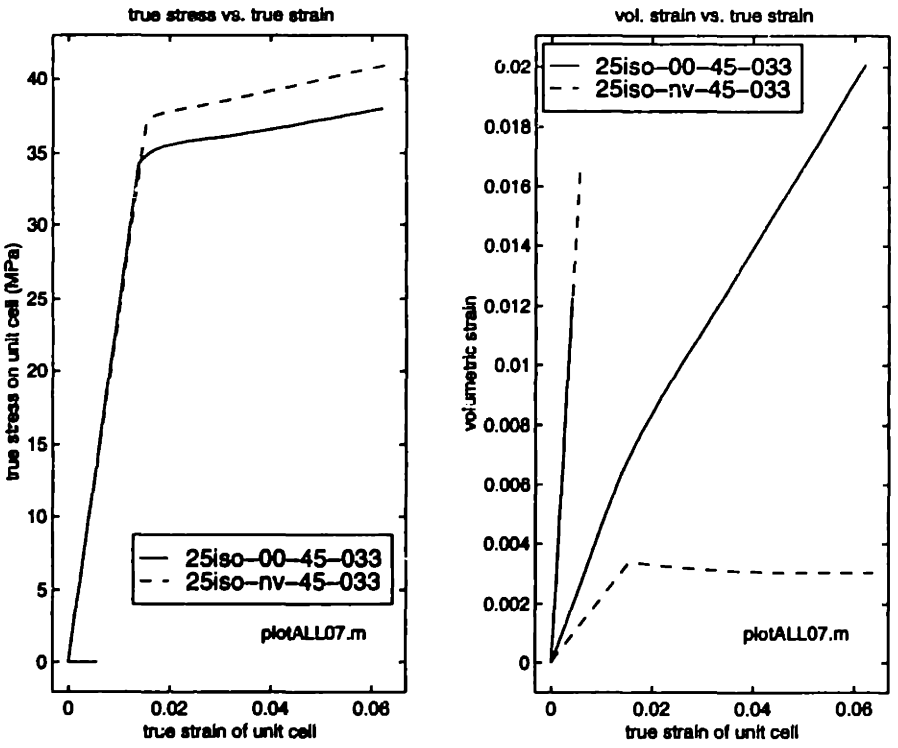

Figure 5-48: (a) macroscopic true axial stress σ_{zz} and cell volumetric strain Ψ as functions of macroscopic axial true strain ε_{zz}. Isosotropic matrix. $\Sigma = 0.33$.

before the particle cavitates a small effect of the cavitation is noticeable during at most 1.5% additional axial strain after the cavitation event. After that the stress-strain curves are nearly indistinguishable. Only in anisotropic matrices under high triaxiality this effect can remain noticeable over larger additional strains. As can be seen in figures 5-46a and 5-47a, a small difference between the stress-strain response of the unit cell with the newly generated cavity and that with a pre-existing cavity persists over larger additional axial strain than 1.5%.

If no particle cavitation occurs, the macroscopic axial stress can be more than double than the stresses supported by unit cells containing cavitating particles or hollow cavities within the first 6.5% axial strain, especially at high levels of triaxiality.

5.5.3 Effect of Varying P_{cr} on the Matrix Plasticity

In this section the effect of varying the particle's cavitation strength P_{cr} on the onset, evolution and magnitudes of matrix plasticity is evaluated by studying the contour

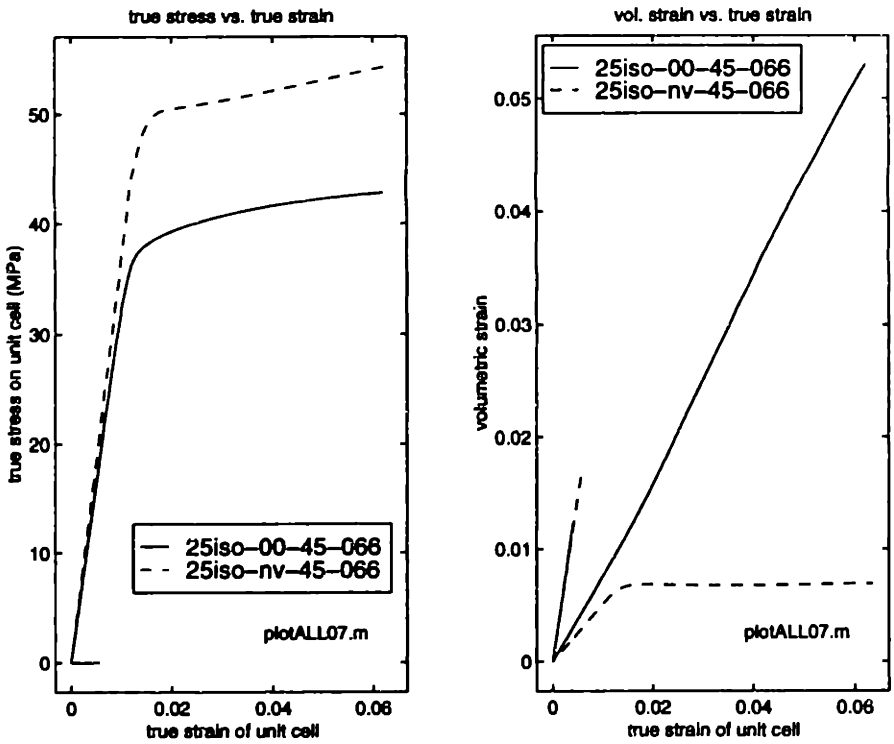

Figure 5-49: (a) macroscopic true axial stress σ_{zz} and cell volumetric strain Ψ as functions of macroscopic axial true strain ε_{zz}. Isosotropic matrix. $\Sigma = 0.66$.

plots of equivalent plastic strain ε^p_{equiv} (PEEQ). Considering a series of simulations where at fixed triaxiality the unit cell contains one of the following. A particle cavitation at either $P_{cr} = -40MPa$ or $-60MPa$, a pre-existing cavity or a non-cavitating particle.

In the case of simple tension the comparison is limited to the cavity and the non-cavitating particle. Under $\Sigma = 0.66$, the case of $P_{cr} = -40MPa$ is added, and at 1.33 and 2.33 triaxiality all four cases are considered.

Anisotropic Matrix

Comparing the plots of ε^p_{equiv} in the unit cells under simple tension with a pre-existing cavity (figures 5-32a-f) with that containing a non-cavitating particle (figures 5-24a-f). The two matrices yield in a similar fashion. Both plots of ε^p_{equiv} at $\varepsilon_{zz} = 1.5\%$ show a plastic zone in the upper right-hand corner. Only the unit cell with the pre-existing cavity has the zone of initial yield drawn out toward the lateral boundary along the

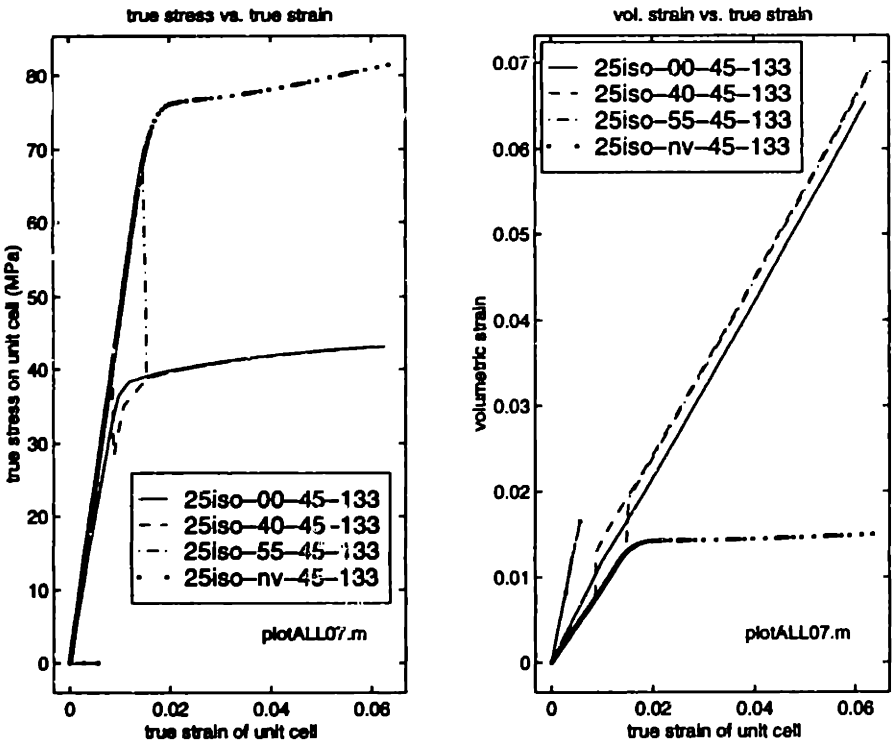

Figure 5-50: (a) macroscopic true axial stress σ_{zz} and cell volumetric strain Ψ as functions of macroscopic axial true strain ε_{zz}. Isosotropic matrix. $\Sigma = 1.33$.

direction in which the first shear band later develops. At $\varepsilon_{zz} = 2.5\%$ the shear band I begins to emerge in the unit cell with the pre-existing cavity ("00"). At higher axial strains the plastic deformation in the unit cells with the cavtity continues to localize in the shear band and to some degree along the cavity surface. The localization of plasticty in the unit cell with the non-cavitating particle is discernable but overall less pronounced. At $\varepsilon_{zz} = 5.5\%$, ε^p_{equiv} reaches 11% in the case of the pre-existing cavity and 7.5% in the matrix surrounding the non-cavitating particle.

At $\Sigma = 0.66$, the previously observed trends are confirmed. Considering the unit cells containing a cavity from the start (case "00", figures 5-33a-f), a particle cavitating at $P_{cr} = -40MPa$ (case "40", figures 5-52a-f) and a non cavitating particle (case "nv", figures 5-25a-f). Case "00" yields at $\varepsilon^y_{zz} = 1.1\%$ and cases "40" and "nv" at 0.9%. Comparing the plots of ε^p_{equiv} at $\varepsilon_{zz} = 1.5\%$ and 2.5%, it can be seen that the "40" and "nv" cases reach higher levels of ε^p_{equiv} because of their yielding at lower axial strain. They show the typical pattern of plasticity of a unit cell containing a particle, whereas case "00" shows the typical pattern of a matrix surrounding a cavity

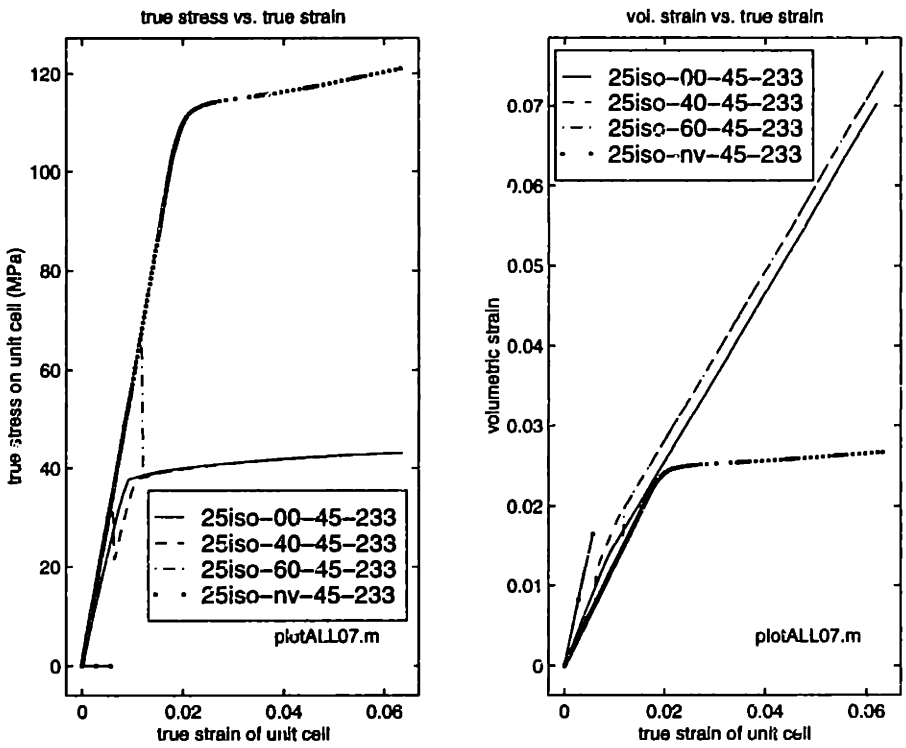

Figure 5-51: (a) macroscopic true axial stress σ_{zz} and cell volumetric strain Ψ as functions of macroscopic axial true strain ε_{zz}. Isosotropic matrix. $\Sigma = 2.33$.

with the formation of a shear band etc. At $\varepsilon_{zz} = 2.5\%$, the "00" matrix develops localization of plasticity in the shear band and ε^p_{equiv} reaches 3%, whereas ε^p_{equiv} in the two other cases remains at 2.3% and show only moderate levels of localization. The particle of the "40" case cavitates at $\varepsilon_{zz} = 3\%$. Its ε^p_{equiv} contour plot at $\varepsilon_{zz} = 3.5\%$ has changed in terms of distribution of the plasticity toward that of the unit cell surrounding a pr-existing cavity (case "00"). ε^p_{equiv} has become more localized and reaches levels of over 4.6%, whereas that of the "nv" case reaches 4.0% at the same strain. In the "00" case, ε^p_{equiv} reaches 7.5% at that same strain. At $\varepsilon_{zz} = 4.5\%$ the ε^p_{equiv} contour plot of case with $P_{cr} = -40MPa$ has gotten even more similar to that of the pre-existing cavity. Its maximum ε^p_{equiv} is 9.6% wherease that of the "00" case is 11% and that of the non-cavitating case 5.9%. At $\varepsilon_{zz} = 5.5\%$ axial strain the ε^p_{equiv} contour plots of the "00" and "40" cases are very similar and the maximum levels of ε^p_{equiv} are 14% and 12% respectively.

Moving now on to $\Sigma = 1.33$ simulatons with a pre-existing cavity ("00" figures 5-34a-f), particles cavitating at $P_{cr} = -40MPa$ ("40", figures 5-53a-f) and $P_{cr} =$

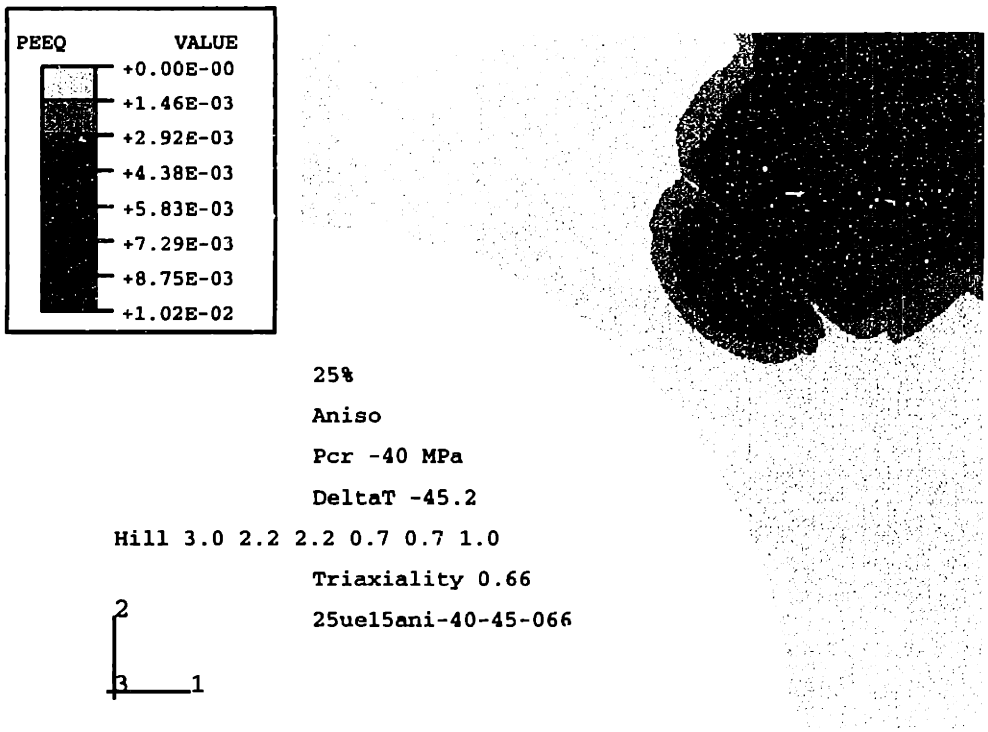

Figure 5-52a: 25ani-40-45-066: Contour plots of ε^p_{equiv} at $\varepsilon_{zz} = 1.5\%$.

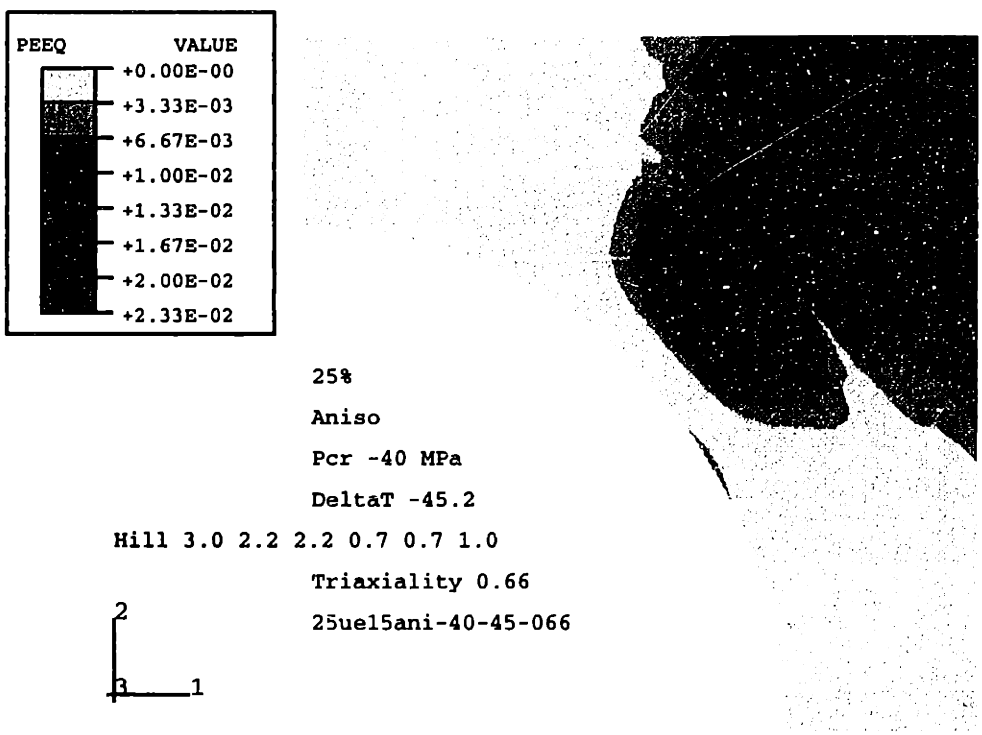

Figure 5-52b: 25ani-40-45-066: Contour plots of ε^p_{equiv} at $\varepsilon_{zz} = 2.5\%$.

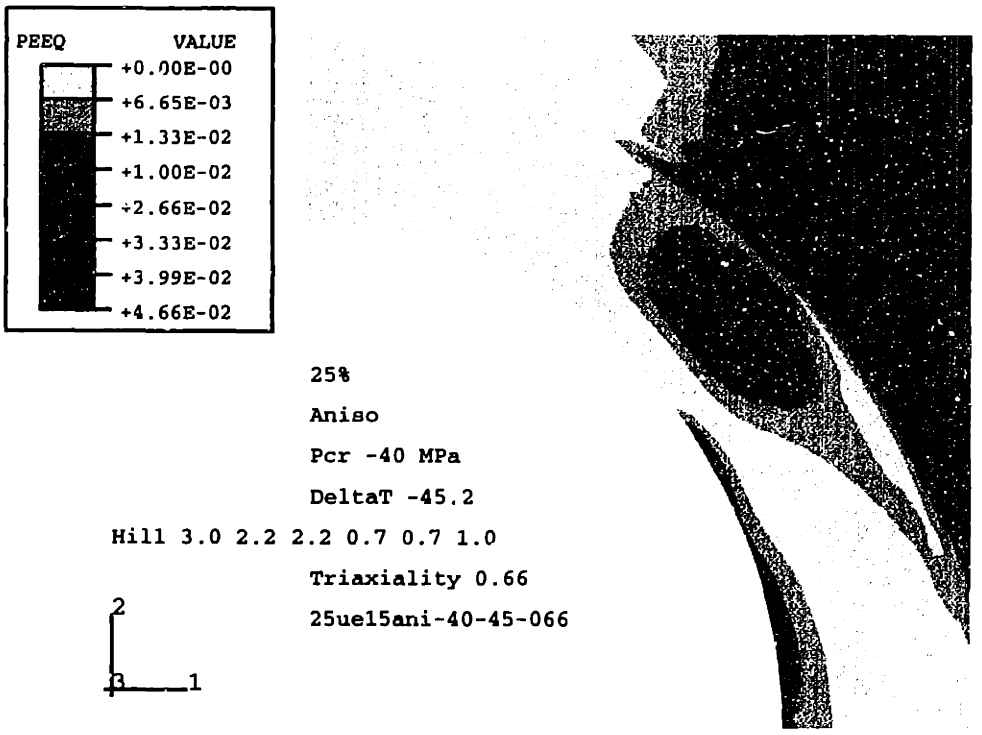

Figure 5-52c: 25ani-40-45-066: Contour plots of ε^p_{equiv} at $\varepsilon_{zz} = 3.5\%$.

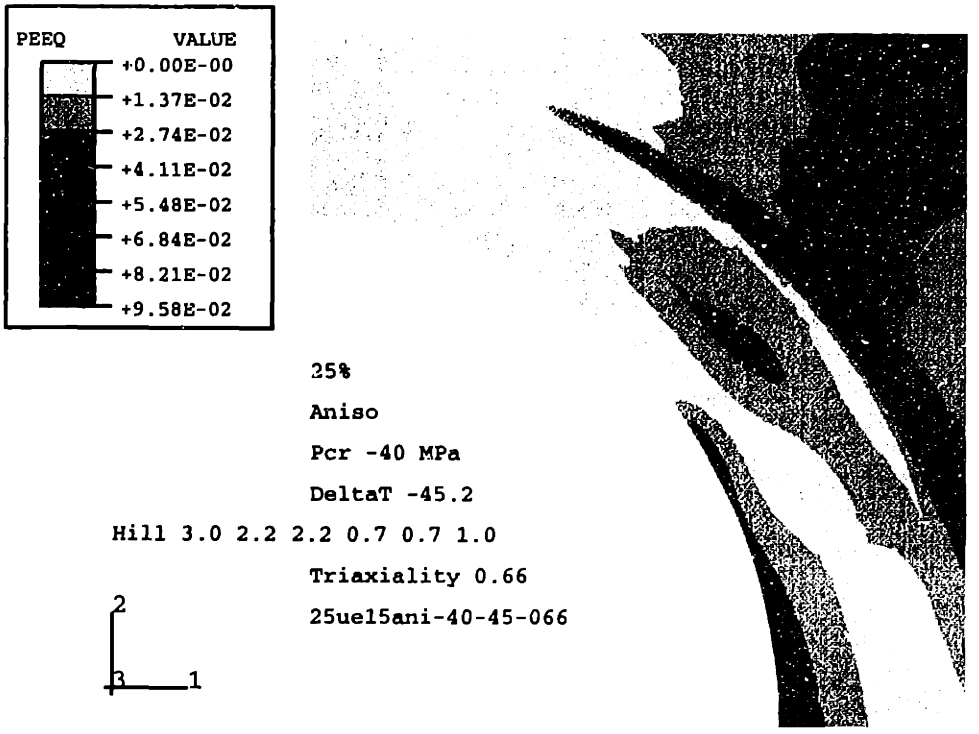

Figure 5-52d: 25ani-40-45-066: Contour plots of ε^p_{equiv} at $\varepsilon_{zz} = 4.5\%$.

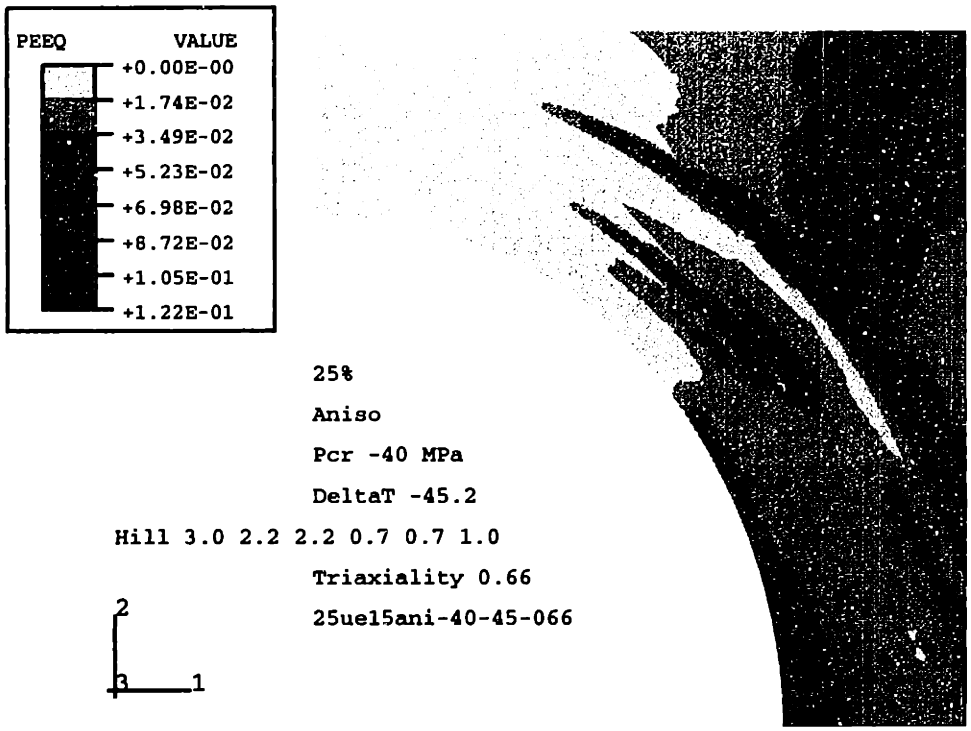

Figure 5-52e: 25ani-40-45-066: Contour plots of ε^{p}_{equiv} at $\varepsilon_{zz} = 5.5\%$.

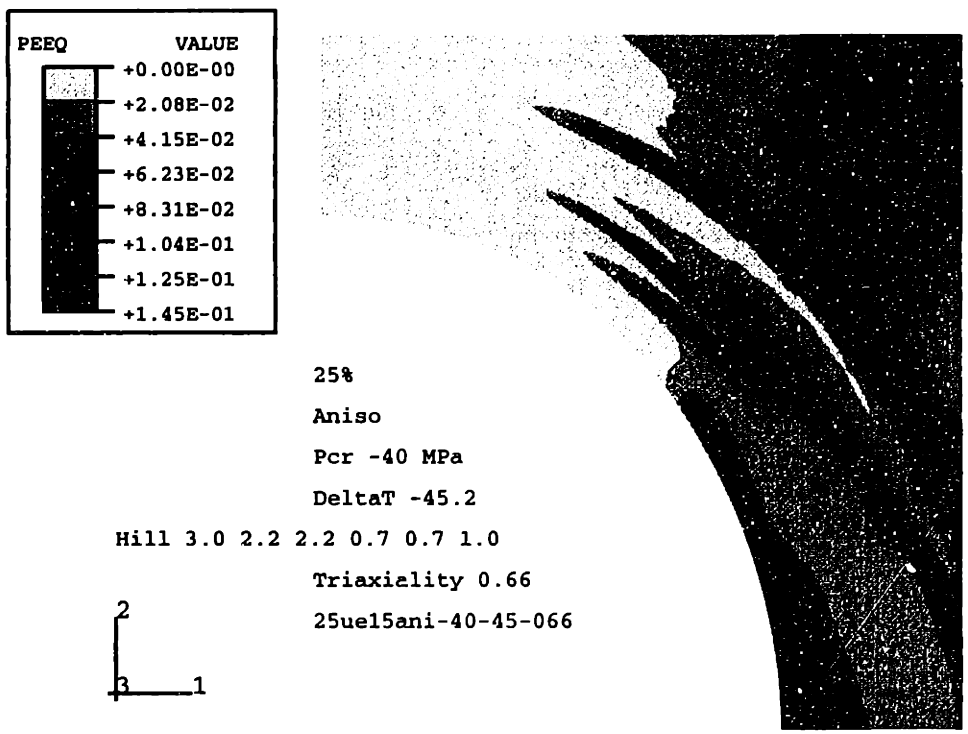

Figure 5-52f: 25ani-40-45-066: Contour plots of ε^{p}_{equiv} at $\varepsilon_{zz} = 6.5\%$.

$-60MPa$ ("60", figures 5-9a-e), and a non-cavitating particle ("nv", figures 5-26a-f). The "00" and "40" unit cells yield before the axial strain reaches 1.5%, probably at strains larger than 1.2%. The "40" particle cavitates at $\varepsilon_{zz} = 0.8\%$, which is still in the elastic regime of the matrix's deformation. Therefore the ε^p_{equiv} contour plots of these two cases are the same throughout the simulation. The "60" particle cavitates at approximately $\varepsilon_{zz} = 2.8\%$ and hence after the matrix has yielded. Therefore the ε^p_{equiv} contour plots of the "60" case are the same as the "nv" case up to axial strains of 2.8%. Comparing the ε^p_{equiv} contour plots of the "00" and "nv" cases at $\varepsilon_{zz} = 2.5\%$, the typical difference between the matrix plasticity of a unit cell with a pre-existing cavity and that with a non-cavitating particle emerges. In the "00" case, most of the matrix plasticity is concentrated in the shear bands I and the shear band II which has developed at the cavity surface. The maximum ε^p_{equiv} is 5.1%. In the "nv" case shows the plasticity spread out over a large area, with a maximum ε^p_{equiv} of 2.0%. When the strain reaches 3.5% the ε^p_{equiv} contour plot of the unit cell with $P_{cr} = -60MPa$ with the now cavitated particle has already changed into that of a matrix surrounding a cavity although its ε^p_{equiv} levels have not yet caught up with those of the case with a pre-existing. The maximum ε^p_{equiv} of the "00" case is 18%, that of the "60" case is 8.4% and that of the "nv" case is 3.7%. At $\varepsilon_{zz} = 6.5\%$, the ε^p_{equiv} contour plot of the "60" case looks quite similar to that of the "00" case. Its maximum ε^p_{equiv} reaches 42%, while that of the "00" case reaches 56%. The "nv" case reaches a ε^p_{equiv} of 9.2% and displays the typical distribution of plasticity as found under other triaxialities in the cases of non-cavitating particles.

The cases of unit cells under a triaxialitiy of 2.33, it is sufficient to study the pre-existing cavity case ("00", figures 5-35a-f) and the non-cavitating particle case ("nv", 5-27a-f). The particles with cavitating strengths of $P_{cr} = -40MPa$ and $-60MPa$ cavitate at $\varepsilon_{zz} = 0.6\%$ and 1.1% resprectively, which is at strains that are smaller than that at which the matrix yields. The "00" matrix yields at 1.4% macroscopic axial strain and that surrounding the non-cavitating particle at 1.3%. When comparing the ε^p_{equiv} contour plots of the "00" case and the "nv" case the same trends as those observed for $\Sigma = 1.33$ emerge. At $\varepsilon_{zz} = 6.5\%$, ε^p_{equiv} reaches 9.6% in

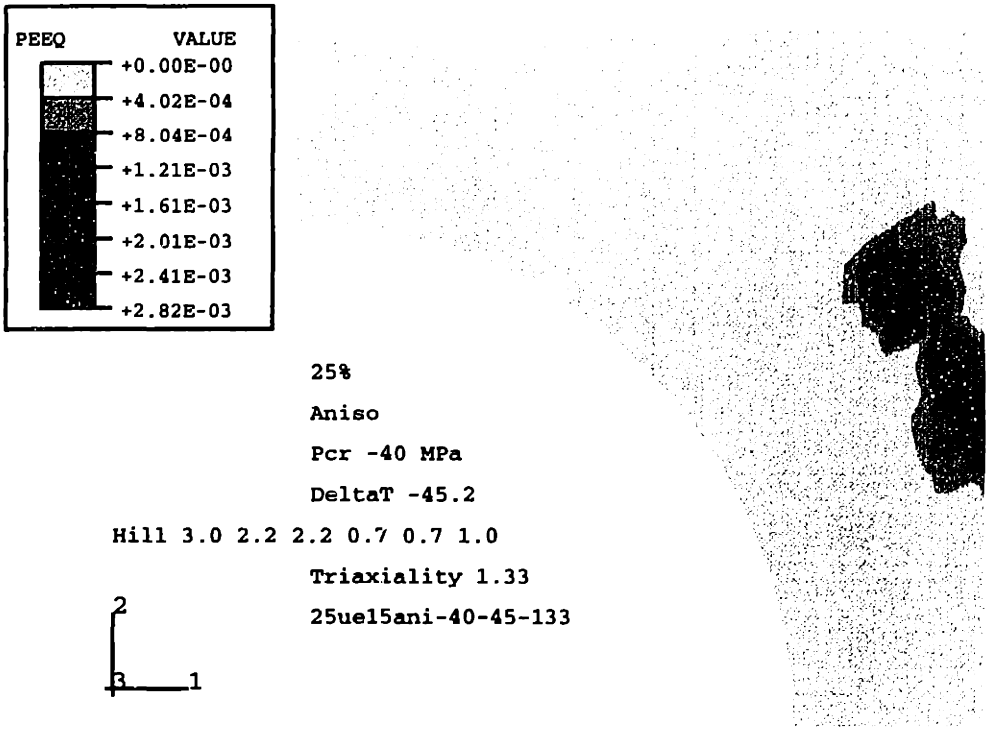

Figure 5-53a: 25ani-40-45-133: Contour plots of ε^p_{equiv} at $\varepsilon_{zz} = 1.5\%$.

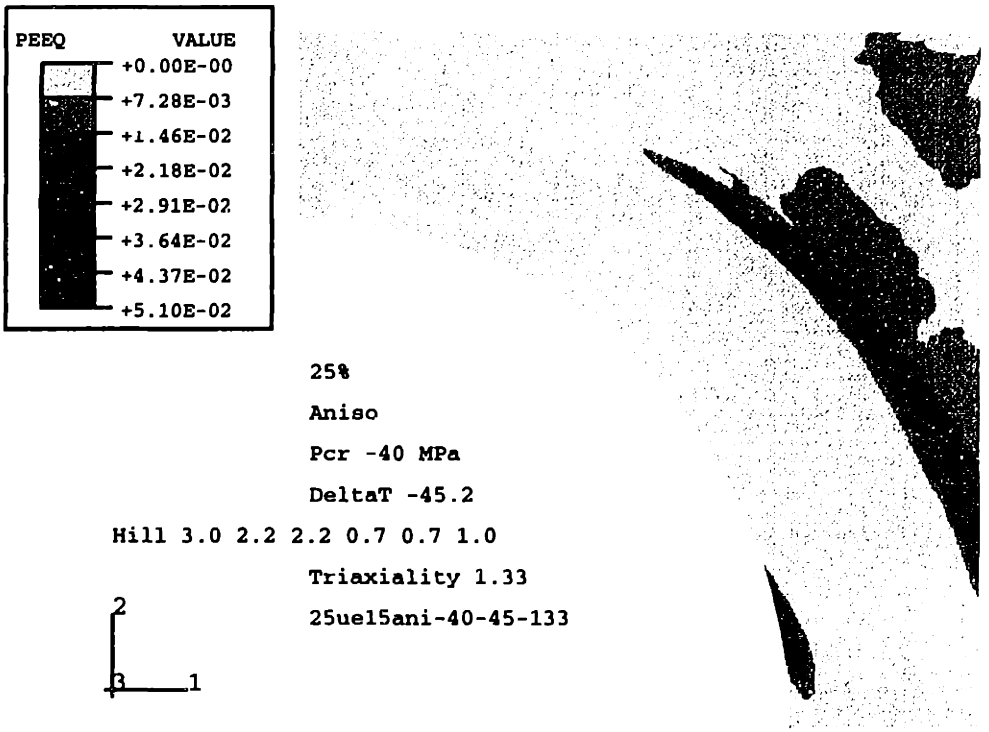

Figure 5-53b: 25ani-40-45-133: Contour plots of ε^p_{equiv} at $\varepsilon_{zz} = 2.5\%$.

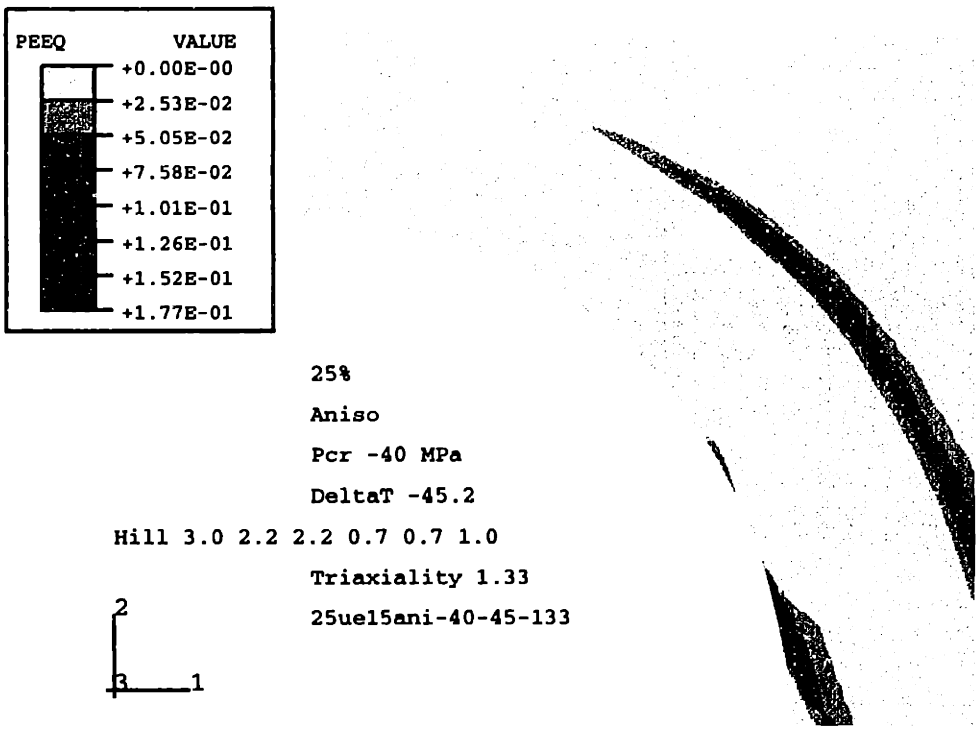

Figure 5-53c: 25ani-40-45-133: Contour plots of ε^p_{equiv} at $\varepsilon_{zz} = 3.5\%$.

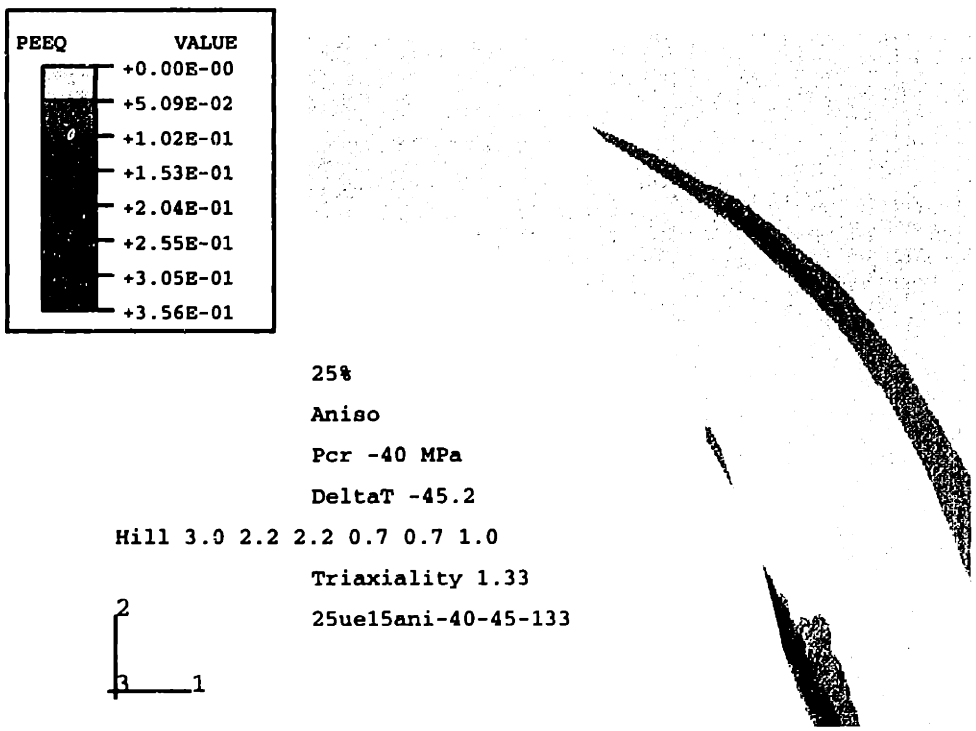

Figure 5-53d: 25ani-40-45-133: Contour plots of ε^p_{equiv} at $\varepsilon_{zz} = 4.5\%$.

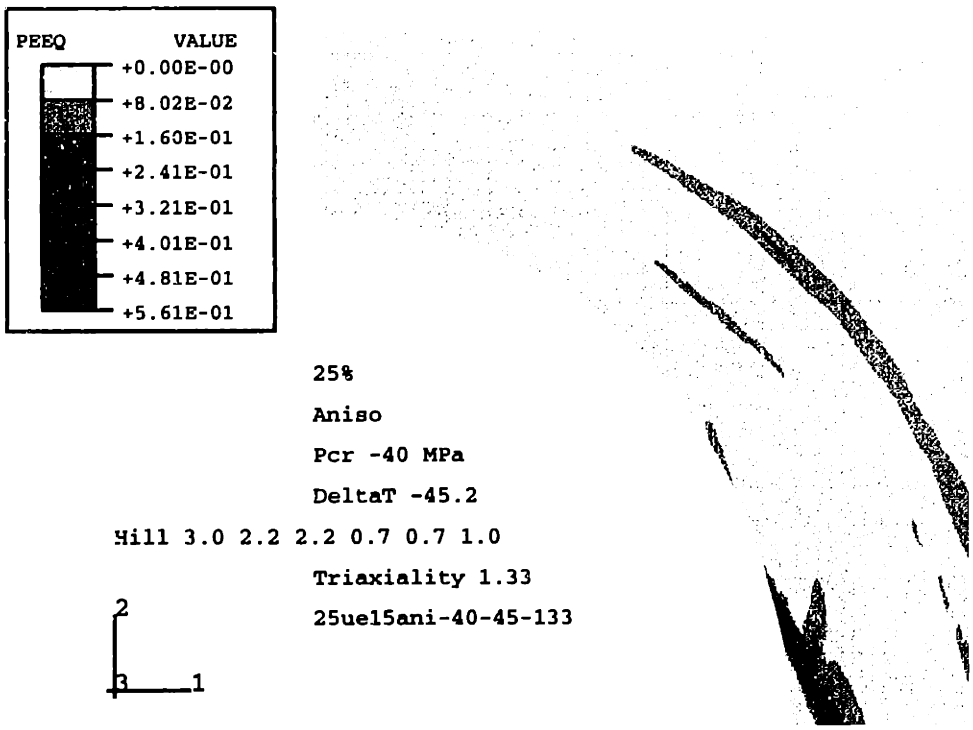

Figure 5-53e: 25ani-40-45-133: Contour plots of ε^p_{equiv} at $\varepsilon_{zz} = 5.5\%$.

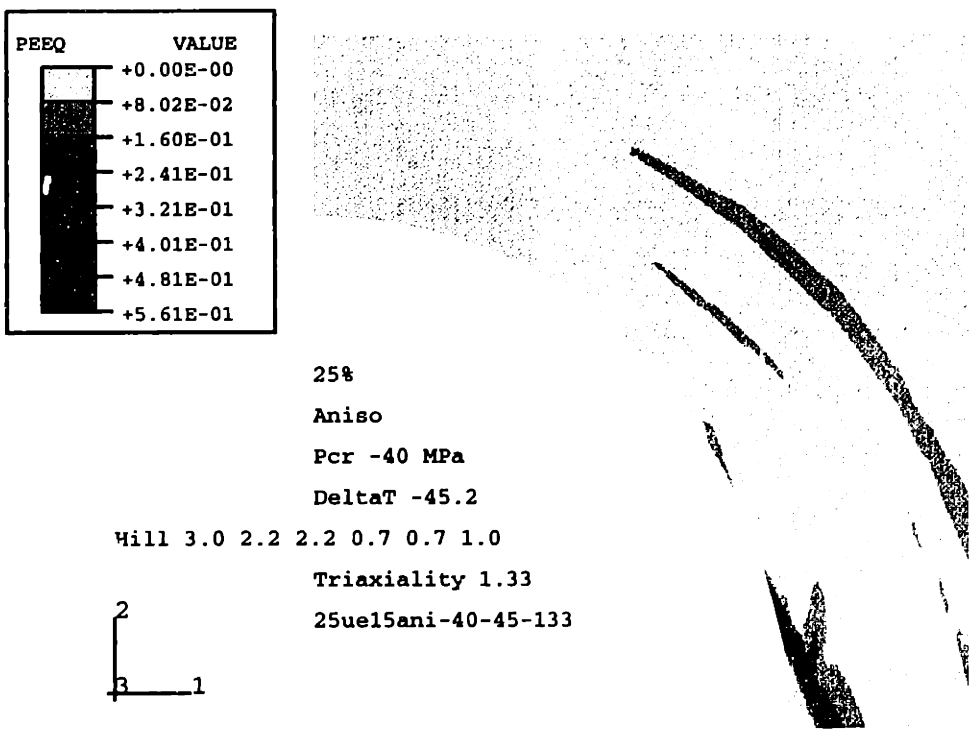

Figure 5-53f: 25ani-40-45-133: Contour plots of ε^p_{equiv} at $\varepsilon_{zz} = 6.5\%$.

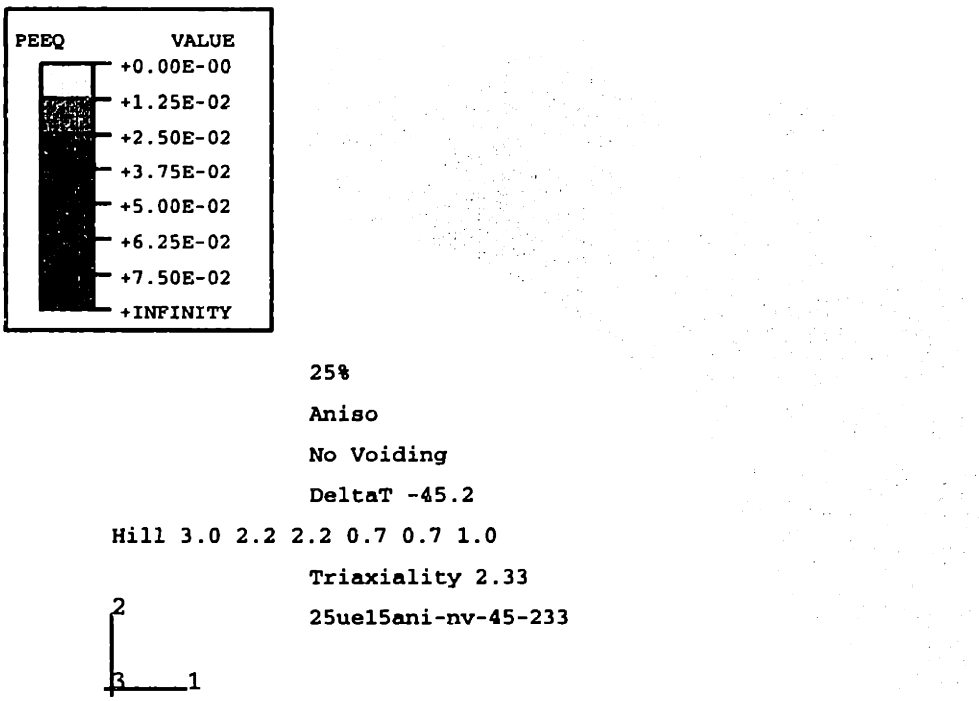

Figure 5-54a: 25ani-nv-45-233: Contour plots of ε^p_{equiv} at $\varepsilon_{zz} = 1.5\%$. $Cmax = 7.5\%$.

the "nv" case and over 200% in the "00" case.

In order to better visualize how the matrix plasticity evolves, the displayed levels of the equivalent plastic strain ε^p_{equiv} have been limited in figures 5-36a-f and 5-54a-f. The cut-off levels of ε^p_{equiv} are 1.25%, 2.50%, 3.75%, 5.00%, 6.25% and 7.50%. ε^p_{equiv} larger than 7.50% is displayed in the darkest contour shade of the highest category. At $\varepsilon_{zz} = 1.5\%$ no $\varepsilon^p_{equiv} > 1.25\%$ is displayed in the "00" (figures 5-36a-f) and "nv" (figures 5-54a-f) unit cells. At $\varepsilon_{zz} = 2.5\%$, the "00" unit cell exhibits strong localizations of plasticity in the two shear bands I and II. At the same strain, the "nv" matrix displays only small amounts of plasticity in the upper right-hand corner. When the axial strain reaches 3.5% all four shear bands have emerged in the "00" cell as previously discussed. At $\varepsilon_{zz} = 4.5\%$, shear bands III and IV have connected.

Isotropic Matrix

As in the anisotropic case, the particle pressure inside the unit cell under simple tension does not reach a critical value of $P =_{cr} = -40MPa$ within the first 6.5%

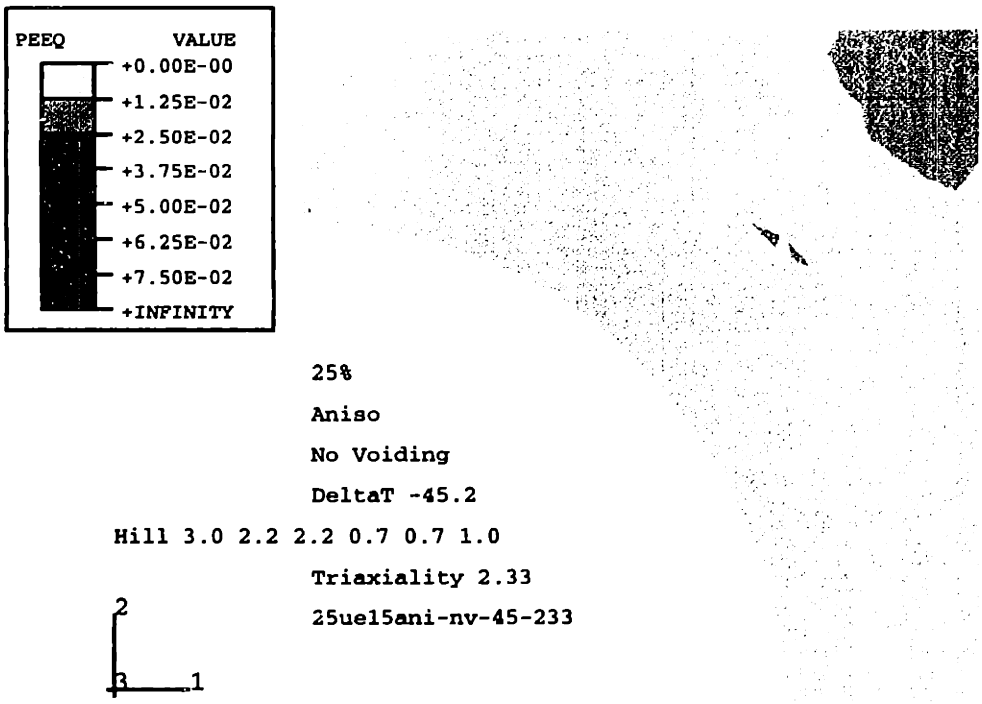

Figure 5-54b: 25ani-nv-45-233: Contour plots of ε^{p}_{equiv} at $\varepsilon_{zz} = 2.5\%$. $Cmax = 7.5\%$.

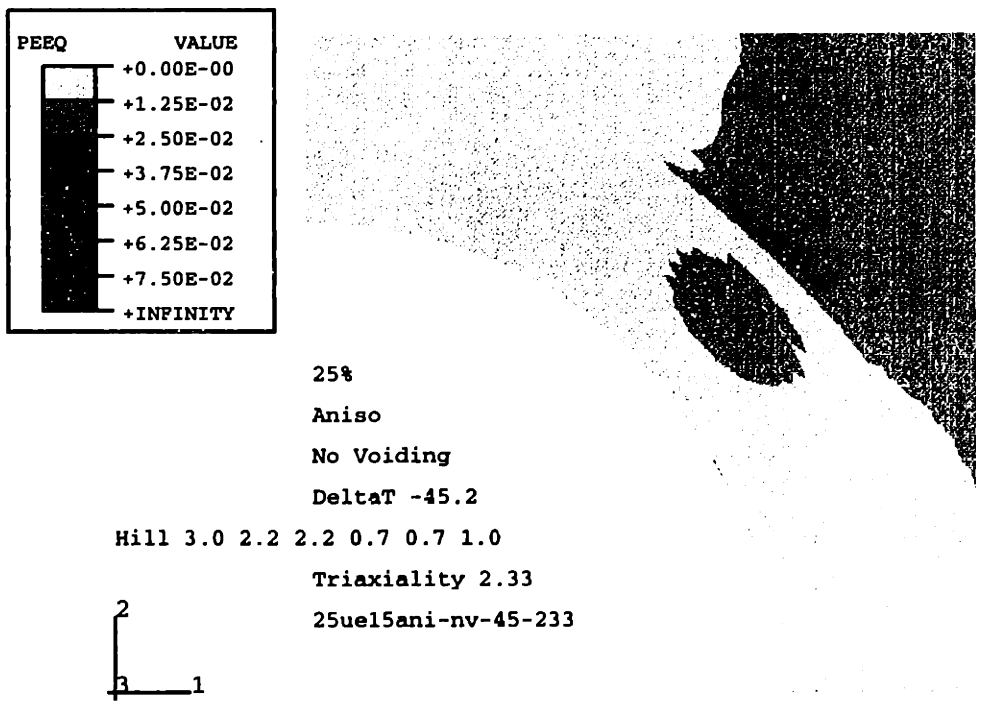

Figure 5-54c: 25ani-nv-45-233: Contour plots of ε^{p}_{equiv} at $\varepsilon_{zz} = 3.5\%$. $Cmax = 7.5\%$.

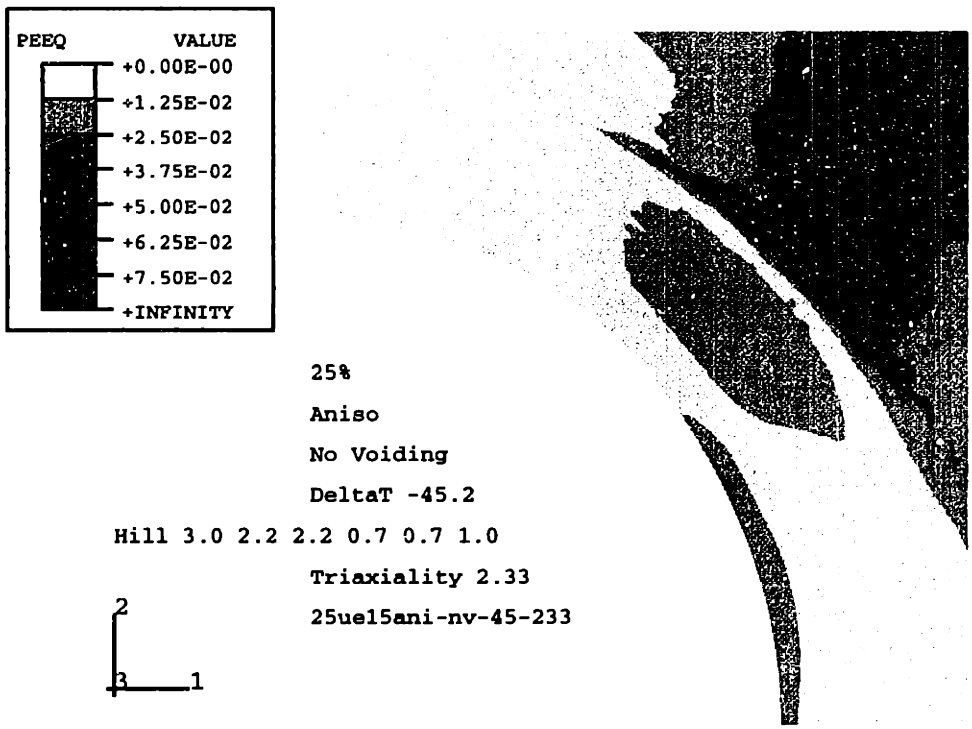

Figure 5-54d: 25ani-nv-45-233: Contour plots of ε^p_{equiv} at $\varepsilon_{zz} = 4.5\%$. $Cmax = 7.5\%$.

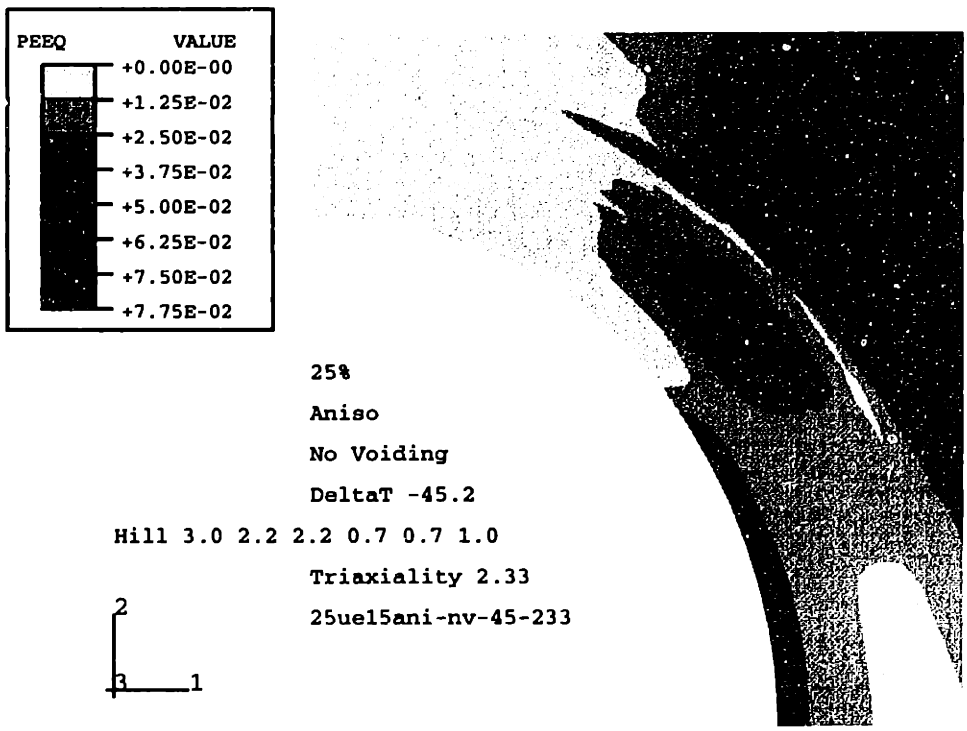

Figure 5-54e: 25ani-nv-45-233: Contour plots of ε^p_{equiv} at $\varepsilon_{zz} = 5.5\%$. $Cmax = 7.5\%$.

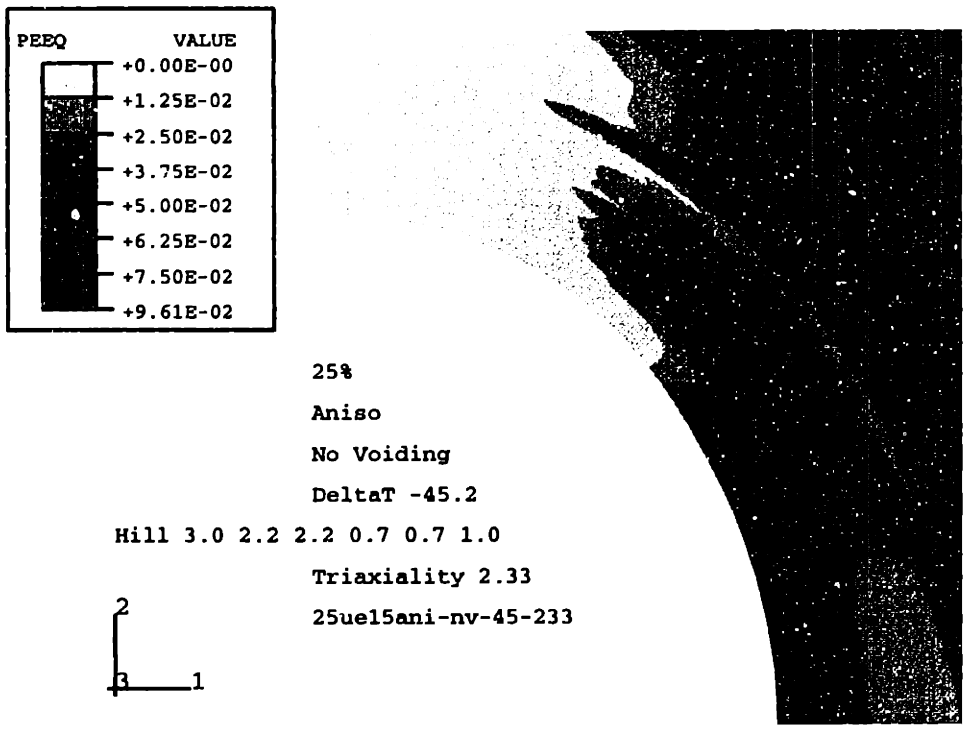

Figure 5-54f: 25ani-nv-45-233: Contour plots of ε^p_{equiv} at $\varepsilon_{zz} = 6.5\%$. $Cmax = 7.5\%$.

of macroscopic axial strain. Therefore no cavitation event is observed at $\Sigma = 0.33$. Figures 5-5a-f show the ε^p_{equiv} contour plots of the isotropic unit cell with a pre-existing cavity ("00") and figures 5-28a-f those for the non-cavitating case ("nv"), both under uniaxial tension. At $\varepsilon_{zz} = 1.5\%$ both simulations exhibit the typical plasticity patterns for their type of particle. The "00" case yields in the lower part of the matrix near the particle equator, and the "nv" matrix yields near the particle pole, as well as the upper right-hand corner of the unit cell. As the axial strain increases to 6.5%, the ε^p_{equiv} contour plots for the "00" case evolve as described in section 5.4 by spreading the plastic zone radially outward and axially upward. The maximum ε^p_{equiv} reaches 9.8% at $\varepsilon_{zz} = 6.5\%$. The ε^p_{equiv} contours of the "nv" case also spread out and ε^p_{equiv} finally reaches a maximum of 8.4%.

In the case of $\Sigma = 1.33$ the particle pressure reaches both $P_{cr} = -40MPa$ and $-55MPa$ within the limits of axial strain considered. Figures 5-38a-f, 5-55a-f, 5-56a-f and 5-30a-f are contour plots of ε^p_{equiv} for unit cells with a pre-existing cavity ("00"), with particles cavitating at $P_{cr} = -40MPa$ ("40") and at $-55MPa$ ("55"), and with

a non-cavitating particle ("nv"). The "40" particle cavitates at $\varepsilon_{zz} = 0.9\%$ at which the matrix is sitll fully elastic. The evolution of the plasticity in the "40" case is therefore identical to that of the "00" case. The axial cavitation strain for the "55" particle is 1.5%, which is just after matrix yield. The ε^p_{equiv} contour plots of the "00" and the "55" cases at $\varepsilon_{zz} = 1.5\%$ are very similar: both the location of the plastic zone and the magnitudes of ε^p_{equiv} are similar. The maximum ε^p_{equiv} is 3.5% for the "00" case and 3.4% for the "55" case. This is explained by the small amount of plastic deformation that has occured between matrix yield and particle cavitation in the "55" case. However, it also indicates that although the two simulations follow quite different evolutions in terms of their stress-strain curves, the resulting ε^p_{equiv} contour plots are nearly identical. The plastic deformation that occured between $\varepsilon_{zz} = 0.9\%$ and 1.5%, while the unit cell followed the "00" stress-strain curve is nearly identical to the plastic deformation that occured between $\varepsilon_{zz} = 1.4\%$ and 1.5% while the unit cell first followed the "nv" stress-strain curve and then dropped down to that of the "00" curve. At $\varepsilon_{zz} = 6.5\%$ the maximum ε^p_{equiv} is 34% for the "00" and "55" cases, and 7.8% in the unit cell with the non-cavitating particle.

Under a triaxiality of 2.33, the "40" particle cavitates at $\varepsilon_{zz} = 0.6\%$, and the "60" particle cavitates at $\varepsilon_{zz} = 1.2\%$. Since the unit cell with a particle intact yields at an axial strain of 1.7%, both cavitation events occure before matrix yield. See figures 5-57a-f, 5-58a-f and 5-31a-f. However, the unit cell with the pre-existing cavity yields at $\varepsilon_{zz} = 0.8\%$, so that the "60" unit cell experiences a drop from the stress-strain curve of the not-yet-yielded "nv" to that of the "00" case. As in the similar case under $\Sigma = 1.33$, the ε^p_{equiv} contour plots of the "00" and "60" cases are nearly identical at $\varepsilon_{zz} \geq 1.5\%$. The maximum ε^p_{equiv} reached at the end of the simulations ($\varepsilon_{zz} = 6.5\%$) are 35% for the case of the pre-existing cavity and the cavitated particles, and 7.2% in the case of the non-cavitating particle.

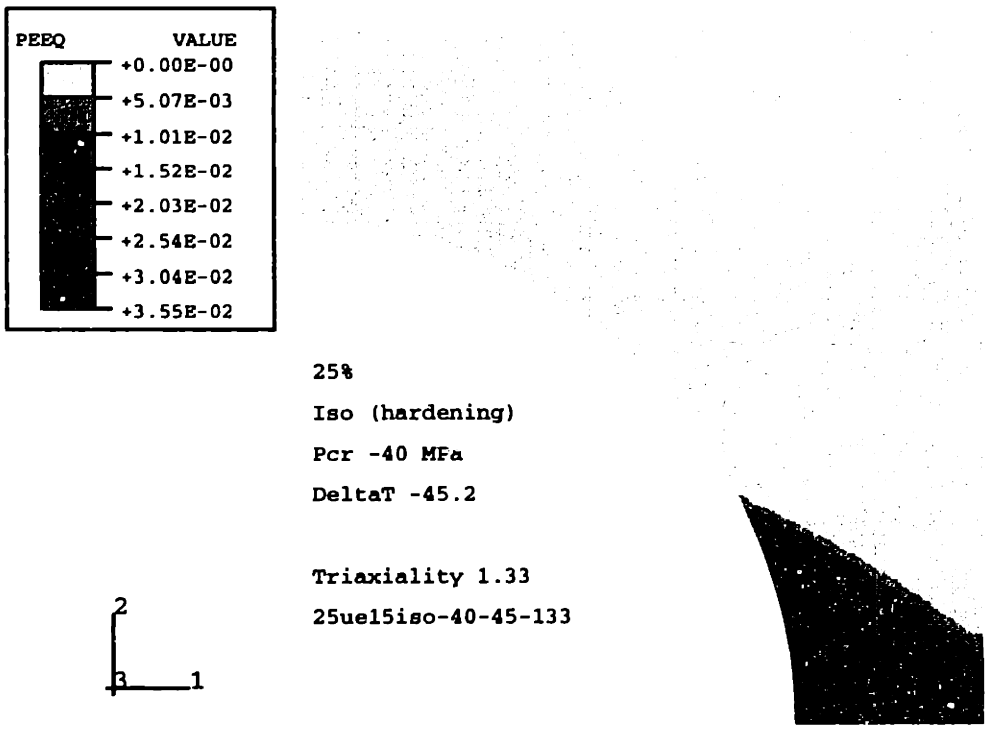

Figure 5-55a: 25iso-40-45-133: Contour plots of ε^{p}_{equiv} at $\varepsilon_{zz} = 1.5\%$.

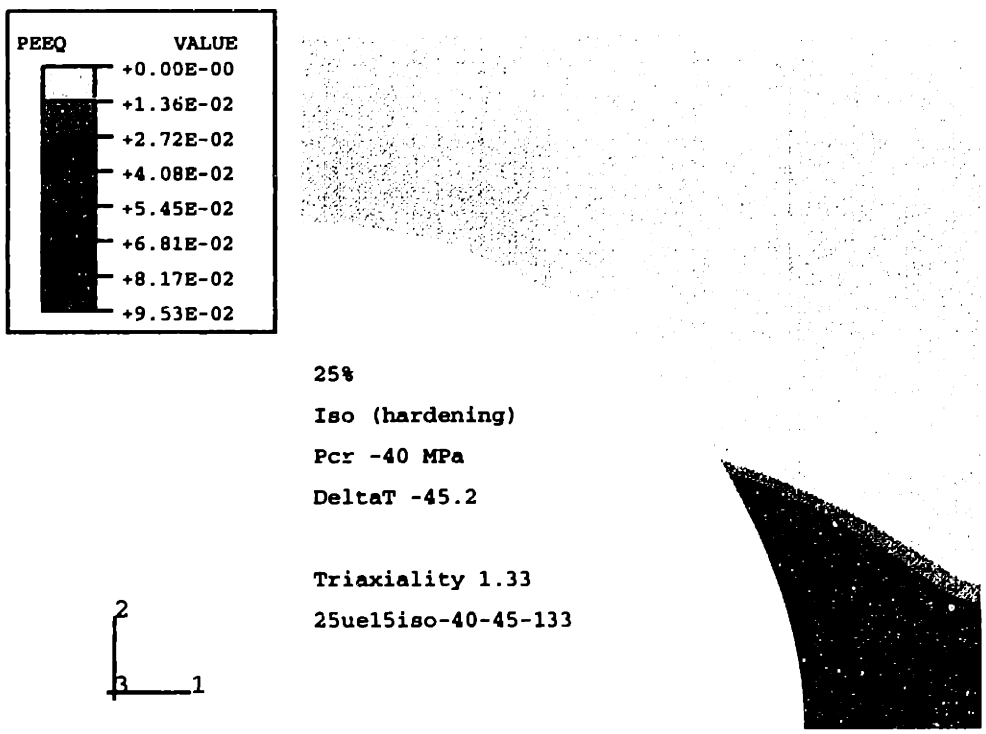

Figure 5-55b: 25iso-40-45-133: Contour plots of ε^{p}_{equiv} at $\varepsilon_{zz} = 2.5\%$.

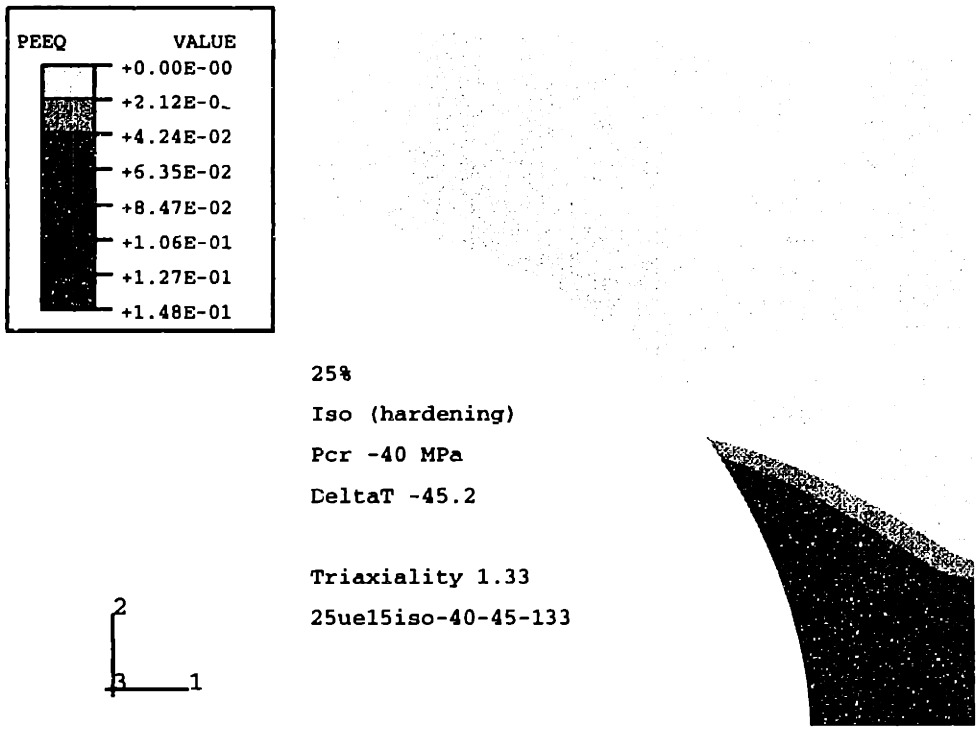

Figure 5-55c: 25iso-40-45-133: Contour plots of ε^p_{equiv} at $\varepsilon_{zz} = 3.5\%$.

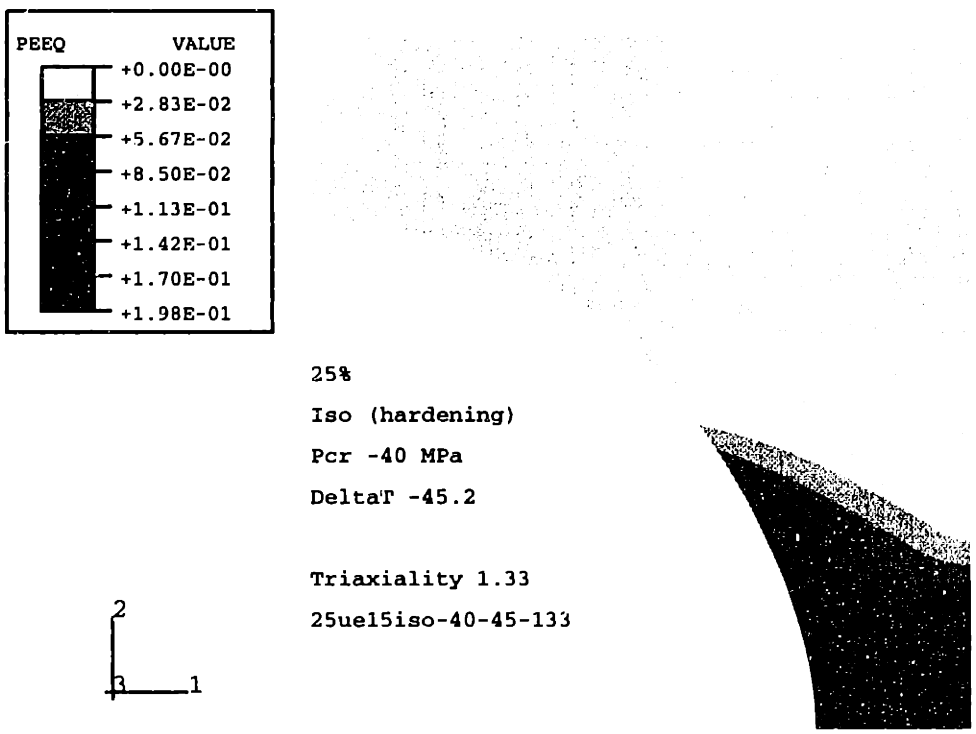

Figure 5-55d: 25iso-40-45-133: Contour plots of ε^p_{equiv} at $\varepsilon_{zz} = 4.5\%$.

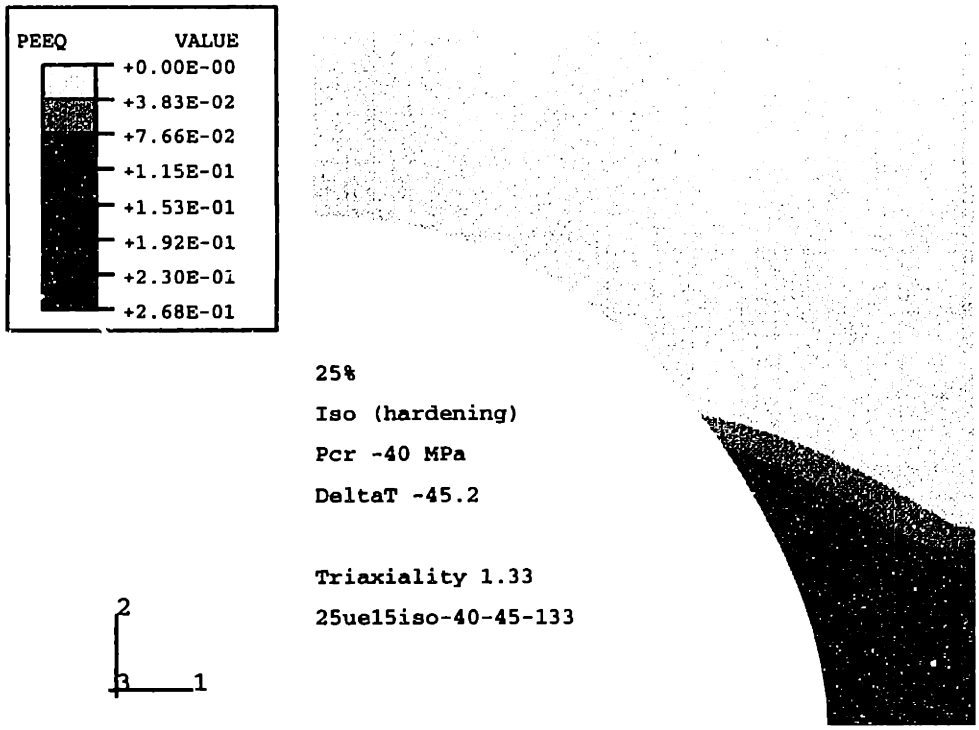

Figure 5-55e: 25iso-40-45-133: Contour plots of ε^p_{equiv} at $\varepsilon_{zz} = 5.5\%$.

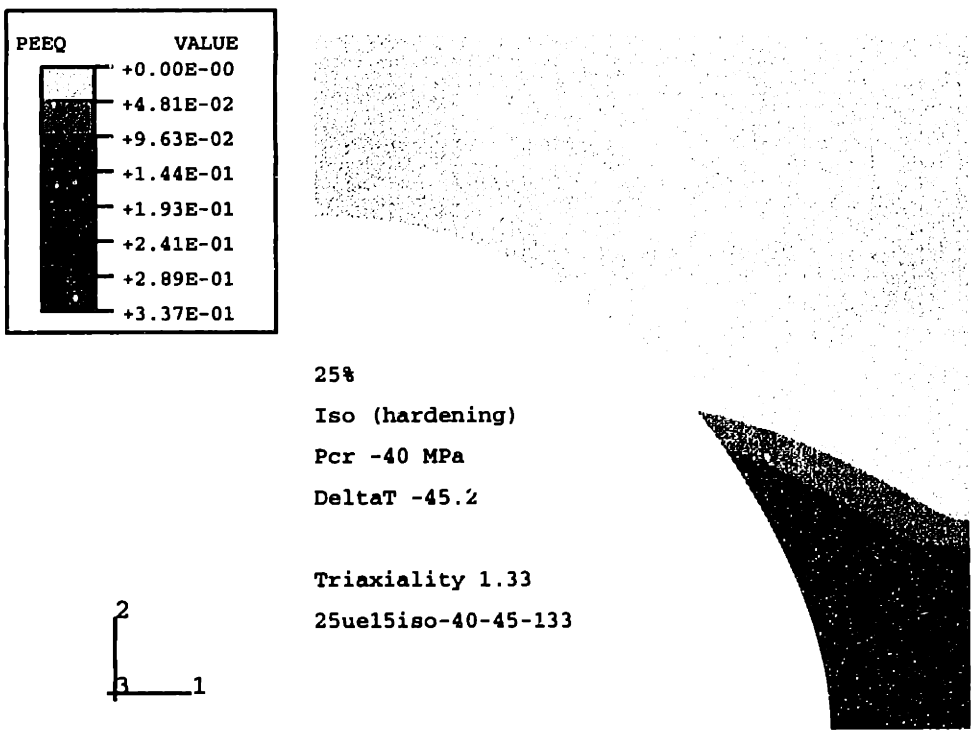

Figure 5-55f: 25iso-40-45-133: Contour plots of ε^p_{equiv} at $\varepsilon_{zz} = 6.5\%$.

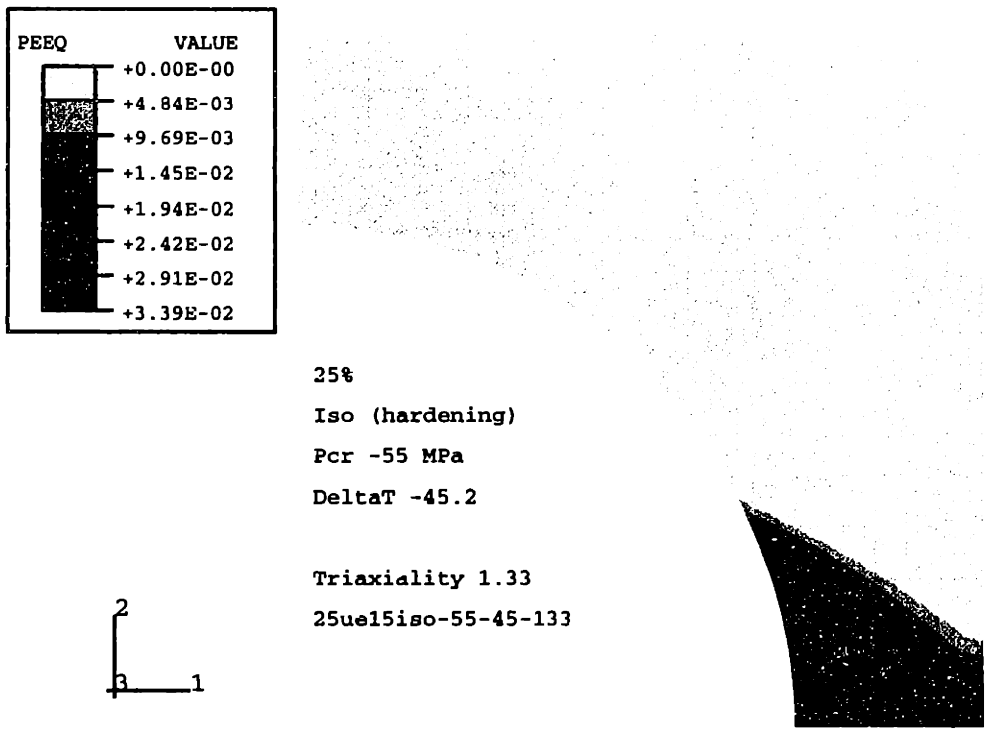

Figure 5-56a: 25iso-55-45-133: Contour plots of ε^p_{equiv} at $\varepsilon_{zz} = 1.5\%$.

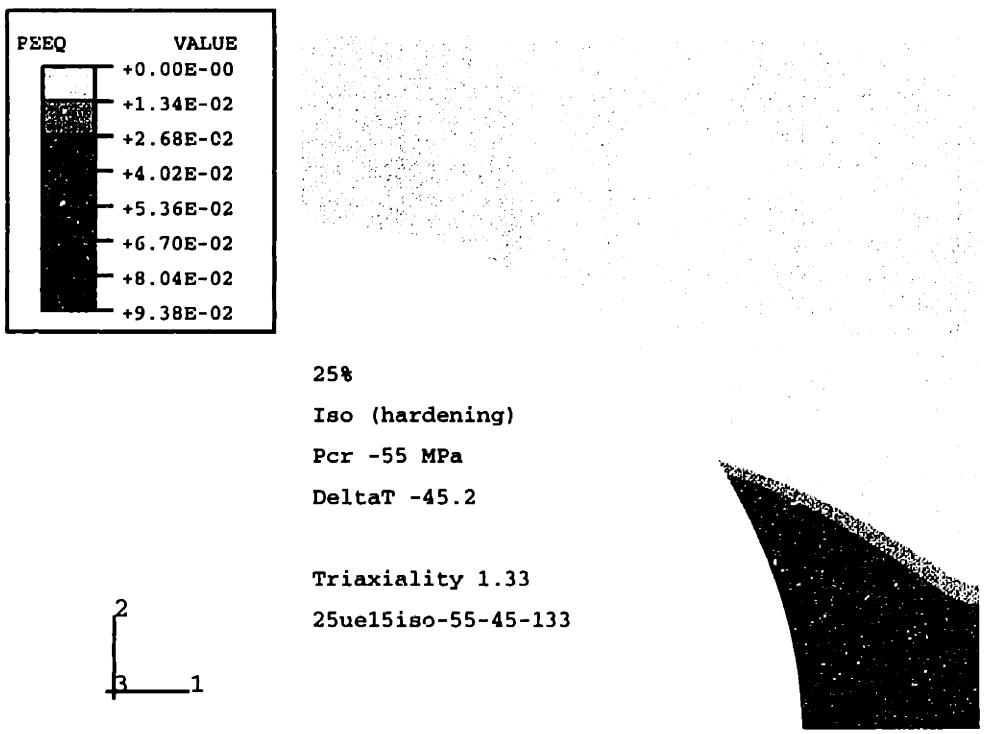

Figure 5-56b: 25iso-55-45-133: Contour plots of ε^p_{equiv} at $\varepsilon_{zz} = 2.5\%$.

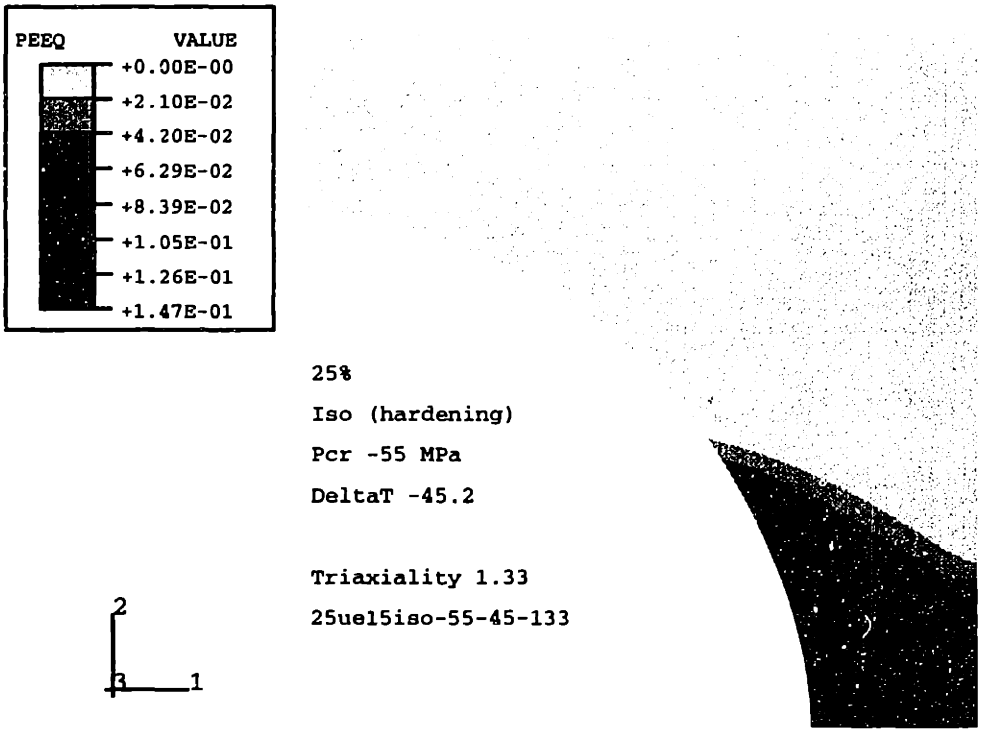

Figure 5-56c: 25iso-55-45-133: Contour plots of ε^{p}_{equiv} at $\varepsilon_{zz} = 3.5\%$.

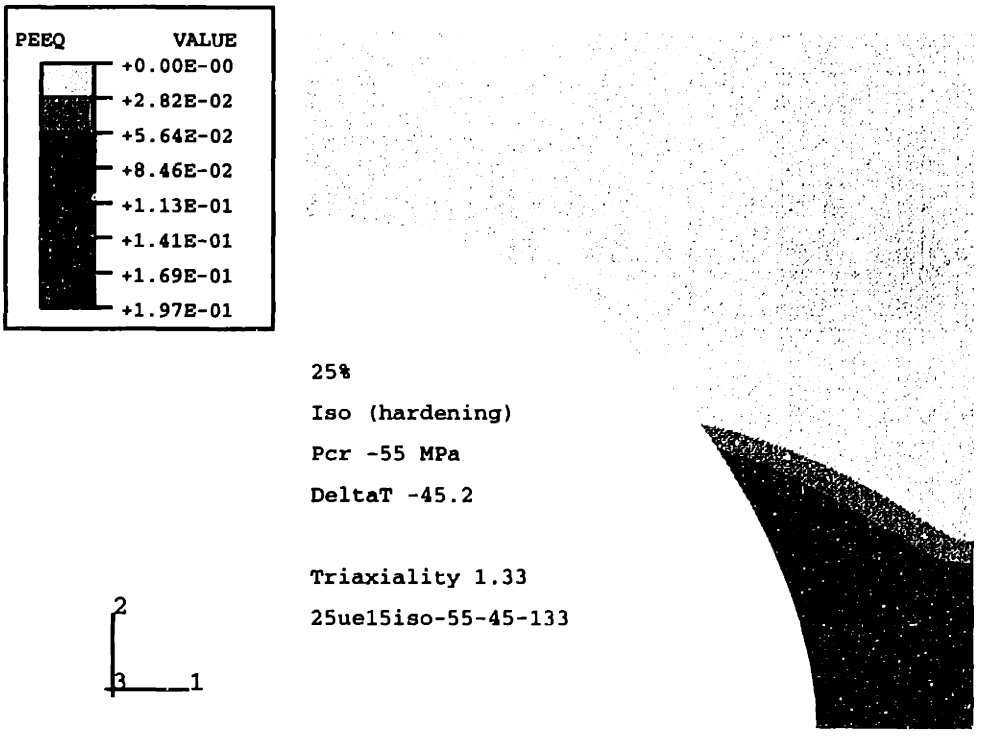

Figure 5-56d: 25iso-55-45-133: Contour plots of ε^{p}_{equiv} at $\varepsilon_{zz} = 4.5\%$.

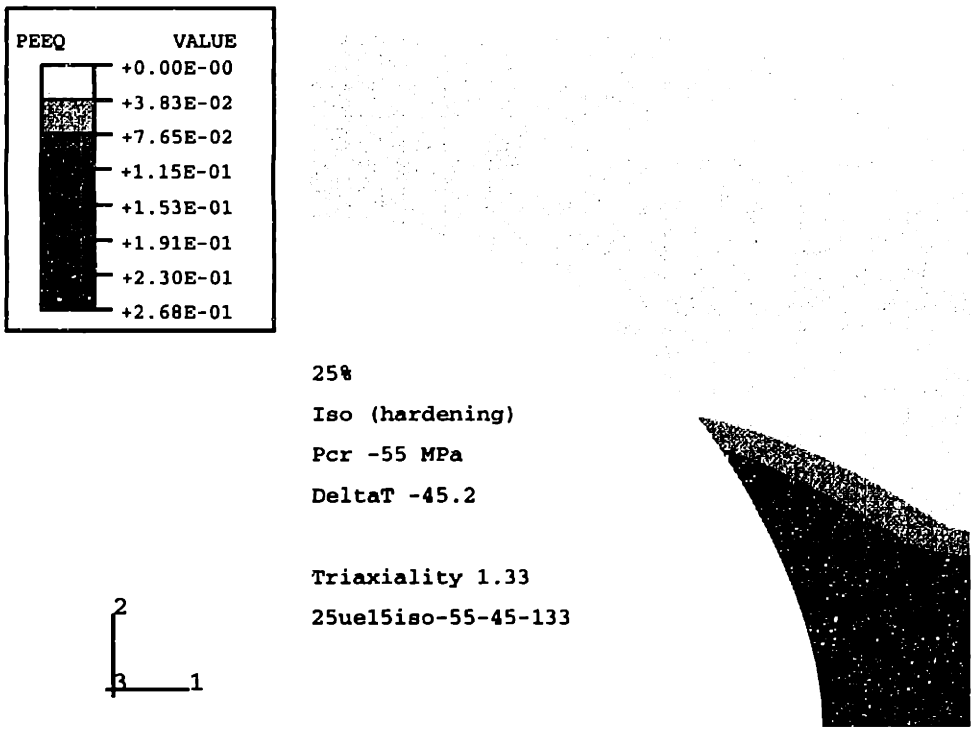

Figure 5-56e: 25iso-55-45-133: Contour plots of ε^{p}_{equiv} at $\varepsilon_{zz} = 5.5\%$.

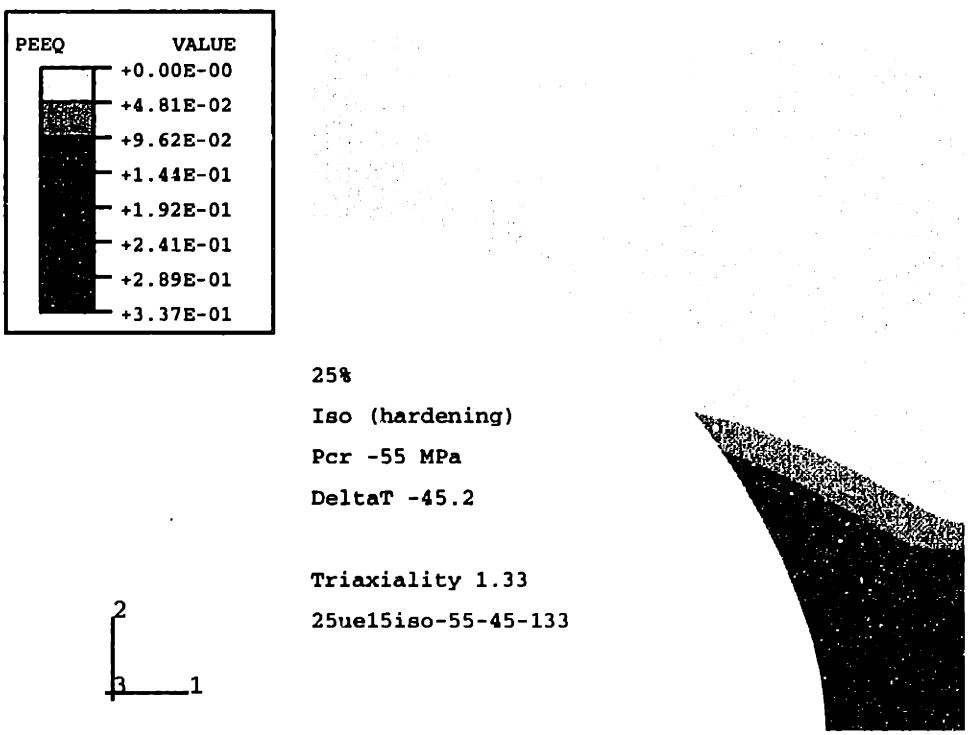

Figure 5-56f: 25iso-55-45-133: Contour plots of ε^{p}_{equiv} at $\varepsilon_{zz} = 6.5\%$.

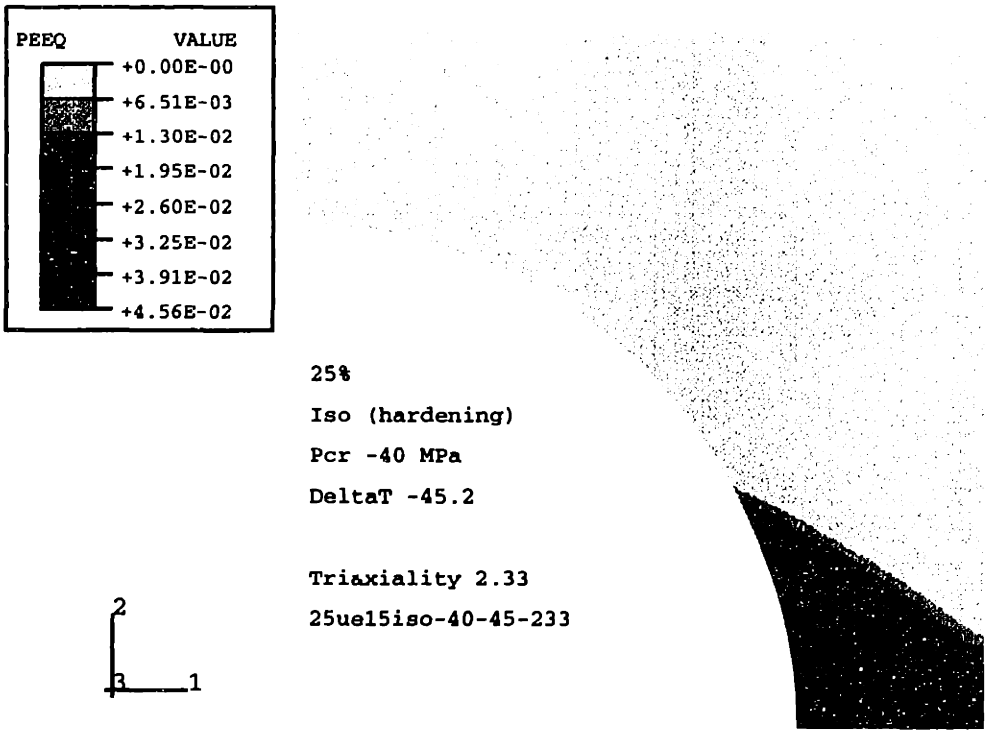

Figure 5-57a: 25iso-40-45-233: Contour plots of ε^{p}_{equiv} at $\varepsilon_{zz} = 1.5\%$.

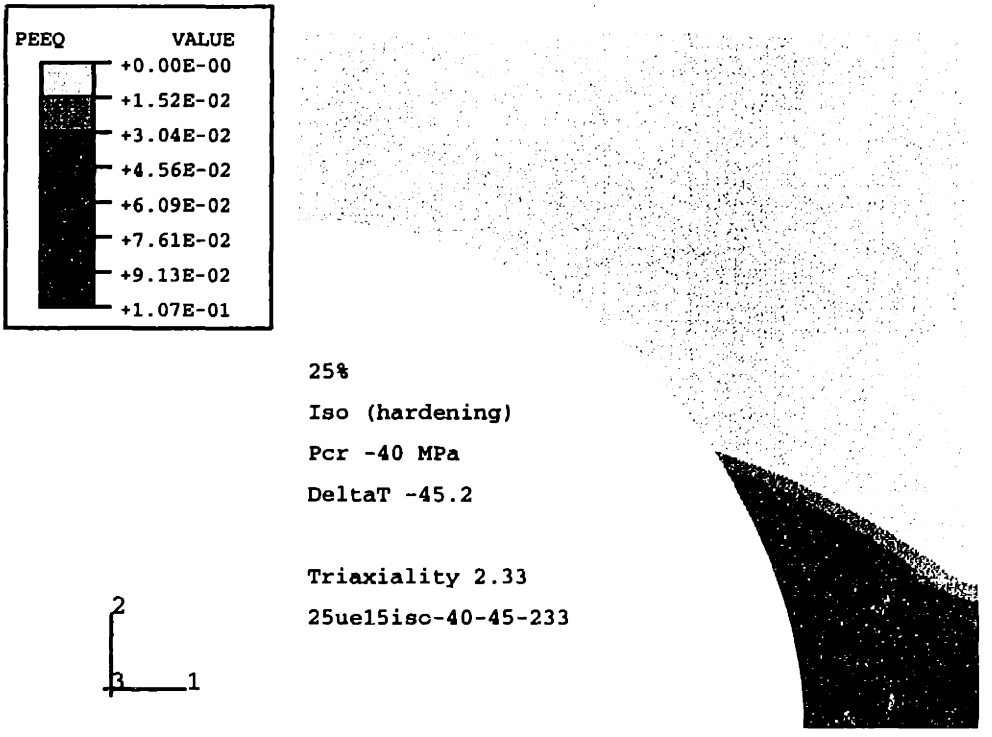

Figure 5-57b: 25iso-40-45-233: Contour plots of ε^{p}_{equiv} at $\varepsilon_{zz} = 2.5\%$.

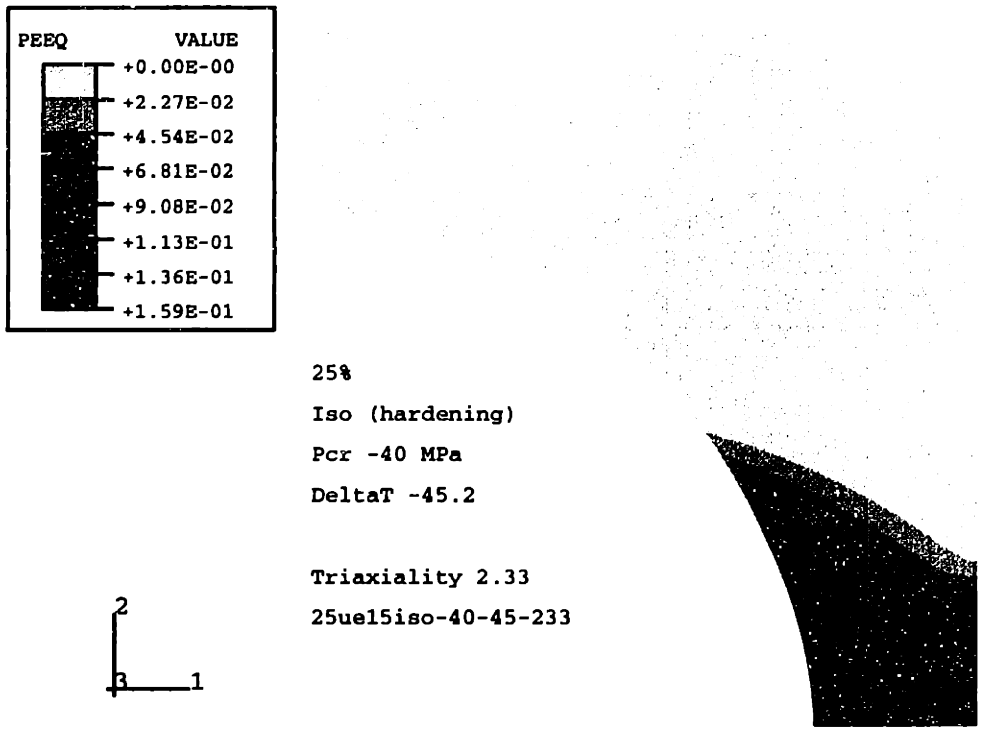

Figure 5-57c: 25iso-40-45-233: Contour plots of ε^p_{equiv} at $\varepsilon_{zz} = 3.5\%$.

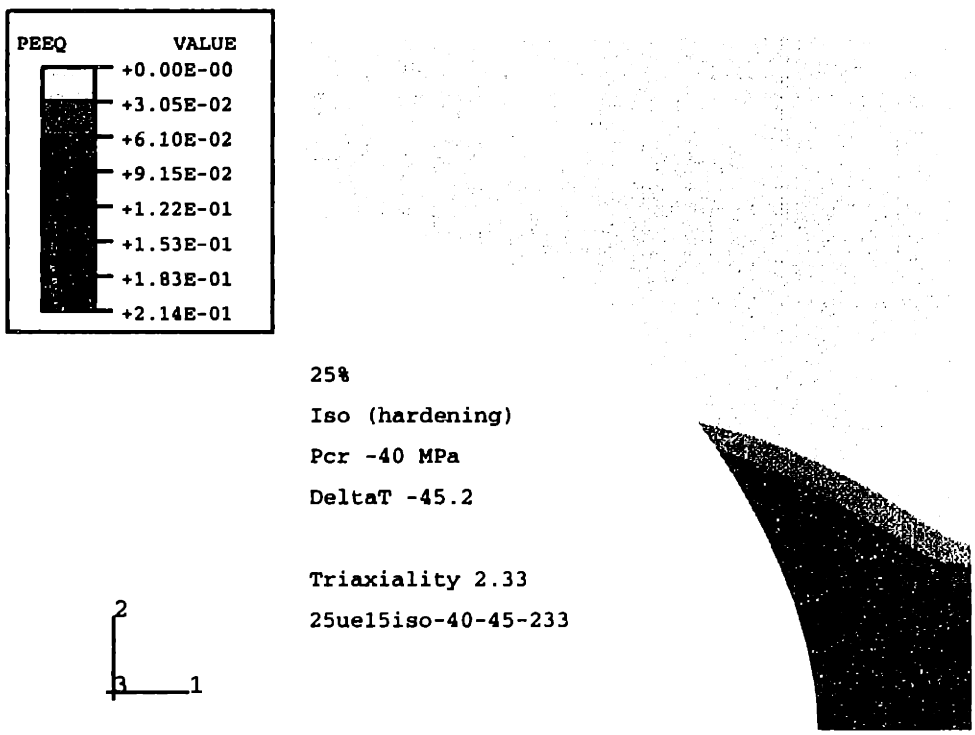

Figure 5-57d: 25iso-40-45-233: Contour plots of ε^p_{equiv} at $\varepsilon_{zz} = 4.5\%$.

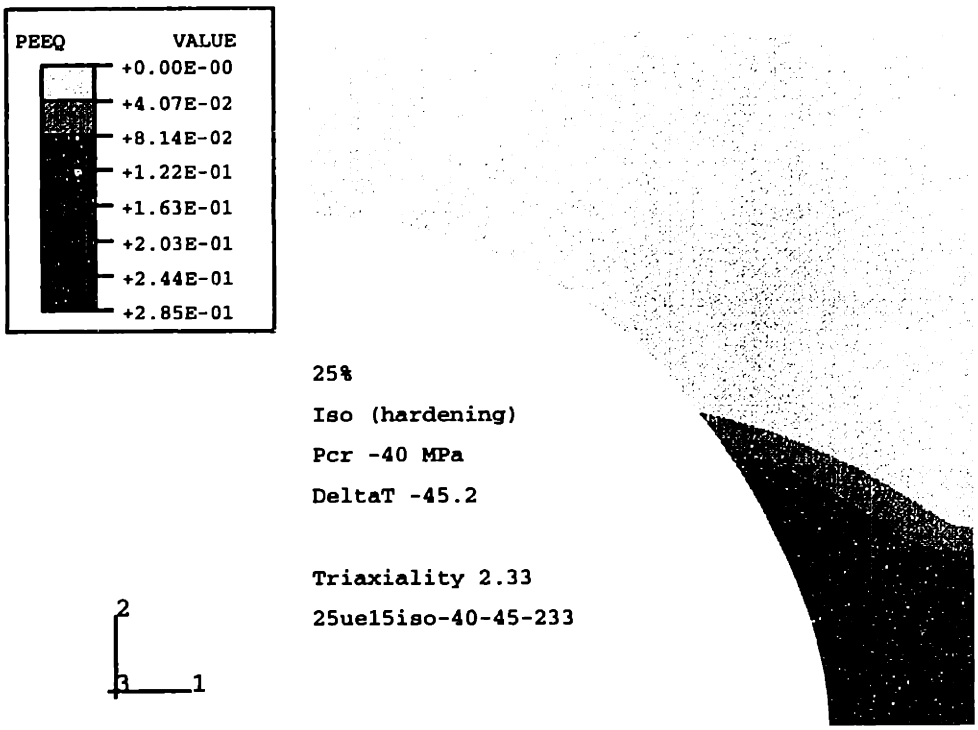

Figure 5-57e: 25iso-40-45-233: Contour plots of ε^p_{equiv} at $\varepsilon_{zz} = 5.5\%$.

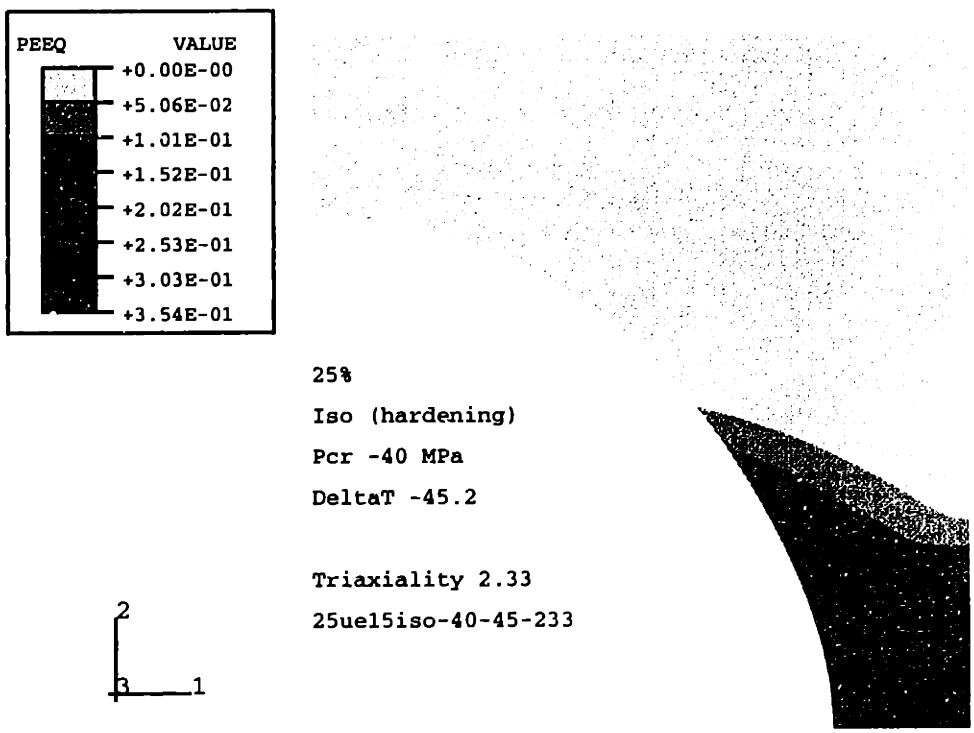

Figure 5-57f: 25iso-40-45-233: Contour plots of ε^p_{equiv} at $\varepsilon_{zz} = 6.5\%$.

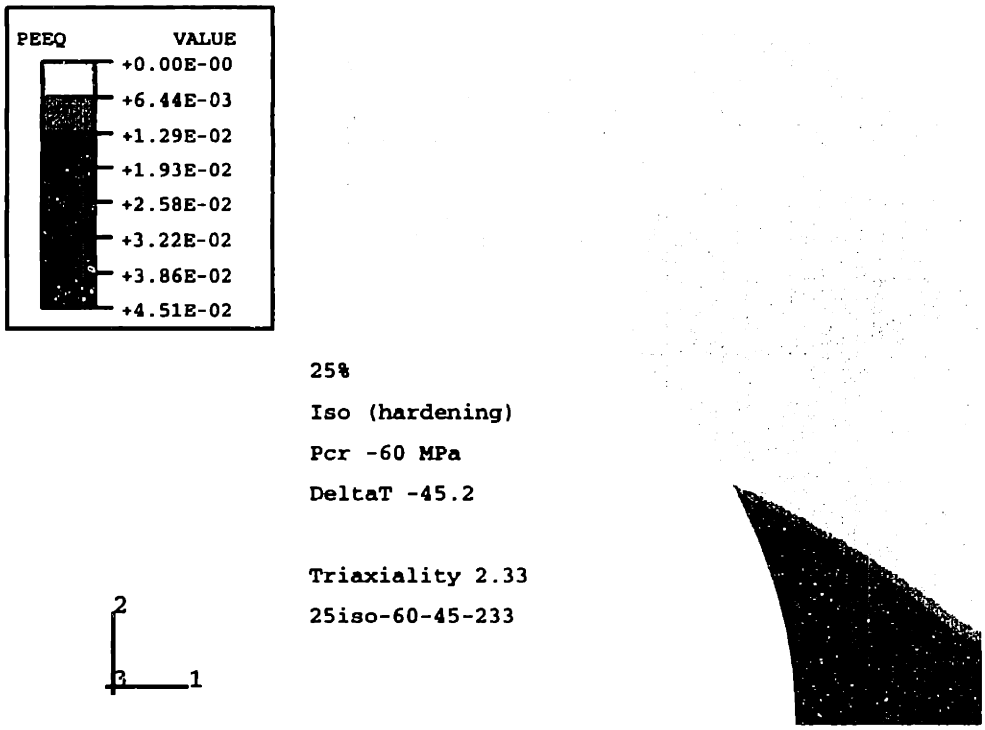

Figure 5-58a: 25iso-60-45-233: Contour plots of ε^p_{equiv} at $\varepsilon_{zz} = 1.5\%$.

Summary

Within the limits of a macroscopic axial strain of 6.5% and particle cavitation strengths of up to $-60MPa$, the effect on the matrix plasticity of varying the particle cavitation strength at fixed triaxiality is found to be very small. In many cases the particles are found to cavitate at a point in the deformation where very little or no plastic deformation has occurred in the matrix. In cases where the particles cavitate before matrix yield, the matrix plasticity is identical with that of the pre-existing cavity case. At $\varepsilon_{zz} = 6.5\%$ the difference between the maximum ε^p_{equiv} found in matrices with particles cavitating after matrix yield and that containing a cavity from the start is found to be smaller than one quarter of the maximum ε^p_{equiv} under the $\Sigma = 1.33$.

Large differences in equivalent plastic strain are observable between anisotropic matrices surrounding cavities and those containing non-cavitating particles. In the case of cavities, ε^p_{equiv} reaches levels more than 30 times the maximum ε^p_{equiv} of the non-cavitating particle case under $\Sigma = 2.33$. Under $\Sigma = 1.33$ this factor is on the order of 6, and for $\Sigma = 0.66$ it is approximately 2.5. In the unit cell under uniaxial

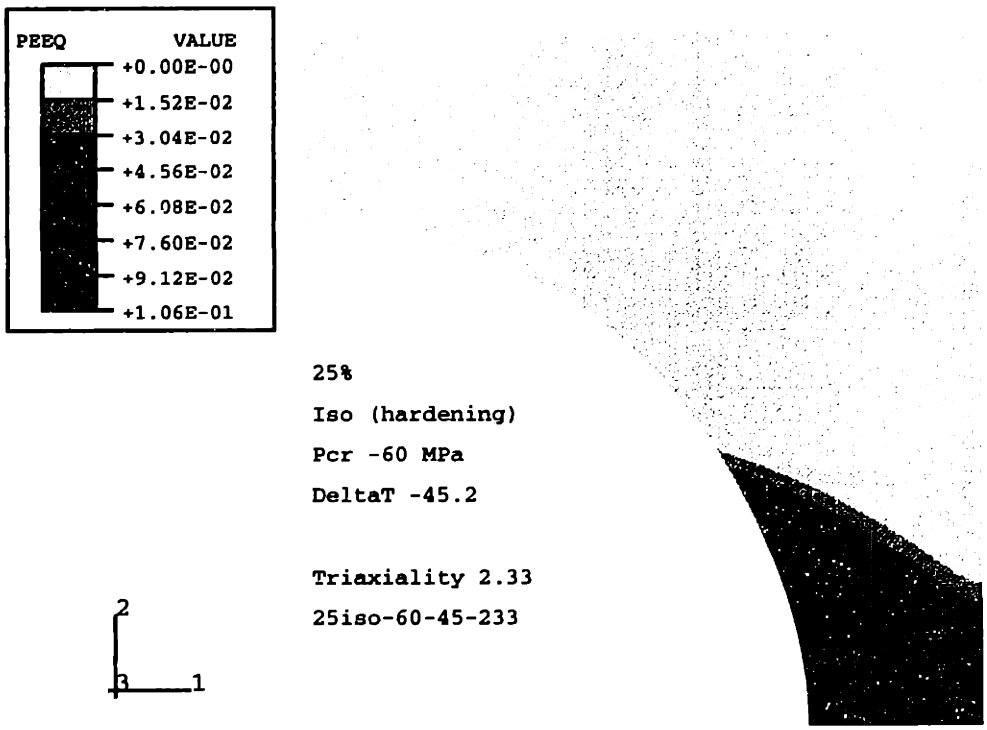

Figure 5-58b: 25iso-60-45-233: Contour plots of ε^p_{equiv} at $\varepsilon_{zz} = 2.5\%$.

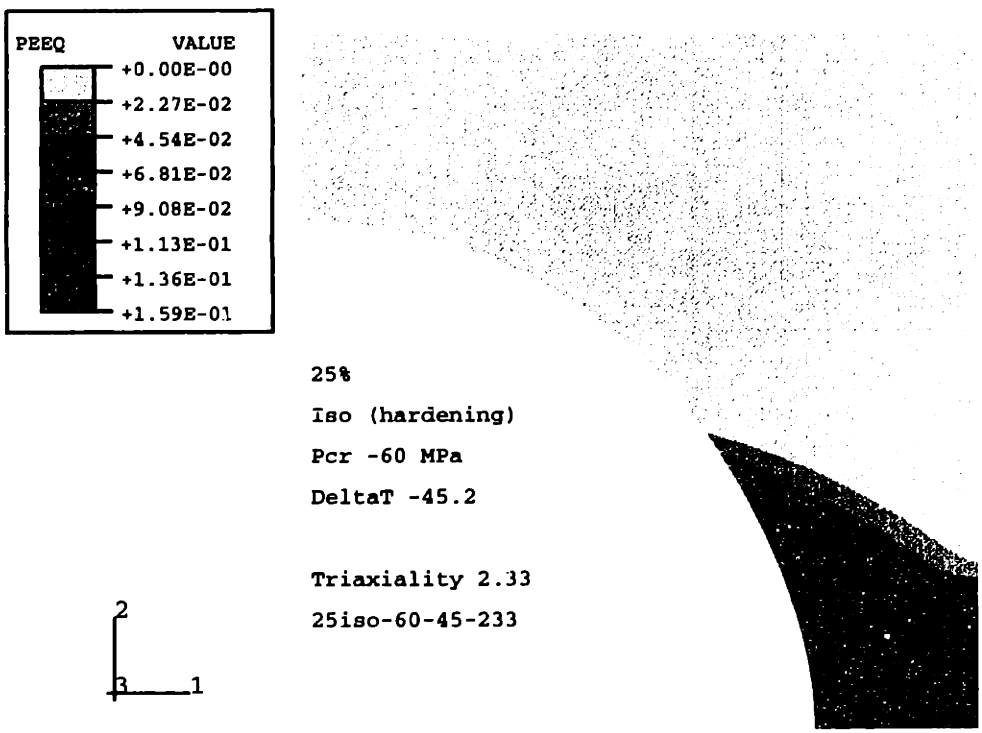

Figure 5-58c: 25iso-60-45-233: Contour plots of ε^p_{equiv} at $\varepsilon_{zz} = 3.5\%$.

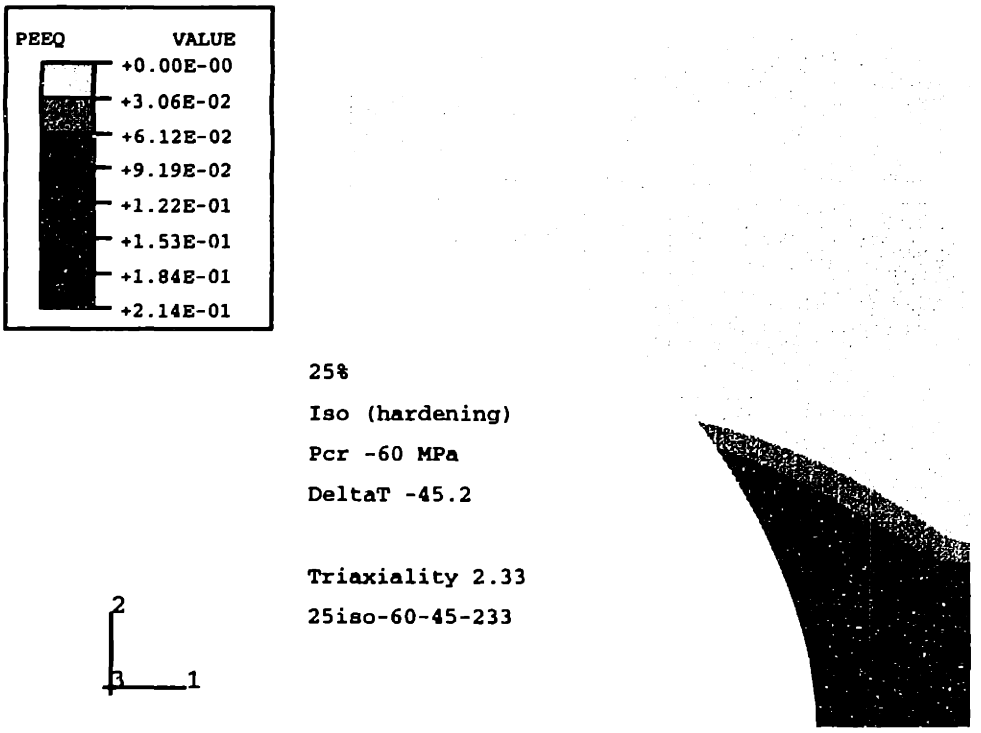

Figure 5-58d: 25iso-60-45-233: Contour plots of ε^p_{equiv} at $\varepsilon_{zz} = 4.5\%$.

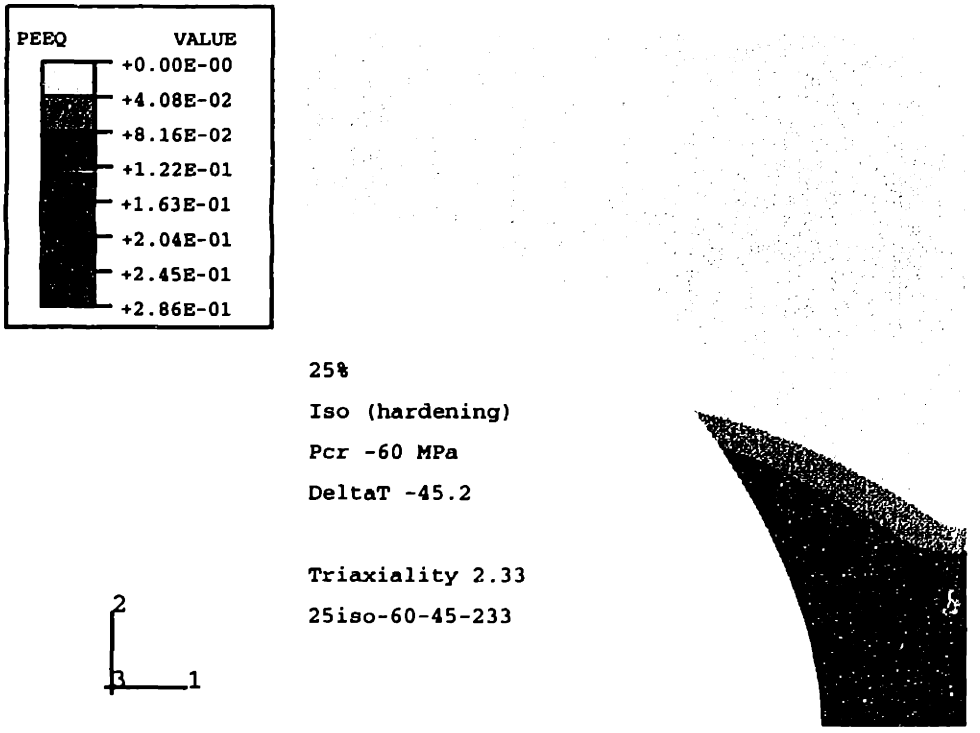

Figure 5-58e: 25iso-60-45-233: Contour plots of ε^p_{equiv} at $\varepsilon_{zz} = 5.5\%$.

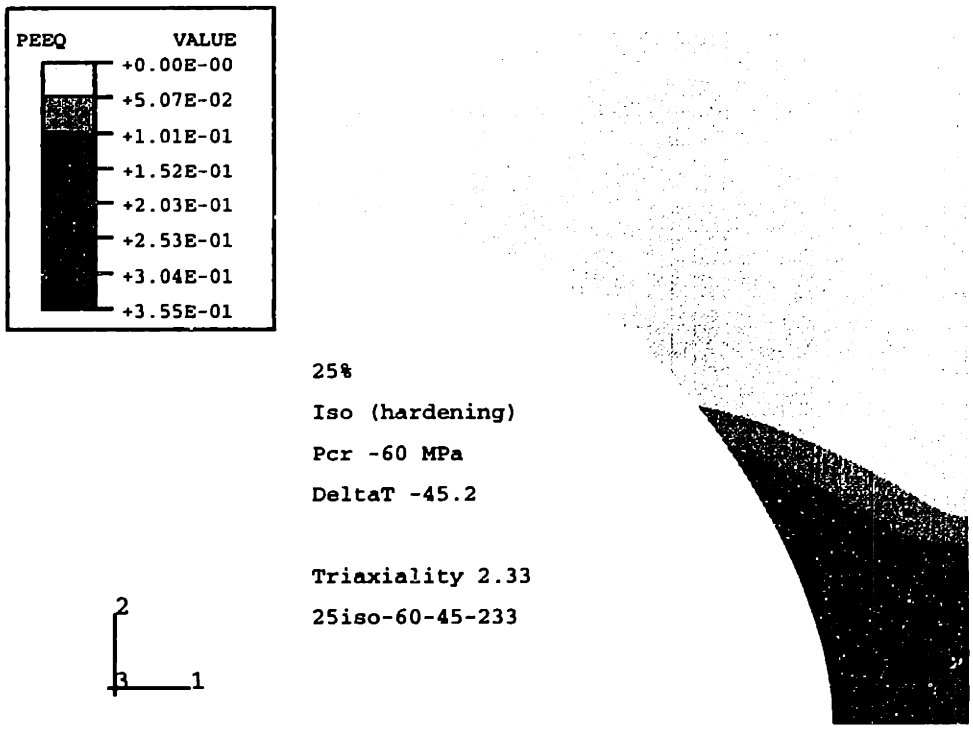

Figure 5-58f: 25iso-60-45-233: Contour plots of ε^{p}_{equiv} at $\varepsilon_{zz} = 6.5\%$.

tension this factor is on the order of 1.5.

5.5.4 Effect of Varying P_{cr} on the Yield Point of the Unit Cell

Comparing the yield points of anisotropic unit cells with cavities with that with non-cavitating particles at fixed triaxiality ratio, it is found that the unit cells with non-cavitating particles yield at ε_{zz} than those with cavities. The difference in ε^{y}_{zz} is on the order of 1% to 2%. Figure 5-40 shows a plot of ε^{y}_{zz} as a function of Σ.

The stresses at which the matrix yields, however, do not follow such a clear trend in the anisotropic case. At $\Sigma = 0.33$ and 0.66, σ^{y}_{zz} of the unit cells with cavities are approximately $2MPa$ or 8% higher than those of the unit cells with non-cavitating particles. At $\Sigma = 1.33$, σ^{y}_{zz} in the case of the non-cavitating particle is $3MPa$ or 6% higher than that in the case of the hollow cavity. Under $\Sigma = 2.33$, σ^{y}_{zz} in the case of the non-cavitating particle is $15MPa$ or 25% higher than in the case of the hollow cavity. See figure 5-41.

5.5.5 Summary

The above results show that relative to their macroscopic stress-strain response and their matrix plasticity, the undertaken simulations can be grouped into those where the unit cell contains either a cavitating particle or a pre-existing cavity, and those where the unit cell contains a non-cavitating particle. The simulations where the anisotropic unit cell contains a pre-existing cavity or a cavitating particle are characterized by a strong localization of matrix plasticity in shear bands and a much smaller level of macroscopic stress than that sustained by a unit cell containing a non-cavitating particle.

The level of negative pressure at which the particle cavitates is found to have an insignificant effect on the unit cell's stress-strain response and its matrix plasticity.

Whether the particle cavitates within the limitations of the chosen parameters depends on the particle's cavitation strength and the triaxiality ratio. Under uniaxial tension particles with strengths more negative than $P_{cr} = -30MPa$ do not cavitate at axial strains of up to 6.5%. In the case of $\Sigma = 2.33$, particles of $P_{cr} \geq -60MPa$ (less negative than $-60MPa$) cavitate at axial strains at which little or no plastic deformation has occurred in the matrix. The cases in which the particle cavitation strength has any significant effect are therefore limited to unit cells where the particles have a cavitation strength that is high enough for the cavitation to occur after matrix yield and that is low enough for the particle to yield before the macroscopic stress of the unit cell reaches levels at which the composite might fail in a brittle mode. In the simulations that were performed, such a case did not arise.

In preliminary studies of anisotropic and isotropic unit cells under simple tension it was shown that a particle with a cavitation strength on the order of $-10MPa$ or less does not have any significant effect on the matrix plasticity or the unit cell's stress-strain response, even for ε_{zz} of up to 30%.

At high triaxialities, if the particle has a cavitation strength of $-60MPa$ or less (less negative), it cavitates when the unit cell has undergone such low levels of axial strain that only small amounts of plastic deformation have occurred in the matrix.

The unit cell containing the cavitating particle therefore behaves very much like a unit cell with a cavity from the start.

5.6 Effect of Matrix Properties: Anisotropic vs. Isotropic

In this section the influence that the change from isotropic to anisotropic matrix properties has on the behavior of the unit cell will be discussed. As introduced in chapter 4, the choice of an either fully anisotropic or fully isotropic matrix is a simplified model of the behavior of a semi-crystalline matrix surrounding a heterogeneity, and the changes in the degree of crystallinity that occur when the inter-particle distance is varied.

5.6.1 Effect of Changing the Matrix Properties on the Yield Point of the Unit Cell

Figures 5-59 and 5-61 are plots of the macroscopic axial strain ε_{zz} at which the matrix yielding occurs as a function of triaxial loading condition Σ. Figures 5-60 and 5-62 are the corresponding plots of σ^y_{zz} vs. Σ.

Figure 5-59 shows how in the case of a pre-existing cavity the strain at which the anisotropic matrix yields $\varepsilon^y_{zz,ani}$ is smaller than that at which the isotropic matrix yields $\varepsilon^{y,iso}_{zz}$ under simple tension, with $\varepsilon^y_{zz,iso} - \varepsilon^y_{zz,ani} = 0.5\%$. At $\Sigma \geq 0.66$, $\varepsilon^y_{zz,ani} > \varepsilon^y_{zz,iso}$ where $\varepsilon^y_{zz,ani} - \varepsilon^y_{zz,iso}$ increases with Σ. The difference $\varepsilon^y_{zz,ani} - \varepsilon^y_{zz,iso}$ is 0.1%, 0.3% and 0.6% for $\Sigma = 0.66, 1.33$ and 2.33, respectively. The corresponding σ^y_{zz} confirm this trend. Under simple tension, $\sigma^y_{zz,ani} < \sigma^y_{zz,iso}$, whereas at $\Sigma \geq 0.66$, $\sigma^y_{zz,ani} > \sigma^y_{zz,iso}$. The differences in macroscopic yield stress increases from $9MPa$ inder simple tension to $-24MPa$ under $\Sigma = 2.33$.

The yield point of unit cells with pre-existing cavities is found to be very sensitive relative to the choice of matrix properties. Whereas $\varepsilon^y_{zz,ani}$ and $\sigma^y_{zz,ani}$ increase with increasing Σ, $\varepsilon^y_{zz,iso}$ and $\sigma^y_{zz,iso}$ show the opposite trend. Under simple tension, ε^y_{zz} and σ^y_{zz} can be depressed by switching from an isotropic to an anisotropic matrix, where as for $\Sigma \geq 0.66$ the reverse is true.

In the case of unit cells with coherent (non-cavitating) particles (figures 5-61 and 5-

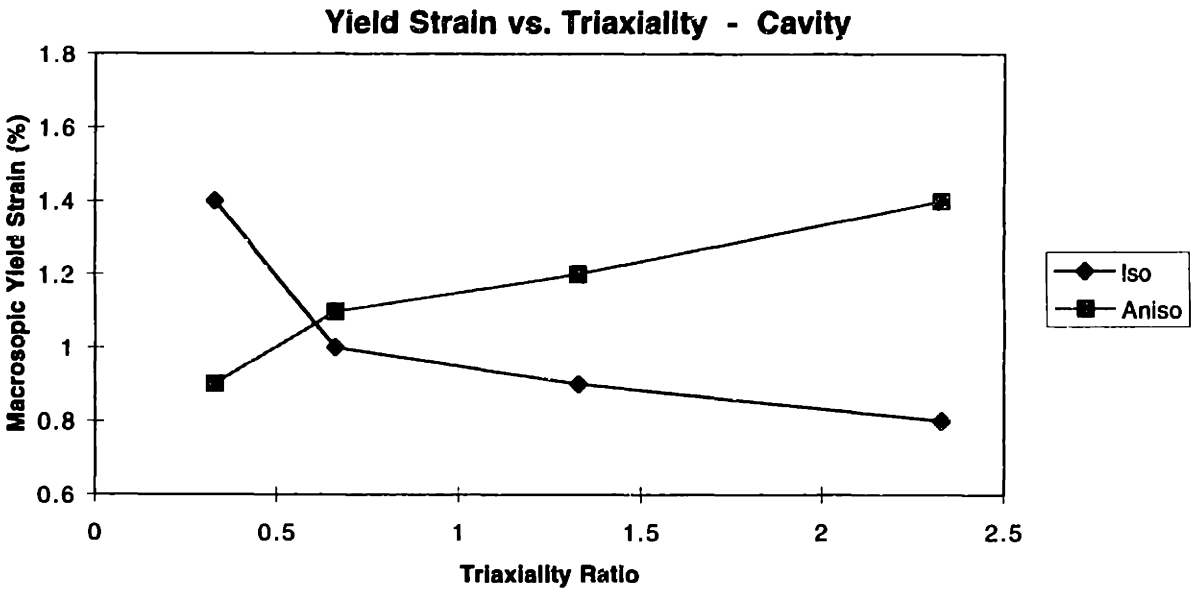

Figure 5-59: Anisotropic vs. isotropic matrix: macroscopic yield strain ε_{zz}^{y} as function of Σ. Pre-existing cavity.

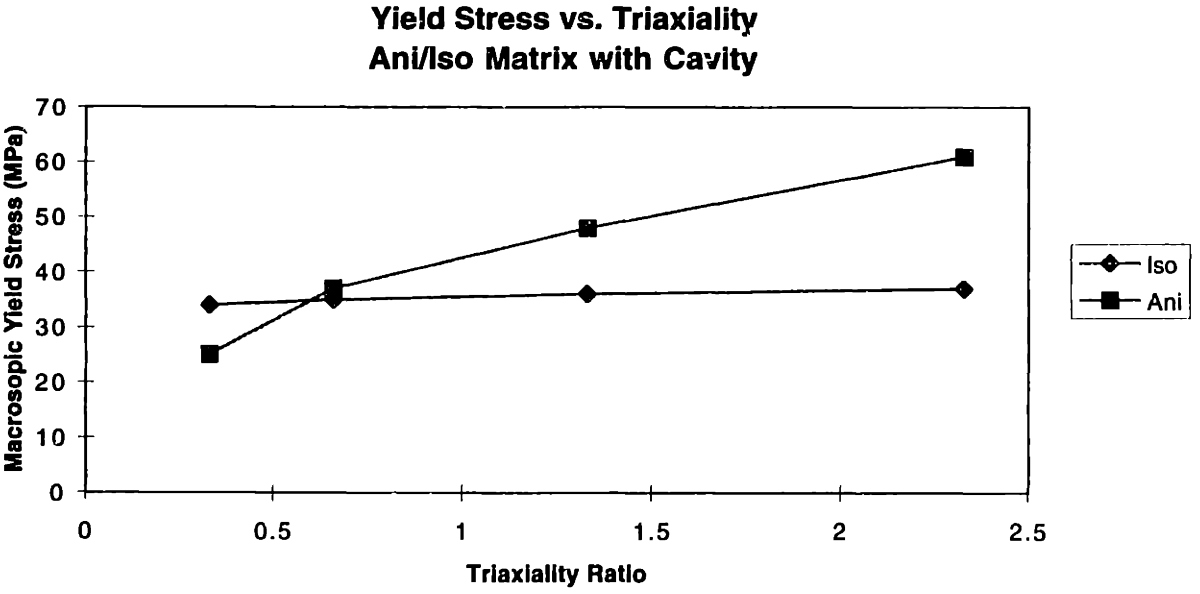

Figure 5-60: Anisotropic vs. isotropic matrix: macroscopic yield stress σ_{zz}^{y} as function of Σ. Pre-existing cavity.

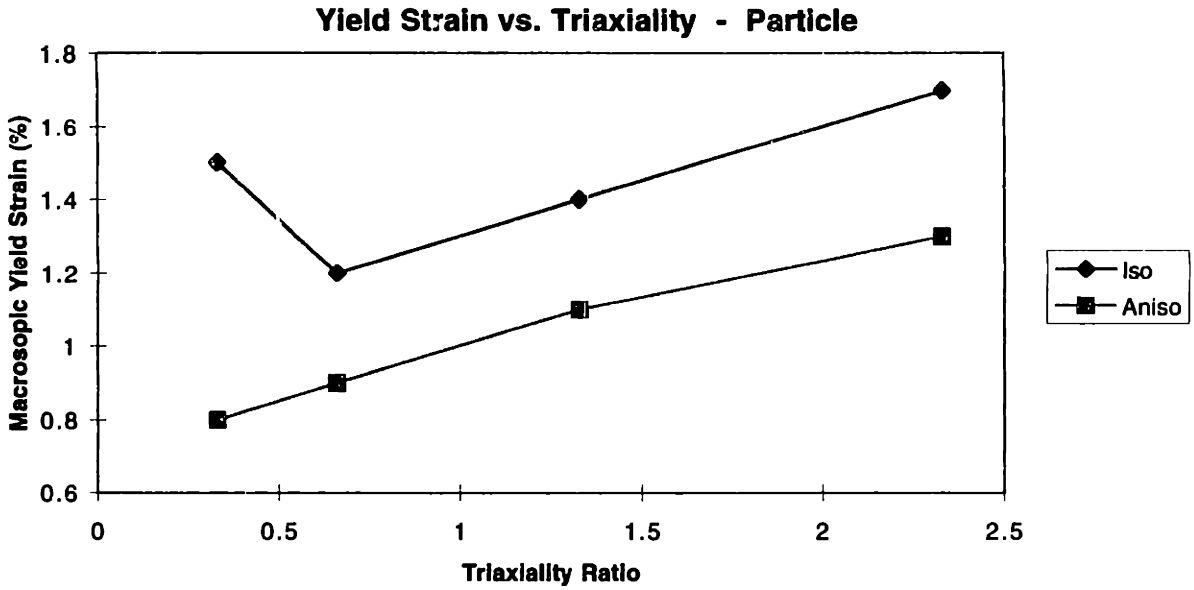

Figure 5-61: Anisotropic vs. isotropic matrix: macroscopic yield strain ε^y_{zz} as function of Σ. Coherent particle.

62), the anisotropic matrix is found to yield at lower ε_{zz} than the isotropic matrix. The difference varies from $\varepsilon^y_{zz,iso} - \varepsilon^y_{zz,ani} = 0.7\%$ under simple tension to a near constant 0.3% and 0.4% for $\Sigma \geq 0.66$. The yield stress σ^y_{zz} follows a somewhat similar trend, in that the initial difference between the yield stresses of the two matrices $\sigma^y_{zz,iso} - \sigma^y_{zz,ani}$ is $14MPa$ under simple tension, drops to $-2MPa$ at $\Sigma = 0.66$, and then increases to $15MPa$ and $26MPa$ at $\Sigma = 1.33$ and 2.33 respectively. With the exception of the case of simple tension, the unit cells with the two matrix properties both exhibit similar dependencies on Σ.

5.6.2 Effect of Changing the Matrix Properties on the Macroscopic Stress-Strain Response of Unit Cell with a Pre-Existing Cavity

Figures 5-63a through 5-66a are plots of macroscopic axial true stress σ_{zz} as a function of macroscopic true axial strain ε_{zz}. Each figure contains the plots of a unit cell with an anisotropic matrix and that of an isotropic matrix under the same triaxial loading condition and with a pre-existing cavity.

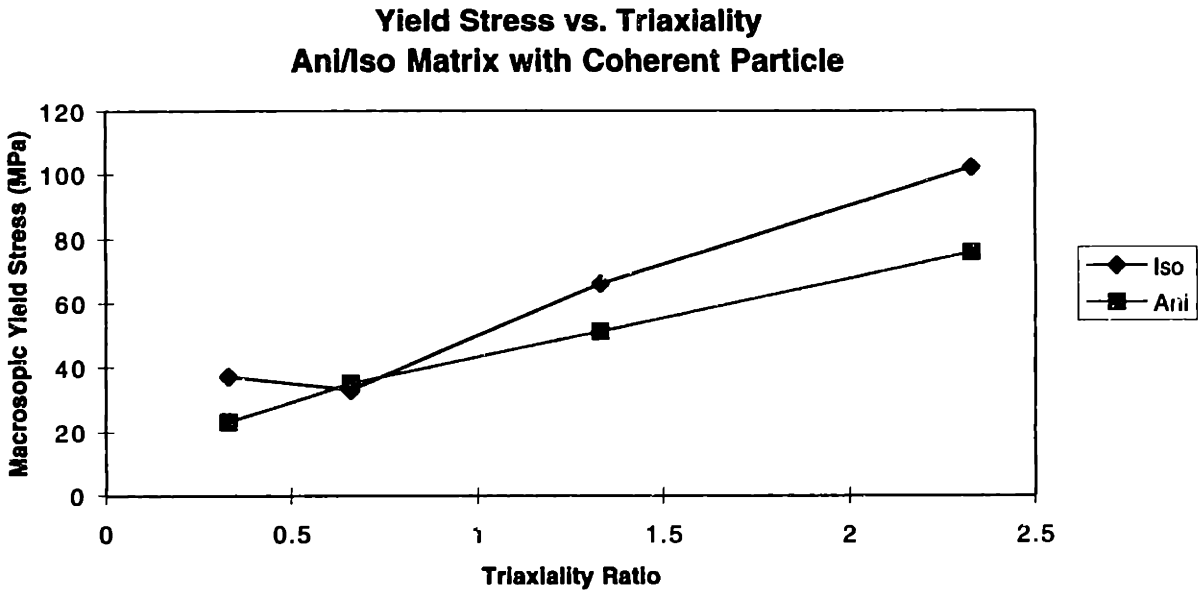

Figure 5-62: Anisotropic vs. isotropic matrix: macroscopic yield stress σ_{zz}^{y} as function of Σ. Coherent particle.

Up to the yield point of the matrix the stress-strain response of the unit cells is independent of the matrix properties, since the anisotropy of the matrix model is limited to its plastic regime. The general trend observed in the stress-strain plots after matrix yield is the larger stress reached in the unit cells with anisotropic matrices. The ratio of axial stress of the anisotropic matrix to that of the isotropic matrix $\sigma_{zz}^{ani}/\sigma_{zz}^{iso}$ at $\varepsilon_{zz} = 5\%$ is on the order of 1.3 under simple tension (figure 5-63a), increases to 1.5 for $\Sigma = 0.66$ (figure 5-64a) and to 1.9 in the case of 1.33 triaxiality (figure 5-65a). At very high triaxiality ($\Sigma = 2.33$, figure 5-66a) the maximum of this ratio is observed at $\varepsilon_{zz} = 2.7\%$ with a value of over 2.2. However, the drop-off in σ_{zz} decreases the ratio of $\sigma_{zz}^{ani}/\sigma_{zz}^{iso}$ to 1.3 at $\varepsilon_{zz} = 5\%$.

Compared to the isotorpic matrix, the anisotropic matrix exhibits a large capacity to harden under tensile deformation. Whereas the axial stress increases only very lightly after yield in the isotropic matrix, it continues to increase in the anisotropic matrix. The stress-strain plot of the 2.33 triaxiality case suggests that the anisotropic matrix has the ability to harden until some condition is satisfied that then allows for increased plastic deformation and a load drop. A mechanistical explanation can be developed from the observation that the spherical texture orientation of the anisotropy

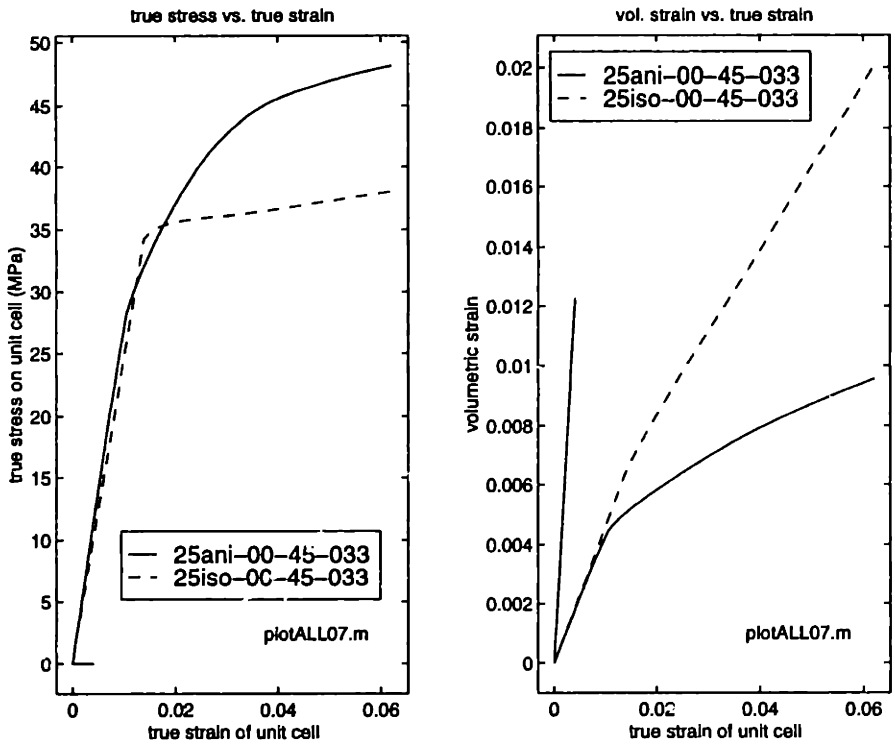

Figure 5-63: 25xxx-00-45-033: (a) macroscopic axial true stress σ_{zz} and (b) cell volumetric strain Ψ as function macroscopic true axial strain ε_{zz}. $\Sigma = 0.33$. Cavity.

is not allowed to evolve during the deformation. It therefore requires some critical level of axial straining to allow for the initiation of additional deformation mechanism than the initially observed shear bands. This is discussed below.

5.6.3 Effect of Changing the Matrix Properties on the Macroscopic Stress-Strain Response of Unit Cell with a Non-Cavitating Particle

Figures 5-67a through 5-70a are plots of macroscopic axial true stress σ_{zz} as a function of macroscopic true axial strain ε_{zz}. Each figure contains the plots of a unit cell with an anisotropic matrix and that of an isotropic matrix under the same triaxial loading condition and with a non-cavitating particle.

The general trend of a higher macroscopic axial true stress in unit cells with anisotropic matrices that was observed for cavities is also found to be true for solid particles. The ratio of axial stress of the anisotropic cell σ_{zz}^{ani} to that of the isotropic

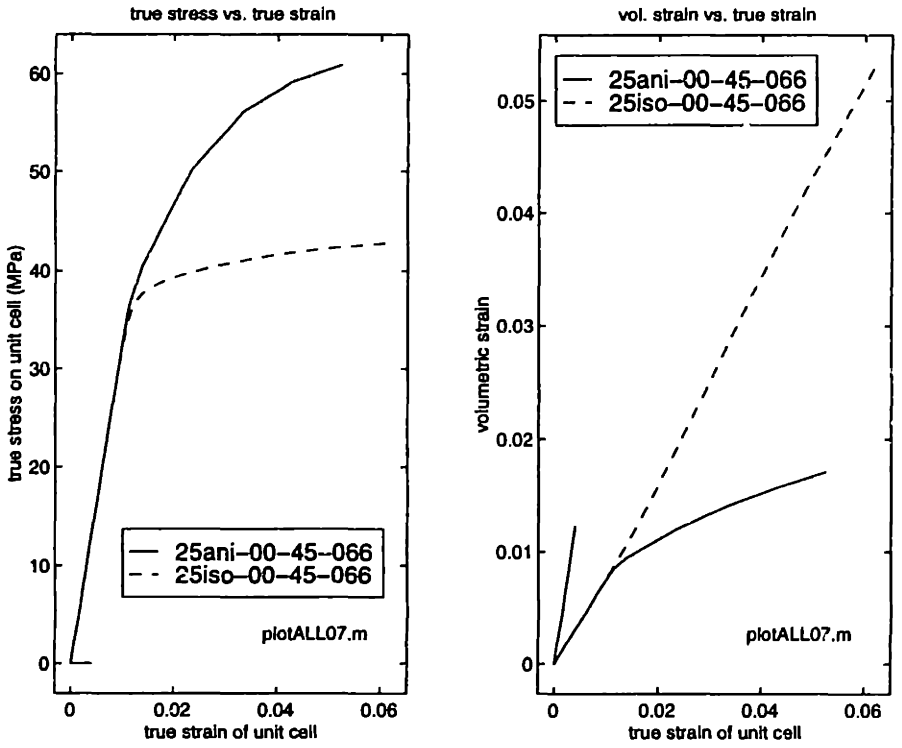

Figure 5-64: 25xxx-00-45-066: (a) macroscopic axial true stress σ_{zz} and (b) cell volumetric strain Ψ as function macroscopic true axial strain ε_{zz}. $\Sigma = 0.66$. Cavity.

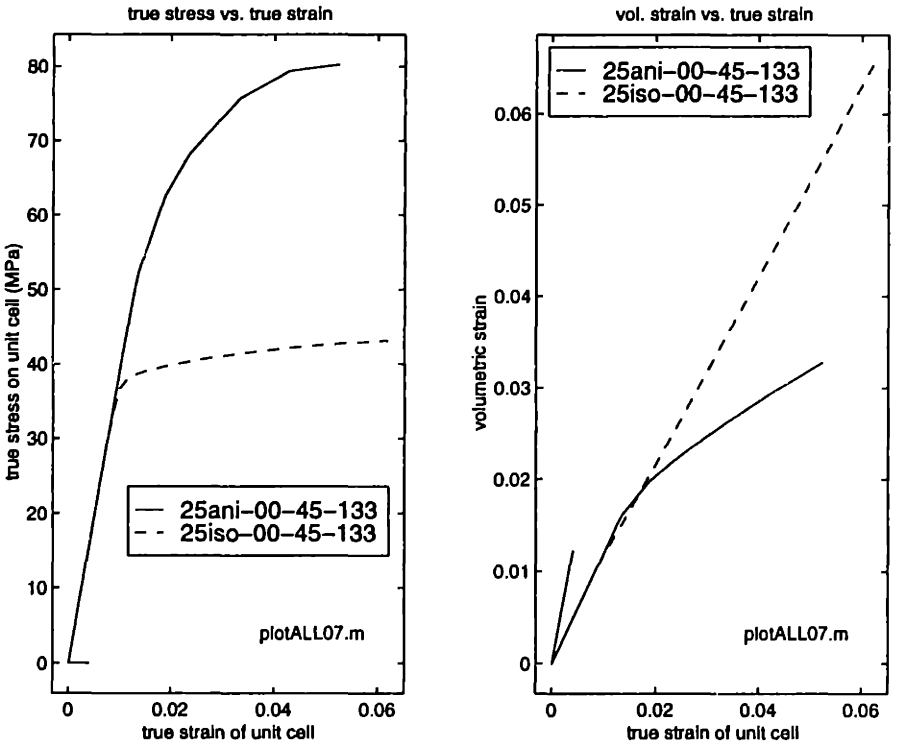

Figure 5-65: 25xxx-00-45-133: (a) macroscopic axial true stress σ_{zz} and (b) cell volumetric strain Ψ as function macroscopic true axial strain ε_{zz}. $\Sigma = 1.33$. Cavity.

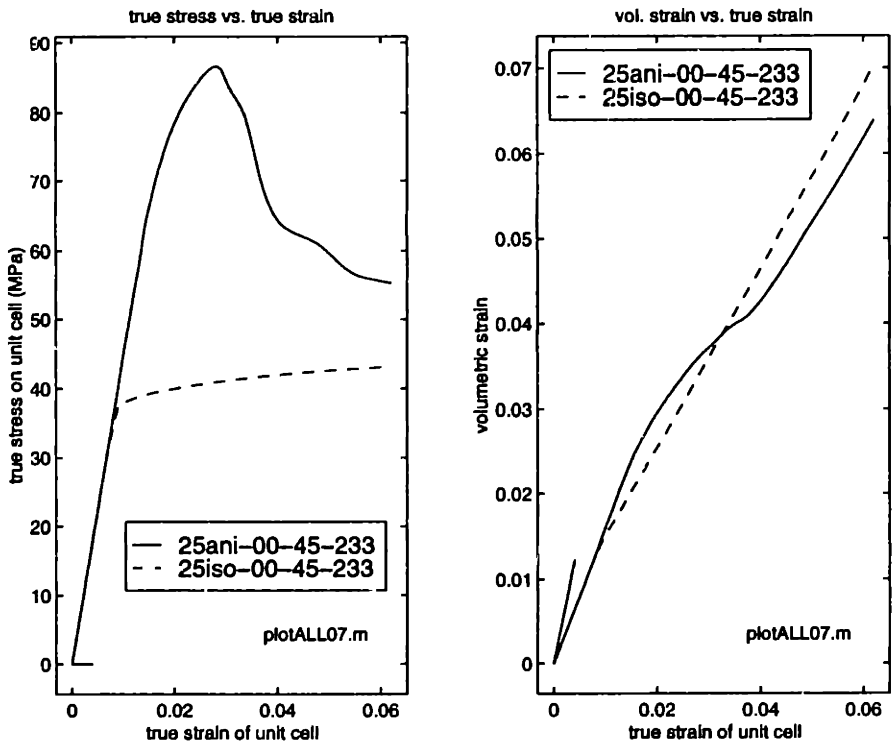

Figure 5-66: 25xxx-00-45-233: (a) macroscopic axial true stress σ_{zz} and (b) cell volumetric strain Ψ as function macroscopic true axial strain ε_{zz}. $\Sigma = 2.33$. Cavity.

cell σ_{zz}^{iso} at axial strains of 5% is found to be roughly constant at approximately 1.2 for all triaxialities. As seen from the plots of deviatoric true axial stress vs. true axial strain above (figures 5-17 and 5-19) the axial stresses correlate with the super-posed hydrostatic stress state introduced by the triaxial loading condition. The effects of the matrix properties therefore seem to be identical for all triaxialities.

The higher axial stresses observed in the anisotropic matrices can be attributed to the same "shell" mechanisms as discussed above. The fact that the difference in axial stresses is relatively small compared to the differences observed in the case of a cavity is due to the additional constraints on the matrix due to the non-zero tractions along the particle/matrix interface. These tractions provide a stabilization in the isotropic matrix where they prevent the early thinning in the matrix ligament near the particle equator and cause additional yielding in the matrix near the particle pole. In the case of the anisotropic matrix the interface tractions provide a stabilization of the matrix deformation that prevents the matrix to activate additional shear bands as is the case of a cavity (compare figure 5-35f.

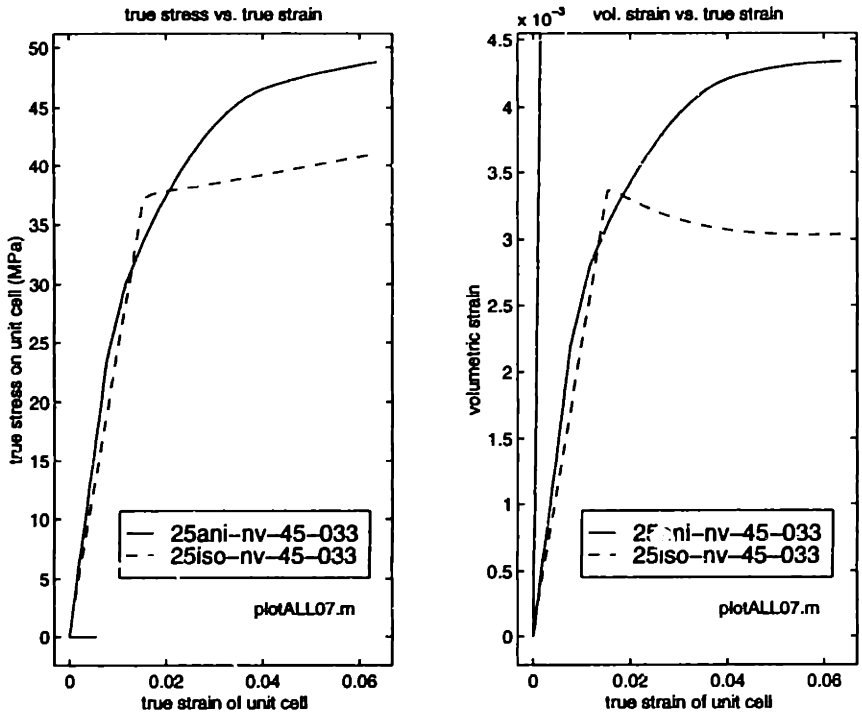

Figure 5-67: 25xxx-nv-45-033: (a) macroscopic axial true stress σ_{zz} and (b) cell volumetric strain Ψ as function macroscopic true axial strain ϵ_{zz}. $\Sigma = 0.33$. Coherent particle.

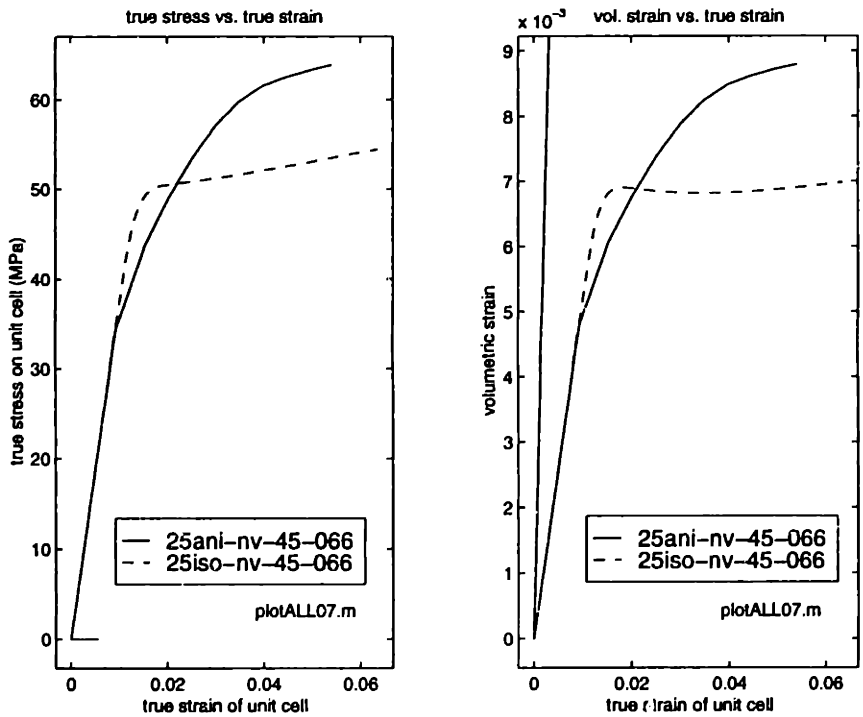

Figure 5-68: 25xxx-nv-45-066: (a) macroscopic axial true stress σ_{zz} and (b) cell volumetric strain Ψ as function macroscopic true axial strain ϵ_{zz}. $\Sigma = 0.66$. Coherent particle.

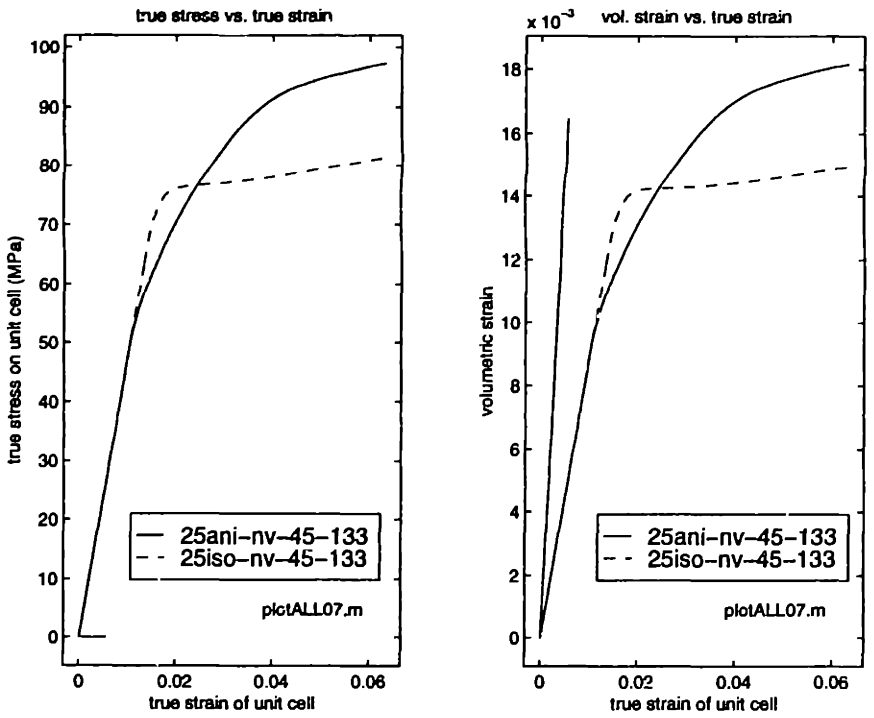

Figure 5-69: 25xxx-nv-45-133: (a) macroscopic axial true stress σ_{zz} and (b) cell volumetric strain Ψ as function macroscopic true axial strain ε_{zz}. $\Sigma = 1.33$. Coherent particle.

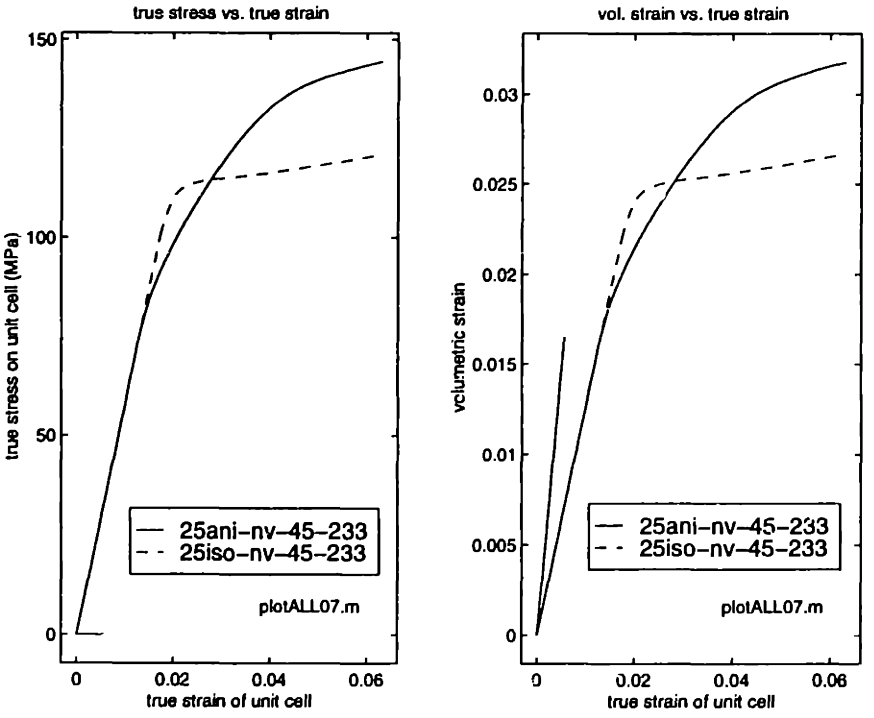

Figure 5-70: 25xxx-nv-45-233: (a) macroscopic axial true stress σ_{zz} and (b) cell volumetric strain Ψ as function macroscopic true axial strain ε_{zz}. $\Sigma = 2.33$. Coherent particle.

5.6.4 Effect of Changing the Matrix Properties on the Evolution of Matrix Plasticity in Unit Cells with a Pre-Existing Cavity

In previous sections the contour plots of equivalent plastic strain ε^p_{equiv} at different levels of axial strains have been introduced and discussed (see figures 5-32a through 5-39a-f). When comparing the general trends in matrix evolution between that of anisotropic matrices and that of isotropic matrices the following trends can be observed.

Comparing the plots of ε^p_{equiv} of the anisotropic and the isotropic matrices with cavities in the case of uniaxial tension (figures 5-32a-e and 5-5a-e), the difference in the evolution of matrix plasticity becomes apparent from the onset of deformation. Whereas the matrix yields in the upper right-hand corner of the anisotropic unit cell, it yields near the cavity equator in the isotropic cell. From axial strains of 2.5% on, the anisotropic matrix exhibits increasing localization of plasticity in shear bands along the unit cell diagonal and the cavity's free surface, whereas the plastic zone in the isotropic matrix gradually spreads out toward the upper right-hand corner of the unit cell and remains in its distribution relatively constant. The levels of ε^p_{equiv} are comparable in the two matrices within the limits of the studied axial strains of 5.5%. They reach 11% in the anisotropic and 10% in the isotropic matrix.

The same general trends are observed in the case of 0.66 triaxiality (figures 5-33a-e and 5-37a-f). The anisotropic matrix is found to yield in the upper right-hand corner and its plastic deformation localizes in shear bands, whereas the isotropic matrix yields near the cavity equator and its plasticity essentially concentrates in that area. The levels of ε^p_{equiv} reached are 14% in the anistocropic and 22% in the isotropic matrix.

Under 1.33 triaxiality the maximum observed ε^p_{equiv} at $\varepsilon_{zz} = 5.5\%$ increases to 54% in the anisotropic matrix and to 27% in the isotropic matrix (figures 5-34a-f and 5-38a-f).

Under very high triaxiality ($\Sigma = 2.33$) the anisotropic matrix forms additional

shear bands as discussed on page 195 (shear bands III and IV) whereas the distribution of plastic strains in the isotropic matrix remains essentially unchanged from that of the isotropic unit cells at lower triaxialities (figures 5-35a-f and 5-39a-f). The maximum values of ε^p_{equiv} at $\varepsilon_{zz} = 6.5\%$ are over 200% in the anisotropic and 35% in the isotropic case. The difference in the degree of localization becomes apparent when the contour plots of ε^p_{equiv} of the anisotropic unit cell in which the range of values is limited to 7.5% (figure 5-36a-f) are compared with the ε^p_{equiv}-plots of the isotropic unit cell (figure 5-39a-f).

5.6.5 Effect of Changing the Matrix Properties on the Evolution of Matrix Plasticity in Unit Cells with a Non-Cavitating Particle

In the case of non-cavitating particles the trends in the effects of changing the matrix properties from anisotropic to isotropic are somewhat different from those identified above. Figures 5-24a through 5-31e are the relevant contour plots of equivalent plastic strain ε^p_{equiv} at different levels of axial strains.

In the case of uniaxial tension (figures 5-24a-f and 5-28a-f), the isotropic matrix yields near the pole of the cavity and in the upper right-hand corner of the unit cell. With increasing axial strain the plastic zones spreads out to connect and the plastic deformation becomes somewhat more pronounced in the corner area of the unit cell. ε^p_{equiv} reaches a maximum of 7.0% at an axial strain of 5.5%. In the anisotropic case the matrix yields in the upper right-hand corner of the unit cell but quickly develops the characteristic concentration of ε^p_{equiv} along the diagonal of the unit cell. The degree of localization, however, is far less than that in the case of a pre-existing cavity. The maximum ε^p_{equiv} is 7.5% at an axial strain of 5.5% and is therefore on the same order of magnitude as that of the isotropic matrix.

At 0.66, 1.33 and 2.33 triaxialities the same trends and distributions of plasticity as under simple tension are observed. The maximum values of ε^p_{equiv} at 5.5% axial strain increase to 7.5%, 7.6% and 7.8% in the anisotropic matrix and decrease to 6.8%,

6.4% and 5.8% for 0.66, 1.33 and 2.33 triaxiality respectively. The relative amounts of ε^{p}_{equiv} are not found to be significantly different in the unit cells of different matrix properties.

5.6.6 Effect of Changing the Matrix Properties on the Macroscopic Strain Response of Unit Cell and Particle

In this section the effect on the macroscopic strain response of isotropic and anisotropic matrices under varying triaxial loading conditions and with varying particle properties will be discussed. Two types of plots will be referred to:

- Macroscopic strain space evolution of the unit cell. Figures 5-71 through 5-78 show the macroscopic radial strain ε_{rr} of the unit cell plotted along the abscissa, and the macroscopic axial strain ε_{zz} along the ordinate.
- Volumetric strain of the unit cell Ψ_m as a function of the macroscopic axial strain ε_{zz}: figures 5-63b - 5-70b.

Each figure contains the plots of a unit cell with an anisotropic matrix and that of an isotropic matrix under the same triaxial loading condition. The unit cells contain either a pre-existing cavity ("00") or a non-cavitating particle ("nv").

Unit Cells with Pre-Existing Cavities

In the case of the unit cells containing a pre-existing cavity, the isotropic unit cell generally undergoes more volumetric straining than the anisotropic unit cell. As seen in figures 5-63b ($\Sigma = 0.33$), 5-64b ($\Sigma = 0.66$) and 5-65b ($\Sigma = 1.33$), the ratio of the volumetric strains of the isotropic to that of the anisotropic unit cell Ψ^{iso}/Ψ^{ani} ranges from 1.6 to 2.5 at $\varepsilon_{zz} = 5\%$. Under very high triaxiality ($\Sigma = 2.33$) the volumetric strains of the two unit cells are not very different, as shown in figure 5-66b. The isotropic matrix exhibits more of a "spherical growth" mode than the anistoropic matrix.

Comparing the strain space evolution of the four pairs of triaxiality cases (figures 5-71, 5-72, 5-73, 5-74), it is seen that the slope of the radial strain ε_{11} as a function of axial strain ε_{22} is always larger in the isotropic case than in the anisotropic case. The difference in growth mode between the two matrices is very limited in the case of uniaxial tension, becomes more noticeable in the case of 0.66 triaxiality and is quite dramatic in the case of 1.33 triaxiality. At 1.33 triaxiality the isotropic matrix undergoes practically no radial straining after yield; ε_{11} remains constant. The anisotropix matrix, however, undergoes substantial straining in the radial direction after yielding. In fact, the slope of ε_{22} relative to ε_{11} is on the order of -2.5 after matrix yield. In the cases of high triaxiality (1.33 and 2.33) the unit cells are found to undergo positive radial straining which is explained by the mechanism in which the triaxial loading condition is applied.

More interestingly in the cases of pre-existing cavities, the generally higher levels of axial strain at which the anisotropic matrix yields appear here as an indication of a different mechanical response of the two unit cells. While the isotropic unit cell exhibits increasing straining in the matrix ligament close to the particle's equator, the anisotropic unit cell was found to concentrate the plastic deformation in shear bands. Since the orientation of the shear bands is mostly tangential to the particle/matrix or cavity/matrix interface, the growth mode of the anisotropic unit cell is interpreted as that of a structure which is composed of a number of shells which slide over eachother. This interpretation is in agreement with the spherical anisotropy of the matrix properties. This deformation model allows to explain the overall greater capacity of the anisotropic unit cell to harden under tension.

Unit Cells with Non-Cavitating Particles

In the case of the unit cells with non-cavitating particles (figures 5-75 - 5-78), the macroscopic strain-space elvolution of the anisotropic and the isotropic matrices are very close to each other. This is easily explained with the much smaller volumetric extension of the solid particle when compared to that of the a cavity. The general trend between the volumetric strains of the isotropic and anisotropic unit cells is

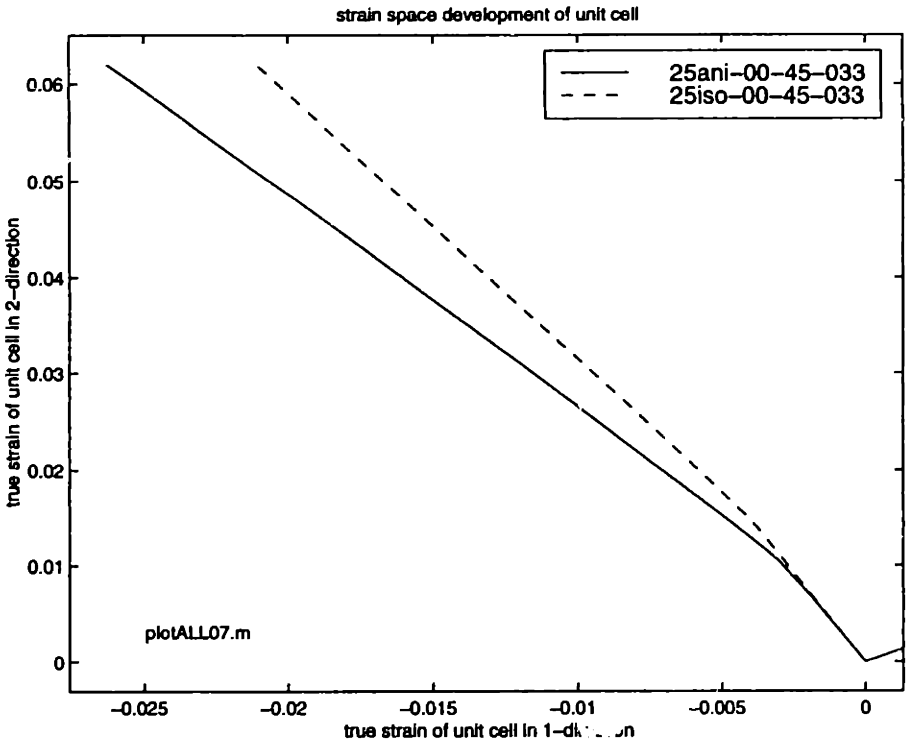

Figure 5-71: 25xxx-00-45-033: Macroscopic strain space evolution: ε_{zz} vs. ε_{rr}. $\Sigma = 0.33$. Cavity.

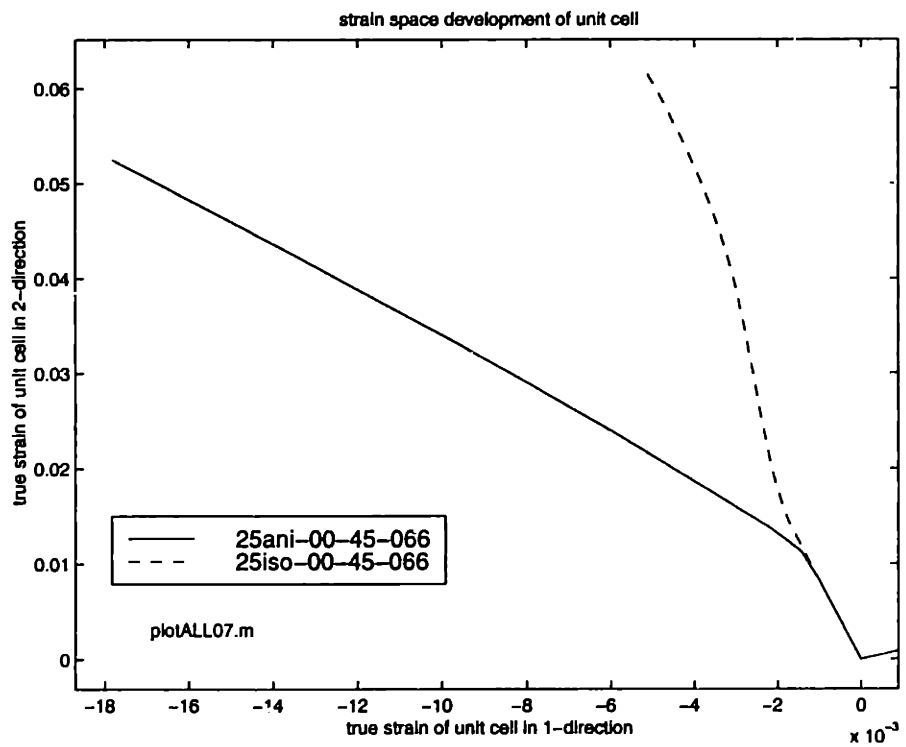

Figure 5-72: 25xxx-00-45-066: Macroscopic strain space evolution: ε_{zz} vs. ε_{rr}. $\Sigma = 0.66$. Cavity.

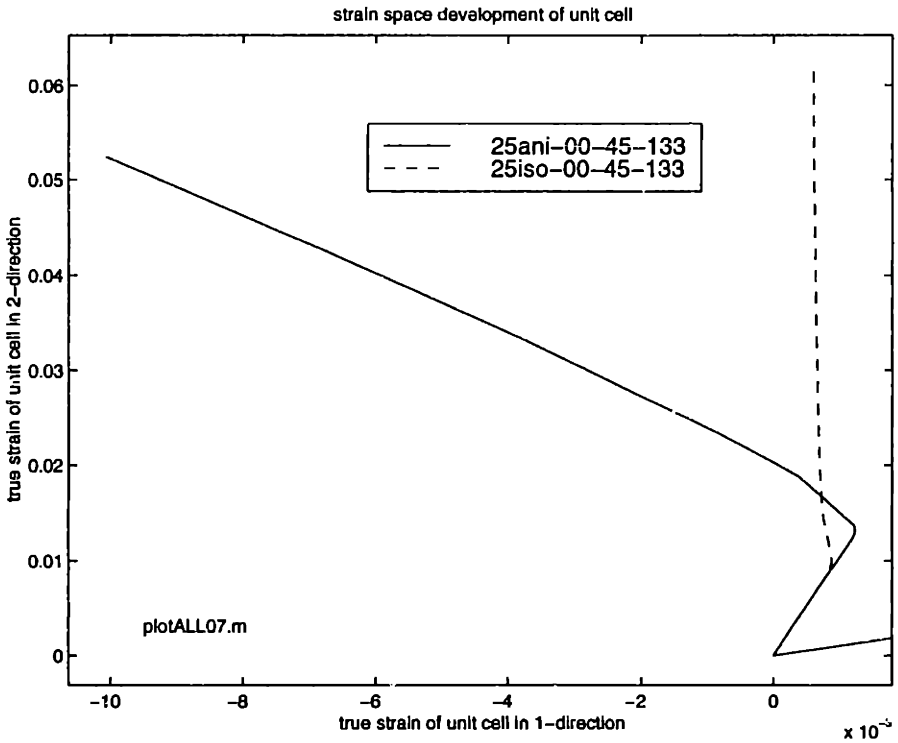

Figure 5-73: 25xxx-00-45-133: Macroscopic strain space evolution: ε_{zz} vs. ε_{rr}. $\Sigma = 1.33$. Cavity.

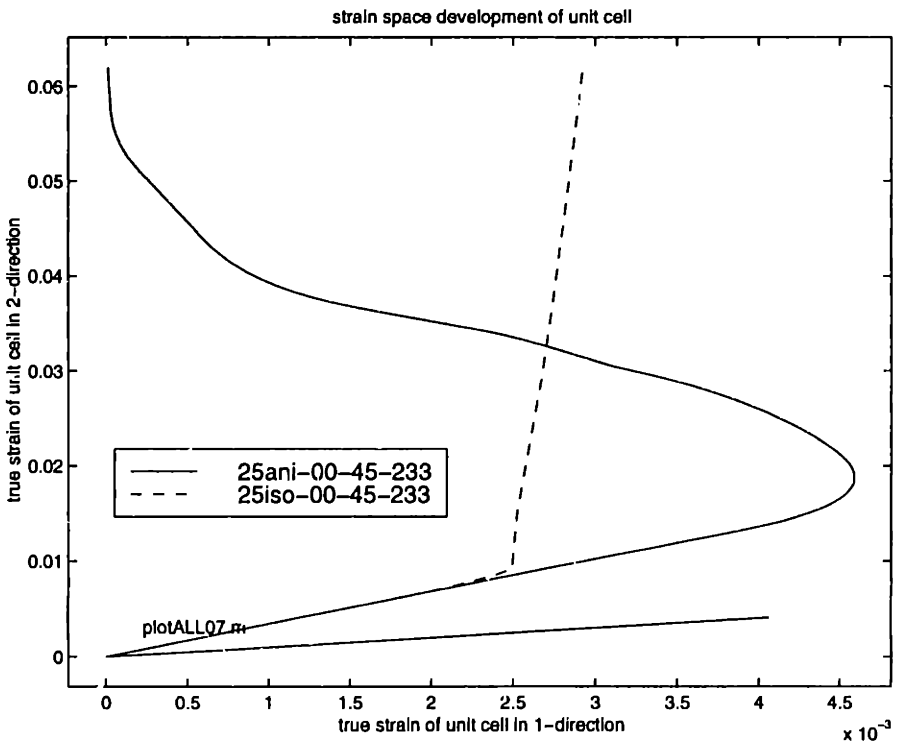

Figure 5-74: 25xxx-00-45-233: Macroscopic strain space evolution: ε_{zz} vs. ε_{rr}. $\Sigma = 2.33$. Cavity.

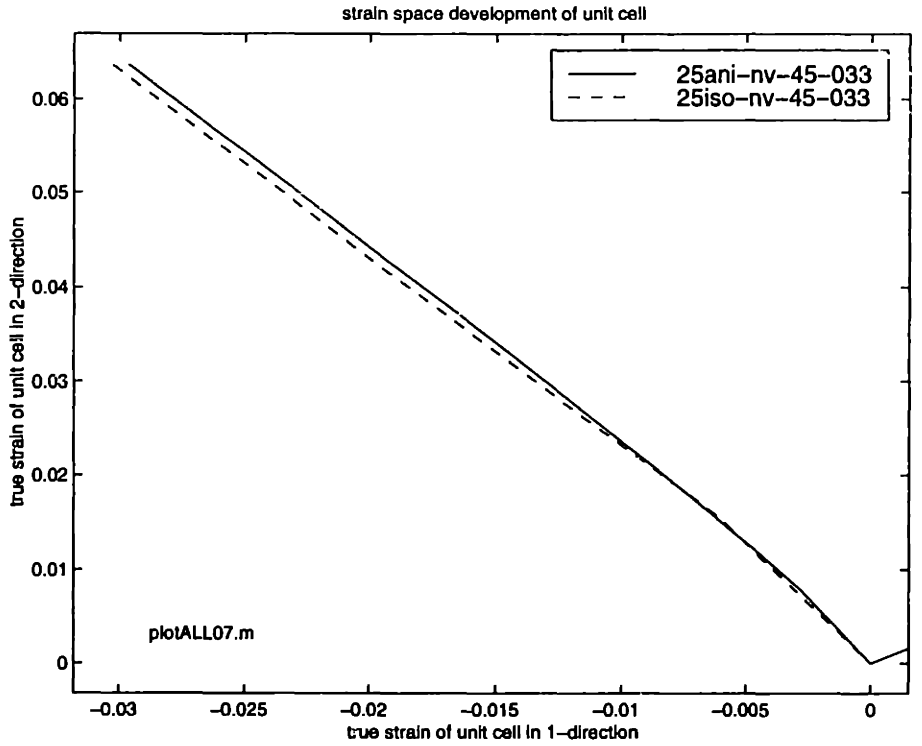

Figure 5-75: 25xxx-00-45-033: Macroscopic strain space evolution: ε_{zz} vs. ε_{rr}. $\Sigma = 0.33$. Coherent particle.

reversed from the case of the pre-existing cavity. In the case of the non-cavitating particle it is the anisotropic unit cell that undergoes larger volumetric strains than the isotropic unit cell. This is explained by use of the above-mentioned shell-structure model for the anisotropic matrix.

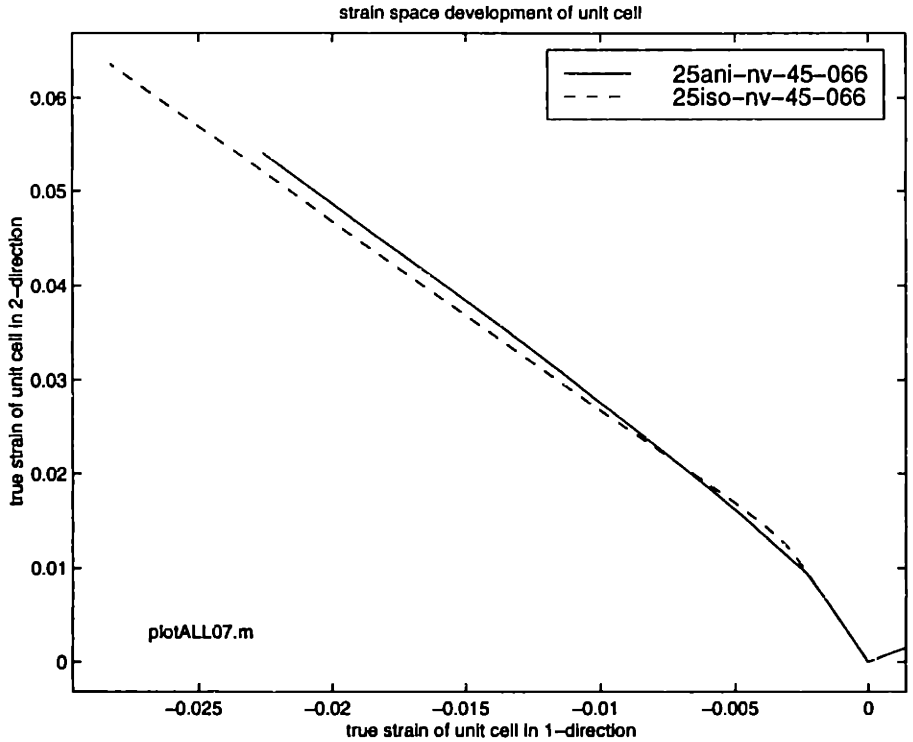

Figure 5-76: 25xxx-00-45-066: Macroscopic strain space evolution: ε_{zz} vs. ε_{rr}. $\Sigma = 0.66$. Cavity.

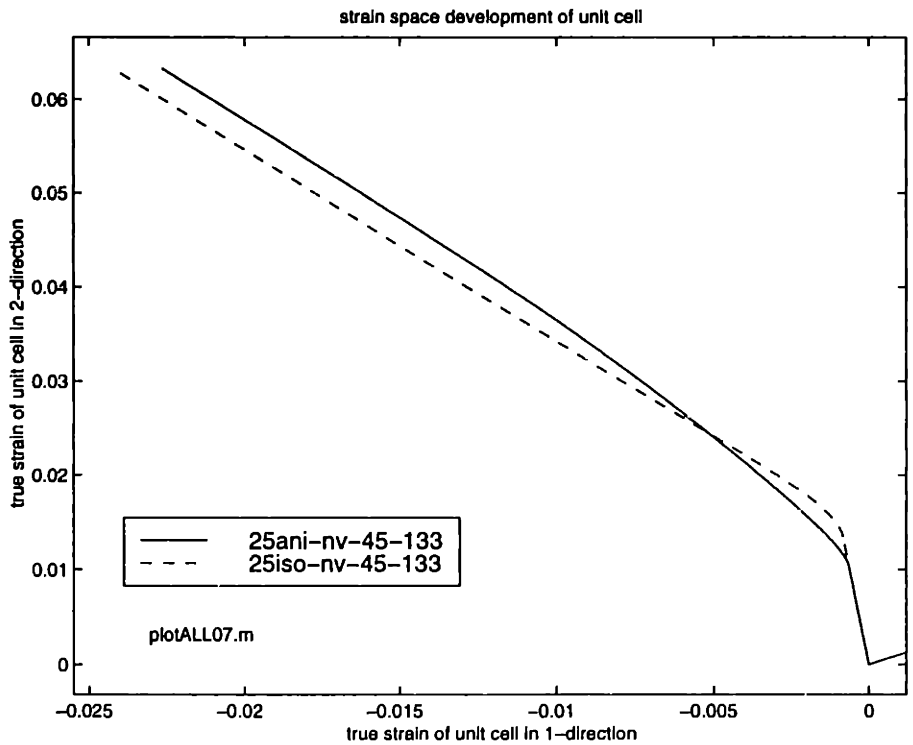

Figure 5-77: 25xxx-00-45-133: Macroscopic strain space evolution: ε_{zz} vs. ε_{rr}. $\Sigma = 1.33$. Cavity.

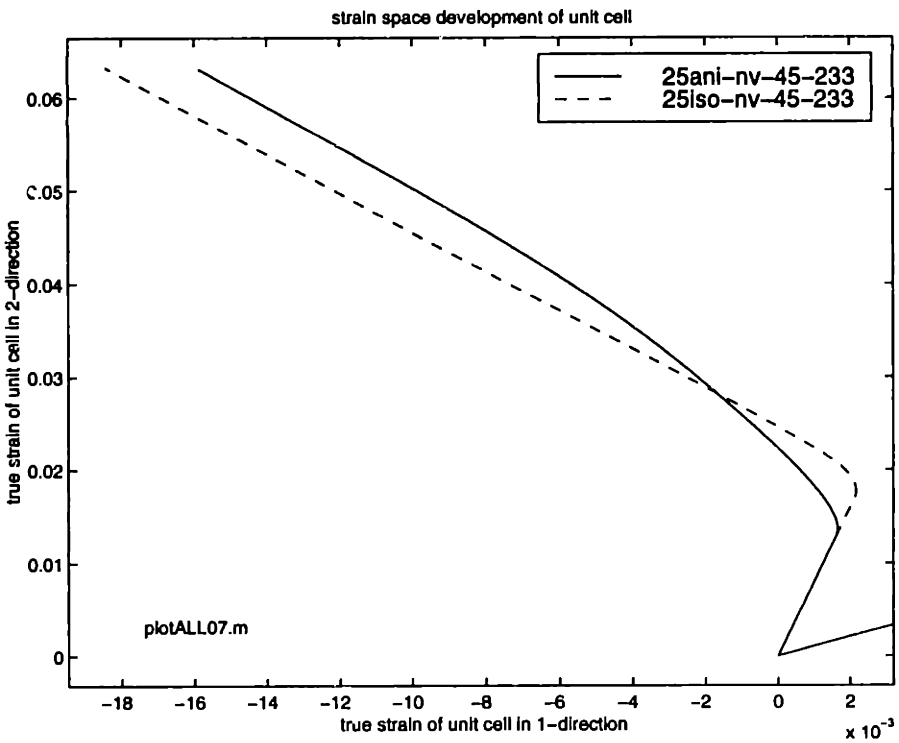

Figure 5-78: 25xxx-00-45-233: Macroscopic strain space evolution: ε_{zz} vs. ε_{rr}. $\Sigma = 2.33$. Cavity.

Chapter 6

Discussion

In this chapter, possible conclusions to be drawn from the numerical simulations regarding the nature of the particle-toughening mechanisms of polymers, and in particular regarding the role of the particle cavitation event in these mechanisms, will be discussed.

The numerical analysis of the unit cell-based micromechanical model presented in this thesis allows to identify important characteristics of the deformation response of particle-modified polymer systems. First of all, the numerical results show that a change in matrix properties causes the character of the deformation in the modelled polymer system to be fundamentally altered. The change from an isotropic plasticity to an anisotropic plasticity model has a very strong effect on the magnitudes and the distribution of matrix plasticity, especially when the particle is allowed to cavitate during the deformation or the matrix contains a pre-existing cavity. The macroscopic stress-strain response and the macroscopic strains at which particle cavitation occurs were also found to heavily depend on the matrix properties.

The change in matrix properties was motivated by the observation of a changing degree of crystallographic texturing in the matrix near the particle/matrix interface, and the resulting plastic anisotropy, in Nylon/rubber systems. Our results therefore support the idea of Argon and co-workers [8, 11, 13] that the main factor in the sudden

increase in toughening in Nylon-6/rubber blends is the change in the deformation behavior of the matrix polymer due to the presence of the particle surface and the resulting preferential orientation.

The degree of triaxiality of the applied stress state was found to be another important factor in the onset and evolution of matrix plasticity, as well as in the stress-strain response of the model and the particle cavitation event. Varying the macroscopic applied stress state from simple tension to that of high triaxiality, as encountered in the vicinity of a crack or notch tip, the simulations showed that the magnitudes of matrix plasticity are highly sensitive to changes in the triaxiality, in some cases varying by factors of more than 20. The macroscopic axial stress σ_{zz} varied by factors of up to 2. It must therefore be concluded that the notch-sensitivity of polymer systems cannot be studied by subjecting models to uniaxial tension alone without risking of neglecting important phenomena. Simple tension models do not realistically take in to account the effect of the stress state under notched conditions.

As discussed in chapter 2, the notch brittleness of a polymer system can be alleviated by either increasing its brittle strength σ_B, by reducing its yield strength σ_Y or by a combination of the two. Lowering the yield strength of a polymer may be achieved by various methods. One method is the modification of the local stress state, such as in the vicinity of an inhomogeneity like a rubber particle or a cavity. Another method is the modification of the polymer's microstructure with the goal of increasing the availablility of certain slip systems, such as influencing the location and the orientation of the crytalline part of the Nylon matrix in rubber-toughened Nylon-6 [49, 11].

The simulations that were undertaken in the present work are suited for investigating the first of the two methods, within certain limitations. Because of its small size compared to the length scales over which stress fields in multi-particle systems need to be considered, the unit cell cannot fully convey these stresses, neither macroscopically, nor on a multi-particle level. The stress state that appears as a macroscopic stress state on the level of the unit cell, is an approximation of an average stress state across the modeled polymer system. In a real system the strains and strain rates

are so high that they cannot be realistically modelled within the confines of a unit cell. In fact, the strain gradients encountered in the vicinity of an advancing crack are on the order of 100% or 200% across the dimension of a single unit cell[1], which compares poorly with the 6% tensile strain that the unit cells underwent in our simulations. On the other hand, the changes in the stress state in the immediate vicinity of the particle/matrix or cavity/matrix interface can be studied in our unit cell-based model, and compared directly to the stress field analys of Dijkstra and Ten Bolscher [28]. As discussed on page 38, the authors found a strong increase in σ_{mises} across the "cavitation event", accompanied by a relatively unchanged σ^h, which the authors interpreted as proof for particle cavitation to act as trigger of matrix yielding.

From our results, however, the subject seems more complex. It is not sufficient to limit the analysis of the yield event to saying that the stress deviator in a matrix next to a cavitating particle increases under certain conditions to such levels that matrix yielding is to be expected. The numerical results have shown that matrix yielding occurs, whether the particle is coherent or cavitated. Our results have shown that under simple tension, neither the macroscopic yield stress σ^y_{zz}, nor the corresponding yield strain ε^y_{zz} differ significantly whether a particle or a void is present in the isotropic matrix (figures 5-43 and 5-42). Although under high triaxiality the matrix with the cavity yields sooner than the matrix with the coherent particle, the corresponding stress also increases. Equations 6.1 and 6.2 summarize these observations:

$$\Sigma = 0.33: \quad \left\{ \begin{array}{l} \varepsilon^y_{zz,nv} \simeq \varepsilon^y_{zz,00} \\ \sigma^y_{zz,nv} \simeq \sigma^y_{zz,00} \end{array} \right\} \tag{6.1}$$

$$\Sigma = 2.33: \quad \left\{ \begin{array}{l} \varepsilon^y_{zz,nv} \simeq 2\varepsilon^y_{zz,00} \\ \sigma^y_{zz,nv} \simeq 3\sigma^y_{zz,00} \end{array} \right\} \tag{6.2}$$

With $\Sigma = 0.33$, the increase in yield stress is in part due to the hydrostatic stress added by the triaxial stress state. However, certainly not all of it are solely due to the triaxiality, as can be inferred from figure 5-19 when considering the deviatoric

[1]From conversations with Professor Parks.

stresses at the relevant levels of macroscopic axial strain. Therefore, our results are in good agreement with those of Dijkstra and Ten Bolscher regarding ε_{zz}^{y} in an isotropic matrix under uniaxial and highly triaxial or "biaxial" tension. In the case of the anisotropic matrix, ε_{zz}^{y} and σ_{zz}^{y} show little sensitivity to the presence or absence of a particle, as seen from figures 5-40 and 5-41. Due to the highly anisotropic nature of the plastic behavior in these cases, matrix yielding is relatively independent of the local stress state. Ten Bolscher and Dijkstra's model and results are therefore not applicable to particle-modified polymer systems in which local texturing plays a significant role, such as in rubber/Nylon-6 and rubber/HDPE with a subcritical inter-particle distance ($ID \leq ID_{cr}$). For systems with isotropic matrix plasticity, they are valid.

It is not possible to extend the above results for the isotropic matrix to saying that the cavitation event "triggers" matrix yield. For the particle cavitation to trigger matrix yielding, the particle cavitation strength must be of precisely such a value that the particle cavitates at a point in the deformation when the stress state in the matrix is such that the relief of tractions along the particle/matrix interface causes the deviatoric stress to increase by a critical amount, thereby inducing yielding.

Our results showed that there is a connection between the stress state in the matrix and the stress state of the particle. Within the limitations of the undertaken simulations and under high triaxiality, the particle cavitation event was found to occur at strains that are either smaller than the strains at which the matrix yields (elastic regime) or very close to them.

$$\varepsilon_{zz}^{cav} \leq \text{ or } \simeq \varepsilon_{zz}^{y} \tag{6.3}$$

This means that no or only very little plastic deformation has occurred in the matrix at the time when the particle cavitates. Therefore it must be concluded that it is not the event of particle cavitation that triggers matrix yielding, but the stress state due to the presence of a cavity that facilitates matrix yielding in certain cases.

Considering now the effect of the cavitation event in cases where the particle cavi-

tation strength is so high that the particle cavitates at strains up to which the matrix has already undergone substantial yielding. This possibility is not realistic for high levels of triaxiality, since our results show that the pressures the particles experience under high triaxiality ratios, reach exceedingly high levels at axial strains of 2% or 3% (see figures 5-14 and 5-15). In the case of low triaxiality it was shown that the matrix plasticity is not very different for the cases of a solid particle and a cavity. Therefore, it is not expected that particle cavitation has a large effect at low triaxialities, even if occurring at higher axial strains. The reports by numerous investigators, that the rubber particles were observed to cavitate before matrix yielding occurs [2, 59, 16], have therefore limited relevance.

Regarding the evolution of matrix plasticity and in particular the observed magnitudes, spatial distribution and degree of localization of plasticity, our results allow for a fundamental statement: as long as the particle does cavitate in a simulation, it does not matter at what macroscopic strain $\varepsilon_{zz,cav}$ it cavitates. The results of section 5.5 have shown that no significant difference exists between the plasticity of a matrix surrounding a pre-existing cavity, and that in a matrix that surrounds a newly created cavity. Even the stress-strain responses of both anisotropic and isotropic unit cells with cavitating particles were found to approach those of unit cells with pre-existing cavities. Some short-term effects of the cavitation event were observed, but disappeared within 0.5% to 1.0% of axial strain after the cavitation event. The validity of all of these conclusions is limited to the volume fraction $\Phi = 25\%$ and macroscopic axial strains of up to 6%.

The second route to toughening, i.e. the lowering of the yield strength by modifying the matrix polymer's plastic resistance, was successfully modelled in the work presented here. The availability of an easy slip system parallel to the particle/matrix interface was simulated by a change of the matrix properties from isotropic to anisotropic, using the Hill plasticity model. Under simple tension, it was found from figures 5-59,

5-60, 5-61 and 5-62, that for both matrices with particles and with cavities:

$$\varepsilon^{y}_{zz,iso} > 1.5\varepsilon^{y}_{zz,ani} \tag{6.4}$$

$$\sigma^{y}_{zz,iso} > 1.3\sigma^{y}_{zz,ani} \tag{6.5}$$

Hence for the case of simple tension, our model supports the theory that yield strain and stress can be decreased by introducing a preferential orientation into the matrix. For $\Sigma \geq 0.66$, only the case of a matrix with a coherent particle was found to confirm the theory. In the case of a unit cell with a cavity, the trend was reversed and the result contradicts the theory. A possible explanation of the trend's reversal is the high radial load-bearing capacity of the anisotropic matrix, an effect whose importance increases with increasing σ^{h}, and hence with increasing Σ. To explain the consequences of the anisotropic properties on the load-bearing capability of the matrix and on the deformation patterns in the matrix, the concept of the 'stacked-shell structur' will be discussed.

A remarkable result of the numerical simulations is the discovery that the behavior of the anisotropic matrix can be characterized as that of a stacked-shell structure. This behavior is most pronounced in simulations under high triaxiality and with pre-existing cavities or cavitating particles. The key observations are:

- the great capacity of the matrix to harden after yield;
- the tangential orientation of the matrix shear bands;
- the emergence of non-tangential shear bands under the very high constraints.

In opposition to the isotropic matrix, the anisotropic matrix was found to exhibit considerable strain hardening after matrix yielding. Whereas the isotropic unit cell displayed a very light increase in the macroscopic stress-strain plots after yield, the anisotropic unit cell hardened to stresses that were larger than the yield stress by roughly a factor of 1.5 in the case of a cavity, and a factor of 2 in the case of the solid particle, under very high triaxiality and for axial strains of up to 6%. At

lower triaxialities this effect is less pronounced but certainly manifest. The spherical arrangement of the matrix anisotropy makes the normal plastic deformation of the matrix very difficult in the tangential and radial directions, whereas the deformation in shear on the spherical surfaces between the imagined shells is very easy[2].

Under very high triaxiality of the applied stresses, the stress state inside of the unit cell has a large hydrostatic component in tension. Because the plastic deformation in the tangential direction $\varepsilon^p_{\theta\theta}$ and radial direction ε^p_{rr} require so much higher stresses relative to those required for the plastic deformations in shear $\varepsilon^p_{r\theta}$ and $\varepsilon^p_{r\phi}$, the shells can carry large loads in radial tension while effectively acting as a dome under tension. The strong localization of the matrix plasticity in shear bands is then thought of as the tangential sliding of the shells over each other, since this is the easiest deformation mode of the matrix. As previously pointed out, the plastic shear strain $\varepsilon^p_{r\theta}$ on the plane normal to the radial direction accounts for nearly all of the plastic deformation in the anisotropic unit cells (figures 5-36a-f).

As the macroscopic deformation continues, the radial tensile load on the shells increases. Since the geometric boundary conditions do not allow for plastic flow across the boundaries of the unit cell, the need for additional modes of deformation in the matrix becomes increasingly large. The local deformation of the mesh along the cavity surface in figure 5-36f near the cavity equator is the result of such a new deformation mode. This phenomenon is not, however, due to the activation of additional slip systems. When examining the shape of the deformed mesh elements, the shear band IV (see page 195 for an explanation) is found to consist of a row of elements that each deformed in $r\theta$-shear.

Another indication of the shell-like behavior and structure of the anisotropic matrix are obtained from the study of the effects of Σ on the particle pressure. As seen from section 5.4, the particles inside an anisotropic matrix experience a monotonic increase of negative pressure as ε_{zz} increases, at all levels of Σ. In the case of an isotropic matrix this is only the case at low triaxiality ratios. At high Σ the particle

[2]Recall the use of the Hill plasticity model and our choice of $H_{11} = 3.0$ and $H_{12} = 0.7$ as explained in section 4.4.2 on page 72.

inside an isotropic matrix experiences a peak negative pressure at matrix yield and a subsequent drop in pressure. The explanation for this observation lies in the mode of deformation of the matrix, whose shell-like deformation leaves the boundary of particle/matrix or cavity/matrix interface deforming in a very gradual manner, not allowing for large shape changes and hence loading the particle more gradually.

Another interesting result of our simulations is the high degree in the localization of matrix plasticity that was observed to occur in matrices with the anisotropic material model. This result will be compared with those of Fukui, Kikuchi and Inoue [66] who have undertaken a two-dimensional finite element analysis on rubber-toughened Nylon using an isotropic elastic-plastic material model for the matrix. Inside a unit cell, 5 octahedral rubber particles or voids were arranged in a BCC-like pattern. The authors observed more localized plastic straining in the void/matrix system, and concluded from their results that the particle/matrix system was expected to be tougher than the void/matrix system because at a given strain after matrix yield, the number of elements that had deformed plastically was higher in the particle/matrix system than in the void/matrix system.

Comparing our results to those of Fukui, Kikuchi and Inoue [66] it appears that the authors' reasoning followed the idea that it is not the magnitude of plastic strains, but the volume over which it occurs that determines the amount of energy being dissipated during a deformation process. The higher the area (or volume) over which energy is dissipation, they reasoned, the tougher the reponse of the system, and therefore, they concluded, the emphasis in the toughening should be put on the reinforcement of the particle/matrix interface in order to prevent premature debonding. Fukui et al. did not take into account Wu's criterion for the critical inter-particle distance, which seems to indicate that their reasoning should only apply to scale-independent polymer systems. Also, no effects of local orientation were taken into account. The results of Fukui et al. confirm our findings that the degree of localization is generally higher in cavity/matrix systems than in particle/matrix systems. This phenomenon can be

explained by the load-bearing capacity of the particle which causes the stress deviator in the matrix with a solid particle to be smaller than that of a matrix surrounding a cavity. Our findings confirm that in the particle/matrix system the plastic zone is spread out further, in both anisotropic and isotropic matrices. Strain localization, however, was experimentally observed by several investigators. Some even reported a connection between the toughness of a blend and the degree of observed strain localization.

Huang and Kinloch [45] performed a finite element analysis on an axisymmetric particle/matrix and void/matrix system that was modelled after rubber-modified epoxy. The reported distribution of the equivalent plastic strain contours of Huang and Kinloch's 19% void volume fraction model are in excellent agreement with our results for isotropic matrices as reported in chapter 5, such a in figures 5-5c and 5-5f. However, the authors' levels of plastic strains are generally much lower than those obtained by us. Huang and Kinloch also report a stress-strain curve for the same simulation. Comparing it with our results for the isotropic matrix with a cavity under uniaxial tension (figure 5-4a), it is found to be in excellent agreement as well.

Two of the major shortcoming of the numerical simulations undertaken, are the lack of texture evolution and the lack of connection between mesoscopic and macroscopic effects. The mesoscopic effects are characterized by the length scale of the unit cells and particles, whereas the macroscopic effects are characterized by the length scale of the macroscopic defects that govern certain aspects of the fracture and toughening behavior of modified polymer.

In the present model the anisotropic plastic behavior of the matrix polymer (Nylon) was modeled using the Hill anisotropic plasticity model as it is available as a standard feature in finite element software. The disadvantage of this implementation is that the orientation of the local directions and therefore the local orientation of the plastic matrix anisotropy does not evolve with the inelastic deformations. Within the unit cell the easy slip systems are always oriented relative to the boundaries of the

elements. (See section 4.4.2) They do not rotate freely or evolve in accordance with a realistic model of crystal plasticity. In order to alleviate this problem an appropriate plasticity model needs to be adapted to the behavior of the crystalline polymer matrix and implemented by means of user-defined material descriptions. In ABAQUS this could be done using a UMAT subroutine.

At small strains the Hill plasticity model is a reasonably good approximation of the anisotropic plasticity of a crystalline matrix material. The limitation on the magnitude of the plastic strains applies only indirectly to the macroscopic strains the unit cell undergoes, whereas they apply directly to the local strains within the unit cell. In the simulations the local strains are shown to reach levels of over 200% while the macroscopic strains remain on the order of a few percent. At the levels of local plastic strains encountered, the applicability of the Hill plasticity model is doubtfull.

The second major shortcoming of our simulation lies in the fact that our simulations have been limited to small volume elements that do not connect the length scales of the macroscopic defects that dominate the failure of the blend, and the length scale of the particles and inter-particle ligaments that determine the plastic response of the toughened material. A critical point is that in the vicinity of a notch or crack the plastic strains to be expected in the matrix are on the order of at least 100%. This is 2 orders of magnitude larger than the strains to which the unit cells were macroscopically strained in the simulations. Together with the locally encountered plastic strain levels this indicates that large interactions between the matrix material around several particles are to be expected, in both stresses and plastic flow. The resulting percolation of a plastic zone through a multi-particle system is not captured in our simulations, but is to be expected when the constraint of the periodic boundary conditions is removed.

Some of the issues in modeling large strain texture evoluton have already been studied by Lee, Argon, Parks, Ahzi and Bartczak for HDPE [6, 7], Arruda, Boyce and Quintus-Bosz for initially anisotropic glassy polymers [15], Parks for semi-crystalline polymers [30] and others. Some of the techniques required for an implementation of a multi-level finite element analysis have been developed [19].

Another aspect that was neglected in our micromechanical model is the pressure sensitivity of the slip resistances in Nylon. Lin [10] reported experimental findings indicating that shear deformations in the crystalline domains of Nylon are highly sensitive to stresses that are applied normal to the slip planes. This could, in fact, cause the shear deformation to be even easier available than currently modeled, thus increasing the anisotropy of the matrix and making deformation by shear even more dominant in the matrix plasticity.

Appendix A

Codes and Abreviations

Figure A-1 shows the structure of the code used for identifying individual simulations.

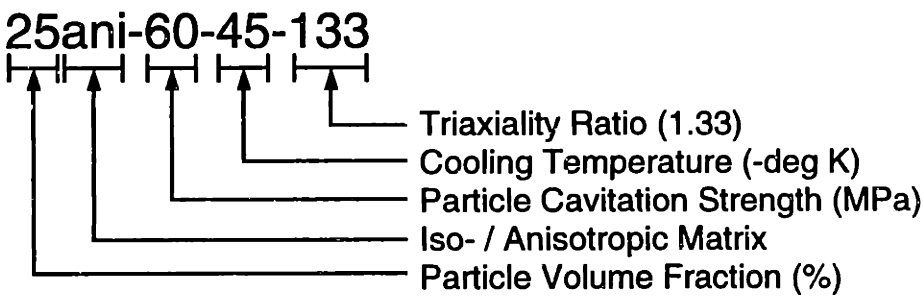

Figure A-1: Explanation of Simulation Code

Table A.1 below lists some of the variables used in this thesis and their meaning.

Symbol	Meaning
E	Young's modulus.
K	Bulk modulus.
P	Particle pressure.
r^0	Initial radius of the particle.
R^0	Initial radius of the cylindrical unit cell.
$S11, S22, S33$ and $S12$	Stress components in contour plots. Correspond to $\sigma_{11}, \sigma_{22}, \sigma_{33}$ and σ_{12}. In the case of simulations with an isotropic matrix, the directions correspond to the global directions: $S11 = \sigma_{11} = \sigma_{rr}$. In the case of anisotropic matrices, they correspond to the local directions, as explained in section 4.4.2.
ε	True strain.
σ	True stress.
ν	Poisson's ratio.
Φ	Particle volume fraction.
Ψ	Volumetric strain.
Σ	Triaxiality ratio (see equation 4.16)

Table A.1: Symbols and their meaning.

Appendix B

Formulation of the Rubber Particle User Element

B.1 The Particle Element

The user element for the cavitating fluid particle was designed for simmulations with axial symmetry. It is therefore a 2-D element that takes into account the radial variation of the surface area at the element's boundary.

The element has a minimum of 3 nodes. The first and last nodes have to lie on the model's axis of symmetry. The axial coordinate of the first node must be larger than that of the last node. All other nodes are free to lie on or off the axis of symmetry and above or below the first and last nodes. The numbering of the nodes starts with the top node (1) and ends with the bottom node (n). It is clockwise. Figure B-1 shows two examples of possible user elements as defined in the UEL subroutine.

B.2 Constitutive Model

The rubber particle is modeled as a fluid-filled cavity. Its stress state is characterized by a constant hydrostatic pressure P and zero shear stresses throughout the particle. The stress state is therefore determined from the volumetric strain Ψ the rubber phase undergoes and the rubber bulk modulus K. Equation B.1 shows the dependence of

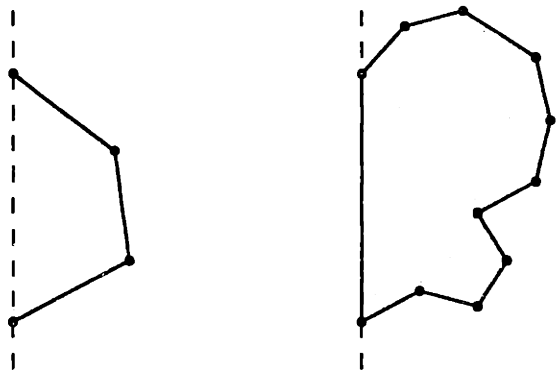

Figure B-1: Examples of axisymmetric elements that can be modeled using the UEL subroutine

P on the volumetric strain $\frac{V-V_0}{V_0}$.

$$P = -K\Psi = -K\frac{V - V_0}{V_0} \tag{B.1}$$

where V is the current volume of the particle and V_0 is the volume of the undeformed particle. The tractions on the particle boundary act exactly normal to the boundary and have the same magnitudes everywhere along the boundary. Therefore the nodal forces are the sums of the incremental weighted areas multiplied by the current pressure.

B.3 Subroutine Calls

During each equilibrium iteration, the finite element software, HKS ABAQUS, calls the subroutine UEL. During each call, ABAQUS provides the subroutine with the original radial and axial node coordinates $\mathbf{R}^0$ and $\mathbf{Z}^0$, a displacement field $\mathbf{u}$ and a measure of time t. The measure of time essentially serves verification purposes and to determine when the reference volume of the fluid particle is to be reduced for the purpose of simulating thermal shrinkage.

The subroutine returns a force vector $\mathbf{f}$, a jacobian $\mathbf{J} = \frac{\partial \mathbf{f}}{\partial \mathbf{u}}$ and number of "housekeeping" parameters.

B.4 Algorithm

B.4.1 Computing the Volume

Using the Divergence Theorem, the volume of the particle can be expressed as the dot product of the outward surface normal **n** and the position vector **m** integrated over the particle surface S.

$$V = \frac{1}{3}\int_S \mathbf{m}\cdot\mathbf{n}\,dS \tag{B.2}$$

The discretized form of equation B.2 is equation B.3:

$$V = \frac{1}{3}\sum_{i=1}^{n-1} \mathbf{m}_i\cdot\mathbf{n}_i\,S_i \tag{B.3}$$

where the summation is done over the $n-1$ surface elements corresponding to an element with n nodes. Figure B-2 shows the continuous and discrete form of the surface integral corresponding to equations B.2 and B.3.

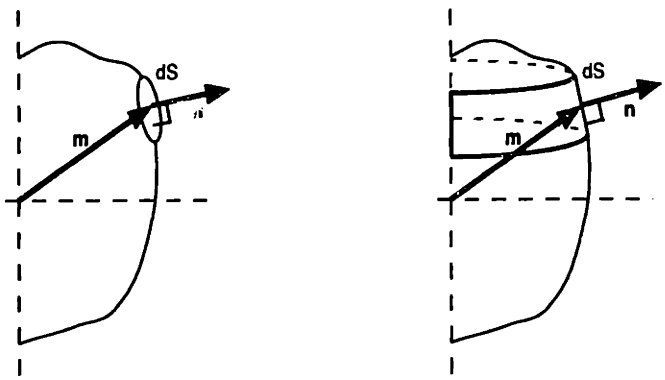

Figure B-2: Continuous and discrete version of the surface integral.

During the first call of the subroutine the undeformed volume V_0 is recorded and stored so that during later subroutine calls the current volume V can be compared with V_0 and the current volumetric strain can be computed.

B.4.2 Computing Volumetric Strain and Pressure

The pressure P is obtained by multiplying the bulk modulus by the volumetric strain as shown in equation B.1.

B.4.3 Computing Nodal Forces

Because of its axisymmetry, the user element is implemented as a 2-D element as shown in figure B-1. Each surface element i is delimited by two nodes i and j. The surface area A_i of each surface element i has to be scaled by the radius r at which it is located as shown in equation B.4 where the area of surface segment i is expressed as the integral of surface area increments dA_i from the radial coordinate R_i of node i to the radial coordinate R_j of node j[1].

$$A_i = \int_{R_i}^{R_j} dA_i = \int_{R_i}^{R_j} \frac{2\pi}{sin\theta_i} r\, dr = \pi(R_i + R_j)\sqrt{(R_j - R_i)^2 + (Z_j - Z_i)^2} \qquad \text{(B.4)}$$

where $sin\theta_i = \frac{R_j - R_i}{\sqrt{(R_j - R_i)^2 + (Z_j - Z_i)^2}}$. Z_i and Z_j are the axial coordinates of nodes i and $i+1$ respectively.

To compute the nodal forces the contributions from each of the two surface segments neighboring a node must be taken into account. In other words, each surface segment i makes contributions to the forces on each of the nodes i and j the segment is limited by. An appropriate shape function N_i has to be chosen to weight the contributions of the surface segments, as shown in equation B.5.

$$N^i = \frac{R_j - r}{R_j - R_i} \qquad \text{(B.5)}$$

where r varies from R_i to R_j. The contribution to the force acting on node i due to the neighboring surface segment i is computed by summing the incremental force

[1]Note that the node j is not the same as the node i. Because the force due to each surface incremental dA_i makes a contribution to both nodes at each end of the segment, it can conversely be said that each node receives contributions from surface increments on both neighboring segments. The contributions due to the neighboring segments of node i are called fj_i and fi_{i+1}.

contribution $df_i = P N_i^i dA_i$ from that element to the node as shown in equation B.6.

$$f_i = \int_{R_i}^{R_j} df_i = \int_{R_i}^{R_j} P \frac{R_j - r}{R_j - R_i} \frac{2\pi}{sin\theta_i} r \, dr \tag{B.6}$$

After integrating equation B.6 the expression for f_i is obtained in B.7. Similarly the expression for the force contribution of the surface element i to node j, f_{j_i}, is obtained as in equation B.8.

$$f_i = \frac{P\pi\sqrt{(R_j - R_i)^2 + (Z_j - Z_i)^2}}{(R_j - R_i)^2} \left[\frac{1}{3}R_j^3 - R_i^2 R_j + \frac{2}{3}R_i^3\right] \tag{B.7}$$

$$f_{j_i} = \frac{P\pi\sqrt{(R_j - R_i)^2 + (Z_j - Z_i)^2}}{(R_j - R_i)^2} \left[\frac{2}{3}R_j^3 - R_i R_j^2 + \frac{1}{3}R_i^3\right] \tag{B.8}$$

Using equations B.7 and B.8 the contributions of each surface segment i to each one of the limiting nodes i and j are obtained. Next the force contributions to each node of each of its neighboring surface segments are summed up to give the $2n$ by 1 force vector $\mathbf{f}$. The individual components are given by equation B.9.

$$[\mathbf{f}]_i = f_{i_{mod(i-1)/2+1}} \cdot \mathbf{n}_{mod(i-1)/2+1} + f_{j_{mod(i-1)/2+2}} \cdot \mathbf{n}_{mod(i-1)/2+2} \tag{B.9}$$

where $\mathbf{n}_i$ is the surface normal of surface segment i. Figure B-3 shows how the node and segment numbering works.

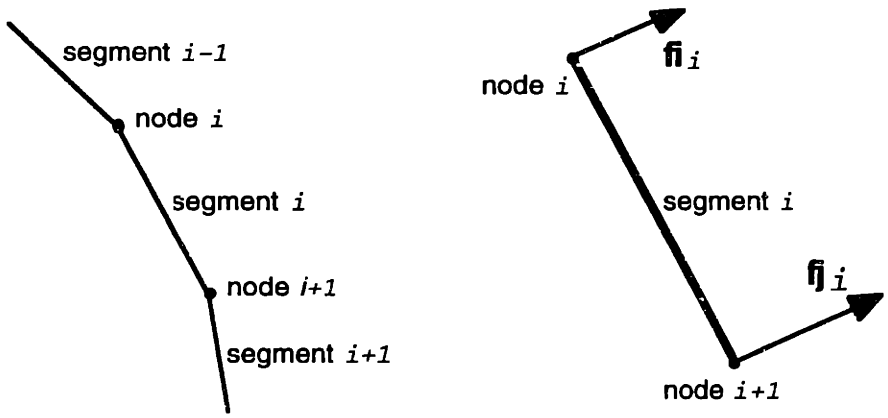

Figure B-3: Illustration of node and surface segment numbering

B.4.4 Computing The Jacobian

The jacobian, or 'stiffness matrix' as it is often called in solid mechanics, expresses how the nodal forces change with a changing displacement field. For a 2-D element of n nodes and $2n$ degrees of freedom, the jacobian is an n by n matrix. Equation B.10 shows the decomposition of the jacobian as applicable in the user element.

$$\mathbf{J} = \frac{\partial \mathbf{f}}{\partial \mathbf{u}} = \frac{\partial \mathbf{f}}{\partial P}\frac{\partial P}{\partial V}\frac{\partial V}{\partial \mathbf{u}} + \left[\frac{\partial \mathbf{f}}{\partial \mathbf{u}}\right]_P \tag{B.10}$$

where $\mathbf{f}$ is the $2n$ by 1 force vector of the element, $\mathbf{u}$ is the $2n$ by 1 displacement vector relative to the $2n$ degrees of freedom, P is the particle pressure and V is the current volume of the particle. The different parts of equation B.10 are calculated as follows.

$\frac{\partial \mathbf{f}}{\partial P}$ is the current force vector divided by the change in pressure P. It is obtained by dividing equation B.9 and hence equations B.7 and B.8 by P. Its dimension is $2n$ by 1.

$\frac{\partial P}{\partial V}$ is just the bulk modulus K; a scalar.

$\frac{\partial V}{\partial \mathbf{u}}$ is the change in volume as a function of the displacements $\mathbf{u}$ obtained by differentiating equation B.3 with respect to the individual degrees of freedom $\mathbf{u}_i$. Its dimension is 1 by $2n$.

$\frac{\partial \mathbf{f}}{\partial \mathbf{u}}$ is obtained by differentiating equation B.9 and hence equations B.7 and B.8 with respect to the displacements $\mathbf{u}_i$ which yields a $2n$ by $2n$ matrix.

B.5 Cavitation

Two different implementations for the simulation of the particle cavitation event have been done. The first consists in a sudden drop of the bulk modulus, whereas the second gradually reduces the effective bulk modulus over a finite amount of macroscopic strain in the model.

B.5.1 Cavitation Criterion

The chosen criterion for the start of the cavitation event is the comparison of the current particle pressure P with the a pre-defined critical pressure P_{cr}. When P reaches the critical value P_{cr} one of the two cavitation algorithms is initiated. P_{cr} isULF passed into the subroutine through a parameter PROPS. Another parameter PVLAW allows to set the desired cavitation algorithm, which is passed into the subroutine through the parameter JPROPS.

B.5.2 Simple Cavitation

This option corresponds to the values 13 and 14 for PVLAW. When P reaches the critical pressure P_{cr}, the bulk modulus K is reduced to $10^{-7}K$. Through equation B.1 this reduces the particle pressure and the forces by the same proportions. A flag SVARS is set in order for the bulk modulus to remain low at the next call of the subroutine. Figure B-4 shows a schematic representation how the particle pressure could evolve as a function of "time" in the case of the "simple cavitation" algorithm.

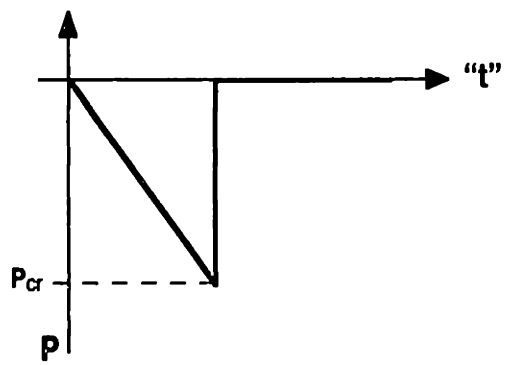

Figure B-4: Constitutive model for the case of "Simple Cavitation"

B.5.3 Force Relaxation

In the case of the force relaxation algorithm the time t_{cav} at which the critical pressure is reached is recorded in a flag SVARS for later use. Over an pre-determined interval

of the simulation parameter "time" Δt_{cav} the bulk modulus is reduced to $10^{-7}K$. During the reduction of the bulk modulus the displacement-dependence of the forces is artificially set to zero, which corresponds to eliminating the last term of equation B.10. The proportion by which the bulk modulus is reduced at every subroutine call is determined by the relative amount of "time" that has elapsed since the start of the relaxation algorithm $t - t_{cav}$ as shown in equation B.11. The interval over which the relaxation is to occur is set by a parameter PROPS passed into the subroutine.

$$K^I = K\left(1 - \frac{t - t_{cav}}{\Delta t_{cav}} + 10^{-7}\right) \tag{B.11}$$

where K is the original and K^I is the "current" bulk modulus.

Figure B-5 shows a schematic representation how the particle pressure could evolve as a function of "time" in the case of the "force relaxation algorithm". The

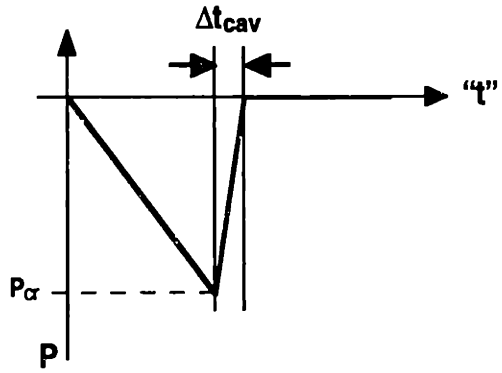

Figure B-5: Constitutive model for the case of "force relaxation algorithm"

amount of "time" over which the cavitation event occurs is in fact chosen to be on the order of 0.01 which translates into macroscopic axial strains of less than 10^{-4}.

Figure B-6 shows the flow diagram for the "force relaxation algorithm".

B.6 Thermal Strain

In the present implementation of the use element, the rubber particle is assumed to be always elastic, i.e. for all imposed displacement fields an elastic solution can be found and the formulation of the jacobian does not change. An exception to this is

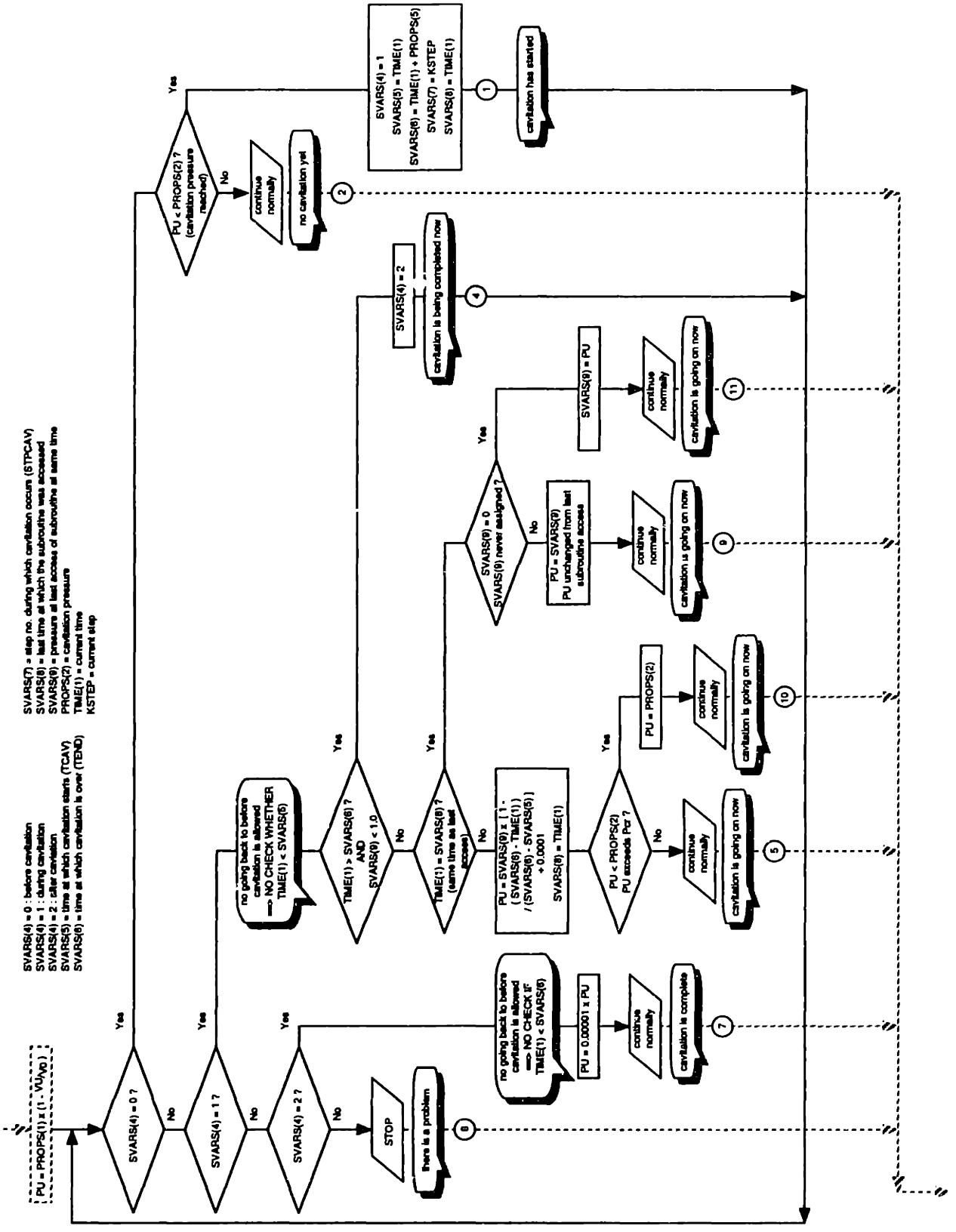

Figure B-6: Flow chart of the "force relaxation algorithm"

the cavitation of the particle as discussed above. However, the two mechanisms of cooling and cavitation do not interfere with each other because the first is taken into account through a measure of temperature, whereas the second takes effect through a measure of "time".

In order to allow the rubber particle to undergo thermal strains, it is sufficient to scale the reference volume V_0 by the volumetric strain that corresponds to a given change in temperature ΔT and the thermal expansion coefficient α of the material. Equation B.12 shows the dependence of the current reference volume V_0' on V_0, α and ΔT:

$$V_0' = V_0 \left(1 + \alpha \Delta T\right)^3 \tag{B.12}$$

The rest of the algorithm does not change; i.e., equations B.1, B.9 and B.10 are still valid.

B.7 Example of a Typical Input Deck

The following is an example of the section of an ABAQUS input deck that illustrates the use of the user element.

Lines 1 and 2 of the code below which start, with the ABAQUS *USER ELEMENT option, characterize the user element. In this example it is of type U1 with 75 nodes and 2 degrees of freedom per node.

Line 5 of the code, which is part of the *UEL PROPERTIES option, contains the parameters that characterize the rubber particle. The rubber bulk modulus is 2000.0MPa and the cavitation strength is −60MPa. The material's thermal expansion coefficient α is $0.00025\frac{1}{\text{deg}\,K}$ and the cooling during the first step in the simulation is over a ΔT of $-45.14\,\text{deg}$. The "time" interval over which the cavitation occurs is $\Delta t_{cav} = 0.01$ which represents 1% of the "duration" of the simulation step in which the cavitation event occurs. The meaning of Δt_{cav} is limited to the cases in which the parameter PVLAW is either 15 or 16. The last parameter in line 5 is PVLAW which is 16 in this example.

In the *ELEMENT option on line 6 the user defines the TYPE of the user element

and on lines 7 through 13 the nodes by which the element is defined are given. The order is clockwise with the first and last nodes on the axis of symmetry of the model.

```
 *USER ELEMENT, TYPE=U1, NODES=75, COORDINATES=2,VARIABLES=9, PROPERTIES=6,
IPROPERTIES=1
1,2
*UEL PROPERTY, ELSET=UEL1
2000.0, -60.0, 0.00025, -45.15, 0.01, 1.0, 16
*ELEMENT,TYPE=U1,ELSET=UEL1
1,9999,7129,7113,7082,7066,7035,7019,6988,6975,6941,
6925,6894,6878,6847,6831,6800,6784,6753,6737,6706,
6690,6659,6643,6612,6596,6565,6549,6518,6502,6471,
6189,6158,6142,6111,6098,6064,6048,6017,6001,5970,                    10
5954,5923,5907,5876,5860,5829,5813,5782,5766,5735,
5719,5688,5672,5641,5625,5594,5578,5547,5531,5500,
5484,5453,5437,5406,9999
```

B.8 Subroutine Code

The FORTRAN code for the rubber particle subroutine is listed below:

```
    SUBROUTINE UEL(RHS,AMATRX,SVARS,ENERGY,NDOFEL,NRHS,NSVARS,
     & PROPS,NPROPS,COORDS,MCRD,NNODE,U,DU,V,A,JTYPE,TIME,DTIME,
     & KSTEP,KINC,JELEM,PARAMS,NDLOAD,JDLTYP,ADLMAG,PREDEF,NPREDF,
     & LFLAGS,MLVARX,DDLMAG,MDLOAD,PNEWDT,JPROPS,NJPROP,PERIOD)
c       User Element subroutine.
c       Version 3.1
c       Varying Triaxiality
c       uel31.f
c ****************************************************************
c **    HISTORY                                                 **          10
c ****************************************************************
c VERSION 3.0 'uel30.f'
c  Implemented force relaxation algorithm.
c  P-V-Laws now implemented:
c    JPROPS(1)=13  First step is displacement with sudden K-drop
```

```
c                 No second step, no cooling
c    JPROPS(1)=14  First step is cooling
c                 Second step is displacement with sudden K-drop
c    JPROPS(1)=15  First step is displacement with force relaxation
c                   in the same step                                    20
c                 No second step, no cooling
c    JPROPS(1)=16  First step is cooling
c                 Second step is displacement with force relaxation
c  New variables:
c    SVARS(4)  cavitation state of the particle
c       0 = before cavitation
c       1 = during cavitation
c       2 = after cavitationa
c    SVARS(5)  time at which cavitation process "starts"
c    SVARS(6)  time at which cavitation process "termiates"              30
c    SVARS(7)  step number in which cavitation takes place
c    SVARS(8)  last time at which the subroutine was accessed
c    SVARS(9)  pressure at last acces of subroutine (at same time)
c    PROPS(5)  time period over which cavitation process occurs
c    PROPS(6)  critical last pressure value (when time reaches the
c                preset end-of-cavitation time, then the second con-
c                dition is that the last pressure be below PROPS(6) )
c  New output parameters:
c    OUT20 = all variables rel.  to P-V-law 15
c VERSION 2.1 Triaxial 'uel21tri.f'                                     40
c  Included the features of Simona's triaxial.f with a second
c   type of uel and a DLOAD subroutine.
c  Added the common block.
c  Added JTYPE identifying what element the UEL is being called for.
c  Integrated uvarm14.f at end.
c VERSION 2.1 'uel21.f'
c  Modified from version 2.0
c  Added use of PROPS(4) (see below).
c  Added P-V law 14.
c VERSION 2.0 is modified from version 1.7                              50
c  Implemented passing of 'state variables' SVARS(NSVARS):
```

```
c     SVARS(1) = step when voiding occurred
c     SVARS(2) = time when voiding occured
c     SVARS(3) = 0 if voiding has not occured yet
c                1 if voiding has occured
c  Implemented passing of PROPS(NPROPS): (real)
c     PROPS(1) = bulk modulus of the particle
c     PROPS(2) = voiding pressure of the particle
c     PROPS(3) = linear thermal expansion coeff of particle
c     PROPS(4) = delta T during first step                                  60
c  Implemented passing of JPROPS(NJPROP): (integer)
c     JPROPS(1) = no.  of P-V law to be used
c  Implemented P-V law 13:
c     Uses PROPS to void
c     Uses SVARS to indicate if particle has voided.
c     BULK modulus is dropped suddenly to 0.0000001 of initial BULK.
c  Inplemented SPECIAL 6:
c     Output condition adapted to SVARS.
c  IMPORTANT:
c     From version 2.0 on, only P-V laws 13 and up can be used.             70
c     From version 2.0 on, only SPECIAL 6 and up can be used.
c VERSION 1.7 is modified from version 1.6 (NOT 1.6B)
c  Modified PV-LAW 12:
c     step 1:  cooling
c     step 2:  deformation and voiding
c     step 3:  further deformation
c        (Exception for T12 > 1.0.  See below definition of T12.)
c  SPECIAL parameter:  option 5 modified:  to be used with PVLAW 12.
c VERSION 1.6 is modified from version 1.4 (NOT 1.5).
c NEW IN VERSION 1.6                                                       80
c  PV-LAW 12 for pre-shrinkage using temperature-dependence.
c  SPECIAL parameter:  option 5 added:  to be used with PVLAW 12.
c NEW IN VERSION 1.4
c  SPECIAL parameter:  option 4 added.
c FROM THE ORIGINAL VERSION:
c  Throughout subroutine:  use WRHS(DOF,NNODE)
c     then at the end assign WRHS values to RHS(NDOFEL,1)
```

```
c  Sign of AMATRX is inverted relative to sign of RHS.
c  If statement in 'computing simplifying variables' for the cases
c    of extremely small UCOORDS(1,KNN) and UCOORDS(1,KNN+1).                  90
c  PVLAW implemented.
c ***************************************************************
c **    HOW TO USE THIS SUBROUTINE (version 2.0 and up)       **
c ***************************************************************
c To be set in the user subroutine:
c   - output and echoing flags OUT1 - OUT20
c   - special output parameter SPECIAL
c To be set in the input deck (example):
c    *USER ELEMENT, TYPE=U1, NODES=9, COORDINATES=2,VARIABLES=3,
c    PROPERTIES=4, IPROPERTIES=1                                             100
c    1,2
c    *USER SUBROUTINE,INPUT=uel21.f
c    *ELEMENT,TYPE=U1,ELSET=PARTICLE
c    1,1,12026,10026,8026,6026,4026,2026,26,1
c    ** enter properties for uel21.f:
c    **   bulk mod.  (real)
c    **   cavitation press (real)
c    **   lin.therm.ex.coeff (real)
c    **   delta T during first step (real) [P-V-law 14]
c    **   time period over which cavitation occurs (real) [P-V-law 15]       110
c    **   no.  of P-V law to be used (integer)
c    *UEL PROPERTY, ELSET=PARTICLE
c    2000.0, -8.0, 0.00025, -32.447, 0.05, 14
c ***************************************************************
c **    P-V LAWS (version 3.0 and up) JPROPS(1)               **
c ***************************************************************
c 13:  No thermal expansion.  Sudden drop of BULK.
c 14:  First step is cooling, second step displacament with sudden K-drop.
c 15:  First step displacement with force relaxation.  No thermal expansion.
c 16:  First step is cooling, second step displacement with force relaxation  120
c ***************************************************************
c **    INCLUDE, DECLARATIONS, DIMENSIONS, PARAMETERS         **
c ***************************************************************
```

```
c ********* include ************************************************
      INCLUDE 'ABA_PARAM.INC'
c ********* parameter declaration *********************************
c *** output and echoing parameters ***
c Whenever a parameter is 1, the corresponding output is done.
      PARAMETER( OUT1 = 0 )
c       output:  UEL entry header, KSTEP, KINC                          130
      PARAMETER( OUT2 = 0 )
c       output:  MCRD, NNODE, NDOFEL, MLVARX, NRHS, JTYPE, JELEM,
c              NSVARS, NPROPS, NJPROP, SVARS, PROPS, JPROPS
      PARAMETER( OUT3 = 0 )
c       output:  COORDS, U
      PARAMETER( OUT4 = 0 )
c       output:  LFLAGS
      PARAMETER( OUT5 = 0 )
c       output:  iteration headers ('now I am doing this...')
      PARAMETER( OUT6 = 0 )                                             140
c       output:  warnings, errors, comments
      PARAMETER( OUT7 = 0 )
c       output:  KY, KX, DFDP, DPDV, DVDU, DFDU
      PARAMETER( OUT8 = 0 )
c       output:  VU, V0, VU-V0, PU
      PARAMETER( OUT9 = 0 )
c       output:  simplifying variables DELR, DELZ, LENS, PARI, PARJ
      PARAMETER( OUT10 = 0 )
c       output:  force magnitudes
      PARAMETER( OUT11 = 0 )                                            150
c       output:  WRHS
      PARAMETER( OUT12 = 0 )
c       output:  DFDP
      PARAMETER( OUT13 = 0 )
c       output:  DPDV
      PARAMETER( OUT14 = 0 )
c       output:  DVDU
      PARAMETER( OUT15 = 0 )
c       output:  DFIDRI, DFIDZI, DFIDRJ, DFIDZJ
```

```
      PARAMETER( OUT16 = 0 )                                              160
c       output:  DFDU
      PARAMETER( OUT17 = 0 )
c       output:  AMATRX
      PARAMETER( OUT18 = 0 )
c       output:  stiffness matrix computed from deltas (skipped)
      PARAMETER( OUT19 = 0 )
c       output:  RHS
      PARAMETER( OUT20 = 0 )
c       output:  all variables rel.  to P-V-law 15, 16
c *** special output parameters ***                                       170
      PARAMETER( SPECIAL = 6 )
c       values for SPECIAL
c         6:  PU, KINC, TIME(1)+KSTEP-1, VU, Step#, X, V0
c              where X = 1 before voiding, and
c                    X = force relaxation factor during voiding
c                          (P-V-Laws 15,16 only)
c                   X = 0.0000001 after voiding
c *** dimensioning parameters ***
      PARAMETER( NMAX=200 )
c       the number of nodes in the element is limited to 100              180
c *** just constants ***
      PARAMETER( PI = 3.141592653598D0)
      PARAMETER( PI03 = 1.0471975511966D0)
c *** tolerances ***
      PARAMETER( TOLERA = 0.001D0)
c       TOLERA is tolerance for the vertical-segment-approximation
      PARAMETER( TOLERB = 1.0E-20 )
      PARAMETER( TOLERC = 1.0E-10 )
c ********* declaration of PASSED-IN variables ******************
c not necessary                                                           190
c ********* declaration of LOCAL variables ***********************
      INTEGER NNODE, MCRD, NDOFEL, LFLAGS
      DOUBLE PRECISION
     &  M, N, LENG, V0, DS,
     &  UCOORDS, UM, UN, ULENG, VU,
```

```
     &  DELR, DELZ, LENS, PARI, PARJ, FI, FJ, FTOT, PU,
     &  DFDP, DPDV, DVDU, DFDU,
     &  DFIDRI, DFIDZI, DFIDRJ, DFIDZJ,
     &  DFJDRI, DFJDZI, DFJDRJ, DFJDZJ,
     &  DFIDP, DFJDP,                                                  200
     &  PARA, PPDR,
     &  RI, RJ, XPARI, XPARJ, XLENS, XPARA, XPPDR,
     &  X1DFIDRI, X1DFIDZI, X1DFIDRJ, X1DFIDZJ,
     &  X1DFJDRI, X1DFJDZI, X1DFJDRJ, X1DFJDZJ,
     &  X2DFIDRI, X2DFIDZI, X2DFIDRJ, X2DFIDZJ,
     &  X2DFJDRI, X2DFJDZI, X2DFJDRJ, X2DFJDZJ,
     &  WRHS
c ********* counter variable declaration ************************
      INTEGER KNN, KX, KY
c ********* dimensioning PASSED-IN variables ********************  210
      DIMENSION RHS(MLVARX,*),AMATRX(NDOFEL,NDOFEL),PROPS(*),
     & SVARS(*),ENERGY(8),COORDS(MCRD,NNODE),U(NDOFEL),
     & DU(MLVARX,*),V(NDOFEL),A(NDOFEL),TIME(2),PARAMS(*),
     & JDLTYP(MDLOAD,*),ADLMAG(MDLOAD,*),DDLMAG(MDLOAD,*),
     & PREDEF(2,NPREDF,NNODE),LFLAGS(*),JPROPS(*)
c ********* dimensioning LOCAL variables ************************
      DIMENSION
     &  M(2,NMAX),  N(2,NMAX),  DS(NMAX),
     & UCOORDS(2,NMAX), UM(2,NMAX), UN(2,NMAX), UDS(NMAX),
     &  DELR(NMAX), DELZ(NMAX), LENS(NMAX), PARI(NMAX),                220
     &  PARJ(NMAX),
     &  FI(NMAX), FJ(NMAX), FTOT(NMAX),
     &  DFDP(NMAX), DVDU(NMAX), DFDU(NMAX,NMAX),
     &  DFIDP(NMAX), DFJDP(NMAX),
     &  DFIDRI(NMAX), DFIDZI(NMAX), DFIDRJ(NMAX), DFIDZJ(NMAX),
     &  DFJDRI(NMAX), DFJDZI(NMAX), DFJDRJ(NMAX), DFJDZJ(NMAX),
     &  WRHS(2,NNODE)
c ********* flags declaration ************************************
      INTEGER WARN8(NMAX)
c ***************************************************************  230
c **    FEEDBACK OF PASSED-IN DATA                          **
```

```
c ***************************************************************
c ********* outputting UCOORDS ************************************
      IF ( OUT1 .EQ. 1 ) THEN
         WRITE(*,*) ' '
         WRITE(*,*) ' '
         WRITE(*,*) '*********************************************',
     &    '********************'
         WRITE(*,*) '*** ENTERING USER SUBROUTINE       ',
     &    '              *****************'                                  240
         WRITE(*,*) '*********************************************',
     &    '********************'
         WRITE(*,*) ' '
         WRITE(*,*) '*********************************'
         WRITE(*,*) '* Feedback of passed-in values:  *'
         WRITE(*,*) '*********************************'
         WRITE(*,*) '* KSTEP=', KSTEP
         WRITE(*,*) '* KINC=', KINC
         WRITE(*,*) '* TIME(1)=', TIME(1)
      ENDIF                                                                 250
      IF ( OUT2 .EQ. 1 ) THEN
         WRITE(*,*) '* MCRD=', MCRD
         WRITE(*,*) '* NNODE=', NNODE
         WRITE(*,*) '* NDOFEL=', NDOFEL
         WRITE(*,*) '* MLVARX=', MLVARX
         WRITE(*,*) '* NRHS=', NRHS
         WRITE(*,*) '* JTYPE=', JTYPE
         WRITE(*,*) '* JELEM=', JELEM
         WRITE(*,*) '* NSVARS=', NSVARS
         WRITE(*,*) '* NPROPS=', NPROPS                                     260
         WRITE(*,*) '* NJPROP=', NJPROP
         WRITE(*,*) '* SVARS:'
         IF (NSVARS .GT. 0) THEN
            DO 21 KNN=1,NSVARS
               WRITE(*,*) '   SVARS(', KNN, ')= ', SVARS(KNN)
   21       CONTINUE
         ELSE
```

```
         WRITE(*,*) 'NSVARS not > 0, so no output for SVARS.'
       ENDIF
       WRITE(*,*) '* PROPS:'                                          270
       IF (NPROPS .GT. 0) THEN
          DO 22 KNN=1,NPROPS
             WRITE(*,*) '   PROPS(', KNN, ')= ', PROPS(KNN)
 22       CONTINUE
       ELSE
          WRITE(*,*) 'NPROPS not > 0, so no output for PROPS.'
       ENDIF
       WRITE(*,*) '* JPROPS:'
       IF (NJPROP .GT. 0) THEN
          DO 23 KNN=1,NJPROP                                          280
             WRITE(*,*) '   JPROPS(', KNN, ')= ', JPROPS(KNN)
 23       CONTINUE
       ELSE
          WRITE(*,*) 'NJPROP not > 0, so no output for JPROPS.'
       ENDIF
    ENDIF
    IF ( OUT3 .EQ. 1 ) THEN
       WRITE(*,*) '* COORDS:'
       WRITE(*,FMT=35) 'NODE#','COORDS'
 35  FORMAT(A7, A32)                                                 290
    DO 39 KNN=1,NNODE
      WRITE(*,FMT=37) KNN,COORDS(1,KNN),COORDS(2,KNN)
 37    FORMAT(I5,3X,E25.13,1X,E21.13)
 39  CONTINUE
    WRITE(*,*) '* U:'
       WRITE(*,FMT=45) 'NODE#','U'
 45    FORMAT(A7, A29)
       DO 49 KNN=1,NNODE
          WRITE(*,FMT=37) KNN, U((2*KNN)-1), U(2*KNN)
 47       FORMAT(I5,3X,E25.13,1X,E21.13)                             300
 49    CONTINUE
    ENDIF
    IF ( OUT4 .EQ. 1 ) THEN
```

```
         WRITE(*,*) '* LFLAGS(3)=', LFLAGS(3)
         WRITE(*,*) '* LFLAGS(1)=', LFLAGS(1)
         WRITE(*,*) '***'
      ENDIF
c ***************************************************************
c **    LFLAGS solution procedure and requirements for element **
c **    calculations                                           **                310
c ***************************************************************
      IF (LFLAGS(3).EQ.1) THEN
      IF (LFLAGS(1).EQ.1 .OR. LFLAGS(1).EQ.2) THEN
c ************************************************** CASE 1 **
c **    LFLAGS(3) = 1  normal incrementation:  define RHS     **
c **   and                                     and AMATRX     **
c **    LFLAGS(1) = 1 or 2  static analysis *STATIC           **
c **                                  or *STATIC,DIRECT      **
c ***************************************************************
      IF ( OUT5 .EQ. 1) THEN                                                    320
         WRITE(*,*) '*******************************************'
         WRITE(*,*) '* Begin STATIC or STATIC,DIRECT analysis    *'
         WRITE(*,*) '* LFLAGS(3)=1 and LFLAGS(1)=1 or 2          *'
         WRITE(*,*) '*******************************************'
      ENDIF
c ***************************************************************
c **    VERIFICATION OF DATA, WRITING WARNINGS                 **
c ***************************************************************
c ******* warning ***************************************************
      IF ( OUT6 .EQ. 1) THEN                                                    330
        WRITE(*,*) '*** Warnings'
         IF ( (NNODE*MCRD) .NE. NDOFEL) THEN
           WRITE(*,*) '* Error 1:  (NNODE * MCRD) .NE. NDOFEL'
         ENDIF
         IF ( ABS(COORDS(1,1)) .GT. TOLERB ) THEN
           WRITE(*,*) '* Error 4:  first node not on axis of symm.'
         ENDIF
         IF ( ABS(COORDS(1,NNODE)) .GT. TOLERB ) THEN
           WRITE(*,*) '* Error 5:  last node not on axis of symm.'
```

```
         ENDIF                                                          340
         IF ( ABS(U(1)) .GT. TOLERB ) THEN
           WRITE(*,*) '* Error 6:  r-disp of first node .NE. zero.'
         ENDIF
         IF ( ABS(U(NDOFEL-1)) .GT. TOLERB ) THEN
           WRITE(*,*) '* Error 7:  r-disp of last node .NE. zero.'
         ENDIF
         IF ( COORDS(2,1) .LE. COORDS(2,NNODE) ) THEN
           WRITE(*,*) '* Error 9:  COORDS(2,1) .LE. COORDS(2,NNODE)'
         ENDIF
       ENDIF                                                            350
c ********************************************************************
c **    ARRANGING VARIABLES                                         **
c ********************************************************************
       IF ( OUT5 .EQ. 1 ) THEN
         WRITE(*,*) '*** Arranging Variables'
       ENDIF
c ******* setting too small COORDS to zero ***********************
       IF ( OUT5 .EQ. 1 ) THEN
         WRITE(*,*) 'setting too small COORDS to zero.'
       ENDIF                                                            360
       DO 60 KNN=1,NNODE
         IF ( COORDS(1,KNN) .LT. TOLERC ) THEN
           COORDS(1,KNN) = 0.0D0
           IF ( OUT6 .EQ. 1 ) THEN
             WRITE(*,*) 'COORDS(1,',KNN,') set to zero.'
           ENDIF
         ENDIF
    60 CONTINUE
c ******* computing current position UCOORDS *********************
       DO 70 KNN=1,NNODE                                                370
         UCOORDS(1,KNN) = COORDS(1,KNN) + U((2*KNN)-1)
         UCOORDS(2,KNN) = COORDS(2,KNN) + U(2*KNN)
         IF (UCOORDS(1,KNN) .LE. 0.0D0) THEN
           IF (KNN .NE.1 .AND. KNN .NE. NNODE) THEN
             IF ( OUT6 .EQ. 1 ) THEN
```

```
                WRITE(*,*) '* Error 3:  r-coord .LT. zero.'
              ENDIF
            ENDIF
          ENDIF
   70 CONTINUE                                                          380
c ********************************************************************
c **    INTIALIZING VARIABLES TO ZERO                              **
c ********************************************************************
      IF ( OUT5 .EQ. 1 ) THEN
         WRITE(*,*) '*** Initializing Variables to Zero'
      ENDIF
      VO = 0.0D0
      VU = 0.0D0
      DO 83 KNN=1,NNODE
         FI(KNN) = 0.0D0                                                390
         FJ(KNN) = 0.0D0
   83 CONTINUE
      DO 85 KX = 1, NDOFEL
         DO 84 KY = 1, NDOFEL
            DFDU(KX,KY) = 0.0D0
            AMATRX(KX,KY) = 0.0D0
   84    CONTINUE
   85 CONTINUE
c ********************************************************************
c **    M, N,UM, UN, VO, VU, FI FJ                                 **  400
c ********************************************************************
c ******* computing N, M, LENG, UN, UM, ULENG ********************
      IF ( OUT5 .EQ. 1 ) THEN
         WRITE(*,*) '*** Computing N, M, LENG, UN, UM, ULENG'
      ENDIF
      DO 100 KNN=1,(NNODE-1)
         M(1,KNN) = ( COORDS(1,KNN) + COORDS(1,(KNN+1)) ) / 2.0D0
         M(2,KNN) = ( COORDS(2,KNN) + COORDS(2,(KNN+1)) ) / 2.0D0
         UM(1,KNN) = ( UCOORDS(1,KNN) + UCOORDS(1,(KNN+1)) ) / 2.0D0
         UM(2,KNN) = ( UCOORDS(2,KNN) + UCOORDS(2,(KNN+1)) ) / 2.0D0    410
         N(1,KNN) = ( COORDS(2,KNN) - COORDS(2,(KNN+1)) )
```

```
      N(2,KNN) = ( COORDS(1,(KNN+1)) - COORDS(1,KNN) )
      UN(1,KNN) = ( UCOORDS(2,KNN) - UCOORDS(2,(KNN+1)) )
      UN(2,KNN) = ( UCOORDS(1,(KNN+1)) - UCOORDS(1,KNN) )
      LENG = SQRT( ((N(1,KNN))**2.0D0) + ((N(2,KNN))**2.0D0) )
      ULENG = SQRT( ((UN(1,KNN))**2.0D0) + ((UN(2,KNN))**2.0D0) )
      IF ( LENG .LE. 0.0D0 ) THEN
        WRITE(*,*) '* Error 2:  LENG is not larger than zero.'
      ENDIF
      IF ( ULENG .LE. 0.0D0 ) THEN                                    420
        WRITE(*,*) '* Error 2b:  ULENG is not larger than zero.'
      ENDIF
      N(1,KNN) = N(1,KNN) / LENG
      N(2,KNN) = N(2,KNN) / LENG
      UN(1,KNN) = UN(1,KNN) / ULENG
      UN(2,KNN) = UN(2,KNN) / ULENG
  100 CONTINUE
c ********* computing the surface increments DS, UDS *************
      IF ( OUT5 .EQ. 1 ) THEN
        WRITE(*,*) '*** Computing the surface increments DS, UDS'     430
      ENDIF
      DO 120 KNN=1,(NNODE-1)
        DS(KNN) = PI * (COORDS(1,KNN) + COORDS(1,(KNN+1))) *
     &             SQRT( ((COORDS(1,KNN) - COORDS(1,(KNN+1)))**2.0D0)
     &                 + ((COORDS(2,KNN) - COORDS(2,(KNN+1)))**2.0D0) )
        UDS(KNN) = PI * (UCOORDS(1,KNN) + UCOORDS(1,(KNN+1))) *
     &             SQRT( ((UCOORDS(1,KNN) - UCOORDS(1,(KNN+1)))**2.0D0)
     &                 + ((UCOORDS(2,KNN) -
     &                                    UCOORDS(2,(KNN+1)))**2.0D0) )
  120 CONTINUE                                                        440
c ********* computing volumes V0 and VU  ************************
      IF ( OUT5 .EQ. 1 ) THEN
        WRITE(*,*) '*** computing volumes V0 and VU'
      ENDIF
      DO 130 KNN=1,(NNODE-1)
        V0 = V0 + ( ( (M(1,KNN)*N(1,KNN)) + (M(2,KNN)*N(2,KNN)) )
     &              * DS(KNN) )
```

```
         VU = VU + ( ( (UM(1,KNN)*UN(1,KNN)) + (UM(2,KNN)*UN(2,KNN)) )
     &               * UDS(KNN) )
  130 CONTINUE                                                          450
      VO = VO / 3.0D0
      VU = VU / 3.0D0
c *****************************************************************
c **    computing the pressure PU                                **
c *****************************************************************
      IF ( OUT5 .EQ. 1 ) THEN
         WRITE(*,*) '*** computing pressure PU'
         IF ( VO .LT. TOLERA ) THEN
            WRITE(*,*) 'P-V-Relations is', JPROPS(1)
         ENDIF                                                          460
      ENDIF
c ********* P-V Law no.  13 ***************************************
      IF ( JPROPS(1) .EQ. 13 ) THEN
         IF ( SVARS(3) .EQ. 0 ) THEN
c           ** Voiding has not occured yet.                  **
c           ** Voiding condition needs to be evaluated.      **
            PU = PROPS(1) * ( 1.0D0 - VU/VO )
            IF ( PU .LT. PROPS(2) ) THEN
c              ** Voiding condition satisfied:  voiding now! **
               SVARS(1) = KSTEP                                         470
               SVARS(2) = TIME(1)
               SVARS(3) = 1
               PU = 0.0000001 * PROPS(1) * ( 1.0D0 - VU/VO )
            ENDIF
         ELSE IF ( SVARS(1) .LE. KSTEP .AND. TIME(1) .LE. SVARS(2) )
     &      THEN
c           ** Abaqus has gone backwards and the voiding con- **
c           ** dition has to be re-evaluated.                 **
            SVARS(3) = 0
            PU = PROPS(1) * ( 1.0D0 - VU/VO )                           480
            IF ( PU .LT. PROPS(2) ) THEN
c              ** Voiding condition satisfied:  voiding now! **
               SVARS(1) = KSTEP
```

```
            SVARS(2) = TIME(1)
            SVARS(3) = 1
            PU = 0.0000001 * PROPS(1) * ( 1.0D0 - VU/V0 )
          ENDIF
        ELSE
c         ** Particle is already voided and Abaqus has not **
c         ** gone backwards.                                **
          PU = 0.0000001 * PROPS(1) * ( 1.0D0 - VU/V0 )
        ENDIF
c ********* P-V Law no.  14 ************************************
      ELSE IF ( JPROPS(1) .EQ. 14 ) THEN
        IF ( KSTEP .EQ. 1) THEN
c         ** Cooling is happening during this step 1       **
          V0 = V0 * ( (1 + (TIME(1)*PROPS(3)*PROPS(4)))**3.0D0 )
        ELSE
c         ** Cooling was completed in step 1              **
          V0 = V0 * ( (1 + (PROPS(3)*PROPS(4)))**3.0D0 )
        ENDIF
        IF ( SVARS(3) .EQ. 0 ) THEN
c         ** Voiding has not occured yet.                 **
c         ** Voiding condition needs to be evaluated.     **
          PU = PROPS(1) * ( 1.0D0 - VU/V0 )
          IF ( PU .LT. PROPS(2) ) THEN
c           ** Voiding condition satisfied:  voiding now! **
            SVARS(1) = KSTEP
            SVARS(2) = TIME(1)
            SVARS(3) = 1
            PU = 0.0000001 * PROPS(1) * ( 1.0D0 - VU/V0 )
          ENDIF
        ELSE IF ( SVARS(1) .LE. KSTEP .AND. TIME(1) .LE. SVARS(2) )
     &      THEN
c         ** Abaqus has gone backwards and the voiding con- **
c         ** dition has to be re-evaluated.                 **
          SVARS(3) = 0
          PU = PROPS(1) * ( 1.0D0 - VU/V0 )
          IF ( PU .LT. PROPS(2) ) THEN
```

```
c              ** Voiding condition satisfied:  voiding now! **                520
               SVARS(1) = KSTEP
               SVARS(2) = TIME(1)
               SVARS(3) = 1
               PU = 0.0000001 * PROPS(1) * ( 1.0D0 - VU/V0 )
            ENDIF
         ELSE
c           ** Particle is already voided and Abaqus has not **
c           ** gone backwards.                                **
            PU = 0.0000001 * PROPS(1) * ( 1.0D0 - VU/V0 )
         ENDIF                                                                  530
c ********* P-V Law no.  15 and 16 *********************************
      ELSE IF ( (JPROPS(1) .EQ. 15) .OR. (JPROPS(1) .EQ. 16) ) THEN
c
         IF ( JPROPS(1) .EQ. 16 ) THEN
            IF ( KSTEP .EQ. 1 ) THEN
c              ** Cooling is happening during this step 1     **
               V0 = V0 * ( (1 + (TIME(1)*PROPS(3)*PROPS(4)))**3.0D0 )
            ELSE
c              ** Cooling was completed in step 1             **
               V0 = V0 * ( (1 + (PROPS(3)*PROPS(4)))**3.0D0 )                   540
            ENDIF
         ENDIF
         PU = PROPS(1) * ( 1.0D0 - VU/V0 )
         IF ( OUT20 .EQ. 1 ) THEN
            WRITE(*,*) ' '
            WRITE(*,*) '*** incoming:'
            WRITE(*,*) 'state         SVARS(4)= ', SVARS(4)
            WRITE(*,*) 't start       SVARS(5)= ', SVARS(5)
            WRITE(*,*) 't end         SVARS(6)= ', SVARS(6)
            WRITE(*,*) 'cav step      SVARS(7)= ', SVARS(7)                   550
            WRITE(*,*) 'last access   SVARS(8)= ', SVARS(8)
            WRITE(*,*) 'last pressure SVARS(9)= ', SVARS(9)
            WRITE(*,*) 'current time  TIME(1)= ', TIME(1)
            WRITE(*,*) 'calc.  press   PU= ', PU
            WRITE(*,*) 'cav.  press    PROPS(2)= ', PROPS(2)
```

```
            WRITE(*,*) 'cav.  period   PROPS(5)= ', PROPS(5)
          ENDIF
  135     IF ( SVARS(4) .EQ. 0 ) THEN
            IF ( PU .LT. PROPS(2) ) THEN
              SVARS(4) = 1                                              560
              SVARS(5) = TIME(1)
              SVARS(6) = TIME(1) + PROPS(5)
              SVARS(7) = KSTEP
              SVARS(8) = TIME(1)
              IF ( OUT20 .EQ. 1 ) THEN
                WRITE(*,*) '** 1 **'
              ENDIF
              GOTO 135
C             ** 1 **
            ELSE                                                        570
              IF ( OUT20 .EQ. 1 ) THEN
                WRITE(*,*) '** 2 **'
              ENDIF
C             ** 2 **
            ENDIF
          ELSE IF ( SVARS(4) .EQ. 1 ) THEN
            IF ( (TIME(1) .GT. SVARS(6))
     &          .AND. (SVARS(9) .LT. PROPS(6)) ) THEN
              SVARS(4) = 2
              IF ( OUT20 .EQ. 1 ) THEN                                  580
                WRITE(*,*) '** 4 **'
              ENDIF
C             ** 4 **
              GOTO 135
            ELSE IF ( TIME(1) .EQ. SVARS(8) ) THEN
              IF ( SVARS(9) .EQ. 0 ) THEN
                SVARS(9) = PU
                IF ( OUT20 .EQ. 1 ) THEN
                  WRITE(*,*) '** 11 **'
                ENDIF                                                   590
C               ** 11 **
```

```
            ELSE
              PU = SVARS(9)
               IF ( OUT20 .EQ. 1 ) THEN
                  WRITE(*,*) '** 9 **'
               ENDIF
c              ** 9 **
            ENDIF
         ELSE
            PU = SVARS(9) * ( (SVARS(6) - TIME(1)) /                    600
     &                        (SVARS(6) - SVARS(5)) + 0.0000001 )
            IF ( OUT20 .EQ. 1 ) THEN
               WRITE(*,*) 'PU-factor= ',
     &          (SVARS(6)-TIME(1))/(SVARS(6)-SVARS(5)) + 0.0000001
            ENDIF
            SVARS(8) = TIME(1)
            IF ( PU .LT. PROPS(2) ) THEN
              PU = PROPS(2)
               IF ( OUT20 .EQ. 1 ) THEN
                  WRITE(*,*) '** 10 **'                                 610
               ENDIF
c              ** 10 **
            ELSE
               IF ( OUT20 .EQ. 1 ) THEN
                  WRITE(*,*) '** 5 **'
               ENDIF
c              ** 5 **
            ENDIF
         ENDIF
       ELSE IF (SVARS(4) .EQ. 2 ) THEN                                  620
         PU = 0.0000001 * PU
c        ** 7 **
       ELSE
c         ** there is a problem                          **
          WRITE(*,*) '*** ERROR: invalid value for SVARS(4)',
     &    'in PU calc.:  ', SVARS(4)
c         ** 8 **
```

```
        ENDIF
        IF ( OUT20 .EQ. 1 ) THEN
           WRITE(*,*) '*** outgoing:'                                    630
           WRITE(*,*) 'state         SVARS(4)= ', SVARS(4)
           WRITE(*,*) 't start       SVARS(5)= ', SVARS(5)
           WRITE(*,*) 't end         SVARS(6)= ', SVARS(6)
           WRITE(*,*) 'cav step      SVARS(7)= ', SVARS(7)
           WRITE(*,*) 'last access   SVARS(8)= ', SVARS(8)
           WRITE(*,*) 'last pressure SVARS(9)= ', SVARS(9)
           WRITE(*,*) 'current time  TIME(1)= ', TIME(1)
           WRITE(*,*) 'calc.  press   PU= ', PU
           WRITE(*,*) 'cav.  press    PROPS(2)= ', PROPS(2)
           WRITE(*,*) 'cav.  period   PROPS(5)= ', PROPS(5)              640
        ENDIF
c ********* test for invalid P-V Law number **********************
      ELSE
        WRITE(*,*) '*** ERROR: invalid value for JPROPS(1) in PU calc:  ',
     &              JPROPS(1)
      ENDIF
c ********* testing V0, PU regarding limits **********************
      IF ( V0 .EQ. 0 ) THEN
        WRITE(*,*) '* Error:  V0= ',V0,' .'
      ENDIF                                                            650
      IF ( PU .GT. 1.0E50 ) THEN
        WRITE(*,*) '*** Error:  PU > 1.0E50'
        PU = 1.0E50
      ENDIF
      IF ( PU .LT. -1.0E50 ) THEN
        WRITE(*,*) '*** Error:  PU < -1.0E50'
        PU = -1.0E50
      ENDIF
c ****************************************************************
c **    computing simplifying variables                       **    660
c ****************************************************************
      IF ( OUT5 .EQ. 1 ) THEN
         WRITE(*,*) '*** computing simplifying variables'
```

```
      ENDIF
      DO 140 KNN=1,(NNODE-1)
         DELR(KNN) = UCOORDS(1,KNN+1) - UCOORDS(1,KNN)
         DELZ(KNN) = UCOORDS(2,KNN+1) - UCOORDS(2,KNN)
         LENS(KNN) = SQRT( DELR(KNN)**2.0D0 + DELZ(KNN)**2.0D0 )
      IF ( OUT5 .EQ. 1 ) THEN
         WRITE(*,*) '*** computing simplifying variables'                    670
      ENDIF
c           WRITE(*,*) 'KNN=',KNN,'  UCOORDS(1,KNN)=',UCOORDS(1,KNN),
c     &                '  UCOORDS(1,KNN+1)=',UCOORDS(1,KNN+1)
      IF ( UCOORDS(1,KNN) .LT. TOLERB ) THEN
c this IF statement because float errors with X**3 when X < E-40
         IF ( OUT5 .EQ. 1 ) THEN
            WRITE(*,*) '*** computing simplifying variables'
         ENDIF
            IF ( OUT6 .EQ. 1 ) THEN
               WRITE(*,*) 'UCOORDS(1,KNN) .LT. TOLERB'                       680
            ENDIF
           PARI(KNN) = ( ((UCOORDS(1,KNN+1)**3.0D0)/3.0D0)
     &                 - (UCOORDS(1,KNN+1)*(UCOORDS(1,KNN  )**2.0D0)) )
           PARJ(KNN) = ( - (UCOORDS(1,KNN  )*(UCOORDS(1,KNN+1)**2.0D0))
     &                 + (2.0D0*(UCOORDS(1,KNN+1)**3.0D0)/3.0D0) )
         ELSE IF ( UCOORDS(1,KNN+1) .LT. TOLERB ) THEN
            IF ( OUT6 .EQ. 1 ) THEN
               WRITE(*,*) 'UCOORDS(1,KNN+1) .LT. TOLERB'
            ENDIF
           PARI(KNN) = ( - (UCOORDS(1,KNN+1)*(UCOORDS(1,KNN  )**2.0D0))     690
     &                 + (2.0D0*(UCOORDS(1,KNN  )**3.0D0)/3.0D0) )
           PARJ(KNN) = ( ((UCOORDS(1,KNN  )**3.0D0)/3.0D0)
     &                 - (UCOORDS(1,KNN  )*(UCOORDS(1,KNN+1)**2.0D0)) )
         ELSE
            IF ( OUT6 .EQ. 1 ) THEN
               WRITE(*,*) 'UCOORDS(1,KNN+1 & KNN) not .LT. TOLERB'
            ENDIF
            PARI(KNN) = ( ((UCOORDS(1,KNN+1)**3.0D0)/3.0D0)
     &                  - (UCOORDS(1,KNN+1)*(UCOORDS(1,KNN  )**2.0D0))
```

```
     &                  + (2.0D0*(UCOORDS(1,KNN  )**3.0D0)/3.0D0) )                700
           PARJ(KNN) = ( ((UCOORDS(1,KNN  )**3.0D0)/3.0D0)
     &                  - (UCOORDS(1,KNN  )*(UCOORDS(1,KNN+1)**2.0D0))
     &                  + (2.0D0*(UCOORDS(1,KNN+1)**3.0D0)/3.0D0) )
         ENDIF
  140 CONTINUE
c ********************************************************************
c **    computing FI, FJ                                            **
c ********************************************************************
      IF ( OUT5 .EQ. 1 ) THEN
         WRITE(*,*) '*** computing FI, FJ'                                      710
      ENDIF
      DO 145 KNN=1,(NNODE-1)
         WARN8(KNN) = 0
         IF ( ABS( DELZ(KNN) ) .GT. (TOLERA**2.0D0) ) THEN
            IF ( ABS((DELR(KNN)/DELZ(KNN))) .LT. TOLERA ) THEN
               WARN8(KNN) = 1
            ENDIF
c checking if the solution breaks down due to two nodes that are
c vertically above eachother.  if yes, approximation is made.
         ELSE                                                                   720
            IF (OUT6 .EQ. 1) THEN
               WRITE(*,*) '* Warning 10:  WARN8 test skipped.'
               WRITE(*,*) 'DELZ(',KNN,') = ',DELZ(KNN)
c don't perform check WARN8 if DELRZ(KNN) = 0 (division by zero).
            ENDIF
         ENDIF
         IF ( OUT6 .EQ. 1 ) THEN
            WRITE(*,*) 'WARN8(',KNN,') =', WARN8(KNN)
         ENDIF
         IF ( WARN8(KNN) .EQ. 1 ) THEN                                          730
            IF (OUT5 .EQ. 1) THEN
               WRITE(*,*) 'Begin computing FI from FTOT, KNN= ', KNN
            ENDIF
            FTOT(KNN) = PU * PI * (UCOORDS(1,KNN)+UCOORDS(1,KNN+1))
     &                           * LENS(KNN)
```

```
            FI(KNN) = FTOT(KNN) / 2.0D0
            FJ(KNN) = FI(KNN)
            IF (OUT6 .EQ. 1) THEN
               WRITE(*,*) '* Warning 8:  Approximation made:',
     &                                        'FI = FJ = 0.5 * FTOT'          740
            ENDIF
         ELSE
            IF ( OUT5 .EQ. 1 ) THEN
               WRITE(*,*) 'Begin computing FI directly, KNN= ', KNN
            ENDIF
            FI(KNN) = PU * PI * LENS(KNN)
     &                       * PARI(KNN) / (DELR(KNN)**2.0D0)
            FJ(KNN) = PU * PI * LENS(KNN)
     &                       * PARJ(KNN) / (DELR(KNN)**2.0D0)
         ENDIF                                                                 750
  145 CONTINUE
c ********************************************************************
c **    computing WRHS                                              **
c ********************************************************************
      IF ( OUT5 .EQ. 1 ) THEN
         WRITE(*,*) '*** computing WRHS'
      ENDIF

      WRHS(1,1) = FI(1) * UN(1,1)
      WRHS(2,1) = FI(1) * UN(2,1)                                            760

      DO 155 KNN=2,NNODE-1
         WRHS(1,KNN) = FI(KNN) * UN(1,KNN)  +  FJ(KNN-1) * UN(1,KNN-1)
         WRHS(2,KNN) = FI(KNN) * UN(2,KNN)  +  FJ(KNN-1) * UN(2,KNN-1)
  155 CONTINUE

      WRHS(1,NNODE) = FJ(NNODE-1) * UN(1,NNODE-1)
      WRHS(2,NNODE) = FJ(NNODE-1) * UN(2,NNODE-1)

      IF ( WRHS(1,NNODE) .GT. 1E50 ) THEN                                    770
         WRITE(*,*) '*** Error WRHS(1,',NNODE,') > E50'
```

```
      ENDIF

      IF ( WRHS(2,NNODE) .GT. 1E50 ) THEN
         WRITE(*,*) '*** Error WRHS(2,',NNODE,') > E50'
      ENDIF
c ********************************************************************
c **    computing DFIDP and DFJDP                                   **
c ********************************************************************
      IF ( OUT5 .EQ. 1 ) THEN                                          780
         WRITE(*,*) '*** computing DFIDP and DFJDP'
      ENDIF
      DO 148 KNN=1,NNODE-1
         IF ( WARN8(KNN) .EQ. 1 ) THEN
            DFIDP(KNN) = 0.5D0 * PI * LENS(KNN)
     &                          * (UCOORDS(1,KNN) + UCOORDS(1,KNN+1))
            DFJDP(KNN) = DFIDP(KNN)
         ELSE
            DFIDP(KNN) = PI * LENS(KNN) * PARI(KNN)
     &                        / (DELR(KNN)**2.0D0)                   790
            DFJDP(KNN) = PI * LENS(KNN) * PARJ(KNN)
     &                        / (DELR(KNN)**2.0D0)
         ENDIF
  148    CONTINUE
c ********************************************************************
c **    computing DFDP                                              **
c ********************************************************************
      IF ( OUT5 .EQ. 1 ) THEN
         WRITE(*,*) '*** computing DFDP'
      ENDIF                                                            800
      DFDP(1) = UN(1,1) * DFIDP(1)
      DFDP(2) = UN(2,1) * DFIDP(1)
c
      DO 175 KNN=2,NNODE-1
         DFDP(2*KNN-1) = UN(1,KNN-1) * DFJDP(KNN-1)
     &                 + UN(1,KNN  ) * DFIDP(KNN  )
         DFDP(2*KNN  ) = UN(2,KNN-1) * DFJDP(KNN-1)
```

```
     &                + UN(2,KNN  ) * DFIDP(KNN  )
  175    CONTINUE
c                                                                       810
      DFDP(NDOFEL-1) = UN(1,NNODE-1) * DFJDP(NNODE-1)
      DFDP(NDOFEL  ) = UN(2,NNODE-1) * DFJDP(NNODE-1)
c ***********************************************************************
c **    computing DPDV                                            **
c ***********************************************************************
      IF ( OUT5 .EQ. 1 ) THEN
         WRITE(*,*) '*** computing DPDV'
      ENDIF
      IF ( JPROPS(1) .EQ. 13 ) THEN
         IF (SVARS(3) .EQ. 0) THEN                                      820
            DPDV = -PROPS(1) / V0
         ELSE
            DPDV = -0.0000001 * PROPS(1) / V0
         ENDIF
      ELSE IF ( JPROPS(1) .EQ. 14 ) THEN
         IF (SVARS(3) .EQ. 0) THEN
            DPDV = -PROPS(1) / V0
         ELSE
            DPDV = -0.0000001 * PROPS(1) / V0
         ENDIF                                                          830
      ELSE IF ( (JPROPS(1) .EQ. 15) .OR. (JPROPS(1) .EQ. 16) ) THEN
         IF ( SVARS(4) .EQ. 0 ) THEN
            DPDV = -PROPS(1) / V0
         ELSEIF ( SVARS(4) .EQ. 1 ) THEN
            DPDV = 0.0
         ELSE
            DPDV = -0.0000001 * PROPS(1) / V0
         ENDIF
      ELSE
         WRITE(*,*) '*** ERROR: invalid value for JPROPS(1) in DPDV: ',  840
     &              JPROPS(1)
      ENDIF
      IF ( DPDV .GT. 1.0E50 ) THEN
```

```
         WRITE(*,*) '*** Error:  DPDV > 1.0E50'
         DPDV = 1.0E50
      ENDIF
      IF ( DPDV .LT. -1.0E50 ) THEN
         WRITE(*,*) '*** Error:  DPDV < -1.0E50'
         DPDV = -1.0E50
      ENDIF                                                              850
c ********************************************************************
c **    computing DVDU                                              **
c ********************************************************************
c see notes 4-2-97 pages 1-3
      IF ( OUT5 .EQ. 1 ) THEN
         WRITE(*,*) '*** computing DVDU'
      ENDIF
      DVDU(1) = PI03 * (UCOORDS(2,1)-UCOORDS(2,2)) * UCOORDS(1,2)
      DVDU(2) = PI03 * (UCOORDS(1,2)**2.0D0)
      DO 185 KNN=2, NNODE-1                                              860
         DVDU(KNN*2-1) = PI03 * (
     &   (UCOORDS(2,KNN-1)-UCOORDS(2,KNN)) *
     &              ( UCOORDS(1,KNN-1) + UCOORDS(1,KNN)*2.0D0 )
     & + (UCOORDS(2,KNN)-UCOORDS(2,KNN+1)) *
     &              ( UCOORDS(1,KNN+1) + UCOORDS(1,KNN)*2.0D0 ) )
         DVDU(KNN*2  ) = PI03 * (
     &   - UCOORDS(1,KNN-1) * ( UCOORDS(1,KNN) + UCOORDS(1,KNN-1) )
     &   + UCOORDS(1,KNN+1) * ( UCOORDS(1,KNN) + UCOORDS(1,KNN+1) ) )
  185 CONTINUE
      DVDJ(NDOFEL-1) = PI03 * (UCOORDS(2,NNODE-1)-UCOORDS(2,NNODE))      870
     &                      * UCOORDS(1,NNODE-1)
      DVDU(NDOFEL)   = - PI03 * (UCOORDS(1,NNODE-1)**2.0D0)
c ********************************************************************
c **    computing DFIDRI, DFIDZI, DFIDRJ, DFIDZJ                    **
c ********************************************************************
c revised 97Mar28
      IF ( OUT5 .EQ. 1 ) THEN
         WRITE(*,*) '*** computing DFIDRI, etc.'
      ENDIF
```

```
      DO 190 KNN = 1, NNODE-1                                                  880
         IF ( DELR(KNN) .EQ. 0 ) THEN
            WRITE(*,*) '* Warning 12:  Approxmation for DFDU(',KNN,
     &             ') has been made.'
c compute DFIDRI as average of DFIDRI at RI = RJ - 0.001
c                          and DFIDRI at RI = RJ + 0.001
c same for all others
            RJ = UCOORDS(1,KNN+1)
c first RI = RJ - 0.01 and X1-computations
            RI = UCOORDS(1,KNN  ) - 0.001D0
            XDELR = RJ-RI                                                      890
            XPARI = (RJ**3.0D0)/3.0D0 - RJ*RI*RI + 2.0D0*(RI**3.0D0)/3.0D0
            XPARJ = (RI**3.0D0)/3.0D0 - RI*RJ*RJ + 2.0D0*(RJ**3.0D0)/3.0D0
            XLENS = SQRT( ((RJ-RI)**2.0D0) + (DELZ(KNN)**2.0D0) )
            XPARA = 2.0D0*XLENS/(XDELR**2.0D0) - (1.0D0/XLENS)
            XPPDR = PU * PI / XDELR
            X1DFIDRI =  XPPDR * ( XPARI*XPARA - 2.0D0*RI*XLENS )
            X1DFIDZI = -XPPDR * DELZ(KNN) * XPARI / ( XLENS * XDELR )
            X1DFIDRJ =  XPPDR * ( XPARI*(-XPARA) + (RI+RJ)*XLENS )
            X1DFIDZJ = -X1DFIDZI
            X1DFJDRI =  XPPDR * ( XPARJ*XPARA - (RI+RJ) * XLENS )              900
            X1DFJDZI = -XPPDR * DELZ(KNN) * XPARJ / ( XLENS * XDELR )
            X1DFJDRJ =  XPPDR * ( XPARJ*(-XPARA) + 2.0D0 * RJ * XLENS )
            X1DFJDZJ = -X1DFJDZI
c then RI = RJ + 0.01 and X2-computations
            RI = RI + 0.002D0
            XDELR = RJ-RI
            XPARI = (RJ**3.0D0)/3.0D0 - RJ*RI*RI + 2.0D0*(RI**3.0D0)/3.0D0
            XPARJ = (RI**3.0D0)/3.0D0 - RI*RJ*RJ + 2.0D0*(RJ**3.0D0)/3.0D0
            XLENS = SQRT( ((RJ-RI)**2.0D0) + (DELZ(KNN)**2.0D0) )
            XPARA = 2.0D0*XLENS/(XDELR**2.0D0) - (1.0D0/XLENS)                 910
            XPPDR = PU * PI / XDELR
            X2DFIDRI =  XPPDR * ( XPARI*XPARA - 2.0D0*RI*XLENS )
            X2DFIDZI = -XPPDR * DELZ(KNN) * XPARI / ( XLENS * XDELR )
            X2DFIDRJ =  XPPDR * ( XPARI*(-XPARA) + (RI+RJ)*XLENS )
            X2DFIDZJ = -X2DFIDZI
```

```
            X2DFJDRI =  XPPDR * ( XPARJ*XPARA - (RI+RJ) * XLENS )
            X2DFJDZI = -XPPDR * DELZ(KNN) * XPARJ / ( XLENS * XDELR )
            X2DFJDRJ =  XPPDR * ( XPARJ*(-XPARA) + 2.0D0 * RJ * XLENS )
           X2DFJDZJ = -X2DFJDZI                    -
c calculating averages                                                    920
            DFIDRI(KNN) = 0.5D0 * ( X1DFIDRI + X2DFIDRI )
            DFIDZI(KNN) = 0.5D0 * ( X1DFIDZI + X2DFIDZI )
            DFIDRJ(KNN) = 0.5D0 * ( X1DFIDRJ + X2DFIDRJ )
            DFIDZJ(KNN) = 0.5D0 * ( X1DFIDZJ + X2DFIDZJ )
            DFJDRI(KNN) = 0.5D0 * ( X1DFJDRI + X2DFJDRI )
            DFJDZI(KNN) = 0.5D0 * ( X1DFJDZI + X2DFJDZI )
            DFJDRJ(KNN) = 0.5D0 * ( X1DFJDRJ + X2DFJDRJ )
            DFJDZJ(KNN) = 0.5D0 * ( X1DFJDZJ + X2DFJDZJ )
c normal calculation
         ELSE                                                            930
            PPDR = PU * PI / DELR(KNN)
            PARA = 2.0D0*LENS(KNN)/(DELR(KNN)**2.0D0)
     &                                          - (1.0D0/LENS(KNN))
            DFIDRI(KNN) = PPDR * ( PARI(KNN)*PARA
     &         - 2.0D0 * UCOORDS(1,KNN) * LENS(KNN)  )
            DFIDZI(KNN) = -PPDR * DELZ(KNN) * PARI(KNN)
     &                          / ( LENS(KNN) * DELR(KNN) )
            DFIDRJ(KNN) = PPDR * ( PARI(KNN)*(-PARA)
     &         + (UCOORDS(1,KNN) + UCOORDS(1,KNN+1)) * LENS(KNN)  )
            DFIDZJ(KNN) = -DFIDZI(KNN)                                   940
            DFJDRI(KNN) = PPDR * ( PARJ(KNN)*PARA
     &         - (UCOORDS(1,KNN) + UCOORDS(1,KNN+1)) * LENS(KNN)  )
            DFJDZI(KNN) = -PPDR * DELZ(KNN) * PARJ(KNN)
     &                        / ( LENS(KNN) * DELR(KNN) )
            DFJDRJ(KNN) = PPDR * ( PARJ(KNN)*(-PARA)
     &         + 2.0D0 * UCOORDS(1,KNN+1) * LENS(KNN)  )
            DFJDZJ(KNN) = -DFJDZI(KNN)
         ENDIF
  190 CONTINUE
c ***************************************************************          950
c **    computing DFDU                                          **
```

```
c ****************************************************************
      IF ( OUT5 .EQ. 1 ) THEN
         WRITE(*,*) '*** computing DFDU'
      ENDIF
c -- first and second row -- << i = 1 >> ------------------------
c  first row
      DFDU(1,1) = UN(1,1) * DFIDRI(1)
      DFDU(1,2) = UN(1,1) * DFIDZI(1)
      DFDU(1,3) = UN(1,1) * DFIDRJ(1)                                  960
      DFDU(1,4) = UN(1,1) * DFIDZJ(1)
c  second row
      DFDU(2,1) = UN(2,1) * DFIDRI(1)
      DFDU(2,2) = UN(2,1) * DFIDZI(1)
      DFDU(2,3) = UN(2,1) * DFIDRJ(1)
      DFDU(2,4) = UN(2,1) * DFIDZJ(1)
c -- rows in body of matrix -------------------------------------
      DO 215 KNN = 2, NNODE-1
c  contribution from first (KNN-1 th) node pair << i = KNN-1 >>
c  and contribution from second (KNN th) node pair << i = KNN >>    970
c  first row of pair
         DFDU(KNN*2-1,KNN*2-3) = UN(1,KNN-1) * DFJDRI(KNN-1)
         DFDU(KNN*2-1,KNN*2-2) = UN(1,KNN-1) * DFJDZI(KNN-1)
         DFDU(KNN*2-1,KNN*2-1) = UN(1,KNN-1) * DFJDRJ(KNN-1)
     &                         + UN(1,KNN  ) * DFIDRI(KNN  )
         DFDU(KNN*2-1,KNN*2  ) = UN(1,KNN-1) * DFJDZJ(KNN-1)
     &                         + UN(1,KNN  ) * DFIDZI(KNN  )
         DFDU(KNN*2-1,KNN*2+1) = UN(1,KNN  ) * DFIDRJ(KNN  )
         DFDU(KNN*2-1,KNN*2+2) = UN(1,KNN  ) * DFIDZJ(KNN  )
c  second row of pair                                               980
         DFDU(KNN*2  ,KNN*2-3) = UN(2,KNN-1) * DFJDRI(KNN-1)
         DFDU(KNN*2  ,KNN*2-2) = UN(2,KNN-1) * DFJDZI(KNN-1)
         DFDU(KNN*2  ,KNN*2-1) = UN(2,KNN-1) * DFJDRJ(KNN-1)
     &                         + UN(2,KNN  ) * DFIDRI(KNN  )
         DFDU(KNN*2  ,KNN*2  ) = UN(2,KNN-1) * DFJDZJ(KNN-1)
     &                         + UN(2,KNN  ) * DFIDZI(KNN  )
         DFDU(KNN*2  ,KNN*2+1) = UN(2,KNN  ) * DFIDRJ(KNN  )
```

```
        DFDU(KNN*2  ,KNN*2+2) = UN(2,KNN  ) * DFIDZJ(KNN  )
  215 CONTINUE
c -- 2nd-to-last and last row -- << i = NNODE-1 >> ---------------                990
c  2nd-to-last row
      DFDU(NDOFEL-1,NDOFEL-3) = UN(1,NNODE-1) * DFJDRI(NNODE-1)
      DFDU(NDOFEL-1,NDOFEL-2) = UN(1,NNODE-1) * DFJDZI(NNODE-1)
      DFDU(NDOFEL-1,NDOFEL-1) = UN(1,NNODE-1) * DFJDRJ(NNODE-1)
      DFDU(NDOFEL-1,NDOFEL  ) = UN(1,NNODE-1) * DFJDZJ(NNODE-1)
c  last row
      DFDU(NDOFEL  ,NDOFEL-3) = UN(2,NNODE-1) * DFJDRI(NNODE-1)
      DFDU(NDOFEL  ,NDOFEL-2) = UN(2,NNODE-1) * DFJDZI(NNODE-1)
      DFDU(NDOFEL  ,NDOFEL-1) = UN(2,NNODE-1) * DFJDRJ(NNODE-1)
      DFDU(NDOFEL  ,NDOFEL  ) = UN(2,NNODE-1) * DFJDZJ(NNODE-1)               1000
c ***************************************************************
c **    assembling AMATRX                                       **
c ***************************************************************
      IF ( OUT5 .EQ. 1 ) THEN
         WRITE(*,*) '*** assembling AMATRX'
      ENDIF
      DO 310 KY = 1, NDOFEL
        DO 305 KX = 1, NDOFEL
           IF ( OUT7 .EQ. 1 ) THEN
              WRITE(*,*) 'KY=',KY                                              1010
              WRITE(*,*) 'KX=',KX
              WRITE(*,*) 'DFDP(KY)', DFDP(KY)
              WRITE(*,*) 'DPDV', DPDV
              WRITE(*,*) 'DVDU(KX)', DVDU(KX)
              WRITE(*,*) 'DFDU(KY,KX)', DFDU(KY,KX)
           ENDIF
           AMATRX(KY,KX) = DFDP(KY) * DPDV * DVDU(KX) + DFDU(KY,KX)
           AMATRX(KY,KX) = DFDP(KY) * DPDV * DVDU(KX) + DFDU(KY,KX)
           AMATRX(KY,KX) = DFDP(KY) * DPDV * DVDU(KX) + DFDU(KY,KX)
           AMATRX(KY,KX) = DFDP(KY) * DPDV * DVDU(KX) + DFDU(KY,KX)            1020
           AMATRX(KY,KX) = - AMATRX(KY,KX)
  305    CONTINUE
  310 CONTINUE
```

```
c ***************************************************************
c **    OUTPUT OF COMPUTED DATA                                  **
c ***************************************************************
      IF ( OUT5 .EQ. 1 ) THEN
         WRITE(*,*) '*******************************************'
         WRITE(*,*) '*** Output of computed data                *'
         WRITE(*,*) '*******************************************'                1030
      ENDIF
c ********* outputting UCOORDS **********************************
      IF ( OUT5 .EQ. 1 ) THEN
         WRITE(*,*) '* DEFORMED NODE COORDINATES'
         WRITE(*,*) ' NODE#                UCOORDS'
      DO 1183 KNN=1,NNODE
          WRITE(*,FMT=1180) KNN,UCOORDS(1,KNN),UCOORDS(2,KNN)
 1180     FORMAT(I5,3X,E21.13,1X,E21.13)
 1183   CONTINUE
      WRITE(*,*) '***'                                                           1040
      ENDIF
c ********* outputting N, M, LENG, VO ***************************
      IF ( OUT5 .EQ. 1 ) THEN
         WRITE(*,*) '* UNDEFORMED COORDINATES OF M, N, LENG, and DS'
         WRITE(*,FMT=1184) 'NODE#','M','N','LENG','DS'
 1184    FORMAT(A7,A15,A28,A22,A16)
         DO 1190 KNN=1,(NNODE-1)
            LENG = SQRT( ((N(1,KNN))**2.0) + ((N(2,KNN))**2.0) )
            WRITE(*,FMT=1185) KNN, M(1,KNN), M(2,KNN),
     c                        N(1,KNN), N(2,KNN), LENG, DS(KNN)                1050
 1185       FORMAT(I5,2(3X,E12.6,1X,E12.6),2(3X,E12.6))
 1190    CONTINUE
         WRITE(*,*) '***'
      ENDIF
c ********* outputting UN, UM, ULENG ****************************
      IF ( OUT5 .EQ. 1 ) THEN
         WRITE(*,*) '* DEFORMED COORDINATES OF UM, UN, ULENG, and UDS'
         WRITE(*,FMT=1184) 'NODE#','UM','UN','ULENG','UDS'
         DO 1199 KNN=1,(NNODE-1)
```

```
            ULENG = SQRT( ((UN(1,KNN))**2.0) + ((UN(2,KNN))**2.0) )
            WRITE(*,FMT=1185) KNN, UM(1,KNN), UM(2,KNN),
     &                        UN(1,KNN), UN(2,KNN), ULENG,
     &                        UDS(KNN)
 1199    CONTINUE
      ENDIF
c ********* outputting V0, VU, VU-V0 ****************************
      IF ( OUT8 .EQ. 1 ) THEN
         WRITE(*,*) '* VU=',VU
         WRITE(*,*) '* V0=',V0
         WRITE(*,*) '* VU-V0=', VU-V0
         WRITE(*,*) '***'
      ENDIF
c ********* outputting PU ***************************************
      IF ( OUT8 .EQ. 1 ) THEN
         WRITE(*,*) '* PU=', PU
         WRITE(*,*) '***'
      ENDIF
c ********* outputting Simplifying Variables ********************
      IF ( OUT9 .EQ. 1 ) THEN
         WRITE(*,*) '* SIMPLIFYING VARIABLES'
         WRITE(*,FMT=1203) 'NODE#','DELR','DELZ','LENS','PARI','PARJ'
 1203    FORMAT(A7,A10,4(A17))
         DO 1205 KNN=1,(NNODE-1)
            WRITE(*,FMT=1204) KNN, DELR(KNN), DELZ(KNN), LENS(KNN),
     &                        PARI(KNN), PARJ(KNN)
 1204       FORMAT(I5,5(2X,E15.9))
 1205    CONTINUE
         WRITE(*,*) '***'
      ENDIF
c ********* outputting FI, FJ, FTOT *****************************
      IF ( OUT10 .EQ. 1 ) THEN
         WRITE(*,*) '*  FORCE MAGNITUDES'
         WRITE(*,FMT=1207) 'NODE#','FI','FJ','FI+FJ','FTOT','WARN8'
 1207    FORMAT(A7,A10,A18,A19,A17,A14)
         DO 1209 KNN=1,(NNODE-1)
```

```
            WRITE(*,FMT=1208) KNN, FI(KNN), FJ(KNN), FI(KNN)+FJ(KNN),
     &                              FTOT(KNN), WARN8(KNN)
 1208       FORMAT(I5,4(3X,E15.9),5X,I1)
 1209    CONTINUE
         WRITE(*,*) '***'                                                1100
      ENDIF
c ********* outputting WRHS ***************************************
      IF ( OUT11 .EQ. 1 ) THEN
         WRITE(*,*) '* WRHS matrix'
         WRITE(*,FMT=1210) 'NODE#','r-WRHS','z-WRHS'
 1210    FORMAT(A7,A12,A15)
         DO 1215 KNN=1, NNODE
            WRITE(*,FMT=1213) KNN, WRHS(1,KNN), WRHS(2,KNN)
 1213       FORMAT(I5,2(3X,E15.9))
 1215    CONTINUE                                                        1110
         WRITE(*,*) '***'
      ENDIF
c ********* outputting DFDP ***************************************
      IF ( OUT12 .EQ. 1 ) THEN
         WRITE(*,*) '* DFDP ='
         WRITE(*,*) ' NDOF#'
         DO 1225 KX = 1, NDOFEL / 5 + 1
            WRITE(*,FMT=1223) KX*5-4, ' -' , KX*5, DFDP(KX*5-4),
     &         DFDP(KX*5-3), DFDP(KX*5-2),DFDP(KX*5-1),DFDP(KX*5)
 1223       FORMAT(I5,A2,I5,5(2X,E12.6))                                1120
 1225    CONTINUE
         WRITE(*,*) '***'
      ENDIF
c ********* outputting DPDV ***************************************
      IF ( OUT13 .EQ. 1 ) THEN
         WRITE(*,FMT=1230) '* DPDV =', DPDV
 1230    FORMAT(A10,E21.13)
         WRITE(*,*) '***'
      ENDIF
c ********* outputting DVDU ***************************************      1130
      IF ( OUT14 .EQ. 1 ) THEN
```

```
        WRITE(*,*) '* DVDU ='
        WRITE(*,*) ' NDOF#'
        DO 1235 KX = 1, NDOFEL/5+1
          WRITE(*,FMT=1233) KX*5-4, ' -' , KX*5, DVDU(KX*5-4),
     &       DVDU(KX*5-3), DVDU(KX*5-2), DVDU(KX*5-1), DVDU(KX*5)
 1233      FORMAT(I5,A2,I5,5(2X,E12.6))
 1235   CONTINUE
        WRITE(*,*) '***'
      ENDIF                                                          1140
c ********* outputting DFIDRI, DFIDZI, ...  ***********************
      IF ( OUT15 .EQ. 1 ) THEN
        WRITE(*,*) '* DFIDRI etc.  ='
        WRITE(*,FMT=1240) 'NDOF#','DFIDRI','DFIDZI','DFIDRJ','DFIDZJ'
 1240   FORMAT(A5,A14,3(1X,A16))
        DO 1245 KX = 1, NNODE-1
          WRITE(*,FMT=1242) KX, DFIDRI(KX), DFIDZI(KX), DFIDRJ(KX),
     &                          DFIDZJ(KX)
 1242      FORMAT(I5,4(1X,E17.8))
 1245   CONTINUE                                                      1150
        WRITE(*,*) ' '
        WRITE(*,FMT=1246) 'NDOF#','DFJDRI','DFJDZI','DFJDRJ','DFJDZJ'
 1246   FORMAT(A5,A14,3(1X,A16))
        DO 1249 KX = 1, NNODE-1
          WRITE(*,FMT=1247) KX, DFJDRI(KX), DFJDZI(KX), DFJDRJ(KX),
     &                          DFJDZJ(KX)
 1247      FORMAT(I5,4(1X,E17.8))
 1249   CONTINUE
        WRITE(*,*) '***'
      ENDIF                                                          1160
c ********* outputting DFDU ***************************************
      IF ( OUT16 .EQ. 1 ) THEN
        WRITE(*,*) '* DFDU ='
        DO 1259 KX = 1, NDOFEL/6+1
          WRITE(*,FMT=1250) KX*6-5,KX*6-4,KX*6-3,KX*6-2,KX*6-1,KX*6
 1250        FORMAT(I14,5(2X,I12))
          DO 1255 KY = 1, NDOFEL
```

```
            WRITE(*,FMT=1253) KY, DFDU(KY,KX*6-5), DFDU(KY,KX*6-4),
     &           DFDU(KY,KX*6-3), DFDU(KY,KX*6-2), DFDU(KY,KX*6-1),
     &           DFDU(KY,KX*6)                                          1170
 1253        FORMAT(I5,6(2X,E12.6))
 1255      CONTINUE
         WRITE(*,*) ' '
 1259 CONTINUE
      WRITE(*,*) '***'
      ENDIF
c ********* outputting AMATRX ************************************
      IF ( OUT17 .EQ. 1 ) THEN
      WRITE(*,*) '* AMATRX='
      DO 1275 KX = 1, NDOFEL/6+1                                        1180
         WRITE(*,FMT=1260) KX*6-5,KX*6-4,KX*6-3,KX*6-2,KX*6-1,KX*6
 1260      FORMAT(I14,5(2X,I12))
         DO 1265 KY = 1, NDOFEL
            WRITE(*,FMT=1263) KY,
     &      AMATRX(KY,KX*6-5), AMATRX(KY,KX*6-4), AMATRX(KY,KX*6-3),
     &      AMATRX(KY,KX*6-2), AMATRX(KY,KX*6-1), AMATRX(KY,KX*6)
 1263       FORMAT(I5,6(2X,E12.6))
 1265    CONTINUE
         WRITE(*,*) ' '
 1275 CONTINUE                                                          1190
      WRITE(*,*) '***'
      ENDIF
c ****************************************************************
c **    computing AMATRX from deltas                            **
c ****************************************************************
      IF ( OUT18 .EQ. 1 ) THEN
      GOTO 1301
      WRITE(*,*) '* Stiffness matrix computed from deltas='
      DO 1300 KX = 1,NDOFEL
         IF (U(KX) .NE. 0) THEN                                         1200
            WRITE(*,FMT=1290) 'NDOF#', 'non-zero DOF=', KX
 1290       FORMAT(A7,A16,I3)
            DO 1295 KY = 1,NDOFEL
```

```
          IF (AMATRX(KY,KX) .EQ. 0) THEN
                WRITE(*,FMT=1292) KY, WRHS(2,INT((KY+1)/2))/U(KX),
     &             '= WRHS(2,',INT((KY+1)/2),') / U(',KX,')',
     &             'AMATRX(', KY,',',KX,') = zero'
 1292          FORMAT(I5,E18.6,A15,I2,A6,I2,A1,A15,I2,A1,I2,A9)
          ELSE
             IF (KY .EQ. 2*INT(KY/2)) THEN                                  1210
                WRITE(*,FMT=1293) KY, WRHS(2,INT((KY+1)/2))/U(KX),
     &             '= WRHS(2,',INT((KY+1)/2),') / U(',KX,')',
     &             '% Error:',
     &             (((WRHS(2,INT((KY+1)/2))/U(KX))-AMATRX(KY,KX))
     &             / AMATRX(KY,KX)) * 100
             ELSE
                WRITE(*,FMT=1293) KY, WRHS(1,INT((KY+1)/2))/U(KX),
     &             '= WRHS(1,',INT((KY+1)/2),') / U(',KX,')',
     &             '% Error:',
     &             (((WRHS(1,INT((KY+1)/2))/U(KX))-AMATRX(KY,KX))         1220
     &             / AMATRX(KY,KX)) * 100
             ENDIF
 1293          FORMAT(I5,E18.6,A15,I2,A6,I2,A1,A15,F8.2)
          ENDIF
 1295       CONTINUE
        ENDIF
 1300 CONTINUE
 1301 WRITE(*,*) '***'
      ENDIF
c ********* assigning WRHS to RHS ***********************************       1230
      DO 2000 KNN= 1,NNODE
         RHS(KNN*2-1,1) = WRHS(1,KNN)
         RHS(KNN*2  ,1) = WRHS(2,KNN)
 2000 CONTINUE
c ********* outputting WRHS ***************************************
      IF ( OUT19 .EQ. 1 ) THEN
         WRITE(*,*) '* RHS matrix'
         WRITE(*,FMT=2210) 'NODE#','RHS'
 2210    FORMAT(A7,A12)
```

```
        DO 2215 KNN=1, NDOFEL                                              1240
          WRITE(*,FMT=2213) KNN, RHS(KNN,1)
2213       FORMAT(I5,3X,E15.9)
2215    CONTINUE
        WRITE(*,*) '***'
      ENDIF
c ***************************************************************
c **    SPECIAL OUTPUTS                                          **
c ***************************************************************
c ** titles **
      IF ( (SPECIAL .EQ. 6) .AND. (KINC .EQ. 1) .AND. (KSTEP .EQ. 1) )     1250
     &  THEN
        WRITE(*,*) '                      TIME(1)+'
        WRITE(*,FMT=2225) 'PU     ', 'KINC', ' KSTEP-1', 'VU', 'KSTEP',
     &         'P-drop', 'V0'
 2225   FORMAT(A15, x, A5, A9, A6, A7, A8, A8)
      ENDIF
c ** P-V-laws 13 and 14 **
      IF ( (SPECIAL .EQ. 6) .AND.
     &     ((JPROPS(1) .EQ. 13) .OR. (JPROPS(1) .EQ. 14 ))
     &   ) THEN                                                            1260
        IF (SVARS(3) .EQ. 0) THEN
c          ** Voiding has not occured yet                  **
           WRITE(*,FMT=2231) PU, KINC, TIME(1)+KSTEP-1, VU, KSTEP,
     &                       1, V0
        ELSE
c          ** Voiding has occured                          **
           WRITE(*,FMT=2231) PU, KINC, TIME(1)+KSTEP-1, VU, KSTEP,
     &                       0.0000001, V0
        ENDIF
 2231   FORMAT(E15.9,X,I5, F8.5,F10.7,I2,X,F10.7,F10.7)                    1270
c ** P-V-law 15 and 16 **
      ELSE IF ( (SPECIAL .EQ. 6) .AND.
     &  ( (JPROPS(1) .EQ. 15) .OR. (JPROPS(1) .EQ.16) ) )  THEN
        IF (SVARS(4) .EQ. 0) THEN
c          ** Voiding has not occured yet                  **
```

```
            WRITE(*,FMT=2231) PU, KINC, TIME(1)+KSTEP-1, VU, KSTEP,
     &                        1, VO
         ELSE IF (SVARS(4) .EQ. 1) THEN
            WRITE(*,FMT=2231) PU, KINC, TIME(1)+KSTEP-1, VU, KSTEP,
     &          ( (SVARS(6) - TIME(1))/(SVARS(6) - SVARS(5)) ), VO
         ELSE
c           ** Voiding has occured                              **
            WRITE(*,FMT=2231) PU, KINC, TIME(1)+KSTEP-1, VU, KSTEP,
     &                        0.0000001, VO
         ENDIF
       ELSE
         WRITE(*,*) '*** ERROR: invalid value for SPECIAL: ',
     &              SPECIAL
       ENDIF
c ********************************************************************
       ENDIF
c ** is the ENDIF for LFLAGS(1) = 1 or 2 ************************
c ************************************      not CASE 1      **
c **    LFLAGS(3) is not =3 :  no normal incrementation      **
c ********************************************************************
       ELSE
c ** is the ELSE for LFLAGS(3) = 3 ******************************
       PRINT *, '*****************************************'
       PRINT *, 'LFLAGS(3) is not = 3, so subroutine returns',
     & 'without computations!'
       ENDIF
c ********************************************************************
c **    output before return                                  **
c ************************************************************
       IF ( OUT1 .EQ. 1 ) THEN
          WRITE(*,*) '*********************************************'
          WRITE(*,*) '* Output of state variables before return    *'
          WRITE(*,*) '*********************************************'
          WRITE(*,*) '* KSTEP=', KSTEP
          WRITE(*,*) '* KINC=', KINC
       ENDIF
```

```
      IF ( OUT2 .EQ. 1 ) THEN
         WRITE(*,*) '* SVARS at return:'
         IF (NSVARS .GT. 0) THEN
            DO 9921 KNN=1,NSVARS
               WRITE(*,*) '* SVARS(', KNN, ')= ', SVARS(KNN)
 9921       CONTINUE
         ELSE
            WRITE(*,*) 'NSVARS not > 0, so no output for SVARS.'
         ENDIF                                                          1320
      ENDIF
      IF ( OUT1 .EQ. 1 ) THEN
         WRITE(*,*) ' '
         WRITE(*,*) ' '
         WRITE(*,*) '*********************************************',
     &    '*******************'
         WRITE(*,*) '*** LEAVING USER SUBROUTINE        ',
     &    '               *****************'
         WRITE(*,*) '*********************************************',
     &    '*******************'                                        1330
      ENDIF
      RETURN
      END
```

Appendix C

Formulation of the Triaxial Loading Condition

For the undertaken simulations it was necessary to subject the unit cell to a macroscopic stress state of constant triaxiality during the deformation. However, since the displacement history of the two moving boundaries, top and lateral, cannot be known in advance, a mechanism needed to be implemented that regulates the boundary conditions at the unit cell's top and lateral boundaries.

Two approaches have been taken to the implementation of the triaxial loading condition. The first is a "closed" solution what involves a user-defined multi-part constraint and spring elements. The second involves the use of a unser element for measuring the current axial force acting on the unit cell and for the computation of a lateral distributed load that is then applied using a user subroutine for distributed loads.

C.1 MPC Implementation

The first, but unsuccessful, attempt at this was to use a user-defined multi-point constraints (USER MPC) in conjunction with spring elements. Figure C-1 shows a schematic of the unit cell with the two spring elements and the node numbering corresponding to the USER MPC.

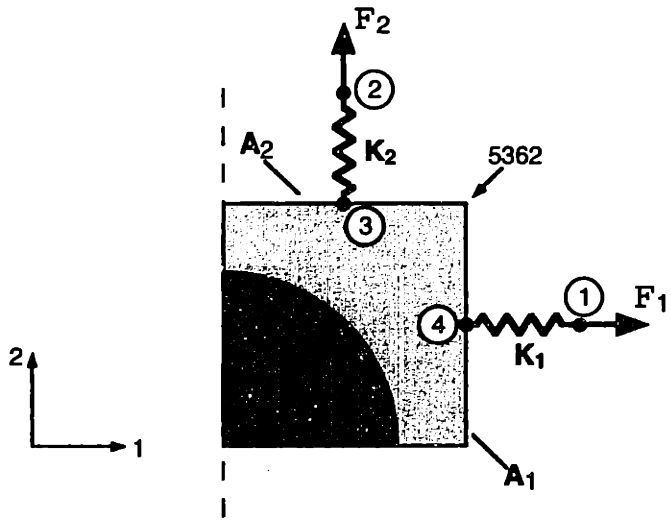

Figure C-1: Schematic of the USER MPC implementation

Starting with the expressions for the areas A_1 and A_2,

$$A_1 = 2\pi \left(x_2^3 + u_2^3\right)\left(x_1^4 + u_1^4\right) \tag{C.1}$$

$$A_2 = \pi \left(x_1^4 + u_1^4\right)^2 \tag{C.2}$$

and the expressions for the reaction forces F_1 and F_2,

$$F_1 = K_1 \left(u_1^1 - u_1^4\right) \tag{C.3}$$

$$F_2 = K_2 \left(u_2^2 - u_2^3\right) \tag{C.4}$$

Using an appropriate triaxiality parameter Ω

$$\sigma_r = \frac{F_1}{A_1} = \Omega \frac{F_2}{A_2} = \Omega \sigma_z \tag{C.5}$$

an expression for the displacement u_1^1 of node 1 in the 1-direction can be found which generates the correct triaxial stress state in the unit cell. u_1^1 is a function of the displacements of the three other nodes involved as shown in equation C.6.

$$u_1^1 = 2\Omega \frac{K_2}{K_1} \left(u_2^2 - u_2^3\right) \frac{x_2^3 + u_2^3}{x_1^4 + u_1^4} + u_1^4 \tag{C.6}$$

where x_2^3 and x_1^4 are the undisplaced coordinates of the nodes involved. Note that the parameter Ω is equal to the parameter TRIMULT below, and not the "triaxiality ratio" Σ. Ω is simply the ratio of the radial stress σ_r to the axial stress σ_z.

The finite element software passes the current displacement field **u** and the initial (undeformed) coordinates **x** of the involved nodes into the MPC subroutine. The information passed back from the subroutine to the main program is the correct displacement of the constrained node u_1^1 and the stiffness matrix of the MPC or jacobian **J** which is obtained by differentiating equation C.6 with respect to the four degrees of freedom involved as seen in equation C.7.

$$\mathbf{J} = \frac{\partial \mathbf{f}}{\partial \mathbf{u}} \tag{C.7}$$

Discussion of the Implemenation

After the implementation it was found that USER MPCs cannot be used in ABAQUS in the way planned. The finite element program interprets simulations with such a displacement constraint as "over-constrained"[1] and therefore does not calculate a correct result.

The advantage of this method would be its accuracy and simplicity. Since the radial displacement of node 1 is directly constrained as a function of the other 3 degrees of freedom involved, and the stffness matrix is complete for the entire simulation, the solver of the finite element software can make a correct guess of the next displacement field from one iteration to the next. This accuracy was lost in the second but successful attempt for the triaxiality implementation, as discussed below.

FORTRAN code of the USER MPC

```
      SUBROUTINE MPC(UE,A,JDOF,MDOF,N,JTYPE,X,U,UINIT,MAXDOF,
     & LMPC,KSTEP,KINC,TIME,NT,NF,TEMP,FIELD,LTRAN,TRAN)
C
```

[1] From discussions with Dr. S. Socrate and from a private communication between Professor D. M. Parks of MIT and representatives of Hibbit, Karlsson & Sorensen, Inc.

```
c       User Multi Point Constraint subroutine.
c       Version 1.0
c       mpc10.f
c
c ***************************************************************
c **    HOW TO USE THIS SUBROUTINE                             **
c ***************************************************************
c ** JTYPE = 1
c     4-point MPC with Simona's triax ratio = 1.33
c       which corresponds to a stress state where the laterally
c       applied stress is 1/2 the axially applied stress.
c     TRIRAT = 0.5
c ** JTYPE = 2
c     4-point MPC with Simona's triax ratio = infinity
c       which corresponds to a hydrostatic stress state.
c     TRIRAT = 1
c ***************************************************************
c **    INCLUDE, DECLARATIONS, DIMENSIONS, PARAMETERS          **
c ***************************************************************
      INCLUDE 'ABA_PARAM.INC'
c ** output parameters for debugging purposes
      PARAMETER( OUT1 = 1 )
c       output:  all variables for JTYPE = 1, 2
c ********* declaration of PASSED-IN variables ******************
c not necessary
c ********* declaration of LOCAL variables ***********************
      DOUBLE PRECISION UCOORD, TRIRAT
c ********* dimensioning PASSED-IN variables *********************
      DIMENSION A(N),JDOF(N),X(6,N),U(MAXDOF,N),UINIT(MAXDOF,N),
     & TIME(2),TEMP(NT,N),FIELD(NF,NT,N),LTRAN(N),TRAN(3,3,N)
c ********* dimensioning LOCAL variables *************************
      DIMENSION UCOORD(N)
c ***************************************************************
c **    MAIN PROGRAM                                           **
c ***************************************************************
c ********************************** BEGIN JTYPE = 1,2 **
```

```
      IF ( (JTYPE .EQ. 1) .OR. (JTYPE .EQ. 2) ) THEN                    40
c ** ratio between axial and lateral loading, as def.  in U's notes.
         IF ( JTYPE .EQ. 1 ) THEN
            TRIRAT = 0.5
         ELSE
            TRIRAT = 1.0
         ENDIF
         JDOF(1) = 1
         JDOF(2) = 2
         JDOF(3) = 2
         JDOF(4) = 1                                                    50
c ** derivatives of constraint function
         A(1) = -1.0
         A(2) =  2.0 * TRIRAT * (X(2,3)+U(2,3)) / (X(1,4)+U(1,4))
         A(3) =  2.0 * TRIRAT * ( U(2,2) - (2*U(2,3)) - X(2,3) )
     &                        / (X(1,4)+U(1,4))
         A(4) = ( - 2.0 * TRIRAT * (U(2,2)-U(2,3)) *
     &                       (X(2,3)+U(2,3)) / ((X(1,4)+U(1,4))**2)
     &          ) + 1.0
c ** value of constrained dof
         UE = ( 2.0 * TRIRAT * (U(2,2)-U(2,3)) * (X(2,3)+U(2,3))        60
     &                                        / (X(1,4)+U(1,4))
     &        ) + U(1,4)
c ** output before return for debugging
         IF ( OUT1 .EQ. 1 ) THEN
            WRITE(*,*) '****************************************'
            WRITE(*,*) 'KINC= ', KINC
            WRITE(*,*) 'JTYPE= ', JTYPE
            WRITE(*,*) 'TRIRAT= ', TRIRAT
            WPITE(*,*) 'X(1,1)= ', X(1,1)
            WRITE(*,*) 'U(1,1)= ', U(1,1)                               70
            WRITE(*,*) 'X(2,2)= ', X(2,2)
            WRITE(*,*) 'U(2,2)= ', U(2,2)
            WRITE(*,*) 'X(2,3)= ', X(2,3)
            WRITE(*,*) 'U(2,3)= ', U(2,3)
            WRITE(*,*) 'X(1,4)= ', X(1,4)
```

```
            WRITE(*,*) 'U(1,4)= ', U(1,4)
            WRITE(*,*) 'A(1)= ', A(1)
            WRITE(*,*) 'A(2)= ', A(2)
            WRITE(*,*) 'A(3)= ', A(3)
            WRITE(*,*) 'A(4)= ', A(4)                                    80
            WRITE(*,*) 'UE= ', UE
          ENDIF
c ** total value of eliminated degree of freedom
c ** not necessary
c ********************************************** END JTYPE = 1,2 **
      ELSE
            WRITE(*,*) '* MPC: JTYPE has illegal value.'
      ENDIF
c
      RETURN                                                             90
      END
```

C.2 UEL and DLOAD Implementation

The second attempt at finding a suitable implementation of a triaxiality constraint was successful. Following Socrate's[64] approach a user element subroutine (UEL2) was used in conjunction with a user-defined distributed load (USER DLOAD). The purpose of the user element is to measure the current axial force acting at the top boundary of the unit cell and to compute the distributed load to be applied at the lateral boundary so that the disired macroscopic triaxial stress state is generated in the unit cell. Figure C-2 shows a schematic of the implementation.

The user element UEL2 consists of the nodes numbered 1, 2 and 3 and is thought to include the spring between node 1 and 2 of stiffness K. From the passed-in displacement field the reaction forces at the nodes 1 and 2 are computed as in equation C.8.

$$f_z^1 = K\left(u_z^2 - u_z^1\right) \qquad f_z^2 = -f_z^1 \tag{C.8}$$

The user defines the desired level of triaxiality and the stiffness of the user element's spring through the parameters PROPS in the ABAQUS input deck as shown

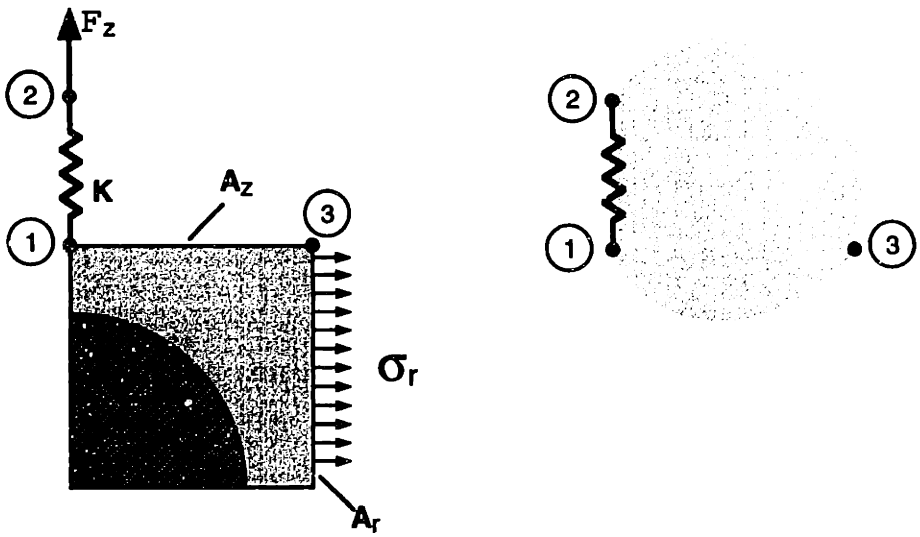

Figure C-2: Schematic of the triaxiality implementation using a UEL

below. From the triaxiality ratio a parameter TRIMULT is computed which is the ratio of the radial stress σ_r to the axial stress σ_z (equal to Ω above). Taking into account the current area of the top boundary of the unit cell, the lateral stress is the obtained as in equation C.9.

$$\sigma_r = \text{TRIMULT} \frac{f_z^1}{\pi \left(x_r^3 + u_r^3\right)^2} \tag{C.9}$$

The computed σ_r is passed into the DLOAD subroutine through a COMMON block as shown below. From the DLOAD subroutine it is passed back to the finite element program where the appropriate distributed load is applied to the elements along the lateral boundary of the unit cell.

C.2.1 Discussion of the Implementation

The disadvantage of this method of introducing the triaxial loading condition into the model is that the solver of the finite element software is left with an incomplete stiffness matrix and therefore has to make guesses for the displacement field without all of the necessary information. As can be seen from the listing of the UEL2 subroutine below, the stiffness matrix computed in the subroutine lacks the dependency of the radial degree of freedom corresponding to node 3, although this dependency exists.

Since the laterally applied distributed load is computed inside the UEL2 subroutine, but it is applied through the DLOAD subroutine, the solver of the finite element program does not know of this dependence.

In spite of these obstacles, this implementation of the triaxial loading condition has been successful. In some cases very small increments had to be chosen for the solutions to converge. Under certain conditions no solution was obtained. A critical parameter for the UEL2 implementation of the triaxiality is the choice of the stiffness K of the spring in the user element. It was chosen to be 2 to 3 orders of magnitude larger than the effective stiffness of the unit cell. This choice was motivated by Socrate's [64] arguments that a too-high value of K leads to an ill-conditioning of the stiffness matrix, and that a too-low choice of K causes the elastic energy in the spring to make too much of a contribution to the discontinuous processes in the unit cell, such as particle cavitation.

Below are listed:

- the FORTRAN code of the UEL2 subroutine
- the FORTRAN code of the DLOAD subroutine
- an example of the section of an ABAQUS input deck that defines the user element UEL2
- an example of the section of an ABAQUS input deck to illustrate the application of the distributed load to the lateral boundary

FORTRAN code of the UEL2 subroutine

```
      SUBROUTINE UEL(RHS,AMATRX,SVARS,ENERGY,NDOFEL,NRHS,NSVARS,
     1 PROPS,NPROPS,COORDS,MCRD,NNODE,U,DU,V,A,JTYPE,TIME,DTIME,
     2 KSTEP,KINC,JELEM,PARAMS,NDLOAD,JDLTYP,ADLMAG,PREDEF,NPREDF,
     3 LFLAGS,MLVARX,DDLMAG,MDLOAD,PNEWDT,JPROPS,NJPROP,PERIOD)
C
      ../..  (insert declaration parts here)
C *********** include ***********************************************
```

```
      INCLUDE 'ABA_PARAM.INC'
      common/kspress/sigr
c                                                                       10
        ZERO = 0.D0
        ONE = 1.D0
        TWO =2.D0
        THREE = 3.D0
        PII = TWO*TWO*DATAN(ONE)
c       DATAN(ONE) is Pi / 4 (Ulf 98Jan21)
C
        AK = PROPS(1)
        TRIAX = PROPS(2)
C                                                                       20
C Zeroing
          do k1=1,ndofel
            do krhs=1,nrhs
           rhs(k1,krhs) = zero
            enddo
            do k2=1,ndofel
           amatrx(k2,k1) = zero
             enddo
          enddo
C                                                                       30
         delu = u(4) - u(2)
         force = ak * delu
         rhs(2,1) = force
         rhs(4,1) = -force
C
         amatrx(2,2) = ak
         amatrx(4,4) = ak
         amatrx(2,4) = -ak
         amatrx(4,2) = -ak
C                                                                       40
         trimult = (three*triax - one)/(two + three*triax)
         radius = coords(1,3) + u(5)
         sigz = force/(pii*radius**2)
```

```
          sigr = sigz*trimult
          svars(1) = sigr
          svars(2) = sigz - sigr
          if(svars(2).ne.zero)then
           svars(3) = (2.0*sigr+sigz)/(3.0*(sigz-sigr))
          else
           svars(3) = 0.33                                          50
          endif
C
          svars(4) = sigz
C
   ../..  (return statement etc.)
```

FORTRAN code of the DLOAD subroutine

```
      SUBROUTINE DLOAD(F,KSTEP,KINC,TIME,NOEL,NPT,COORDS,JLTYP)
C
         INCLUDE 'ABA_PARAM.INC'
      common/kspress/sigr
C
      f = -sigr
C
      RETURN
      END
```

Example of the section of an ABAQUS input deck that defines the user element UEL2

```
 *USER ELEMENT, TYPE=U2, NODES=3, COORDINATES=2,VARIABLES=7, PROPERTIES=2
1,2
*UEL PROPERTY, ELSET=UEL2
500000, 2.33
```

```
************************ element generation:  uel2
*ELEMENT,TYPE=U2,ELSET=UEL2
2,4747,8888,5362
```

Example of the section of an ABAQUS input deck to illustrate the application of the distributed load to the lateral boundary

```
 *DLOAD
RIGELS,P2NU
```

Note: The element set RIGELS consists of all the element along the lateral boundary of the unit cell.

Appendix D

Matlab Scripts

The following is a Matlab script used to take the data from ABAQUS Post (.fil file) and data from the .dat file, and to compute the following stress and strain measures:

- macroscopic axial true stress of unit cell;
- macroscopic axial true deviatoic stress of unit cell;
- macroscopic radial true strain of unit cell;
- macroscopic radial true strain of unit cell computed from end of cooling on;
- macroscopic axial true strain of unit cell;
- macroscopic axial true strain of unit cell;
- volumetric strain of unit cell;
- volumetric strain of unit cell computed from end of cooling on;
- volumetric strain in particle;

```
name = 'sprocess06.m';
% ************************************************
% Modified from sprocess05.m on 98Apr07.
% Modified from sprocess04.m on 98Mar17.
% Modified from process03.m on 98Feb15.
```

```
%
% modified from process02.m on 97Nov23 to incorporate
%   strain measured from beginning of step 2 on.
% modified from plotA01.m on 97Nov18
% modified from plotA25ue8.m on 97Nov09                                    10
% modified from plotA25ue7.m;
% ************************************************
% This tool calculates
%  true stress of unit cell       vs. true strain of cell
%  volumetric strain of cell      vs. true strain of cell
%  volumetric strain of particle vs. true strain of cell
%  pressure in particle           vs. true strain of cell
%
% Required input files for this tool are:
%  data (copied from the .dat file, cleaned with clean6.f)                  20
%  rf2u (extracted from the .fil file using scyrf2u)
%    Attention: rf2u needs a zero value line.
%
% ************************************************
% column 1 rf2u: contains time
% column 2 rf2u: contains rf2u2 at node 8888
% column 3 rf2u: contains u2 at node 4747
% column 4 rf2u: contains u1 at node 5362
% column 5 rf2u: volumetric strain of cell: V / V0
% column 6 rf2u: true strain in u2-direction.                              30
% column 7 rf2u: true stress: rf2u2 / inst.area
% column 8 rf2u: pressure in particle
% column 9 rf2u: volumetric strain of particle
% column 10 rf2u: true strain as measured from end of cooling step.
% column 11 rf2u: vol.strain of cell measured from end of cooling step.
% column 12 rf2u: true strain in u1-direction.
% column 13 rf2u: tru strain in 1-direction measured from end of cooling step.
%
% column 1 data: pressure in particle
% column 2 data: increment number                                          40
% column 3 data: time
```

```
% column 4 data: current volume
% column 5 data: step number
% column 6 data: pressure multiplyer ( no voiding ==> =1 )
% column 7 data: reference volume
% column 8 data: true strain of cell in form of a curve fit of the
%               true strain in column 6 of rf2u1.
% column 9 data: vol.strain of particle computed from cols 4 and 7
%               of data.
% column 10 data: true strain of cell measured from end of cooling
%               in form of a curve fit of column 10 of rf2u1.
%
% ************************************************
%
%
% ------------------------------------------------
% LOADING DATA SETS FROM 'data' and 'rf2u'
% ------------------------------------------------
load data;
data1 = data;
linesdata = length(data1);
load rf2u;
rf2u1 = rf2u;
linesrf2u = length(rf2u1);
%
% -----------------
% WORK IN 'rf2u1'
% -----------------
% column 1 of rf2u: contains time
% column 2 of rf2u: contains rf2u2 at node 8888
% column 3 of rf2u: contains u2 at node 4747
% column 4 of rf2u: contains u1 at node 5362

% column 5 of rf2u: volumetric strain of cell: V / V0
for i = 1:linesrf2u
rf2u1(i,5) = (((rf2u1(i,4)+1.0)^2) * (rf2u1(i,3)+1.0))-1;
end
```

```
% column 6 of rf2u: true strain in u2-direction:
for i = 1:linesrf2u,                                                    80
rf2u1(i,6) = log(rf2u1(i,3)+1.0);
end

% column 7 of rf2u: true stress: rf2u2 / inst.area
for i = 1:linesrf2u,
rf2u1(i,7) = rf2u1(i,2) / (((rf2u1(i,4)+1.0)^2)*pi);
end

% column 8 of rf2u: particle pressure as curve fit vs. time
% from data1                                                            90
p1r = polyfit(data1(:,3),data1(:,1),10);
for i = 1:linesrf2u,
rf2u1(i,8) = (polyval(p1r,rf2u1(i,1)));
end


% ---------------------
%  WORK IN 'data1'
% ---------------------
% column 1 data: pressure in particle                                   100
% column 2 data: increment number
% column 3 data: time
% column 4 data: current volume
% column 5 data: step number
% column 6 data: parameter indicating voiding has
%                happened or not
% column 7 data: reference volume

% column 8 of data1: true strain of cell in form of a
% curve fit of the true strain in column 6 of rf2u1                     110
p1d = polyfit(rf2u1(:,1),rf2u1(:,6),10);
for i = 1:linesdata,
data1(i,8) = polyval(p1d,data1(i,3));
```

```
end

% column 9 of data1: vol.strain of particle computed
% from cols 4 and 7 of data:
for i = 1:linesdata,
data1(i,9) = (data1(i,4)/data1(i,7)) - 1.0;
end                                                                    120


% ---------------------
%  WORK IN 'rf2u1'
% ---------------------
% column 9: volumetric strain of particle
% create curve fit of vol.strain vs. time in columns 9 and 1 of data1
% then evaluate it into column 9 of rf2u1
p1r = polyfit(data1(:,3),data1(:,9),10);
for i = 1:linesrf2u,                                                   130
rf2u1(i,9) = (polyval(p1r,rf2u1(i,1)));
end

% finding the row number of the last step 1 entry
for i = 1:linesrf2u,
if rf2u1(i,1) == 1.000
  lastrowst1 = i;
end
end
                                                                       140
% column 10: true strain measured from end of ccoling
for i = 1:linesrf2u,
rf2u1(i,10) = log((rf2u1(i,3)+1.0)/(rf2u1(lastrowst1,3)+1.0));
end

% column 11: volumetric strain of cell measured from end of cooling
for i = 1:linesrf2u
rf2u1(i,11) = ((((rf2u1(i,4)+1.0)^2) * (rf2u1(i,3)+1.0))/(((rf2u1(lastrowst1,4)+1.0)^2) * (rf2u1(lastrowst1,3)+1.0))
end
```

```
% column 12: true strain in 1-direction:
for i = 1:linesrf2u,
rf2u1(i,12) = log(rf2u1(i,4)+1.0);
end

% column 13: true strain in 1-direction measured from end of cooling
for i = 1:linesrf2u,
rf2u1(i,13) = log((rf2u1(i,4)+1.0)/(rf2u1(lastrowst1,4)+1.0));
end

% ---------------------
% WORK IN 'data1'
% ---------------------
% column 10 of data1: true strain of cell as measured
% from end of cooling computed in form of a curve fit
% of the true strain in column 10 of rf2u1:
p1d = polyfit(rf2u1(:,1),rf2u1(:,10),10);
for i = 1:linesdata,
data1(i,10) = polyval(p1d,data1(i,3));
end


% ------------------------
% CORRECTIONS
% ------------------------
data1(1,8) = 0;
rf2u1(1,9) = 0;


% ---------------------
% SAVING
% ---------------------
save rf2u.mout rf2u1 -ascii
save data.mout data1 -ascii
save last.mout lastrowst1 -ascii
```

Bibliography

[1] Version 5.6. *ABAQUS/Standard, User's Manual.* Hibbit, Karlsson & Sorensen, Inc., Pawtucket, RI.

[2] Lazzeri A. *Toughening of nylons.* Ph. d. thesis, Cranfield Institute of Technology, U.K., 1991. Thesis work under Prof. C B Bucknall.

[3] McClintock F. A. *Crack Growth in Fully Plastic Grooved Tensile Specimens*, page 307. A. S. Argon, 1969.

[4] Stringfellow R Abeyaratne R. Cavitation in an elastomer: Comparison of theory with experiment. *Materials Science and Engineering*, A112:127–131, 1989.

[5] Broutman L.J. Agarwal B.D. *Fibre Sci. Tech.*, 7:63, 1974.

[6] Bartczak Z. Ahzi S., Argon A.S., Lee B.J., and Parks D.M. Simulation of large strain plastic deformation and texture evolution in high density polyethylene. *Polymer*, 34:3555–, 1993.

[7] Parks D.M. Ahzi S., Lee B.J. Micromechanical modeling of large plastic deformation and texture evolution in semi-crystalline polymers. *J. Mech. Phys. Solids.*, 41(10):1651–1687, 1993.

[8] Cohen R E Argon A S, Bartczak Z and Muratoglu O K. Novel mechanisms of toughening semi-crystalline polymers. *Proceedings of the 18th Riso International Symposium on Materials Science: Polymeric Composites - Expandin the Limits*, 1997.

[9] Lin L Argon A S. Deformation resistance in oriented nylon 6. *Macromolecules*, 25:4011–4024, 1992.

[10] Lin L Argon A S. Rate mechanism of plasticity in the crystalline component of semicrystalline nylon 6. *Macromolecules*, pages 6903–, 1994.

[11] Muratoglu O K Argon A S, Cohen C E and Weinberg M. Toughening mechanism of rubber-modified polyamides. *Polymer*, 36(5):921–930, 1995.

[12] Schwier C E Argon A S, Cohen R E. Craze plasticity in a series of polystyrene/polybutadiene di-block copolymers with spherical morphology. *Philosophical Magasine A*, 52(5):581–603, 1985.

[13] Muratoglu O.K. Argon A.S., Cohen R.E. Toughness of particle modified semi-crystalline polymers: General principles and specific examples. *ASME*, 1995.

[14] Boyce M.C. Arruda E.M. On modelling the mechanics of rubber elasticity: State of deformation dependence.

[15] Quintus-Bosz H. Arruda E.M., Boyce M.C. Effects of initial anisotropy on the finite strain deformation behavior of glassy polymers. *International Journal of Plasticity*, 9:783–811, 1993.

[16] Gaymans R J Borggreve R J M. Impact behaviour of nylon-rubber blends: 6. influence of stucture on voiding processes; toughening mechanisms. *Polymer*, 30:78–83, 1989.

[17] Magalhaes A M L Borggreve R J M. Contribution of the crasing process to the toughness of rubber-modified polystyrene. *Macromolecules*, 28:5841–5851, 1995.

[18] M C Boyce. Craze initiation in heterogeneous polymers. Master's thesis, MIT, 1984.

[19] Smit R.J.M Brekelmans W.A.M., Meijer H.E.H. Prediction of the mechanical behavior of non-linear heterogeneous systems by multi-level finite element modeling. *to appear.*

[20] Stabenow J. Breuer H., Haaf F. Stress witening and yielding mechanism of rubber-modified pvc. *Journal of Macromolecular Science, Physics*, B14(3):387–417, 1977.

[21] Panizza G. Broutman L.J. *Int. J. Polym. Mat.*, 1:95, 1971.

[22] Kramer E J Bubeck R A, Buckley D J and Brown H R. Modes of deformation in rubber-modified thermoplastics during tensile impact. *J. Mat. Sc.*, 26:6249–6259, 1991.

[23] Jones D P Bucknall C B. Deformation and fracture of thermoplastics containing spherical particles: a comparison between rigid spheres and rubber particles. *Fifth International Conference on Deformation, yield and fracture of polymers*, 29 March to 1 April, 1982.

[24] Lazzeri A Bucknall C B. Dilatational bands in rubber-toughened polymers. *J.Mat.Sc.*, 28:6799–6808, 1993.

[25] Lazzeri A Bucknall C B. Application of a dilatational yielding model to rubber-toughened polymers. *Polymer*, 36(15):2895–2902, 1995.

[26] Lazzeri A Bucknall C B, Heather P S. Rubber toughening of plastics. part 12: Deformation mechanisms in toughened nylon 6,6. *J.Mat.Sc.*, 16:2255–2261, 1989.

[27] Zhang X C Bucknall C B, Karpodinis A. A model for particle cavitation in rubber-toughened plastics. *J.Mat.Sc*, 29:3377–3383, 1994.

[28] Ten Bolscher G H Dijkstra K. Nylon-6/rubber blends: Part iii: Stress in and around rubber particles and cavities in a nylon matrix. *J.Mat.Sc.*, 29:4286–4293, 1994.

[29] Van der Wal A Dijkstra K, Gaymans R J. Nylon 6 - rubber blends: Part iv cavitation and yield in nylon-rubber blends. *J.Mat Sc.*, 29:3489–3496, 1994.

[30] Parks D.M. Large plastic deformation of semi-crystalline polymers. *Mechanics of Plastics and Plastic Composites*, 68, 1995.

[31] Groeninckx G Dompas D. Toughening behaviour of rubber-modified thermoplastic polymers involving very small rubber particles: 2. rubber cavitation behaviour in poly(vinyl chloride)/methyl methacrylate-butadiene-styrene graft copolymer blends. *Polymer*, 35(22):4750.

[32] Groeninckx G Dompas D. Toughening behaviour of rubber-modified thermoplastic polymers involving very small rubber particles: 1. a criterion for internal rubber cavitation. *Polymer*, 35(22):4743, 1994.

[33] Groeninckx G Dompas D. Toughening behaviour of rubber-modified thermoplastic polymers involving very small rubber particles: 3. impact mechanical behaviour of poly(vinyl chloride)/methyl methacrylate-butadiene-styrene graft copolymer blends. *Polymer*, 35(22):4760, 1994.

[34] Yerzley F.L. Adhesion of neoprene to metal. *Ind. Engng Chem.*, 31:950–956, 1939.

[35] Schirrer R. Fond C. A mechanical model for the onset of damage in rubber modified amorphous polymers. *Journal de Physique IV Colloq.*, 6(6):375–384.

[36] Schirrer R. Fond C., Lobbrecht A. Polymers toughened with rubber microspheres: an analytical solution for stresses and strains in the rubber particles at equilibrium and rupture. *International Journal of Fracture*, 77:141–59, 1996.

[37] Schirrer R Fond C, Lobbrecht A. Volume change and light scattering during mechanical damage in polymethylmethacrylate toughened with core-shell rubber particles. *J.Mat.Sc.*, 31:6409–6422, 1996.

[38] Heim P. Gaillard P., Wrotecki C. Rubber toughening of poly(methyl methacrylate). part ii: Effect of a twin population of particle size. *Polymer Engineering and Science*, 31(4):218–222, February 1991.

[39] Lindley P B Gent A N. Internal rupture of bonded rubber cylinders in tension. *Proc. Roy. Soc. A*, 249:195, 1958.

[40] Jonas J.J. G'Sell C. Yield and transient effects during the plastic deformation of solid polymers. *Journal of Materils Science*, 16:1956–1974, 1981.

[41] Kinloch A J Guild F J. Modeling the properties of rubber-toughened epoxy polymers. 1995.

[42] Lovell P. A. Guild F.J., Young R.J. The influence of material properties on the predicted behaviour of rubber-toughened polymers. *Journal of Materials Science Letters*, 13:10–14, 1994.

[43] Sue H-J. Craze-like damage in a core-shell rubber-modified epoxy system. *J.Mat.Sc.*, 27:3098–3107, 1992.

[44] Sue H-J Huang J, Parker D S and Yee A F. Toughening mechanisms in core-shell rubber modified polycarbonate *Polymer*, 31:2267–, 1990.

[45] Kinloch A.J. Huang Y. Modeling of the toughening mechanisms in rubber-modified epoxy polymers. part i: Finite element analysis studies. *J. Mater. Sci.*, 27:2753, 1992.

[46] Kinloch A.J. Huang Y. The role of plastic void growth in the fracture of rubber-toughened epoxy polymers. *Journal of Materials Science Letters*, 11:484–487, 1992.

[47] Ball J.M. Dicontinuous equilibrium solutions and cavitation in nonlinear elasticity. *Phil. Trans. R. Soc. Lond., A*, 306:557–611, 1982.

[48] Rice J. R. Johnson M. A. *The Role of Large Crack Tip Geometry Changes in Plane Strain Fracture*, page 641. McGraw-Hill Book Company. Editors: M. F. Kanninen, W. F. Adler, A. R. Rosenfield and R. I. Jafee.

[49] Muratoglu O K. *Toughening and Frature Mechanisms of Rubber Modified Polyamides.* Ph. d. thesis, MIT, 1995.

[50] D W Van Krevelen. *Properties of Polymers*, page 271. 1976. Editor: D W Van Krevelen. Publisher: Elsevier Scientific, Amsterdam.

[51] Lin L. *An Experimental Study of Deformation Mechanisms and Resistances of Semi-Crystalline Polymers.* Ph.d. thesis, MIT, 1991.

[52] Yee A.F. Li D., Li X. The role of the cavitation in rubber particles in the deformation of rubber toughened epoxy under contrained conditions.

[53] R Lhila M Morton, MCizmecioglu. Model studies of rubber addititves in high-impact plastics. *Advances in Chemisty Series*, pages 221–230, 1984.

[54] Goodier J N. Concentration of stress around spherical and cylindrical inclusions and flaws. 1933.

[55] Vicky Nguyen. Effect of thermal expansion misfit and crystallization volume change ... Technical report, MIT, 1988.

[56] Paul D R Oshinski A J, Keskkula H. Rubber toughening of polyamides with functionalized block copolymers: 1. nylon-6. *Polymer*, 33(2):268–, 1992.

[57] Paul D R Oshinski A J, Keskkula H. Rubber toughening of polyamides with functionalized block copolymers: 2. nylon-6,6. *Polymer*, 33(2):284–, 1992.

[58] Tzika P. Master's thesis, MIT, 1998. in progress.

[59] Yee A F Pearson R A. Toughening mechanisms in elastomer-modified epoxies. *J.Mat.Sc*, 21:2462–2474, 1986.

[60] A Wiley-Interscience publication. *Polymer Handbook.* Wiley etc., New York, 1989.

[61] Sorensen E. P. Rice J. R. Continuing crack-tip deformation and fracture for plane-strain crack growth in elastic-plastic solids. *J. Mech. Phys. Solids*, 26:163–186, 1978.

[62] Wu S. A generalized criterion for rubber toughening: The critical matrix ligament thickness. *Journal of Applied Polymer Science*, 35:549–561.

[63] Wu S. Phase structure and adhesion in polymer blends: A criterion for rubber toughening. *Polymer*, 26:1855–, 1985.

[64] Socrate Simona. *Mechanics of Microvoid Nucleation and Growth in High-Strength Austenitic Steels.* PhD dissertation, MIT, 1995.

[65] Wu Souheng. Control of intrinsic brittleness and toughness of polymers and blends by chemical structure: a review. *Polymer International*, 29:229–247, 1992.

[66] Takashi Inoue Takayuki Fukui, Yutaka Kikuchi. Elastic-plastic analysis of the toughening mechanim in rubber-modified nylon: matrix yielding and cavitation. *Polymer*, 32(13):2367–, 1991.

[67] Yutaka Kikuchi Takayuki Fukui. Elastic-plastic analysis of the toughening mechanism in rubber-modified nylon. matrix yielding and cavitation. *Polymer*, 32:no.13, 1991.

[68] Tvergaard V. On localization in ductile materials containing spherical voids. *Int. J. Fract.*, 18:237–, 1982.

[69] R E Cohen Z Bartczak, A S Argon and M Weinberg. Toughness mechanism in semi-crystalline polymer blends i, ii and iii. *Polymer*, 1998. to appear.